

TECHNISCHE UNIVERSITÄT MÜNCHEN

Lehrstuhl für Numerische Mechanik

Mortar Methods for Computational Contact Mechanics Including Wear and General Volume Coupled Problems

Philipp Wagih Farah

Vollständiger Abdruck der von der Fakultät für Maschinenwesen der Technischen Universität München zur Erlangung des akademischen Grades eines

Doktor-Ingenieurs (Dr.-Ing.)

genehmigten Dissertation.

Vorsitzender: Prof. Dr.-Ing. Karsten Stahl

Prüfer der Dissertation:

1. Prof. Dr.-Ing. Wolfgang A. Wall
2. Prof. Dr.-Ing. habil. Manfred Bischoff

Die Dissertation wurde am 29.06.2017 bei der Technischen Universität München eingereicht und durch die Fakultät für Maschinenwesen am 20.03.2018 angenommen.

Abstract

While computations of classical single-field problems defined on one considered body are well-investigated, since they have been in the focus of research from the beginning of the finite element method, numerical treatments of interface and volume coupled problems with multiple bodies being involved are still topic of current research. They can be found in nearly all challenging engineering applications, such as crash tests, metal forming, joints for aircraft engines, brakes and implantation of artificial joint prostheses. Simulations of all these problems require adequate coupling strategies for their spatial discretizations to guarantee highest possible accuracy and robustness. For this purpose, mortar methods are chosen as the basis for all developments made in this thesis due to their superior performance, their sound mathematical foundation and their numerical stability.

In this thesis, the applicability of mortar finite element methods to contact problems leading to 0D, 1D and 2D contact zones and general 3D volume coupled problems is explored. In addition, the incorporation of interface effects such as wear with and without thermo-mechanical interactions is investigated. For all these points of interest, dual mortar methods based on biorthogonality conditions are employed, which naturally lead to very efficient solution procedures.

In particular, a novel strategy for computational contact mechanics of vertices, edges and surfaces being simultaneously involved in a finite deformation regime is presented. The well-known contact conditions are separately enforced for the occurring point contact, line contact and surface contact by employing three different sets of Lagrange multipliers. The line contact resulting therein is for the first time realized with the mortar finite element method and a novel technique for its numerical evaluation is presented. The discrete unknowns due to the Lagrange multiplier approach are eliminated from the global system of equations by employing the aforementioned dual (biorthogonal) shape functions for the line and surface Lagrange multipliers. In order to guarantee a consistent formulation and fulfill the fundamental requirement of partition of unity, a shape function modification is introduced for the line and surface Lagrange multipliers. For the combined algorithm, no transition parameters are required and the decision between point contact, line contact and surface contact is implicitly made by the variationally consistent framework. The algorithm is supported by a penalty regularization for the scenario of non-parallel edge-to-edge contact. The robustness and applicability of the proposed algorithms are demonstrated with several challenging benchmark examples.

Next, a finite element framework based on dual mortar methods is presented for simulating fretting wear effects in the finite deformation regime. Fretting wear effects are modeled in an incremental scheme with the help of Archard's law and the worn material is considered as additional contribution to the gap function. Numerical examples demonstrate the robustness and accuracy of the presented algorithm. In order to extend the applicability of the fretting wear algorithm, finite deformation contact problems with frictional effects and finite shape changes due to wear are investigated. To capture the finite shape changes, a third configuration besides the well-known reference and spatial configurations is introduced, which represents the time-dependent, worn state. Consistent interconnections between these configurations are realized by an Arbitrary-Lagrangian-Eulerian formulation. The newly developed partitioned and fully implicit algorithm is based on a Lagrangian step and a shape evolution step. Within the Lagrangian step, contact constraints as well as the wear equations are weakly enforced following the well-established mortar framework. Additional unknowns due to the employed Lagrange multiplier

method for contact constraint enforcement and due to wear are again eliminated by condensation procedures based on the aforementioned concept of biorthogonality of the employed shape functions. Several numerical examples in both 2D and 3D are provided to demonstrate the performance and accuracy of the proposed numerical algorithm. The developed finite wear algorithm is then for the first time included in a thermo-structure interaction framework and validated with a numerical reference example in 2D. Its applicability to 3D finite wear problems is also demonstrated.

Finally, the presented work demonstrates that dual mortar methods are also extendable beyond classical domain decomposition and contact applications towards general volume couplings. More precisely, a generic 3D coupling operator based on biorthogonal shape functions is developed, which allows for highly accurate nodal information transfer while requiring low computational effort. This operator is utilized to develop a novel and generally applicable methodology for the volumetric coupling of different meshes within a monolithic solution scheme for multi-field simulations, which allows for great flexibility with respect to spatial discretizations. In addition, this scheme is extended towards contact phenomena, which naturally arise for example in thermo-structure interaction problems. At the end, the coupling operator is incorporated in a novel grid motion approach for fluid-structure interaction problems to demonstrate that the implemented functionality is extremely flexible with respect to further applications. For all investigations, the performance of the mortar operator is carefully compared to standard collocation operators.

Altogether, this thesis presents novel and consistent extensions of mortar methods towards applications in 0D to 3D.

Zusammenfassung

Während Berechnungen von klassischen Einfeldproblemen mit einem betrachteten Körper gut erforscht sind, sind gekoppelte Interface- und Volumenprobleme mit mehreren Körpern immer noch Gegenstand aktueller Untersuchungen. Diese treten bei annähernd allen anspruchsvollen Ingenieursanwendungen, wie zum Beispiel Crashtests, Umformprozessen von metallischen Werkstoffen, mechanischen Verbindungen in Turbinen, Bremsen und Knieimplantaten, auf. Die Simulation von all diesen Problemen erfordert passende Kopplungsstrategien für ihre räumlichen Diskretisierungen, um größtmögliche Genauigkeit und Robustheit zu garantieren. Aus diesem Grund werden Mortar-Methoden als Basis für alle Entwicklungen in dieser Arbeit gewählt, da sie sich durch hervorragende Leistung, einer fundierten mathematischen Basis und numerische Stabilität auszeichnen.

In dieser Arbeit wird die Anwendung der Mortar-Finite-Elemente-Methode auf Kontaktprobleme mit 0D-, 1D- und 2D-Kontaktzonen und allgemeine 3D-Volumenprobleme erforscht. Zudem wird das Zusammenspiel mit Interface-Effekten, wie Abrieb mit und ohne thermischen Einfluss, untersucht. Für alle erwähnten Bereiche werden duale Mortar-Methoden verwendet, welche auf Biorthogonalitätsbedingungen basieren und natürlicher Weise zu sehr effizienten Lösungsverfahren führen.

Konkret wird eine neuartige Strategie zur Berechnung von simultan auftretenden Ecken-, Kanten- und Flächenkontakt unter Berücksichtigung großer Deformationen präsentiert. Dabei werden die Kontaktbedingungen separat für den auftretenden Punkt-, Linien- und Flächenkontakt mit Hilfe von drei verschiedenen Sets von Lagrange-Multiplikatoren definiert. Der Linienkontakt wird zum ersten Mal mit der Mortar-Methode umgesetzt und eine neuartige numerische Integrationstechnik wird präsentiert. Die diskreten Unbekannten, welche durch die Lagrange-Multiplikator-Ansätze begründet sind, werden von dem globalen Gleichungssystem unter Verwendung von dualen (biorthogonalen) Ansatzfunktionen für den Linien- und Flächenkontakt eliminiert. Der kombinierte Algorithmus benötigt keinerlei Parameter für den Übergang von Punkt-, Linien- und Flächenkontakt, da diese Entscheidung implizit von der variationell-konsistenten Formulierung getroffen wird. Der entwickelte Algorithmus wird durch eine Regularisierung mittels der Strafterm-Methode unterstützt, um den Fall des nicht-parallelen Kante-zu-Kante-Kontakt zu realisieren. Die Robustheit und Anwendbarkeit der vorgestellten Methode werden mit einigen herausfordernden Beispielen demonstriert.

Des Weiteren wird ein Finite-Elemente-Ansatz basierend auf dualen Mortar-Methoden präsentiert, welcher die Simulation von Reibverschleiß für große Deformationen ermöglicht. Der Reibverschleiß wird hierbei inkrementell mit Hilfe von Archard's Abriebgesetz modelliert und im Rahmen der Kontaktformulierung als zusätzlichen Beitrag zur Abstandsfunktion gewertet. Die bereitgestellten numerischen Beispiele demonstrieren auch hier die Robustheit und Genauigkeit des entwickelten Algorithmus. Um das Anwendungsspektrum zu erweitern, wird dieser Ansatz anschließend um reibungsbehaftete Abriebsphänomene erweitert, welche zu großen Gestaltänderungen führen. Um diese Gestaltänderungen abzubilden, wird neben der bekannten Referenzkonfiguration und der räumlichen Konfiguration eine weitere Konfiguration eingeführt, welche den zeitabhängigen, abgeriebenen Zustand beschreibt. Eine konsistente Verbindung dieser Konfigurationen wird durch eine "Arbitrary-Lagrangian-Eulerian"-Formulierung erreicht. Der neu entwickelte, partitionierte und zugleich voll implizite Algorithmus basiert auf einem Lagrange-Schritt und einem Euler-Schritt. Im Lagrange-Schritt werden die Kontaktbedingungen und die

Abriebgleichung im schwachen Sinne mit Hilfe der Mortar-Methode berechnet. Hierbei werden zusätzliche Unbekannte durch den Lagrange-Multiplikator-Ansatz und durch die zusätzlichen Abriebsgrößen mittels der bereits erwähnten Biorthogonalitätseigenschaft der Ansatzfunktion eliminiert. Mehrere 2D-und 3D-Beispiele werden präsentiert, um den entwickelten Ansatz zu validieren. Danach wird der Algorithmus für große Gestaltänderungen durch Abrieb zum ersten Mal überhaupt um thermische Effekte erweitert. Die entwickelte Methodik wird mit einem 2D-Validierungsbeispiel mit Referenzlösung und einem 3D-Beispiel getestet.

Abschließend wird in der vorliegenden Arbeit die Erweiterung von dualen Mortar-Methoden – über klassische Gebietszerlegungs- und Kontaktanwendungen hinaus – auf allgemeine Volumenkopplungen demonstriert. Zu diesem Zweck wird ein generischer 3D-Kopplungsoperator, basierend auf biorthogonalen Ansatzfunktionen, entwickelt, welcher knotenbasierten Informationsaustausch mit höchster Genauigkeit bei zugleich niedrigem Berechnungsaufwand erlaubt. Dieser Operator wird anschließend verwendet, um einen allgemeinen Lösungsansatz für monolithische, volumengekoppelte Mehrfeldprobleme auf nicht passenden Netzen zu entwickeln. Dieser ermöglicht eine bis zum jetzigen Zeitpunkt nicht bekannte Flexibilität hinsichtlich räumlicher Vernetzungsanforderungen. Des Weiteren wird dieser Ansatz um Kontaktphänomene erweitert, welche beispielsweise bei Thermo-Struktur-Interaktionsproblemen auftreten. Am Ende wird der Kopplungsoperator in einem neuartigen Netzbewegungsansatz für Fluid-Struktur-Interaktionsprobleme eingebettet, welches die flexible Implementierung hinsichtlich folgender Anwendungen beweist.

Zusammenfassend werden in der vorliegenden Arbeit neuartige und konsistente Erweiterungen der Mortar-Methoden hinsichtlich Anwendungen in 0D bis 3D präsentiert.

Danksagung

Die vorliegende Dissertation entstand in der Zeit von 2013 bis 2017 während meiner Tätigkeit als wissenschaftlicher Mitarbeiter am Lehrstuhl für Numerische Mechanik (LNM) der Technischen Universität München (TUM). In diesen Jahren wurde ich von vielen Personen, ohne die diese Arbeit nicht entstanden wäre, fachlich und moralisch unterstützt. An dieser Stelle möchte ich all jenen Wegbegleitern herzlich danken.

Zuallererst danke ich meinem Doktorvater, Prof. Dr.-Ing. Wolfgang A. Wall, für das mir entgegengebrachte Vertrauen, am LNM promovieren zu dürfen. Die von ihm gewährte wissenschaftliche Freiheit habe ich im Laufe meiner Promotion sehr zu schätzen gelernt und seine fachlichen Impulse haben entscheidend zu dem Erfolg dieser Arbeit beigetragen. Weiterhin möchte ich Prof. Dr.-Ing. habil. Manfred Bischoff vom Institut für Baustatik und Baudynamik der Universität Stuttgart für die Übernahme des Mitberichts danken. Für die Übernahme des Vorsitzes meiner Prüfungskommission danke ich Prof. Dr.-Ing. Karsten Stahl vom Lehrstuhl für Maschinenelemente. Ein besonderer Dank gilt auch Prof. Dr.-Ing. Alexander Popp, welcher bereits als Betreuer meiner Masterarbeit und anschließend als Post-Doc während meiner Promotion entscheidend zum Gelingen dieser Arbeit beigetragen hat. Zudem bedanke ich mich bei Renata Nagl, die mir stets bei allen organisatorischen Aufgaben mit Rat und Tat zur Seite gestanden hat.

Diese Arbeit wäre auch undenkbar ohne die Unterstützung einiger meiner damaligen Kollegen, die ich mittlerweile zu meinen guten Freunden zähle. Deshalb gilt mein großer Dank Andreas Rauch (alias Chuck), Michael Hiermeier, Dr.-Ing. Anh-Tu Vuong, Rui Fang und Andy Wirtz. Besonders die vielen Diskussionen bei den gemeinsamen Mittagessen mit Chuck, Michael und Anh-Tu haben mir über die Jahre sehr geholfen. Zudem bedanke ich mich bei Karl Wichmann und Georg Hammerl für die vielen guten Ratschläge und Tipps hinsichtlich der Softwareimplementierung.

Ich danke auch Christoph Schwarz und Christine Moos für die großartige Freundschaft seit meinem Studienbeginn 2008, welche mir einige schwere Phasen bedeutend erleichtert hat. Des Weiteren danke ich auch meinen langjährigen Freunden aus meiner Heimatstadt Chemnitz für die schönen Urlaube und verlängerten Wochenenden, an denen ich herrlich abschalten und neue Kraft tanken konnte. Es gibt auch noch viele andere Kollegen, Studenten und Freunde, die dazu beigetragen haben, dass diese Promotion erfolgreich verlaufen ist. Jedoch sind es zu viele, um sie alle hier namentlich zu erwähnen. Deshalb danke ich allen Studenten, die ich betreuen durfte, allen meinen Korrekturlesern und allen weiteren Personen, die mir fachlich wie auch privat meine Promotion erleichtert haben.

Ein weiterer großer Dank geht an meine Freundin Jasmin Pospiech, die mich vor allem im letzten Drittel meiner Promotion in vielen Gesprächen aufgebaut und mir Kraft gegeben hat. Mein größter Dank gilt jedoch meinen Eltern, Astrid Farah und Dr. rer. nat. Muhsen Farah, die mich zu jeder Zeit von ganzem Herzen unterstützt haben und ohne deren bedingungslosen Rückhalt weder mein Studium noch meine Promotion erfolgreich verlaufen wären.

Philipp Farah

Contents

1. Introduction	1
1.1. Motivation	1
1.2. Fundamental approaches to mortar methods	2
1.3. Research objective	4
1.3.1. General specification of requirements	4
1.3.2. Proposal for novel mortar approaches	6
1.4. Outline	7
2. Governing Equations and Finite Element Formulation	9
2.1. Continuum mechanics	9
2.1.1. Nonlinear kinematics, strain and stress	9
2.1.2. Constitutive laws	12
2.1.3. Balance equations	13
2.1.4. Initial boundary value problem	15
2.2. Finite element formulation and solution scheme for nonlinear solid mechanics .	16
2.2.1. Weak formulation	16
2.2.2. Discretization in space	17
2.2.3. Discretization in time	18
2.2.4. Solution techniques	20
3. Fundamentals on Mortar Methods for Computational Contact Mechanics	23
3.1. Contact kinematics	23
3.2. Contact constraints	26
3.2.1. Tied contact constraints	26
3.2.2. Normal contact constraints	26
3.2.3. Frictional contact constraints	27
3.3. Weak formulation for contact	27
3.4. Mortar finite element discretization	29
3.4.1. Discrete Lagrange multiplier spaces	32
3.4.2. Numerical evaluation	34
3.5. Time integration and global solution scheme	36
3.5.1. Time integration for computational contact mechanics	36
3.5.2. Global solution scheme	37
3.5.3. Algebraic form	39
4. Mortar Methods for Contact of Vertices, Edges and Surfaces	41
4.1. Fundamental approaches and research objective	42
4.1.1. Fundamental approaches	42

4.1.2. Specification of requirements	43
4.1.3. Proposal for contact of vertices, edges and surfaces	45
4.2. Problem statement	46
4.3. Weak formulation	50
4.4. Finite element displacement discretization and nodal normal computation	53
4.4.1. Node-to-surface projection	54
4.4.2. Node-to-line projection	55
4.4.3. Node-to-node projection	56
4.4.4. Closest-point projections with multiple solutions	56
4.4.5. Line-to-line projection	57
4.5. Point contact	58
4.5.1. Vertex contact	58
4.5.2. Contact of non-parallel edges	59
4.6. Line contact	61
4.6.1. Spatial discretization of line contact	61
4.6.2. Numerical evaluation of line contact	63
4.7. Surface contact	67
4.8. All entity contact – combined formulation	69
4.8.1. Semi-smooth Newton method	70
4.8.2. Algebraic representation	71
4.8.3. Conservation laws	72
4.8.4. Post-processing	75
4.8.5. Restrictions and special cases	76
4.8.6. Numerical efficiency	77
4.9. Numerical examples	78
4.9.1. Consistency – patch tests	79
4.9.2. Non-parallel edge-to-edge contact	85
4.9.3. Transition between contact scenarios – bending plate	87
4.9.4. Conservation properties – falling coin	91
4.9.5. Frictional contact – plate on plate	95
5. Mortar Methods for Wear Modeling	99
5.1. Fundamental approaches to computational wear modeling and research objective	100
5.1.1. Fundamental approaches	100
5.1.2. Specification of requirements	101
5.1.3. Proposal for mortar based wear approaches	103
5.2. Fundamentals on wear phenomena	103
5.2.1. Frictional wear phenomena	103
5.2.2. Archard's wear law	105
5.2.3. Continuum mechanics for finite wear	107
5.3. Finite element approaches for wear discretization	108
5.3.1. Internal state variable approach	109
5.3.2. Primary variable approach	110
5.4. Formulation for fretting wear	112
5.4.1. Problem setting for fretting wear	112

5.4.2. Fretting wear algorithm	113
5.4.3. Numerical examples	115
5.5. Formulation for finite wear – ALE formulation	122
5.5.1. Problem setting for finite wear modeling	122
5.5.2. Implicit partitioned algorithm for finite wear	123
5.5.3. Lagrangian step	125
5.5.4. Shape evolution step	128
5.5.5. Numerical examples	130
5.6. Thermo-structure-contact-wear interaction with finite shape changes	143
5.6.1. Problem setting	143
5.6.2. Solution method	145
5.6.3. Numerical examples	146
6. Mortar Methods for Volume Coupled Problems	153
6.1. Fundamental approaches and research objective	154
6.1.1. Fundamental approaches and applications	154
6.1.2. Specification of requirements	156
6.1.3. Proposal for a mortar approach for general volume coupled problems .	157
6.2. Fundamentals on volume projection of nodal information	157
6.2.1. Derivation of the mortar method	159
6.2.2. Degeneration to collocation method	160
6.2.3. Dual shape functions	161
6.2.4. Integration schemes	165
6.2.5. Boundary problems	167
6.2.6. Conservation properties of the projections	169
6.2.7. Numerical examples	170
6.3. Volumetric coupling approaches for multiphysics on non-matching meshes . .	176
6.3.1. General methodology	176
6.3.2. Boundary conditions	178
6.3.3. Contact mechanics for multiphysics on non-matching meshes	179
6.3.4. Numerical examples	180
6.4. Further applications	192
6.4.1. A novel grid motion approach for fluid-structure interaction	192
6.4.2. Algorithmic flexibility – the Hu-Washizu principle	201
7. Summary and Outlook	203
7.1. Mortar methods for computational contact of vertices, edges and surfaces . .	203
7.2. Mortar methods for wear modeling	205
7.3. Mortar methods for volume coupled problems	207
A. Comparison of Segment-Based and Element-Based Integration	209
A.1. Theoretical comparison	209
A.1.1. Choice of integration rule	209
A.1.2. Geometry approximation and discrete projection	211
A.1.3. Boundary problems	213

A.1.4.	Second-order interpolation	215
A.1.5.	Frictional contact	216
A.1.6.	Conservation of linear and angular momentum	217
A.2.	Numerical examples	218
A.2.1.	Consistency – patch test	218
A.2.2.	Accuracy – bending beam	220
A.2.3.	Efficiency – two tori impact	222
A.2.4.	Frictional sliding – ironing	225
A.3.	Concluding remarks	227
B.	Details on Consistent Linearization for Line Contact	229
B.1.	General linearizations	230
B.2.	Linearization of integration segment Jacobian determinant	231
B.3.	Linearization of integration segment vertices	232
B.4.	Linearization of normal and tangent vectors	233
B.4.1.	Auxiliary plane normal:	233
B.4.2.	Nodal normal for node-to-surface CPP:	233
B.4.3.	Nodal normal for node-to-line CPP:	234
B.5.	Linearization of integration points	235
B.6.	Linearization of gap function	236
Bibliography		237

Nomenclature

Representation of scalars, tensors and other quantities

q, Q	Scalar quantity
\mathbf{q}	Vector
Q	Second-order tensor
\mathbf{q}	Discrete vector
\mathbf{Q}	Discrete matrix
\mathcal{Q}	Scalar-valued function space
\mathbf{Q}	Vector-valued function space

Operators and symbols

$(\cdot)^T$	Transpose of a tensor
$(\cdot)^{-1}$	Inverse of a tensor
$(\cdot)^{-T}$	Transpose of the inverse of a tensor
$(\dot{\cdot})$	First time derivative at a fixed reference position
$(\ddot{\cdot})$	Second time derivative at a fixed reference position
$(\hat{\cdot})$	Prescribed quantity
$\langle \cdot, \cdot \rangle_\Omega$	Duality (energy) pairing on Ω
\det	Determinant
tr	Trace operator
\log	Logarithm
\ln	Natural logarithm
div	Spatial divergence operator
Lin	Linearization operator
grad	Spatial gradient
Grad	Material gradient
\max	Maximum function
\otimes	Dyadic product
$\delta(\cdot)$	Virtual quantity
δ_{jk}	Kronecker delta
\mathcal{L}	Lie derivative
\mathbf{I}	Identity tensor
\mathbf{I}_i	Identity matrix $\in \mathbb{R}^{i \times i}$

Domains and boundaries

Ω_0	Reference configuration
Ω_t	Spatial configuration
Ω_m	Material configuration
$\partial\Omega_0$	Boundary in reference configuration
$\partial\Omega_t$	Boundary in spatial configuration
$\partial\Omega_m$	Boundary in material configuration
$\Gamma_u, \gamma_u, \Gamma_{m,u}$	Dirichlet partition of boundary in reference, spatial and material configuration
$\Gamma_\sigma, \gamma_\sigma, \Gamma_{m,\sigma}$	Neumann partition of boundary in reference, spatial and material configuration
$\Gamma_c, \gamma_c, \Gamma_{m,c}$	Potential contact partition of boundary in reference, spatial and material configuration
Γ_a	Active contact zone in reference configuration
Γ_i	Inactive contact zone in reference configuration
Γ_o, γ_o	Potential contact boundary of surfaces without vertices and edges in reference and spatial configuration
Γ_l, γ_l	Potential contact boundary of edges without vertices in reference and spatial configuration
Γ_*, γ_*	Potential contact boundary of vertices in reference and spatial configuration
Γ_x, γ_x	Set of potential contact points resulting from crossing edges in reference and spatial configuration
$\Gamma_\bullet, \gamma_\bullet$	Set of potential point contact in reference and spatial configuration
$\Gamma_\theta, \gamma_\theta, \Gamma_{m,\theta}$	Partition of boundary with prescribed temperatures in reference, spatial and material configuration
$\Gamma_q, \gamma_q, \Gamma_{m,q}$	Partition of boundary with prescribed heat fluxes in reference, spatial and material configuration
Γ_{FSI}	Fluid-structure interface in reference configuration

Kinematics

e_1, e_2, e_3	Basis vectors of Cartesian coordinate system
X	Position in reference configuration
x	Position in spatial configuration
φ	Mapping between reference and spatial configuration
u	Physical displacements
\dot{u}	Physical velocity
\ddot{u}	Physical acceleration
F	Deformation gradient

J	Jacobian determinant, determinant of \mathbf{F}
j_a	Area transformation factor
V_0, V	Reference and current volume
A_0, A	Reference and current area
\mathbf{N}	Unit normal in reference configuration
\mathbf{n}	Unit normal in spatial configuration
\mathbf{E}	Green-Lagrange strain tensor

Stresses and constitutive laws

\mathbf{t}	Traction vector in current configuration
$\boldsymbol{\sigma}$	Cauchy stress tensor
\mathbf{P}	First Piola-Kirchhoff stress tensor
\mathbf{S}	Second Piola-Kirchhoff stress tensor
\mathbf{C}	Constitutive tensor for linear elasticity
Ψ	General strain energy function
Ψ_{SVK}	Strain energy function for Saint-Venant-Kirchhoff material model
Ψ_{NH1}	Strain energy function for classical Neo-Hookean material model
Ψ_{NH2}	Strain energy function for alternative Neo-Hookean material model
E	Young's modulus
ν	Poisson's ratio
λ, μ	Lamé coefficients

Governing equations

t	Time
T	Total simulation time
m	Mass
ρ_0, ρ	Density in reference and material configuration
$\hat{\mathbf{b}}_0$	Body force in reference configuration
$\hat{\mathbf{t}}_0$	Prescribed pseudo-traction in reference configuration
$\hat{\mathbf{u}}_0$	Initial displacement at $t = 0$
$\hat{\mathbf{u}}_0$	Initial velocity at $t = 0$
\mathcal{W}	Work

FE space discretization and solution scheme

$\delta\mathcal{W}_{\text{kin}}$	Kinetic virtual work contribution
$\delta\mathcal{W}_{\text{int}}$	Internal virtual work contribution
$\delta\mathcal{W}_{\text{ext}}$	External virtual work contribution
\mathcal{U}	Solution space for displacement field
\mathcal{V}	Weighting space for displacement field
n_{dim}	Number of spatial dimensions
n_{dof}	Number of degrees of freedom
n_{nod}	Number of nodes
n_{ele}	Number of elements
N_k	FE shape function of node k
\mathbf{f}_{int}	Internal force vector
\mathbf{f}_{ext}	External force vector
\mathbf{K}_{mass}	Global mass matrix
\mathbf{K}_0	Global initial tangent stiffness matrix
\mathbf{K}_{damp}	Global damping matrix due to Rayleigh damping model
r_m, r_k	Parameter for Rayleigh damping model
n	Time step index
Δt	Time step size
\mathbf{d}_n	Discrete displacements at time t_n
\mathbf{v}_n	Discrete velocities at time t_n
\mathbf{a}_n	Discrete accelerations at time t_n
β, γ	Parameters of Newmark's method
α_m, α_f	Parameters of generalized- α method
ρ_∞	Spectral radius
θ_t	Parameter for One-Step- θ scheme
\mathbf{r}	Discrete residual of balance of linear momentum
\mathbf{K}	Dynamic effective tangential stiffness matrix
$\Delta\mathbf{d}_{n+1}^{i+1}$	Displacement increment within Newton-Raphson scheme
\mathbf{d}_{n+1}^0	Start estimate for nonlinear solution scheme

Contact mechanics

$\mathcal{B}^{(1)}$	Slave body
$\mathcal{B}^{(2)}$	Master body
$\hat{\mathbf{x}}^{(2)}$	Closest master point to slave point $\mathbf{x}^{(1)}$
\mathbf{g}	Gap vector
g_n	Gap function
$\mathbf{v}_{\tau,\text{rel}}$	Relative tangential velocity
$\tilde{\mathfrak{F}}$	Coefficient of friction
p_n	Normal contact pressure

t_τ	Tangential contact traction
t_c	Contact traction
d	Interface dissipation rate density in spatial configuration
\dot{D}	Interface dissipation rate density in material configuration
Υ	Slip function
β	Complementarity parameter for frictional sliding

Mortar methods for contact

λ	Lagrange multiplier
λ_n	Normal part of Lagrange multiplier
λ_τ	Tangential part of Lagrange multiplier
\mathcal{T}	Restriction space for Lagrange multiplier in tangential plane
\mathcal{M}	Solution space for Lagrange multiplier
\mathcal{W}	Trace space of weighting space of displacement field
χ	Contact interface mapping
χ_h	Discrete contact interface mapping
$n^{(1)}$	Number of slave nodes
$n^{(2)}$	Number of master nodes
$m^{(1)}$	Number of slave nodes carrying discrete Lagrange multipliers
Φ_j	Lagrange multiplier shape function of node j
λ_j	Discrete Lagrange multiplier of slave node j
$\tilde{g}_{n,j}$	Discrete weighted gap of slave node j
$(\tilde{\mathbf{v}}_{\tau,\text{rel}})_j$	Discrete weighted relative tangential velocity of slave node j
$(\tilde{\mathbf{u}}_{\tau,\text{rel}})_j$	Discrete weighted relative tangential slip increment of slave node j
\mathbf{D}	Slave side mortar matrix
\mathbf{M}	Master side mortar matrix
\mathbf{C}_e	Coefficient matrix for dual shape functions
$\mathbf{D}_e, \mathbf{M}_e$	Auxiliary coefficient matrices for dual shape functions
$\mathbf{x}_0^{(1)}$	Slave element center
$\mathbf{n}_0^{(1)}$	Unit normal vector at slave element center
$\tilde{\mathbf{x}}$	Projected node on auxiliary plane
$C_{n,j}$	Nonlinear complementarity function in normal direction for slave node j
$C_{\tau,j}$	Nonlinear complementarity function in tangential direction for slave node j
c_n	Complementarity parameter for contact in normal direction
c_t	Complementarity parameter for contact in tangential direction
\mathbf{P}	Mortar projection operator
\mathcal{S}	Set of all slave nodes
\mathcal{M}	Set of all master nodes
\mathcal{N}	Set of all interior nodes
\mathcal{A}	Set of all active slave nodes
\mathcal{I}	Set of all inactive slave nodes

$\mathcal{S}_{\mathcal{L}}$	Set of all active slave nodes in the slip state
$\mathcal{S}_{\mathcal{T}}$	Set of all active slave nodes in the stick state

Mortar methods for contact of vertices, edges and surfaces

$(\cdot)_o$	Quantity related to surface contact
$(\cdot)_l$	Quantity related to line contact
$(\cdot)_*$	Quantity related to point contact of vertices
$(\cdot)_x$	Quantity related to point contact of crossing edges
$(\cdot)_.$	Quantity related to general point contact
f_c	Force vector for point contact
l_c	Line load vector for line contact
λ_o	Surface Lagrange multiplier
λ_l	Line Lagrange multiplier
λ_*	Point Lagrange multiplier
\mathcal{M}_o	Solution space for surface Lagrange multiplier
\mathcal{M}_l	Solution space for line Lagrange multiplier
\mathcal{M}_*	Solution space for point Lagrange multiplier
ϵ_n	Penalty parameter for normal contact of non-parallel edges
ϵ_τ	Penalty parameter for frictional sliding of non-parallel edges
ϖ	Scalar-valued distance
$\mathbf{n}_{j,ei}$	Outward pointing unit normal vector of the adjacent element ei at node j
$\mathbf{n}_{j,aux}^{(1)}$	Auxiliary slave normal vector
\mathbf{p}	Trajectory vector
$\hat{\mathbf{n}}_x^{(1)}$	Closest distance vector between two edges
$\hat{\mathbf{x}}_x^{(i)}$	Closest points between two edges
$\xi_x^{(i)}$	Parameter space coordinate on edge element associated with $\hat{\mathbf{x}}_x^{(i)}$
λ_*	Discrete counterpart of λ_*
Λ_j	Point Lagrange multiplier shape function for node j
$n_*^{(i)}$	Nodes of physical vertices
\mathbf{D}_*	Slave side mortar matrix for Lagrange multiplier point contact
\mathbf{M}_*	Master side mortar matrix for Lagrange multiplier point contact
$g_{*,j}$	Discrete gap function for point contact of vertices for node j
$(\mathbf{v}_{*,\tau,rel})_j$	Discrete relative tangential velocity for point contact of vertices for node j
\mathbf{f}_x	Nodal penalty force vector for contact of non-parallel edges
\mathbf{f}_{pen}	Penalty force vector for contact of non-parallel edges
$\mathbf{f}_{pen,\tau}^{\text{trial}}$	Tangential part of penalty force vector for assumed trial state for contact of non-parallel edges
λ_l	Discrete counterpart of λ_l
Θ_j	Line Lagrange multiplier shape function for node j
$n_{ }^{(i)}$	Nodes of physical edges except for nodes $n_*^{(i)}$

$\mathbf{D}_{\text{l}}, \mathbf{D}_{\text{l}*}$	Slave side mortar matrices for line contact
\mathbf{M}_{l}	Master side mortar matrix for line contact
$g_{\text{l},j}$	Discrete gap function for line contact for node j
$(\mathbf{v}_{\text{l},\tau,\text{rel}})_j$	Discrete relative tangential velocity for line contact for node j
$\boldsymbol{\lambda}_{\text{o}}$	Discrete counterpart of $\boldsymbol{\lambda}_{\text{o}}$
n_{e}	Number of nodes associated with a surface element
\bar{n}_{e}	Number of nodes out of n_{e} that carry point or line Lagrange multipliers
ς	Transformation coefficient for shape function modification
\mathbf{T}_{ς}	Discrete transformation matrix for shape function modification
$n_{\text{o}}^{(i)}$	Nodes of physical surfaces except for nodes $n_{\star}^{(i)}$ and $n_{\text{l}}^{(i)}$
$\mathbf{D}_{\text{o}\text{o}}, \mathbf{D}_{\text{o}\text{l}}, \mathbf{D}_{\text{l}\text{o}}$	Slave side mortar matrices for surface contact
\mathbf{M}_{o}	Master side mortar matrix for surface contact
$g_{\text{o},j}$	Discrete gap function for surface contact for node j
$(\mathbf{v}_{\text{o},\tau,\text{rel}})_j$	Discrete relative tangential velocity for surface contact for node j
\mathbf{f}_{c}	Global contact force vector containing information of all contact types
\mathbf{f}_{λ}	Global contact force vector of scenarios enforces with Lagrange multipliers
\mathbf{A}	Diagonal matrix containing area information

Mortar methods for wear modeling

V_{w}	Worn Volume
w	Wear depth in spatial configuration
W	Wear depth in material configuration
k_{w}	Wear coefficient in spatial configuration
K_{w}	Wear coefficient in material configuration
κ	Energy wear coefficient
$\tilde{\mathbf{X}}$	Position in material configuration
ϕ	Mapping between reference and material configuration
ψ	Mapping between reference and spatial configuration
φ	Mapping between material and spatial configuration. Compared to Chapter 2-4, the mathematical definition of φ is changed. Nevertheless, it describes for all problems the physical motion.
$\Theta_{\text{w},j}$	Wear shape function of node j
g_{n}^{w}	Modified gap function
\tilde{w}_j	Discrete weighted wear depth of slave node j
\mathbf{E}	First wear matrix
\mathbf{T}	Second wear matrix
\mathbf{r}_{w}	Discrete wear residual
Ξ_j	Open non-uniform knot vector associated with the j -th dimension
ξ_i^j	i -th knot value associated with the j -th dimension
$N_{i,j,k}$	NURBS basis function
B_j	B-spline basis function

$h_{i,j,k}$	Control point weight
(i, j, k)	Control point
\mathbf{F}_φ	Physical deformation gradient
\mathbf{P}_φ	First Piola-Kirchhoff stress tensor for physical deformation
\mathbf{S}_φ	Second Piola-Kirchhoff stress tensor for physical deformation
\mathbf{u}_φ	Physical motion
\mathbf{F}_ϕ	Artificial deformation gradient for material mapping
\mathbf{P}_ϕ	First Piola-Kirchhoff stress tensor for material mapping
\mathbf{S}_ϕ	Second Piola-Kirchhoff stress tensor for material mapping
\mathbf{u}_ϕ	Material motion
\mathbf{d}^m	Discrete material displacements
\mathbf{S}	Matrix resulting from linearization of wear residual \mathbf{r}_w with respect to displacements \mathbf{d}
\mathbf{F}	Matrix resulting from linearization of wear residual \mathbf{r}_w with respect to Lagrange multipliers λ

Thermo-structure interaction

$\theta^{(i)}$	Temperature field on body $\mathcal{B}^{(i)}$
θ_0	Reference temperature
θ_d	Damage temperature
θ_c	Temperature at contact interface
$\Delta\theta$	Relative temperature
m_0	Stress-temperature modulus
α_θ	Thermal expansion coefficient
C_V	Specific heat capacity
\mathfrak{F}_0	Friction coefficient at reference temperature
r	Heat source per unit mass
\mathcal{H}	Heating due to Joule effect
k_θ	Thermal conductivity
\mathbf{Q}	Heat flux in material configuration
q_c	Heat flux in normal direction in spatial configuration
β_c	Thermal parameter for influence of frictional dissipation for contact
δ_c	Thermal parameter for influence of temperature difference for contact
α_c	Heat transfer parameter
$\bar{\alpha}_c$	Original heat transfer parameter
E_θ	Thermal energy
θ_j^m	Discrete temperature at relocated node j

Mortar methods for volume coupled problems

Ω_i	Mesh i
\mathbf{P}_{ji}	Nodal projection operator from mesh Ω_i to mesh Ω_j
\mathbf{P}_{ji}^m	Nodal projection operator based on mortar approach
\mathbf{P}_{ji}^c	Nodal projection operator based on collocation approach
\mathbf{D}_i	First mortar matrix for mesh Ω_i
$\tilde{\mathbf{D}}_i$	Transformed first mortar matrix for mesh Ω_i
\mathbf{M}_{ij}	Second mortar matrix for transfer from mesh Ω_j to mesh Ω_i
s_i	Exemplary primary field
d_i	Exemplary dual field
\mathbf{s}_i	Exemplary discrete primary field
\mathbf{d}_i	Exemplary discrete dual field
\mathbf{N}_i	Shape function matrix for primary field s_i
Φ_i	Shape function matrix for dual field d_i
\mathcal{S}	Exemplary solution space
\mathbf{T}_e	Element transformation matrix
\mathbf{T}_i	Global transformation matrix for mesh Ω_i
α_T	Parameter for shape function transformation
\tilde{N}	Modified shape function due to basis transformation
\mathbf{r}_1^α	Discrete residual of partial differential equation α on mesh Ω_1
\mathbf{p}, \mathbf{q}	Discrete unknowns for coupled volume problem
λ, Λ	Discrete unknowns for coupled interface problem
$\hat{\mathbf{P}}_{ij}$	Interface projection operator from mesh Ω_i to mesh Ω_j

Porous medium – pseudo 2D

d^S	Structural displacements
κ	Bulk modulus
p^F	Fluid pressure
v^F	Fluid velocity
ρ_0^F	Fluid density
μ^F	Dynamic viscosity of the fluid
k	Permeability in spatial configuration
K_0	Permeability in material configuration

Fluid-structure interaction

$(\cdot)_\Gamma$	Quantity at fluid-structure interface
p^F	Fluid pressure

\mathbf{v}^F	Fluid velocity
\mathbf{c}^F	ALE convective velocity
\mathbf{v}^G	Fluid grid velocity
\mathbf{u}^G	Fluid grid displacements
ρ_0^F	Fluid density
$\boldsymbol{\epsilon}$	Strain rate tensor of Newtonian fluid
μ^F	Dynamic viscosity of the fluid
\mathbf{b}^F	Fluid body force
\mathbf{t}_Γ^F	Fluid surface traction
\mathbf{u}^S	Structural displacements
ρ_0^S	Structural density
\mathbf{t}_Γ^S	Structure surface traction
\mathbf{d}^S	Discrete structural displacements
\mathbf{d}^G	Discrete fluid grid displacements
\mathbf{v}^F	Discrete fluid velocities
\mathbf{d}^O	Discrete overlay grid displacements
$\tilde{\mathbf{d}}^O$	Discrete overlay grid displacements without correction at interface
\mathbf{P}_S	Operator for projection of structural interface displacements on overlay grid
\mathbf{P}_G	Operator for projection of complete overlay grid displacements on fluid grid
\mathbf{P}_c	Operator for correction step
\mathbf{P}_Γ	Interface coupling operator for non-matching fluid and structure mesh
$\Delta \mathbf{d}_{\Gamma,c}^G$	Interface correction displacements for fluid grid
$\alpha_{FSI,ij}$	Correction factor for displacements for interface node i and bulk node j
l_{ij}	Distance between interface node i and bulk node j
L	Maximum distance for correction step

Hu-Washizu principle

\mathbf{e}	Discrete strains
\mathbf{s}	Discrete stresses
$(\cdot)_u$	Quantity related to displacements
$(\cdot)_e$	Quantity related to strains
$(\cdot)_s$	Quantity related to stresses

Abbreviations

ALE	Arbitrary-Lagrangian-Eulerian
BVP	Boundary value problem
CPU	Central processing unit
CPP	Closest point projection

DD	Domain decomposition
EAS	Enhanced assumed strains
FE	Finite element
FEM	Finite element method
FSI	Fluid-structure interaction
FV	Finite volume
IBVP	Initial boundary value problem
IGA	Isogeometric analysis
NCP	Nonlinear complementarity
NTN	Node-to-node
NTS	Node-to-segment
NURBS	Non-uniform rational B-spline
PDASS	Primal-dual active set strategy
STS	Segment-to-segment
TSI	Thermo-structure interaction

1. Introduction

The presented thesis is concerned with dual mortar methods for non-smooth contact problems including wear and general volume coupled problems. This chapter motivates the use of mortar methods for the mentioned topics and highlights their importance. Then, a state-of-the-art review for the most fundamental mortar approaches is provided and from these, the objectives of this thesis are introduced. Finally, an outline of the following chapters is given.

1.1. Motivation

The finite element method as numerical tool for simulation of various problems arising in engineering applications has been under investigations since the 1960s. Nowadays, it is the dominating spatial discretization technique for the solution of partial differential equations in various single-field problems, such as structural mechanics and thermodynamics and it is not possible to imagine engineering practice without it. Despite its wide spread acceptance and over five decades of intensive research, there are still many unanswered questions and challenging tasks, which can often be identified as complex multi-field interface and volume coupled problems. This thesis will focus on such unresolved problems in the field of computational contact mechanics. Beside many other scenarios, the highly complex application of material drilling, where point, line and surface contact simultaneously occur at the drilling head with strong heating due to frictional dissipation could be considered. In addition, interface damage due to wear for pure surface contact in roller bearings and in automobile brakes represent well-known engineering problems. If at all, these scenarios can only hardly be analyzed with experimental procedures and, even when possible, they cause considerable costs. Furthermore, analytical solutions for the mentioned problems are nearly impossible to find due to their inherent nonlinear characteristic. Therefore, simulation of these effects is highly desirable and motivates the following investigations. In order to address numerical modeling of such phenomena with the finite element method, accurate and robust spatial discretization approaches for the interface and volume couplings are required. Classical and frequently employed discretizations for coupling effects are based on a strong (point-wise) enforcement of constraints or information transfer, which is mainly due to their easy implementation. However, they generally lack in robustness and negatively influence the solution quality, especially for strongly nonlinear problems. In contrast, weak constraint enforcement strategies naturally fit in the finite element philosophy and eliminate nearly all drawbacks of point-wise couplings at the prize of increased computational costs due to the required numerical integration. The arguably most well-investigated scheme from this class is the mortar method, but the vast amount of work was restricted to interface problems without sharp edges and vertices, i.e. only 2D, smooth surfaces have been considered. Due to the great results gained from these investigations, it is very promising to take the mortar method into account in the context of 0D to 2D interfaces in order to address point, line and surface contact scenarios. This

would allow for an accurate prediction of acting loads at the contact regions, regardless of the actual contact situation and consequently many aspects of engineering practice would heavily benefit from this information. Furthermore, application of mortar methods to interface damage due to wear as an example for complex interface physics is desirable in order to predict and possibly prevent machine failure. Finally, general volume coupled multi-field problems are usually simulated on matching meshes, meaning that equal discretizations for all involved fields are employed. In order to allow highest possible flexibility in terms of spatial discretization, different meshes should be employed for each field individually. This naturally requires proper information transfer schemes between these non-matching discretizations, where the mortar methods naturally provides best perspectives to work well. All these aspects motivate the extension of already existing mortar methods towards 0D and 1D boundaries, complex interface effects for 2D boundaries and abstract information transfer for 3D problems.

1.2. Fundamental approaches to mortar methods

From a historical point of view, mortar methods were originally introduced in the context of non-overlapping domain decomposition (DD) approaches to allow for coupling of nonconforming discretizations across subdomain boundaries. A first work can be found for spectral element discretizations in Maday et al. [160]. Further investigations and extensions towards the finite element method (FEM) can be found in Ben Belgacem [18], Bernardi et al. [25, 26] and Seshaiyer and Suri [247]. The main characteristic of the mortar method is the enforcement of a continuity condition at the subdomain boundaries in an integral (weak) sense, which perfectly suits the finite element approach. This can be realized by the construction of an appropriate nonconforming space of approximation through the introduction of a new intermediary mortar space. Alternatively, the mortar method can be formulated with help of Lagrange multipliers from a suitable Lagrange multiplier space, which also results in a well-posed problem, see Ben Belgacem [18]. In Bernardi et al. [26] it was shown, that the mortar method for DD applications guarantees for conservation of the optimal convergence rates from the FEM, when a proper mortar space is chosen. Consequently, it was shown that such a space will also satisfy the well-known Babuska-Brezzi stability condition. At the beginning of the century, a new choice for the Lagrange multiplier space for mortar methods in the context of DD was proposed in Wohlmuth [288, 289], which is the so-called dual Lagrange multiplier approach. In contrast to its standard counterpart, it localizes the coupling effect at the subdomain interfaces and thus causes an easier realization of the domain coupling while still guaranteeing for the optimality of the mortar method. This means, that the overall discretization error is bounded by the individual errors of the subdomains, see again Wohlmuth [289]. Due to their proven mathematical optimality, mortar methods became the state-of-the-art discretization technique for general non-matching interface problems, which will be outlined in detail in the following.

In the past two decades, mortar methods have been successfully applied for linear and nonlinear solid mechanics. First DD methods related to mortar approaches can be found in Dohrmann et al. [62], Flemisch et al. [83], Krause and Wohlmuth [140], Puso [216] and Puso and Laursen [217]. Then, mortar methods have been applied to contact interaction problems, since early contact formulations such as the node-to-node (NTN) approach or the node-to-segment (NTS) approach suffered poor performance regarding accuracy and robustness, especially for large de-

formation applications. For this purpose, the classical mortar approach is modified in order to be applicable to inequality constraints characterizing contact problems. First contributions regarding mortar methods for computational contact mechanics are the work in Ben Belgacem et al. [20], Hild [107] and McDevitt and Laursen [168], but these developments were restricted to small deformations. Extensions towards finite deformation problems can be found in various following publications, such as 2D approaches in combination with a penalty regularization in Fischer and Wriggers [80, 81], Laursen [151] and Yang et al. [301] and 3D penalty methods in Puso and Laursen [218] and Puso et al. [220]. Augmented Lagrangian mortar contact formulations are published in Puso and Laursen [219] and Cavalieri and Cardona [38]. Mortar contact formulations with a classical Lagrange multiplier approach can be found in Hesch and Betsch [106] and in Tur et al. [273]. First applications of dual Lagrange multipliers to mortar based contact mechanics in a small deformation regime can be found in Brunßen et al. [34], Flemisch and Wohlmuth [82], Hüeber and Wohlmuth [115] and Hüeber et al. [117]. Successful implementations of a dual Lagrange multiplier approach for finite deformation mortar contact formulations are performed for 2D problems in Popp et al. [211] and Gitterle et al. [88] and for 3D problems in Gitterle [87], Hartmann et al. [98], Popp [210], Popp et al. [212, 213] and Wohlmuth [290]. Additionally, it should be mentioned, that in the context of isogeometric analysis (IGA) dual mortar methods have been very recently developed in Brivadis et al. [33] and Seitz et al. [244]. When considering all the mentioned publications regarding mortar methods for computational contact mechanics, it can be noticed that the classical definition of mortar methods from DD methods changed significantly in the past years. Nowadays, from an illustrative, slightly unmathematical perspective, they could be described as segment-to-segment (STS) contact formulations with explicitly employed balance of linear momentum in a sense that only the contact traction at one of the two interacting sides is employed to state the problem formulation for two bodies. Herein, the mentioned contact traction at one side could be identified as penalization of constraint violation in the context of penalty based mortar methods, or as additional Lagrange multiplier. However, all contributions given above are based on the assumption that the interfaces of the involved bodies are smooth, which means that surface-to-surface contact is expected. Contact of non-smooth boundaries, such as vertices and edges are neglected in all previous mortar publications.

Beyond classical contact problems (i.e. pure structural problems), the mortar method has successfully been applied to complex multiphysics contact problems and general interface problems. Here, thermo-mechanical contact problem formulations with mortar approaches can be found in Hüeber and Wohlmuth [116] and Seitz et al. [245]. The therein included Robin-type constraints are enforced with dual Lagrange multipliers. A similar strategy was very recently employed for electrochemistry problems in Fang et al. [68] in order to couple anode/cathode and electrolyte. Mortar methods for DD of porous media flow can be found in Kim et al. [136] and Vuong [277]. Also an early finite deformation contact formulation of two porous bodies based on mortar methods can be found in Vuong [277]. Mortar approaches for DD in the context of fluid dynamics have been developed in Achdou et al. [1], Ben Belgacem [19] and Ben Belgacem et al. [21] for standard mortar methods. An extension towards dual mortar methods can be found in Ehrl et al. [65]. Fluid-structure interaction problems with the dual mortar method being used for the interface coupling have been introduced in Klöppel et al. [138]. Also a general methodology based on mortar methods for multiscale problems of second-order elliptic equations has been developed in Arbogast et al. [6]. However, the complex contact interface phenomenon of wear is only very rarely addressed in the existing literature. The only

known publications concerning mortar methods for wear modeling are Cavalieri and Cardona [36] and Cavalieri et al. [37], but with several limitations, such as the assumption of frictionless contact and small amounts of wear. In addition, they are based on a standard Lagrange multiplier approach within an augmented Lagrangian framework and the extension towards dual Lagrange multipliers is still an open question.

Finally, the mortar method is employed as abstract projection operator for nodal information transfer and applied towards volume coupled multiphysics on different meshes in Dureisseix and Bavestrello [64] and Néron and Dureisseix [181]. Therein, only 2D problems are considered. Moreover, the multiphysics problems are solved with a partitioned solution scheme and the constructed mortar projection operator is based on a standard mortar approach. Such a standard mortar projection operator was also employed in Bussetta et al. [35] for remeshing applications. However, construction of a real 3D projection operator for nodal information transfer has never been outlined for a dual mortar approach. In addition, a general methodology for the application of mortar projectors towards monolithic multiphysics being defined on different meshes has not been developed in the existing literature.

Despite the great work done in the mentioned publications, there are still various unresolved questions in the context of mortar methods, especially for contact of non-smooth boundaries, complex interface effects such as wear modeling and volume coupled problems. These three aspects mark the points of origin for this thesis.

1.3. Research objective

The methods developed in this thesis are aiming to consistently extend the well-established mortar methods in the context of the FEM towards contact of non-smooth geometries, wear modeling and general volume coupled problems. For all three aspects, dual Lagrange multipliers (i.e. dual mortar methods) are very promising since they have been successfully employed in various applications outlined in the previous section. Thus, the general research objective of this thesis is specified in the following. In addition, detailed specifications of requirements are given for each of the three mentioned topics individually at the beginning of the corresponding chapters.

1.3.1. General specification of requirements

Based upon the explanations stated in the previous section, the most important requirements for the improvements of mortar methods are listed and illustrated in the following.

Mortar formulations for point, line and surface contact General interactions of two arbitrarily formed bodies could not only lead to contacting surfaces, but also contact of edges and vertices. For these scenarios, the existing mortar methods are not desirable, since well-known drawbacks such as large penetrations at vertices and edges would occur. The mentioned large penetrations could be avoided by a node-to-segment scheme at vertices and edges. However, contact stress oscillations for edge (line) contact are inevitable. Thus, it would be desirable to create suitable mortar contact formulations which directly address the interaction of vertices, edges and surface in one comprehensive model. Up to now, there is no such a model available in the existing literature on computational contact mechanics and mortar methods. In addition,

dual Lagrange multipliers are the preferred discretization approach for the development of a combined point, line and surface contact formulation since they naturally allow for an easy and efficient elimination of the arising Lagrange multiplier unknowns.

Fretting wear modeling within mortar contact framework The fretting wear phenomenon is usually modeled as an additional contribution to the gap function, which leads to slightly overlapping bodies up to an extent which is equivalent to the wear depth. For 3D mortar contact, such an approach for wear modeling is published in Cavalieri and Cardona [36] and Cavalieri et al. [37]. But, this model does not consider frictional effects and no beneficial dual Lagrange multipliers are employed. The only frictional contact formulation based on dual mortar methods for fretting wear has been published in Gitterle [87], being restricted to 2D problems. The accurate and efficiently calculated results from Gitterle [87] motivate to realize a general 3D wear formulation based on dual mortar methods, which will be presented in this thesis.

Finite wear modeling within mortar contact framework The effect of material loss at the contact interface due to wear resulting into finite shape changes is only rarely addressed in the existing literature on mortar methods for computational contact mechanics. The only known publications which address this topic are Doca [61] and Gitterle [87], but only for 2D models and explicit time integration of the wear phenomena. In Stupkiewicz [263], it has been demonstrated that implicit treatment of wear effects is necessary in order to obtain stable results, especially when performing simulations based on a steady-state assumption with large time step sizes. However, the construction of an implicit finite wear framework based on dual mortar methods is a hitherto unanswered question.

Dual mortar methods for 3D projection operator For a large variety of applications, projection of nodal information between two different meshes is required. Despite classical collocation methods being well-established for this purpose, nodal information transfer methods based on weak conservation properties are often beneficial to satisfy overall conservation demands. Mortar projection operators for nodal information transfer of 2D problems have been developed and applied in Dureisseix and Bavestrello [64] and Néron and Dureisseix [181]. In addition, the mortar method as basis of a 3D projection operator has already been employed in Bussetta et al. [35]. But, all mentioned publications are based on the standard mortar approach. Consequently, their construction becomes very costly. A volume projection operator based on dual mortar methods has not been developed in the existing literature, although numerical efficiency of dual mortar methods has been demonstrated by several authors for DD and contact applications, see for example Gitterle et al. [88], Popp et al. [212] and Wohlmuth [289]. Consequently, it is very promising in terms of computational efficiency to develop such a projection operator with help of dual mortar methods.

Volume coupled multiphysics on non-matching meshes Classical mortar methods are designed in order to allow for flexible discretization via interface coupling of subdomains with non-matching meshes. Transferring this idea towards the context of coupled multiphysics, it would be desirable to allow for different bulk discretizations of the involved fields. Such an approach has been published in Dureisseix and Bavestrello [64] and Néron and Dureisseix [181], but it is restricted to 2D problems, which are solved within a partitioned solution scheme. Mono-

lithic solution schemes are often proven to be of superior robustness compared to partitioned counterparts. This causes the need for having a general methodology, which allows for solving volume coupled multiphysics on non-matching meshes within a monolithic approach. In addition, contact interaction of two bodies with multiphysics effects and non-matching interface and volume discretizations has never been considered in the existing literature. Aiming for highest possible flexibility with respect to spatial discretization, these topics need further exploration.

1.3.2. Proposal for novel mortar approaches

This thesis describes the consistent extension of the mortar finite element method to computational contact mechanics of complex geometries, wear simulations and general volume coupled problems. The most important ingredients and new scientific contributions of the presented approaches are given in the following:

- the first consistent extension of the dual mortar contact formulation to point, line and surface contact scenarios of vertices, edges and surfaces being involved in a finite deformation regime, see also Farah et al. [71].
- development of the first dual mortar formulation for the calculation of fretting wear problems in 3D, see also Farah et al. [69].
- implementation of the first fully implicit finite wear algorithm in a non-steady-state regime based on dual mortar methods with an Arbitrary-Lagrangian-Eulerian approach and first extensions towards thermo-structure interaction problems, see also Farah et al. [74].
- successful extension of the dual mortar method to a 3D information transfer scheme with application to monolithic volume coupled multi-field problems, e.g. porous media, thermo-structure interaction, fluid-structure interaction and thermo-structure-contact interaction, see also Farah et al. [70] and La Spina et al. [145].

All methods and models devised as part of this work have been implemented in the in-house C++ code BACI (cf. Wall et al. [282]) of the Institute for Computational Mechanics at the Technical University of Munich. This code integrated open-source libraries of the Trilinos Project conducted by Sandia National Laboratories, see Heroux et al. [102]. The basic data structures and existing features like time integration schemes or iterative solution techniques were reused within this thesis. Other modules have been adapted or were written completely from scratch.

1.4. Outline

This thesis is split into three major parts, namely **Chapters 4, 5 and 6**, which extend and adapt the mortar method to be applicable to contact scenarios with vertices, edges and surfaces being involved, complex wear interface phenomena and information transfer operators for general volume coupled problems. Parts of this thesis are taken from, derived from or also published in the articles Farah et al. [69, 70, 71, 73, 74], La Spina et al. [145] and Seitz et al. [244]. The remainder of this thesis is structured as follows:

In **Chapter 2**, the governing equations for nonlinear solid mechanics are outlined in their strong formulation. Additionally, the concept of the weak formulation and spatial discretization based on the finite element method are given. The chapter is completed with explanations on time integration of the provided equations for nonlinear solid mechanics and proper linear and nonlinear solution schemes.

The structural problem is extended towards contact mechanics in **Chapter 3**, where the basics on contact kinematics and the constraints for normal contact and frictional sliding are introduced for classically considered surface-to-surface contact scenarios. Then, the weak form of the contact problem is reviewed based on a Lagrange multiplier approach. This problem formulation is afterwards spatially discretized with the mortar finite element method. Here, commonly used Lagrange multiplier interpolations, namely the standard and the dual approach, are introduced and detailed explanations on the complex numerical integration scheme are provided. Information about the time integration of computational contact mechanics and the global solution scheme complete this chapter.

The main focus of **Chapter 4** is the development of a computational approach for finite deformation contact of vertices, edges and surfaces based on mortar methods. First, the chapter provides a detailed overview of already existing numerical approaches for such complex contact scenarios with emphasis on finite element methods followed by a concrete definition of the most important requirements for the algorithm developed in this thesis. For the purpose of dealing with the aforementioned requirements, the contact kinematics and suitable notations for point contact, line contact and surface contact are introduced and contact constraints for all scenarios are given. Then, a consistent weak formulation is derived with three sets of Lagrange multipliers and an additional penalty regularization for special scenarios. The naturally following spatial discretization is firstly outlined for the contact interface displacement field and suitable and robust definitions for discrete nodal normals are provided. Following the mortar idea, appropriate discretizations with suitable discrete Lagrange multiplier spaces and numerical evaluation procedures are separately given for point contact, line contact and surface contact scenarios. Finally, the introduced algorithms are combined to a comprehensive contact framework, which is validated with help of several numerical examples.

In **Chapter 5**, the complex interface phenomenon of wear is modeled within the mortar finite element framework. Starting point of this chapter is an overview about existing numerical approaches for simulation of wear effects and the consequently arising requirements for the wear algorithms developed in this thesis. Then, the fundamentals on wear effects are reviewed with special focus on the wear law postulated by Archard and the continuum mechanical consideration of finite wear effects. This is followed by two mortar related approaches of spatially discretizing wear effects which are employed in the following for algorithms valid for small wear and finite wear. These algorithms are validated with respect to already existing numerical results

1. Introduction

from the literature and further challenging 3D tests. Finally, the proposed finite wear algorithm is extended towards the interaction with thermal effects and again its accuracy is validated with results from the literature and its applicability is demonstrated by one complex 3D problem.

Chapter 6 successfully extends the mortar method beyond interface problems related to solid mechanics towards general volume coupled problems. Therefore, it is considered as an abstract projection method for nodal information transfer. Again, an overview of existing methods for nodal information transfer and of the various fields of applications of such methods are given. This is followed by a specification of requirements for the developed numerical methods. Then, the basics on nodal information transfer methods are provided and an abstract derivation of the mortar method is given including details on the numerical evaluation and the degeneration to collocation methods. Then, a general methodology for the incorporation of projection operators within a monolithic multiphysics problem is given which allows for different spatial discretization of the involved single-fields. The accuracy of the mortar projection operators is validated with several benchmark examples and the introduced scheme for solving monolithic multiphysics on different meshes is tested for thermo-structure interaction problems and porous media applications. Finally, the versatility of the proposed projection operators is demonstrated by the development of a novel grid motion approach for fluid-structure interaction problems and further applications of the implemented numerical method are outlined.

Finally, **Chapter 7** summarizes the most important achievements gained in this thesis, but also addresses the aspects of the developed approaches which still have potential for improvements.

2. Governing Equations and Finite Element Formulation

In this thesis, various single-field and multi-field problems are considered, but special focus is set on nonlinear solid mechanics since it serves as starting point for all following derivations concerning mortar methods for contact mechanics. Thus, in this chapter, the fundamental concepts of nonlinear continuum mechanics are recapitulated with emphasis on the governing equations for solid dynamics. In addition, the concept of the weak formulation and spatial discretization with the finite element method are explained. Finally, discretization in time is briefly introduced with help of finite differences and solution techniques for nonlinear and linear equations are outlined.

2.1. Continuum mechanics

The following section introduces classical continuum mechanics for nonlinear structures based on the literature Bonet and Wood [31], Holzapfel [113], Ogden [185] and Simo and Hughes [254]. Structural models with special kinematic assumptions, such as beams and plates are not considered in this thesis.

2.1.1. Nonlinear kinematics, strain and stress

In this section, the kinematic relationships as well as strain and stress measurements are introduced to describe the deformation of a homogeneous body \mathcal{B} without material loss. Therefore, a classical Boltzmann continuum in 3D is considered and all following relations are formulated with respect to a global Cartesian coordinate system $\{e_1, e_2, e_3\}$, see Figure 2.1. Basically, it can be distinguished between two different configurations, namely the *reference configuration* $\Omega_0 \subset \mathbb{R}^3$, which represents the positions of all material points \mathbf{X} at the initial time $t = 0$ and the *spatial configuration* $\Omega_t \subset \mathbb{R}^3$, which is occupied by all spatial points \mathbf{x} . In the context of structural mechanics, the reference configuration is also known as the *material configuration* and thus both terms are used in the following. However, for bodies with mass loss due to wear, it is important to distinguish between material and reference configuration, see Chapter 5. By postulating a Lagrangian formulation, the so called *Lagrangian observer* follows the material particles in their motion and thus it is linked to the reference configuration. Consequently, all kinematics and general governing equations are stated in terms of the material coordinates \mathbf{X} . This methodology is the classical formulation in structural dynamics since it allows for computationally advantageous treatment of problems with history dependent variables, such as plasticity and visco-elasticity. Thus, only the nonlinear and bijective deformation map φ is required to

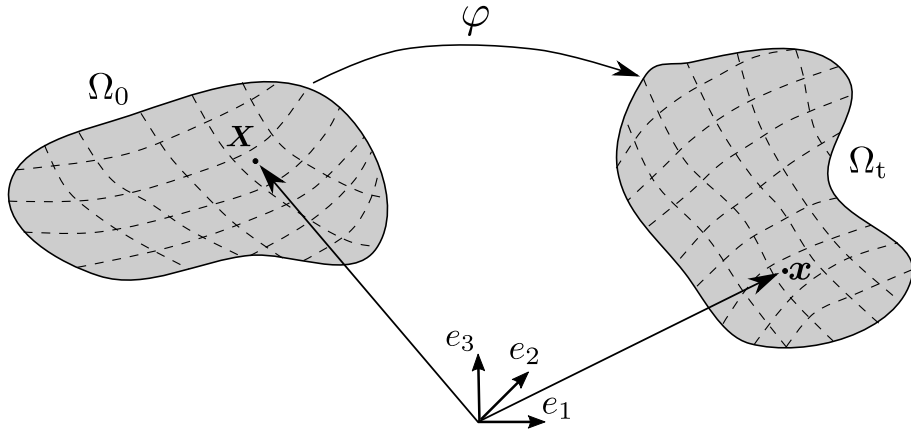


Figure 2.1: The considered homogeneous body \mathcal{B} in reference configuration $\Omega_0 \subset \mathbb{R}^3$ and spatial configuration $\Omega_t \subset \mathbb{R}^3$ with the motion φ , which acts as mapping between these configurations.

describe the motion of a material point:

$$\varphi : \begin{cases} \Omega_0 \rightarrow \Omega_t(t), & (\mathbf{X}, t) \rightarrow \mathbf{x}, \\ & \varphi(\mathbf{X}, t) = \mathbf{x}. \end{cases} \quad (2.1)$$

Furthermore, the *absolute displacement vector* \mathbf{u} of a reference point can be described as

$$\mathbf{u}(\mathbf{X}, t) = \mathbf{x}(\mathbf{X}, t) - \mathbf{X}. \quad (2.2)$$

The deformation gradient is introduced as fundamental measurement for deformation and strain and is defined as gradient of the current position with respect to the material position:

$$\mathbf{F} = \frac{\partial \mathbf{x}(\mathbf{X}, t)}{\partial \mathbf{X}} = \mathbf{I} + \frac{\partial \mathbf{u}(\mathbf{X}, t)}{\partial \mathbf{X}}, \quad (2.3)$$

with \mathbf{I} being the second-order identity tensor. Physically, the deformation gradient can be interpreted as mapping of an infinitesimal line element $d\mathbf{X}$ in the reference configuration to the corresponding line element $d\mathbf{x}$ in spatial configuration, i.e.

$$\mathbf{F} \cdot d\mathbf{X} = d\mathbf{x}. \quad (2.4)$$

This operation is known as *push-forward* operation. Due to the assumed bijectivity of the deformation map φ in (2.1) the corresponding *pull-back* operation can be defined by employing the inverse of the deformation gradient:

$$d\mathbf{X} = \mathbf{F}^{-1} \cdot d\mathbf{x}. \quad (2.5)$$

Thus, the determinant J of the deformation gradient is guaranteed to be positive

$$J = \det \mathbf{F} > 0. \quad (2.6)$$

For the special case of a completely incompressible body, the deformation gradient's determinant is equal to 1. This determinant J is employed to describe the relation of an infinitesimal volume element in the material configuration and the spatial configuration:

$$dV = J dV_0. \quad (2.7)$$

Here, dV is the infinitesimal volume element in spatial configuration and dV_0 represents the counterpart in material configuration. After introducing the transformation of line elements and volume elements, the change of an infinitesimal area element has to be defined. Therefore, the well-known Nanson's formula is employed:

$$dA = J F^{-T} \cdot dA_0, \quad (2.8)$$

with the infinitesimal area element dA in spatial configuration and the corresponding area element in material configuration dA_0 . These elements are interpreted as vectors via

$$dA = dAn, \quad dA_0 = dA_0N, \quad (2.9)$$

with N and n denote unit normal vectors in the material configuration and in the spatial configuration, respectively. As a suitable and very common choice for the strain measure, the so-called *Green-Lagrange strain tensor* is employed and defined as

$$E = \frac{1}{2}(F^T \cdot F - I). \quad (2.10)$$

It fulfills the natural requirement of zero strain in the undeformed state and is valid in the regime of moderate stretch and compression. Alternative strain measures, such as the Euler-Almansi strains and the logarithmic strains can be found in the abundant literature referenced at the beginning of this chapter. However, the Green-Lagrange strains are uniquely utilized throughout this thesis.

In order to describe the kinematic of a body, the first and second derivative in time of the displacement vector, i.e. the velocity vector $\dot{\mathbf{u}}(\mathbf{X}, t)$ and the acceleration vector $\ddot{\mathbf{u}}(\mathbf{X}, t)$, are required. They are defined as

$$\dot{\mathbf{u}}(\mathbf{X}, t) = \left. \frac{\partial \mathbf{u}(\mathbf{X}, t)}{\partial t} \right|_{\mathbf{X}} = \frac{d\mathbf{u}(\mathbf{X}, t)}{dt}, \quad (2.11)$$

$$\ddot{\mathbf{u}}(\mathbf{X}, t) = \left. \frac{\partial \dot{\mathbf{u}}(\mathbf{X}, t)}{\partial t} \right|_{\mathbf{X}} = \frac{d\dot{\mathbf{u}}(\mathbf{X}, t)}{dt} = \frac{d^2\mathbf{u}(\mathbf{X}, t)}{dt^2}. \quad (2.12)$$

Correspondingly, the rate forms of the deformation measures namely the material velocity gradient $\mathbf{L} = \dot{\mathbf{F}}$ or the material strain rate tensor $\dot{\mathbf{E}} = \frac{1}{2}(\dot{\mathbf{F}}^T \cdot \dot{\mathbf{F}} + \mathbf{F}^T \cdot \dot{\mathbf{F}})$ are readily defined.

Generally, elastic bodies are characterized by an inner stress state induced by deformations. Since strains and stresses are naturally connected by the notion of energy conjugate pairs, they cannot be chosen arbitrarily and independently in practice. Instead, definitions of different stress measures depending on the employed problem formulation and the considered continuum mechanical configuration are possible. Considering the spatial configuration, the current *boundary*

traction t is defined as the limit value of the resulting force Δf acting on a vanishing surface area Δa :

$$t = \lim_{\Delta a \rightarrow 0} \frac{\Delta f}{\Delta a}. \quad (2.13)$$

The spatial boundary traction can be related to the *Cauchy stress tensor σ* with an outward pointing unit normal vector \mathbf{n} in spatial configuration, via

$$\mathbf{t} = \boldsymbol{\sigma}(\mathbf{x}, t) \cdot \mathbf{n}. \quad (2.14)$$

This is known as Cauchy theorem and can be derived from equilibrium considerations using an infinitesimal tetrahedral volume element. With the Cauchy stress tensor, the *first Piola-Kirchhoff stress tensor P* can be defined as

$$\mathbf{P} = J \boldsymbol{\sigma} \cdot \mathbf{F}^{-T}. \quad (2.15)$$

In contrast to the spatial stress tensor $\boldsymbol{\sigma}$, the first Piola-Kirchhoff stress tensor \mathbf{P} represents a mapping from the material configuration to the spatial configuration. The *second Piola-Kirchhoff stress tensor S* is a pure material stress tensor and is defined as the pull-back of the Cauchy stress:

$$\mathbf{S} = \mathbf{F}^{-1} \cdot \mathbf{P} = J \mathbf{F}^{-1} \cdot \boldsymbol{\sigma} \cdot \mathbf{F}^{-T}. \quad (2.16)$$

With this measure, the material boundary traction can be defined as

$$\mathbf{T} = \mathbf{S} \cdot \mathbf{N}, \quad (2.17)$$

with the outward pointing unit normal \mathbf{N} in the material configuration.

2.1.2. Constitutive laws

The constitutive relations link the introduced stress and strain measurements and describe the material response of a body due to deformations. Throughout this thesis, only purely homogeneous bodies without any internal dissipation effects are considered. Thus, the existence of a so-called *strain energy function Ψ* is postulated, which depends only on the current deformation state. This is known as *hyperelastic material behavior*. A commonly employed formulation of hyperelastic material is given as

$$\mathbf{S} = \frac{\partial \Psi}{\partial \mathbf{E}}, \quad (2.18)$$

which generally states a nonlinear relationship between the second Piola-Kirchhoff stress tensor and the Green-Lagrange strains. Especially for finite element approaches, the fourth-order material elasticity tensor C is required and can be defined by

$$\mathbf{C} = \frac{\partial \mathbf{S}}{\partial \mathbf{E}} = \frac{\partial^2 \Psi}{\partial \mathbf{E}^2}. \quad (2.19)$$

Thus, the choice of the strain energy function determines the constitutive behavior of the considered body. In the following, three very common material models for the strain energy functions

are introduced, which are employed for all investigations in this thesis. First, the *Saint-Venant-Kirchhoff* material is considered, which is one of the simplest models. It is an isotropic, hyper-elastic model and represents the extension of the linear constitutive theory formulated for large deformations. The corresponding strain energy function reads

$$\Psi_{\text{SVK}} = \frac{\lambda}{2}(\text{tr}\mathbf{E})^2 + \mu\mathbf{E} : \mathbf{E}, \quad (2.20)$$

with λ and μ representing the so-called Lamé parameters. For these parameters, a correlation with Young's modulus E and Poisson's ratio ν can be stated via

$$\lambda = \frac{E\nu}{(1+\nu)(1-2\nu)}, \quad \mu = \frac{E}{2(1+\nu)}. \quad (2.21)$$

The second popular material law is the compressible *Neo-Hookean* model, with the strain energy function

$$\Psi_{\text{NH1}} = \frac{\mu}{2}(\text{tr}(\mathbf{F}^T \cdot \mathbf{F}) - 3) - \mu\ln(J) + \frac{\lambda}{2}(\ln(J))^2. \quad (2.22)$$

Based on the classical New-Hookean model in (2.22), a third strain energy function is introduced, which reads

$$\Psi_{\text{NH2}} = \frac{\mu}{2}(\text{tr}(\mathbf{F}^T \cdot \mathbf{F}) - 3) - \mu\log(J) + \frac{\lambda}{2}(J - 1)^2. \quad (2.23)$$

It is employed for a validation example in the context of finite wear modeling. For other constitutive laws, the interested reader is exemplarily referred to Holzapfel [113] and Simo and Hughes [254].

2.1.3. Balance equations

In the following subsections, the fundamental balance equations and conservation laws for mechanical systems are given. All balance equations can be formulated in an integral (global) manner or in a point-wise (local) form.

2.1.3.1. Conservation of mass

When considering classical elastodynamics without growth, wear or other degradation effects, the mass of the body needs to be conserved. Thus, balance of mass can be written in global form as

$$\frac{dm}{dt} = \frac{d}{dt} \int_{\Omega_t} \rho dV = \int_{\Omega_t} (\dot{\rho} + \rho \text{div}\dot{\mathbf{u}}) dV = 0, \quad (2.24)$$

with ρ being the spatial mass density of the spatial volume element dV and $\text{div}(\cdot)$ representing the spatial divergence operator. For obtaining the relation (2.24), Reynolds' theorem was used. The corresponding formulation in material configuration reads

$$\frac{dm}{dt} = \frac{d}{dt} \int_{\Omega_0} \rho_0 dV_0 = \int_{\Omega_0} \dot{\rho}_0 dV_0 = 0. \quad (2.25)$$

Here, the material density ρ_0 of the material volume element dV_0 is related with the spatial density via the determinant of the deformation gradient:

$$\rho_0 = J \rho. \quad (2.26)$$

Furthermore, in (2.25) the rate of the material density is assumed to be zero, which implies that the density does not depend on time. The corresponding local form of mass conservation reads

$$\dot{\rho} + \rho \operatorname{div} \dot{\mathbf{u}} = 0, \quad (2.27)$$

$$\dot{\rho}_0 = 0. \quad (2.28)$$

2.1.3.2. Balance of linear momentum

The global form of balance of linear momentum states, that the time derivative of linear momentum equals all external forces acting on the considered body. This can be written as

$$\frac{d}{dt} \int_{\Omega_t} \rho \dot{\mathbf{u}} dV = \int_{\Omega_t} \hat{\mathbf{b}} dV + \int_{\partial\Omega_t} \hat{\mathbf{t}} dA, \quad (2.29)$$

with the external body force $\hat{\mathbf{b}}$ acting on a spatial volume element and the external boundary traction $\hat{\mathbf{t}}$ defined on the spatial boundary $\partial\Omega_t$. When applying Reynolds' theorem and local mass conservation (2.27) to the left-hand side and reformulating the right-hand side with help of Gauss divergence theorem, the more convenient form of balance of linear momentum is obtained:

$$\int_{\Omega_t} \rho \ddot{\mathbf{u}} dV = \int_{\Omega_t} (\operatorname{div} \boldsymbol{\sigma} + \hat{\mathbf{b}}) dV \quad (2.30)$$

The corresponding form in material configuration reads

$$\int_{\Omega_0} \rho_0 \ddot{\mathbf{u}} dV_0 = \int_{\Omega_0} (\operatorname{Div} \mathbf{P} + \hat{\mathbf{b}}_0) dV_0, \quad (2.31)$$

with the material divergence operator $\operatorname{Div}(\cdot)$ and the external volume force $\hat{\mathbf{b}}_0$ being defined on the undeformed unit volume. Finally, the local forms of the balance of linear momentum can be stated in the spatial configuration and the material configuration:

$$\rho \ddot{\mathbf{u}} = \operatorname{div} \boldsymbol{\sigma} + \hat{\mathbf{b}}, \quad (2.32)$$

$$\rho_0 \ddot{\mathbf{u}} = \operatorname{Div} \mathbf{P} + \hat{\mathbf{b}}_0. \quad (2.33)$$

This is also known as Cauchy's first equation of motion.

2.1.3.3. Balance of angular momentum

The balance of angular momentum is defined by the requirement, that the time derivative of the angular momentum with respect to a fixed point of origin equals the sum of all external moments acting on the considered body. Therefore, the global form is formulated in the spatial configuration via

$$\frac{d}{dt} \int_{\Omega_t} (\rho \mathbf{x} \times \dot{\mathbf{u}}) dV = \int_{\Omega_t} (\mathbf{x} \times \hat{\mathbf{b}}) dV + \int_{\partial\Omega_t} (\mathbf{x} \times \hat{\mathbf{t}}) dA. \quad (2.34)$$

The counterpart in the material configuration is defined as

$$\frac{d}{dt} \int_{\Omega_0} (\rho_0 \mathbf{x} \times \dot{\mathbf{u}}) dV_0 = \int_{\Omega_0} (\mathbf{x} \times \hat{\mathbf{b}}_0) dV_0 + \int_{\partial\Omega_0} (\mathbf{x} \times \hat{\mathbf{t}}_0) dA_0, \quad (2.35)$$

with the traction $\hat{\mathbf{t}}_0$ being defined on the boundary $\partial\Omega_0$ in material configuration. Without pointing out details on the local form of balance of angular momentum, it leads to the equivalent requirement, that the Cauchy stress tensor $\boldsymbol{\sigma}$ and the second-Piola-Kirchhoff stress tensor are symmetric:

$$\boldsymbol{\sigma}^T = \boldsymbol{\sigma}, \quad \mathbf{S}^T = \mathbf{S}. \quad (2.36)$$

This is also known as Cauchy's second law of motion.

2.1.3.4. Balance of energy

Balance of mechanical energy is not in the focus of this thesis, since it requires adequate spatial and temporal discretizations in the context of computational mechanics. However, since only spatial discretization approaches for interface and volume couplings based on the mortar method are investigated later on, the balance of mechanical energy is generally not guaranteed for the developed approaches for computational contact mechanics. However, for the sake of completeness, balance of mechanical energy requires that the change in total energy equals the introduced external power:

$$\frac{d}{dt} \int_{\Omega_t} \frac{1}{2} \rho \dot{\mathbf{u}} \cdot \dot{\mathbf{u}} dV + \int_{\Omega_t} \boldsymbol{\sigma} : (\mathbf{F}^{-T} \cdot \dot{\mathbf{E}} \cdot \mathbf{F}^{-1}) dV = \int_{\Omega_t} \hat{\mathbf{b}} \cdot \dot{\mathbf{u}} dV + \int_{\partial\Omega_t} \hat{\mathbf{t}} \cdot \dot{\mathbf{u}} dA. \quad (2.37)$$

Herein, the first two terms are the rate of kinetic energy and the internal mechanical power. The two terms on the right-hand side represent the external power due to interface and body forces. For purely mechanical systems, balance of energy is a consequence of the balance of linear momentum and thus its local form does not provide any additional information and is not given here.

2.1.4. Initial boundary value problem

Resulting from the previous sections, the initial boundary value problem (IBVP) of nonlinear solid mechanics is stated in the following. It represents a set of coupled second-order partial differential equations with given initial conditions and boundary conditions. For the entire thesis, the IBVP is defined in the material configuration. However, the corresponding definition in the spatial configuration is also possible. For defining suitable boundary conditions, $\partial\Omega_0$ is divided into two disjoint subsets as

$$\partial\Omega_0 = \Gamma_u \cup \Gamma_\sigma, \quad (2.38)$$

$$\Gamma_u \cap \Gamma_\sigma = \emptyset. \quad (2.39)$$

Here, Γ_u is the Dirichlet boundary which is subjected to a given displacement $\hat{\mathbf{u}}$ and Γ_σ denotes the Neumann boundary, where the tractions $\hat{\mathbf{t}}_0$ are acting. With these definitions, the IBVP of

finite deformation elastodynamics can be stated as follows:

$$\text{Div} \boldsymbol{P} + \hat{\boldsymbol{b}}_0 = \rho_0 \ddot{\boldsymbol{u}} \quad \text{in } \Omega_0 \times [0, T], \quad (2.40)$$

$$\boldsymbol{u} = \hat{\boldsymbol{u}} \quad \text{on } \Gamma_u \times [0, T], \quad (2.41)$$

$$\boldsymbol{P} \cdot \boldsymbol{N} = \hat{\boldsymbol{t}}_0 \quad \text{on } \Gamma_\sigma \times [0, T], \quad (2.42)$$

$$\boldsymbol{u}(\boldsymbol{X}, 0) = \hat{\boldsymbol{u}}_0(\boldsymbol{X}) \quad \text{in } \Omega_0, \quad (2.43)$$

$$\dot{\boldsymbol{u}}(\boldsymbol{X}, 0) = \hat{\dot{\boldsymbol{u}}}_0(\boldsymbol{X}) \quad \text{in } \Omega_0. \quad (2.44)$$

Herein, T denotes the considered time interval. Due to the time dependency in the balance of linear momentum (2.40), proper initial conditions for the displacements and the velocity have to be defined in (2.43) and (2.44). Therefore, $\hat{\boldsymbol{u}}_0(\boldsymbol{X})$ and $\hat{\dot{\boldsymbol{u}}}_0(\boldsymbol{X})$ are introduced, which represent the displacements and velocities at the initial time $t = 0$. Equations (2.40)-(2.44) are commonly denoted as *strong* formulation, since they are enforced at each point within the material domain Ω_0 .

2.2. Finite element formulation and solution scheme for nonlinear solid mechanics

In the following, the finite element formulation for spatial discretization is briefly derived, the employed time integration scheme is introduced and details on the solution schemes are provided.

2.2.1. Weak formulation

In order to derive a suitable finite element representation of the IBVP defined in (2.40)-(2.44), it has to be transformed into a so-called weak or variational formulation. Therefore, the *principle of virtual work* (PVW) can be applied. Without pointing out the details on the derivation, the resulting weak formulation reads

$$\delta\mathcal{W} = \underbrace{\int_{\Omega_0} \rho_0 \ddot{\boldsymbol{u}} \cdot \delta \boldsymbol{u} \, dV_0}_{-\delta\mathcal{W}_{\text{kin}}} + \underbrace{\int_{\Omega_0} \boldsymbol{S} : \delta \boldsymbol{E} \, dV_0}_{-\delta\mathcal{W}_{\text{int}}} - \underbrace{\int_{\Omega_0} \hat{\boldsymbol{b}}_0 \delta \boldsymbol{u} \, dV_0}_{-\delta\mathcal{W}_{\text{ext}}} - \underbrace{\int_{\Gamma_\sigma} \hat{\boldsymbol{t}}_0 \delta \boldsymbol{u} \, dA_0}_{-\delta\mathcal{W}_{\text{ext}}} = 0. \quad (2.45)$$

Herein, the virtual quantities are denoted with $\delta(\cdot)$. Furthermore, three different virtual work contributions can be identified: the kinetic virtual work contribution $\delta\mathcal{W}_{\text{kin}}$, the internal virtual work contribution $\delta\mathcal{W}_{\text{int}}$ and the external virtual work contribution $\delta\mathcal{W}_{\text{ext}}$. It can easily be shown that solutions of the strong problem formulation (IBVP) also satisfy the weak formulation in (2.45). But, the weak formulation makes lower demands on the differentiability requirements to the solution functions \boldsymbol{u} , because only first derivatives of \boldsymbol{u} with respect to \boldsymbol{X} appear in (2.45) instead of second derivatives in (2.40). Thus, the solution spaces \mathcal{U} and weighting spaces \mathcal{V} for the displacement field can be defined as

$$\mathcal{U} = \left\{ \boldsymbol{u} \in [H^1(\Omega)]^3 \mid \boldsymbol{u} = \hat{\boldsymbol{u}} \text{ on } \Gamma_u^{(i)} \right\}, \quad (2.46)$$

$$\mathcal{V} = \left\{ \delta \boldsymbol{u} \in [H^1(\Omega)]^3 \mid \delta \boldsymbol{u} = \mathbf{0} \text{ on } \Gamma_u \right\}. \quad (2.47)$$

Here, $H^1(\Omega)$ denotes the usual Sobolev space of functions with square integrable values and first derivatives, respectively. Finally, the weak formulation of the nonlinear solid mechanics problems can be stated as follows: Find $\mathbf{u} \in \mathcal{U}$ such that

$$\delta\mathcal{W} = 0 \quad \forall \delta\mathbf{u} \in \mathcal{V}. \quad (2.48)$$

2.2.2. Discretization in space

Throughout this thesis, spatial discretization is exclusively considered in the context of the finite element method. Thus, basic ideas and notations will be given but mathematical details on the derivation of the method are omitted. For more information, the interested reader is referred to the abundant literature, e.g. Bathe [13], Belytschko et al. [16], Reddy [228] and Zienkiewicz and Taylor [305]. The basic idea of the finite element method is to find a numerical solution to (2.48) at discrete points, commonly denoted as nodes. These nodes are connected to form elements, which approximate the partitioning of the considered domain Ω_0 , via

$$\Omega_0 \approx \bigcup_{e=1}^{n_{\text{ele}}} \Omega_0^{(e)}, \quad (2.49)$$

with the number of all elements n_{ele} and an individual element $\Omega_0^{(e)}$. Spatial discretization in the finite element context is commonly done with low-order Lagrangian polynomials, which satisfy differentiability requirements of the weak formulation. Thus, usually first order polynomials are adequate for the weak formulation derived in Section 2.2.1. These polynomials are employed to approximate the sought-after discrete solution, i.e. the displacement field for classical structure mechanics. In detail, they define the local interpolation functions $N_k(\xi)$, also known as shape functions, which are defined in a so-called parameter space ξ . Consequently, each element $\Omega_0^{(e)}$ is mapped to this parameter space.

The interpolation of the displacement field, the current geometry and the reference geometry can then be written as

$$\mathbf{u}_h(\xi, t) = \sum_{k=1}^{n_{\text{nod}}^{(e)}} N_k(\xi) \mathbf{d}_k(t), \quad (2.50)$$

$$\mathbf{x}_h(\xi, t) = \sum_{k=1}^{n_{\text{nod}}^{(e)}} N_k(\xi) \mathbf{x}_k(t), \quad (2.51)$$

$$\mathbf{X}_h(\xi) = \sum_{k=1}^{n_{\text{nod}}^{(e)}} N_k(\xi) \mathbf{X}_k. \quad (2.52)$$

Here, all spatially discretized quantities are denoted with $(\cdot)_h$ and the nodal positions in reference and spatial configuration are denoted with \mathbf{X}_k and $\mathbf{x}_k(t)$, respectively. The use of equal shape functions for the interpolation of reference and spatial geometry is based on the so-called isoparametric concept. The definitions given above allow for the use of several commonly employed finite element types. In this thesis, the following well-known 2D finite elements are employed: 3-node triangular (tri3), 6-node triangular (tri6), 4-node quadrilateral (quad4), 8-node

quadrilateral (quad8) and 9-node quadrilateral (quad9). In addition, the following 3D elements are used: 4-node tetrahedral (tet4), 10-node tetrahedral (tet10), 8-node hexahedral (hex8), 20-node hexahedral (hex20) and 27-node hexahedral (hex27). For the pure structural problem, the virtual displacements and the displacements are interpolated using the same shape functions, which is commonly referred to as Bubnov-Galerkin approach.

The contributions to the weak formulations are integrated element-wise by performing Gauss quadrature and then sorted into global vectors and matrices with a so-called assembly operator:

$$\int_{\Omega_0} (\cdot) dV_0 \approx \sum_{e=1}^{n_{ele}} \int_{\Omega_{0,h}^{(e)}} (\cdot) dV_0 . \quad (2.53)$$

When inserting the interpolation of the discrete quantities into the weak formulation, the spatially discrete problem formulation arises as

$$\delta \mathbf{d}^T (\mathbf{K}_{\text{mass}} \ddot{\mathbf{d}} + \mathbf{f}_{\text{int}}(\mathbf{d}) - \mathbf{f}_{\text{ext}}) = \mathbf{0} , \quad (2.54)$$

with the global mass matrix \mathbf{K}_{mass} , the global vector of nonlinear internal forces \mathbf{f}_{int} and the external forces \mathbf{f}_{ext} . The global vectors $\delta \mathbf{d}$, \mathbf{d} and $\ddot{\mathbf{d}}$ contain all discrete values of virtual displacements, displacements and accelerations. The vector length is equivalent to the number of degrees of freedom in the considered system and reads $n_{\text{dof}} = n_{\text{dim}} \cdot n_{\text{nod}}$, with the number of spatial dimensions n_{dim} and the total number of all nodes n_{nod} . Due to the demand, that (2.54) must hold for arbitrary virtual displacements $\delta \mathbf{d}$, it can equivalently be reformulated as

$$\mathbf{K}_{\text{mass}} \ddot{\mathbf{d}} + \mathbf{f}_{\text{int}}(\mathbf{d}) - \mathbf{f}_{\text{ext}} = \mathbf{0} , \quad (2.55)$$

which is also known as the semi-discrete equations of motion. In order to consider viscous damping effects, the Rayleigh damping model is usually introduced into the system (2.55), via

$$\mathbf{K}_{\text{mass}} \ddot{\mathbf{d}} + \mathbf{K}_{\text{damp}} \dot{\mathbf{d}} + \mathbf{f}_{\text{int}}(\mathbf{d}) - \mathbf{f}_{\text{ext}} = \mathbf{0} . \quad (2.56)$$

Here, the global vector $\dot{\mathbf{d}}$ contains all discrete nodal velocities and the matrix \mathbf{K}_{damp} represents the global damping matrix. It is defined in a purely phenomenological manner and reads:

$$\mathbf{K}_{\text{damp}} = r_m \mathbf{K}_{\text{mass}} + r_k \mathbf{K}_0 , \quad (2.57)$$

with the scalars r_m and r_k and the initial tangent stiffness matrix \mathbf{K}_0 .

2.2.3. Discretization in time

Since the focus of this thesis is on mortar methods, which represent spatial discretization schemes, the temporal discretization methods are only briefly introduced. For more details on time discretization in the context of nonlinear solid mechanics, the interested reader is exemplary referred to Belytschko et al. [16]. The spatially discretized system in (2.56) is going to be discretized in time by approximating the time derivatives by their difference quotients. Therefore, the considered time interval of interest $t \in [0, T]$ is subdivided into several intervals of equal and constant time step size Δt . In the following, a discrete time step is denoted as t_n with $n \in \mathbb{N}_0$.

Despite the computational efficiency of explicit time integration scheme, implicit methods are exclusively employed throughout this thesis due to their unconditionally stable characteristic. Thus, the final system to be solved is fully coupled and consists of n_{dof} nonlinear discrete algebraic equations for the n_{dof} unknown discrete displacements, which are represented by the unknown displacement vector \mathbf{d}_{n+1} at time step t_{n+1} . Consequently, the implicit methods require a more challenging implementation and more complex solution schemes compared to explicit time integrators. This is manifested in the requirement of a comprehensive and consistent linearization of the finite element formulation, which is a basic part of the following investigations in the context of mortar methods.

For all following investigations in the presence of nonlinear structures, the generalized- α method is employed, which was firstly introduced by Chung and Hulbert [43]. It is a so-called one-step time integration scheme and allows for expressing the unknown velocities \mathbf{v}_{n+1} and accelerations \mathbf{a}_{n+1} at the end of the considered time interval in terms of previously calculated quantities and the currently unknown displacement state \mathbf{d}_{n+1} :

$$\mathbf{v}_{n+1} = \frac{\gamma}{\beta \Delta t} (\mathbf{d}_{n+1} - \mathbf{d}_n) - \frac{\gamma - \beta}{\beta} \mathbf{v}_n - \frac{\gamma - 2\beta}{2\beta} \Delta t \mathbf{a}_n, \quad (2.58)$$

$$\mathbf{a}_{n+1} = \frac{1}{\beta \Delta t^2} (\mathbf{d}_{n+1} - \mathbf{d}_n) - \frac{1}{\beta \Delta t} \mathbf{v}_n - \frac{1 - 2\beta}{2\beta} \mathbf{a}_n. \quad (2.59)$$

Herein, $\beta \in [0, 0.5]$ and $\gamma \in [0, 1]$ are two basic parameters which characterize the method. By exclusively considering the above stated relations for the velocity and the acceleration, the well-known Newmark method results, which can be interpreted as basis for the following derivation. As its name implies, the generalized- α method introduces intermediate time levels $t_{n+1-\alpha_m}$ and $t_{n+1-\alpha_f}$, at which the terms in (2.56) are evaluated by employing linear interpolation rules. In consequence, the space and time discretized finite element formulation for nonlinear solid mechanics reads

$$\mathbf{K}_{\text{mass}} \mathbf{a}_{n+1-\alpha_m} + \mathbf{K}_{\text{damp}} \mathbf{v}_{n+1-\alpha_f} + \mathbf{f}_{\text{int}}(\mathbf{d}_{n+1-\alpha_f}) - \mathbf{f}_{\text{ext}, n+1-\alpha_f} = \mathbf{0}. \quad (2.60)$$

The set of time integration parameters β, γ, α_m and α_f can be harmonized by introducing the spectral radius ρ_∞ , which directly controls the numerical dissipation of the generalized- α scheme. Under consideration of the required properties of second-order accuracy and unconditional stability, the parameters can be optimized for minimal numerical dissipation and read

$$\alpha_m = \frac{2\rho_\infty - 1}{\rho_\infty + 1}, \quad \alpha_f = \frac{\rho_\infty}{\rho_\infty + 1}, \quad \beta = \frac{1}{4}(1 - \alpha_m + \alpha_f)^2, \quad \gamma = \frac{1}{2} - \alpha_m + \alpha_f. \quad (2.61)$$

For the special case of $\rho_\infty = 1$, no numerical dissipation is introduced into the system.

Finally, it should be noted that the generalized- α scheme is not able to conserve the total energy of the considered system over time. In order to achieve conservation of energy by construction, energy-momentum schemes have been developed in Gonzalez [90], Kuhl and Crisfield [142], Kuhl and Ramm [143] and Simo and Tarnow [252]. However, these types of time integrators are beyond the scope of this thesis and the generalized- α method is exclusively employed for all dynamic simulations.

2.2.4. Solution techniques

The derived system of nonlinear equations discretized in space and time in (2.60) has to be solved within each time step to obtain the displacements \mathbf{d}_{n+1} . In this thesis, the Newton-Raphson scheme is exclusively employed as iterative nonlinear solution technique. It is based on the definition of the discrete residual \mathbf{r} , which reads for the discrete nonlinear solution step i :

$$\mathbf{r}(\mathbf{d}_{n+1}^i) = \mathbf{K}_{\text{mass}} \mathbf{a}_{n+1-\alpha_m}^i + \mathbf{K}_{\text{damp}} \mathbf{v}_{n+1-\alpha_f}^i + \mathbf{f}_{\text{int}}(\mathbf{d}_{n+1-\alpha_f}^i) - \mathbf{f}_{\text{ext}, n+1-\alpha_f}. \quad (2.62)$$

In order to apply a Newton-Raphson scheme, the residual in (2.62) has to be linearized by a truncated Taylor expansion:

$$\text{Lin } \mathbf{r}(\mathbf{d}_{n+1}^i) = \mathbf{r}(\mathbf{d}_{n+1}^i) + \underbrace{\frac{\partial \mathbf{r}(\mathbf{d}_{n+1})}{\partial \mathbf{d}_{n+1}} \Big|_{\mathbf{d}_{n+1}^i}}_{\mathbf{K}(\mathbf{d}_{n+1}^i)} \Delta \mathbf{d}_{n+1}^{i+1}. \quad (2.63)$$

Herein, the partial derivative of the residual with respect to the displacements is identified as $\mathbf{K}(\mathbf{d}_{n+1}^i)$, which is the well-known dynamic effective tangential stiffness matrix of size $n_{\text{dof}} \times n_{\text{dof}}$. Then, it is searched for a displacement solution \mathbf{d}_{n+1} , for which the residual $\mathbf{r}(\mathbf{d}_{n+1})$ vanishes. This is achieved by requiring that the linearized residual vanishes for each nonlinear solution step:

$$\text{Lin } \mathbf{r}(\mathbf{d}_{n+1}^i) = \mathbf{0}. \quad (2.64)$$

Consequently, the linear system to be solved reads

$$\mathbf{K}(\mathbf{d}_{n+1}^i) \Delta \mathbf{d}_{n+1}^{i+1} = -\mathbf{r}(\mathbf{d}_{n+1}^i). \quad (2.65)$$

When the system in (2.65) is solved, the displacement solution is updated via

$$\mathbf{d}_{n+1}^{i+1} = \mathbf{d}_{n+1}^i + \Delta \mathbf{d}_{n+1}^{i+1} \quad (2.66)$$

and the iteration counter is increased by one, i.e. $i \rightarrow i + 1$. The solving step in (2.65) and the update in (2.66) are repeatedly performed until a certain user-defined convergence criterion is met. This criterion is usually stated as L^2 -norm of the residual $\|\mathbf{r}(\mathbf{d}_{n+1}^i)\|$. If the start estimate \mathbf{d}_{n+1}^0 is sufficiently close to the solution \mathbf{d}_{n+1} , the residual norm approaches zero with a quadratic convergence rate. In other words, the start estimate should be chosen to be within the problem-dependent convergence radius in order to achieve optimal expected (quadratic) convergence for the Newton-Raphson scheme.

For all following problems in this thesis, the complete (full) Newton-Raphson scheme as explained above is exclusively utilized. For computational contact problems, its semi-smooth variants with contact constraints being included are introduced in the next chapter. For problems with multiple unknowns, i.e. contact (displacements, Lagrange multipliers) or general monolithic multiphysics problems such as thermo-structure interaction, the Newton-Raphson scheme is extended and the partial derivatives of the residual are performed with respect to all unknown vectors. However, the computational costs for creating the respective system matrices, i.e. $\mathbf{K}(\mathbf{d}_{n+1}^i)$ for structural problems, could be considerably high because it requires a consistent

linearization of all involved terms within each Newton-Raphson step. Alternative solution procedures are quasi-Newton methods or modified Newton methods, which are based on a cheaper approximation of the system matrix, but are not able to achieve quadratic convergence rates.

The solution procedures for the linear system of equations in (2.65) are not in the focus of this thesis, even though it could be identified as most expensive part of the overall solution process for large finite element models. For more information concerning the solution of sparse linear systems, the interested reader is referred to the books of Quarteroni et al. [222] and Saad [237].

3. Fundamentals on Mortar Methods for Computational Contact Mechanics

In this chapter, the basics on computational contact mechanics employing the mortar method are given. All following explanations are referred to classically assumed surface-to-surface contact scenarios in 3D and novel extensions towards more general scenarios are introduced in Chapter 4. The first two sections provide a brief introduction to the most important notations and concepts of contact mechanics including contact kinematics and the constraint equations for unilateral contact as well as frictional sliding. Further details on these topics can be found in classical textbooks on contact mechanics, such as Johnson [130], Kikuchi and Oden [134], Laursen [151] and Wriggers [293]. Then, the derivation of the variationally consistent weak formulation of the surface-to-surface contact problem employing a Lagrange multiplier approach is briefly explained followed by the introduction of the mortar finite element discretization. Finally, information concerning the global solution scheme is provided. All given details on the mortar method in the context of computational contact mechanics have already been well investigated and can be found in Gitterle [87], Gitterle et al. [88], Popp [210], Popp et al. [211, 212] and Puso and Laursen [218, 219].

3.1. Contact kinematics

In order to describe the kinematics of contact, multiple different scenarios could be considered, such as contact of an elastic body with a rigid foundation, selfcontact of a flexible structure or multi-body contact. While the creation of specific algorithms for these scenarios could become essential for numerical simulations, their kinematics and the contact constraints are derived with the classical model of two interacting elastic bodies. Thus, the two deformable bodies $\mathcal{B}^{(1)}$ and $\mathcal{B}^{(2)}$ with one shared contact interface are considered as visualized in Figure 3.1. In the following, the well-established nomenclature of $\mathcal{B}^{(1)}$ being the *slave* body and $\mathcal{B}^{(2)}$ being the *master* body is used. The distinction into slave and master body is not necessarily required for the continuum mechanical contact model, but becomes very advantageous in the context of finite element discretizations. The open sets $\Omega_0^{(i)} \subset \mathbb{R}^3$ and $\Omega_t^{(i)} \subset \mathbb{R}^3$ for $i = 1, 2$ represent the bodies in the material configuration and the spatial configuration, respectively. Due to the potential contact interaction of the two bodies, their material boundaries are divided into three disjoint sets as

$$\partial\Omega_0^{(i)} = \Gamma_u^{(i)} \cup \Gamma_\sigma^{(i)} \cup \Gamma_c^{(i)}, \quad (3.1)$$

$$\Gamma_u^{(i)} \cap \Gamma_\sigma^{(i)} = \Gamma_u^{(i)} \cap \Gamma_c^{(i)} = \Gamma_\sigma^{(i)} \cap \Gamma_c^{(i)} = \emptyset, \quad (3.2)$$

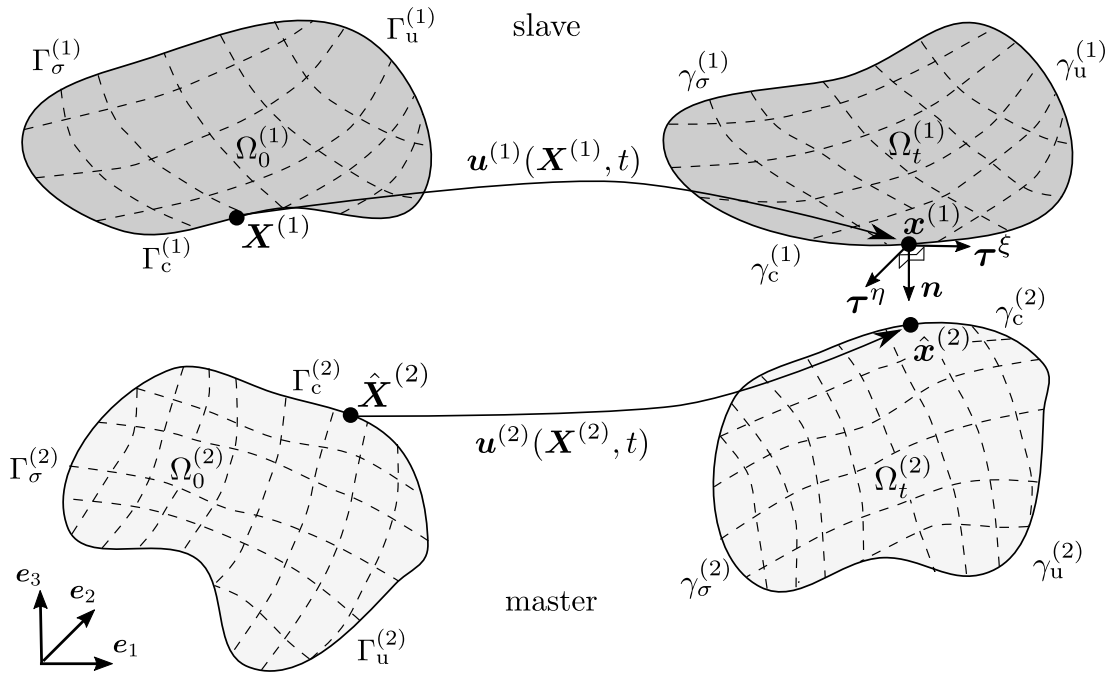


Figure 3.1: Kinematic and basic notation for the contact description of two deformable bodies.

where additionally to the Dirichlet and Neumann boundaries, the boundaries of potential contact $\Gamma_c^{(i)}$ are introduced. Their counterparts in the spatial configuration are denoted as $\gamma_u^{(i)}$, $\gamma_\sigma^{(i)}$ and $\gamma_c^{(i)}$. One of the characteristics of contact problems is that the actual, so-called active part of the contact boundary $\Gamma_a^{(i)} \subseteq \Gamma_c^{(i)}$ is a-priori unknown and possibly changing over time. Consequently, the currently inactive part of the contact boundary is defined by $\Gamma_i^{(i)} = \Gamma_c^{(i)} \setminus \Gamma_a^{(i)}$.

The fundamental quantity for describing contact kinematics is the *gap vector*

$$\mathbf{g}(\mathbf{X}, t) = [\mathbf{x}^{(1)}(\mathbf{X}^{(1)}, t) - \hat{\mathbf{x}}^{(2)}(\hat{\mathbf{X}}^{(2)}(\mathbf{X}^{(1)}, t), t)]. \quad (3.3)$$

It represents the relative position vector between a spatial point $\mathbf{x}^{(1)}$ on the slave side and the corresponding master point $\hat{\mathbf{x}}^{(2)}$. The master point can be identified by performing a so-called closest point projection (CPP), which is mathematically written as

$$\hat{\mathbf{x}}^{(2)} = \arg \min_{\mathbf{x}^{(2)} \in \gamma_c^{(2)}} \|\mathbf{x}^{(1)} - \mathbf{x}^{(2)}\|, \quad (3.4)$$

with $\|\cdot\|$ denoting the L^2 -norm in \mathbb{R}^3 . A general CPP for all possibly arising contact scenarios introduces a broad range of difficulties, such as non-uniqueness and a lot of pathological effects, see Konyukhov and Schweizerhof [139]. Following the concept presented in Popp et al. [212], the outward unit normal to the current slave surface $\gamma_c^{(1)}$ is considered as contact normal \mathbf{n} to overcome the mentioned problems. However, this is only a valid assumption when smooth surface-to-surface contact scenarios are considered. Later on in Chapter 4, a modified version of the CPP based on smoothed interface mappings is employed to provide a proper normal definition for contact of vertices, edges and surfaces. Then, the master point $\hat{\mathbf{x}}^{(2)}$ is calculated via a projection of the slave point $\mathbf{x}^{(1)}$ along the master side outward unit normal and consequently

this normal with changed sign is defined to act as slave normal. Details on the numerical evaluation in the context of spatial finite element discretization is given in Section 4.4. Together with the two tangential vectors τ^ξ and τ^η from the tangential plane, the normal \mathbf{n} forms a set of orthonormal basis vectors in the slave point $\mathbf{x}^{(1)}$.

Derived from the gap vector \mathbf{g} , the so-called *gap function* g_n in the spatial configuration acts as fundamental measure for proximity and penetration and is introduced as:

$$g_n = -\mathbf{n} \cdot \mathbf{g}. \quad (3.5)$$

While the gap function obviously characterizes the contact interaction in normal direction, the primary geometrical quantity for the tangential contact interaction is the *relative tangential velocity* $\mathbf{v}_{\tau,\text{rel}}$. In contrast to the gap function, it represents a rate measure, which introduces additional complexity. For the definition of the relative tangential velocity, a perfect sliding state is assumed. This leads to the requirement, that the gap vector in (3.3) and its time derivative vanish

$$\mathbf{g} = \mathbf{0}, \quad \frac{d}{dt} \mathbf{g} = \mathbf{0}. \quad (3.6)$$

Considering the time derivative of the gap vector in detail yields

$$\frac{d}{dt} \mathbf{g} = \frac{d}{dt} (\mathbf{x}^{(1)} - \hat{\mathbf{x}}^{(2)}) \quad (3.7)$$

$$= \dot{\mathbf{x}}^{(1)} - \dot{\hat{\mathbf{x}}}^{(2)} - \mathbf{v}_{\text{rel}} = \mathbf{0}. \quad (3.8)$$

Here, the relative velocity \mathbf{v}_{rel} follows from the time derivative of the geometrical point projection and can be written in two different ways. First, the formulation using so-called *slip advected bases* is widely employed in the context of node-to-segment contact, see Chawla and Laursen [40], Laursen [151], Laursen and Simo [154], Pietrzak and Curnier [207] and Wriggers [293]. However, this formulation is not considered in this contribution and mathematical details are omitted. Instead, the relative velocity is expressed in terms of material velocities. Therefore, (3.8) is employed under the assumption of perfect sliding, which yields

$$\mathbf{v}_{\text{rel}} = \dot{\mathbf{x}}^{(1)} - \dot{\hat{\mathbf{x}}}^{(2)}. \quad (3.9)$$

In case of strongly curved surfaces, the relative velocity is not completely defined in the tangential plane. This can be ensured by explicitly performing a projection in the tangential plane, which yields the relative tangential velocity:

$$\mathbf{v}_{\tau,\text{rel}} = (\mathbf{I} - \mathbf{n} \otimes \mathbf{n}) \cdot [\dot{\mathbf{x}}^{(1)} - \dot{\hat{\mathbf{x}}}^{(2)}]. \quad (3.10)$$

Note that in contrast to the formulation in slip advected bases, the expression in (3.10) does not fulfill the fundamental requirement of frame indifference since it does not include the CPP of the slave point $\mathbf{x}^{(1)}$. However, it is commonly used for mortar finite element discretizations and also employed in this thesis. The lack of consistency is tackled by the spatial discretization in Section 3.4.

In analogy to the gap function and the relative tangential velocity, the contact traction vector $\mathbf{t}_c^{(1)}$ on the slave side can be split into its normal and tangential components, yielding

$$\mathbf{t}_c^{(1)} = p_n \mathbf{n} + \mathbf{t}_\tau^{(1)}. \quad (3.11)$$

Here, the normal pressure is denoted with p_n and the tangential traction reads \mathbf{t}_τ . Due to the balance of linear momentum, the traction vectors on the slave side and on the master side are identical except for the opposite signs:

$$\mathbf{t}_c^{(1)} = -\mathbf{t}_c^{(2)}. \quad (3.12)$$

With the contact traction being introduced, the so-called *interface dissipation rate density* can be defined in spatial configuration via

$$\dot{d} = \|\mathbf{t}_\tau\| \|\mathbf{v}_{\tau,\text{rel}}\|. \quad (3.13)$$

Here, it is obvious that the dissipation rate density occurs only if tangential tractions are present. Thus, it is also known as frictional dissipation rate density. It is related with its counterpart \dot{D} in the material configuration via the area transformation factor $j_a = \frac{dA}{dA_0}$:

$$\dot{D} = j_a \dot{d}. \quad (3.14)$$

3.2. Contact constraints

In the following, the constraints for tied contact, normal contact and frictional sliding are given.

3.2.1. Tied contact constraints

Tied contact, also known as mesh tying in the context of finite element discretization does not classically belong to contact problems, but shares a lot of conceptual similarities. It is a well-established domain decomposition technique for nonlinear solid mechanics problems and is employed in this thesis to allow for mesh refinement near the contact interfaces by simply creating a fine finite element layer around the body. The condition for tied contact is that no relative movement at the interface between the two domains is allowed. This can be stated as vector valued constraint:

$$\mathbf{g} = \mathbf{0}. \quad (3.15)$$

Thus, no distinction between normal and tangential directions at the interface is necessary. Details on mortar mesh tying formulations are not given in this thesis, but the interested reader is exemplarily referred to Hesch and Betsch [103], Puso [216], Puso and Laursen [217] and Wohlmuth [288].

3.2.2. Normal contact constraints

The normal contact constraints are necessary to define that the two considered bodies are not allowed to overlap. This is mathematically written in form of the well-known Hertz-Signorini-Moreau conditions:

$$g_n \geq 0, \quad p_n \leq 0, \quad p_n g_n = 0. \quad (3.16)$$

Here, the introduced gap function g_n and the normal contact pressure p_n are utilized to describe the normal contact. The first condition in (3.16) describes that either the points are not in contact ($g_n > 0$) or the gap function equals zero, while a penetration state ($g_n < 0$) is not allowed. The second condition implies that no adhesion stresses are allowed in the contact zone. Finally, the third condition in (3.16) is the well-known complementarity condition, which forces the gap to be zero if stresses occur and the contact pressure to be zero if the gap is open.

Remark 3.1. *In the context of dynamics, the so-called persistency condition is employed in order to construct energy conserving algorithms. It can be written as*

$$p_n \dot{g}_n = 0. \quad (3.17)$$

Here, the first time derivative \dot{g}_n of the gap function is utilized to demand that the contact pressure is only non-zero when the bodies are in contact and remain in contact. This is called persistent contact. However, this condition is not employed in this thesis since the main focus is set on mortar methods and not on time integration schemes. For more details on this condition in the context of energy conserving time integrators, the interested reader is exemplarily referred to Laursen and Chawla [152] and Laursen and Love [153].

3.2.3. Frictional contact constraints

The tangential contact constraints are defined by the frictional response to tangential loading. In this thesis, tangential effects are considered in a pure macroscopic manner. Thus, for the law of dry friction, *Coulomb's law* is utilized. It is given by

$$\Upsilon := \|\mathbf{t}_\tau\| - \mathfrak{F}|p_n| \leq 0, \quad \mathbf{v}_{\tau,\text{rel}} + \beta \mathbf{t}_\tau = \mathbf{0}, \quad \beta \geq 0, \quad \Upsilon \beta = 0. \quad (3.18)$$

Here, the friction coefficient $\mathfrak{F} \geq 0$ is assumed to be constant, which is a simplification to load depending coefficients resulting from experimental data, see for example Ben-David and Fineberg [22] and Persson et al. [204]. However, the algorithms presented in the following chapters are not restricted to this assumption and could easily be extended towards a state or temperature dependent friction law. In addition, Υ is the so-called slip function and the parameter β is a complementarity parameter, which is necessary to describe the separation of the stick and slip branch. In the case of $\beta = 0$, no relative movement is allowed and thus it represents the stick state, see the second statement in (3.18). The last relation (3.18) describes the complementarity condition, which states that if $\beta > 0$, the slip function yields zero. This is achieved when the tangential stress is equivalent to the Coulombs limit of $\mathfrak{F}|p_n|$.

Coulomb's law is not the only frictional model available in literature. Alternatively, *Tresca's friction law* could be used, which is independent from the contact pressure. However, Coulomb's law is exclusively considered in the following.

3.3. Weak formulation for contact

Throughout this thesis, the inequality constraints arising from normal contact in (3.16) and tangential contact in (3.18) are predominantly enforced with the Lagrange multiplier method. Thus,

the following explanations are completely devoted to this approach and are based on the investigations made in Gitterle [87], Gitterle et al. [88], Popp [210], Popp et al. [211, 212, 214] and Wohlmuth [290]. However, special scenarios resulting from contact of vertices, edges and surfaces are treated with a penalty regularization, which is explained later on in Chapter 4. It is worth to mention, that in the existing literature on computational contact mechanics, also various publications of mortar methods with penalty regularization and augmented Lagrangian methods can be found, see for example Cavalieri and Cardona [38], Fischer and Wriggers [81], Laursen [151], Puso and Laursen [218, 219], Puso et al. [220] and Yang et al. [301]. In addition, Nitsche's method, which was originally published in Nitsche [183], becomes more and more topic of current research and approaches for computational contact mechanics can be found in Chouly and Hild [41], Mlika et al. [174] and Wriggers and Zavarise [295].

Starting point for deriving a weak formulation is the recapitulation of the well-known solution spaces $\mathcal{U}^{(i)}$ and weighting spaces $\mathcal{V}^{(i)}$ for the displacement field:

$$\mathcal{U}^{(i)} = \left\{ \mathbf{u}^{(i)} \in H^1(\Omega) \mid \mathbf{u}^{(i)} = \hat{\mathbf{u}}^{(i)} \text{ on } \Gamma_u \right\}, \quad (3.19)$$

$$\mathcal{V}^{(i)} = \left\{ \delta \mathbf{u}^{(i)} \in H^1(\Omega) \mid \delta \mathbf{u}^{(i)} = \mathbf{0} \text{ on } \Gamma_u \right\}. \quad (3.20)$$

In order to define a variationally consistent weak formulation of the contact constraints and the contact contributions to the balance of equations, a vector-valued Lagrange multiplier $\boldsymbol{\lambda}$ is introduced as negative slave side contact traction:

$$\boldsymbol{\lambda} = -\mathbf{t}_c^{(1)}. \quad (3.21)$$

In complete analogy to the contact traction, it can be decomposed into its normal part and tangential parts, via

$$\boldsymbol{\lambda} = \lambda_n \mathbf{n} + \boldsymbol{\lambda}_\tau. \quad (3.22)$$

Obviously, the normal part of the Lagrange multiplier λ_n can be identified as negative normal contact pressure $-p_n$ on the slave side and the tangential part $\boldsymbol{\lambda}_\tau$ equals the negative slave side tangential traction $-\mathbf{t}_\tau$. In the following, the contact constraints are reformulated in a variationally consistent manner as stated in Christensen et al. [42], Hüeber [114], Strömberg [260], Wohlmuth [290] and Wriggers [293]. For this purpose, the normal part of the Lagrange multiplier is utilized to enforce the contact constraints in normal direction (3.16) and the tangential Lagrange multiplier vector is used for the frictional constraints in (3.18):

$$\lambda_n \in \mathbb{R}_0^+ : g_n(\delta \lambda_n - \lambda_n) \geq 0 \quad \forall \delta \lambda_n \in \mathbb{R}_0^+, \quad (3.23)$$

$$\boldsymbol{\lambda}_\tau \in \mathcal{T}(\mathfrak{F}\lambda_n) : \mathbf{v}_{\tau,\text{rel}}(\delta \boldsymbol{\lambda}_\tau - \boldsymbol{\lambda}_\tau) \leq 0 \quad \forall \delta \boldsymbol{\lambda}_\tau \in \mathcal{T}(\mathfrak{F}\lambda_n). \quad (3.24)$$

Herein, the normal part of the Lagrange multiplier is only allowed to be in the semi-positive real half space \mathbb{R}_0^+ . In addition, the projection of the Lagrange multiplier into the tangential plane is restricted to $\mathcal{T}(\mathfrak{F}\lambda_n)$, which represents a circle with center $\mathbf{0}$ and radius $\mathfrak{F}\lambda_n$ and can be interpreted as principle of maximum dissipation in the context of Coulomb's law of friction, see Strömberg [260]. Equivalence of the contact constraints in (3.16) and (3.18) and their counterparts formulated as variational inequalities in (3.23) and (3.24) is shown in Wohlmuth [290].

According to investigations in Hüeber [114], the solution space \mathcal{M} for the Lagrange multiplier is defined as the convex cone

$$\mathcal{M}(\boldsymbol{\lambda}) = \left\{ \boldsymbol{\mu} \in \mathcal{M} \mid \langle \boldsymbol{\mu}, \mathbf{v} \rangle_{\gamma_c^{(1)}} \leq \langle \mathfrak{F}\lambda_n, \|\mathbf{v}_\tau\| \rangle_{\gamma_c^{(1)}}, \quad \mathbf{v} \in \mathcal{W} \text{ with } v_n \leq 0 \right\}, \quad (3.25)$$

which accommodates the restrictions in (3.23) and (3.24). In (3.25), \mathcal{M} is the dual space of the trace space $\mathcal{W}^{(1)}$ of $\mathcal{V}^{(1)}$ restricted to $\gamma_c^{(1)}$, i.e. $\mathcal{M} = H^{-1/2}(\gamma_c^{(1)})$ and $\mathcal{W}^{(1)} = H^{1/2}(\gamma_c^{(1)})$, where \mathcal{M} and $\mathcal{W}^{(1)}$ denote single scalar components of the corresponding vector-valued spaces \mathcal{M} and $\mathcal{W}^{(1)}$.

The definition of the weak formulation for frictional contact problems can be achieved by extending the standard weak form for nonlinear solid mechanics in (2.45) to two bodies and adding the specific Lagrange multiplier contributions. Thus, the weak saddle point type formulation can be summarized as: Find $\mathbf{u}^{(i)} \in \mathcal{U}^{(i)}$ and $\boldsymbol{\lambda} \in \mathcal{M}(\boldsymbol{\lambda})$ such that

$$-\delta\mathcal{W}_{\text{kin,int,ext}}(\mathbf{u}^{(i)}, \delta\mathbf{u}^{(i)}) - \delta\mathcal{W}_{\text{co}}(\boldsymbol{\lambda}, \delta\mathbf{u}^{(i)}) = 0 \quad \forall \delta\mathbf{u}^{(i)} \in \mathcal{V}^{(i)}, \quad (3.26)$$

$$\delta\mathcal{W}_{\lambda_n}(\mathbf{u}^{(i)}, \delta\lambda_n) \geq 0 \quad \forall \delta\boldsymbol{\lambda} \in \mathcal{M}(\boldsymbol{\lambda}),$$

$$\delta\mathcal{W}_{\lambda_\tau}(\mathbf{u}^{(i)}, \delta\lambda_\tau) \leq 0 \quad \forall \delta\boldsymbol{\lambda} \in \mathcal{M}(\boldsymbol{\lambda}) \quad (3.27)$$

Here, the kinetic contribution $\delta\mathcal{W}_{\text{kin}}$ as well as the internal and external virtual work $\delta\mathcal{W}_{\text{int,ext}}$ are independent from the contact terms. In contrast to the standard terms, the contact virtual work $\delta\mathcal{W}_{\text{co}}$ and the corresponding weak constraints in normal and tangential direction $\delta\mathcal{W}_{\lambda_n}$ and $\delta\mathcal{W}_{\lambda_\tau}$ shall be presented for the sake of clarity:

$$-\delta\mathcal{W}_{\text{co}} = \int_{\gamma_c^{(1)}} \boldsymbol{\lambda}(\delta\mathbf{u}^{(1)} - \delta\mathbf{u}^{(2)} \circ \chi) \, dA, \quad (3.28)$$

$$\delta\mathcal{W}_{\lambda_n} = \int_{\gamma_c^{(1)}} (\delta\lambda_n - \lambda_n) g_n \, dA, \quad (3.29)$$

$$\delta\mathcal{W}_{\lambda_\tau} = \int_{\gamma_c^{(1)}} (\delta\boldsymbol{\lambda}_\tau - \boldsymbol{\lambda}_\tau) \mathbf{v}_{\tau,\text{rel}} \, dA. \quad (3.30)$$

Within the contact virtual work, a suitable contact interface mapping $\chi : \gamma_c^{(1)} \rightarrow \gamma_c^{(2)}$ is required because the identity of the two involved boundaries $\gamma_c^{(1)}$ and $\gamma_c^{(2)}$ cannot be guaranteed in general.

3.4. Mortar finite element discretization

Mortar methods were originally introduced as domain decomposition method for spectral elements in Maday et al. [160] and were successfully applied to finite elements. They became the state-of-the-art discretization approach for various coupled problems. In the context of computational contact mechanics, mortar finite element methods are applied for discretizing the contact interfaces of the two bodies. Thus, spatial discretization of the displacement field and the geometry at the interfaces are required. For the spatial discretization of the considered frictional contact problem using finite elements, the finite dimensional subsets $\mathcal{U}_h^{(i)}$ and $\mathcal{V}_h^{(i)}$ representing approximations of the continuous solution spaces $\mathcal{U}^{(i)}$ and $\mathcal{V}^{(i)}$ are introduced. In the following, the exclusive focus is on the finite element discretization of the contact terms. Therefore, the Lagrange multiplier as well as the displacement interpolation must be defined on the potential

contact boundaries $\Gamma_{c,h}^{(i)}$ based on the trace space of the underlying problem discretization. Again, the subscript $(\cdot)_h$ refers to a spatially discretized quantity. First, the displacement interpolation and the geometry representation read

$$\boldsymbol{x}_h^{(1)}|_{\Gamma_{c,h}^{(1)}} = \sum_{k=1}^{n^{(1)}} N_k^{(1)} \boldsymbol{x}_k^{(1)}, \quad \boldsymbol{x}_h^{(2)}|_{\Gamma_{c,h}^{(2)}} = \sum_{l=1}^{n^{(2)}} N_l^{(2)} \boldsymbol{x}_l^{(2)}, \quad (3.31)$$

$$\boldsymbol{u}_h^{(1)}|_{\Gamma_{c,h}^{(1)}} = \sum_{k=1}^{n^{(1)}} N_k^{(1)} \boldsymbol{d}_k^{(1)}, \quad \boldsymbol{u}_h^{(2)}|_{\Gamma_{c,h}^{(2)}} = \sum_{l=1}^{n^{(2)}} N_l^{(2)} \boldsymbol{d}_l^{(2)}. \quad (3.32)$$

Here, the total number of slave and master interface nodes is given by $n^{(1)}$ and $n^{(2)}$. Additionally, the discrete nodal displacements are represented by $\boldsymbol{d}_k^{(1)}$ and $\boldsymbol{d}_l^{(2)}$. Based on the usually employed finite element parameter space for 2D surfaces $\boldsymbol{\xi}^{(i)} = (\xi^{(i)}, \eta^{(i)})$, the shape functions $N_k^{(1)}$ and $N_l^{(2)}$ are introduced. Throughout this thesis, well established first- and second-order element types in 2D and 3D settings are employed for the bulk discretization, see Section 2.2.2. Thus, the discretization of the contact interfaces naturally results from the bulk elements. As an example, a finite element mesh of hex8 elements yields a contact interface discretization that consists of quad4 elements.

In addition to the displacements, an adequate discretization of the vector-valued Lagrange multiplier is required and will be based on the discrete approximation $\boldsymbol{\mathcal{M}}_h(\boldsymbol{\lambda}_h)$ of $\boldsymbol{\mathcal{M}}(\boldsymbol{\lambda})$. The choice of $\boldsymbol{\mathcal{M}}_h(\boldsymbol{\lambda}_h)$ is widely discussed in the literature and the Subsection 3.4.1 is completely devoted to this topic. Thus, only a very general notation is given here:

$$\boldsymbol{\lambda}_h = \sum_{j=1}^{m^{(1)}} \Phi_j \boldsymbol{\lambda}_j, \quad (3.33)$$

with the total number of all nodes $m^{(1)}$ carrying discrete Lagrange multipliers. Commonly, all nodes on the slave side carry discrete Lagrange multiplier degrees of freedom, i.e. $m^{(1)} = n^{(1)}$. However, in the context of second-order finite elements it could be beneficial to adapt this choice to $m^{(1)} < n^{(1)}$, which is explained in detail in Popp et al. [213], Puso et al. [220] and Wohlmuth et al. [291]. The shape functions for the Lagrange multiplier interpolation in (3.33) are denoted with Φ_j . Inserting (3.32) and (3.33) into the contact virtual work in (3.28) yields

$$-\delta \mathcal{W}_{co,h} = \sum_{j=1}^{m^{(1)}} \sum_{k=1}^{n^{(1)}} \boldsymbol{\lambda}_j^T \left(\int_{\gamma_{c,h}^{(1)}} \Phi_j N_k^{(1)} dA \right) \delta \boldsymbol{d}_k^{(1)} - \sum_{j=1}^{m^{(1)}} \sum_{l=1}^{n^{(2)}} \boldsymbol{\lambda}_j^T \left(\int_{\gamma_{c,h}^{(1)}} \Phi_j (N_l^{(2)} \circ \chi_h) dA \right) \delta \boldsymbol{d}_l^{(2)}, \quad (3.34)$$

with the discrete mapping $\chi_h : \gamma_{c,h}^{(1)} \rightarrow \gamma_{c,h}^{(2)}$ from the slave to the master side, see Dickopf and Krause [60] and Puso [216] for more information about the interface mapping. By considering (3.34), the well-known mortar matrices \mathbf{D} and \mathbf{M} can be identified, which consist of the following nodal blocks:

$$\mathbf{D}[j, k] = D_{jk} \mathbf{I}_3 = \int_{\gamma_{c,h}^{(1)}} \Phi_j N_k^{(1)} dA \mathbf{I}_3, \quad j = 1, \dots, m^{(1)}, \quad k = 1, \dots, n^{(1)}, \quad (3.35)$$

$$\mathbf{M}[j, l] = M_{jl} \mathbf{I}_3 = \int_{\gamma_{c,h}^{(1)}} \Phi_j (N_l^{(2)} \circ \chi_h) dA \mathbf{I}_3, \quad j = 1, \dots, m^{(1)}, \quad l = 1, \dots, n^{(2)}, \quad (3.36)$$

where $\mathbf{I}_3 \in \mathbb{R}^{3 \times 3}$ is the identity matrix. Details on the numerical integration procedures are given in Section 3.4.2. In order to guarantee for an easy notation, all displacement degrees of freedom in the global displacement vector \mathbf{d} are sorted into three groups: a group where all degrees of freedom associated to bulk nodes are contained \mathcal{N} , a group with all degrees of freedom on the slave interface \mathcal{S} and a group with all degrees of freedom on the master interface \mathcal{M} . Consequently, the global displacement vector can be written as

$$\mathbf{d} = (\mathbf{d}_{\mathcal{N}}, \mathbf{d}_{\mathcal{M}}, \mathbf{d}_{\mathcal{S}}). \quad (3.37)$$

Based on this split, the discrete contact virtual work can be stated in algebraic form

$$-\delta \mathcal{W}_{\text{co},h} = \delta \mathbf{d}^T [\mathbf{0} \quad -\mathbf{M} \quad \mathbf{D}]^T \boldsymbol{\lambda} = \delta \mathbf{d}^T \mathbf{f}_c(\mathbf{d}, \boldsymbol{\lambda}), \quad (3.38)$$

with the vector of discrete contact forces \mathbf{f}_c . With the discrete contact virtual work being defined, the semi-discrete form of balance of linear momentum in (2.56) can be extended to contact problems via

$$\mathbf{r} := \mathbf{K}_{\text{mass}} \ddot{\mathbf{d}} + \mathbf{K}_{\text{damp}} \dot{\mathbf{d}} + \mathbf{f}_{\text{int}}(\mathbf{d}) - \mathbf{f}_{\text{ext}} + \mathbf{f}_c(\mathbf{d}, \boldsymbol{\lambda}) = \mathbf{0}. \quad (3.39)$$

Here, the global contact force vector \mathbf{f}_c , which depends on the current deformation state (i.e. \mathbf{d}) and the Lagrange multipliers $\boldsymbol{\lambda}$, is added to the classic balance of linear momentum.

Discretization of the weak contact constraint in normal direction in (3.29) yields a discrete weighted gap at each slave node j , viz.

$$\tilde{g}_{n,j} = \int_{\gamma_{c,h}^{(1)}} \Phi_j g_{n,h} \, dA. \quad (3.40)$$

Herein, $g_{n,h}$ is the discrete counterpart of the gap function g_n introduced in (3.5). The discrete weighted gap $\tilde{g}_{n,j}$ represents a volumetric measure, since it results from integrating a distance quantity ($g_{n,h}$) over the discrete slave contact surface $\gamma_{c,h}^{(1)}$. Nevertheless, it is utilized as node-wise measure for proximity and is included in the discrete set of node-wise Hertz-Signorini-Moreau conditions:

$$\tilde{g}_{n,j} \geq 0 \quad \lambda_{n,j} \geq 0, \quad \lambda_{n,j} \tilde{g}_{n,j} = 0, \quad j = 1, \dots, m^{(1)}. \quad (3.41)$$

It is shown in great detail in Hüeber [114], that this set of discrete conditions is equivalent to the discretized version of the weak formulation in (3.28) and (3.29).

Remark 3.2. *The shape function Φ_j for the definition of the discrete weighted gap function in (3.40) represents the interpolation of the variation of the discrete Lagrange multiplier vector $\delta \boldsymbol{\lambda}$. For this, it is implicitly assumed that a well-known Bubnov-Galerkin approach was followed which leads to same shape functions for the Lagrange multiplier and its variation. By employing so-called dual shape functions, which will be explained in Section 3.4.1.2, it could be advantageous to follow a Petrov-Galerkin approach and employ the introduced displacement shape functions N_j for the interpolation of the variation of the discrete Lagrange multipliers.*

This is explained in great detail in Popp et al. [214]. Consequently, the discrete weighted gap for a Petrov-Galerkin approach would read

$$\tilde{g}_{n,j} = \int_{\gamma_{c,h}^{(1)}} N_j g_{n,h} dA. \quad (3.42)$$

In this thesis, the Petrov-Galerkin approach is also employed for mortar contact of non-smooth geometries in Chapter 4.

Similar to the discrete weighted gap, the relative tangential velocity in its discrete form $(\tilde{\mathbf{v}}_{\tau,\text{rel}})_j$ results from discretizing the weak frictional sliding constraint (3.30), viz.

$$(\tilde{\mathbf{v}}_{\tau,\text{rel}})_j = (\mathbf{I}_3 - \mathbf{n}_j \otimes \mathbf{n}_j) \cdot \left[\sum_{l=1}^{n^{(2)}} \dot{\mathbf{M}}[j, l] \mathbf{x}_l^{(2)} - \sum_{k=1}^{n^{(1)}} \dot{\mathbf{D}}[j, k] \mathbf{x}_k^{(1)} \right]. \quad (3.43)$$

Here, \mathbf{n}_j is the discrete unit normal at slave node j . Comparing (3.43) with its continuous form in (3.10), the material velocities of the points are expressed as time derivatives of the mortar matrices. This guarantees the satisfaction of the fundamental requirement of frame indifference, which was originally shown in Puso and Laursen [218] and was later on applied in Farah et al. [69, 73, 74], Gitterle et al. [88], Puso and Laursen [219], Yang and Laursen [298] and Yang et al. [301]. The discrete form of the variational inequality in (3.30) can equivalently be reformulated into the following discrete set of equations:

$$\begin{aligned} \Upsilon_j &:= \|(\boldsymbol{\lambda}_\tau)_j\| - \mathfrak{F}|\lambda_{n,j}| \leq 0, \\ (\tilde{\mathbf{v}}_{\tau,\text{rel}})_j + \beta_j (\boldsymbol{\lambda}_\tau)_j &= \mathbf{0}, \quad \beta_j \geq 0, \quad \Upsilon_j \beta_j = 0, \quad j = 1, \dots, n^{(1)}. \end{aligned} \quad (3.44)$$

Finally, the semi discrete problem formulation for frictional contact problems consists of the discrete balance of linear momentum with contact terms being applied in (3.39) together with the discrete equations for the non-penetration conditions in (3.41) and the conditions for the frictional sliding in (3.44).

3.4.1. Discrete Lagrange multiplier spaces

The discrete counterpart \mathcal{M}_h of the continuous Lagrange multiplier space \mathcal{M} was already introduced in the previous section, but not yet specified in detail. However, the choice of the Lagrange multiplier space determines the mathematical properties of the employed mortar approach and thus the two predominantly used approaches, namely *standard* and so-called *dual* Lagrange multipliers will be introduced. These two Lagrange multiplier families are also used later on in all following chapters.

Mathematical details on the choice of the Lagrange multiplier spaces are not in the focus of this thesis, but the interested reader is referred to Ben Belgacem [18], Bernardi et al. [26], Seshaiyer and Suri [247] and Wohlmuth [288].

3.4.1.1. Standard Lagrange multiplier interpolation

Standard Lagrange multipliers can be taken from the finite dimensional subset $\mathcal{W}_h^{(1)}$ of the trace space $\mathcal{W}^{(1)}$ of $\mathcal{V}^{(1)}$. Thus, it usually leads to identical shape functions for the slave side displace-

ment interpolation and the Lagrange multiplier interpolation:

$$\Phi_j = N_j^{(1)}. \quad (3.45)$$

Consequently, the shape functions have equal polynomial degree and the finite dimensional subsets \mathcal{M}_h and $\mathcal{W}_h^{(1)}$ have equal reproduction order.

3.4.1.2. Dual Lagrange multiplier interpolation

Dual Lagrange multipliers have the beneficial property of allowing a localization of the coupling problems. This means, that the algebraic form of the slave side mortar matrix \mathbf{D} in (3.35) becomes a diagonal matrix. Therefore, the complete algebraic structure of the mortar contact formulation results in a node-to-segment type representation, which allows for computationally efficient solution procedures, see Section 3.5.3. In the following, the basic principles of dual shape functions and their construction rules are briefly outlined based on the explanations in Flemisch and Wohlmuth [82], Lamichhane and Wohlmuth [146], Lamichhane et al. [147], Popp [210], Scott and Zhang [242], Wohlmuth [289] and Wohlmuth et al. [291]. A commonly used notation for the biorthogonality condition of dual shape functions is

$$\int_{\gamma_{c,h}^{(1)}} \Phi_j N_k \, dA = \delta_{jk} \int_{\gamma_{c,h}^{(1)}} N_k \, dA, \quad j, k = 1, \dots, m^{(1)} \quad (3.46)$$

with δ_{jk} being the well-known Kronecker delta. For the condition mentioned above, it is assumed that the most common choice of nodes carrying Lagrange multipliers equal the slave interface nodes (i.e. $m^{(1)} = n^{(1)}$) holds. To allow for an easier implementation of this condition, it is commonly reformulated in a local, element-wise form, i.e.

$$\int_e \Phi_j N_k \, de = \delta_{jk} \int_e N_k \, de, \quad j, k = 1, \dots, n_e. \quad (3.47)$$

In this thesis, it is implicitly assumed for the global and the element-wise formulation that the dual shape functions have the same polynomial order as their standard counterparts. However, in the context of higher-order finite elements, it was shown in Popp [210], Popp et al. [213] and Se-shaiyer and Suri [247], that a lower polynomial order for the Lagrange multiplier interpolation could be advantageous. Furthermore, the dual shape functions fulfill a partition of unity property, see Flemisch and Wohlmuth [82]. Since the biorthogonality condition has to be fulfilled in physical space, and not simply in the finite element parameter space, dual shape functions can only be formulated a priori for elements with constant Jacobians. For example, for 2-node line elements in 1D, the standard and dual shape functions are visualized in Figure 3.2 and read

$$N_1(\xi) = \frac{1}{2}(1 - \xi) \quad \Phi_1(\xi) = \frac{1}{2}(1 - 3\xi) \quad (3.48)$$

$$N_2(\xi) = \frac{1}{2}(1 + \xi) \quad \Phi_2(\xi) = \frac{1}{2}(1 + 3\xi). \quad (3.49)$$

Moreover, for 3-node triangle elements in 2D, the standard and dual shape functions are given as

$$N_1(\xi, \eta) = 1 - \xi - \eta \quad \Phi_1(\xi, \eta) = 3 - 4(\xi + \eta) \quad (3.50)$$

$$N_2(\xi, \eta) = \xi \quad \Phi_2(\xi, \eta) = -1 + 4\xi \quad (3.51)$$

$$N_3(\xi, \eta) = \eta \quad \Phi_3(\xi, \eta) = -1 + 4\eta. \quad (3.52)$$

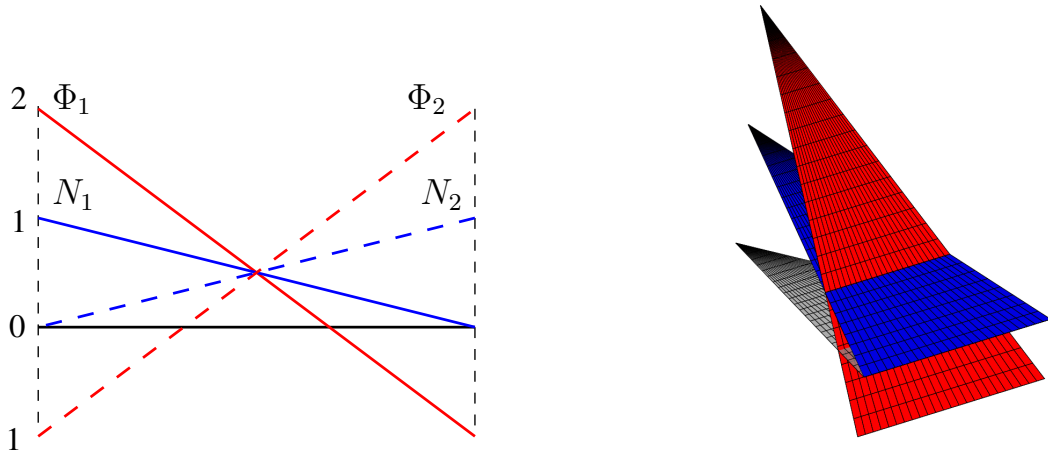


Figure 3.2: Visualization of dual shape functions Φ_j for first-order elements in 1D and 2D cases: standard shape functions are colored blue and dual shape functions are given in red. The figure is based on Farah et al. [70].

However, for elements with non-constant Jacobians, the dual shape functions have to be constructed for each element individually. For this purpose, it is assumed that the dual shape functions can be expressed as linear combination of the standard shape functions, which is algebraically represented by a multiplication of a vector containing standard shape functions within each element with an element coefficient matrix \mathbf{C}_e

$$\Phi_j(\xi) = c_{jk} N_k(\xi), \quad \mathbf{C}_e = [c_{jk}] \in \mathbb{R}^{n_e \times n_e}. \quad (3.53)$$

The construction of this coefficient matrix is then realized by inverting a local, element-wise matrix with mass matrix characteristics and size $n_e \times n_e$, i.e. the size being defined by the number of nodes associated with this element:

$$\mathbf{C}_e = \mathbf{D}_e \mathbf{M}_e^{-1}, \quad (3.54)$$

$$\mathbf{D}_e = [d_{jk}] \in \mathbb{R}^{n_e \times n_e}, \quad d_{jk} = \delta_{jk} \int_e N_k(\xi) J(\xi) de, \quad (3.55)$$

$$\mathbf{M}_e = [m_{jk}] \in \mathbb{R}^{n_e \times n_e}, \quad m_{jk} = \int_e N_j(\xi) N_k(\xi) J(\xi) de. \quad (3.56)$$

3.4.2. Numerical evaluation

Accurately and efficiently computing the mortar quantities is one of the main challenges of mortar contact algorithms. This is due to the fact that evaluating the second mortar matrix \mathbf{M} , and thus also the weighted gap \tilde{g}_n and the relative tangential velocity $\tilde{\mathbf{v}}_{\tau,\text{rel}}$, requires an integration over the slave contact surface with an integrand containing quantities from both master and slave side. In the case of non-matching meshes, the integrand represents a non-smooth function which cannot be evaluated exactly by using standard Gauss rules. This non-smoothness stems from the locally supported Lagrange polynomials on master and slave side having kinks at the respective element nodes and edges. Thus, the preferred integration technique is based on the prevention of

all possibly occurring discontinuities in the integrand of mortar matrix \mathbf{M} , the weighted gap \tilde{g}_n and the relative tangential velocity $\tilde{\mathbf{v}}_{\tau,\text{rel}}$ by creating smooth integrable segments. Consequently, it is named *segment-based integration* in the following. This method was firstly developed in its present form in Puso and Laursen [217] and slight adoptions and extensions can for example be found in Farah et al. [73], Popp et al. [212], Puso and Laursen [218, 219] and Puso et al. [220].

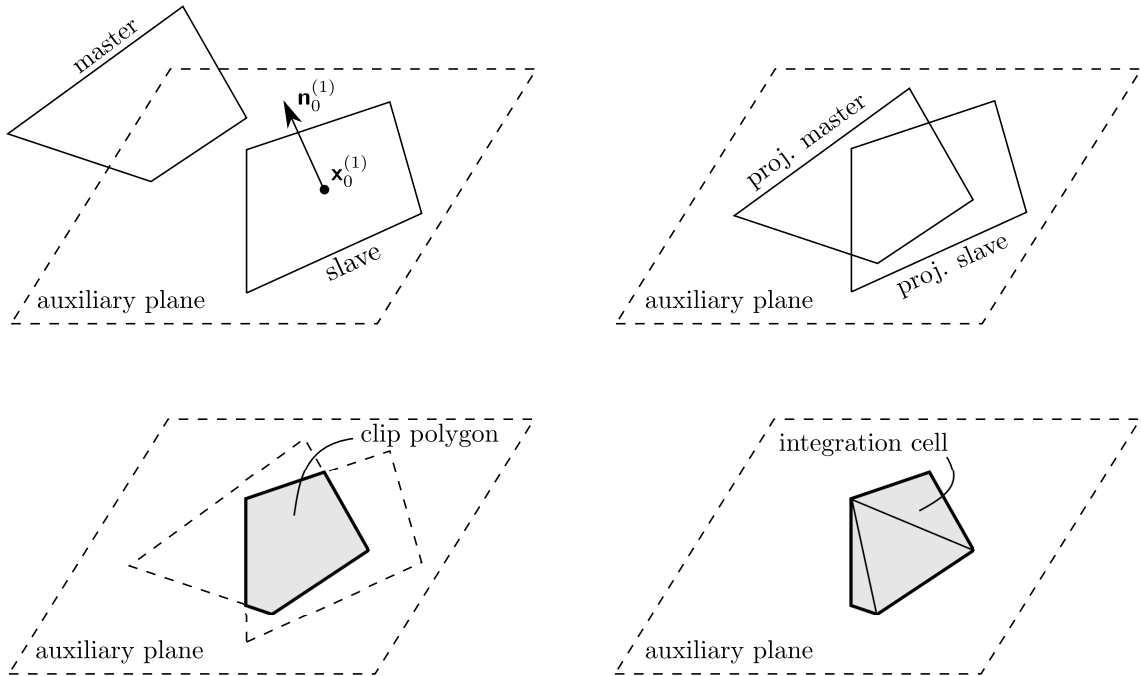


Figure 3.3: Main steps of the segment-based integration scheme for the surface contact algorithm: Construct an auxiliary plane (top left), project slave and master nodes onto the auxiliary plane (top right), perform polygon clipping (bottom left), divide polygon into triangular integration segments and perform numerical integration (bottom right). The figure is taken from Farah et al. [71].

Keeping in mind the idea of integrating just smooth contributions over the slave side, precise information concerning the position of the involved discontinuities of the integrand is required. This information is obtained by working with pairs of one slave and master element each. In a first step, both slave and master nodes are projected onto an auxiliary plane. Then, a polygon clipping algorithm is applied in order to determine the overlap of the slave and master element pair, i.e. the region where the integrands in (3.35) and (3.36) are C^1 -continuous. The whole process is illustrated in Figure 3.3 and summarized for the integration of the mortar matrices in the algorithm below. Of course, the information which slave and master element pairs have to be considered must first be obtained by an efficient contact search algorithm, see e.g. Yang and Laursen [298, 299].

Algorithm 3.1. Segment-based integration

1. Construct an auxiliary plane for numerical integration based on the slave element center $\mathbf{x}_0^{(1)}$ and the corresponding unit normal vector $\mathbf{n}_0^{(1)}$.
2. Project all $n_e^{(1)}$ slave element nodes $\mathbf{x}_k^{(1)}$, $k = 1, \dots, n_e^{(1)}$ along $\mathbf{n}_0^{(1)}$ onto the auxiliary plane to create auxiliary slave nodes $\tilde{\mathbf{x}}_k^{(1)}$.
3. Project all $n_e^{(2)}$ master element nodes $\mathbf{x}_l^{(2)}$, $l = 1, \dots, n_e^{(2)}$ along $\mathbf{n}_0^{(1)}$ onto the auxiliary plane to create the projected master nodes $\tilde{\mathbf{x}}_l^{(2)}$.
4. Perform polygon clipping in the auxiliary plane to find the overlapping region of projected slave and master element. Clipping algorithms are illustrated in more detail in Hughes et al. [119].
5. Perform a decomposition of the clip polygon to define easy-to-integrate subdomains which will be used for numerical integration and are therefore called integration cells. If no geometrical subdivision is performed, then the polygon itself represents the sole integration cell.
6. Define suitable integration points on the triangular integration cells and find their counterparts on the slave and master element by an inverse mapping.
7. Perform numerical integration of the mortar matrices (3.35) and (3.36), the weighted gap (3.40) and the weighted relative tangential velocity (3.43).

The decomposition mentioned in step 5 is carried out to create integration cells with well-known predefined integration rules. Almost all contributions in the available literature that employ segment-based integration use some kind of triangulation to create triangular subdomains. To the best of the author's knowledge, the only exception is the work in Wilking and Bischoff [287], where triangular and quadrilateral integration cells are created. However, the most efficient method to create triangular cells is the so-called Delaunay triangulation (see Lee and Schachter [156]) as illustrated exemplarily in Figure 3.3. Note that numerical evaluation procedures for 2D contact problems resulting into 1D contact zones are not explained, since this thesis focuses on 3D problems. However, also 2D examples are shown in the following and for information about segment-based integration schemes for 2D contact problems the interested reader is referred to Popp et al. [211] and Yang et al. [301].

3.5. Time integration and global solution scheme

3.5.1. Time integration for computational contact mechanics

No matter which spatial discretization scheme is employed, computational contact mechanics introduce an increased complexity with regard to time discretization than standard solid mechanics. This is due to the non-smooth characteristic of contact phenomena, which can be identified by discontinuities of the interface velocities in the event of an impact, see Laursen and Love

[153]. Standard time integration methods, such as the One-Step- θ scheme or the generalized- α scheme, which was introduced in Section 2.2.3, implicitly assume that the time derivatives of the displacement unknowns \mathbf{d} are continuous. Consequently, they lack in accuracy for some mechanical conservation laws when applied to computational contact mechanics. However, in this thesis, the introduced generalized- α scheme is exclusively employed for time integration of the contact problems since non-smooth time integration schemes are beyond the scope of this work. Thus, the final space and time discretized version of the frictional contact problem reads:

$$\mathbf{K}_{\text{mass}} \mathbf{a}_{n+1-\alpha_m} + \mathbf{K}_{\text{damp}} \mathbf{v}_{n+1-\alpha_f} + \mathbf{f}_{\text{int}}(\mathbf{d}_{n+1-\alpha_f}) + \mathbf{f}_c(\mathbf{d}_{n+1-\alpha_f}, \boldsymbol{\lambda}_{n+1-\alpha_f}) - \mathbf{f}_{\text{ext}, n+1-\alpha_f} = \mathbf{0}. \quad (3.57)$$

Herein, the contact term arises in complete analogy to the internal forces, i.e. with linear interpolation rules. Additionally, all constraints are enforced at the time t_{n+1} . This time integration scheme provides a sufficient level in accuracy and robustness for all tested numerical examples later on. For a detailed discussion about conservation properties for linear and angular momentum as well as for energy conservation, the interested reader is referred to Popp [210]. Conservation properties of the algorithm for contact of vertices, edges and surfaces developed in Chapter 4 in combination with the generalized- α scheme are discussed in Section 4.8.3.

3.5.2. Global solution scheme

To consider the additional contact nonlinearities stemming from the inequality constraints for normal direction (3.41) and tangential direction (3.44), the idea of a *primal-dual active set strategy* (PDASS) is employed. It is well-known from literature on constrained optimization (cf. Qi and Sun [221]). When applying a PDASS, the set of all slave nodes \mathcal{S} is split into an active set \mathcal{A} for nodes with positive Lagrange multiplier values and an inactive set \mathcal{I} for nodes which are currently not in contact. In addition, frictional contact requires the splitting of all active nodes \mathcal{A} into a slip set $\mathcal{S}_{\mathcal{L}}$ and a stick set $\mathcal{S}_{\mathcal{T}}$. These introduced sets allow for a reformulation of the inequality constraints into equality constraints for the corresponding nodal sets. To solve the fully discretized system of nonlinear equations within each time step, the well-known primal-dual active set strategy is re-interpreted as a semi-smooth Newton method, see Christensen et al. [42] and Hintermüller et al. [109]. For this purpose, nodal *nonlinear complementarity functions* (NCP) are introduced, which are non-smooth but equivalently express the inequality constraints in (3.41) and (3.44).

First, the normal contact constraints in (3.41) are considered, see Figure 3.4. The complementarity function for the normal direction has been discussed in Hüeber and Wohlmuth [115] and Popp et al. [211] and is defined as

$$C_{n,j}(\boldsymbol{\lambda}_j, \mathbf{d}) = \lambda_{n,j} - \max(0, \lambda_{n,j} - c_n \tilde{\mathbf{g}}_{n,j}), \quad c_n > 0. \quad (3.58)$$

The distinction between the active set \mathcal{A} and the inactive set \mathcal{I} is implicitly contained in this complementarity function through its two different solution branches for the non-smooth max-function. The normal contact constraints are exactly fulfilled when

$$C_{n,j}(\boldsymbol{\lambda}_j, \mathbf{d}) = 0. \quad (3.59)$$

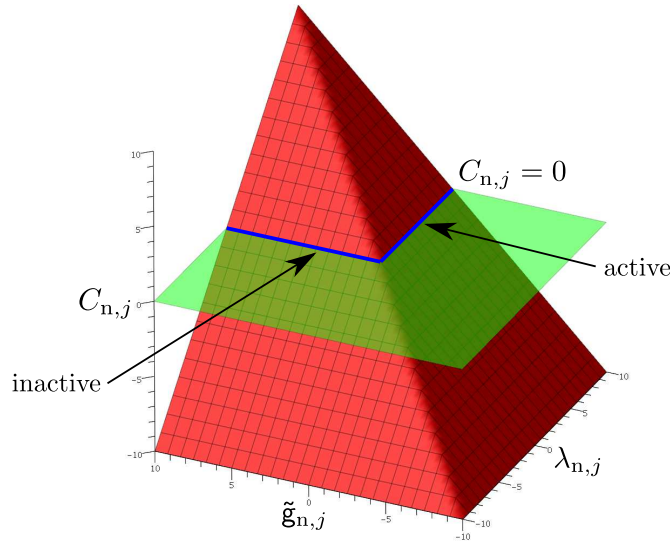


Figure 3.4: Nodal complementarity function $C_{n,j}$ for the normal direction (here with $c_n = 1$). Normal contact constraints are fulfilled for $C_{n,j} = 0$. The figure is taken from Farah et al. [74].

The parameter c_n does not affect the accuracy of results, but may influence the convergence behavior of the semi-smooth Newton method depending on the specific problem setup. The choice of c_n has been suggested to be at the order of Young's modulus E of the involved contacting bodies to obtain optimal convergence, see Hüeber and Wohlmuth [115]. Numerical investigations in Popp et al. [211, 212] have shown only a small influence on the convergence behavior of the semi-smooth Newton method. However, unless otherwise stated, all numerical examples in this thesis are realized with $c_n = 1$.

Second, the frictional sliding constraints in (3.44) are reformulated to again apply a semi-smooth Newton scheme. There is not only one possibility to define a suitable complementarity function for this set of constraints, see for example Alart and Curnier [3] and Christensen et al. [42]. In the following, the formulation introduced in Hüeber et al. [117] and successfully validated in Gitterle et al. [88] is employed. It is visualized in Figure 3.5 and reads

$$C_{\tau,j}(\boldsymbol{\lambda}_j, \mathbf{d}) = \max(\mathfrak{F}(\lambda_{n,j} - c_n \tilde{g}_{n,j}), \|\boldsymbol{\lambda}_{\tau,j} + c_t \tilde{\mathbf{u}}_{\tau,\text{rel},j}\|) \lambda_{\tau,j} - \mathfrak{F} \max(0, \lambda_{n,j} - c_n \tilde{g}_{n,j})(\boldsymbol{\lambda}_{\tau,j} + c_t \tilde{\mathbf{u}}_{\tau,\text{rel},j}), \quad c_n, c_t > 0. \quad (3.60)$$

Herein, the nodal weighted relative slip increment $\tilde{\mathbf{u}}_{\tau,\text{rel}}$ directly arises by multiplication of the relative tangential velocity $\tilde{\mathbf{v}}_{\tau,\text{rel}}$ with a time increment Δt . In analogy to the NCP function corresponding to the non-penetration constraints (3.59), the solution of Coulomb's friction law is equivalently expressed as

$$C_{\tau,j}(\boldsymbol{\lambda}_j, \mathbf{d}) = 0. \quad (3.61)$$

Again, the parameters c_n as well as c_t do not influence the accuracy of the results, but may control the convergence behavior. Considering (3.60), c_t can be interpreted as a parameter that balances the different scales of the tangential part of the Lagrange multiplier $\boldsymbol{\lambda}_\tau$ and the weighted

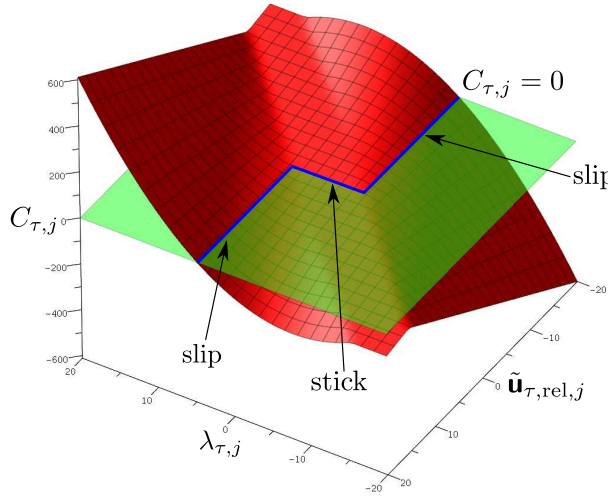


Figure 3.5: Nodal complementarity function $C_{\tau,j}$ for the tangential direction (here with $c_n = 1$ and $c_t = 1$). Tangential contact constraints are fulfilled for $C_{\tau,j} = 0$. Note that this is a 1D visualization of the tangential contact constraints and thus valid for 2D contact problems only. The figure is taken from Farah et al. [74].

relative tangential slip increment $\tilde{u}_{\tau,rel}$, see also H  eber et al. [117]. Consequently, it depends on the current deformation and load. Thus, it is suggested to initially choose c_t at the order of c_n and adapt it by the ratio of the tangential part of the Lagrange multiplier λ_τ and the weighted relative tangential slip increment $\tilde{u}_{\tau,rel}$ of the completed previous time step. Eventually, the global problem formulation to be solved consists of equations (3.39), (3.59) and (3.61). Herein, the nodal sets \mathcal{A} , \mathcal{I} , \mathcal{S}_L and \mathcal{S}_T can be updated after each Newton iteration.

3.5.3. Algebraic form

Finally, an algebraic representation of the linearized system to be solved within each semi-smooth Newton step is provided. It is based on the work in Gitterle [87] and Popp [210]. The resulting system of equations is of saddle-point type and looks in an abstract form as follows:

$$\begin{bmatrix} \mathbf{K}_{NN} & \mathbf{K}_{NM} & \mathbf{K}_{NS} & \mathbf{0} \\ \mathbf{K}_{MN} & \tilde{\mathbf{K}}_{MM} & \tilde{\mathbf{K}}_{MS} & -\mathbf{M}^T \\ \mathbf{K}_{SN} & \tilde{\mathbf{K}}_{SM} & \tilde{\mathbf{K}}_{SS} & \mathbf{D}^T \\ \mathbf{0} & \mathbf{C}_M & \mathbf{C}_S & \mathbf{C}_\lambda \end{bmatrix}^i \begin{bmatrix} \Delta \mathbf{d}_N \\ \Delta \mathbf{d}_M \\ \Delta \mathbf{d}_S \\ \Delta \lambda \end{bmatrix}^{i+1} = - \begin{bmatrix} \mathbf{r}_N \\ \mathbf{r}_M \\ \mathbf{r}_S \\ \mathbf{r}_c \end{bmatrix}^i. \quad (3.62)$$

The system of equations in (3.62) is of increased system size compared to classical structural problems, as both displacements and Lagrange multipliers show up as primary unknowns. Again, the solution vector contains increments of discrete displacements $\Delta \mathbf{d}$ and Lagrange multipliers $\Delta \lambda$. Furthermore, the displacement unknowns are distinguished between interior nodes $(\cdot)_N$, slave nodes $(\cdot)_S$ and master nodes $(\cdot)_M$. The matrix blocks denoted with \mathbf{K} contain terms from linearization of the internal force vector \mathbf{f}_{int} , damping terms \mathbf{K}_{damp} and mass matrix contributions \mathbf{K}_{mass} . The upper tilde symbol $(\tilde{\cdot})$ indicates additional contributions from the linearized

Lagrange multiplier contact force vector \mathbf{f}_c . The \mathbf{C} matrices represent the linearization of the complementarity functions in (3.58) and (3.60). One of the main advantages of dual mortar methods is the node-wise decoupling of the slave side contact virtual work resulting in a diagonal slave mortar matrix \mathbf{D} , see the explanation in Section 3.4.1.2. Thus, it allows for a computationally efficient elimination of the additional Lagrange multiplier unknowns as done in Farah et al. [74], Gitterle et al. [88], Popp et al. [211, 212] and Wohlmuth [289]. For this purpose, the third row of (3.62) is utilized to express the Lagrange multiplier increment in terms of displacement increments:

$$\Delta\lambda^{i+1} = -\mathbf{D}^{i,-T}(\mathbf{K}_{SN}^i \Delta\mathbf{d}_N^{i+1} + \tilde{\mathbf{K}}_{SM}^i \Delta\mathbf{d}_M^{i+1} + \tilde{\mathbf{K}}_{SS}^i \Delta\mathbf{d}_S^{i+1} + \mathbf{r}_c^i). \quad (3.63)$$

Here, the inversion of the diagonal slave side mortar matrix \mathbf{D} is of negligible cost and all other operations are computationally cheap vector matrix multiplications. By inserting (3.63) into (3.62), the final condensed system of equations becomes:

$$\begin{bmatrix} \mathbf{K}_{NN} & \mathbf{K}_{NM} & \mathbf{K}_{NS} \\ \mathbf{K}_{MN} + \mathbf{P}^T \mathbf{K}_{SN} & \tilde{\mathbf{K}}_{MM} + \mathbf{P}^T \tilde{\mathbf{K}}_{SM} & \tilde{\mathbf{K}}_{MS} + \mathbf{P}^T \tilde{\mathbf{K}}_{SS} \\ -\mathbf{C}_\lambda \mathbf{D}^{-T} \mathbf{K}_{SN} & \mathbf{C}_M - \mathbf{C}_\lambda \mathbf{D}^{-T} \tilde{\mathbf{K}}_{SM} & \mathbf{C}_S - \mathbf{C}_\lambda \mathbf{D}^{-T} \tilde{\mathbf{K}}_{SS} \end{bmatrix}^i \begin{bmatrix} \Delta\mathbf{d}_N \\ \Delta\mathbf{d}_M \\ \Delta\mathbf{d}_S \end{bmatrix}^{i+1} = -[\mathbf{r}_N \mid \mathbf{r}_M + \mathbf{P}^T \mathbf{r}_S \mid \mathbf{r}_c - \mathbf{C}_\lambda \mathbf{D}^{-T} \mathbf{r}_S]^{i,T}, \quad (3.64)$$

with the well-known mortar projection operator

$$\mathbf{P} = \mathbf{D}^{-1} \mathbf{M}. \quad (3.65)$$

The final system of equations in (3.64) is of constant system size and the only remaining degrees of freedom are the displacement unknowns. The discrete Lagrange multipliers can be easily obtained by performing a recovery step based on (3.63).

The solution of the linear saddle-point type system in (3.62) or the condensed system in (3.64) with iterative solution techniques is beyond the scope of this thesis. Details on algebraic and geometric multigrid methods for this purpose can be found in Brunßen et al. [34], Krause [141], Wiesner [286] and Wohlmuth and Krause [292].

4. Mortar Methods for Contact of Vertices, Edges and Surfaces

Contact interaction of bodies with vertices, edges and surfaces is the main focus of this chapter. Under macroscopic considerations, sharp edges and vertices naturally occur and should be modeled as only C^0 -continuous part of the boundary. But, in a zoom in view small roundings can always be detected, since accurate fabrication of such bodies can only be achieved in a certain tolerance range. In addition, small roundings are often deliberately introduced in components. Therefore, it is essential to define vertices and edges from a modeling point of view, see Figure 4.1. Here, the decision whether the model consists of rounded boundaries or sharp edges and vertices strongly depends on the application and the quantities of interest, which should be obtained from FEM simulations. As can be seen in the mentioned Figure, an adequate finite element resolution for a rounded part of the geometry is rather costly, but the arising contact situations could still be classified as surface-to-surface contact. However, when considering the overall mechanical properties of a contacting body, the small roundings at vertices and edges play a minor role. Thus, it would be efficient to characterize them as non-smooth parts of the geometry, i.e. parts of the surface which are not C^1 -continuous. When doing so, the well-known and robust mortar schemes for contact problems are not applicable anymore. This is due to the inherent drawback of a classical mortar based contact formulation that leads to large penetrations at non-smooth geometries. This causes the need for a contact formulation, which inherits all beneficial properties from the mortar method but is applicable to interactions of non-smooth geometries. Up to now, this topic is only rarely addressed in the existing literature on computational contact mechanics, especially for mortar based contact formulations. Nevertheless, computational contact mechanics of nonlinear solids and structures with sharp edges and vertices represent a major complexity in many classical engineering tasks and in applied sciences and thus the investigation of such contact scenarios is of high importance.

In the following, the main focus is set on the development of a variationally consistent framework for computational contact of non-smooth geometries based on dual mortar methods. Therein,

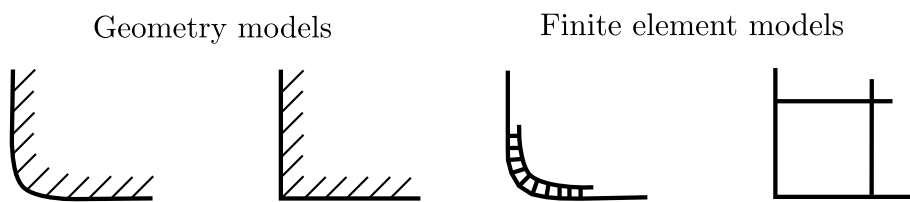


Figure 4.1: Zoom in view of a vertex: Possible geometry models (left) and corresponding finite element discretizations at the critical part of the geometry (right).

point contact, line contact and surface contact are treated with three different sets of Lagrange multipliers and a suitable definition of the appropriate discrete Lagrange multiplier spaces prevents the final system to be over-constrained. The presented algorithms and numerical examples are basically taken from the author's publication Farah et al. [71].

4.1. Fundamental approaches and research objective

4.1.1. Fundamental approaches

In the past years, the main focus of research was based on the assumption of smooth physical surfaces, and thus pure surface-to-surface contact settings have been almost exclusively considered in the literature. In the context of this thesis, the naming "smooth" is employed for surfaces that can be considered as being at least C^1 -continuous in a strong form of the problem formulation. Thus, the aim for surface-to-surface contact discretizations was to calculate the corresponding smooth contact stress distributions and to exactly represent the geometries (i.e. the contact surfaces) of the involved bodies. For this purpose, non-uniform-rational-B-splines (NURBS) have become of high interest because with these types of shape functions an exact geometry representation can be reached, see for example De Lorenzis et al. [53], Kim and Youn [135], Matzen and Bischoff [163], Matzen et al. [164], Seitz et al. [244], Temizer [268] and Temizer et al. [270]. Nevertheless, classical finite elements based on first-order and second-order Lagrangian polynomials are still the most commonly employed discretization type and are also considered in this thesis.

As fundamental technique for discretizing the contact constraints, mortar methods are well-established nowadays because they allow for a variationally consistent treatment of contact conditions despite the presence of non-matching surface meshes, see the explanations in Chapter 3 and Gitterle et al. [88], Popp et al. [211, 212], Puso and Laursen [219], Puso et al. [220] and Yang et al. [301]. These methods have already been successfully extended to resolve complex interface phenomena such as wear in Cavalieri and Cardona [36] and Farah et al. [69, 74], lubrication in Yang and Laursen [300] and thermal effects in Hüeber and Wohlmuth [116]. Despite the superior robustness of mortar methods, their applicability is strongly restricted by the requirement of smooth geometries (i.e. surface-to-surface contact). From an illustrative, slightly unmathematical perspective, this is due to their weak enforcement of the contact constraints, which results in a surface-based weighting of the gap function. Consequently large penetrations at vertices and sharp edges would occur, and therefore contact of non-smooth geometries such as vertex-to-vertex, vertex-to-edge, vertex-to-surface, edge-to-edge and edge-to-surface contact cannot be acceptably resolved with classical mortar methods. Finite element based contact discretization schemes that naturally lead to an adequate satisfaction of non-penetration conditions at non-smooth geometric entities are for example the well-known node-to-segment methods, see for example Bathe and Chaudhary [14], Erhart et al. [67], Hallquist et al. [96], Laursen and Simo [154], Papadopoulos and Taylor [195], Simo et al. [253] and Wriggers et al. [296]. In combination with a Lagrange multiplier approach for constraint enforcement, they lead to an exact constraint fulfillment at each slave node and thus no penetration at the nodes occurs. However, node-to-segment methods often lack important accuracy requirements as can be demonstrated with classical patch tests, see Papadopoulos and Taylor [195].

In addition to the problem of constraint discretization, the numerical evaluation of a suitable contact normal direction is a highly complex task for arbitrary geometries, see Konyukhov and Schweizerhof [139]. Eventually, a discrete nodal normal field is required for defining the non-penetration constraints based on the gap measurement between two bodies. This constitutes a classical, well-established approach in computational contact mechanics. An alternative non-penetration condition can be formulated by employing the intersection volume instead of the gap function, see Kane et al. [132] and Pandolfi et al. [194]. These methods were originally restricted to geometrically linear tetrahedral elements, but have later been extended to more general element types, see Cirak and West [46], Haikal [94] and Haikal and Hjelmstad [95]. Similar to these procedures, the *contact domain method* has been developed in Hartmann et al. [99, 100], Oliver et al. [186] and Weyler et al. [285]. The contact domains can be interpreted as regions connecting the potential contact surfaces of the involved bodies and are utilized to formulate the constraints. These methods are also able to pass classical contact patch tests.

When considering contact of vertices, edges and surfaces, the so-called *discontinuous deformation analysis* should also be mentioned, which was originally introduced in Shi [250]. This method shares similarities with the finite element method since it is based on solving for displacements and stresses of discrete elements, but these elements are not connected in a finite element sense. Instead, they are disconnected discrete elements that interact with each other via contact constraints. Thus, it also contains characteristics of discrete element methods, see Cundall [50]. This method is well-established in simulating jointed rock mass behavior, where edge-to-edge contact scenarios (cf. Yeung et al. [302]) and vertex-to-surface contact scenarios (cf. Jiang and Yeung [129]) occur permanently.

Besides the finite element approaches, non-smooth contact scenarios are usually treated within rigid multi-body simulations, see Fetecau et al. [79] and Stewart [259], but these approaches, while being highly efficient in calculating physically correct contact kinematics, are not able to determine accurate contact stresses in finite deformation settings. Therefore, this type of simulation is not considered in this thesis.

It can be seen from the review given above, that despite the abundant literature on numerical approaches for the simulation of surface-to-surface contact, methods for the contact treatment of non-smooth geometries (i.e. vertices, edges and surfaces) can only rarely be found in the existing literature. Therefore, the aim of this thesis is to develop a unified mortar-based finite element framework for an accurate and robust calculation of the displacements and contact stresses for contacting vertices, edges and surfaces in a finite deformation regime. To the best knowledge of the author, this is not possible with any other mortar-based approach from the literature.

4.1.2. Specification of requirements

Based upon the explanations stated in the previous section, the most important requirements for the development of a general mortar finite element approach with dual Lagrange multipliers in the context of fully nonlinear contact dynamics of vertices, edges and surfaces being involved are listed and illustrated in the following.

Mortar contact formulation for 1D boundaries of 3D bodies Considering general contact mechanics problems in 3D, it becomes obvious that not only smooth C^1 -continuous surfaces could be in contact, but also vertices and edges could be involved. The contact scenarios result-

ing from interaction of these entities can be identified as point contact (0D contact zone) and line contact (1D contact zone). When utilizing the classic mortar contact methods for these scenarios, well-known drawbacks such as large penetrations at vertices and edges occur, which highlight the need for alternative contact approaches for non-smooth geometries. The nature of point contact of a vertex naturally fits the NTS approach since constraints can be directly enforced at the vertex node and no weighting and integration is necessary. Consequently, the mortar idea degenerates to the NTS approach for this application. However, line contact of an exemplary edge-to-surface scenario needs a suitable strategy of constraint enforcement over the contact line and accurate and robust numerical evaluation and solution procedures to be applicable in a finite deformation regime. Applying dual mortar methods to this scenario is very promising since excellent results have been achieved with this methodology for surface-to-surface contact interaction in Gitterle [87] and Popp et al. [212]. However, realization of such a dual mortar approach for line contact scenarios is a completely unanswered question.

Exact enforcement of contact constraints at vertices, edges and surfaces Mortar methods for computational contact mechanics in combination with the Lagrange multiplier method guarantee exact contact constraint enforcement in a weak sense, which causes the superior robustness and accuracy of these schemes for surface contact. But, again, this naturally leads to unphysically large penetration at non-smooth geometries, i.e. at vertices and edges, and thus these methods lack in accuracy for such critical scenarios. In contrast, classical node-to-segment schemes could guarantee for a strong, node-wise fulfillment of the non-penetration constraints when defined with the Lagrange multiplier approach. Thus, they are perfectly suited for point contact of vertices, but in the context of surface contact they perform very poorly in terms of accuracy as they fail patch test requirements. This causes the need for a combined contact algorithm together with a Lagrange multiplier approach. When aiming to do so, it is of high importance to carefully define the Lagrange multipliers for point, line and surface contact to prevent the final system from being overconstrained. Up to now, there is no algorithm available in the existing literature, which takes care of the dimension of the contacting boundary and enforces the contact constraints individually over the respective domain, i.e. a point (0D), a line (1D) or a surface (2D).

Variationally consistent transition between point, line and surface contact without any heuristic transition parameter Numerical modeling of contact scenarios with completely different characteristics, such as point contact, line contact and surface contact requires different contact algorithms for these scenarios. An analogy can be found in beam-to-beam contact simulations, where it is generally distinguished between point and line contact. Very recently, the point contact model and the line contact model in the context of beam interaction have been combined by the introduction of a transition parameter, see Meier et al. [171] and Meier [170]. Whereas this transition parameter is a valid modeling approach for beam-to-beam contact since it is based on a simple angle measure between two involved beams and allows for robust numerical treatment of the employed penalty regularization, its introduction to contact of fully 3D solids is not desirable. This is due to the increased complexity of the 3D solid, where it is extremely intricate to define a proper measure for such a transition parameter. The decision whether the actual contact situation represents a point contact, line contact or surface contact scenario should arise from the variational formulation itself. Up to now, such a formulation is not available in the

existing literature on computational contact mechanics.

Condensation of discrete Lagrange multipliers for all contact scenarios When dealing with a Lagrange multiplier approach for enforcement of contact constraints, additional unknowns inevitably arise in the system of equations and, depending on the size of the contact interface, could drastically affect the efficiency of the contact algorithm. This can be avoided for classical mortar contact algorithms by the use of dual shape functions, which allow for elimination of the additional Lagrange multiplier unknowns by an easy condensation procedure, see Chapter 3 and Popp et al. [211, 212] and Wohlmuth [288]. This makes the dual Lagrange multipliers again the preferred discretization approach for the combined contact framework for point contact, line contact and surface contact.

Fully consistent linearization for the finite deformation regime In this thesis, contact interaction is considered in the context of nonlinear finite element methods with implicit time integration schemes in a finite deformation regime. Therefore, the developed contact formulation has to be consistently linearized in order to achieve the desired quadratic convergence rates within the employed Newton-Raphson scheme. It is well known, that the consistent linearization of mortar based contact contributions is very intricate, since many geometrical operations have to be consistently included in the linearization process. This was firstly outlined for 2D contact of only smooth geometries being involved in Yang and Laursen [298] and was extended towards dual mortar contact for 2D problems in Popp et al. [211]. Also 3D surface-to-surface contact has been consistently linearized for dual mortar methods in Popp et al. [212] and Popp [210]. However, a fully consistent linearization of the line contact interaction is still an unanswered question.

4.1.3. Proposal for contact of vertices, edges and surfaces

The most important ingredients and new scientific contributions of the presented non-smooth contact approach is given in the following:

- the first successful implementation of a dual mortar formulation for line contact in a finite deformation realm, see also Farah et al. [71].
- development and implementation of the first variationally consistent framework for combined point contact, line contact and surface contact in a finite deformation regime, see also Farah et al. [71].

In other words, this chapter consistently extends the well-investigated mortar contact approach towards point contact, line contact and surface contact within one numerical model.

4.2. Problem statement

Starting point for the derivation of a contact formulation being valid for various different contact scenarios is the standard initial boundary value problem (IBVP) for finite deformation elastodynamics as introduced in Section 2.1.4. For the sake of completeness, it is restated here for the two considered bodies $\mathcal{B}^{(1)}$ and $\mathcal{B}^{(2)}$:

$$\text{Div} \mathbf{P}^{(i)} + \hat{\mathbf{b}}_0^{(i)} = \rho_0^{(i)} \ddot{\mathbf{u}}^{(i)} \quad \text{in } \Omega_0^{(i)} \times [0, T], \quad (4.1)$$

$$\mathbf{u}^{(i)} = \hat{\mathbf{u}}^{(i)} \quad \text{on } \Gamma_u^{(i)} \times [0, T], \quad (4.2)$$

$$\mathbf{P}^{(i)} \cdot \mathbf{N}^{(i)} = \hat{\mathbf{t}}_0^{(i)} \quad \text{on } \Gamma_\sigma^{(i)} \times [0, T], \quad (4.3)$$

$$\mathbf{u}^{(i)}(\mathbf{X}^{(i)}, 0) = \hat{\mathbf{u}}_0^{(i)}(\mathbf{X}^{(i)}) \quad \text{in } \Omega_0^{(i)}, \quad (4.4)$$

$$\dot{\mathbf{u}}^{(i)}(\mathbf{X}^{(i)}, 0) = \hat{\dot{\mathbf{u}}}_0^{(i)}(\mathbf{X}^{(i)}) \quad \text{in } \Omega_0^{(i)}. \quad (4.5)$$

As explained for standard surface-to-surface contact in Section 3.1, these bodies share one potential contact interface, which is defined by the potential contact boundaries in the reference configuration $\Gamma_c^{(i)}$. Again, the overall boundary of each body is divided into three disjoint sets as

$$\partial\Omega_0^{(i)} = \Gamma_u^{(i)} \cup \Gamma_\sigma^{(i)} \cup \Gamma_c^{(i)}, \quad (4.6)$$

$$\Gamma_u^{(i)} \cap \Gamma_\sigma^{(i)} = \Gamma_u^{(i)} \cap \Gamma_c^{(i)} = \Gamma_\sigma^{(i)} \cap \Gamma_c^{(i)} = \emptyset, \quad (4.7)$$

with the Dirichlet boundaries $\Gamma_u^{(i)}$ and the Neumann boundaries $\Gamma_\sigma^{(i)}$. Since the special focus of this chapter is to investigate contact situations involving non-smooth geometries, the potential contact boundaries $\Gamma_c^{(i)}$ are further divided into three disjoint subsets, viz.

$$\Gamma_c^{(i)} = \Gamma_o^{(i)} \cup \Gamma_i^{(i)} \cup \Gamma_\star^{(i)}, \quad (4.8)$$

$$\Gamma_o^{(i)} \cap \Gamma_i^{(i)} = \Gamma_o^{(i)} \cap \Gamma_\star^{(i)} = \Gamma_i^{(i)} \cap \Gamma_\star^{(i)} = \emptyset, \quad (4.9)$$

where $\Gamma_o^{(i)}$ are the potential contact boundaries of surfaces, $\Gamma_i^{(i)}$ represent edges and $\Gamma_\star^{(i)}$ are the sets of all vertices within the contact boundaries, see also Figure 4.2. Similar to the other boundaries, their spatial counterparts are denoted as $\gamma_o^{(i)}$, $\gamma_i^{(i)}$ and $\gamma_\star^{(i)}$. Due to the assumed finite deformation regime, the geometrical contact entities, namely surfaces, edges and vertices can deform significantly, meaning that an initial vertex could be flattened to become part of a new surface, or a surface could be deformed in a way to create a new edge. However, in this thesis it is assumed that the spatial points are assigned to the set definition of its reference boundary and consequently extreme deformations, such as a complete flattening of an edge, are not allowed. In order to define suitable contact conditions the possibly arising contact scenarios have to be specified. For this purpose, it is assumed that the contact entity with the lower geometrical dimension acts as slave part and the corresponding contact entity of equal or higher geometrical order is defined to be the master boundary. Concretely, the first class of possible contact scenarios is characterized by the active contacting area reducing to a point, see Figure 4.3. Namely, these scenarios are vertex-to-vertex, vertex-to-edge, vertex-to-surface and non-parallel edge-to-edge settings. These contact situations are denoted as point contact in the following. The next class is defined by the contacting area being a 1D line, which could arise due to edge-to-surface

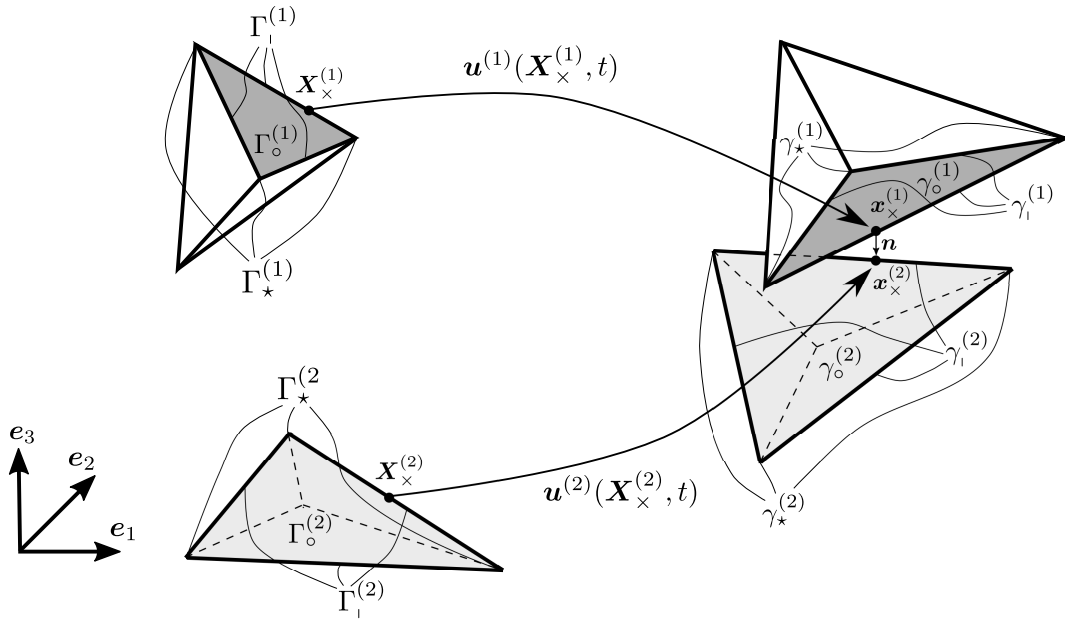


Figure 4.2: Kinematics and basic notation for the description of contact of vertices, edges and surfaces for two elastic bodies. Note, only the grey surface represent the potential contact regions and thus all notations are restricted to these zones. The figure is taken from Farah et al. [71].

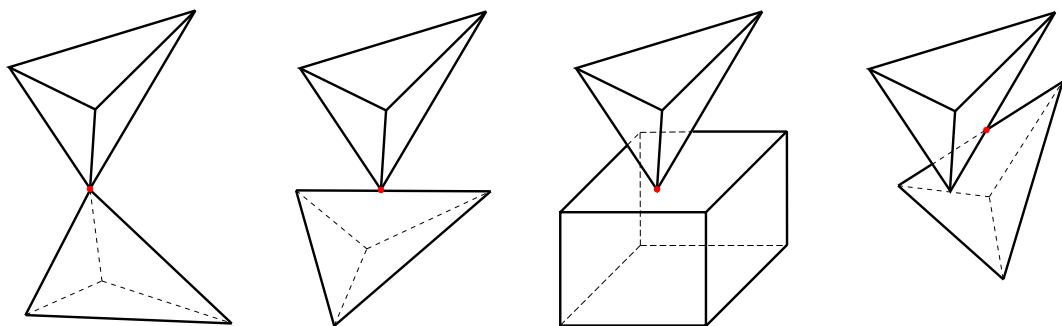


Figure 4.3: Classification of contact scenarios leading to point contact. From left to right: vertex-to-vertex, vertex-to-edge, vertex-to-surface and non-parallel edge-to-edge. Contact point is highlighted in red. The figure is taken from Farah et al. [71].

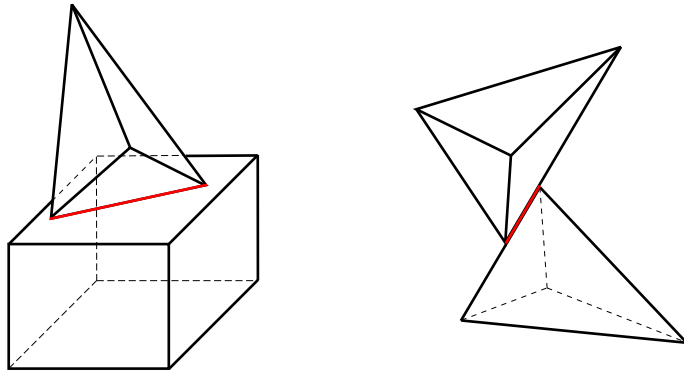


Figure 4.4: Classification of contact scenarios leading to line contact: edge-to-surface (left) and parallel edge-to-edge (right). Contact line is highlighted in red. The figure is taken from Farah et al. [71].

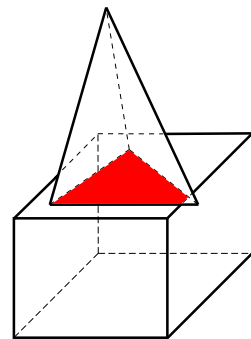


Figure 4.5: Classical surface contact scenario with contact area highlighted in red. The figure is taken from Farah et al. [71].

and parallel edge-to-edge contact, see Figure 4.4. The last setting is the classical surface contact scenario, which is well-investigated in the context of computational contact mechanics and is schematically visualized in Figure 4.5. This classification represents a hierarchy of contact situations, where the contact boundary on which the contact constraints are going to be formulated is the involved slave entity with the lowest dimension. The only exception to this scheme is the non-parallel edge-to-edge contact. Here, the geometrical slave entity is an edge but the contact scenario reduces to a point contact. Therefore, these special contact points are denoted as x_\times and the set of all slave contact points resulting from crossing edges is $\gamma_\times^{(1)}$. For the non-parallel edge-to-edge setting the discrete enforcement of the contact constraints will be treated in a special way later on. However, in order to keep a convenient notation, it is postulated that the set of edge-to-edge crossing points and the set of all vertices are united to the set of potential point contacts $\gamma_\bullet^{(1)}$:

$$\gamma_\bullet^{(1)} = \gamma_\star^{(1)} \cup \gamma_\times^{(1)}. \quad (4.10)$$

Furthermore, it is assumed that the potential line contact setting is defined on $\gamma_\circ^{(1)}$ and the potential surface contact scenario is defined on $\gamma_\circ^{(1)}$. The corresponding contact force quantity which acts on the slave contact boundary is now different for point, line and surface contact. The point

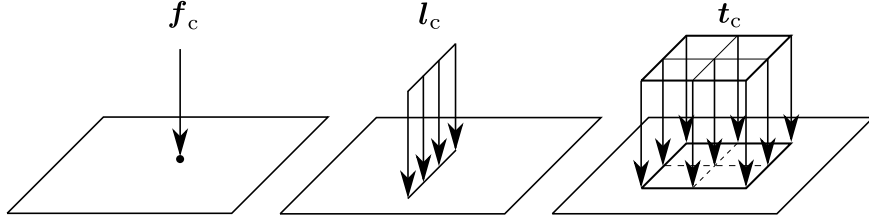


Figure 4.6: Contact force quantities for different contact scenarios: point contact (left), line contact (middle) and surface contact (right). The figure is taken from Farah et al. [71].

contact formulation is subjected to the force vector $f_c^{(1)}$, which is a concentrated load on the contact point. For the line contact setting, a line load vector $l_c^{(1)}$ is introduced, and consequently a surface traction vector $t_c^{(1)}$ is employed for the surface contact. Due to the balance of linear momentum, the corresponding master load vectors are identical except for the opposite sign, i.e.

$$f_c^{(1)} = -f_c^{(2)}, \quad l_c^{(1)} = -l_c^{(2)}, \quad t_c^{(1)} = -t_c^{(2)}. \quad (4.11)$$

Similar to the gap function and the relative tangential velocity in Chapter 3, the contact load vectors $f_c^{(1)}$, $l_c^{(1)}$ and $t_c^{(1)}$ on the slave surface can be split into their normal and tangential components, yielding

$$f_c^{(1)} = f_n \mathbf{n} + \mathbf{f}_\tau, \quad l_c^{(1)} = l_n \mathbf{n} + \mathbf{l}_\tau, \quad t_c^{(1)} = t_n \mathbf{n} + \mathbf{t}_\tau. \quad (4.12)$$

Thus, the contact constraints in normal direction are given in form of the well-known Hertz-Signorini-Moreau conditions for the point, line and surface contact scenarios:

$$g_n \geq 0 \quad \text{on } \gamma_c^{(1)} \times [0, T], \quad (4.13)$$

$$f_n \leq 0, \quad f_n g_n = 0 \quad \text{on } \gamma_\bullet^{(1)} \times [0, T], \quad (4.14)$$

$$l_n \leq 0, \quad l_n g_n = 0 \quad \text{on } \gamma_i^{(1)} \times [0, T], \quad (4.15)$$

$$t_n \leq 0, \quad t_n g_n = 0 \quad \text{on } \gamma_o^{(1)} \times [0, T]. \quad (4.16)$$

In addition, frictional sliding is formulated under the assumption that Coulomb's law is also valid for point contact and line contact, see Pandolfi et al. [194]. The frictional sliding constraints for point contact read

$$\Upsilon_\bullet := \|f_\tau\| - \mathfrak{F}|f_n| \leq 0, \\ v_{\tau,\text{rel}} + \beta_\bullet f_\tau = \mathbf{0}, \quad \beta_\bullet \geq 0, \quad \Upsilon_\bullet \beta_\bullet = 0 \quad \text{on } \gamma_\bullet^{(1)} \times [0, T]. \quad (4.17)$$

The corresponding constraints for line contact are given as

$$\Upsilon_i := \|l_\tau\| - \mathfrak{F}|l_n| \leq 0, \\ v_{\tau,\text{rel}} + \beta_i l_\tau = \mathbf{0}, \quad \beta_i \geq 0, \quad \Upsilon_i \beta_i = 0 \quad \text{on } \gamma_i^{(1)} \times [0, T]. \quad (4.18)$$

Finally, the tangential part of surface contact is defined by

$$\Upsilon_o := \|t_\tau\| - \mathfrak{F}|t_n| \leq 0, \\ v_{\tau,\text{rel}} + \beta_o t_\tau = \mathbf{0}, \quad \beta_o \geq 0, \quad \Upsilon_o \beta_o = 0 \quad \text{on } \gamma_o^{(1)} \times [0, T]. \quad (4.19)$$

In (4.17)-(4.19) the friction coefficient $\mathfrak{F} \geq 0$ is assumed to be equal for all contact scenarios for the sake of simplicity. Again, $\|\cdot\|$ denotes the L^2 -norm in \mathbb{R}^3 and the parameters β_i are complementarity parameters that are necessary to describe the separation of the stick and slip branch. These parameters will vanish by reformulating the sets of tangential constraints within so-called nonlinear complementarity functions, see Section 3.5.

4.3. Weak formulation

For the derivation of a weak variational formulation, the solution spaces $\mathcal{U}^{(i)}$ and weighting spaces $\mathcal{V}^{(i)}$ for the displacement field are repeated:

$$\mathcal{U}^{(i)} = \left\{ \mathbf{u}^{(i)} \in [H^1(\Omega)]^3 \mid \mathbf{u}^{(i)} = \hat{\mathbf{u}}^{(i)} \text{ on } \Gamma_u^{(i)} \right\}, \quad (4.20)$$

$$\mathcal{V}^{(i)} = \left\{ \delta \mathbf{u}^{(i)} \in [H^1(\Omega)]^3 \mid \delta \mathbf{u}^{(i)} = \mathbf{0} \text{ on } \Gamma_u^{(i)} \right\}. \quad (4.21)$$

Here, $H^1(\Omega)$ denotes the usual Sobolev space of functions with square integrable values and first derivatives, respectively. In order to enforce the normal and tangential contact constraints, three vector-valued Lagrange multipliers are introduced. The first one is the surface Lagrange

multiplier $\lambda_o = -t_c$, which represents the negative slave side contact traction and is chosen from the convex cone $\mathcal{M}_o(\lambda_o) \subset \mathcal{M}_o$ given by

$$\mathcal{M}_o(\lambda_o) = \left\{ \boldsymbol{\mu} \in \mathcal{M}_o \mid \langle \boldsymbol{\mu}, \mathbf{v} \rangle_{\gamma_o^{(1)}} \leq \langle \mathfrak{F}\lambda_{o,n}, \|\mathbf{v}_\tau\| \rangle_{\gamma_o^{(1)}}, \mathbf{v} \in \mathcal{W}_o \text{ with } \mathbf{v}_n \leq 0 \right\}. \quad (4.22)$$

Herein, $\langle \cdot, \cdot \rangle_{\gamma_o^{(1)}}$ stands for the scalar or vector-valued duality pairing between $H^{(-1/2)}$ and $H^{(1/2)}$ on the surface contact boundary $\gamma_o^{(1)}$. Moreover, \mathcal{M}_o is the dual space of the trace space \mathcal{W}_o of $\mathcal{V}^{(1)}$ restricted to the surface contact boundary $\gamma_o^{(1)}$. The second vector-valued Lagrange multiplier represents the negative slave side line traction $\lambda_i = -l_c$ and is utilized to enforce the line contact constraints. It is chosen from the convex cone $\mathcal{M}_i(\lambda_i) \subset \mathcal{M}_i$ defined by

$$\mathcal{M}_i(\lambda_i) = \left\{ \boldsymbol{\mu} \in \mathcal{M}_i \mid \langle \boldsymbol{\mu}, \mathbf{v} \rangle_{\gamma_i^{(1)}} \leq \langle \mathfrak{F}\lambda_{i,n}, \|\mathbf{v}_\tau\| \rangle_{\gamma_i^{(1)}}, \mathbf{v} \in \mathcal{W}_i \text{ with } \mathbf{v}_n \leq 0 \right\}. \quad (4.23)$$

In complete analogy to (4.22), \mathcal{M}_i is the dual space of the trace space \mathcal{W}_i of $\mathcal{V}^{(1)}$ restricted to the edge contact boundary $\gamma_i^{(1)}$. Finally, the constraint enforcement for the point contact has to be defined. Since the Lagrange multipliers for the surface contact and line contact are already defined on all points of the potential slave contact boundary except the set of all vertices, only these vertices are free of constraints. Thus, the point contact for the vertices can be enforced by the vector-valued Lagrange multiplier λ_* , which is chosen from the convex cone $\mathcal{M}_*(\lambda_*) \subset \mathcal{M}_*$ given by

$$\mathcal{M}_*(\lambda_*) = \left\{ \boldsymbol{\mu} \in \mathcal{M}_* \mid \langle \boldsymbol{\mu}, \mathbf{v} \rangle_{\gamma_*^{(1)}} \leq \langle \mathfrak{F}\lambda_{*,n}, \|\mathbf{v}_\tau\| \rangle_{\gamma_*^{(1)}}, \mathbf{v} \in \mathcal{W}_* \text{ with } \mathbf{v}_n \leq 0 \right\}. \quad (4.24)$$

Again, \mathcal{M}_* is the dual space of the trace space \mathcal{W}_* of $\mathcal{V}^{(1)}$ restricted to the vertex contact boundary $\gamma_*^{(1)}$. With λ_* , only the point contact scenarios acting on vertices are defined and the edge-to-edge setting is not affected by this Lagrange multiplier. Unfortunately, it is mathematically impossible to define the point Lagrange multiplier also on the points of crossing edges, since the edges are already subjected to the line Lagrange multiplier. From an engineering point of view, the scenario of two Lagrange multipliers acting on the same point can be considered as being over-constrained. Thus, the enforcement of the edge-to-edge contact constraints is relaxed via a penalty regularization. Therein, the contact constraints are explicitly removed by a penalization of any occurring constraint violation. Consequently, the normal part of the force vector reads

$$f_n = \begin{cases} \epsilon_n(-g_n) & \text{if } g_n \leq 0 \\ 0 & \text{if } g_n > 0 \end{cases} \quad \text{on } \gamma_\times^{(1)} \times [0, T]. \quad (4.25)$$

The parameter ϵ_n penalizes the penetration of the two bodies. The tangential part of the force vector is defined via

$$\begin{aligned} \mathcal{L}\mathbf{f}_\tau &= \epsilon_\tau [\mathbf{v}_{\tau,\text{rel}} - \beta_\times \mathbf{f}_\tau], \\ \Upsilon_\times := \|\mathbf{f}_\tau\| - \mathfrak{F}|f_n| &\leq 0, \quad \beta_\times \geq 0, \quad \Upsilon_\times \beta_\times = 0 \quad \text{on } \gamma_\times^{(1)} \times [0, T]. \end{aligned} \quad (4.26)$$

Herein, \mathcal{L} is the *Lie derivative* of the tangential force and ϵ_τ is the frictional penalty parameter, see Laursen [151]. The scalar parameter β_\times has the same interpretation as in (4.17)-(4.19).

Finally, the weak saddle point type formulation can be summarized as: Find $\mathbf{u}^{(i)} \in \mathcal{U}^{(i)}$, $\boldsymbol{\lambda}_* \in \mathcal{M}_*(\boldsymbol{\lambda}_*)$, $\boldsymbol{\lambda}_i \in \mathcal{M}_i(\boldsymbol{\lambda}_i)$ and $\boldsymbol{\lambda}_o \in \mathcal{M}_o(\boldsymbol{\lambda}_o)$ such that

$$-\delta\mathcal{W}_{\text{kin,int,ext}}(\mathbf{u}^{(i)}, \delta\mathbf{u}^{(i)}) - \delta\mathcal{W}_{\text{co}}(\boldsymbol{\lambda}_*, \boldsymbol{\lambda}_i, \boldsymbol{\lambda}_o, \delta\mathbf{u}^{(i)}) - \delta\mathcal{W}_{\text{pen}}(\mathbf{u}^{(i)}, \delta\mathbf{u}^{(i)}) = 0 \quad \forall \delta\mathbf{u}^{(i)} \in \mathcal{V}^{(i)}, \quad (4.27)$$

$$\delta\mathcal{W}_{\boldsymbol{\lambda}_*}(\mathbf{u}^{(i)}, \delta\boldsymbol{\lambda}_*) \geq 0 \quad \forall \delta\boldsymbol{\lambda}_* \in \mathcal{M}_*(\boldsymbol{\lambda}_*), \quad (4.28)$$

$$\delta\mathcal{W}_{\boldsymbol{\lambda}_i}(\mathbf{u}^{(i)}, \delta\boldsymbol{\lambda}_i) \geq 0 \quad \forall \delta\boldsymbol{\lambda}_i \in \mathcal{M}_i(\boldsymbol{\lambda}_i), \quad (4.29)$$

$$\delta\mathcal{W}_{\boldsymbol{\lambda}_o}(\mathbf{u}^{(i)}, \delta\boldsymbol{\lambda}_o) \geq 0 \quad \forall \delta\boldsymbol{\lambda}_o \in \mathcal{M}_o(\boldsymbol{\lambda}_o). \quad (4.30)$$

Here, the kinetic contribution $\delta\mathcal{W}_{\text{kin}}$ as well as the internal and external virtual work $\delta\mathcal{W}_{\text{int,ext}}$ are independent from the contact terms and their derivation is well-known in nonlinear continuum mechanics and thus omitted here. The contact virtual work $\delta\mathcal{W}_{\text{co}}$ due to the Lagrange multipliers is given as

$$\begin{aligned} -\delta\mathcal{W}_{\text{co}} = & \sum_{x \in \gamma_*^{(1)}} (\delta\mathbf{u}^{(1)} - \delta\mathbf{u}^{(2)} \circ \chi) \\ & + \int_{\gamma_i^{(1)}} \boldsymbol{\lambda}_i (\delta\mathbf{u}^{(1)} - \delta\mathbf{u}^{(2)} \circ \chi) \, dL \\ & + \int_{\gamma_o^{(1)}} \boldsymbol{\lambda}_o (\delta\mathbf{u}^{(1)} - \delta\mathbf{u}^{(2)} \circ \chi) \, dA, \end{aligned} \quad (4.31)$$

with a suitable contact interface mapping $\chi : \gamma_c^{(1)} \rightarrow \gamma_c^{(2)}$ which is required due to the generally non-identical contact boundaries $\gamma_c^{(1)}$ and $\gamma_c^{(2)}$. The weak form of the normal and tangential contact constraints for the point Lagrange multiplier reads

$$\delta\mathcal{W}_{\boldsymbol{\lambda}_*} = \sum_{x \in \gamma_*^{(1)}} (\delta\lambda_{*,n} - \lambda_{*,n}) g_n - \sum_{x \in \gamma_*^{(1)}} (\delta\boldsymbol{\lambda}_{*,\tau} - \boldsymbol{\lambda}_{*,\tau}) \mathbf{v}_{\tau,\text{rel}}. \quad (4.32)$$

The weak constraints for the line Lagrange multiplier are given as

$$\delta\mathcal{W}_{\boldsymbol{\lambda}_i} = \int_{\gamma_i^{(1)}} (\delta\lambda_{i,n} - \lambda_{i,n}) g_n \, dL - \int_{\gamma_i^{(1)}} (\delta\boldsymbol{\lambda}_{i,\tau} - \boldsymbol{\lambda}_{i,\tau}) \mathbf{v}_{\tau,\text{rel}} \, dL. \quad (4.33)$$

Finally, the weak constraints due to the surface Lagrange multiplier read

$$\delta\mathcal{W}_{\boldsymbol{\lambda}_o} = \int_{\gamma_o^{(1)}} (\delta\lambda_{o,n} - \lambda_{o,n}) g_n \, dA - \int_{\gamma_o^{(1)}} (\delta\boldsymbol{\lambda}_{o,\tau} - \boldsymbol{\lambda}_{o,\tau}) \mathbf{v}_{\tau,\text{rel}} \, dA. \quad (4.34)$$

The penalty contribution $\delta\mathcal{W}_{\text{pen}}$ that becomes inevitable to avoid over-constraining due to the point contact contribution of crossing edges is schematically given by

$$\delta\mathcal{W}_{\text{pen}} = \sum_{x \in \gamma_X^{(1)}} \mathbf{f}_c^{(1)} (\delta\mathbf{u}^{(1)} - \delta\mathbf{u}^{(2)} \circ \chi), \quad (4.35)$$

where the normal and tangential contributions to the contact force vector $\mathbf{f}_c^{(1)}$ are computed according to (4.25)-(4.26).

4.4. Finite element displacement discretization and nodal normal computation

For the spatial discretization of the considered frictional contact problem using finite elements, the finite dimensional subsets $\mathcal{U}_h^{(i)}$ and $\mathcal{V}_h^{(i)}$, which represent approximations of the continuous solution spaces $\mathcal{U}^{(i)}$ and $\mathcal{V}^{(i)}$ are employed. In the following, the focus lies on 3D linear and tri-linear Lagrangian finite elements and thus the contact surface discretization may consist of 3-node triangular (tri3) elements and of 4-node quadrilateral (quad4) elements. Accordingly, the slave and master geometry and displacement interpolation are given as

$$\mathbf{x}_h^{(1)}|_{\Gamma_{c,h}^{(1)}} = \sum_{k=1}^{n^{(1)}} N_k^{(1)} \mathbf{x}_k^{(1)}, \quad \mathbf{x}_h^{(2)}|_{\Gamma_{c,h}^{(2)}} = \sum_{l=1}^{n^{(2)}} N_l^{(2)} \mathbf{x}_l^{(2)}, \quad (4.36)$$

$$\mathbf{u}_h^{(1)}|_{\Gamma_{c,h}^{(1)}} = \sum_{k=1}^{n^{(1)}} N_k^{(1)} \mathbf{d}_k^{(1)}, \quad \mathbf{u}_h^{(2)}|_{\Gamma_{c,h}^{(2)}} = \sum_{l=1}^{n^{(2)}} N_l^{(2)} \mathbf{d}_l^{(2)}. \quad (4.37)$$

Here, $n^{(1)}$ and $n^{(2)}$ represent the number of nodes on the discrete slave contact surface $\Gamma_{c,h}^{(1)}$ and on the discrete master contact surface $\Gamma_{c,h}^{(2)}$, respectively. The discrete nodal positions and discrete nodal displacements are given by $\mathbf{x}_k^{(1)}$, $\mathbf{x}_l^{(2)}$, $\mathbf{d}_k^{(1)}$ and $\mathbf{d}_l^{(2)}$. Based on the usually employed finite element parameter space for 2D surfaces $\xi^{(i)} = (\xi^{(i)}, \eta^{(i)})$, the shape functions $N_k^{(1)}$ and $N_l^{(2)}$ are defined. These shape functions are naturally derived from the underlying bulk shape functions.

The nodal normal vectors are of utmost importance for the formulation of a non-smooth contact framework, since they define the local direction in which the contact force acts. Thus, contact kinematics are strongly influenced by the way the normal vectors are defined. However, it is not aimed here at giving a comprehensive solution for all problems arising from defining nodal normals between two arbitrary geometries. The fact that already the simple vertex-to-vertex contact scenario can lead to various problems in defining suitable normal directions illustrates the complexity of this topic, see Bao and Zhao [11, 12]. In contrast, robust numerical approximations of rather classical closest-point-projections are discussed. Here, the idea is to project a physical point onto C^1 -continuous geometries, see Konyukhov and Schweizerhof [139]. Specifically, three different types of closest-point-projections of a point onto a C^1 -continuous surface, edge and a point are performed. From an algorithmic perspective, these procedures are denoted as node-to-surface projection, node-to-line projection and node-to-node projection and are explained in Sections 4.4.1, 4.4.2 and 4.4.3. The resulting nodal normals $\mathbf{n}^{(1)}$ on the slave side are then interpolated by the already introduced displacement shape functions N_k via

$$\mathbf{n}^{(1)} = \sum_{k=1}^{n^{(1)}} N_k^{(1)} \mathbf{n}_k^{(1)}. \quad (4.38)$$

This results in a C^0 -continuous field of normals, and the procedure can be interpreted as numerical smoothing of the normal field to guarantee robust contact projection and evaluation algorithms. However, in rare cases the closest-point-projections fail the slave side nodal normals are calculated via the well-established averaging procedure described in Popp et al. [212].

4.4.1. Node-to-surface projection

The classical closest-point-projection of a node onto a surface is realized by projecting the slave node j along the master side normal $\mathbf{n}^{(2)}$ onto the discretized master surface. This procedure can be stated as follows:

$$\varpi \mathbf{n}^{(2)}(\hat{\xi}^{(2)}) + \sum_{l=1}^{n^{(2)}} N_l^{(2)}(\hat{\xi}^{(2)}) \mathbf{x}_l^{(2)} = \mathbf{x}_j^{(1)}. \quad (4.39)$$

Here, the sought-after quantities are the scalar-valued distance ϖ between the slave point \mathbf{x}_j and the master surface, and the projection point coordinates in the 2D master parameter space $\hat{\xi}^{(2)}$. The projection in (4.39) is nonlinear in terms of the unknowns ϖ and $\hat{\xi}^{(2)}$ and can be solved with a local Newton-Raphson scheme. Since this procedure assumes to project a point onto a C^1 -continuous surface, the typical first-order finite element approximation does not guarantee solvability of this projection. To overcome well-known problems arising from this closest-point-projection, such as degenerated cases of crossing normals or non-uniqueness of the CPP, the master surface nodal normal field $\mathbf{n}^{(2)}$ is formulated based on a C^0 -continuous field of normals, viz.

$$\mathbf{n}^{(2)}(\hat{\xi}^{(2)}) = \sum_{l=1}^{n^{(2)}} N_l^{(2)}(\hat{\xi}^{(2)}) \mathbf{n}_l^{(2)}, \quad (4.40)$$

with the master side displacement shape functions $N_l^{(2)}$. As mentioned above for the slave side, this can be interpreted as numerical smoothing procedure without changing the actual finite element geometry representation. The nodal normal vectors $\mathbf{n}_l^{(2)}$ are based on an averaging procedure in order to create a unique normal at each master node, see Figure 4.7. This procedure has been suggested for 2D contact scenarios in Yang et al. [301] and was used for 3D applications in Popp et al. [212]. Thus, it is only briefly explained in the following. The outward pointing unit

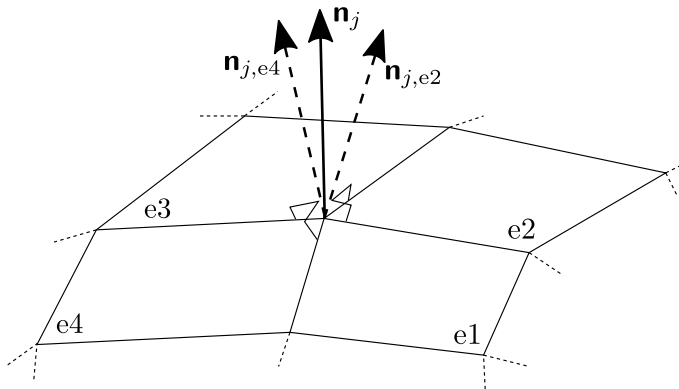


Figure 4.7: Nodally averaged normal vector \mathbf{n}_j at node j with four adjacent elements. Element normal vectors are exemplarily visualized for element e_2 and e_4 . The figure is taken from Farah et al. [71].

normal vectors $\mathbf{n}_{j,ei}$ of the adjacent master elements ei at master node j are employed to create

the unique master normal \mathbf{n}_j via

$$\mathbf{n}_j = \frac{\sum_{i=1}^{n_j^{\text{adj}}} \mathbf{n}_{j,\text{ei}}}{\left\| \sum_{i=1}^{n_j^{\text{adj}}} \mathbf{n}_{j,\text{ei}} \right\|}. \quad (4.41)$$

Herein, the number of adjacent elements is denoted as n_j^{adj} . Finally, the slave side nodal normal vector $\mathbf{n}_j^{(1)}$ at node j is defined as

$$\mathbf{n}_j^{(1)} = -\mathbf{n}^{(2)}(\hat{\xi}^{(2)}). \quad (4.42)$$

4.4.2. Node-to-line projection

The closest distance between a slave node and a master edge is computed with a node-to-line projection. The unit normal vector at slave node j reads

$$\mathbf{n}_j = \frac{\mathbf{x}_j^{(1)} - \sum_{l=1}^{n^{(2)}} N_l^{(2)}(\hat{\xi}^{(2)}) \mathbf{x}_l^{(2)}}{\left\| \mathbf{x}_j^{(1)} - \sum_{l=1}^{n^{(2)}} N_l^{(2)}(\hat{\xi}^{(2)}) \mathbf{x}_l^{(2)} \right\|}, \quad (4.43)$$

with the corresponding master point being defined by the line coordinate $\hat{\xi}^{(2)}$ in 1D parameter space. Note, that the expression in (4.43) does not guarantee that the unit normal is pointing in outward direction of the slave body. Thus, an auxiliary slave normal vector $\mathbf{n}_{j,\text{aux}}^{(1)}$ has to be computed to determine the sign of the slave nodal normal. Therefore, $\mathbf{n}_{j,\text{aux}}^{(1)}$ is defined as nodally averaged normal vector of all adjacent slave elements, which is a similar procedure as in (4.41) but performed on the slave side. If the angle between $\mathbf{n}_{j,\text{aux}}^{(1)}$ and \mathbf{n}_j is larger than 90° , the sign of \mathbf{n}_j has to be switched. The idea of a signed normal was already developed in Belytschko et al. [17]. The master parameter space coordinate $\hat{\xi}^{(2)}$ can be computed by solving the following scalar projection equation:

$$\boldsymbol{\tau}^{(2)}(\hat{\xi}^{(2)}) \left[\mathbf{x}_j^{(1)} - \sum_{l=1}^{n^{(2)}} N_l^{(2)}(\hat{\xi}^{(2)}) \mathbf{x}_l^{(2)} \right] = 0, \quad (4.44)$$

with $\hat{\xi}^{(2)}$ being the only unknown. Like for the node-to-surface projection, this nonlinear equation can be solved with a local Newton-Raphson scheme. To allow for a robust iteration process and unique solution, a pseudo C^1 -continuous curve in space is created by construction of a nodal tangent field:

$$\boldsymbol{\tau}^{(2)}(\xi^{(2)}) = \sum_{k=1}^{n^{(2)}} N_k^{(2)}(\xi^{(2)}) \boldsymbol{\tau}_k^{(2)}. \quad (4.45)$$

This field is again interpolated by the master displacement shape functions $N_k^{(2)}$. The tangent interpolation in (4.45) requires a unique tangent definition at each master node, and thus the normal averaging procedure in (4.41) is also employed for the tangents, yielding

$$\boldsymbol{\tau}_j = \frac{\sum_{i=1}^{n_j^{\text{adj}}} \boldsymbol{\tau}_{j,\text{ei}}}{\left\| \sum_{i=1}^{n_j^{\text{adj}}} \boldsymbol{\tau}_{j,\text{ei}} \right\|}. \quad (4.46)$$

4.4.3. Node-to-node projection

The unit nodal normal vector resulting from a node-to-node projection is given by the difference vector of the spatial nodal positions scaled to unit length. For a slave node j and a master node k , the slave nodal normal reads

$$\mathbf{n}_j = \frac{\mathbf{x}_j^{(1)} - \mathbf{x}_k^{(2)}}{\|\mathbf{x}_j^{(1)} - \mathbf{x}_k^{(2)}\|}. \quad (4.47)$$

Like in (4.43), the expression in (4.47) does not guarantee to produce an outward unit normal vector. Thus, the direction of the nodal normal vector \mathbf{n}_j has to be assessed by comparing with an auxiliary slave normal vector $\mathbf{n}_{j,\text{aux}}^{(1)}$, see Section 4.4.2.

4.4.4. Closest-point projections with multiple solutions

The projections in Sections 4.4.1, 4.4.2 and 4.4.3 generally yield a locally unique solution, since they are based on nodal averaged normals and tangents on the master side. However, multiple local solutions could occur as illustrated for 2D setups in Figure 4.8. To overcome this problem,

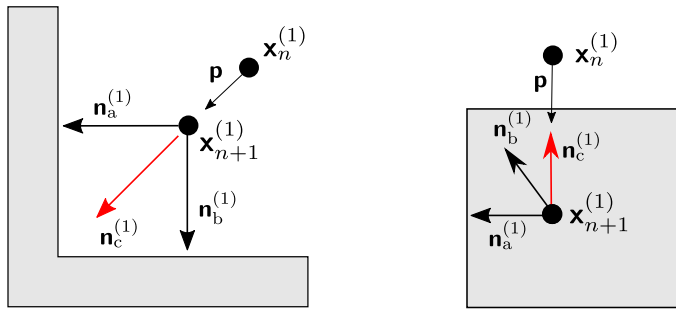


Figure 4.8: Situations with multiple solutions for the closest-point projections. The figure is taken from Farah et al. [71].

the past trajectory of the considered slave node is used to decide which projection is physically more reasonable. Therefore, a trajectory vector \mathbf{p}_j for the j -th node is created via

$$\mathbf{p}_j = \mathbf{x}_{j,n+1}^{(1)} - \mathbf{x}_{j,n}^{(1)}. \quad (4.48)$$

Here, $\mathbf{x}_{j,n+1}^{(1)}$ is the current spatial coordinate and $\mathbf{x}_{j,n}^{(1)}$ is the spatial coordinate of the last converged time step. To decide which nodal normal should be employed, the angles between the trajectory vector and the considered normals are calculated. Furthermore, the angles between the negative trajectory vector and the nodal normals are computed. Eventually, the nodal normal candidate that encloses the smallest angle with \mathbf{p} or $-\mathbf{p}$ is utilized as normal vector for the computation of the contact terms. This procedure is also shown in Figure 4.8. In the left part of Figure 4.8, three different solutions for the closest-point-projection are available. The normal $\mathbf{n}_c^{(1)}$ represents the solution with the largest distance from slave to master surface, but it encloses the smallest angle with \mathbf{p} and thus it is chosen to be the slave normal. In the right part of

Figure 4.8, the penetration of a slave node is visualized, which could occur within the predictor step of a dynamic contact analysis. Here, the normal $\mathbf{n}_c^{(1)}$ encloses the smallest angle with $-\mathbf{p}$, and again it is employed as physically reasonable choice of the slave normal.

4.4.5. Line-to-line projection

For the evaluation of contact between two crossing edges it is necessary to detect the pair of points that minimizes the distance between the edges. For this purpose, a closest-point-projection between two lines is introduced. In the spatially discretized setup, an edge is represented by 1D line elements. Since only first-order interpolations are considered, each line element consists of two nodes. The closest-point-projection between two line elements is realized by the following two conditions

$$\begin{aligned} \tau^{(1)}(\hat{\xi}_{\times}^{(1)}) \left[\sum_{k=1}^{n^{(1)}} N_k^{(1)}(\hat{\xi}_{\times}^{(1)}) \mathbf{x}_k^{(1)} - \sum_{l=2}^{n^{(2)}} N_l^{(2)}(\hat{\xi}_{\times}^{(2)}) \mathbf{x}_l^{(2)} \right] &= 0, \\ \tau^{(2)}(\hat{\xi}_{\times}^{(2)}) \left[\sum_{k=1}^{n^{(1)}} N_k^{(1)}(\hat{\xi}_{\times}^{(1)}) \mathbf{x}_k^{(1)} - \sum_{l=2}^{n^{(2)}} N_l^{(2)}(\hat{\xi}_{\times}^{(2)}) \mathbf{x}_l^{(2)} \right] &= 0. \end{aligned} \quad (4.49)$$

These conditions enforce the distance vector between the closest points to be orthogonal to the corresponding tangents on both slave side and master side, see Figure 4.9. Similar procedures are employed for closest point projections in the context of beam-to-beam contact scenarios, see Meier et al. [171]. In (4.49), the slave tangent $\tau^{(1)}(\hat{\xi}_{\times}^{(1)})$ and master tangent $\tau^{(2)}(\hat{\xi}_{\times}^{(2)})$ are

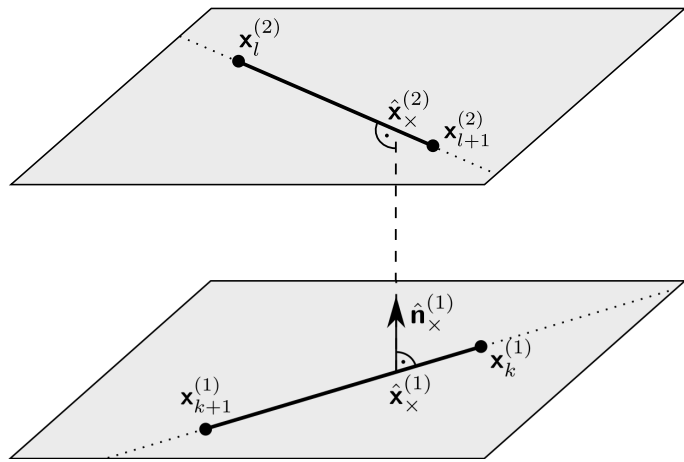


Figure 4.9: Closest point projection between two arbitrarily oriented line elements for edge-to-edge contact. Here, the special case of straight edges is depicted. The figure is taken from Farah et al. [71].

computed according to (4.45) and (4.46) and thus they depend on the parameter space coordinates $\hat{\xi}_{\times}^{(1)}$ and $\hat{\xi}_{\times}^{(2)}$. These parameter space coordinates represent the unknowns in (4.49), which are computed by a local Newton-Raphson scheme. The resulting spatial points are denoted as $\hat{\mathbf{x}}_{\times}^{(1)}$

and $\hat{\mathbf{x}}_{\times}^{(2)}$. Consequently, the normal can easily be defined as cross product of the tangents

$$\hat{\mathbf{n}}_{\times}^{(1)} = \frac{\boldsymbol{\tau}^{(1)}(\hat{\xi}_{\times}^{(1)}) \times \boldsymbol{\tau}^{(2)}(\hat{\xi}_{\times}^{(2)})}{\|\boldsymbol{\tau}^{(1)}(\hat{\xi}_{\times}^{(1)}) \times \boldsymbol{\tau}^{(2)}(\hat{\xi}_{\times}^{(2)})\|}, \quad (4.50)$$

and its orientation is once again determined by comparing with a suitable auxiliary slave normal vector, see Section 4.4.2.

4.5. Point contact

Firstly, the spatial discretization and numerical evaluation of point contact is considered. As stated in Section 4.3, there are two strategies to enforce the point contact scenario depending on the involved geometrical entities. Real point contact with vertices being involved is realized via the vector-valued Lagrange multiplier λ_* , while the point contact that occurs due to crossing edges is treated by a penalty regularization.

4.5.1. Vertex contact

For the Lagrange multiplier constraint enforcement, the discrete counterpart to the vector λ_* is required. It is based on the discrete Lagrange multiplier space $\mathcal{M}_{*,h}$ being an approximation of \mathcal{M}_* . The notation for the discrete point Lagrange multiplier reads

$$\lambda_{*,h} = \sum_{j=1}^{n_*} \Lambda_j \lambda_{*,j}. \quad (4.51)$$

In (4.51), the shape functions Λ_j of the point Lagrange multiplier interpolation reduce to impulse functions being 1 at the nodes of physical slave vertices $n_*^{(1)}$ and zero at all other points:

$$\Lambda_j = \begin{cases} 1 & \text{at } \mathbf{x}_j, \\ 0 & \text{else.} \end{cases} \quad (4.52)$$

Therefore, no interpolation functions are necessary between these points. The use of these Lagrange multipliers at slave vertices can easily be interpreted as the well-known node-to-segment formulation for point contact, see for example Bathe and Chaudhary [14], Erhart et al. [67], Hallquist et al. [96], Laursen and Simo [154], Papadopoulos and Taylor [195], Simo et al. [253] and Wriggers et al. [296]. Nevertheless, in the following, computational details on the numerical evaluation are briefly given. When inserting the introduced finite element discretizations (4.36) and (4.51) into the contact virtual work corresponding to the point contact contribution (4.31), the point contact matrices $\mathbf{D}_* \in \mathbb{R}^{3n_*^{(1)} \times 3n_*^{(1)}}$ and $\mathbf{M}_* \in \mathbb{R}^{3n_*^{(1)} \times 3n_*^{(2)}}$ can be computed by merging the nodal blocks

$$\mathbf{D}_*[j,k] = D_{*,jk} \mathbf{I}_3 = \Lambda_j N_k^{(1)} \mathbf{I}_3 = \mathbf{I}_3, \quad j = 1, \dots, n_*^{(1)}, \quad k = 1, \dots, n_*^{(1)}, \quad (4.53)$$

$$\mathbf{M}_*[j,l] = M_{*,jl} \mathbf{I}_3 = \Lambda_j (N_l^{(2)} \circ \chi_h) \mathbf{I}_3, \quad j = 1, \dots, n_*^{(1)}, \quad l = 1, \dots, n_*^{(2)}. \quad (4.54)$$

Herein, $\mathbf{I}_3 \in \mathbb{R}^{3 \times 3}$ is the identity and $\chi_h : \gamma_{c,h}^{(1)} \rightarrow \gamma_{c,h}^{(2)}$ represents a suitable discrete approximation of the mapping χ between the contact sides, see e.g. Dickopf and Krause [60] and Puso [216] for more details. Discretization of the non-penetration constraint in (4.32) yields the discrete gap function $g_{\star,j}$ at each node j :

$$g_{\star,j} = g_{n,h} = \mathbf{n}_j \left[\hat{\mathbf{x}}^{(2)}(\mathbf{x}_j^{(1)}) - \mathbf{x}_j^{(1)} \right] \quad j = 1, \dots, n_{\star}^{(1)}. \quad (4.55)$$

Here, $\hat{\mathbf{x}}^{(2)}(\mathbf{x}_j^{(1)})$ is the discrete point on the master side that results from the projection of the slave node position \mathbf{x}_j , while \mathbf{n}_j is the discrete nodal normal at node j . The discrete relative tangential velocity $(\mathbf{v}_{\star,\tau,rel})_j$ at node j yields

$$\begin{aligned} (\mathbf{v}_{\star,\tau,rel})_j &= (\mathbf{I}_3 - \mathbf{n}_j \otimes \mathbf{n}_j) \cdot \left[\sum_{l=1}^{n^{(2)}} \dot{\mathbf{M}}_{\star}[j, l] \mathbf{x}_l^{(2)} - \mathbf{I}_3 \mathbf{x}_j^{(1)} \right] \\ &= (\mathbf{I}_3 - \mathbf{n}_j \otimes \mathbf{n}_j) \cdot \sum_{l=1}^{n^{(2)}} \dot{\mathbf{M}}_{\star}[j, l] \mathbf{x}_l^{(2)} \quad j = 1, \dots, n_{\star}^{(1)}, \end{aligned} \quad (4.56)$$

with the time derivative (\cdot) being shifted from the nodal positions to the contact matrices to guarantee the satisfaction of the fundamental requirement of frame indifference, see Gitterle [87] for a detailed explanation. Finally, the algorithm to evaluate the point contact contributions for one pair of vertex node and possibly contacting master element reads:

Algorithm 4.1. Vertex contact

1. Project the slave node $\mathbf{x}_j^{(1)}$ that corresponds to the vertex along its unit normal $\mathbf{n}_j^{(1)}$ onto the master element to obtain the projected position on the master element $\hat{\mathbf{x}}^{(2)}(\mathbf{x}_j^{(1)})$.
2. Evaluate the contact matrices (4.53) and (4.54), gap function (4.55) and relative tangential velocity (4.56) at these points.

4.5.2. Contact of non-parallel edges

The penalty regularization of the point contact scenario resulting from edge-to-edge contact is considered in the following. Since the non-parallel edge-to-edge scenario results in contact points that are generally not coincident with finite element nodes, stability requirements for the Lagrange multipliers at these points are hardly predictable. Additionally, a point Lagrange multiplier would be located in the interior of the support of the already defined edge Lagrange multipliers. Thus, from an engineering point of view, these situations could be described as being over-constrained. Therefore, the exact (point-wise) enforcement of the contact constraints on $\gamma_{\times,h}$ is relaxed via a penalty regularization.

Remark 4.1. Note that the scenario of non-parallel edges being in contact is the only inevitable situation in the overall algorithm, where a penalty regularization is needed. To the best of knowledge of the author, no suitable Lagrange multiplier space can be a priori constructed for such a scenario and consequently the penalty approach cannot be avoided at this point.

By inserting the spatial discretization (4.36) into (4.35), the discrete penalty force vector of crossing edges results in

$$\mathbf{f}_\times = \mathbf{f}_\times^{(1)} - \mathbf{f}_\times^{(2)}, \quad (4.57)$$

with the discrete slave force vector $\mathbf{f}_\times^{(1)}$ and the discrete master force vector $\mathbf{f}_\times^{(2)}$. These can be computed by merging the nodal vectors

$$\mathbf{f}_\times^{(1)}[k] = \mathbf{f}_{\text{pen}} N_k^{(1)}(\hat{\xi}_\times^{(1)}) , \quad k = 1, \dots, n^{(1)}, \quad (4.58)$$

$$\mathbf{f}_\times^{(2)}[l] = \mathbf{f}_{\text{pen}} N_l^{(2)}(\hat{\xi}_\times^{(2)}) , \quad l = 1, \dots, n^{(2)}. \quad (4.59)$$

Here, the expression in (4.35) reduces to a point-wise evaluation at the parameter space coordinates $\hat{\xi}_\times^{(1)}$ and $\hat{\xi}_\times^{(2)}$. These points represent the parameter space counterparts to the points in physical space $\hat{\mathbf{x}}_\times^{(1)}$ and $\hat{\mathbf{x}}_\times^{(2)}$ at which the closest distance between two line elements can be measured, see Section 4.4.5. Generally, these points are not coincident with finite element nodes and thus they have to be computed via a closest-point-projection between two line elements. In (4.58) and (4.59), the discrete penalty force vector \mathbf{f}_{pen} can be split into its normal part $\mathbf{f}_{\text{pen},n}$ and its tangential part $\mathbf{f}_{\text{pen},\tau}$. The normal force can be obtained by inserting the finite element discretization into (4.25):

$$\mathbf{f}_{\text{pen},n} = \begin{cases} \epsilon_n(-g_{\times,n}) \hat{\mathbf{n}}_\times^{(1)} & \text{if } g_{\times,n} \leq 0 \\ 0 & \text{if } g_{\times,n} > 0 \end{cases}. \quad (4.60)$$

Herein, $g_{\times,n}$ is the discrete gap function between $\hat{\mathbf{x}}_\times^{(1)}$ and $\hat{\mathbf{x}}_\times^{(2)}$ and $\hat{\mathbf{n}}_\times^{(1)}$ is the unit normal vector defined along the connecting line between $\hat{\mathbf{x}}_\times^{(1)}$ and $\hat{\mathbf{x}}_\times^{(2)}$, but pointing in outward direction of the slave body, see again Figure 4.9. For defining the discrete frictional penalty force, the discrete relative tangential velocity at $\hat{\mathbf{x}}_\times^{(1)}$ has to be defined as

$$\mathbf{v}_{\times,\tau,\text{rel}} = (\mathbf{I}_3 - \hat{\mathbf{n}}_\times^{(1)} \otimes \hat{\mathbf{n}}_\times^{(1)}) \cdot \left[\sum_{l=1}^{n^{(2)}} \dot{N}_l^{(2)}(\hat{\xi}_\times^{(2)}) \mathbf{x}_l^{(2)} - \sum_{k=1}^{n^{(1)}} \dot{N}_k^{(1)}(\hat{\xi}_\times^{(1)}) \mathbf{x}_k^{(1)} \right]. \quad (4.61)$$

Again, the time derivative is shifted to the discrete interpolation, which guarantees frame indifference, see Gitterle [87]. There, the time derivative stems from the changing geometrical projection, which can be directly expressed as change of the parameter space coordinate. The Lie derivative in (4.26) is defined as

$$\mathcal{L} \mathbf{f}_{\text{pen},\tau} = (\mathbf{I}_3 - \hat{\mathbf{n}}_\times^{(1)} \otimes \hat{\mathbf{n}}_\times^{(1)}) \dot{\mathbf{f}}_{\text{pen},\tau}. \quad (4.62)$$

This expression contains only material time derivatives of the penalty force itself and no time derivatives of base vectors are present. Thus, the Lie derivative in (4.62) is frame indifferent. For the calculation of the Coulomb frictional forces at the edge-to-edge contact points, a trial state-return map strategy is employed, which is an algorithmic time stepping procedure, see Laursen [151] and Yang et al. [301]. Here, a trial state is computed by assuming a perfect stick state during the time increment Δt :

$$\mathbf{f}_{\text{pen},\tau_{n+1}}^{\text{trial}} = \mathbf{f}_{\text{pen},\tau_n}^{\text{trial}} - \epsilon_\tau \mathbf{v}_{\times,\tau,\text{rel}}. \quad (4.63)$$

Again, the lower index n is the time step counter. With this trial force at hand, the final tangential force can be computed with

$$\mathbf{f}_{\text{pen},\tau_{n+1}} = \begin{cases} \mathbf{f}_{\text{pen},\tau_{n+1}}^{\text{trial}} & \text{if } \|\mathbf{f}_{\text{pen},\tau_{n+1}}^{\text{trial}}\| - \mathfrak{F}\|\mathbf{f}_{\text{pen},n}\| \leq 0 \\ \frac{\mathfrak{F}\|\mathbf{f}_{\text{pen},n}\|}{\|\mathbf{f}_{\text{pen},\tau_{n+1}}^{\text{trial}}\|} \mathbf{f}_{\text{pen},\tau_{n+1}}^{\text{trial}} & \text{if } \|\mathbf{f}_{\text{pen},\tau_{n+1}}^{\text{trial}}\| - \mathfrak{F}\|\mathbf{f}_{\text{pen},n}\| > 0 \end{cases}. \quad (4.64)$$

Here, the first case represents the perfect stick situation, which was assumed for the trial state and thus the final tangential force is identical to the trial force. The second case is the slip state where the final force has the absolute value of the Coulomb friction limit but points in the direction of the trial force. To sum up, the discrete penalty forces for the non-parallel edge-to-edge contact setting are no independent unknowns but can rather be expressed in terms of the discrete nodal displacements.

The algorithm for the non-parallel edge-to-edge contact is summarized in the following for a pair of two line elements:

Algorithm 4.2. Contact of non-parallel edges

1. Check if the line elements are parallel: If yes, no point contact of crossing edges will occur, otherwise continue.
2. Compute the points $\hat{\mathbf{x}}_x^{(1)}$ and $\hat{\mathbf{x}}_x^{(2)}$ with their corresponding parameter space coordinates $\xi_x^{(1)}$ and $\xi_x^{(2)}$. If the parameter space coordinates are outside of the defined intervals of their line elements, i.e. $\xi_x^{(i)} < -1$ or $\xi_x^{(i)} > 1$, the two line elements do not represent an edge-to-edge contact pair and the algorithm is completed.
3. Compute the normal part of penalty force vector $\mathbf{f}_{\text{pen},n}$ with (4.60) and the tangential force $\mathbf{f}_{\text{pen},\tau}$ with (4.64).
4. If the penalty regularization is active and the force vector is non-zero, compute the slave and master side force vectors $\mathbf{f}_x^{(1)}$ and $\mathbf{f}_x^{(2)}$ via (4.58) and (4.59).

4.6. Line contact

Now, the discretization of the line contact is considered. Afterwards, the numerical evaluation of the arising mortar terms for line contact is explained. Therefore, two different strategies for numerical integration are provided.

4.6.1. Spatial discretization of line contact

All possible contact scenarios that result in line contact are treated with a mortar-based approach defined on an edge. Thus, Lagrange multipliers are employed for constraint enforcement at 1D slave entities. Therefore, a discrete counterpart of the line Lagrange multiplier must be introduced, which is based on the subset $\mathcal{M}_{\text{l,h}}$ being an approximation of the continuous space \mathcal{M}_{l} .

The interpolation of the discrete line Lagrange multipliers reads

$$\boldsymbol{\lambda}_{\text{t},\text{h}} = \sum_{j=1}^{n_{\text{t}}^{(1)}} \Theta_j \boldsymbol{\lambda}_{\text{t},j} . \quad (4.65)$$

The shape functions Θ_j are based on the finite element parameter space for 1D curves ξ . The discrete line Lagrange multipliers are carried by the nodes $n_{\text{t}}^{(1)}$, which are defined on physical slave edges except for the nodes $n_{\star}^{(1)}$ attached to vertices. Basically, there are two different types of Lagrange multiplier interpolation for mortar methods. First, so-called standard shape functions can be employed, which are identical to the displacement interpolation of a 2-node line element. Second, shape functions based on a biorthogonality condition can be utilized, which are also commonly known as dual shape functions, see Chapter 3 for dual shape functions in the context of surface contact. These dual shape functions are very advantageous, since they allow for a computationally efficient condensation procedure of the discrete Lagrange multipliers. More details on dual shape functions for contact elements with 1D parameter space can be found in Popp et al. [211] and Wohlmuth [289]. If a line element is connected to a vertex, it would now carry one discrete line Lagrange multiplier and one discrete point Lagrange multiplier. Thus, partition of unity would not be guaranteed anymore. In order to guarantee partition of unity for these elements, the line Lagrange multiplier shape functions have to be modified in the vicinity of the vertex node, see Figure 4.10. Here, modification of the shape function of the line Lagrange

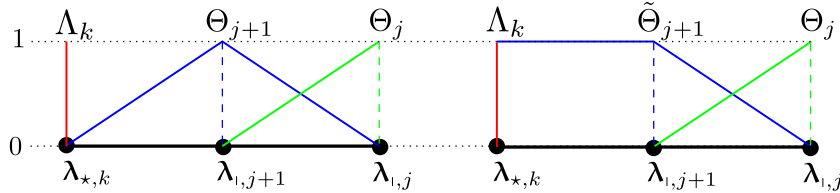


Figure 4.10: Modification of line Lagrange multiplier interpolation for standard shape functions due to the presence of a point Lagrange multiplier: unmodified shape function (left) and modified shape function (right). The figure is taken from Farah et al. [71].

multiplier yields a constant interpolation to the point Lagrange multiplier. The modified shape functions are denoted by $\tilde{\Theta}_j$. This modification is also applicable for dual shape functions as shown in Figure 4.11. It should be pointed out that such modifications are well-established in mortar finite element methods in the context of Dirichlet boundary conditions at slave nodes or so-called crosspoints, which arise when multiple mortar subdomains meet at one point, see Puso and Laursen [217] and Wohlmuth [289].

By discretizing the contact virtual work related to line contact, the two slave side line contact matrices $\mathbf{D}_{\parallel} \in \mathbb{R}^{3n_{\text{t}}^{(1)} \times 3n_{\text{t}}^{(1)}}$ and $\mathbf{D}_{\star\text{t}} \in \mathbb{R}^{3n_{\text{t}}^{(1)} \times 3n_{\star}^{(1)}}$ arise:

$$\mathbf{D}_{\parallel}[j, k] = D_{\parallel,jk} \mathbf{I}_3 = \int_{\gamma_{\text{t},\text{h}}^{(1)}} \Theta_j N_k^{(1)} dL \mathbf{I}_3 , \quad j = 1, \dots, n_{\text{t}}^{(1)}, \quad k = 1, \dots, n_{\text{t}}^{(1)} , \quad (4.66)$$

$$\mathbf{D}_{\star\text{t}}[j, k] = D_{\star\text{t},jk} \mathbf{I}_3 = \int_{\gamma_{\text{t},\text{h}}^{(1)}} \Theta_j N_k^{(1)} dL \mathbf{I}_3 , \quad j = 1, \dots, n_{\text{t}}^{(1)}, \quad k = 1, \dots, n_{\star}^{(1)} . \quad (4.67)$$

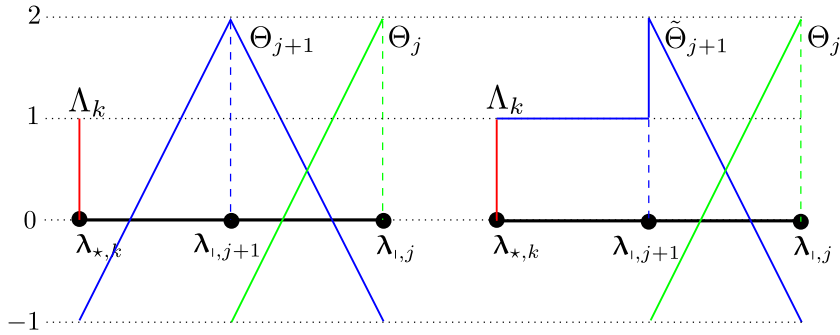


Figure 4.11: Modification of line Lagrange multiplier interpolation for dual shape functions due to the presence of a point Lagrange multiplier: unmodified shape function (left) and modified shape function (right). The figure is taken from Farah et al. [71].

Here, \mathbf{D}_{\parallel} couples the line Lagrange multipliers with the edge displacements and \mathbf{D}_{\star} couples the line Lagrange multipliers with the displacements of vertex nodes. Both matrices can be assembled to the matrix $\mathbf{D}_i \in \mathbb{R}^{3n_i^{(1)} \times 3n_i^{(1)}}$

$$\mathbf{D}_i = [\mathbf{D}_{\parallel} \quad \mathbf{D}_{\star}] , \quad (4.68)$$

which allows for an easier notation later on. In addition, the master side line contact matrix $\mathbf{M}_i \in \mathbb{R}^{3n_i^{(1)} \times 3n_i^{(2)}}$ reads:

$$\mathbf{M}_i[j, l] = M_{i,jl} \mathbf{I}_3 = \int_{\gamma_{i,h}^{(1)}} \Theta_j(N_l^{(2)} \circ \chi_h) dL \mathbf{I}_3 , \quad j = 1, \dots, n_i^{(1)}, \quad l = 1, \dots, n_i^{(2)}. \quad (4.69)$$

These slave and master matrices can readily be interpreted as mortar matrices, since they result from an integration of a shape function product over the Lagrange multiplier support. Thus, they have mass matrix characteristics. When inserting the finite element discretization (4.36) and (4.65) into the normal part of the constraint equations for line contact (4.33), the discrete weighted gap $\tilde{g}_{i,j}$ at node j for line contact emerges:

$$\tilde{g}_{i,j} = \int_{\gamma_{i,h}^{(1)}} \Phi_j g_{n,h} dL \quad j = 1, \dots, n_i^{(1)}. \quad (4.70)$$

Additionally, the weighted relative tangential velocity $(\mathbf{v}_{i,\tau,rel})_j$ for line contact follows from discretizing the weak frictional sliding constraint in (4.33), viz.

$$(\tilde{\mathbf{v}}_{i,\tau,rel})_j = (\mathbf{I}_3 - \mathbf{n}_j \otimes \mathbf{n}_j) \cdot \left[\sum_{l=1}^{n_i^{(2)}} \dot{\mathbf{M}}_i[j, l] \mathbf{x}_l^{(2)} - \sum_{k=1}^{n_i^{(1)}} \dot{\mathbf{D}}_i[j, k] \mathbf{x}_k^{(1)} \right]. \quad (4.71)$$

Again, frame indifference is achieved by formulating $(\mathbf{v}_{i,\tau,rel})_j$ in terms of time derivatives of the mortar matrices.

4.6.2. Numerical evaluation of line contact

In contrast to the point contact formulation in Section 4.5, a numerical integration procedure has to be carried out to evaluate the mortar matrices in (4.67) and (4.69) and the kinematic

quantities (4.70) and (4.71). Since the mortar matrix \mathbf{M}_i , the weighted gap $\tilde{g}_{i,j}$ and the weighted relative tangential velocity $(\tilde{\mathbf{v}}_{i,\tau,\text{rel}})_j$ all require an integration over the slave side line contact boundary $\gamma_{i,h}^{(1)}$ with integrands containing quantities from both sides, an exact evaluation cannot be achieved by standard Gauss quadrature rules simply being applied on each slave line element. This is due to the generally non-matching meshes that result from arbitrary line contact situations in the finite deformation regime. To overcome this problem, a so-called segment-based integration scheme is employed, which is based on the idea of preventing all possible discontinuities in the integrands by creating smooth integrable segments. This idea was firstly outlined for classical segment-to-segment contact formulations in Simo et al. [253] and in Zavarise and Wriggers [304] and then applied in the context of mortar formulations in McDevitt and Laursen [168] and in Puso and Laursen [217]. Here, the basic principle is adopted for the line contact integration. In order to create line segments that contain only C^1 -continuous integrands in (4.69), (4.70) and (4.71), the nodes of a considered slave line element and a master element are projected onto an auxiliary plane. Then, a line clipping algorithm is applied to determine the part of the line element that is located within the master element or the master element edges. The whole procedure is visualized in Figure 4.12.

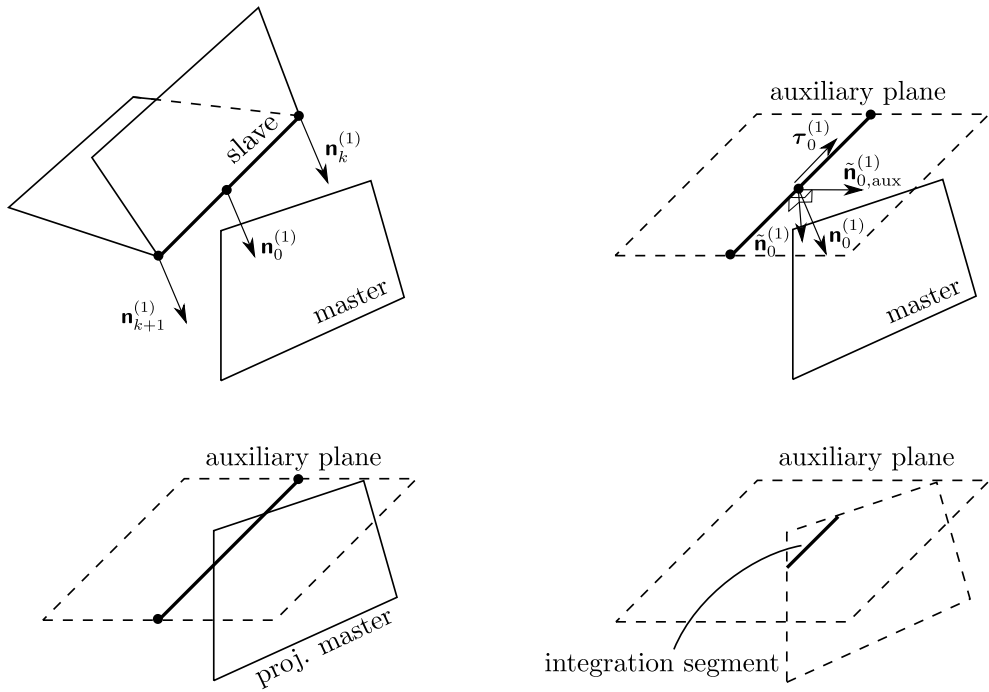


Figure 4.12: Main steps of the segment-based integration scheme for the line contact algorithm: Create an averaged normal vector at the middle of the slave line element (top left), project the averaged normal vector into the normal plane of the line element and construct an auxiliary plane (top right), project slave and master nodes onto the auxiliary plane (bottom left) and perform line clipping to identify line segments in which the numerical integration is performed (bottom right).

Additionally, the evaluation process is given in the following algorithm:

Algorithm 4.3. Segment-based integration for line contact

1. Create an averaged normal vector $\mathbf{n}_0^{(1)}$ based on the nodal normal vectors $\mathbf{n}_k^{(1)}$ and $\mathbf{n}_{k+1}^{(1)}$.
2. Project the averaged normal vector $\mathbf{n}_0^{(1)}$ into the normal plane of the considered line element to create the normal vector $\tilde{\mathbf{n}}_0^{(1)}$. In detail: $\tilde{\mathbf{n}}_0^{(1)} = (\mathbf{I}_3 - \boldsymbol{\tau}_0^{(1)} \otimes \boldsymbol{\tau}_0^{(1)}) \mathbf{n}_0^{(1)}$.
3. Construct an auxiliary plane for numerical integration based on the slave element center $\mathbf{x}_0^{(1)}$ and the corresponding normal vector $\tilde{\mathbf{n}}_0^{(1)}$.
4. Project all $n_e^{(2)}$ master element nodes $\mathbf{x}_l^{(2)}$, $l = 1, \dots, n_e^{(2)}$ along $\tilde{\mathbf{n}}_0^{(1)}$ onto the auxiliary plane to create the auxiliary master nodes $\tilde{\mathbf{x}}_l^{(2)}$.
5. Project all $n_e^{(1)}$ slave line element nodes $\mathbf{x}_k^{(1)}$, $k = 1, \dots, n_e^{(1)}$ along $\tilde{\mathbf{n}}_0^{(1)}$ onto the auxiliary plane to create the auxiliary slave nodes $\tilde{\mathbf{x}}_k^{(1)}$. This step is not required for first-order elements and can be considered as possible demand for extensions towards second-order elements.
6. Perform line clipping in the auxiliary plane in order to find the overlapping line segment of projected slave and master nodes. Adequate line clipping algorithms can be found in Hughes et al. [119].
7. Define suitable integration points on the created line segment and find their counterparts on the slave and master element by an inverse mapping.
8. Perform numerical integration of the mortar matrices (4.67), (4.69), the weighted gap (4.70) and the weighted relative tangential velocity (4.71).

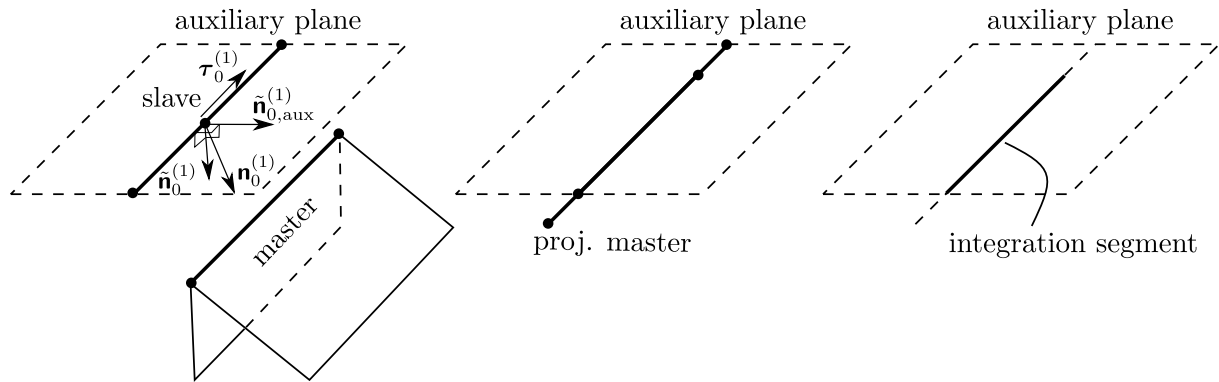


Figure 4.13: Special case of parallel edge-to-edge contact for segment based integration scheme:
Already constructed auxiliary plane (left), projected master and slave edge nodes onto auxiliary plane (middle) and line-to-line clipping (right).

In the presented algorithm, the edge-to-surface contact scenario is employed to explain the segmentation procedure. However, the proposed integration scheme is also valid for parallel

edges being in contact. This is visualized in Figure 4.13. Here, again an auxiliary plane is built in complete analogy to Figure 4.12. Then, a master line element is projected onto the slave side auxiliary plane, see middle part of Figure 4.13. Afterwards, a line-to-line clipping algorithm is performed, which shares a lot of similarities with segment-based integration schemes for 2D bodies with mortar contact, see Popp et al. [211] and Yang et al. [301]. Consequently, the integration segment end points can be directly identified as projected slave or master nodes. For the edge-to-surface segmentation scheme, the integration segment end points could also be identified as crossing of projected element edges. More information concerning the node projection and consistent linearization of the geometrical procedures can be found in the Appendix B. The robustness and accuracy of the segment-based integration scheme for edge-to-surface and edge-to-edge contact scenarios is demonstrated at several numerical examples in Section 4.9.

The algorithm explained above performs robustly and guarantees for highest accuracy in all tested numerical examples. However, an alternative segment-based integration scheme is given in the following, which requires less algorithmic steps and can thus be implemented more efficiently. However, this increase in efficiency is dearly bought by the prize of less robustness compared to the first algorithm. For the sake of completeness, the alternative procedure is illustrated in Figure 4.14 and the corresponding algorithm reads:

Algorithm 4.4. Alternative segment-based integration for line contact

1. Construct an auxiliary plane for numerical integration based on the master element center $\mathbf{x}_0^{(2)}$ and the corresponding element normal vector $\mathbf{n}_0^{(2)}$.
2. Project all $n_e^{(2)}$ master element nodes $\mathbf{x}_l^{(2)}$, $l = 1, \dots, n_e^{(2)}$ along $\mathbf{n}_0^{(2)}$ onto the auxiliary plane to create the auxiliary master nodes $\tilde{\mathbf{x}}_l^{(2)}$.
3. Project all $n_e^{(1)}$ slave line element nodes $\mathbf{x}_k^{(1)}$, $k = 1, \dots, n_e^{(1)}$ along their nodal normal $\mathbf{n}_k^{(1)}$ onto the auxiliary plane to create the auxiliary slave nodes $\tilde{\mathbf{x}}_k^{(1)}$.
4. Perform line clipping in the auxiliary plane in order to find the overlapping line segments of projected slave and master nodes. Adequate line clipping algorithms can be found in Hughes et al. [119].
5. Define suitable integration points on the created line segment and find their counterparts on the slave and master element by an inverse mapping.
6. Perform numerical integration of the mortar matrices (4.67), (4.69), the weighted gap (4.70) and the weighted relative tangential velocity (4.71).

Here, the integration is performed on line segments being defined on the master side auxiliary plane. The calculation of the projection normal is much easier and consequently less terms to be linearized occur. Again, the alternative integration procedure performs less robust in the numerical examples but also guarantees an exact integral evaluation. Both algorithms are implemented in the employed in-house code BACI (cf. Wall et al. [282]), but it is recommended to use the first algorithm, see Figure 4.12.

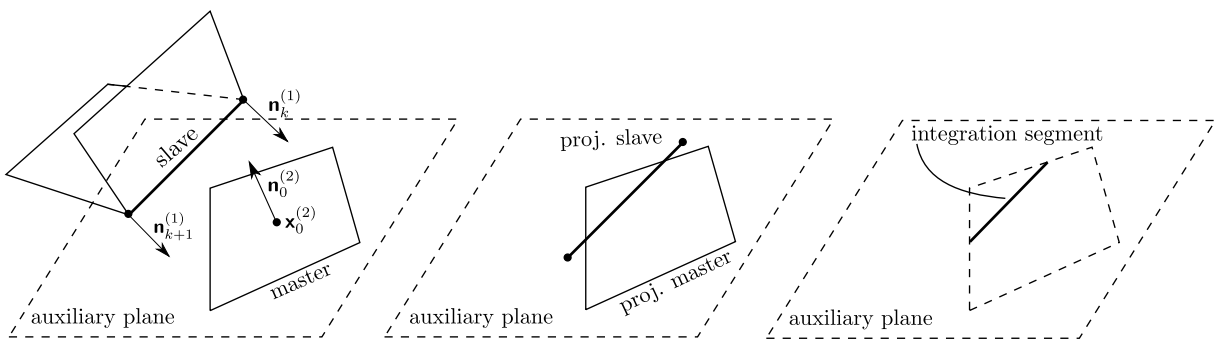


Figure 4.14: Main steps of the alternative segment-based integration scheme for the line contact algorithm: Construct an auxiliary plane (left), project slave and master nodes onto the auxiliary plane (middle) and perform line clipping to identify line segments in which the numerical integration is performed (right). The figure is taken from Farah et al. [71].

4.7. Surface contact

Finally, numerical treatment of surface contact is considered. In the following, it is focused on special aspects of surface contact with respect to the non-smooth contact framework. However, the fundamental basics of mortar surface contact have already been introduced in Chapter 3. The discretization of surface contact is realized by introducing a mortar finite element approximation of the surface Lagrange multiplier. It is based on the discrete Lagrange multiplier subset $\mathcal{M}_{o,h}$, which is an approximation of \mathcal{M}_o . The discretization of the surface Lagrange multiplier reads

$$\lambda_{o,h} = \sum_{j=1}^{n_o} \Phi_j \lambda_{o,j}, \quad (4.72)$$

with the shape functions Φ_j being based on the finite element parameter space for 2D surfaces $\xi^{(i)} = (\xi^{(i)}, \eta^{(i)})$. Again, the shape functions Φ_j can be chosen as standard shape functions or dual shape functions based on a biorthogonality condition. Dual shape functions for 2D surfaces can be found in Popp et al. [212] and Wohlmuth [288]. As for the interpolation of the discrete line Lagrange multipliers (4.65), the shape functions Φ_j have to be modified in the case of elements that are at the same time attached to different types of discrete Lagrange multipliers, i.e. line or point Lagrange multipliers. This is necessary to guarantee partition of unity. In contrast to the line Lagrange multiplier interpolation Θ_j , which is based on a 1D parameter space, this modification becomes more complex for the surface shape functions Φ_j . Thus, a general procedure based on a transformation of shape functions is defined for this modification. Starting point for deriving a suitable shape function transformation, which guarantees partition of unity, is a surface element with n_e nodes. Out of this n_e nodes, it is assumed that \bar{n}_e nodes carry discrete line Lagrange multipliers or point Lagrange multipliers. Thus, a transformation coefficient ς can be defined as

$$\varsigma = (n_e - \bar{n}_e)^{-1}. \quad (4.73)$$

It becomes obvious that the transformation is only valid when at least one node carries no other discrete Lagrange multiplier than a surface Lagrange multiplier, i.e. when $\bar{n}_e < n_e$. The final transformation is exemplified for a 4-node surface element with the first two nodes carrying surface Lagrange multipliers:

$$\begin{bmatrix} \tilde{\Phi}_1 \\ \tilde{\Phi}_2 \\ \tilde{\Phi}_3 \\ \tilde{\Phi}_4 \end{bmatrix} = \underbrace{\begin{bmatrix} 1 & 0 & \varsigma & \varsigma \\ 0 & 1 & \varsigma & \varsigma \\ 0 & 0 & 0 & 0 \\ 0 & 0 & 0 & 0 \end{bmatrix}}_{\mathbf{T}_\varsigma} \cdot \begin{bmatrix} \Phi_1 \\ \Phi_2 \\ \Phi_3 \\ \Phi_4 \end{bmatrix}, \quad (4.74)$$

with the transformed shape functions $\tilde{\Phi}_j$ and the element transformation matrix \mathbf{T}_ς . The transformation coefficient for the example given in (4.74) is obviously $\varsigma = 0.5$, since $n_e = 4$ and $\bar{n}_e = 2$. Applying the transformation procedure to different shape functions, i.e. 3-node linear surface shape functions, is absolutely straightforward. The shape function modification is exemplarily shown in Figure 4.15. When applying the transformation scheme to the line Lagrange multiplier

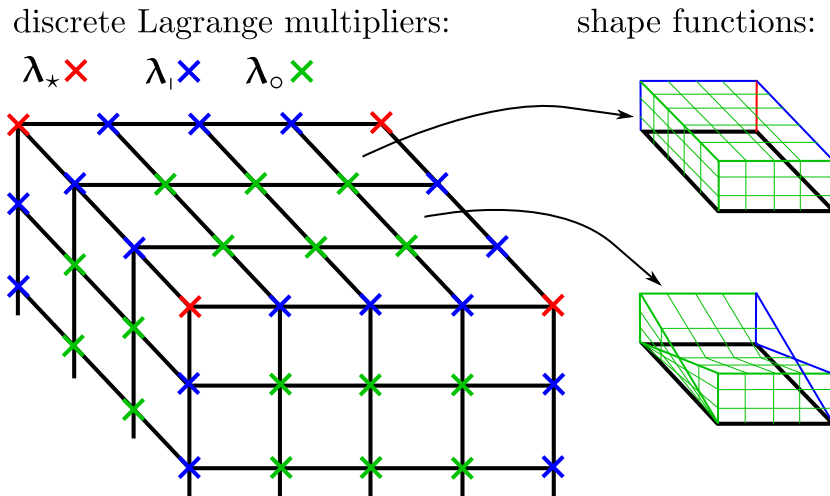


Figure 4.15: Discrete Lagrange multipliers on vertices, edges and surfaces with two exemplary modifications for standard shape functions. The figure is taken from Farah et al. [71].

interpolation Θ_j , the constant interpolation of the shape function that has already intuitively been given in Figure 4.10 would be formally obtained.

When inserting the finite element discretization for the displacement fields (4.36) and the surface Lagrange multiplier (4.72) into the surface contact virtual work contribution (4.31), the three slave side mortar matrices for surface contact $\mathbf{D}_{oo} \in \mathbb{R}^{3n_o^{(1)} \times 3n_o^{(1)}}$, $\mathbf{D}_{oi} \in \mathbb{R}^{3n_o^{(1)} \times 3n_i^{(1)}}$

and $\mathbf{D}_{\circ\star} \in \mathbb{R}^{3n_{\circ}^{(1)} \times 3n_{\star}^{(1)}}$ can be computed, viz.

$$\mathbf{D}_{\circ\circ}[j, k] = D_{\circ\circ, jk} \mathbf{I}_3 = \int_{\gamma_{\circ,h}^{(1)}} \Phi_j N_k^{(1)} d\gamma \mathbf{I}_3 , \quad j = 1, \dots, n_{\circ}^{(1)}, \quad k = 1, \dots, n_{\circ}^{(1)} , \quad (4.75)$$

$$\mathbf{D}_{\circ\mid}[j, k] = D_{\circ\mid, jk} \mathbf{I}_3 = \int_{\gamma_{\circ,h}^{(1)}} \Phi_j N_k^{(1)} d\gamma \mathbf{I}_3 , \quad j = 1, \dots, n_{\circ}^{(1)}, \quad k = 1, \dots, n_{\mid}^{(1)} , \quad (4.76)$$

$$\mathbf{D}_{\circ\star}[j, k] = D_{\circ\star, jk} \mathbf{I}_3 = \int_{\gamma_{\circ,h}^{(1)}} \Phi_j N_k^{(1)} d\gamma \mathbf{I}_3 , \quad j = 1, \dots, n_{\circ}^{(1)}, \quad k = 1, \dots, n_{\star}^{(1)} . \quad (4.77)$$

These matrices represent the coupling of the surface Lagrange multipliers to surface, edge and vertex nodes, respectively. The complete slave side mortar matrix reads

$$\mathbf{D}_{\circ} = [\mathbf{D}_{\circ\circ} \quad \mathbf{D}_{\circ\mid} \quad \mathbf{D}_{\circ\star}] . \quad (4.78)$$

Furthermore, the master side mortar matrix $\mathbf{M}_{\circ} \in \mathbb{R}^{3n_{\circ}^{(1)} \times 3n^{(2)}}$ is given as

$$\mathbf{M}_{\circ}[j, l] = M_{\circ, jl} \mathbf{I}_3 = \int_{\gamma_{\circ,h}^{(1)}} \Phi_j (N_l^{(2)} \circ \chi_h) d\gamma \mathbf{I}_3 . \quad j = 1, \dots, n_{\circ}^{(1)}, \quad l = 1, \dots, n^{(2)} . \quad (4.79)$$

The discrete counterpart of the gap function for surface contact is also a mortar-typical weighted gap, since it is integrated over the boundary $\gamma_{\circ,h}^{(1)}$, via

$$\tilde{\mathbf{g}}_{\circ,j} = \int_{\gamma_{\circ,h}^{(1)}} \Phi_j g_{n,h} dA \quad j = 1, \dots, n_{\circ}^{(1)} . \quad (4.80)$$

Additionally, the weighted relative tangential velocity for surface contact is given as

$$(\tilde{\mathbf{v}}_{\circ,\tau,\text{rel}})_j = (\mathbf{I}_3 - \mathbf{n}_j \otimes \mathbf{n}_j) \cdot \left[\sum_{l=1}^{n^{(2)}} \dot{\mathbf{M}}_{\circ}[j, l] \mathbf{x}_l^{(2)} - \sum_{k=1}^{n_{\circ}^{(1)}} \dot{\mathbf{D}}_{\circ}[j, k] \mathbf{x}_k^{(1)} \right] . \quad (4.81)$$

The evaluation of these discrete quantities requires an accurate numerical integration procedure. Here, the well-known segment-based integration scheme for surface mortar methods is employed, which was already explained in Section 3.4.2. A schematic visualization can be found in Figure 3.3. This segmentation scheme was already developed and investigated in the abundant literature and can be found for example in Farah et al. [73], Popp et al. [212] and Puso and Laursen [217].

4.8. All entity contact – combined formulation

When combining all previously presented contact contributions, the semi-discrete balance of linear momentum that results from mortar finite element discretization reads

$$\mathbf{r} := \mathbf{K}_{\text{mass}} \ddot{\mathbf{d}} + \mathbf{K}_{\text{damp}} \dot{\mathbf{d}} + \mathbf{f}_{\text{int}}(\mathbf{d}) - \mathbf{f}_{\text{ext}} + \mathbf{f}_c(\mathbf{d}, \boldsymbol{\lambda}) = \mathbf{0} , \quad (4.82)$$

with the mass matrix \mathbf{K}_{mass} and the damping matrix \mathbf{K}_{damp} , which is based on the widely used Rayleigh model for viscous damping. Furthermore, the internal and external force vectors are denoted as $\mathbf{f}_{\text{int}}(\mathbf{d})$ and \mathbf{f}_{ext} . The contact contribution $\mathbf{f}_c(\mathbf{d}, \boldsymbol{\lambda})$ is split into the Lagrange multiplier

force vector denoted as $\mathbf{f}_\lambda(\mathbf{d}, \boldsymbol{\lambda})$ and the penalty force vector for contact of crossing edges $\mathbf{f}_x(\mathbf{d})$, which was already defined in (4.57):

$$\mathbf{f}_c(\mathbf{d}, \boldsymbol{\lambda}) = \mathbf{f}_\lambda(\mathbf{d}, \boldsymbol{\lambda}) + \mathbf{f}_x(\mathbf{d}). \quad (4.83)$$

The Lagrange multiplier force vector is defined via the global slave and master side mortar matrices $\mathbf{D} \in \mathbb{R}^{3m^{(1)} \times 3n^{(1)}}$ and $\mathbf{M} \in \mathbb{R}^{3m^{(1)} \times 3n^{(2)}}$

$$\mathbf{D} = [\mathbf{D}_o \quad \mathbf{D}_l \quad \mathbf{D}_s], \quad \mathbf{M} = [\mathbf{M}_o \quad \mathbf{M}_l \quad \mathbf{M}_s]. \quad (4.84)$$

Here, the row dimension of the matrices is given as $m^{(1)} = n_o^{(1)} + n_l^{(1)} + n_s^{(1)} = n^{(1)}$. With these matrices, the global contact force vector due to Lagrange multiplier based contact reads

$$\mathbf{f}_\lambda = [\mathbf{0} \quad -\mathbf{M} \quad \mathbf{D}]^T \boldsymbol{\lambda}, \quad (4.85)$$

with the global Lagrange multiplier vector

$$\boldsymbol{\lambda} = [\lambda_o \quad \lambda_l \quad \lambda_s]^T. \quad (4.86)$$

Obviously, all discrete Lagrange multipliers for point, line and surface contact are contained in $\boldsymbol{\lambda}$. The inequality constraints for normal and tangential contact are generally stated in semi-discrete form as

$$g_j \geq 0, \quad \lambda_{n,j} \geq 0, \quad \lambda_{n,j} g_j = 0, \quad j = 1, \dots, n^{(1)}, \quad (4.87)$$

$$\Upsilon_j := \|(\boldsymbol{\lambda}_\tau)_j\| - |\mathfrak{F}|(\lambda_n)_j \leq 0,$$

$$(\mathbf{v}_{\tau,\text{rel}})_j + \beta_j (\boldsymbol{\lambda}_\tau)_j = \mathbf{0}, \quad \beta_j \geq 0, \quad \Upsilon_j \beta_j = 0, \quad j = 1, \dots, n^{(1)}. \quad (4.88)$$

The semi-discrete problem formulation given in (4.82)-(4.88) is particularly elegant, since it is no longer distinguished between point, line and surface contact. For example, in (4.87) and (4.88), the gap g_j , the relative tangential velocity $(\mathbf{v}_{\tau,\text{rel}})_j$, the complementarity parameter β_j and the Lagrange multiplier λ_j have different physical interpretations for vertex, edge and surface nodes, respectively. Although it contains point, line and surface contact formulations, the semi-discrete problem formulation remains as simple and compact as for pure surface contact, see e.g. Popp et al. [212] and Chapter 3.

4.8.1. Semi-smooth Newton method

As described in Section 3.5.2, a primal-dual active set strategy is employed in order to consider the additional nonlinearities stemming from the contact inequality constraints. Thus, the split of the set of all slave nodes \mathcal{S} into an active set \mathcal{A} , inactive set \mathcal{I} as well as a stick set \mathcal{S}_T and a slip set \mathcal{S}_L is performed regardless of the fact whether the actual Lagrange multiplier belongs to the point, line or surface contact. Also the introduced nonlinear complementarity functions in (3.59) and (3.61) are reused without any modification for the different contact scenarios. Consequently, all arising nonlinearities can be solved within one Newton-Raphson scheme. Again, the introduced parameters c_n and c_t in (3.59) and (3.61) only influence the convergence behavior and do not affect the result when the algorithm is converged. Having in mind that the tangential

parameter c_t balances the different scales of the tangential part of the Lagrange multiplier and the relative tangential slip increment, it becomes obvious, that the different units of the point, line and surface Lagrange multipliers influence the choice of c_t . Consequently, it depends on the current load, deformation and contact status. However, for all numerical examples a constant value for c_t for all slave nodes is employed over the entire simulations without recognizing any deterioration of convergence.

Note, the node-wise decoupled enforcement of the contact constraints in (4.87) and (4.88) is only valid for a diagonal slave side contact matrix \mathbf{D} . This cannot be achieved for the combined contact formulation presented in this contribution, due the off-diagonal blocks $\mathbf{D}_{\circ\circ}$, $\mathbf{D}_{\circ\star}$ and $\mathbf{D}_{\star\circ}$. But, the main diagonal blocks $\mathbf{D}_{\circ\circ}$, $\mathbf{D}_{\parallel\parallel}$ and $\mathbf{D}_{\star\star}$ can be created in diagonal form by employing dual shape functions and thus most of the nodes are decoupled. However, a rigorous variational form would require a coupled NCP function containing all coupled slave nodes or suitable lumping techniques, see Blum et al. [29]. Nevertheless, node-wise NCP functions are utilized throughout this thesis without any negative influence on the numerical examples.

4.8.2. Algebraic representation

In this section, an algebraic representation of the linearized system to be solved within each semi-smooth Newton step is provided for the developed all entity contact formulation. The general resulting system of equations is of saddle-point type and can be formulated in complete analogy to the one for surface contact from (3.62). For the sake of clarity, it is briefly repeated:

$$\begin{bmatrix} \mathbf{K}_{NN} & \mathbf{K}_{NM} & \mathbf{K}_{NS} & \mathbf{0} \\ \mathbf{K}_{MN} & \tilde{\mathbf{K}}_{MM} & \tilde{\mathbf{K}}_{MS} & -\mathbf{M}^T \\ \mathbf{K}_{SN} & \tilde{\mathbf{K}}_{SM} & \tilde{\mathbf{K}}_{SS} & \mathbf{D}^T \\ \mathbf{0} & \mathbf{C}_M & \mathbf{C}_S & \mathbf{C}_\lambda \end{bmatrix}^i \begin{bmatrix} \Delta\mathbf{d}_N \\ \Delta\mathbf{d}_M \\ \Delta\mathbf{d}_S \\ \Delta\lambda \end{bmatrix}^{i+1} = - \begin{bmatrix} \mathbf{r}_N \\ \mathbf{r}_M \\ \mathbf{r}_S \\ \mathbf{r}_c \end{bmatrix}^i. \quad (4.89)$$

Again, the system of equations in (4.89) is of increased system size compared to classical structural problems, as both displacements and Lagrange multipliers show up as primary unknowns. Thus, the solution vector contains increments of discrete displacements $\Delta\mathbf{d}$ and Lagrange multipliers $\Delta\lambda$. The discrete global vector of Lagrange multipliers is split into point, line and surface Lagrange multipliers as stated in (4.86). Like for surface-to-surface contact from Section 3.5.3, the displacement unknowns are distinguished between bulk nodes $(\cdot)_N$, slave nodes $(\cdot)_S$ and master nodes $(\cdot)_M$. The matrix blocks denoted with \mathbf{K} contain terms from linearization of the internal force vector \mathbf{f}_{int} , damping terms \mathbf{K}_{damp} and mass matrix contributions \mathbf{K}_{mass} . The upper tilde symbol $(\tilde{\cdot})$ indicates additional contributions from the linearized penalty force vector \mathbf{f}_\times and the linearized Lagrange multiplier contact force vector \mathbf{f}_λ . The matrix blocks denoted with \mathbf{C} represent the linearization of the complementarity functions in (3.58) and (3.60). Following the explanations in Section 3.5.3, elimination of additional Lagrange multiplier unknowns can be achieved by utilizing the third row of (4.89). This yields a Lagrange multiplier expression in terms of displacement increments:

$$\Delta\lambda^{i+1} = -\mathbf{D}^{i,-T}(\mathbf{K}_{SN}^i \Delta\mathbf{d}_N^{i+1} + \tilde{\mathbf{K}}_{SM}^i \Delta\mathbf{d}_M^{i+1} + \tilde{\mathbf{K}}_{SS}^i \Delta\mathbf{d}_S^{i+1} - \mathbf{r}_S^i). \quad (4.90)$$

In classical dual mortar methods, inverting the diagonal matrix \mathbf{D} is of negligible computational cost. In this thesis, not all slave nodes completely decouple due to the three different sets of

Lagrange multipliers. Therefore, the complete slave side mortar matrix reads in block structure:

$$\mathbf{D} = \begin{bmatrix} \mathbf{D}_{\text{oo}} & \mathbf{D}_{\text{o}\text{l}} & \mathbf{D}_{\text{o}\star} \\ \mathbf{0} & \mathbf{D}_{\text{l}\text{l}} & \mathbf{D}_{\text{l}\star} \\ \mathbf{0} & \mathbf{0} & \mathbf{D}_{\star\star} \end{bmatrix}. \quad (4.91)$$

Here, it is obvious that \mathbf{D} is an upper triangular matrix and its inversion is not as trivial as for classic dual mortar methods. Nevertheless, its inversion reads

$$\mathbf{D}^{-1} = \begin{bmatrix} \mathbf{D}_{\text{oo}}^{-1} & \mathbf{0} & \mathbf{0} \\ \mathbf{0} & \mathbf{D}_{\text{l}\text{l}}^{-1} & \mathbf{0} \\ \mathbf{0} & \mathbf{0} & \mathbf{D}_{\star\star}^{-1} \end{bmatrix} \begin{bmatrix} \mathbf{I} & -\mathbf{D}_{\text{o}\text{l}}\mathbf{D}_{\text{l}\text{l}}^{-1} & \mathbf{D}_{\text{o}\text{l}}\mathbf{D}_{\text{l}\text{l}}^{-1}\mathbf{D}_{\text{l}\star}\mathbf{D}_{\star\star}^{-1} - \mathbf{D}_{\text{o}\star}\mathbf{D}_{\star\star}^{-1} \\ \mathbf{0} & \mathbf{I} & -\mathbf{D}_{\text{l}\star}\mathbf{D}_{\star\star}^{-1} \\ \mathbf{0} & \mathbf{0} & \mathbf{I} \end{bmatrix}. \quad (4.92)$$

Herein, only the main diagonal blocks \mathbf{D}_{oo} , $\mathbf{D}_{\text{l}\text{l}}$ and $\mathbf{D}_{\star\star}$ have to be inverted. By employing dual shape functions, these main diagonal blocks are again of diagonal shape and thus inverting the global \mathbf{D} matrix is still computationally efficient. By expressing the discrete Lagrange multiplier unknowns in terms of displacement unknowns as stated in (4.90), the final condensed system of equations arises:

$$\begin{bmatrix} \mathbf{K}_{\mathcal{N}\mathcal{N}} & \mathbf{K}_{\mathcal{N}\mathcal{M}} & \mathbf{K}_{\mathcal{N}\mathcal{S}} \\ \mathbf{K}_{\mathcal{M}\mathcal{N}} + \mathbf{P}^T \mathbf{K}_{\mathcal{S}\mathcal{N}} & \tilde{\mathbf{K}}_{\mathcal{M}\mathcal{M}} + \mathbf{P}^T \tilde{\mathbf{K}}_{\mathcal{S}\mathcal{M}} & \tilde{\mathbf{K}}_{\mathcal{M}\mathcal{S}} + \mathbf{P}^T \tilde{\mathbf{K}}_{\mathcal{S}\mathcal{S}} \\ -\mathbf{C}_\lambda \mathbf{D}^{-T} \mathbf{K}_{\mathcal{S}\mathcal{N}} & \mathbf{C}_\lambda \mathbf{D}^{-T} \tilde{\mathbf{K}}_{\mathcal{S}\mathcal{M}} & \mathbf{C}_\lambda \mathbf{D}^{-T} \tilde{\mathbf{K}}_{\mathcal{S}\mathcal{S}} \end{bmatrix}^i \begin{bmatrix} \Delta \mathbf{d}_{\mathcal{N}} \\ \Delta \mathbf{d}_{\mathcal{M}} \\ \Delta \mathbf{d}_{\mathcal{S}} \end{bmatrix}^{i+1} = - [\mathbf{r}_{\mathcal{N}} \mid \mathbf{r}_{\mathcal{M}} + \mathbf{P}^T \mathbf{r}_{\mathcal{S}} \mid \mathbf{r}_{\mathcal{S}} - \mathbf{C}_\lambda \mathbf{D}^{-T} \mathbf{r}_{\mathcal{S}}]^{i,T}. \quad (4.93)$$

Again, the mortar projection operator can be identified in its general form

$$\mathbf{P} = \mathbf{D}^{-1} \mathbf{M}. \quad (4.94)$$

The final system of equations in (4.93) is of constant system size and the only remaining degrees of freedom are the displacement unknowns. All information of the point, line and surface contact are included in the modified system matrix and no saddle-point structure occurs anymore. The discrete Lagrange multipliers can be easily obtained by a simple post-processing step based on (4.90).

4.8.3. Conservation laws

The fundamental conservation laws have been already introduced for mechanical systems in Section 2.1.3 and are now analyzed in the context of the proposed all entity contact formulation. Therefore, all following explanations are referred to the semi-discrete setting, meaning that the problem is discrete in space but continuous in time.

4.8.3.1. Balance of linear momentum

First, as elaborated e.g. in Puso and Laursen [218] the requirement for linear momentum conservation can be expressed as balance of all forces acting on the slave and master side. In the context of the newly developed all entity contact formulation this requirement reads:

$$\mathbf{f}_c^{(1)} - \mathbf{f}_c^{(2)} = \mathbf{D}^T \boldsymbol{\lambda} + \mathbf{f}_x^{(1)} - (\mathbf{M}^T \boldsymbol{\lambda} + \mathbf{f}_x^{(2)}). \quad (4.95)$$

As explained in the previous sections, the slave and master side forces can be split into penalty force vectors $\mathbf{f}_\times^{(i)}$ and Lagrange multiplier force vectors $\mathbf{f}_\lambda^{(i)}$. The overall balance of linear momentum at the contact interface can be investigated by first considering the balance of penalty forces and then the balance of forces due to the Lagrange multipliers. Thus, the balance of penalty forces reads

$$\mathbf{f}_\times^{(1)} - \mathbf{f}_\times^{(2)} = \sum_{k=1}^{n^{(1)}} \mathbf{f}_{\text{pen}} N_k^{(1)}(\hat{\xi}_\times^{(1)}) - \sum_{l=1}^{n^{(2)}} \mathbf{f}_{\text{pen}} N_l^{(2)}(\hat{\xi}_\times^{(2)}) = \mathbf{0}. \quad (4.96)$$

Since the displacement shape functions fulfill the fundamental requirement of partition of unity, i.e. $\sum_{k=1}^{n^{(1)}} N_k^{(1)} = 1$ and $\sum_{l=1}^{n^{(2)}} N_l^{(2)} = 1$, the balance of linear momentum can be written as

$$1(\mathbf{f}_{\text{pen}} - \mathbf{f}_{\text{pen}}) = \mathbf{0}. \quad (4.97)$$

Here, it can be clearly seen that conservation of linear momentum is *always* guaranteed for the penalty forces resulting from contact of crossing edges.

Conservation of linear momentum for the Lagrange multiplier force vectors can be stated as

$$\mathbf{f}_\lambda^{(1)} - \mathbf{f}_\lambda^{(2)} = \sum_{j=1}^{m^{(1)}} \left(\sum_{k=1}^{n^{(1)}} \mathbf{D}[j, k] \boldsymbol{\lambda}_j - \sum_{l=1}^{n^{(2)}} \mathbf{M}[j, l] \boldsymbol{\lambda}_j \right) = \mathbf{0}, \quad (4.98)$$

which is identical to the investigations in Popp [210] and Puso and Laursen [218]. In contrast to these publications, the mortar matrices \mathbf{D} and \mathbf{M} are created in a different way and contain now information from point contact, line contact and surface contact. In addition, the global Lagrange multiplier vector $\boldsymbol{\lambda}$ contains now information from all three contact scenarios. The expression in (4.98) can be reformulated for considering each Lagrange multiplier individually:

$$\sum_{k=1}^{n^{(1)}} \mathbf{D}[j, k] - \sum_{l=1}^{n^{(2)}} \mathbf{M}[j, l] = \mathbf{0} \quad \forall j = 1, \dots, m^{(1)}. \quad (4.99)$$

This means, that the sum of all contributions from slave and master side matrices associated with one Lagrange multiplier has to vanish. For the line contact terms, this reads in detail:

$$\sum_{k=1}^{n^{(1)}} \left(\int_{\gamma_{i,h}^{(1)}} N_k^{(1)} \Theta_j dL \right) - \sum_{l=1}^{n^{(2)}} \left(\int_{\gamma_{i,h}^{(1)}} N_l^{(2)} \Theta_j dL \right) = 0, \quad (4.100)$$

where it is not distinguished between the entries for \mathbf{D}_{\parallel} and $\mathbf{D}_{\perp\star}$. When employing the aforementioned partition of unity property for the displacement shape functions, the conservation of linear momentum finally reads

$$1 \int_{\gamma_{i,h}^{(1)}} \Theta_j dL - 1 \int_{\gamma_{i,h}^{(1)}} \Theta_j dL = 0, \quad (4.101)$$

which is *always* fulfilled when the integration of the slave and master side mortar matrix is performed over the same discrete domain. This was already stated in Puso and Laursen [218] and also holds for the line contact algorithm. It is also valid for the surface contact as elaborated in Popp [210]. For the point contact of vertices, the same reasoning holds without performing a numerical integration but rather a simple term evaluation. For the sake of brevity, these investigations are not outlined here in detail since they are in complete analogy to the explanations for the line contact.

4.8.3.2. Balance of angular momentum

Enforcing an exact conservation of angular momentum is rather challenging in the context of computational contact mechanics. The basic requirement for conservation of angular momentum is given as

$$\mathbf{m}_c^{(1)} - \mathbf{m}_c^{(2)} = \sum_{k=1}^{n^{(1)}} \mathbf{x}_k^{(1)} \times \mathbf{f}_{c,k}^{(1)} - \sum_{l=1}^{n^{(2)}} \mathbf{x}_l^{(2)} \times \mathbf{f}_{c,l}^{(2)} = \mathbf{0}, \quad (4.102)$$

which means that the sum of slave and master interface momentum should vanish. In (4.102), the vectors $\mathbf{f}_{c,k}^{(1)}$ and $\mathbf{f}_{c,l}^{(2)}$ represent the nodal forces at slave node k and master node l , respectively. As discussed in Popp [210], Puso and Laursen [218], Yang et al. [301], expression (4.102) is zero when at least one of the two following requirements is fulfilled:

- the discrete form of the displacement jump vector (gap vector) \mathbf{g} vanishes,
- the force vectors and the discrete displacement jump vector are collinear.

Since the discrete nodal force vectors $\mathbf{f}_{c,k}^{(1)}$ and $\mathbf{f}_{c,l}^{(2)}$ can be split into contributions from the penalty regularization of the contact interaction of crossing edges and Lagrange multiplier contributions, the above mentioned requirements for conservation of angular momentum are investigated separately for these two types of force vectors. First, the penalty force vectors are considered. The discrete form of the displacement jump vector (gap vector) reads for the contact of non-parallel edges:

$$\mathbf{g}_{\times,h} = \sum_{l=1}^{n^{(1)}} N_l^{(1)}(\hat{\boldsymbol{\xi}}_{\times}^{(1)}) \mathbf{x}_l^{(1)} - \sum_{k=1}^{n^{(2)}} N_k^{(2)}(\hat{\boldsymbol{\xi}}_{\times}^{(2)}) \mathbf{x}_k^{(2)}, \quad (4.103)$$

which points per definition in the normal direction $\hat{\mathbf{n}}_{\times}^{(1)}$, see Section 4.4.5. The resulting forces due to the non-penetration condition point in the same direction, as can be seen in (4.60). Thus, all normal force vectors and the discrete gap vector are collinear and thus conservation of angular momentum is *guaranteed* for contact without frictional effects. Note, that the other requirement of a vanishing gap vector can never be achieved due to the penalty regularization, i.e. $\epsilon_n \rightarrow \infty$. For frictional contact, the force vectors and the gap may not be collinear and thus conservation of angular momentum is not always fulfilled. This is due to the rate form of the frictional contact problem.

When considering the nodal forces resulting from Lagrange multipliers, the conservation of angular momentum in (4.102) can be rewritten as

$$\mathbf{m}^{(1)} - \mathbf{m}^{(2)} = \sum_{j=1}^{m^{(1)}} \left[\sum_{k=1}^{n^{(1)}} \mathbf{x}_k^{(1)} \times (\mathbf{D}[j, k] \boldsymbol{\lambda}_j) - \sum_{l=1}^{n^{(2)}} \mathbf{x}_l^{(2)} \times (\mathbf{M}[j, l] \boldsymbol{\lambda}_j) \right] = \mathbf{0}. \quad (4.104)$$

Thus, for contact force vectors resulting from Lagrange multipliers, the requirement of collinear force and displacement jump vectors can be reformulated into the requirement of collinearity between the Lagrange multiplier vectors and the displacement jump vector, see Puso and Laursen [218] and Yang et al. [301]. For the presented mortar contact formulation from Chapter 3 and the

current chapter, this is neither guaranteed for contact without friction nor for frictional contact, see again Popp [210] and Yang et al. [301]. A possible remedy for contact without frictional effects would be a reformulation of the contact approach without an a-priori split of the Lagrange multipliers into a normal and a tangential part from (3.22). Instead, the normal direction should be included in the integrals for the mortar matrices \mathbf{D} and \mathbf{M} in order to account for the varying normal direction over the integration domain. But, when doing so, the diagonal form of the subblocks in \mathbf{D} cannot be achieved anymore with dual shape functions, and the computationally efficient solution procedure in Section 4.8.2 cannot be performed anymore. Furthermore, variation of the mortar integrals when deriving the discrete contact virtual work contribution would lead to conservation of angular momentum, see Hesch and Betsch [106]. These variations are commonly neglected, since they require second derivatives of the mortar matrices \mathbf{D} and \mathbf{M} , and thus the computational complexity would strongly increase, see Popp et al. [214], Puso and Laursen [218] and Puso and Laursen [219]. However, the numerical example in Section 4.9.4 demonstrates that the violation of angular momentum conservation is very small and from an engineering point of view negligible in practice.

For investigating the collinearity condition, the corresponding displacement jump vector has to be stated for the Lagrange multiplier node j :

$$\mathbf{g}_{h,j} = \sum_{l=1}^{n^{(1)}} \mathbf{D}[j, l] \mathbf{x}_l^{(1)} - \sum_{k=1}^{n^{(2)}} \mathbf{M}[j, k] \mathbf{x}_k^{(2)}. \quad (4.105)$$

It is again a quantity with different interpretations depending on the actual Lagrange multiplier. For contact of vertices, this quantity becomes a distance measure, but for surface contact it represents a volumetric measure. However, vanishing of the jump vector cannot be guaranteed since only the normal part of it is forced to zero. Thus, the approaches for Lagrange multiplier contact slightly violate both required conditions, which was already investigated by several authors for surface contact, see for example Popp [210] and Yang et al. [301]. Therefore, conservation of angular momentum may not be guaranteed for the all entity contact formulation.

4.8.4. Post-processing

Since the discrete Lagrange multiplier unknowns contained in the global vector $\boldsymbol{\lambda}$ in (4.86) are utilized to enforce different contact scenarios, they also have different physical interpretations. Concretely, the point Lagrange multipliers $\boldsymbol{\lambda}_*$ represent discrete point forces, the line Lagrange multipliers $\boldsymbol{\lambda}_l$ represent line loads, i.e. a force divided by a distance quantity, and the surface Lagrange multipliers $\boldsymbol{\lambda}_o$ represent classical interface tractions, i.e. a force divided by an area quantity. In order to evaluate and assess the accuracy of computational results, a uniform interface traction quantity is very helpful for post-processing. Thus, the discrete nodal forces (in a finite element sense) acting on the slave side are considered first. They result from multiplying the global vector of Lagrange multipliers $\boldsymbol{\lambda}$ with the transpose of the slave side mortar matrix \mathbf{D} and adding the penalty force contributions from the contact of crossing edges:

$$\mathbf{f}_c^{(1)} = \mathbf{D}^T \boldsymbol{\lambda} + \mathbf{f}_x^{(1)}. \quad (4.106)$$

This vector contains discrete forces acting on slave nodes. In order to compute discrete tractions for post-processing, the global slave side force vector $\mathbf{f}_c^{(1)}$ is scaled by the diagonal matrix \mathbf{A}

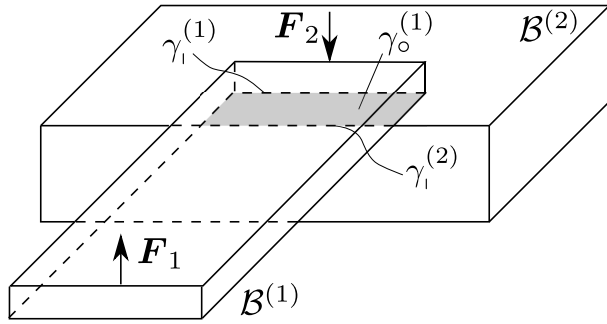


Figure 4.16: Special case for all entity contact formulation: 2 blocks are in surface-to-surface contact (gray area), but slight deflections could cause an active edge-to-surface contact scenario, where the active edge could be on $\gamma_i^{(1)}$ (positive forces $\mathbf{F}_1, \mathbf{F}_2$) or $\gamma_i^{(2)}$ (negative forces $\mathbf{F}_1, \mathbf{F}_2$).

that contains support area information of the slave nodes. It can be computed by assembling the nodal blocks

$$\mathbf{A}[j, k] = A_{jk} \mathbf{I}_3 = \delta_{jk} \int_{\gamma_{c,h}^{(1)}} N_j^{(1)} d\gamma \mathbf{I}_3, \quad j, k = 1, \dots, n^{(1)}, \quad (4.107)$$

with δ_{jk} being the well-known Kronecker delta. The effective slave side interface tractions containing the effect of point, line and surface contact then follow as

$$\mathbf{t}^{(1)} = \mathbf{A}^{-1} \mathbf{f}_c^{(1)}. \quad (4.108)$$

Remark 4.2. *The area matrix \mathbf{A} is basically a slave side mortar matrix \mathbf{D}_o with surface Lagrange multipliers being defined on all slave nodes including edge nodes and vertex nodes. By employing dual shape functions, \mathbf{D}_o automatically becomes a diagonal matrix and thus identical to \mathbf{A} .*

Remark 4.3. *The scaling presented in (4.108) is also applicable for the master side. The master side tractions can be computed by employing the discrete master force vector $\mathbf{f}_c^{(2)}$ and performing the scaling with an area matrix that is integrated over the master surface.*

4.8.5. Restrictions and special cases

As stated in the problem description for contact of vertices, edges and surfaces in Section 4.2, the geometrical entity with lower or equal dimension is implicitly assumed to be on the slave side. With this assumption, a large variety of problems can be sufficiently treated as can be seen at the numerical examples in Section 4.9. However, there are some special contact scenarios, where this assumption is not realizable. Such a scenario is shown in Figure 4.16. Here, 2 blocks $B^{(1)}$ and $B^{(2)}$ are in surface-to-surface contact but slight deflections caused by the forces \mathbf{F}_1 and \mathbf{F}_2 could lead an edge-to-surface contact scenario. For positive force vectors, the edge on $\gamma_i^{(1)}$ becomes active and the initial slave-master assumption is valid. In contrast, when the forces are negative, the edge on $\gamma_i^{(2)}$ characterizes the line contact and the slave-master definition is not

valid anymore, since the slave contact entity (surface) is of higher dimension than the master contact entity (edge). By simply changing the definition of the edge on $\gamma_i^{(2)}$ to $\gamma_i^{(1)}$ and keeping the other definitions, the problem would be over-constrained since too many Lagrange multipliers act on the same region. A dynamically changing assignment of the complete slave and master definition helps avoid these scenarios. The algorithms necessary for the dynamic change of slave and master side are strongly related to self contact approaches, see Yang and Laursen [298, 299]. Without pointing out the details, the basic ingredient described in the mentioned publications is the efficient contact search, which was adopted in Popp [210] and reused for the all entity contact algorithm proposed in this thesis. However, when the external loads lead to a contact scenario where surface and line contact occur and no strict distinction can be made, then the proposed algorithm is at its limit and no dynamic change in master and slave definition could help. This could occur in the considered finite deformation regime of relatively soft bodies.

A simple but efficient workaround is to employ a penalty regularization for master edges and vertices. For the vertex contact, the penalty regularization is realized in complete analogy to the contact of non-parallel edges in Section 4.5.2. For the mortar-based line contact in Section 4.6, the penalization is done as described for classic surface contact formulations with the mortar methods, see for example Fischer and Wriggers [81], Laursen [151], Puso and Laursen [218, 219], Puso et al. [220] and Yang et al. [301]. However, for all numerical examples presented in Section 4.9, this workaround was not employed. But, it has been implemented by the author. A more sophisticated solution for this problem could be developed based on a so-called two-pass formulation, which is usually employed for improving the performance of classical node-to-segment formulations, see Park et al. [196] and Taylor and Papadopoulos [266]. But, these two-pass formulations usually suffer from locking or over-constraint behavior. Therefore, the following investigations concerning the outlined issues are the basis for potential future work.

4.8.6. Numerical efficiency

The presented all entity contact formulation requires several evaluation and integration procedures for all possibly arising contact scenarios. Therefore, the point contact evaluations (cf. 4.5) as well as the segment-based numerical integration schemes for the line contact (cf. 4.6.2) and the surface contact (cf. 3.4.2) have to be performed in order to evaluate the mortar matrices, the gap functions and the relative tangential velocities. Here, especially the segment-based integration schemes significantly contribute to the high computational effort of the proposed mortar based methods. Thus, the entire implementation is designed for the use on computer systems with many central processing units (CPUs) and is based on the already existing multicore framework in the in-house code BACI (cf. Wall et al. [282]). Herein, the finite element meshes, global vectors and global matrices are distributed into several independent processes that are assigned to corresponding processors. The parallel decomposition functionality is based on the third-party library Zoltan, see Boman et al. [30] and Devine et al. [57]. For the calculation of contact interactions, a simple load balancing technique was employed in Popp [210], that allows for a dynamic redistribution of the CPU ownership during a simulation depending on the actual contact zone. The algorithms developed in this thesis are designed in order to fit into this framework and to inherit these parallel computing features.

Despite ability of parallel computing, the costly numerical evaluation procedures themselves, namely the segment-based integration schemes, can be optimized. Therefore, the so-called element-based integration scheme can be employed, which allows for significant time savings at the costs of accuracy. Such an integration scheme was employed in Fischer and Wriggers [80, 81]. A detailed comparison of both integration schemes can be found in Farah et al. [73] and is also provided in the Appendix A. The basic algorithm is given in the following:

Algorithm 4.5. General element-based integration scheme

1. Define suitable integration points on the slave element parameter space.
2. Try to project each integration point from the slave element to the master elements to get the corresponding integration point position in master element parameter space. The projection is performed along the normal field of the slave side. If the projection algorithm does not converge for any involved master element or if the integration points lie outside all master element parameter spaces, then this integration point is sorted out.
3. Perform numerical integration on the entire slave element of the mortar matrices, the weighted gap and the weighted relative tangential velocity.

Here, it does not matter whether the surface contact evaluation or the line contact evaluation is considered. The only difference is the definition of a suitable integration point number. Obviously, a 1D integration rule has to be chosen for the line contact and a 2D rule, depending on the element shape, has to be chosen for the surface contact evaluation. As can be seen at the provided algorithm, no subdivision of the integration domain has to be performed. In addition, the overall number of integration points could be significantly decreased compared to the segment-based integration scheme. Altogether, the element-based integration technique drastically saves computation time, see Appendix A. The loss in accuracy is also investigated in Appendix A, but it is summarized that from an engineering point of view the element-based integration scheme performs acceptably accurate. Details concerning the consistent linearization for the element-based integration technique can be found in Farah [72].

4.9. Numerical examples

In this section, the theoretically introduced contact algorithms and all entity contact formulation is validated with several numerical examples. First, the consistency of the developed shape function modifications for surface-to-surface scenarios of tied contact is proved, see Section 4.7. Afterwards, the all entity contact formulation is tested with a patch test setting, which is usually employed for surface contact problems. Then, the line contact formulation is tested with an edge-to-surface and an edge-to-edge contact scenario. Here, it is also compared to classic surface mortar methods and the node-to-segment scheme. Next, the contact of non-parallel edges is analyzed with special focus on the robustness of the proposed algorithm and conservation of linear and angular momentum. Afterwards, the contact transition between point contact, line contact and surface contact is demonstrated with a bending plate example. Next, an example

from implicit dynamics, a falling coin, is considered to investigate linear and angular momentum conservation for the developed all entity contact formulation. Finally, frictional line contact is analyzed with two contacting plates in order to demonstrate the robustness of the developed line contact scheme in a frictional setting.

4.9.1. Consistency – patch tests

In order to demonstrate and validate the consistency of numerical methods or element formulations, patch tests are the most common choice, see e.g. Irons [126] and Taylor et al. [267]. In the context of mortar methods for computational contact mechanics, these tests are utilized to demonstrate the ability of the methods to represent a constant stress state across the active contact interface. First, this is investigated for a tied surface contact setting in 4.9.1.1 in order to validate the consistency of the shape function modification in Section 4.7. Second, a frictionless contact setting is analyzed with the combined point, line and surface contact algorithm in Section 4.9.1.2 to demonstrate the consistency of the combined contact framework of point, line and surface contact. Finally, a line contact scenario is considered where the active contact interface reduces to a curve and the algorithm is tested with regard to represent a constant stress state across this curve.

4.9.1.1. Mortar mesh tying with boundary modification

The first patch test investigated in this thesis is a 3D cuboid, which consists of six differently discretized subdomains connected by the mortar mesh tying scheme, see left part of Figure 4.17. It is well-known that the employed mortar method with its variationally consistent interpolation of the interface traction via discrete Lagrange multipliers naturally guarantees for a satisfaction of classical patch tests. Nevertheless, this example is challenging, because it inevitably leads to crossing mesh tying interfaces, which require special treatment of the Lagrange multipliers at so-called crosspoints and crosslines in order to achieve a properly stated problem. Therefore, the discrete Lagrange multipliers at the nodes attached to crosspoints and crosslines are removed and the shape functions of neighbored Lagrange multipliers are modified according to Section 4.7. Since the matrices arising for mortar mesh tying schemes are strongly related to the matrices from mortar based computational contact mechanics, this example can be interpreted as validation for the shape function modification. In order to test the shape function modification for all commonly employed first-order and second-order finite elements, 4-node and 10-node tetrahedral elements and 8-node, 20-node and 27-node hexahedral elements are employed, see again the left part of Figure 4.17. The cuboids dimensions in x-, y- and z-direction are $3 \times 3 \times 8$ and the employed material model is of Saint-Venant-Kirchhoff type with Young's modulus $E = 22500$ and Poisson's ratio $\nu = 0.0$. It is completely fixed at its lower surface and subjected to a load $p = 1000$ in positive z-direction at its upper surface. The resulting displacement state and the Cauchy stresses are visualized in Figure 4.17. Here, the consistent shape function modification at crosspoints and crosslines allows for an exact representation of the constant stress state within the cuboid and consequently of the linear distribution of the displacement field. This demonstrates the consistency of the employed shape function modification regardless of which element type is employed.

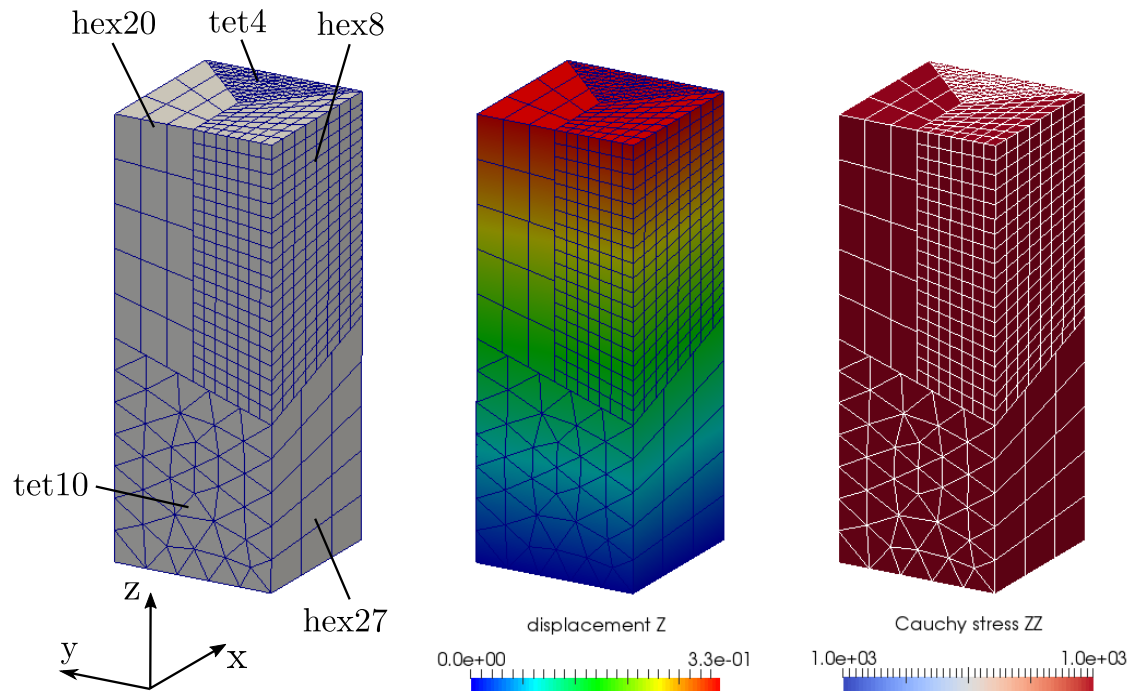


Figure 4.17: 3D patch test for mortar meshing with boundary modification of Lagrange multiplier shape functions: Finite element mesh (left), displacement solution (middle) and Cauchy stress (right).

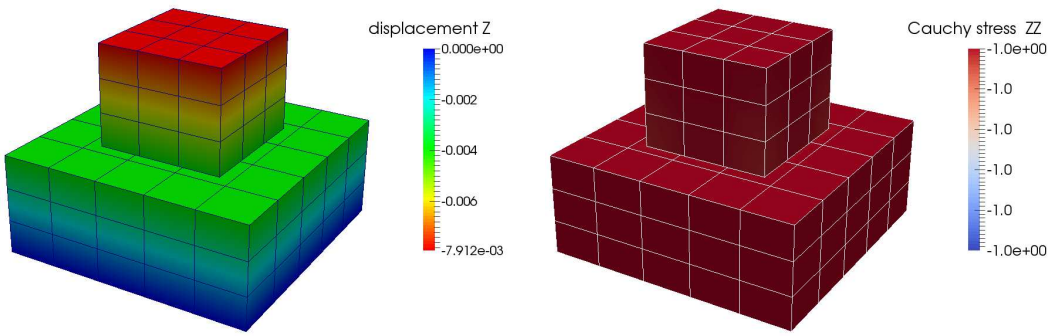


Figure 4.18: Result for patch test with combined non-smooth contact formulation: displacement (left) and Cauchy stresses (right). The figure is taken from Farah et al. [71].

4.9.1.2. Mortar surface-to-surface contact

The next example is a simple patch test for a surface contact scenario, which is investigated to show the ability of the proposed method to represent a constant stress state across non-matching discretizations at the contact interface. It is well-known that mortar contact formulations are able to successfully pass this test setup, whereas classical node-to-segment formulations would fail, see El-Abbasi and Bathe [66] and Taylor and Papadopoulos [266]. However, the method that has been introduced in this contribution modifies the mortar contact formulation at vertices and edges of the contact boundary, and thus the patch test has to be revisited to demonstrate that these modifications have no negative influence on the solution accuracy as compared with pure surface contact. The test setup consists of a large block with dimensions $10 \times 10 \times 4$ and a small block with dimensions $5 \times 5 \times 4$. The larger block is completely supported at its lower surface and its upper surface acts as master contact side. The smaller block lies on top of the larger one and acts as slave body. The employed finite element meshes are shown in Figure 4.18. The nodes attached to vertices carry point Lagrange multipliers, the nodes on edges carry line Lagrange multipliers and all other slave nodes are subject to surface Lagrange multipliers. The upper surface of the slave body and the non-contact part of the upper surface of the lower body are loaded with the constant pressure $p = -1.0$ in Z-direction. The employed material model for both bodies is based on a compressible Neo-Hookean material law with Young's modulus $E = 1000$ and Poisson's ratio $\nu = 0.0$. In addition, frictionless contact is assumed for the simulation. The resulting displacements and Cauchy stresses are shown in Figure 4.18. It can be seen that the contact patch test requirements are perfectly fulfilled, i.e. the test is passed to machine precision. In addition, the resulting Lagrange multiplier values are visualized in the left part of Figure 4.19. Here, only the four Lagrange multiplier vectors of the inner surface nodes have noteworthy non-zero values. This is due to the surface Lagrange multipliers being able to represent the constant stress state within the contact interface and thus are able to completely fulfill the contact constraints. Consequently, the point and the line Lagrange multipliers do not significantly contribute to the contact virtual work. Instead, their contact status can be described as limit case where the gap values are zero but no noteworthy non-zero Lagrange multiplier values occur. Numerically, this could lead to problems due to an arbitrarily changing contact status of the vertex nodes and the edge nodes for this example, while the constraint residual as well as the structural residual

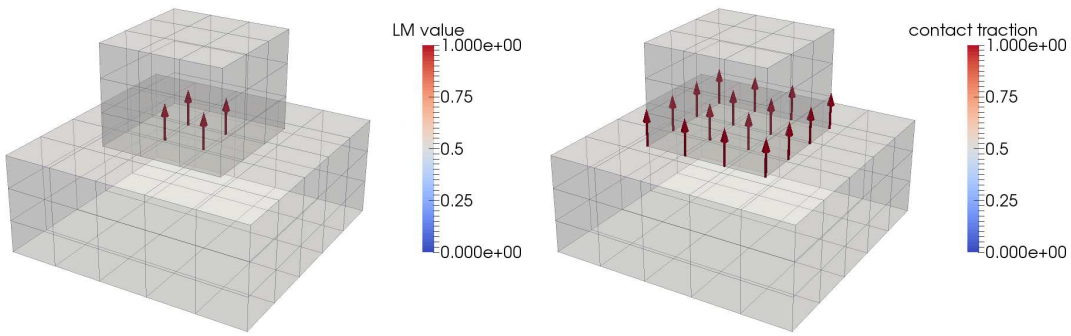


Figure 4.19: Result for patch test with combined non-smooth contact formulation: Lagrange multiplier vectors (left) and scaled interface tractions (right). The figure is taken from Farah et al. [71].

converge perfectly. Therefore, convergence behavior of the Lagrange multiplier increment and the gap function are tracked and changes in the active set are ignored as convergence criterion when both quantities simultaneously approach zero.

However, the Lagrange multiplier solution in the left part of Figure 4.19 cannot be interpreted as interface traction since the shape function modification in (4.74) has been applied to the surface Lagrange multiplier shape functions. Taking into account the post-processing procedure explained in Section 4.8.4, a representative solution for the contact traction can be derived, which is visualized in the right part of Figure 4.19. There, the expected constant stress state at each slave node can be observed.

4.9.1.3. Mortar Edge-to-Surface contact

The next example is introduced to demonstrate the ability of the proposed contact algorithm to represent a constant stress state for edge-contact situations, i.e. it can be interpreted as an edge-to-surface contact patch test. The example consists of a rigid plate that is completely fixed and an elastic cube. The edge length of the cube is $l = 2$ and its material model is of Neo-Hookean type with Young's modulus $E = 22.5 \cdot 10^5$ and Poisson's ratio $\nu = 0.0$. It is rotated by 45° twice around two different axes, such that its contact edge equals the diagonal of the fixed plate. The cube acts as slave body and the plate as master body, respectively. During the entire simulation, inertia effects and damping are neglected. The initial distance between the bodies is $d = 2.29 \cdot 10^{-2}$ and the cube is pressed against the plate with a total prescribed displacement at its upper surfaces of $d_{\max} = 0.2$. This displacement boundary condition is applied within 12 quasi-static load steps. This setup is calculated with three different contact algorithms. First, the proposed algorithm with its combination of point, line and surface Lagrange multipliers. Second, with a classical mortar contact algorithm, and finally with a classical node-to-segment formulation. The resulting displacement solutions are shown in Figure 4.20. Here, the left part shows the solution for the proposed contact algorithm, which successfully enforces the non-penetration conditions and leads to a physically correct displacement state. The right part shows a solution computed with a classical node-to-segment algorithm, which also shows a reasonable displacement state. The classical mortar formulation in the middle of Figure 4.20 obviously produces a

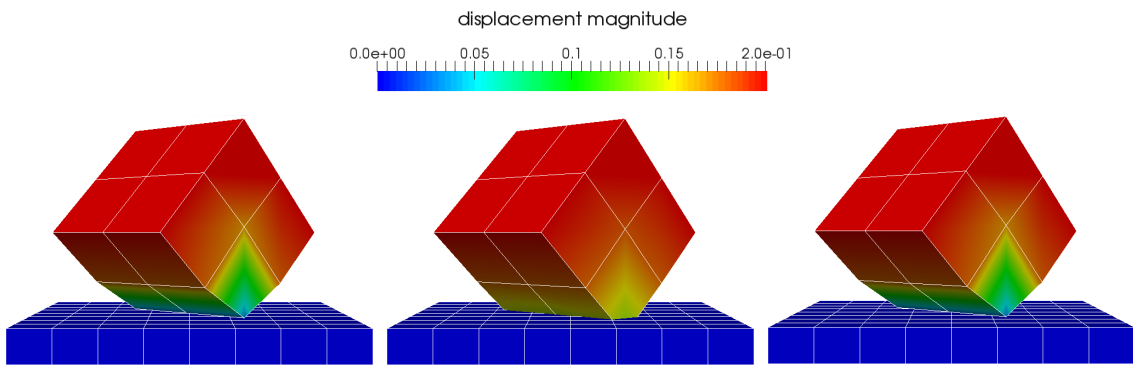


Figure 4.20: Displacement solution for the patch test for edge contact: combined formulation (left), classical mortar contact (middle) and classical node-to-segment algorithm (right). The figure is taken from Farah et al. [71].

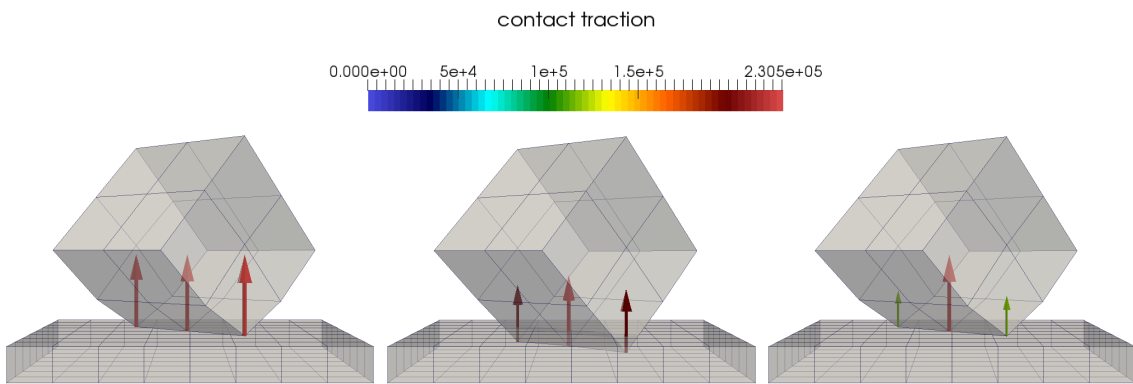


Figure 4.21: Contact tractions for the patch test for edge contact: combined formulation (left), classical mortar contact (middle) and classical node-to-segment algorithm (right). The figure is taken from Farah et al. [71].

large penetration and the contact is only detected very late. This is due to the surface weighted gap function which inherently arises for the classical mortar formulation, see Popp et al. [212]. In Figure 4.21, the interface tractions are visualized. From this, it can be further deduced that the proposed algorithm with its line Lagrange multipliers perfectly passes the patch test by producing a constant stress state, which is to be expected for this test setup. In order to compare the results, the visualized stress state is based on a post-processing procedure that considers element dimensions of the setup. The only discrete Lagrange multiplier with a non-zero value is the line Lagrange multiplier at the middle node of the contacting edge. The vertex Lagrange multipliers again exhibit the limit case, where the gap functions are zero but no noteworthy non-zero value for the point Lagrange multiplier arises. Consequently, the entire set of contact constraints are consistently enforced with only one discrete line Lagrange multiplier. In contrast, the classical mortar algorithm produces smaller stresses, since the predicted penetration is far from the physically meaningful state of being zero. Finally, the node-to-segment algorithm, while yielding

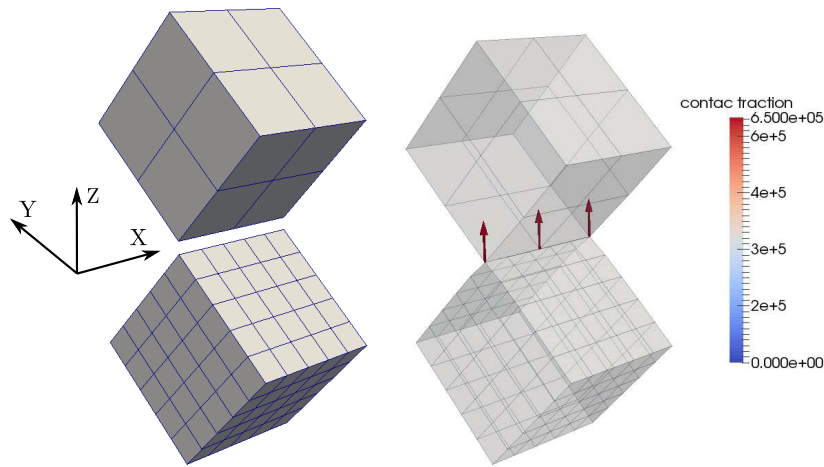


Figure 4.22: Parallel edge-to-edge contact: initial setting (left) and deformed state with contact tractions (right). The figure is taken from Farah et al. [71].

plausible results from a qualitative point of view, is not able to produce a constant stress state, which is, of course, a well-known deficiency of this type of contact discretization.

4.9.1.4. Mortar parallel edge-to-edge contact

The next example is a parallel edge-to-edge contact situation of two elastic cubes. Here, the robustness of the proposed numerical evaluation of the line contact algorithm shall be demonstrated. The material model for both cubes is identical to the elastic cube from the edge-contact example in Section 4.9.1.3. Both cubes are rotated by 45° around their individual X-axis such that their edges are perfectly parallel, see Figure 4.22. The cubes have identical dimensions of $1 \times 1 \times 1$, and tri-linear hexahedral elements are employed for the spatial discretization. The finite element meshes are non-matching at the contacting edges as visualized in Figure 4.22. The upper block is defined as slave side and the lower body represents the master side. The lower cube is supported at its lower surfaces and the upper cube is subjected to a prescribed motion at its upper surfaces. Their initial distance is $d = 0.083$ and the total prescribed displacement in negative Z-direction is $d_{\max} = 0.166$, which is enforced within 50 quasi-static load steps. The resulting contact tractions and the deformed meshes are again shown in Figure 4.22. The proposed contact algorithm yields perfectly identical contact tractions at all slave nodes. This is due to the highly accurate segment-based integration scheme explained in Section 4.6.2. Furthermore, the introduced definition for the nodal normal field leads to a perfect edge-to-edge contact scenario, which can again be interpreted as a special kind of (edge-to-edge) contact patch test. It should be pointed out, however, that the solution of this example represents an academic limit case and is therefore rather sensitive with respect to nodal normal definitions and other numerical evaluation procedures.

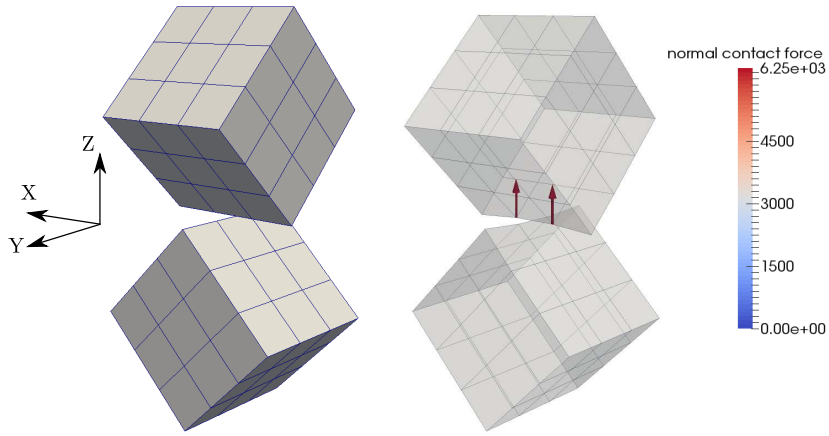


Figure 4.23: Non-parallel edge-to-edge contact: initial setting (left) and deformed state with normal contact force at $t = 5$ (right). The figure is taken from Farah et al. [71].

4.9.2. Non-parallel edge-to-edge contact

In the following, a scenario of non-parallel edges being in frictional contact is investigated. Again, two cubes with identical dimensions of $1 \times 1 \times 1$ are considered with the same material properties as in the previous examples, i.e. the material model is of Neo-Hookean type with Young's modulus $E = 22.5 \cdot 10^5$ and Poisson's ratio $\nu = 0.0$. Both cubes are discretized equally with tri-linear hexahedral elements as shown in Figure 4.23. The upper cube is rotated by 45° around its X-axis and the lower cube is rotated by 45° around the Y-axis. The initial distance between the two bodies is $d_i = 0.01$. The lower block is completely fixed at its two lower surfaces and acts as master body for the contact description. Consequently, the upper block is defined as slave body. The two top surfaces of the upper block are subjected to a prescribed displacements $\mathbf{d}_{dbc} = [d_x, d_y, d_z]$, which is split into two different motions. First, in the time interval $0 < t \leq 5$, the displacements in X- and Y-direction are fixed, i.e. $d_x = d_y = 0$, and the displacements in Z-direction are defined by $d_z = -0.012 t$. Afterwards, in the time interval $5 < t \leq 25$, the displacements in Z-direction are fixed at $d_z = -0.06$ and the displacements in X and Y direction are defined as $d_x = d_y = 0.015 (t - 5)$. The time step size is chosen as $\Delta t = 0.1$. The resulting point contact of the non-parallel edge-to-edge scenario is realized with a penalty regularization as explained in Section 4.5.2. The required penalty parameters are defined to be at the order of the Young's modulus, i.e. $\epsilon_n = \epsilon_\tau = 22.5 \cdot 10^5$ and the Coulomb friction coefficient is chosen as $\mathfrak{F} = 0.9$.

The resulting slave side normal contact forces $\mathbf{f}_{x,n}^{(1)}$ and the deformation state are visualized for $t = 5$ in Figure 4.23. The contact point is exactly in the middle of an edge (line) element, and according to (4.58) the contact force due to the penalization of the penetration is equally distributed between the adjacent nodes. The tangential contact forces are shown in Figure 4.24. As expected, they point in the opposite direction of the tangential movement and are consistently split between the two involved nodes of an edge (line) element. In the middle part of Figure 4.24 it can be seen that the contact point is located near the left involved node, and thus its part of the overall tangential force is much larger than for the other involved node. The final state of the simulation is shown in the right part of Figure 4.24. Here, the contact point has moved from

4. Mortar Methods for Contact of Vertices, Edges and Surfaces

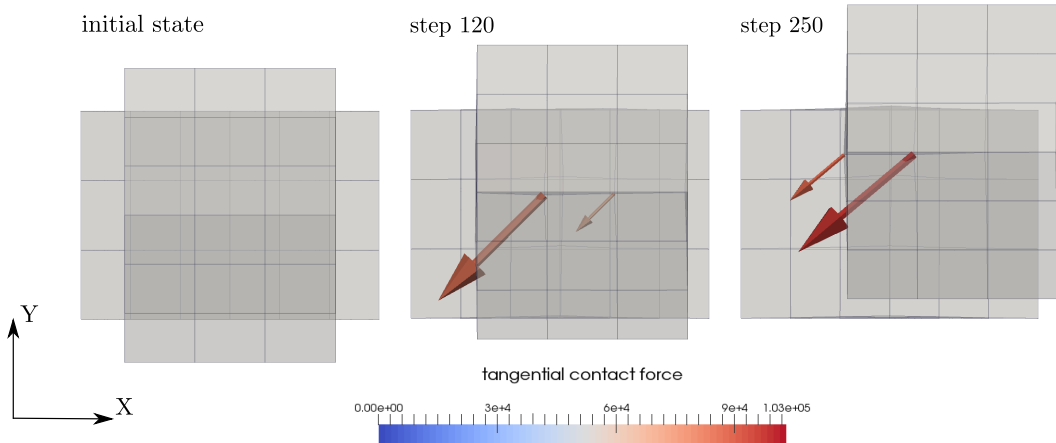


Figure 4.24: Deformed state and tangential contact forces for non-parallel edge-to-edge contact: initial setting (left), solution at step 100 (middle) and solution at step 250 (right). The figure is taken from Farah et al. [71].

the initial slave line element to its left neighbor, and consequently the outer left node now gets a share of the contact force. This transition from one line element to another only works in a robust manner when C^1 -continuous nodal tangent fields are used. These fields are based on unique tangent definitions at each node, see (4.45) and (4.46).

Finally, the conservation of linear and angular momentum is investigated. According to the explanations in Section 4.8.3, conservation of linear and angular momentum can be formulated as conservation requirement of interface forces and moments acting on the slave and master side, respectively. Thus, the resulting plots for the absolute interface forces and moments in this numerical example are given in Figure 4.25. It can be seen, that the slave and master sides behave

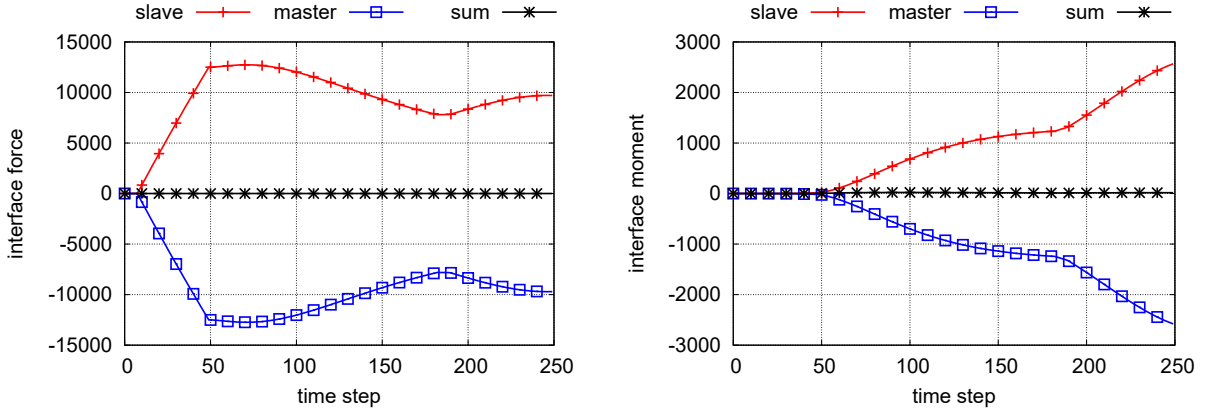


Figure 4.25: Absolute values of interface forces (left) and moments (right) for frictional contact of non-parallel edges. Master quantities are defined to be negative for visualization. The figure is taken from Farah et al. [71].

identically, which leads to an excellent balance of forces and moments at the contact interface.

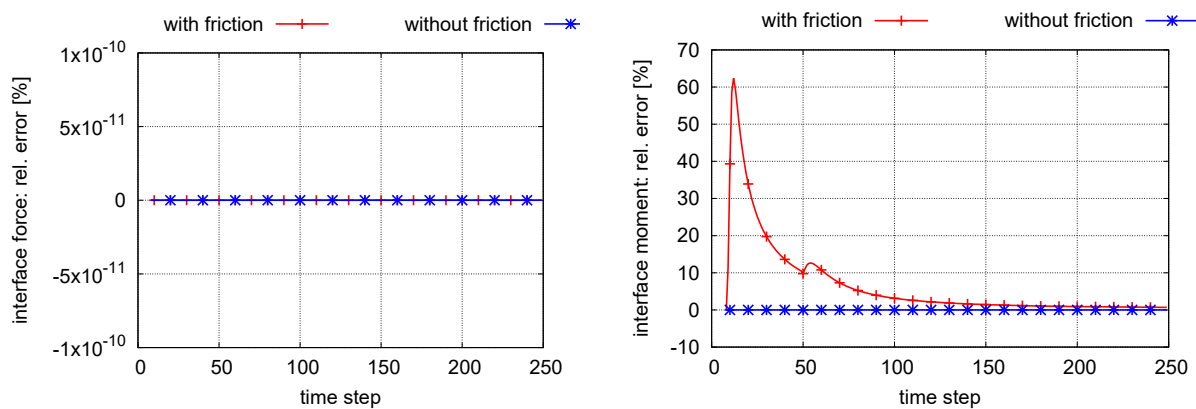


Figure 4.26: Relative errors of interface forces (left) and moments (right) for contact of non-parallel edges. Comparison of contact with friction (red) and contact without friction (blue). The figure is taken from Farah et al. [71].

The interface moments only take non-zero values after the time step 50, since then the tangential movement begins. The kink arising in all curves at ca. time step 185 occurs due to the transition of the contact point from one line element to another. A detailed view on the conservation of forces and moments is provided in Figure 4.26. In the left subfigure, the relative error of the sum of interface forces from slave and master side with respect to the slave side force is plotted for contact with friction and frictionless contact. It can be seen, that the interface forces and thus the linear momentum is *exactly* conserved for both scenarios, i.e. an accuracy up to machine precision is reached, which was expected from the investigations in Section 4.8.3. The right plot in Figure 4.26 shows the same error calculation for the interface moments. As explained in Section 4.8.3, conservation of moments and consequently the angular momentum is only guaranteed for contact without frictional effects. For the simulation without friction, again, an accuracy up to machine precision can be achieved. However, the relative error for contact with friction seems to be significant at the beginning of the simulation. Yet, as can be seen in the right part of Figure 4.25, the absolute value of the moments for the slave and master side is practically zero at the beginning of the simulation. Thus, the large relative error that can be observed in Figure 4.26 until time step 50 is not relevant in practice. As soon as the absolute value of the interface moment increases after time step 50, the relative error decreases towards circa 0.5%, which is acceptable from an engineering point of view. It should be noted that with an increasing penalty parameter ϵ_n and for finer meshes, the accuracy in conservation of interface moments, i.e. angular momentum, can be further improved.

4.9.3. Transition between contact scenarios – bending plate

The next example is utilized to demonstrate the consistent transition between point, line and surface contact. To this end, an elastic plate is pressed against a rigid foundation. The problem setup is visualized in Figure 4.27. The plate is meshed with $70 \times 70 \times 3$ tri-linear hexahedral elements (hex8) with EAS element technology (cf. Simo and Rifai [255]). The employed material model is of Neo-Hookean type with Young's modulus $E = 6.25 \cdot 10^7$ and Poisson's ratio $\nu = 0.0$.

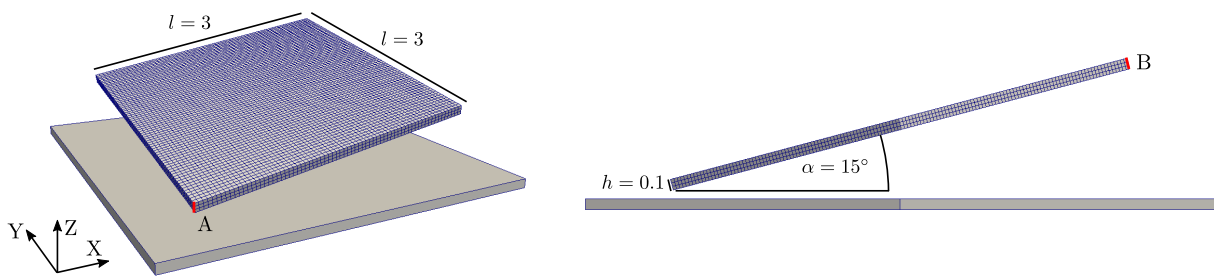


Figure 4.27: Setup for the bending plate example. The figure is taken from Farah et al. [71].

The initial distance between the bodies at their closest points is $d = 0.1$. The nodes at the edge A, which points in thickness direction of the plate, are only allowed to move in Z-direction and the nodes at edge B are subjected to a prescribed total motion of $d_{\max} = 0.72$ in negative Z-direction, which is enforced within 35 steps. All frictional and inertia effects are neglected within this simulation. Obviously, the first contact occurs at the vertex node at the lower end of edge A. The very first steps involving contact are shown in detail in Figure 4.28, where the contact tractions are computed according to (4.108). Specifically, it can be observed that point contact becomes active at the vertex node in step 5. Until step 7, point contact of the vertex node yields the highest stress concentrations during the entire simulation. In step 8, the active contact set increases with the adjacent edge nodes becoming active. Consequently, the contact tractions decrease due to the larger overall contact zone. Solution step 9 is not visualized, but the vertex node and the two edge nodes remain active. In load step 10, the vertex node becomes inactive and the corresponding point Lagrange multiplier takes on a zero value. Nevertheless, the contact tractions still keep their maximum at the vertex node due to the two active edge nodes and their modified shape functions, see shape function visualization in Figure 4.11. The absolute value of the tractions further decreases since the stresses are continuously shifted from the vertex node to the edge nodes. While only being of qualitative nature, this result nevertheless nicely demonstrates the ability of the proposed algorithm to robustly change between point contact formulation and line contact formulation without any heuristic transition parameter.

Until solution step 20, the number of active edge nodes increases and the two active edge sectors separate from the vertex node, see Figure 4.29. Then, in step 21, the first active surface nodes occur, and the active surface area completely connects the two active edge sectors in step 25, see again Figure 4.29. Interestingly, however, the two edge nodes connected to the vertex node on edge A are still in contact and the highest contact tractions still occur at this region. During the following steps, the region of active surface nodes continuously moves towards edge B and the maximum surface stress values increase. Moreover, the number of active edge nodes reduces and the contact tractions at the edge nodes as well as at the vertex node further decrease. This further underlines the robust and consistent transition between point, line and surface contact.

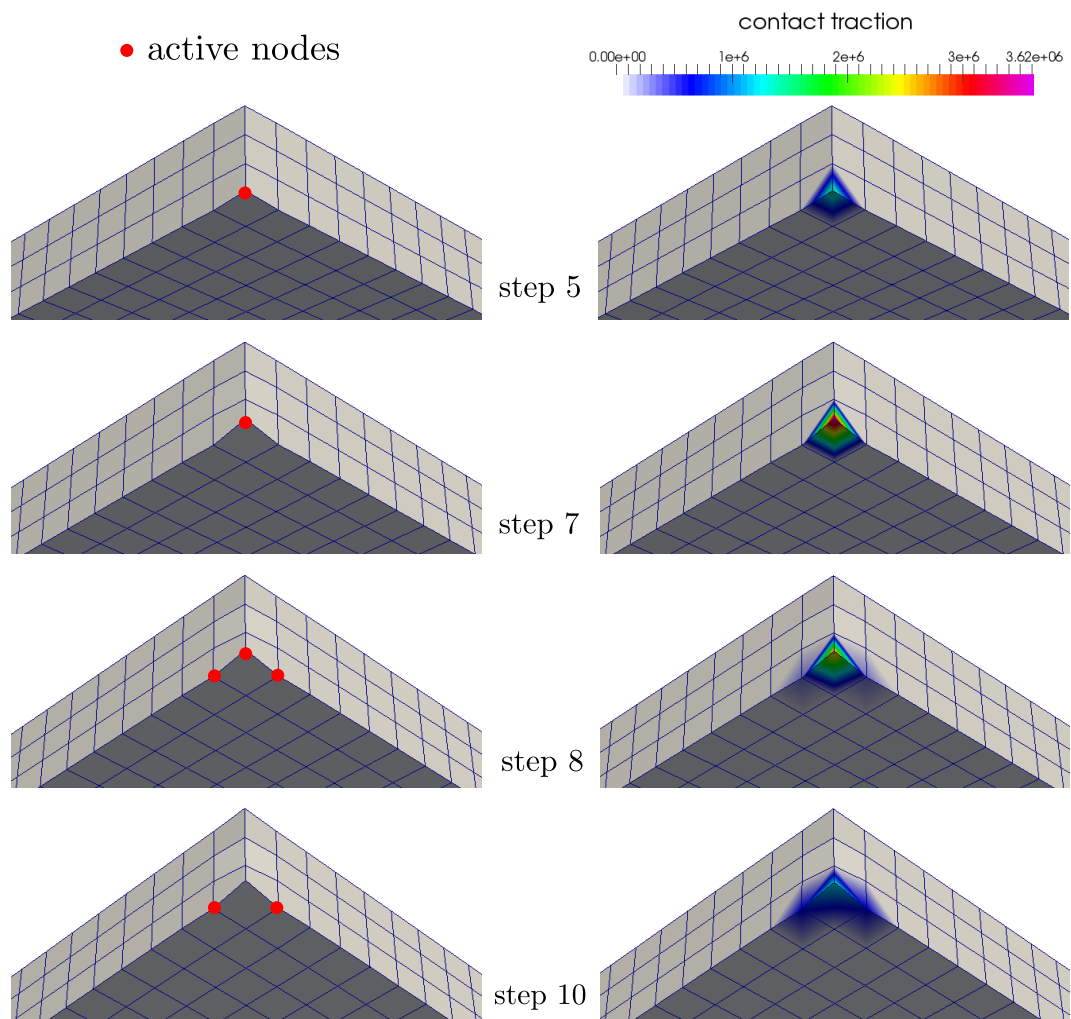


Figure 4.28: Contact tractions and active contact set for the bending plate example at the tip of the plate. The figure is taken from Farah et al. [71].

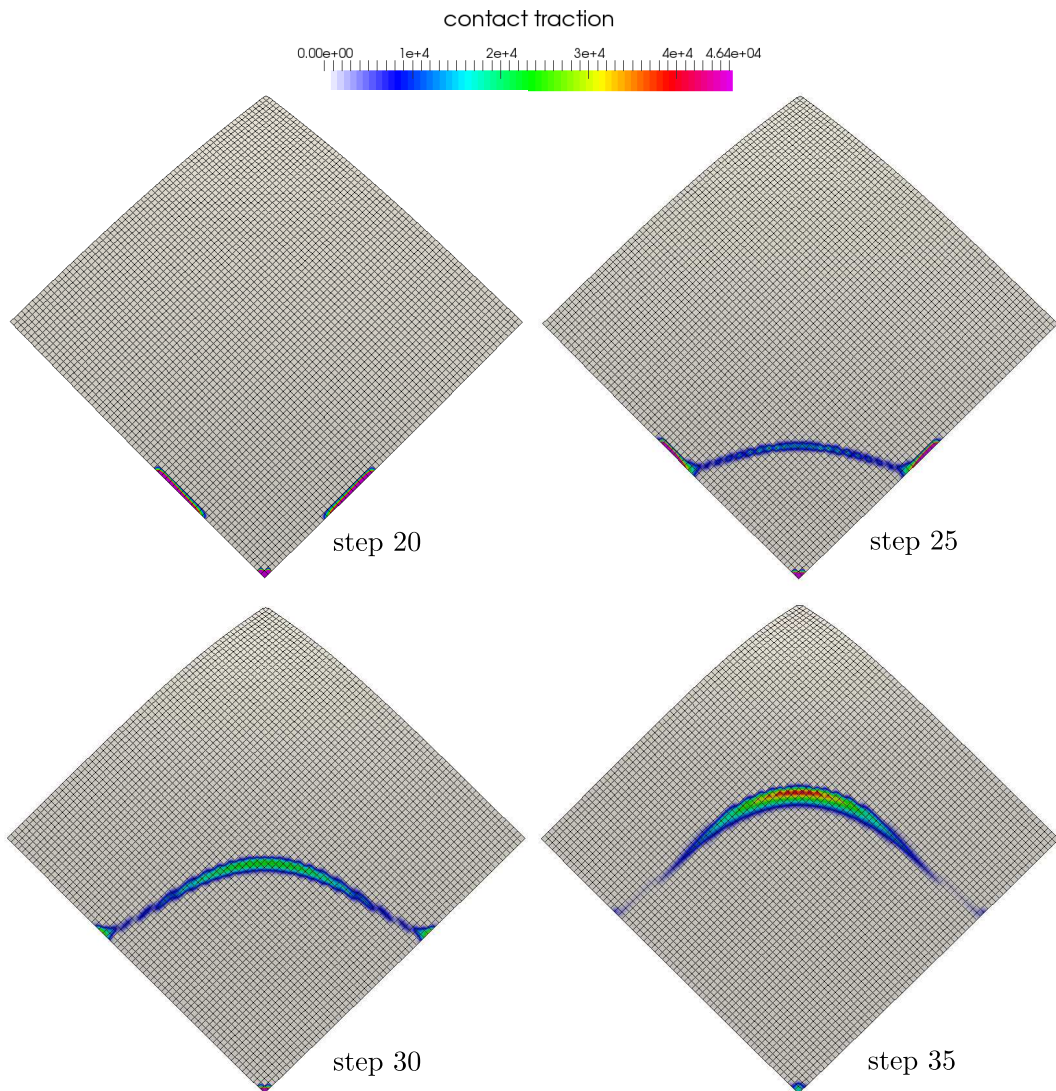


Figure 4.29: Contact tractions for the bending plate example. The figure is taken from Farah et al. [71].

4.9.4. Conservation properties – falling coin

The next example demonstrates the conservation properties of the Lagrange multiplier contact algorithms developed in this thesis, which were previously discussed in Section 4.8.3. In addition, the convergence of the contact algorithms within the semi-smooth Newton scheme is investigated. The example consists of an elastic coin (flat cylinder) and an elastic foundation, see Figures 4.30 and 4.31. The employed material model for both bodies is of Saint-Venant-Kirchhoff

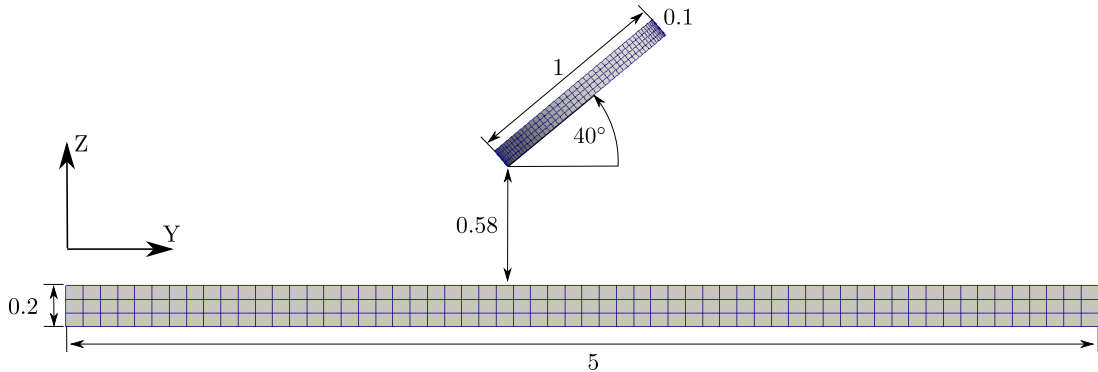


Figure 4.30: Initial setting for the falling coin example. The figure is taken from Farah et al. [71].

type. The material properties of the coin are defined with Young's modulus being $E = 1 \cdot 10^5$, Poisson's ratio being $\nu = 0.0$ and the density being $\rho_0 = 0.3$. The properties of the foundation are the same except for Young's modulus, which is defined as $E = 4 \cdot 10^3$. The dimensions of the bodies can be seen in Figure 4.30. During the entire simulation, the coin is subjected to a constant body force $\hat{b} = -700$ in negative Z-direction. The edges of the lower surface of the foundation are completely fixed during the simulation. The employed finite element discretization can also be seen in the Figures 4.30 and 4.31. All in all, 14248 tri-linear hexahedral elements (hex8) with

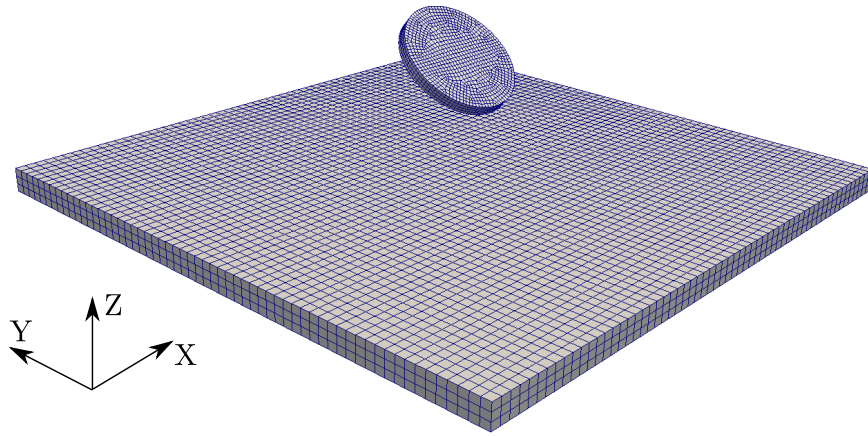


Figure 4.31: 3D view on the initial setting of the falling coin example. The figure is taken from Farah et al. [71].

EAS element technology (cf. Simo and Rifai [255]) are employed. For the simulation, inertia

effects are considered and implicit time integration is done with a generalized- α scheme introduced in Section 2.2.3. The time integration parameter is chosen as $\rho_\infty = 0.95$, which introduces slight numerical dissipation. The overall simulation time is $T = 0.055$ and the time step is defined to be $\Delta t = 5 \cdot 10^{-4}$. The contact scenario is defined with the coin being the slave body and the foundation being the master body, respectively. Contact without any frictional effects is assumed, and line and surface Lagrange multipliers are introduced at the edges and the surfaces of the coin. A Petrov-Galerkin scheme is utilized for the Lagrange multiplier interpolation, which changes the definition of the weighted gaps according to (3.42), see also Popp et al. [214].

The resulting deformation of the coin and the foundation is visualized for characteristic time steps in Figure 4.32. Herein, the deformation corresponding to the first impact is shown in the

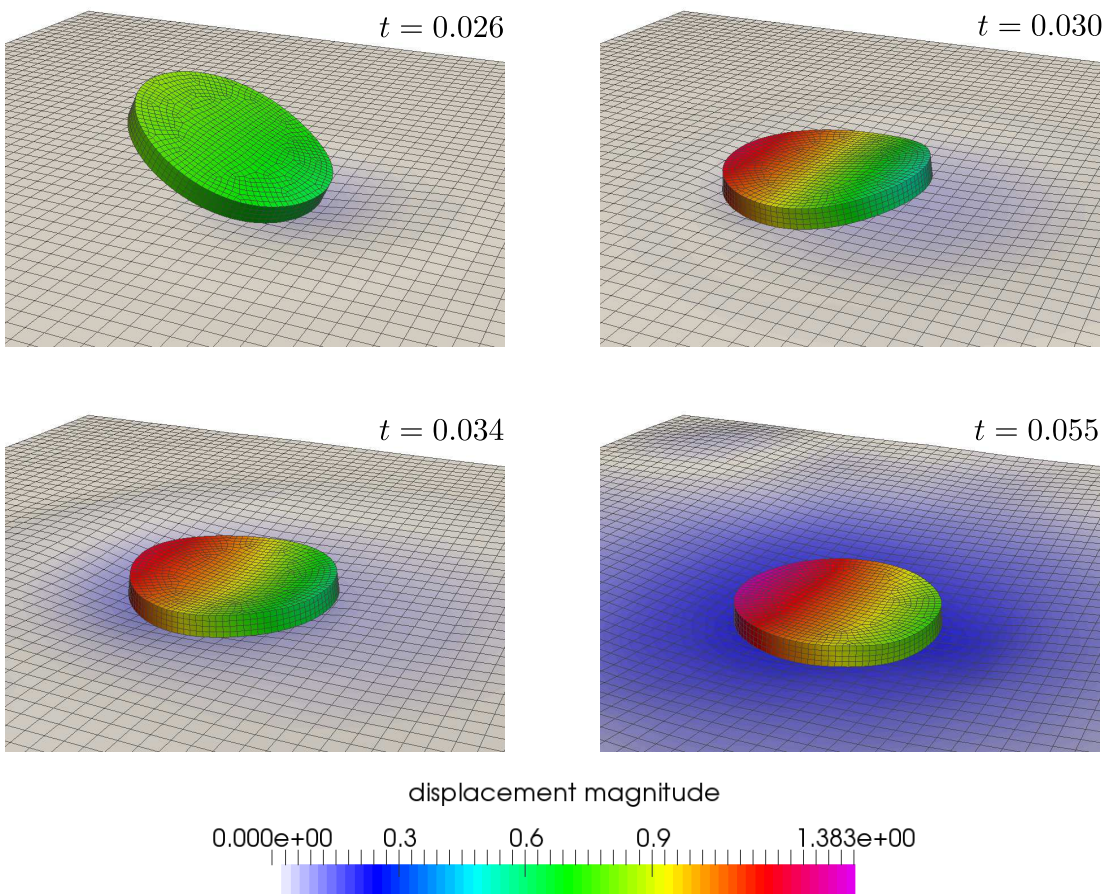


Figure 4.32: Falling coin example: characteristic stages of deformation. The figure is taken from Farah et al. [71].

top left part. This impact is resolved entirely by the line Lagrange multipliers. It introduces a rotation of the coin, which then leads to the next contact situation being dominated by the surface Lagrange multipliers, see top right part of Figure 4.32. The bottom left part of Figure 4.32 illustrates nicely the elastic wave traveling through the foundation after the first impact. The final deformation at the end of the simulation is shown in the bottom right part of Figure 4.32.

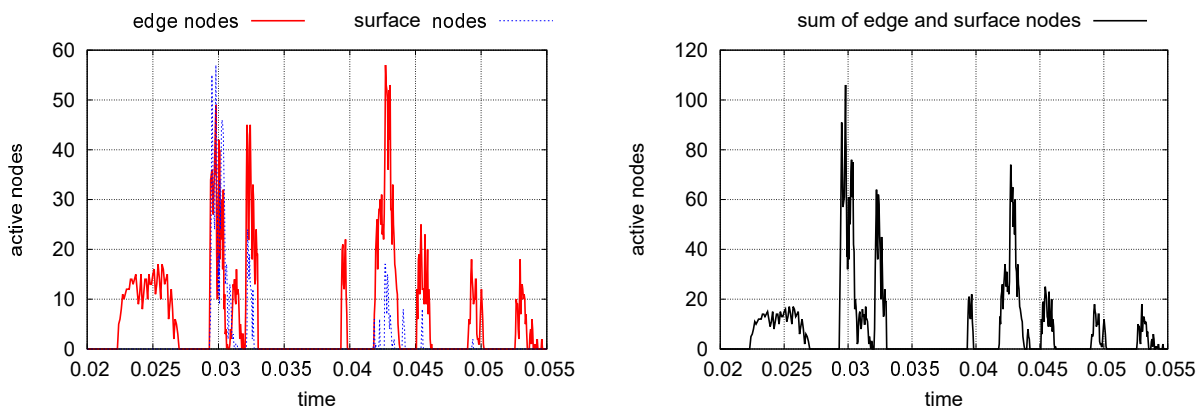


Figure 4.33: Falling coin example: active edge and surface nodes (left) and sum of edge and surface nodes (right). The figure is taken from Farah et al. [71].

The mentioned activation and deactivation of the line- and surface-based Lagrange multipliers is additionally shown in Figure 4.33. Therein, active edge nodes correspond to discrete line Lagrange multipliers. It can be seen that at most points in time contact interaction is actually dominated by the line Lagrange multipliers, while only very few situations, such as the one illustrated in the top right and bottom left corners of Figure 4.32, are characterized by surface contact. Thus, it can be stated that the overall robustness of the simulation is strongly affected by the newly developed segment-based integration scheme for line contact presented in Section 4.6.2.

Again, investigations concerning conservation properties are based on the explanations in Section 4.8.3. Thus, conservation of linear momentum is achieved, when the sum of contact forces that act on slave and master side vanishes. In analogy, conservation of angular momentum is achieved, when the sum of interface moments due to contact forces that act on slave and master side vanishes. For this investigation, the interface forces and moments of slave and master sides are visualized in Figure 4.34. It can be seen that the absolute values of force and moment of slave and master side behave identically at first sight and correspond to the impact situations characterized by the number of active nodes in Figure 4.33. However, an in-depth investigation of the conservation properties requires a closer look at the relative error of the sums with respect to the slave quantity. The corresponding results are plotted in Figure 4.35. As described in Section 4.8.3, conservation of linear momentum is *guaranteed* for the developed contact algorithms, since slave and master forces balance perfectly. This conservation is achieved up to machine precision. Conservation of angular momentum is not guaranteed, since the interface moments do not balance. However, the obtained error is very small (max. 0.025%) and thus can be considered negligible from an engineering point of view. Note that conservation of energy can not be guaranteed with the presented algorithm, since adequate time integration schemes that resolve the discontinuities of the interface velocities in the event of an impact are required for this purpose, see Laursen and Chawla [152] and Laursen and Love [153]. These time integration schemes are not employed and not in the focus of this thesis.

Finally, the convergence rate of the contact algorithms within the semi-smooth Newton scheme is investigated in the following. Therefore, a characteristic time step with line and surface La-

4. Mortar Methods for Contact of Vertices, Edges and Surfaces

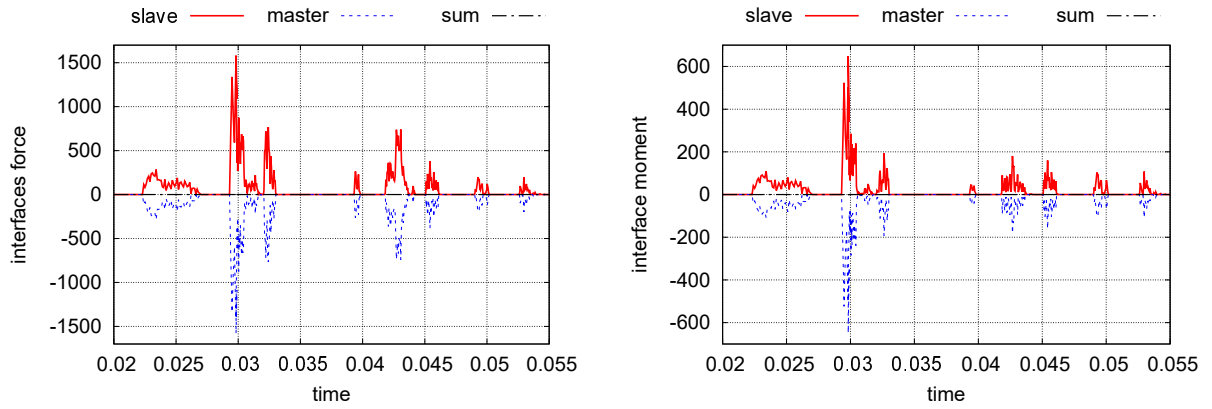


Figure 4.34: Falling coin example: absolute values of interface forces (left) and moments (right) for investigation of conservation of linear momentum and angular momentum. Master quantities are defined to be negative for better visualization. The figure is taken from Farah et al. [71].

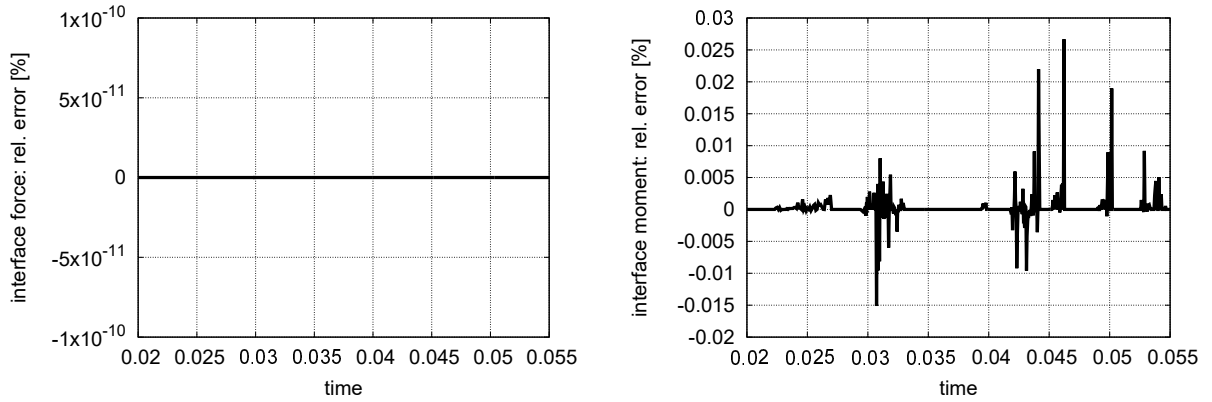


Figure 4.35: Relative errors for balance of interface forces (left) and moments (right) for the falling coin example. The figure is taken from Farah et al. [71].

grange multipliers being active is considered. The convergence behavior is shown in Table 4.1. There, the L^2 -norm of the displacement residual, the displacement increment, the constraint residual and the Lagrange multiplier increment are given for the required Newton steps. In addition, the number of active nodes is provided and the nonlinear solution steps with changing active set are highlighted. At the beginning of the nonlinear solution procedure, 5 changes in the active set are carried out. Within these steps, the considered norms only slowly decrease, which is expected for semi-smooth Newton methods, see Popp [210]. After the correct active set is found, all norms converge approximately quadratic to zero, which is the expected convergence rate for Newton methods when being close enough to the solution, see Section 2.2.4. However, the Lagrange multiplier increment norm approaches latest to zero, which is also expected according to the classic textbook about constrained optimization Bertsekas [27]. For the sake of completeness, it should be noted, that the final number of 88 active nodes consists of 24 edge nodes and 64 surface nodes

step	displ. residual	displ. incr.	constr. residual	LM incr.	active nodes
1	2.86708e + 01	2.49036e - 01	1.78943e + 05	2.86007e + 05	207 (*)
2	1.74212e + 01	2.57951e - 02	1.77194e + 05	3.21509e + 05	130 (*)
3	8.92433e + 00	1.76936e - 02	1.11207e + 05	2.47264e + 05	96 (*)
4	2.92589e + 00	7.29371e - 03	3.16991e + 04	1.30408e + 05	89 (*)
5	3.44270e - 01	1.72936e - 03	2.60689e + 03	3.59133e + 04	88 (*)
6	3.81247e - 03	1.42311e - 04	3.00870e - 01	2.92161e + 03	88
7	5.09491e - 08	3.46040e - 07	4.57391e - 06	1.38196e + 00	88
8	8.51222e - 11	5.54522e - 12	2.81013e - 11	1.68548e - 05	88
9	8.22572e - 11	6.50431e - 15	2.07129e - 11	4.33384e - 09	88

(*) = change in active set

Table 4.1.: Convergence behavior of the all entity contact algorithm in terms of the displacement residual norm, the displacement increment norm, the constraint norm and the Lagrange multiplier increment norm for a characteristic time step. In addition, the change in active set and the number of active nodes are given.

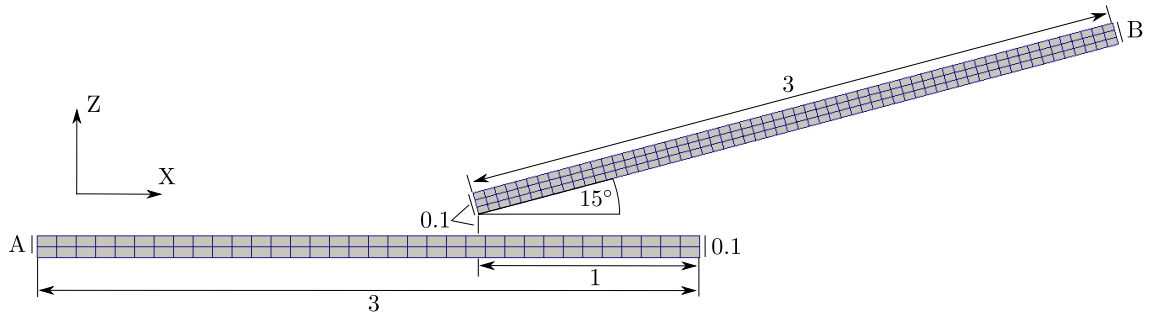


Figure 4.36: Initial setting for the frictional plate on plate example. The figure is taken from Farah et al. [71].

The convergence results demonstrate that the all entity contact formulation developed in this thesis is perfectly incorporated into the semi-smooth Newton methods from Section 3.5.2. Although the Lagrange multipliers for line and surface contact have different physical interpretation and are of different units, an excellent performance of the nonlinear solution scheme could be achieved. One basic aspect of this result is the consistent linearization of the line contact algorithm (cf. Appendix B) with all geometrical operations being considered.

4.9.5. Frictional contact – plate on plate

Finally, it is demonstrated that the developed contact formulation allows for capturing complex frictional effects in the finite deformation realm. For this purpose, two elastic plates are considered, see Figures 4.36 and 4.37. The material model for both plates is of Neo-Hookean type with Poisson's ratio of $\nu = 0.3$. Young's modulus for the lower plate is chosen as $E = 5 \cdot 10^5$ and Young's modulus for the upper plate is $E = 7 \cdot 10^5$. A quasi-static simulation is performed and thus inertia effects are not considered. The dimensions of the plates and their orientation

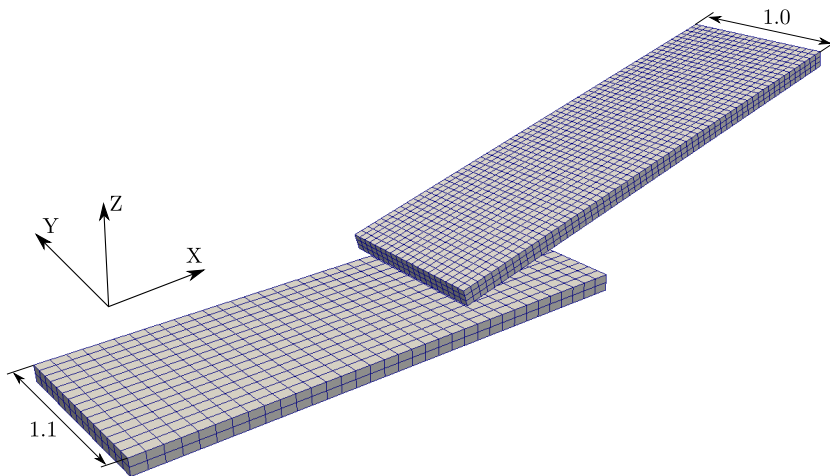


Figure 4.37: 3D view on the initial setting for the frictional plate on plate example. The figure is taken from Farah et al. [71].

can be extracted from Figures 4.36 and 4.37. During the entire simulation, the lower plate is completely fixed at its left face side A and the upper plate is subjected to a prescribed displacement $\mathbf{d}_{dbc} = [d_x, d_y, d_z]$ at its right face side B. In the time interval $0 \leq t < 6$ the displacement component d_z is linearly decreased from 0 to -0.75 and all other displacement components of \mathbf{d}_{dbc} remain zero. Afterwards, in the time interval $6 \leq t < 18$, the displacement component d_x is linearly decreased from 0 to -0.6 , the component d_z is kept constant and $d_y = 0$. Thus, the overall simulation time is $T = 18.0$. The time step size is defined as $\Delta t = 0.05$, and consequently 360 time steps have to be computed. Spatial discretization is realized with tri-linear hexahedral elements (hex8) with EAS element technology (cf. Simo and Rifai [255]) as can be seen in Figures 4.36 and 4.37. All in all, 4620 elements are employed. With regard to contact interaction, the upper plate is defined as slave body and the lower plate acts as master body. Frictional effects are described by a coefficient of friction $\mathfrak{F} = 0.4$. The complementarity parameter for the normal contact is defined to $c_n = 2$ and the parameter for frictional sliding is $c_t = 3000$. Both parameters are constant for the entire simulation. Due to the tilted upper (slave) plate, the resulting contact interaction is of edge-to-surface type, which is governed by the newly developed line contact algorithm. In addition, two vertices of the slave body are also in contact with the master plate, which represent an additional point contact scenario also enforced with Lagrange multipliers. Shortly after the considered simulation time, the contact scenario would change to surface contact.

The resulting normal contact stresses at time $t = 6.0$ are visualized in Figure 4.38. It can be seen that the stress level is comparably low in the middle of the contact line and drastically increases towards the two vertices. These effects near the vertices in flat-on-flat contact interactions are well-known as contact singularities and have already been investigated in several publications, see for example the work in Ciavarella et al. [44], Comninou [47] and Hojjati Talemi [111]. The developed all entity contact algorithm allows for robustly representing the expected stress state. Also the relatively sharp transitions between the low stress level in the middle of the contact line and the contact singularities at the vertices is accurately captured by the algo-

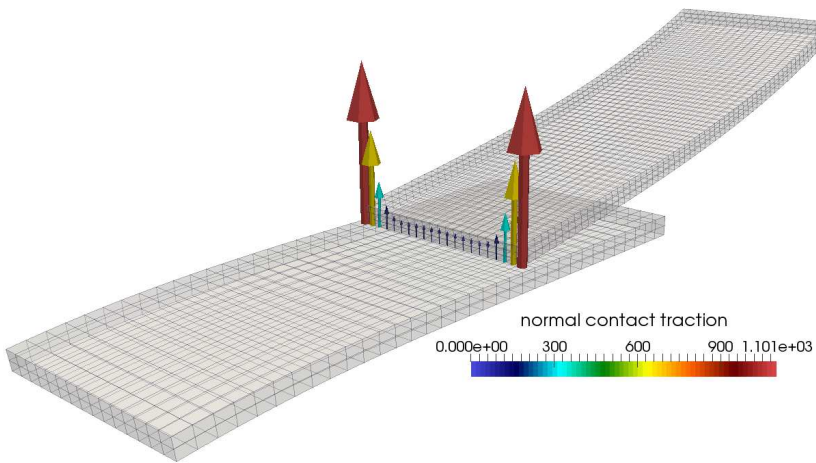


Figure 4.38: Frictional plate on plate example: deformation and normal contact stresses at time $t = 6$. The figure is taken from Farah et al. [71].

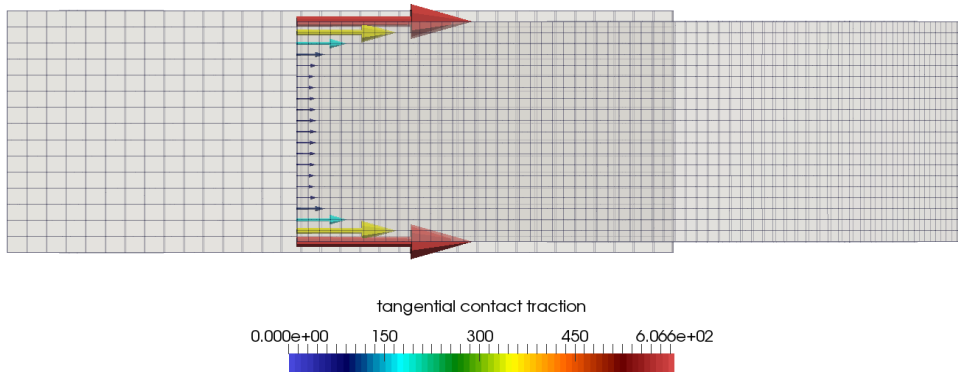


Figure 4.39: Frictional plate on plate example: top view with tangential contact stresses at time $t = 18$. The figure is taken from Farah et al. [71].

rithm. The tangential traction due to frictional effects at the end of the simulation, i.e. $t = 18.0$, are shown in Figure 4.39. Therein, a top view on the two plates can be seen. As expected, the corresponding frictional stresses show the same profile as the normal contact stresses in Figure 4.38. Finally, the L^2 -norms of the resulting normal force vector and tangential force vector are plotted for the entire simulation in Figure 4.40. Both forces linearly increase in the time interval $0 \leq t < 6$, which corresponds to the lowering of the upper plate through the prescribed displacement component d_z . Subsequently, frictional sliding is initiated by the given displacement component d_x , which leads to nearly constant forces in the time interval $6 \leq t < 18$. Slight oscillations occur due to the non-smooth geometry approximation inherent to first-order (hex8) elements.

All in all, the results of this example clearly demonstrate that the novel all entity contact algorithm is also able to robustly calculate frictional contact scenarios.

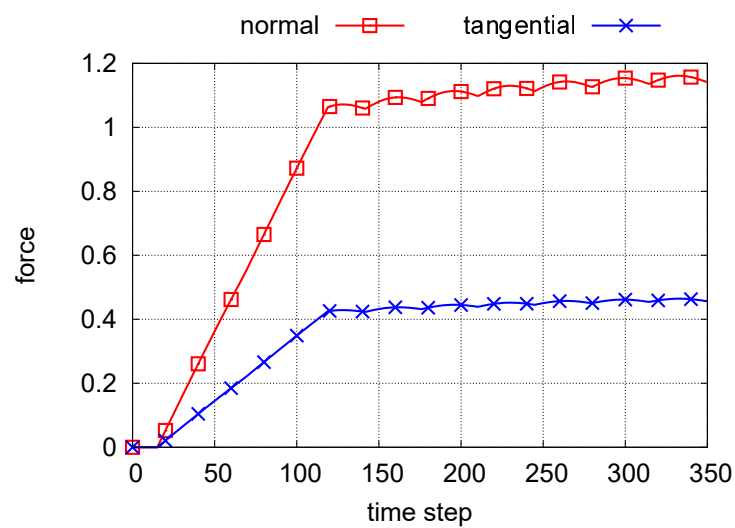


Figure 4.40: Frictional plate on plate example: L^2 -norm of normal force vector (red) and tangential force vector (blue) for the entire simulation. The figure is taken from Farah et al. [71].

5. Mortar Methods for Wear Modeling

Contact mechanics including wear is one of the main causes for subsequent failure of machines and component damage and thus highly important for industrial applications. It is a process of material removal associated with frictional effects, which might result in finite shape changes. Wear is a very complex phenomenon, which relates a geometrical setting including external conditions with tribological material behavior in the contact zone. Therefore correct predictions of wear effects are quite difficult to make, see Meng and Ludema [173]. The main wear types from the classifications in Popov [209] and Rabinowicz [223] are abrasive, adhesive corrosive and fretting wear. Nevertheless, there are many more wear types for different materials and load cases. The formulation predominantly employed for wear calculations is the linear phenomenological law by Archard [7], which is based on first studies from Holm [112]. It relates the worn volume to the normal contact force, a characteristic sliding length and a problem-specific wear parameter. There are also other wear laws available in the literature, such as the nonlinear wear model from Ho and Peterson [110], Pavelescu and Musat [198] and Rhee [230, 231]. However, Archards's law is also employed in this thesis as general wear description without discussing microscopical effects of special wear types. Thus, the wear phenomenon is only considered as macroscopical effect exemplarily driven by Archard's wear law, while the developed formulations could obviously also incorporate with other macroscopic wear laws.

Main focus of this chapter lies on the developed numerical algorithms to treat fretting wear effects and wear resulting into finite shape changes. Therein, the presented algorithm for simulating fretting wear problems is basically taken from the author's publication Farah et al. [69] and the explanations for the finite wear algorithm and the corresponding examples are strongly based on the author's publication Farah et al. [74]. Additionally, an extension of the developed finite wear algorithm towards the interaction of wear phenomena with thermal effects is given based on term paper Pröll [215], which was supervised by the author.

The following chapter starts with a state-of-the-art overview of already existing wear algorithms for considering fretting wear and finite wear phenomena. Afterwards, the fundamental information regarding the wear phenomena for finite wear and fretting wear considerations are given. Then, two developed finite element approach for spatial discretization of wear depth are introduced, which are applied to fretting wear and finite wear simulations. Finally, the framework for finite wear simulations is extended towards thermo-structure-contact-wear interaction.

5.1. Fundamental approaches to computational wear modeling and research objective

5.1.1. Fundamental approaches

In general, there are two different classes of wear treatment in computational contact mechanics: either only the consideration of very small amounts of wear or finite wear resulting in significant shape changes. The first class is usually treated by modifications of the gap function, which results in slightly overlapping bodies, see de Saracibar and Chiumenti [54], Gitterle [87], Rodríguez-Tembleque et al. [235], Serre et al. [246], Strömberg [260] and Strömberg [262]. When the wear depth exceeds a certain amount of material loss, which is usually equivalent to one or more element rows, the modification of the gap function leads to a decrease of robustness and solution accuracy. Thus, the geometry of the bodies, and consequently the mesh, must be adapted properly. In this regard, procedures ensuring an adequate mesh relocation are considered to be in the class of finite wear algorithms. Standard remeshing procedures are employed in various contributions to prevent bulk elements from degeneration, see Hegadekatte et al. [101], McColl et al. [167], Molinari et al. [175], Öqvist [187], Paulin et al. [197], Podra and Andersson [208] and Sfiantos and Aliabadi [249]. An alternative approach to guarantee proper mesh quality is the Arbitrary-Lagrangian-Eulerian (ALE) formulation, where the mesh movement is considered as pseudo-elasticity problem, see Stupkiewicz [263]. Also so-called wear-box models are available, which restrict the zone where the mesh movement takes place and rearrange nodes consistently to guarantee a good mesh quality, see Doca [61].

Most of the solution procedures for wear evolution are based on an explicit forward-Euler time integration scheme. Concretely, the standard contact problem is evaluated and only afterwards wear is calculated as a post-processing quantity for the last time step or even for a certain number of time steps. This incremental procedure is widely employed for the finite element method in Lengiewicz and Stupkiewicz [157], McColl et al. [167], Öqvist [187] and Podra and Andersson [208] and for the boundary element method in Kim et al. [137], Lee et al. [155], Rodríguez-Tembleque et al. [233, 234, 235], Serre et al. [246] and Sfiantos and Aliabadi [248, 249]. Wear algorithms based on implicit time integration schemes are predominantly available for small amounts of wear and usually introduce additional unknowns into the linearized system of equations, see Ben Dhia and Torkhani [23], Jourdan and Samida [131] and Strömberg [260]. To the knowledge of the author, the algorithm shown in Stupkiewicz [263] is the only contribution in the context of finite element analysis that treats wear implicitly in a finite deformation and finite wear regime. Yet, it is limited to quasi-steady-state contact scenarios.

Restrictions to periodic cycling and prescribed relative movement of the involved bodies are often made in order to simplify the wear algorithm, see Argatov [8], Argatov and Tato [9], Lengiewicz and Stupkiewicz [158] and Páczelt et al. [193] for reciprocal sliding and Páczelt and Mróz [191, 192] and Stupkiewicz [263] for general steady-state simulations. This assumption may be valid for classical tribological test configurations like pin-on-cylinder tests, but it is certainly not applicable to general scenarios.

The underlying contact frameworks for the wear algorithms existing in the literature are mostly based on node-to-segment contact formulations, see for example Lengiewicz and Stupkiewicz [157] and Strömberg et al. [261]. Nowadays, the mortar method is undoubtedly the most

preferred choice for robust finite element discretizations in computational contact mechanics. As already introduced in Chapter 3, finite deformation mortar algorithms with and without frictional effects can exemplarily be found in Popp et al. [212], Puso and Laursen [219], Puso et al. [220] and Yang et al. [301]. Still, the only wear algorithm based on a mortar finite element discretization that can be found in the literature is given in Cavalieri and Cardona [36], where only small wear effects without shape changes are considered.

Computational approaches for wear modeling in combination with thermo-structure interaction effects can only very rarely be found in existing literature. In Ireman et al. [125] wear effects within a thermo-structure simulation are considered for material properties corresponding to aluminium and steel in a small deformation, small temperature change regime in combination with a node-to-node contact algorithm. In addition, the wear depth has been taken into account as additional contribution to the gap function. Therein, the wear coefficient and the coefficient of friction were defined to be independent from the temperatures. In Molinari et al. [175] it was suggested to define the wear coefficient to be dependent on the current temperature in order to capture oxidation effects of the surfaces and other chemistry effects, which arise in a high temperature regime. The numerical model therein is based on the experimental observations in Lancaster [150], where a pin is pressed onto a rotating disc for different angular velocities. In the recent publication Pearson et al. [200], it was experimentally observed that an increasing temperature leads to the formation of a glaze-layer from debris particles. Consequently, the wear coefficient and the coefficient of friction decrease for high temperatures. However, to the best knowledge of the author, no general approach for thermo-structure-contact-wear interaction in a finite deformation, finite wear regime is available in the literature.

5.1.2. Specification of requirements

Based on the previous explanations on already existing wear algorithms, the most important requirements for the development of accurate and efficient mortar approaches for wear modeling are listed in the following.

3D fretting wear modeling with frictional mortar method When dealing with fretting wear problems, the underlying contact framework crucially influences the accuracy of displacement and stress results and consequently the overall wear simulation. As mentioned above, almost all existing wear algorithms are based on node-to-segment approaches or even node-to-node contact discretizations. Nowadays, the mortar method is arguably the most robust and accurate spatial discretization technique for computational contact problems and is thus predestinated as basis for the wear algorithms. Implementation of a fretting wear approach within a mortar based contact framework in a finite deformation regime was firstly carried out for 2D problems in Gitterle [87]. In Cavalieri and Cardona [36], modification of the gap function for small amounts of wear has been realized with the mortar method in a 3D regime, but without considering friction. However, no fretting wear algorithm based on a finite deformation mortar framework with frictional effects being included can be found in the existing literature.

Computationally efficient algorithm for fretting wear problems Simulation of fretting wear processes requires an efficient solution procedure since usually a large number of loading cycles has to be performed in order to investigate these effects. Consequently, the amount of

volume loss due to frictional wear effects is usually considered as additional contribution to the gap function, which represents a valid modeling approach when the wear depth per element size is reasonably small. When employing the mortar method in combination with a Lagrange multiplier approach for constraint enforcement, which is undoubtedly the most accurate choice, not only the overall system size but also the effort in solving the system of equations increase. Thus, the already introduced dual shape functions based on biorthogonality conditions to standard shape functions are the preferred discretization approach in order to achieve a computationally efficient wear modeling approach.

Finite element formulation for the computation of finite wear Finite deformation contact problems with frictional effects and finite shape changes due to wear in a non steady-state regime are considered in this chapter. While finite wear effects have already been considered in a steady-state regime (cf. Stupkiewicz [263]), no general formulation, which allows for arbitrarily changing loading conditions was developed in the context of the mortar finite element method so far.

Implicit time integration for finite wear effects The concept of finite wear computation has to be considered not only in the dimension of wear depth per body size, but rather in the ratio of wear depth per element size. Thus, the finer the mesh resolution the earlier should wear effects be considered in a finite manner. Consequently, also small load steps could lead to finite wear effects with respect to the element size and a proper temporal resolution would require a very small time step size. This inevitably leads to the requirement of a fully implicit treatment of the finite wear effects. Up to the knowledge of the author, the only implicit finite wear approach was developed in Stupkiewicz [263], but it is restricted to steady-state loading conditions. Thus, a general implicit algorithm, which allows for the computation of finite wear effects is a completely unanswered question.

Condensation of discrete wear unknowns Depending on the size of the contact interface, the spatial discretization of Archard's law for the finite wear algorithm could lead to an increase in the size of the global linear system of equations. This can be avoided by the use of dual shape functions, which satisfy the biorthogonality condition, see Section 3.4.1.2, since they allow for a computationally efficient elimination of the additional discrete unknowns due to the wear discretization by a static condensation procedure. Thus, the idea of dual shape functions is consequently adopted from the Lagrange multiplier discretization in Popp et al. [211, 212] and applied to frictional wear problems.

Extension to thermo-elastic contact problems with finite shape changes due to wear Since wear phenomena are strongly coupled to frictional dissipation, their interaction with frictional heat generation and general thermal effects plays a significant role in industrial applications. Also for computational contact problems with thermal effects, the mortar method has proven to perform excellently, see Hüeber and Wohlmuth [116] and Seitz et al. [245]. But up to now, neither numerical investigations concerning the interaction of thermal effects in wearing contact for small wear and small deformation nor their extension towards finite deformations and finite shape changes can be found in the existing literature in the context of the finite element method.

5.1.3. Proposal for mortar based wear approaches

The most important ingredients and new scientific contributions of the presented wear approaches are given in the following:

- extension of the finite deformation dual mortar contact formulation towards 3D fretting wear simulations, see also Farah et al. [69].
- implementation of the first fully implicit finite wear algorithm in a non-steady-state, finite deformation regime based on dual mortar methods with an Arbitrary-Lagrangian-Eulerian approach, see also Farah et al. [74].
- extension of the developed finite wear algorithm towards thermo-structure-contact-wear interaction problems.

In summary, the methods proposed in this chapter bring together existing ideas of computational wear modeling and dual mortar finite element methods and extend them towards a comprehensive and more general framework for efficient treatment of wear problems than possible to date.

5.2. Fundamentals on wear phenomena

The main focus of this chapter is on the development of wear algorithms based on mortar methods. For this purpose, any phenomenological wear law could be employed. Thus, the wear phenomena are considered in a macroscopic and very general form. However, the basic types of wear phenomena and their physical background are briefly outlined in the next subsection. Then, the commonly employed wear law of Archard is introduced, which acts as basis for the developed wear algorithms regardless of which wear type is considered, see Subsection 5.2.2. Finally, the continuum mechanical description of wear problems with considerably large material loss is given in Subsection 5.2.3.

5.2.1. Frictional wear phenomena

Wear phenomena can be generally described as volume loss due to frictional dissipation at the contact interface. Thus, according to Popov [209], friction and wear always appear together. However, depending on the application, one could also model wear without friction and friction without wear. In the following of this thesis, the most general assumption of wear with frictional effects is modeled. Despite this very general wear description, it can be distinguished between many types of wear, see Popov [209] and Rabinowicz [223]. The most relevant wear phenomena are *fretting wear* and *abrasive wear*.

5.2.1.1. Fretting wear

Information concerning fretting wear and fretting fatigue can be found in the vast amount of literature existing on this topic, where the interested reader is exemplarily referred to Aldham et al. [5], Hills [108], Hurricks [124] and Waterhouse [284]. In this subsection, only a brief description of these phenomena is given.

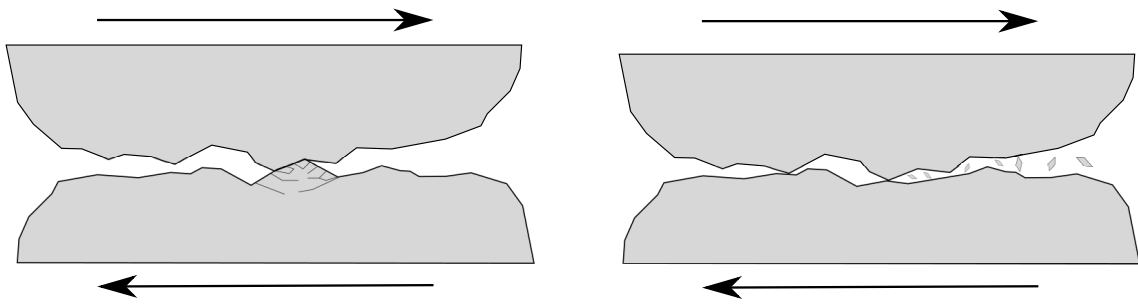


Figure 5.1: Fretting wear: micro crack initiation (left) and fracture of micro cracks which leads to material removal (right).

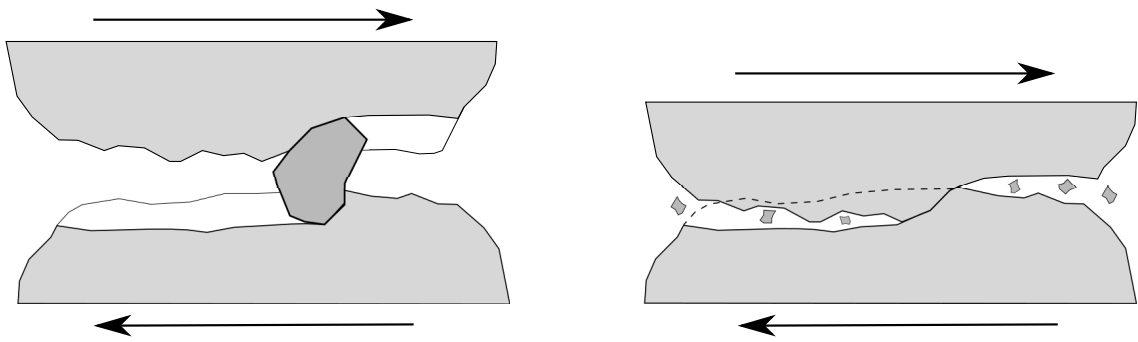


Figure 5.2: Forms of abrasive wear: three body abrasive wear (left) and two body abrasive wear (right).

Fretting wear is a destructive process of interface degradation, which occurs between clamped contacts when subjected to repeated loading cycles and minute relative motion. In each of these cycles, no noticeable change in the surfaces appear, but after a certain number of cycles micro cracks could occur due to the occurring large shearing stresses. Depending on the employed material, the coating and the loading condition, these micro cracks could erode and lead to slight material removal, see Figure 5.1. It is also possible that the introduced cracks propagate and lead to bulk brittle fracture, which is then denoted as fretting fatigue. Distinction between fretting wear, fretting fatigue and other fatigue classifications can also be made based on the length and orientation of the cracks relative to the contact surface and the presence of plasticity near the interface. A detailed classification of these related effects is not required in order to construct a finite element algorithm for macroscopic wear modeling and is therefore beyond the scope of this thesis.

5.2.1.2. Abrasive wear

Abrasive wear is characterized as material loss when two distinctively hard bodies are in contact or when three body contact occurs with hard particles being involved, see Godet [89]. This is schematically visualized in Figure 5.2. During the process of abrasive wear, the harder material penetrates and cuts the softer body. In the left part of Figure 5.2, three body contact is shown

for a zoom in view. The particle is harder than the two contact bodies and thus leads to material loss at them. Two body wear is shown in the right part of Figure 5.2. There, the interaction with the worn debris particles is negligible and the two bodies themselves cause the abrasive behavior. However, for the numerical algorithms developed in this thesis, only two body contact is explicitly modeled. The effect of three body contact could be included in the wear parameter later on (cf. Section 5.2.2), but the debris particles themselves are not modeled as additional bodies.

5.2.1.3. Further wear phenomena

In addition to the aforementioned fretting wear and abrasive wear, there are many more types available in the existing literature. For example, *adhesive wear* occurs when two bodies with comparable hardness are in contact. According to Popov [209], their interaction can be described as welding together of surfaces with micro-roughness followed by tearing processes of particles. Characteristic for this type of wear is the plastic deformation of metals at the contact interface when reaching a certain stress level. Furthermore, *corrosive wear* is caused by chemical modifications of the surface which leads to erosion at the interface layer. Without frictional sliding, the corrosive processes form a film on the contact surfaces, which on the other hand slows down the corrosion. However, when the loading conditions cause frictional sliding, the corrosive layer will be worn away and the interface erosion continues.

5.2.2. Archard's wear law

For the following derivation of the wear algorithms, the wear law from Archard [7] is employed as a phenomenological approach to relate kinematic quantities with the worn volume. The essential aspects of the proposed approach are however not limited to this specific type of law, but can also be applied with other (macroscopic) wear laws. Archard's wear law is a general formulation, which is valid for various physical types of wear, but also ignores some fundamental effects such as thermal relationships and the interaction with worn material within the contact zone. However, when considering only relatively small sliding velocities it is a suitable basis for further algorithmic developments, see Rabinowicz [223]. According to Archard's law, the worn volume V_w is globally expressed as

$$V_w = K \frac{P S}{H}, \quad (5.1)$$

with the normal force P , the sliding length S , the hardness of the softer material H and the dimensionless wear coefficient K . Employing Archard's law within a finite element formulation later on requires a local expression for the loss of material. For this purpose, the amount of worn volume V_w is expressed as wear depth w per area. Thus, the global form of Archard's law is reformulated as rate of the wear depth in spatial configuration:

$$\dot{w} = k_w |p_n| ||\mathbf{v}_{\tau,\text{rel}}||, \quad (5.2)$$

where the local wear coefficient in spatial configuration k_w is not a dimensionless parameter, but has the dimension of an inverse pressure. It can be equivalently expressed in terms of the spatial

frictional dissipation rate density \dot{d} , which has been already introduced in Section 3.1. Based on the considerations in Ramalho and Miranda [224], the rate of the spatial wear depth reads:

$$\dot{w} = \frac{k_w}{\mathfrak{F}} \dot{d} = \mathfrak{K} \dot{d}. \quad (5.3)$$

Here, the original wear coefficient k_w and the Coulomb friction coefficient \mathfrak{F} are combined to the so-called energy wear coefficient \mathfrak{K} . Experiments in Ramalho and Miranda [224] suggest that assuming a constant energy wear coefficient leads to better results than assuming a constant wear coefficient, thus indicating the strong coupling of wear effects and frictional sliding conditions. In the following, a relation between spatial and material wear is derived based on the considerations in Lengiewicz and Stupkiewicz [157]. The transformation of the frictional dissipation rate density \dot{d} to the material configuration (i.e. to \dot{D}) was already outlined in Section 3.1 and is shortly reviewed as

$$\dot{D} = j_a \dot{d}, \quad (5.4)$$

with dA and dA_0 being the areas of an infinitesimal surface segment in spatial and material description, respectively. The relation between the spatial wear rate and its material counterpart \dot{W} can be established by expressing wear as a volume loss per area. For this purpose, it is assumed that the loss of material is defined in the spatial and material unit normal direction, respectively. Thus, mass conservation yields

$$\dot{w} dt = \frac{dV}{dA} = \frac{1}{\rho} \frac{dm}{dA} \quad \text{and} \quad \dot{W} dt = \frac{dV_0}{dA_0} = \frac{1}{\rho_0} \frac{dm}{dA_0}. \quad (5.5)$$

Here, as introduced in Chapter 2, dV represents an infinitesimal volume element in the spatial configuration, whereas dV_0 is the corresponding counterpart in the material configuration. Additionally, ρ is the spatial density and ρ_0 is the density in the material configuration. Enforcing mass conservation yields

$$j_a \dot{w} = J \dot{W}, \quad (5.6)$$

where J is the determinant of the deformation gradient. Assuming a constant friction coefficient and having equations (5.4) and (5.6) at hand, it is obvious that the wear coefficients in spatial and material configuration are related by

$$k_w = J K_w. \quad (5.7)$$

To the author's knowledge, there are no unambiguous and conclusive experimental data, which would justify the choice of a constant wear coefficient in material or spatial configuration as being more physically meaningful. Therefore, both approaches have been implemented and will be evaluated in the numerical examples later on. However, one could think of non-constant wear coefficients in both configurations, which depend on the current normal load or other quantities. For this purpose, it should be mentioned that the work in Pearson and Shipway [199] has indicated that the wear coefficient is independent of the slip amplitude and thus independent from displacement quantities. Employing a backward Euler scheme for local time discretization of (5.2) results in the incremental formulation

$$\Delta w = k_w |p_n| ||\mathbf{v}_{\tau,\text{rel}}|| \Delta t = k_w |p_n| ||\mathbf{u}_{\tau,\text{rel}}||, \quad (5.8)$$

with $\mathbf{u}_{\tau,\text{rel}}$ being the relative tangential slip increment within one pseudo-time step. Assuming that both involved bodies may undergo a process of material loss at the interface, two wear quantities $w^{(1)}$ and $w^{(2)}$ have to be defined for the slave and for the master surface, respectively. Correspondingly, two generally different wear coefficients $k_w^{(1)}$ and $k_w^{(2)}$ are introduced. As the kinematic quantities p_n and $\mathbf{u}_{\tau,\text{rel}}$ are equivalent for slave and master side in the continuous setting, only the wear coefficients cause differences for slave-sided and master-sided wear. Thus, the relation between wear on the slave side and wear on the master side can be directly formulated as ratio of the wear coefficients:

$$\Delta w^{(1)} = \frac{k_w^{(1)}}{k_w^{(2)}} \Delta w^{(2)}. \quad (5.9)$$

Considering the absolute wear depth without taking into account the different signed wear quantities due to opposed interface normals for slave and master side, the cumulative wear depth can be expressed as

$$\Delta w = (k_w^{(1)} + k_w^{(2)}) |p_n| ||\mathbf{u}_{\tau,\text{rel}}||. \quad (5.10)$$

5.2.3. Continuum mechanics for finite wear

When taking into account finite wear, the mechanical configuration to which kinematic quantities are referred constantly changes, which introduces a major additional complexity in continuum modeling as compared with finite deformation contact problems without removal of material due to wear, see Chapter 3. Therefore, an additional configuration of each involved body is introduced: the time-dependent undeformed material (worn) configuration $\Omega_m^{(i)} \subset \mathbb{R}^3$, which represents the unloaded worn state. This concept of a third configuration, which represents the undeformed worn state was successfully employed in Lengiewicz and Stupkiewicz [157] and Stupkiewicz [263] and thus it is the basis for the following considerations. The material configuration is occupied by all material points $\tilde{\mathbf{X}}$ at a certain time t . The Dirichlet, Neumann and contact boundaries of the material configuration read $\Gamma_{m,u}^{(i)}$, $\Gamma_{m,\sigma}^{(i)}$ and $\Gamma_{m,c}^{(i)}$. It is assumed that reference, spatial and material configurations are coincident for the initial time $t = 0$. The interconnections between these configurations are visualized for one exemplary body in Figure 5.3. By introducing the material configuration $\Omega_m^{(i)}$, the reference configuration $\Omega_0^{(i)}$ can be interpreted as observer domain for the material motion ϕ , viz.

$$\phi : \begin{cases} \Omega_0 \rightarrow \Omega_m(t), & (\mathbf{X}, t) \rightarrow \tilde{\mathbf{X}}, \\ & \phi(\mathbf{X}, t) = \tilde{\mathbf{X}}. \end{cases} \quad (5.11)$$

Here, the bijective mapping ϕ connects a material point $\tilde{\mathbf{X}}$ with its observer point in the reference configuration \mathbf{X} . An additional bijective mapping ψ is introduced to describe the connection between observer points \mathbf{X} and spatial points \mathbf{x} , as

$$\psi : \begin{cases} \Omega_0 \rightarrow \Omega_t(t), & (\mathbf{X}, t) \rightarrow \mathbf{x}, \\ & \psi(\mathbf{X}, t) = \mathbf{x}. \end{cases} \quad (5.12)$$

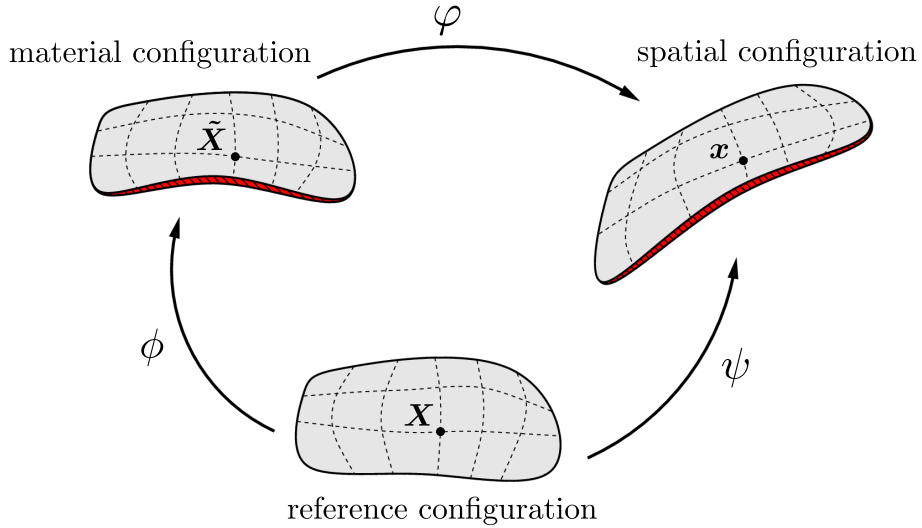


Figure 5.3: Three continuum mechanical configurations and their interconnections: reference configuration, material (worn) configuration and spatial configuration. Figure taken from Farah et al. [74].

Accordingly, the mapping of the physical motion φ originally defined in (2.1) changes and is now expressed with ϕ and ψ as

$$\varphi = \psi \circ \phi^{-1} : \begin{cases} \Omega_m(t) \rightarrow \Omega_t(t), & \tilde{\mathbf{X}}(t) \rightarrow \mathbf{x}(t), \\ \varphi(\tilde{\mathbf{X}}) = \mathbf{x}. \end{cases} \quad (5.13)$$

The mapping φ in its general form is denoted as *Arbitrary-Lagrangian-Eulerian* (ALE) formulation, since the observer is neither fixed at a material point nor fixed at a spatial point. By degeneration of the material mapping ϕ to an identity mapping, the ALE approach reduces to a pure *Lagrangian* representation. On the contrary, when the spatial mapping ψ represents the identity mapping, the approach changes to an *Eulerian* representation. This concept of an ALE formulation is widely used, e.g. for fluid-structure interaction problems Klöppel et al. [138] and Mayr et al. [166] and finite strain plasticity models Armero and Love [10]. More detailed explanations of ALE problems can for example be found in Belytschko et al. [16] and Huerta and Casadei [118].

5.3. Finite element approaches for wear discretization

In the following, it is distinguished between two fundamentally different finite element approaches for discretizing the volume loss, i.e. the wear depth. Again, wear phenomena are considered as a description for material loss driven by Archard's law regardless of the underlying physical effects. First, the so-called *internal state variable approach* is introduced based on the investigations in Farah et al. [69] and Gitterle et al. [88]. It expresses the wear depth in a weak sense and in terms of the already existing quantities. Thus, no additional unknowns enter the discrete system of equations. The alternative method of wear discretization is based on the work

in Farah et al. [74] and is named *primary variable approach*. Here, wear is completely discretized on the contact interface and enters the system of equations as additional set of unknowns.

5.3.1. Internal state variable approach

The internal state variable approach was developed in the context of 2D dual mortar methods in Gitterle [87] and was extended towards 3D applications in Farah et al. [69]. Thus, the following explanations are strongly based on the work in Farah et al. [69]. The internal state variable approach is based on expressing the wear depth in terms of already employed quantities, namely the normal contact pressure p_n and the displacements $\mathbf{u}^{(i)}$. Therefore, the basis for the finite element discretization of wear with the internal state variable approach is the expression of the cumulative wear in (5.10), which reads

$$\Delta w = (k_w^{(1)} + k_w^{(2)}) |p_n| \|\mathbf{u}_{\tau,\text{rel}}\|. \quad (5.14)$$

Here, the wear increment Δw represents the total wear depth per time step of the two involved slave and master surfaces. Now, the cumulative wear coefficient is introduced and reads

$$k_w = k_w^{(1)} + k_w^{(2)}. \quad (5.15)$$

Keeping in mind the well-established slave-master principle of mortar contact discretizations introduced in Chapter 3, all following relations are stated on the slave side. Thus, the weighted wear increment $\Delta \tilde{w}^{(1)}$ is defined on the slave side and is evaluated as integral expression of (5.14) over the slave side, via

$$\Delta \tilde{w}^{(1)} = k_w \int_{\gamma_c^{(1)}} p_n \|\mathbf{u}_{\tau,\text{rel}}\| \, dA. \quad (5.16)$$

Herein, the normal contact pressure p_n can be identified as normal part of the contact Lagrange multiplier λ_n . Thus, the discretized form of the weighted wear increment $\Delta \tilde{w}_j^{(1)}$ for slave node- j reads

$$\Delta \tilde{w}_j^{(1)} = k_w \int_{\gamma_{c,h}^{(1)}} \hat{\Phi}_j \lambda_n \|\mathbf{u}_{\tau,\text{rel}}\| \, dA, \quad (5.17)$$

with $\hat{\Phi}_j$ representing a test function for the wear equation. Its physical interpretation and definition will be discussed in Section 5.4.2.1. Similar to the discrete weighted gap function in (3.40), the discrete weighted wear increment represents a discrete distance quantity, which is integrated over the discrete slave surface. Therefore, the discrete weighted wear could be interpreted as volume loss per slave node.

In addition, it is important to point out that the employed slip increment in (5.17) is not related with the weighted relative tangential velocity in (3.43), but rather a point-wise evaluated quantity. The weighted relative tangential velocity is created by a weighting introduced by the variation of Lagrange multipliers, which is represented by the shape function Φ_j within the time derivative of the mortar matrices \mathbf{D} and \mathbf{M} in (3.43). Employing the frame indifferent relative tangential velocity from (5.17) is only appropriate when assuming a constant normal pressure over the local support of a node and would allow to exclude the normal part of the Lagrange multiplier λ_n .

from the integral in (5.17). However, this simplification would decrease the accuracy of the traction interpolation, which directly affects the quality of the computational results. Therefore, the non-weighted slip increment is employed for the weighted wear and slight discrepancies will be accepted. Further information concerning the choice of the slip increment can be found in Gitterle [87].

5.3.2. Primary variable approach

The second possibility of discretizing the wear depth is the so-called primary variable approach, which was firstly presented in Cavalieri and Cardona [36] for a small amount of wear and has been extended to finite wear simulations in Farah et al. [74]. Here, Archard's wear law is rewritten by employing the method of weighted residuals

$$\int_{\gamma_c^{(i)}} \delta w^{(i)} (w^{(i)} - k_w^{(i)} |p_n| |\mathbf{u}_{\tau,\text{rel}}|) dA = 0, \quad (5.18)$$

with the wear weighting functions $\delta w^{(i)}$. In contrast to the internal state variable approach, the wear depth on slave and master side is explicitly discretized via

$$w_h^{(1)}|_{\Gamma_{c,h}^{(1)}} = \sum_{k=1}^{n_w^{(1)}} N_k^{(1)} w_k^{(1)}, \quad w_h^{(2)}|_{\Gamma_{c,h}^{(2)}} = \sum_{l=1}^{n_w^{(2)}} N_l^{(2)} w_l^{(2)}, \quad (5.19)$$

where $w_k^{(1)}$ and $w_l^{(2)}$ represent discrete nodal wear variables on the slave and the master surface, respectively. As for the displacement interpolation, standard shape functions based on Lagrange polynomials $N_k^{(1)}$ and $N_l^{(2)}$ are employed for wear representation. Moreover, the numbers of nodes carrying discrete wear unknowns are defined to be equal to the total numbers of slave and master nodes, i.e. $n_w^{(1)} = n^{(1)}$ and $n_w^{(2)} = n^{(2)}$. In addition to the discrete wear depth unknowns, discrete weighting functions are introduced as

$$\delta w_h^{(1)}|_{\Gamma_{c,h}^{(1)}} = \sum_{k=1}^{n_z^{(1)}} \Theta_{w,k}^{(1)} \delta w_k^{(1)}, \quad \delta w_h^{(2)}|_{\Gamma_{c,h}^{(2)}} = \sum_{l=1}^{n_z^{(2)}} \Theta_{w,l}^{(2)} \delta w_l^{(2)}, \quad (5.20)$$

with the nodes carrying discrete wear weightings being chosen according to the wear interpolation: $n_z^{(1)} = n^{(1)}$ and $n_z^{(2)} = n^{(2)}$. The shape functions $\Theta_w^{(i)}$ are defined in full analogy to the Lagrange multiplier interpolation Φ , which allows for employing either standard or dual shape functions, see Section 3.4.1. With the discrete wear unknowns and the weighting functions being defined, the calculation of the wear depth $w^{(i)}$ can be stated based on the weak enforcement of Archard's wear law in (5.18). Therefore, the normal contact pressure p_n in (5.18) is identified as normal part of the contact Lagrange multiplier λ_n and the discretized wear depth and the discrete wear weightings are employed, which leads to the resulting discrete wear residuum in global form:

$$\mathbf{r}_w^{(i)} = \mathbf{E}^{(i)} \mathbf{w}^{(i)} - \mathbf{T}^{(i)} \boldsymbol{\lambda} = \mathbf{0}. \quad (5.21)$$

Here, the vector $\mathbf{w}^{(i)}$ contains all discrete wear unknowns. The new mortar matrices $\mathbf{E}^{(i)}$ are created by assembling the nodal values

$$E_{jk}^{(1)} = \int_{\gamma_{c,h}^{(1)}} \Theta_{w,j}^{(1)} N_k^{(1)} dA , \quad j = 1, \dots, n^{(1)}, \quad k = 1, \dots, n^{(1)} , \quad (5.22)$$

$$E_{jl}^{(2)} = \int_{\gamma_{c,h}^{(1)}} (\Theta_{w,j}^{(2)} \circ \chi_h) (N_l^{(2)} \circ \chi_h) dA , \quad j = 1, \dots, n^{(2)}, \quad l = 1, \dots, n^{(2)} . \quad (5.23)$$

It is obvious that $\mathbf{E}^{(1)}$ can be interpreted as standard slave-sided mortar matrix \mathbf{D} with reduced dimension. Thus, employing dual shape functions for the discrete wear weighting and standard shape functions for the wear interpolation yields a Petrov-Galerkin type formulation and consequently a diagonal matrix $\mathbf{E}^{(1)}$ in (5.22). A detailed motivation for such a Petrov-Galerkin approach can be found in Popp et al. [214] in the context of the non-penetration constraint for contact. The beneficial effects of $\mathbf{E}^{(1)}$ becoming a diagonal matrix can be employed for an efficient calculation of the discrete wear unknowns in (5.21), via

$$\mathbf{w}^{(1)} = \mathbf{E}^{(1),-1} \mathbf{T}^{(1)} \boldsymbol{\lambda} . \quad (5.24)$$

Here, the mortar matrix $\mathbf{E}^{(1)}$ is inverted to obtain a solution for the discrete wear unknowns. The matrix $\mathbf{E}^{(2)}$ in (5.23) arises by integrating the two shape functions $\Theta_j^{(2)}$ and $N_l^{(2)}$ defined on the master side over the slave surface. This is realized by applying the already introduced discrete mapping χ_h twice. Integrating this matrix over the master surface would arguably be easier, because no discrete projection would be required, but to keep the established slave-master principle, and thus in some sense the consistency of the mortar integration scheme, all integration procedures are performed on the slave side. But, it is not guaranteed that the matrix $\mathbf{E}^{(2)}$ in (5.23) is strictly diagonal, because the biorthogonality condition of the dual shape functions $\Theta_j^{(2)}$ is enforced over the discrete master surface $\gamma_{c,h}^{(2)}$, but the integral expression in (5.23) is evaluated over the discrete slave surface $\gamma_{c,h}^{(1)}$. A strictly diagonal matrix $\mathbf{E}^{(2)}$ could be created by enforcing the biorthogonality condition between the projected master side shape functions over the slave surface $\gamma_{c,h}^{(1)}$, or performing the integral evaluation over the master surface. However, from an engineering point of view, the resulting error in the problem formulation is negligible. The matrices $\mathbf{T}^{(i)}$ arise from integrating products of weighting and Lagrange multiplier shape functions with the norm of the non-weighted slip increment over the slave side, i.e.

$$T_{jk}^{(1)} = k_w^{(1)} \int_{\gamma_{c,h}^{(1)}} \Theta_{w,j}^{(1)} \Phi_k^{(1)} ||\mathbf{u}_{\tau,\text{rel}}|| dA , \quad j = 1, \dots, n^{(1)}, \quad k = 1, \dots, n^{(1)} , \quad (5.25)$$

$$T_{jl}^{(2)} = k_w^{(2)} \int_{\gamma_{c,h}^{(1)}} (\Theta_{w,j}^{(2)} \circ \chi_h) \Phi_l^{(1)} ||\mathbf{u}_{\tau,\text{rel}}|| dA , \quad j = 1, \dots, n^{(2)}, \quad l = 1, \dots, n^{(1)} . \quad (5.26)$$

These matrices complete the discrete wear equation.

Remark 5.1. *The definition that the wear weighting functions $\Theta_{w,j}$ act as dual shape functions and the interpolation of the discrete wear unknowns is realized by standard shape functions is somehow arbitrary. It is also possible to create a Petrov-Galerkin type formulation by defining the shape functions vice versa. This was also implemented and tested and no negative influence on the solution quality, the stability or robustness of the proposed algorithms was noticed.*

5.4. Formulation for fretting wear

Basically, it is distinguished between wear effects resulting into a relatively small amount of wear (i.e. wear depth) and wear effects which lead to finite shape changes of the considered bodies. In this section, the wear effects of small extent are considered. Here, the most important phenomenon is the fretting wear as introduced in Section 5.2.1.1. First, the problem setting for fretting wear modeling is stated. Afterwards, the internal state variable approach of finite element discretization is applied to this problem. Then, the application of the primary variable approach to modeling fretting wear is discussed. Finally, numerical examples are shown to demonstrate the solution quality of the proposed algorithm.

5.4.1. Problem setting for fretting wear

For modeling fretting wear phenomena, no finite shape change in the geometry of the involved bodies due to material loss is expected. But, the finite deformation regime is still assumed. Thus, the problem formulation for frictional contact is basically still valid and briefly repeated. First, the IVP of elastodynamics reads

$$\text{Div} \boldsymbol{P}^{(i)} + \hat{\boldsymbol{b}}_0^{(i)} = \rho_0^{(i)} \ddot{\boldsymbol{u}}^{(i)} \quad \text{in } \Omega_0^{(i)} \times [0, T], \quad (5.27)$$

$$\boldsymbol{u}^{(i)} = \hat{\boldsymbol{u}}^{(i)} \quad \text{on } \Gamma_u^{(i)} \times [0, T], \quad (5.28)$$

$$\boldsymbol{P}^{(i)} \cdot \boldsymbol{N}^{(i)} = \hat{\boldsymbol{t}}_0^{(i)} \quad \text{on } \Gamma_\sigma^{(i)} \times [0, T], \quad (5.29)$$

$$\boldsymbol{u}^{(i)}(\boldsymbol{X}, 0) = \hat{\boldsymbol{u}}_0^{(i)}(\boldsymbol{X}) \quad \text{in } \Omega_0^{(i)}, \quad (5.30)$$

$$\dot{\boldsymbol{u}}^{(i)}(\boldsymbol{X}, 0) = \hat{\dot{\boldsymbol{u}}}_0^{(i)}(\boldsymbol{X}) \quad \text{in } \Omega_0^{(i)}. \quad (5.31)$$

In addition, the frictional contact constraints remain unchanged and are stated as firstly introduced in (3.18):

$$\Upsilon := \|\boldsymbol{t}_\tau\| - \mathfrak{F}|p_n| \leq 0, \quad \boldsymbol{v}_{\tau,\text{rel}} + \beta \boldsymbol{t}_\tau = \mathbf{0}, \quad \beta \geq 0, \quad \Upsilon \beta = 0. \quad (5.32)$$

All these equations are identical to the standard contact problem in Chapter 3. The only difference affects the Hertz-Signorini-Moreau conditions in (3.16). Here, the gap function g_n is replaced by a modified gap function g_n^w , yielding

$$g_n^w \geq 0, \quad p_n \leq 0, \quad p_n g_n^w = 0. \quad (5.33)$$

Herewith, the wear effects are modeled as additional contribution to the gap function. Such an approach was firstly introduced in Strömberg et al. [261] and employed in Gitterle [87], Salles et al. [240] and Strömberg [260]. This approach results in slightly overlapping bodies, where the overlap represents the material loss due to wear. Considering the spatial finite element discretization, it becomes obvious that this approach is only valid for a very small amount of wear. The author recommends that the wear depth corresponding to the worn material should not exceed a characteristic element length at the contact interface in order to guarantee a proper solution quality.

5.4.2. Fretting wear algorithm

The numerical algorithm for calculating frictional contact with fretting wear is based on the mortar contact framework stated in Chapter 3. As explained in the previous section, only the Hertz-Signorini-Moreau conditions are modified, see (5.33). Herein, the basic modeling assumption for this approach is to directly modify the gap function according to wear effects at the interface. This modification is realized by considering the wear depth as additional contribution to the gap function along the outward normal vector of the contact interface. This modification could be numerically treated with the internal state variable approach and the primary variable approach explained in Section 5.3. But, the internal state variable approach is the preferred finite element approach for simulating fretting wear problems due to its explicit avoidance of additional unknowns. This becomes very beneficial when simulating a large number of cycles, which are usually required for simulating fretting wear problems. However, in general the primary variable approach could also be used for fretting wear problems and its computational efficiency could be drastically increased by employing dual shape functions as explained in Section 5.3.2. But, its complete mortar matrices have to be globally assembled, which is more costly than the evaluation of the internal state variable approach.

5.4.2.1. Internal state variable approach

The presented algorithm aims to be valid for wear phenomena that result in a very small amount of worn volume, thus no macroscopic change of the involved bodies due to wear is expected. Therefore, only the gap function within the Hertz-Signorini-Moreau conditions is modified by the wear effects. For this purpose, the modified gap g_n^w reads

$$g_n^w = g_n + w \quad (5.34)$$

with the wear depth being defined according to Archard's law in Section 5.2.2. In (5.34), modification of the gap function is realized by enforcing the wear depth as additional contribution to the gap function along the normal vector of the contact interface. Consequently, the modified Hertz-Signorini-Moreau conditions read

$$g_n + w \geq 0, \quad p_n \leq 0, \quad p_n(g_n + w) = 0. \quad (5.35)$$

It becomes obvious that these reformulated inequalities allow the two bodies to penetrate to an extent being equivalent to the wear depth. All other equations of the IBVP as well as the frictional sliding constraints remain unchanged. Consequently, the variational contact constraints in (3.23) are adapted to

$$\lambda_n \in \mathbb{R}_0^+ : (g_n + w)(\delta\lambda_n - \lambda_n) \geq 0 \quad \forall \delta\lambda_n \in \mathbb{R}_0^+, \quad (5.36)$$

where the Lagrange multiplier is again chosen from $\mathcal{M}(\lambda)$. Thus, the weak formulation of this constraint results in

$$\int_{\gamma_c^{(1)}} (\delta\lambda_n - \lambda_n) g_n dA + \int_{\gamma_c^{(1)}} (\delta\lambda_n - \lambda_n) w dA \geq 0, \quad (5.37)$$

where the first term yields the weighted gap, and the second term can be interpreted as weighted wear, respectively. Since the weighted gap was already introduced in its discrete form in (3.40),

the following details are only outlined for the weighted wear. It can be written in its discrete form for slave node j as

$$\Delta\tilde{w}_j^{(1)} = k_w \int_{\gamma_{c,h}^{(1)}} \Phi_j \lambda_n ||\mathbf{u}_{\tau,\text{rel}}|| \, dA, \quad (5.38)$$

where it becomes obvious that the shape function $\hat{\Phi}_j$ in (5.17) can directly be identified with the Lagrange multiplier shape function Φ_j . Thus, the discrete weighted wear and consequently the entire frictional contact problem for fretting wear depends only on the already existing discrete Lagrange multipliers and the discrete displacements and no additional unknowns enter the system of equations. By assuming only very small material loss during the overall time interval, the wear state is nearly constant within one discrete time step. Therefore, this approach is realized explicitly, meaning that wear is post-processed after each time step for the considered slave node j , via

$$\tilde{w}_j(t_n) = \tilde{w}_j(t_{n-1}) + \Delta\tilde{w}_j(t_n), \quad (5.39)$$

with the accumulated weighted wear $\tilde{w}_j(t_n)$. Accordingly, the discretized normal constraint reads

$$\tilde{g}_{n,j} + \tilde{w}_j \geq 0, \quad \lambda_{n,j} \leq 0, \quad \lambda_{n,j} (\tilde{g}_{n,j} + \tilde{w}_j) = 0 \quad j = 1, \dots, n^{(1)}. \quad (5.40)$$

These inequality constraints can then be reformulated into nonlinear complementarity functions as explained in Section 3.5. Here, the discrete weighted gap function has to be replaced by the modified gap, but the basic approach remains unchanged. To visualize the wear depth in inward normal direction, the accumulated weighted wear \tilde{w}_j has to be post-processed, because it represents an integral quantity rather than a real physical measure. Therefore, the weighting of the wear is removed by dividing the weighted wear information of a node by the associated area. By definition, this information is stored within the first mortar matrix \mathbf{D} from (3.35). When employing the introduced dual shape functions explained in Section 3.4.1.2, this matrix becomes diagonal and the area information of the nodes is stored in the corresponding diagonal entry. Thus, the physical wear depth can be easily computed via

$$w_j = \frac{\tilde{w}_j}{D_{jj}} \quad j = 1, \dots, n^{(1)}. \quad (5.41)$$

Finally, the algorithm for one time step of the presented internal state variable approach for simulating fretting wear included within the frictional mortar framework is shown:

Algorithm 5.1. Internal state variable approach for fretting wear

1. Solve the frictional mortar contact problem without considering a change of the actual wear state.
2. Post-process the wear increment for this time step as described in (5.17) and update the accumulated wear per node in (5.39).
3. Substitute the nodal weighted gap \tilde{g}_j by the modified gap $\tilde{g}_{n,j}^w$ including the updated accumulated wear

$$\tilde{g}_{n,j}^w(t_{n+1}) = \tilde{g}_{n,j}(t_{n+1}) + \tilde{w}_j(t_n) \quad j = 1, \dots, n^{(1)}. \quad (5.42)$$

By computing the modified gap, the time step is completed.

5.4.2.2. Primary variable approach

The primary variable approach for spatial finite element discretization was introduced in Section 5.3.2 and is not the preferred approach for simulating fretting wear problems. This is due to the necessity of constructing the mortar matrices \mathbf{E} and \mathbf{T} , which is computationally more costly than the simple gap update for the internal state variable approach in the previous section. Thus, its application to fretting wear problems is just briefly outlined in the following for the sake of completeness. Starting point for the derivation of this algorithm is the modeling approach of modifying the gap function, explained in Section 5.4.1. In contrast to the internal state variable approach for fretting in Section 5.4.2.1, the spatial node positions at the contact interface are directly modified for the primary variable approach, via

$$\tilde{\mathbf{x}}^{(i)} = \mathbf{x}^{(i)} - \mathbf{n}^{(i)} w^{(i)} \quad \text{on } \gamma_c^{(i)}. \quad (5.43)$$

Here, the modified spatial coordinates $\tilde{\mathbf{x}}$ automatically yield a modification of the gap function. Note, this modification would only be applied for the calculation of the gap function and thus the involved bodies would also slightly overlap. When performing spatial discretization of the wear depth as described in Section 5.3.2, the discrete wear unknowns can be explicitly calculated via

$$\mathbf{w}^{(i)} = \mathbf{E}^{(i),-1} \mathbf{T}^{(i)} \boldsymbol{\lambda}. \quad (5.44)$$

Again, this procedure is not recommended for fretting wear simulations since the internal state variable approach can be realized in a more efficient manner. Thus, a concluding algorithm is not provided for the primary variable approach.

5.4.3. Numerical examples

In the following, two 2D examples and one 3D example are presented. The first one is an oscillating beam which allows for comparison with results from the literature. The second example is a typical bridge type fretting test. The last example is a Hertzian contact scenario in 3D, which is discretized with NURBS elements.

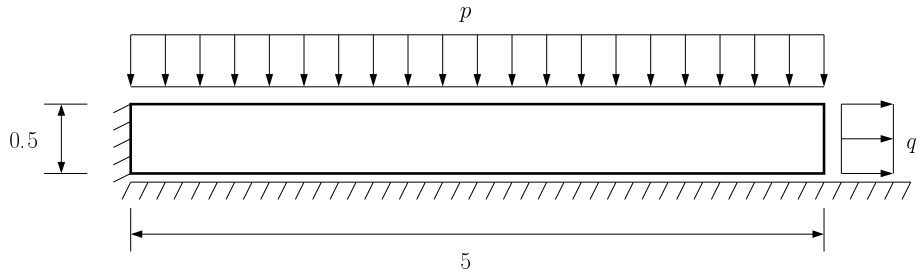


Figure 5.4: Problem setting for 2D oscillating beam. Length measures are given in [cm]. The Figure is taken from Farah et al. [69].

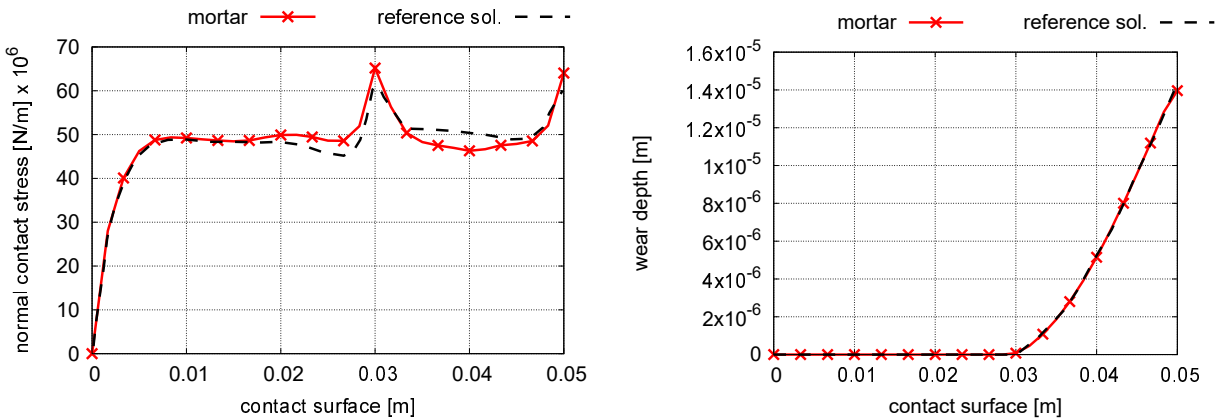


Figure 5.5: Results for 2D oscillating beam after 3000 calculated cycles: normal contact stresses (left) and wear depth (right) compared with reference solution Strömberg [260]. Figure is based on Farah et al. [69].

5.4.3.1. Validation – oscillating beam

The first example is a 2D oscillating beam firstly presented in Strömberg [260] for a node-to-segment approach in combination with an augmented Lagrange method to enforce the contact constraints. This example has already been employed in combination with a mortar contact algorithm in Gitterle [87]. The problem setting is visualized in Fig. 5.4. The beam is fixed in horizontal direction at its left boundary and the lower edge of the beam is in contact with a rigid foundation. It is loaded by a constant pressure $p = 50 \frac{\text{MN}}{\text{m}}$ and by a sinusoidal excitation $q = 50 \frac{\text{MN}}{\text{m}} \sin(2\pi t)$. The friction coefficient is chosen as $\tilde{\gamma} = 0.2$ and the wear coefficient is $k_w = 1.0 \cdot 10^{-11} \text{Pa}^{-1}$. The material model is of Saint-Venant-Kirchhoff type with Poisson's ratio $\nu = 0.3$ and Young's modulus $E = 210 \text{GPa}$. For this simulation, 3000 cycles are calculated, where each cycle is divided into 80 pseudo-time increments and the problem is discretized by 12×30 first-order quadrilateral Lagrangian elements. Fig. 5.5 shows the results compared to the reference solution from the original publication Strömberg [260]. Due to the horizontal load, a back and forth sliding motion of the beam is initiated, which results in a stick-slip transition at the right side of the contact interface. The potential slip region is the zone from the transition point at 0.03m until the end of the beam. The left side remains in stick state for the entire

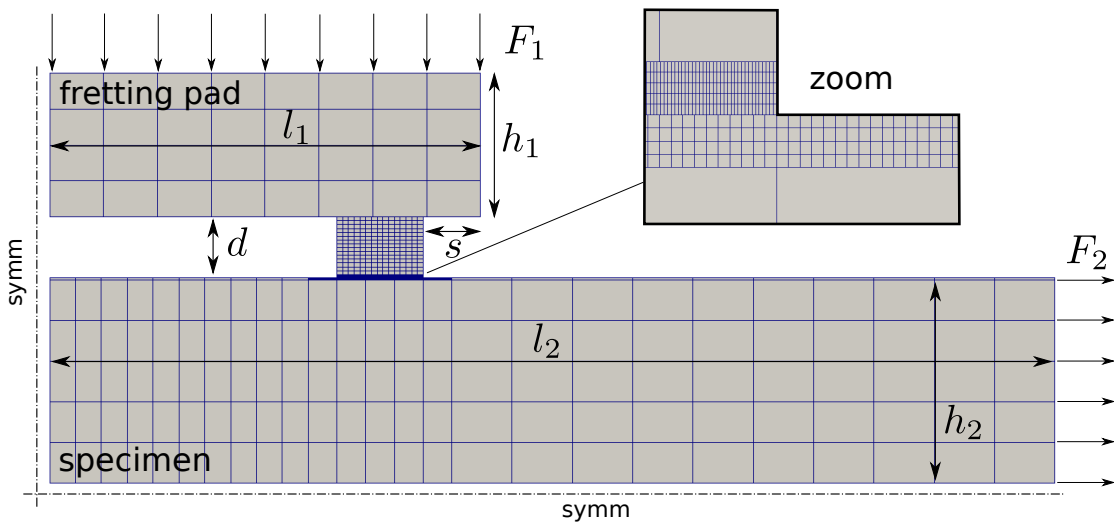


Figure 5.6: Problem setting for the bridge type fretting test with finite element mesh and zoom for the contact interface discretization, taken from Farah et al. [69].

simulation time. This leads to a wear distribution that increases from the transition point to the end of the beam. The calculated wear depth shows an excellent agreement with the reference solution. In addition, also the stress distributions match well and slight differences occur due to the fundamentally different contact formulations.

5.4.3.2. Application – bridge type flat contact

The next example is a bridge type flat contact test where typically two bridge-shaped fretting pads are pushed against a specimen. It is strongly inspired by Hojjati Talemi [111]. The finite element setting with the employed symmetry conditions is shown in Fig. 5.6. The fretting pad is loaded with a constant traction $F_1 = 150 \frac{\text{N}}{\text{mm}}$ and the specimen is loaded with a sinusoidal traction with a magnitude of $F_2 = 150 \frac{\text{N}}{\text{mm}}$. The dimensions of the fretting pad are given as $l_1 = 15\text{mm}$, $h_1 = 5\text{mm}$, $s = 2\text{mm}$, $d = 2.1\text{mm}$ and the contact zone is 3mm wide. The specimen is defined by $l_2 = 35\text{mm}$ and $h_2 = 7.15\text{mm}$. The fretting pad as well as the specimen are spatially discretized by finite elements based on second-order Lagrangian polynomials (quad9). The structured meshes with refinement at the contact zone are created via several non-conforming patches, which are coupled via the mortar mesh tying method. Further details on domain decomposition procedures with mortar methods can be found in Hesch and Betsch [103], Puso [216], Puso and Laursen [217] and Wohlmuth [288]. The material model for both bodies is of Saint-Venant-Kirchhoff type with Poisson's ratio $\nu = 0.33$. The Young's modulus for the pad is $E = 210\text{GPa}$ and the specimen stiffness is defined by $E = 72.1\text{GPa}$. Frictional contact is prescribed by a friction coefficient of $\mathfrak{f} = 0.5$ and fretting wear effects are modeled with a wear coefficient of $k_w = 1.0 \cdot 10^{-6} \frac{1}{\text{GPa}}$. The whole model is restricted to a plane strain setting. Overall, 10.000 load cycles are simulated with 10 pseudo time steps per cycle. This setting generates a partial sliding scenario, where the left part of the contact zone remains in stick

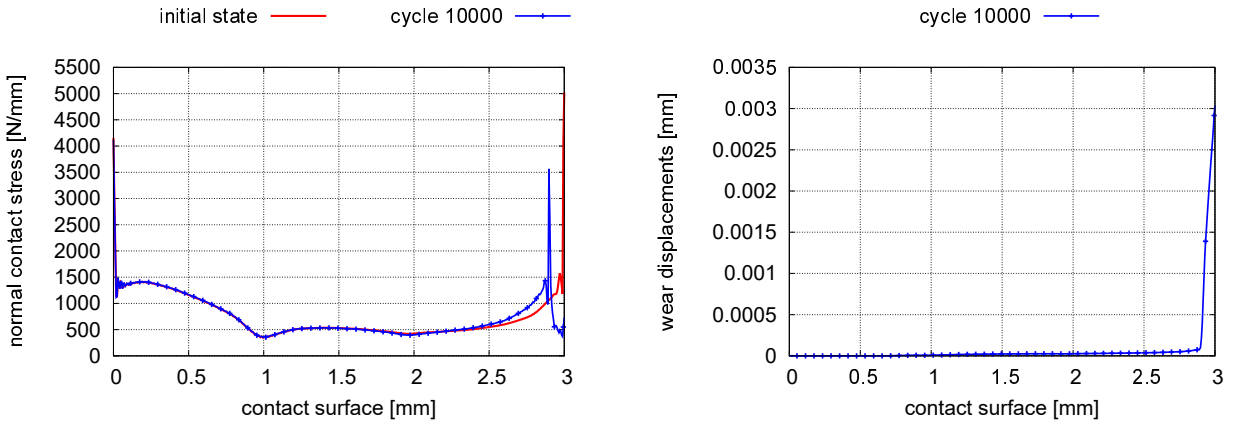


Figure 5.7: Results for the bridge type fretting test: normal contact stress (left) and wear displacements (right), taken from Farah et al. [69].

state and the right part reaches the Coulomb limit and slips. Therefore, wear effects occur predominantly within the right part of the contact zone as shown in Fig. 5.7. In the left subfigure, the normal contact stress is plotted over the contact interface. The stress peak at the outer right side decreases and moves into the contact zone due to fretting wear effects. The corresponding wear depth in inward normal direction is plotted in the right subfigure. There, the highest value occurs at the outer right contact singularity, which corresponds with the stress visualization in the left part of the figure.

5.4.3.3. 3D NURBS – Hertzian contact with wear

This last example represents a 3D Hertzian contact setting, which is discretized with non-uniform-rational-B-splines (NURBS) functions. It is employed to demonstrate the applicability of the proposed fretting wear algorithm towards 3D problem settings and its flexibility with respect to the spatial discretization. Therefore, a very brief introduction to some basics of isogeometric analysis is given in the following. For a comprehensive overview, the interested reader is referred to Piegl and Tiller [206] and Rogers [236] for NURBS functions. NURBS have been the industrial standard for computer aided design (CAD) systems and became a major topic of recent research due to the work of Hughes et al. [122], who used them as shape functions in the finite element framework. In the context of computational contact mechanics, NURBS shape functions or isogeometric analysis in general became famous due to their smooth geometrical representation which results from higher-inter element continuity. In detail, Lagrangian polynomials are limited to C^0 inter-element continuity, while NURBS-based finite elements of polynomial order p lead to C^{p-1} inter-element continuity. For this example, second-order NURBS functions are employed for spatial discretization in 3D. Consequently, 2D surfaces are considered as contact interfaces. Starting point is a tensor product B-spline function space with an open non-uniform knot vector

$$\Xi_j = \{\bar{\xi}_1^j, \dots, \bar{\xi}_{n_j+p_j+1}^j\} \quad (5.45)$$

of knot values $\bar{\xi}_i \in \mathbb{R}$ with $\bar{\xi}_i \leq \bar{\xi}_{i+1}$ associated with the j -th parametric dimension of the considered patch. To guarantee an open knot vector, the first and last entries in the knot vector are repeated $p_j + 1$ times, where p_j is the polynomial order of the B-spline basis function in the j -th direction. A general 3D volume \mathbf{V} is then defined by NURBS basis functions N and control point coordinates \mathbf{X} , via

$$\mathbf{V}(\xi, \eta, \zeta) = \sum_{i=1}^n \sum_{j=1}^m \sum_{k=1}^l N_{i,j,k}(\xi, \eta, \zeta) \mathbf{X}_{i,j,k}. \quad (5.46)$$

As the derivation is restricted to open knot vectors in each parametric direction, the surface representation is defined by the control points and knot vectors on the considered surface of the parametric domain. Consequently, a 2D manifold \mathbf{S} reads

$$\mathbf{S}(\xi, \eta) = \sum_{i=1}^n \sum_{j=1}^m N_{i,j}(\xi, \eta) \mathbf{X}_{i,j}. \quad (5.47)$$

The employed NURBS basis functions of each control point are constructed from B-splines by introducing a weighting function, i.e.

$$N_{i,j,k}(\xi, \eta, \zeta) = \frac{h_{i,j,k} B_i(\xi) B_j(\eta) B_k(\zeta)}{\sum_{i=1}^n \sum_{j=1}^m \sum_{k=1}^l h_{i,j,k} B_i(\xi) B_j(\eta) B_k(\zeta)}, \quad (5.48)$$

where B_l are the B-spline basis functions in each parametric direction and $h_{i,j,k}$ is the weight associated with the control point (i, j, k) . By defining all weights of a patch equally, the NURBS functions reduce to standard B-splines. Thus, they share some fundamental properties with B-splines, i.e. inner-element connectivity, non-negativity and partition of unity. In addition, they have the additional capability to exactly represent many conic geometries such as circles. Applying the introduced concept of isogeometric analysis for isoparametric finite element methods, also the interpolation of discrete displacements is realized with NURBS basis functions

$$\mathbf{u}_h^e(\xi, t) = \sum_{k=1}^{n_{cp}} N_k(\xi) \mathbf{d}_k(t), \quad (5.49)$$

where $n_{cp} = n \cdot m \cdot l$ is the number of control points.

Remark 5.2. *NURBS functions are in general rational function and thus exact integral evaluation is not achievable with standard Gauss quadrature rules. However, it was shown in Hughes et al. [123] that they still lead to accurate results and therefore standard Gauss rules are employed within this work.*

The considered example consists of a half sphere with radius $r = 1.0$ and a rigid foundation, which is modeled with one NURBS-based element of order $p = 2$. The half sphere itself is also meshed with second-order NURBS-based elements and consists of approximately 73.500 control points as visualized in Fig. 5.8. The half sphere material model is chosen to be of Saint-Venant-Kirchhoff type with the Young's modulus $E = 200.000$ and the Poisson's ratio $\nu = 0.3$. The sphere is defined to be the slave body and the rigid foundation represents the master body. The wear coefficient is $k_w = 1.0 \cdot 10^{-8}$ and the friction coefficient is $\mathfrak{F} = 0.2$. Within the

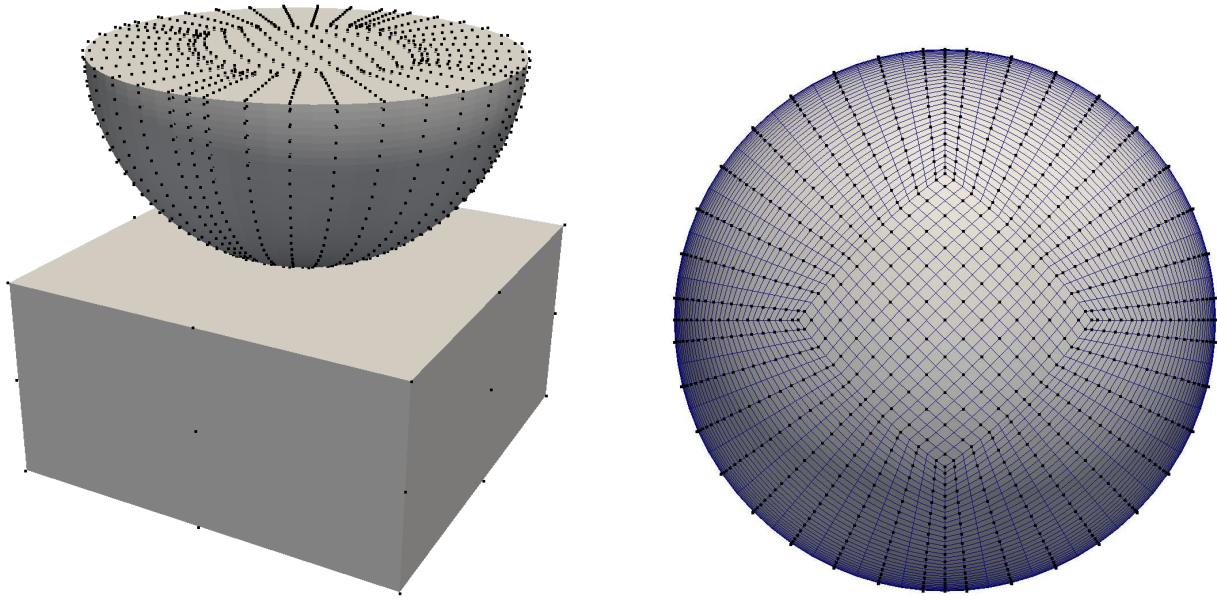


Figure 5.8: Geometry and mesh for the 3D Hertzian contact with wear with visualized control points, taken from Farah et al. [69].

time interval $0 < t < 1$, the half sphere is pressed into the block up to a displacement magnitude of $u_v = 0.06$. After that, u_v remains fixed and the horizontal movement $u_h = 0.02 \cdot \sin(2\pi(t-1))$ is enforced within the time interval $1 \leq t < 1401$, which leads to 1400 cycles. This setup initially generates a partial sliding contact state, which means that the prescribed horizontal movement is not large enough to trigger gross sliding. Thus, the center of the contact zone remains in the stick state, whereas the outer parts of the contact zone reach the Coulomb limit and come into sliding. The resulting normal contact stress distribution is visualized in Fig. 5.9. Here, the circular stress field becomes oval due to the unidirectional sliding and the contact area decreases due to the loss of material. The corresponding wear profile is shown in Fig. 5.10. The sticking center of the contact zone preserves an unworn area that is surrounded by worn material. Summing up, this example demonstrates that the developed fretting wear algorithm with an internal state variable approach is applicable to 3D examples and to isogeometric spatial discretizations, i.e. NURBS. Additionally, even the rather simple problem setting similar to a Hertzian contact leads to complex wear and stress distributions, which can be sufficiently resolved with the introduced algorithm.

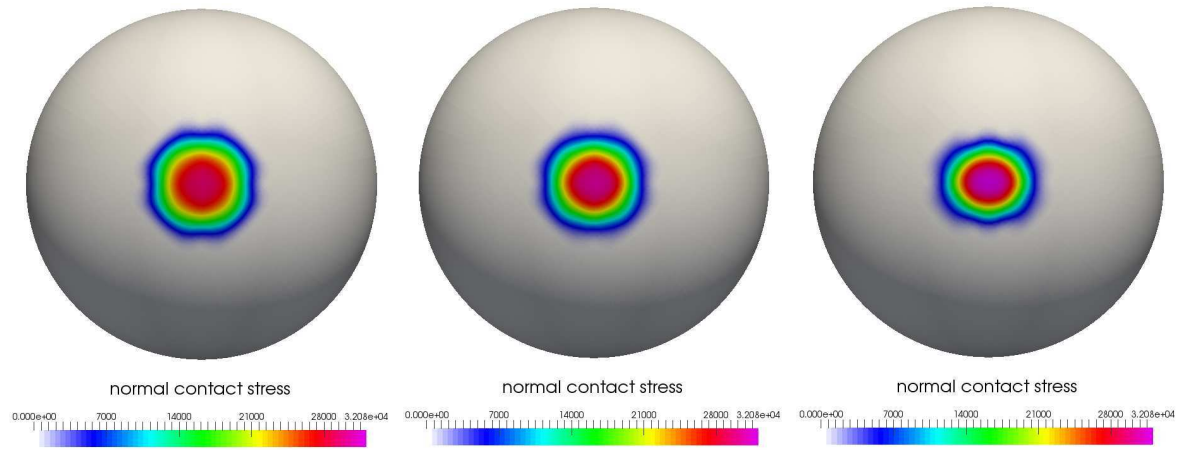


Figure 5.9: Normal contact stress for the 3D Hertzian contact with wear. Results after 500, 1000 and 1400 oscillations from left to right, taken from Farah et al. [69].

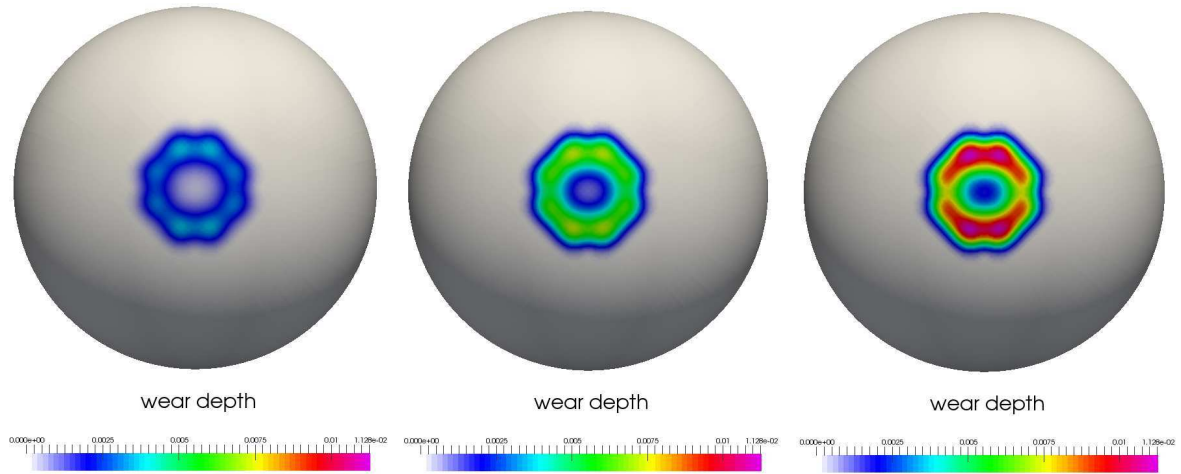


Figure 5.10: Wear depth for the 3D Hertzian contact with wear. Results after 500, 1000 and 1400 oscillations from left to right, taken from Farah et al. [69].

5.5. Formulation for finite wear – ALE formulation

In this section, wear effects that result into finite shape changes are considered. The following derivations and investigations are based on the author's publication Farah et al. [74]. Modeling of finite wear phenomena is realized by an Arbitrary-Lagrangian-Eulerian approach, which allows for considering a changing material configuration being subjected to material loss. The derived numerical approach is based on a partitioned algorithm and consists of a Lagrangian step and a shape evolution step.

Similar to the numeric modeling of fretting wear effects, the introduced internal state variable approach and the primary variable approach are applicable in order to simulate finite wear phenomena. In contrast to fretting wear modeling, the primary variable approach is the preferred discretization type because it strongly simplifies the overall partitioned algorithm. However, the application of the internal state variable approach is also briefly outlined.

5.5.1. Problem setting for finite wear modeling

Considering wear phenomena, which result into finite shape changes requires a fundamentally different problem description. In detail, the pure Lagrangian formulation which was employed for defining elastodynamics including contact mechanics in Chapters 2, 3 and 4 is changed into an Arbitrary-Lagrangian-Eulerian problem formulation. Thus, it allows for a convenient description of a time dependent spatial and material configuration.

By introducing an Arbitrary-Lagrangian-Eulerian approach, the problem formulation of finite deformation elastostatics in equations (2.40)-(2.42) is now referred to the material configuration $\Omega_m^{(i)}$. Consequently, the physical deformation gradient

$$\mathbf{F}_\varphi^{(i)} = \frac{\partial \mathbf{x}^{(i)}}{\partial \tilde{\mathbf{X}}^{(i)}} \quad (5.50)$$

is now employed as fundamental nonlinear deformation measure for physical motion. The first and second Piola-Kirchhoff stress tensors \mathbf{S} and \mathbf{P} are now referred to the material configuration, and thus should be denoted as \mathbf{S}_φ and \mathbf{P}_φ . The physical displacement vector, which defines the motion due to elastic deformation with respect to the material configuration reads

$$\mathbf{u}_\varphi^{(i)} = \mathbf{x}^{(i)} - \tilde{\mathbf{X}}^{(i)}. \quad (5.51)$$

Finally, the problem formulation of finite deformation elastostatics based on the physical displacement vector referred to the material configuration yields

$$\text{Div} \mathbf{P}_\varphi^{(i)} + \hat{\mathbf{b}}_\varphi^{(i)} = 0 \quad \text{in } \Omega_m^{(i)} \times [0, T], \quad (5.52)$$

$$\mathbf{u}_\varphi^{(i)} = \hat{\mathbf{u}}_\varphi^{(i)} \quad \text{on } \Gamma_{m,u}^{(i)} \times [0, T], \quad (5.53)$$

$$\mathbf{P}_\varphi^{(i)} \mathbf{N}_\varphi^{(i)} = \hat{\mathbf{t}}_\varphi^{(i)} \quad \text{on } \Gamma_{m,\sigma}^{(i)} \times [0, T]. \quad (5.54)$$

Here, $\mathbf{N}_\varphi^{(i)}$ denotes the outward unit normal vector in the material configuration.

In addition, the problem formulation describing the material mapping ϕ is based on the material displacement vector

$$\mathbf{u}_\phi^{(i)} = \tilde{\mathbf{X}}^{(i)} - \mathbf{X}^{(i)}, \quad (5.55)$$

which describes the change of the material configuration due to material loss associated with wear. As the material mapping only represents a motion with physical interpretation at the boundary of the material configuration, the bulk problem equation for the material mapping can be chosen arbitrarily. In order to obtain the highest possible solution quality and to guarantee a bijective mapping, the bulk problem is considered as pseudo-elasticity problem in the finite deformation regime. Thus, the artificial deformation gradient for the material mapping ϕ is introduced as

$$\mathbf{F}_\phi^{(i)} = \frac{\partial \tilde{\mathbf{X}}^{(i)}}{\partial \mathbf{X}^{(i)}}. \quad (5.56)$$

This leads to the pseudo-stress tensors \mathbf{S}_ϕ and \mathbf{P}_ϕ . The resulting problem formulation for the material motion reads

$$\text{Div} \mathbf{P}_\phi^{(i)} = \mathbf{0} \quad \text{in } \Omega_0^{(i)} \times [0, T], \quad (5.57)$$

$$\dot{\mathbf{u}}_\phi^{(i)} = -\mathbf{N}_\phi^{(i)} \dot{W}^{(i)} \quad \text{on } \Gamma_{m,c}^{(i)} \times [0, T], \quad (5.58)$$

$$\mathbf{u}_\phi^{(i)} = \mathbf{0} \quad \text{on } \Gamma^{(i)} \setminus \Gamma_c^{(i)} \times [0, T]. \quad (5.59)$$

Here, $\dot{W}^{(i)}$ describes the wear rate in the material configuration, which is applied in the current negative unit normal direction $\mathbf{N}_\phi^{(i)}$ of the material configuration. This rate problem is later on solved within an incremental step strategy, i.e. within the shape evolution step of the partitioned algorithm introduced in Section 5.5.4. Wear acts on the boundary $\Gamma_{m,c}^{(i)}$, which is the counterpart in material configuration to the contact boundary $\gamma_c^{(i)}$ at the current time. The definition of the wear rate was already introduced in Section 5.2.2. The problem description in (5.57), (5.58) and (5.59) represents a purely Dirichlet constrained system. The constraint in (5.59) enforces the equality of the non-worn boundary in reference and spatial configuration.

5.5.2. Implicit partitioned algorithm for finite wear

The algorithm employed in this thesis is based on the partitioning between a so-called *Lagrangian* step and a *shape evolution* step, see Figure 5.11. Here, the discrete displacements and material displacements of the problem are denoted with $\mathbf{d}^{(i)}$ and $\mathbf{d}^{m,(i)}$, with equal interpolation functions from the finite dimensional subspaces $\mathcal{U}_h^{(i)}$ being used for both fields. Within the Lagrangian step, the nonlinear frictional mortar contact problem is solved with respect to a fixed material configuration (fixed $\mathbf{d}^{m,(i)}$). Wear is only considered as an additional contribution to the gap function in this step, which will be explained in detail in Section 5.5.3. After convergence of the Lagrangian step is obtained, the calculated wear results (i.e. wear depth $\mathbf{w}^{(i)}$) are imposed as Dirichlet boundary conditions for the shape evolution step, where now the real geometrical change of the contact surface is considered, see Section 5.5.4. Considering wear as additional displacements of the mesh (and not the material) to the usual elastic displacements and additionally considering the fact that the wear displacements are only enforced at nodes associated with the contact boundary leads to a degeneration of the associated surface-near elements after a certain amount of wear. To prevent this, also the bulk mesh must be properly adapted. Therefore, the shape evolution step is chosen to be treated as ALE problem, see Section 5.5.1. Similarly to the evaluation of the contact terms, wear is calculated on the spatial contact boundary. However,

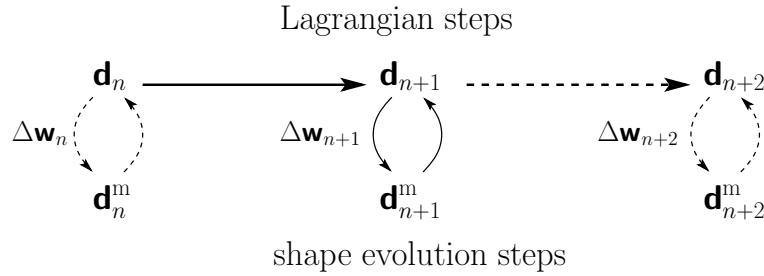


Figure 5.11: Implicit coupling algorithm based on iterations between Lagrangian and shape evolution steps. Transfer variables are the increment of the discrete wear depth $\Delta\mathbf{w}$ and the material displacements \mathbf{d}^m . The figure is taken from Farah et al. [74].

the shape evolution step can then be performed either in the spatial configuration or in the material configuration and the corresponding configuration is updated with help of the advection map, which will be introduced in Section 5.5.4.

After having completed the shape evolution step, both spatial as well as material configuration have been changed by wear. To guarantee convergence of the coupled problem within the considered time step, iterating between Lagrangian and shape evolution step is possible. However, from all numerical experience gathered so far this only becomes necessary for extremely large amounts of wear within one time step.

The general algorithm is summarized in the following:

Algorithm 5.2. Implicit partitioned scheme

1. Solve the nonlinear frictional contact problem for fixed material displacements. Wear effects within the Lagrangian step are considered as additional contribution to the spatial gap function, which leads to slightly overlapping bodies, see Section 5.5.3.
2. Solve the nonlinear shape evolution step as a pseudo-elasticity problem (ALE problem) for a fixed amount of wear, see Section 5.5.4. Then update the material and spatial configurations according to the calculated wear by employing the advection map procedure.
3. Repeat the two steps of the partitioned algorithm until convergence of the structural residual and the residual of the pseudo-elasticity problem is observed.

The details of this implicit algorithm are given in the following sections.

Remark 5.3. A partitioned coupling scheme is preferred over a monolithic coupling scheme here because the wear process itself is in general very slow compared to the fully resolved contact scenario. Therefore, the coupling between the Lagrangian and the shape evolution step is not too strong and convergence of the partitioned algorithm can easily be achieved even without any convergence accelerator, such as the well-known Aitken accelerator in Irons and Tuck [127]. However, for strongly coupled problems such as steady-state wear processes with extremely large time steps, monolithic solution schemes are arguably of superior robustness compared to the

partitioned ones. Yet, it seems that by considering the worn material as an additional gap within the Lagrangian step, the Lagrangian step itself already includes certain information about the wear effects implicitly. Therefore, even for steady-state wear processes with large time steps, the presented partitioned wear algorithm converges for all scenarios tested so far, and monolithic schemes with their increased algorithmic complexity do not seem to be necessary.

5.5.3. Lagrangian step

In this section, the treatment of wear phenomena within the Lagrangian step is explained. Basically, the implicit partitioned algorithm described in the previous section also works when wear phenomena are not considered within the Lagrangian step. Then, a standard contact problem as described in Chapter 3 is solved without any modification. However, the wear depth occurring during one load step is taken into account in order to accelerate the partitioned algorithm. Thus, in complete analogy to fretting wear modeling in Section 5.4.1, wear effects are considered as additional contribution to the gap function, which leads to a modification of the Hertz-Signorini-Moreau conditions:

$$g_n^w \geq 0, \quad p_n \leq 0, \quad p_n g_n^w = 0. \quad (5.60)$$

Again, g_n^w represents the modified gap function. The modified constraints in (5.60) together with the boundary value problem (5.52), (5.53) and (5.54) state the problem formulation for the Lagrangian step.

Remark 5.4. Note that the wear depth $w^{(i)}$, which is utilized to modify the gap function according to (5.34) or (5.43), is generally not the absolute wear depth per time increment, but the increment of the solution procedure with respect to the last Lagrangian step of the partitioned algorithm. By introducing the notation $(\cdot)^p$ for the current iteration step of the partitioned algorithm, the wear depth reads

$$w^{(i)} = w^{(i),p} - w^{(i),p-1}. \quad (5.61)$$

For the first iteration $p = 1$, the initial wear guess is set to zero, i.e. $w^{(i),0} = 0$. However, for the sake of brevity, the iteration counter is skipped for the partitioned algorithm in the following and relation (5.61) is implicitly used.

In the following, the implicit treatment of the gap modification for the Lagrangian step is explained in detail for the primary variable approach and briefly introduced for the internal state variable approach. However, the primary variable approach is the preferred spatial discretization approach because the wear depth, which is a transfer variable in the implicit partitioned algorithm, is directly represented by an additional variable. This is very beneficial in order to iterate between the Lagrangian step and the shape evolution step. The internal state variable approach is only applicable for an explicit partitioned algorithm without iterating between the steps.

5.5.3.1. Primary variable approach

Starting point for the primary variable approach is the discrete residual for the slave and master side wear:

$$\mathbf{r}_w^{(i)} = \mathbf{E}^{(i)} \mathbf{w}^{(i)} - \mathbf{T}^{(i)} \boldsymbol{\lambda} = \mathbf{0}. \quad (5.62)$$

5. Mortar Methods for Wear Modeling

For the application of iterative nonlinear solvers based on a Newton-Raphson scheme, the wear residual (5.21) has to be linearized. Thus, in complete analogy to the explanation for standard structural problems in Section 2.2.4, a truncated Taylor series expansion is carried out

$$\text{Lin } \mathbf{r}_w(\mathbf{d}^i, \boldsymbol{\lambda}^i, \mathbf{w}^i) = \mathbf{r}_w(\mathbf{d}^i, \boldsymbol{\lambda}^i, \mathbf{w}^i) + \frac{\partial \mathbf{r}_w}{\partial \mathbf{d}} \Big| \Delta \mathbf{d}^{i+1} + \frac{\partial \mathbf{r}_w}{\partial \boldsymbol{\lambda}} \Big| \Delta \boldsymbol{\lambda}^{i+1} + \frac{\partial \mathbf{r}_w}{\partial \mathbf{w}} \Big| \Delta \mathbf{w}^{i+1} = \mathbf{0}. \quad (5.63)$$

Here, the index i denotes the previously calculated Newton step. This results in the linearized wear residual

$$-\mathbf{r}_w(\mathbf{d}^i, \boldsymbol{\lambda}^i, \mathbf{w}^i) = \mathbf{S}^i \Delta \mathbf{d}^{i+1} + \mathbf{F}^i \Delta \boldsymbol{\lambda}^{i+1} + \mathbf{E}^i \Delta \mathbf{w}^{i+1}. \quad (5.64)$$

Details on the directional derivatives for the linearized wear residual are omitted here, since they are strongly related to the linearizations well-known for surface mortar contact, see Popp [210] and Popp et al. [212]. The semi-discrete problem formulation in (3.39) remains unchanged, despite the occurring wear phenomena, but the complementarity functions in (3.58) and (3.60) change due to the modified gap. Thus, the linearized system of equations to be solved within each Newton-Raphson step, which is explained in Section 3.5.3, must be extended due to wear considerations. Concretely, linearizations of the complementarity functions with respect to wear and the linearized wear equation itself are introduced. In the following, for the sake of brevity, the algebraic representation of the finite wear problem formulation is given for slave-sided wear. However, an extension towards both-sided wear is straightforward and the described solution procedures are also applicable to both-sided wear. Thus, an exemplary matrix representation of the system of equations, when only slave-sided wear phenomena are considered, looks as follows:

$$\begin{bmatrix} \mathbf{K}_{NN} & \mathbf{K}_{NM} & \mathbf{K}_{NS} & \mathbf{0} & \mathbf{0} \\ \tilde{\mathbf{K}}_{MN} & \tilde{\mathbf{K}}_{MM} & \tilde{\mathbf{K}}_{MS} & -\mathbf{M}^T & \mathbf{0} \\ \mathbf{K}_{SN} & \tilde{\mathbf{K}}_{SM} & \tilde{\mathbf{K}}_{SS} & \mathbf{D}^T & \mathbf{0} \\ \mathbf{0} & \mathbf{C}_M & \mathbf{C}_S & \mathbf{C}_\lambda & \mathbf{C}_w \\ \mathbf{0} & \mathbf{S}_M & \mathbf{S}_S & \mathbf{F} & \mathbf{E} \end{bmatrix}^i \begin{bmatrix} \Delta \mathbf{d}_N \\ \Delta \mathbf{d}_M \\ \Delta \mathbf{d}_S \\ \Delta \boldsymbol{\lambda} \\ \Delta \mathbf{w} \end{bmatrix}^{i+1} = - \begin{bmatrix} \mathbf{r}_N \\ \mathbf{r}_M \\ \mathbf{r}_S \\ \mathbf{r}_c \\ \mathbf{r}_w \end{bmatrix}^i. \quad (5.65)$$

Here, the solution vector contains increments of discrete displacements $\Delta \mathbf{d}$, Lagrange multipliers $\Delta \boldsymbol{\lambda}$ and wear quantities $\Delta \mathbf{w}$. The displacements are split into inner nodes $(\cdot)_N$, master nodes $(\cdot)_M$ and slave nodes $(\cdot)_S$, whereas the Lagrange multipliers and wear quantities are only defined on the slave side anyway. The stiffness blocks \mathbf{K} arise from linearization of the internal force vector, and the tilde symbols indicate additional linearizations due to the contact force vector. The first three rows of the system can be identified as linearized algebraic form of the force equilibrium and row four represents the linearized contact constraints. In addition to the standard frictional contact problem, the last row arises due to the additional wear consideration. As wear is taken into account as an additional gap within the Hertz-Signorini-Moreau conditions, coupling terms only arise in the row associated with the contact constraints and a direct coupling into the force equilibrium is not to be expected.

While this system of equations could be solved directly, this does not seem advisable, since it not only contains displacement degrees of freedom, but also Lagrange multipliers as well as unknowns due to wear. Therefore, it is of increased and even of varying size. Moreover, the introduced Lagrange multipliers cause a saddle point structure of the linearized system of

equations, which may cause difficulties for the performance of common iterative solvers and preconditioners. To get rid of these problems, the condensation procedure explained in Gitterle et al. [88], Popp et al. [211] and Popp et al. [212] and already employed in a similar form in Chapters 3 and 4 is used. Here, dual shape functions for the Lagrange multiplier interpolation are employed to generate a diagonal structure of the mortar matrix \mathbf{D} , which then allows for a computationally cheap condensation of the Lagrange multipliers via

$$\Delta\lambda^{i+1} = \mathbf{D}^{i,-T}(-\mathbf{r}_S^i - \mathbf{K}_{SN}^i \Delta\mathbf{d}_N^{i+1} - \tilde{\mathbf{K}}_{SM}^i \Delta\mathbf{d}_M^{i+1} - \tilde{\mathbf{K}}_{SS}^i \Delta\mathbf{d}_S^{i+1}). \quad (5.66)$$

This results in the system

$$\begin{bmatrix} \mathbf{K}_{NN} & \mathbf{K}_{NM} & \mathbf{K}_{NS} & \mathbf{0} \\ \mathbf{K}_{MN} - \mathbf{P}_d \mathbf{K}_{SN} & \tilde{\mathbf{K}}_{MM} - \mathbf{P}_d \tilde{\mathbf{K}}_{SM} & \tilde{\mathbf{K}}_{MS} - \mathbf{P}_d \tilde{\mathbf{K}}_{SS} & \mathbf{0} \\ -\mathbf{P}_\lambda \mathbf{K}_{SN} & \mathbf{C}_M - \mathbf{P}_\lambda \tilde{\mathbf{K}}_{SM} & \mathbf{C}_S - \mathbf{P}_\lambda \tilde{\mathbf{K}}_{SS} & \mathbf{C}_w \\ -\mathbf{P}_w \mathbf{K}_{SN} & \mathbf{S}_M - \mathbf{P}_w \tilde{\mathbf{K}}_{SM} & \mathbf{S}_S - \mathbf{P}_w \tilde{\mathbf{K}}_{SS} & \mathbf{E} \end{bmatrix}^i \begin{bmatrix} \Delta\mathbf{d}_N \\ \Delta\mathbf{d}_M \\ \Delta\mathbf{d}_S \\ \Delta\mathbf{w} \end{bmatrix}^{i+1} = -[\mathbf{r}_N \mid \mathbf{r}_M - \mathbf{P}_d \mathbf{r}_S \mid \mathbf{r}_S - \mathbf{P}_\lambda \mathbf{r}_S \mid \mathbf{r}_w - \mathbf{P}_w \mathbf{r}_S]^{i,T}. \quad (5.67)$$

Here, the projection operators \mathbf{P} are defined as

$$\mathbf{P}_d^i = \mathbf{M}^{i,T} \mathbf{D}^{i,-T}, \quad \mathbf{P}_\lambda^i = \mathbf{C}_\lambda^i \mathbf{D}^{i,-T}, \quad \mathbf{P}_w^i = \mathbf{F}^i \mathbf{D}^{i,-T}. \quad (5.68)$$

This condensation concept can now be extended to the wear unknowns by using dual shape functions also for the discrete weighting of the wear residual, which then yields a diagonal \mathbf{E} matrix. Consequently, an additional condensation step can be performed, which expresses the wear unknowns in terms of discrete displacements:

$$\begin{aligned} \Delta\mathbf{w}^{i+1} = \mathbf{E}^{i,-1} & (-\tilde{\mathbf{r}}_w^i + \mathbf{P}_w^i \mathbf{r}_S^i + \mathbf{P}_w^i \mathbf{K}_{SN}^i \Delta\mathbf{d}_N^{i+1} - (\mathbf{S}_M^i - \mathbf{P}_w^i \tilde{\mathbf{K}}_{SM}^i) \Delta\mathbf{d}_M^{i+1} \\ & - (\mathbf{S}_S^i - \mathbf{P}_w^i \tilde{\mathbf{K}}_{SS}^i) \Delta\mathbf{d}_S^{i+1}). \end{aligned} \quad (5.69)$$

The resulting condensed system of equations is not explicitly given here for the sake of brevity. However, as the main result, it is only solved for displacement degrees of freedom and all contact and wear information is included in the modified system matrix. This matrix is of constant size and no saddle point structure occurs anymore. Discrete Lagrange multiplier and wear variables can be obtained by simple post-processing steps based on (5.66) and (5.69).

5.5.3.2. Internal state variable approach

The introduced internal state variable approach is also applicable to finite wear problems. This has already been demonstrated for 2D problem settings in Gitterle [87]. However, the primary variable approach is the preferred wear discretization scheme since the internal state variable is not directly controllable in the partitioned algorithm 5.2. This is due to the inherent feature of the internal state variable approach of no additional unknowns entering the system of equations for the Lagrangian step. Thus, the methodology for the internal state variable approach is only briefly outlined. When considering wear as internal state variable in an implicit solution scheme and as additional contribution to the gap function as explained in 5.2, only the linearizations of

the nonlinear complementarity functions are directly affected. The other parts of the system of equations remain unchanged (cf. (3.62)). After the Lagrangian step is completed, wear must be enforced as Dirichlet condition for the shape evolution step. In contrast to the primary variable approach, the internal state wear quantity represents a surface-weighted wear depth, i.e. a worn volume. Consequently, it has to be expressed in distance measure by dividing it by the support area of the attached node. This has already been realized in (5.41). Such a computation is the natural result of a weak enforcement of Dirichlet boundary condition, i.e. wear depth.

The internal state variable approach has been implemented and carefully validated by the author. When no iteration between Lagrangian and shape evolution step is required, no change in solution quality and robustness for both wear discretization schemes are noticeable. However, as already mentioned, the primary variable approach easily allows for a completely implicit partitioned iteration scheme and is thus the preferred discretization technique for finite wear simulations.

5.5.4. Shape evolution step

The shape evolution step is performed to calculate shape changes of the material configuration due to the loss of material at the interface, which is expressed in terms of material displacements. Thus, the connection between observer points \mathbf{X} and material points $\tilde{\mathbf{X}}$ changes. In the semi-discrete setting, this procedure guarantees that bulk elements attached to the contact interface are prevented from degeneration and it also assures a proper mesh quality for all volume elements by distributing the material displacements over the entire domain with an ALE approach. The configuration in which the shape evolution step is performed can be chosen arbitrarily. However, all following explanations are referred to a shape evolution step in the material configuration as explained in Section 5.5.1.

By performing spatial discretization of (5.57)-(5.59) based on the same finite dimensional subspaces \mathcal{U}_h and \mathcal{V}_h as used for the finite deformation frictional contact problem and considering the material motion as nonlinear pseudo-elasticity problem, the linearized system to be solved within each step of a Newton-Raphson scheme reads

$$\tilde{\mathbf{K}} \Delta \mathbf{d}^{m,k+1} = -\mathbf{r}_\phi(\mathbf{d}^{m,k}). \quad (5.70)$$

Here, the linearized pseudo stiffness matrix is denoted with $\tilde{\mathbf{K}}$. After convergence is obtained, the material motion vector \mathbf{d}^m has to be mapped to the spatial configuration to adapt it properly. Based on (5.13), if the material configuration is known and the mapping φ is accordingly defined, the spatial mapping ψ associated with the spatial configuration can be adapted properly. This is possible because the reference configuration Ω_0 , which represents the observer domain, is fixed for the entire simulation. The mapping φ is solved after the converged Lagrangian step, but the material configuration is only updated within the shape evolution step, thus resulting in the additional mesh displacements \mathbf{d}_j^m for the node j . The new material coordinates are then given as

$$\tilde{\mathbf{X}}_j^m = \tilde{\mathbf{X}}_j + \mathbf{d}_j^m. \quad (5.71)$$

In the following, the superscript $(\cdot)^m$ denotes quantities updated due to the shape evolution step. The spatial configuration must be modified to assure that the computed mesh displacements

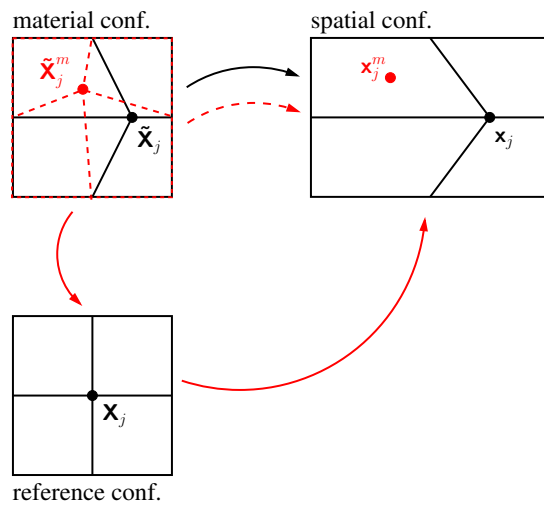


Figure 5.12: Schematically visualized procedure for the advection map between material and spatial configuration: setup after Lagrangean step (black) and after shape evolution step (red), taken from Farah et al. [74].

are stress-free. This is done by the so-called *advection map*, which represents a mapping from material to spatial configuration via the correlation in (5.13). Within a finite element framework, the advection map is realized by exploiting fundamental properties of the isoparametric concept, see Figure 5.12. First, the element into which a considered node is relocated due to the shape evolution step is detected. Then, the parameter space coordinate $\tilde{\xi}_j$ of the updated node within the non-updated element is calculated by solving

$$\mathbf{r}(\tilde{\xi}_j) = \sum_{b=1}^{n_n} N_b(\tilde{\xi}_j) \tilde{\mathbf{x}}_b - \tilde{\mathbf{x}}_j^m = \mathbf{0}. \quad (5.72)$$

Here, $\tilde{\mathbf{x}}_j^m$ is the material coordinate of the considered node j after a displacement update as computed in the shape evolution step (5.71). This nonlinear equation is solved by a local Newton-Raphson scheme for each node. With the parameter space coordinate at hand, the new spatial coordinates can be calculated as

$$\mathbf{x}_j^m = \sum_{b=1}^{n_n} N_b(\tilde{\xi}_j) \mathbf{x}_b. \quad (5.73)$$

Thus, the discrete advection map can simply be interpreted as a proper parameter space mapping.

Remark 5.5. Note that the separation of physical motion and mesh motion naturally leads to convective terms for the total time derivatives. In case of the velocities, they represent the difference between material and mesh velocities. However, it is commonly assumed that inertia effects does not have influence on the solution of typical wear problems. Thus, only quasi-static problems are considered and no total time derivatives are required.

For the considered hyper-elastic material models, the node position mapping described above is sufficient to complete the shape evolution step. However, for more complex material models that require history variables, such as elasto-plastic materials, also the stored history data

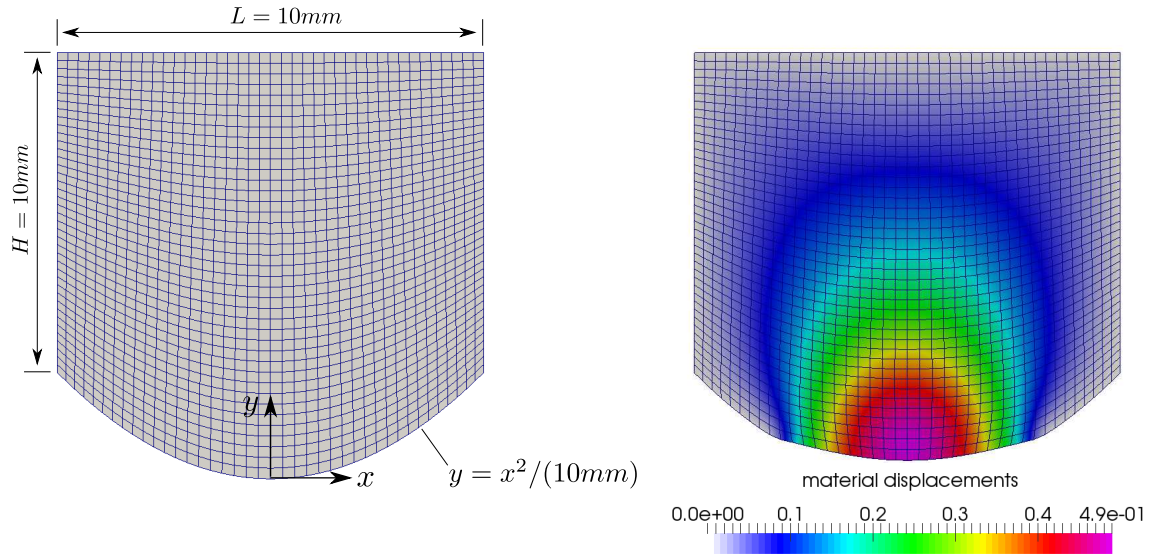


Figure 5.13: 2D pin-on-flat problem: Reference configuration with dimensions (left) and material configuration with material displacements after 5 pseudo time steps (right), taken from Farah et al. [74].

has to be mapped accordingly, see Orlando and Perić [188], Perić et al. [202], Rashid [227] and Rodríguez-Ferran et al. [232].

5.5.5. Numerical examples

In this section, the developed algorithm is validated with four numerical examples. The first example is a 2D pin-on-flat setup, which is analyzed based on a steady-state assumption and the solution is compared to results from literature. The second example is an oscillating beam on a half circle, which is simulated with very high wear coefficients on both sides, therefore resulting in finite shape changes of both bodies. The last numerical study is based on two cylinders where two-sided wear in 3D is investigated.

5.5.5.1. Validation – pin on disc

The first example is adapted from Stupkiewicz [263] to compare the presented implicit wear algorithm with a monolithic steady-state wear algorithm. Steady-state assumptions are valid for periodically repeated contact and frictional sliding problems with many cycles, such as pin-on-disc, reciprocating pin-on-flat, and pin-on-cylinder tribological tests. Usually, these problems are based on splitting the time scale into a fast time of the finite deformation problem and a slow time for the shape evolution due to wear, see Lengiewicz and Stupkiewicz [157, 158] and Stupkiewicz [263]. However, within the developed wear framework, a state-independent fixed slip increment is defined per integration point to simulate a steady-state sliding process. Concretely, the 2D pin-on-flat example consists of a hyper-elastic pin, which is pressed into an infinitely long rigid plane, see Figure 5.13. The pin is moved laterally with a constant velocity of $v = 1000 \frac{\text{mm}}{\text{s}}$. Consequently, the absolute value of the integration point slip increment is given as $\mathbf{u}_{\tau,\text{rel}} = v \Delta t$.

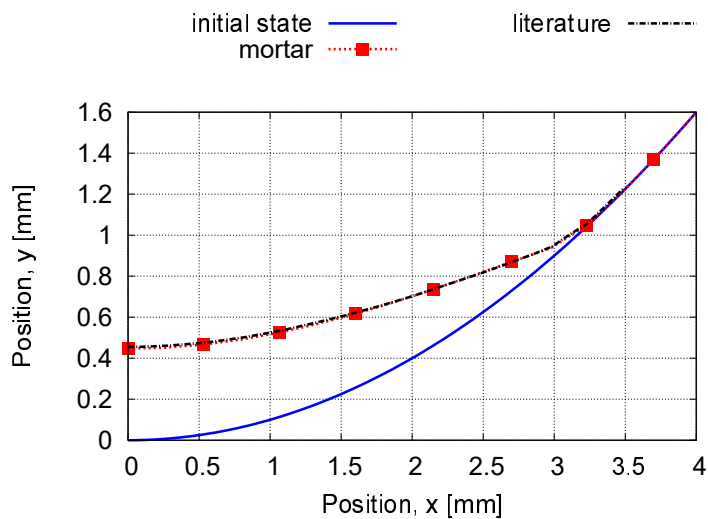


Figure 5.14: Worn shape of the pin after 5 pseudo time steps with $\Delta t = 200\text{s}$ compared to results from Stupkiewicz [263], taken from Farah et al. [74].

The simulation is performed within 5 pseudo-time steps with $\Delta t = 200\text{s}$. Frictionless sliding is assumed, which leads to a formulation of Archard's law in terms of the normal contact pressure, see equation (5.2). The wear coefficient is assumed constant in the material configuration and defined as $k_w = 10^{-7}\text{MPa}^{-1}$. The pin is loaded at its top edge with a normal force $F = 20 \frac{\text{N}}{\text{mm}}$ acting in negative y -direction. The neo-Hookean material model from (2.23) is employed for the pin. Therein, the Young's modulus is chosen as $E = 20\text{MPa}$ and the Poisson's ratio is $\nu = 0.3$. This 2D simulation is based on a plane-strain assumption and volumetric locking effects are avoided by the F-bar formulation for the employed 4-node quadrilateral elements, see de Souza Neto et al. [55]. The resulting material (i.e. worn) configuration is visualized in Figure 5.13. Here, the material displacements, which connect reference and material configuration, are illustrated. It can be clearly seen that not only nodes attached to the contact boundary are relocated but also inner nodes are properly adapted by the developed ALE approach. This guarantees a very good mesh quality in the worn configuration. In addition, the evolution of the contact boundary is shown in Figure 5.14. Here, the results are compared with the simulation from Stupkiewicz [263]. The mortar based method matches the results from literature very well, which demonstrates that the wear algorithm can also be applied for such steady-state wear simulations.

5.5.5.2. Mesh quality – beam on half-sphere

Within the following example, the mesh quality of the material configuration for extremely large material loss is analyzed. The example consists of a 2D oscillating beam and a half circle in a non-steady-state regime. Here, both bodies undergo wear and therefore a shape evolution procedure is required, which results in a change of the material configuration. Both hyper-elastic bodies are modeled based on the classical Neo-Hookean type material model given in (2.22). The chosen material parameters are dimensionless and identical for both bodies, i.e. $E = 100$ and $\nu = 0.3$. The initial setup for the simulation is shown in Figure 5.15. Here, the half circle is fixed at its lower edge and the beam is Dirichlet-controlled at its upper edge. Concretely,

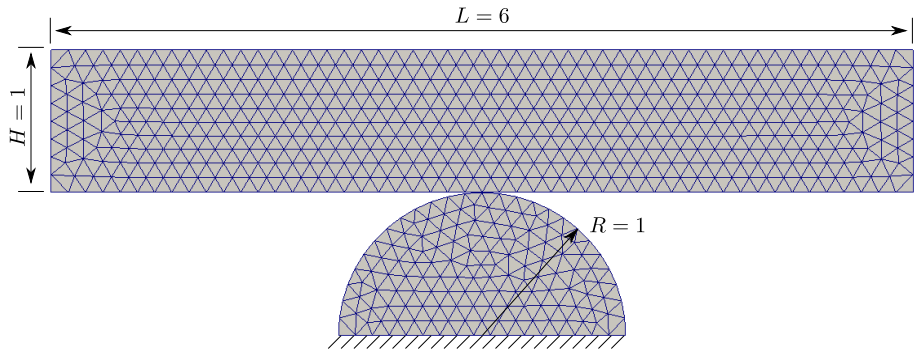


Figure 5.15: Setting for the 2D oscillating beam example with mesh, taken from Farah et al. [74].

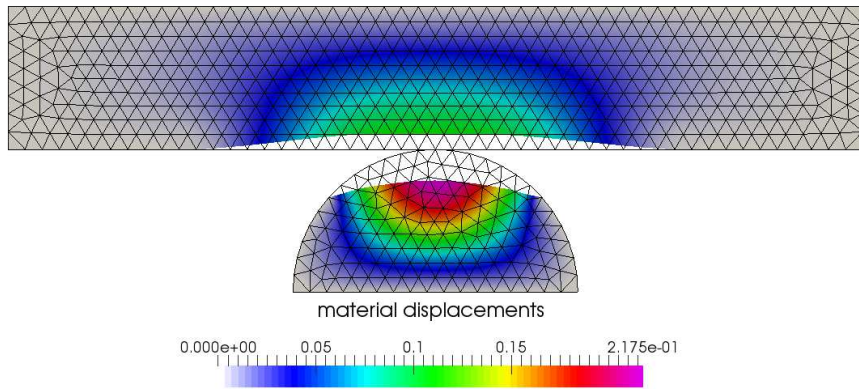


Figure 5.16: Reference configuration (wire frame) and material configuration (colored surface) at the end of the simulation with material displacements, taken from Farah et al. [74].

in the time interval $0 \leq t \leq 1$ the beam is pressed onto the circle vertically with a displacement of $d_v = 0.4$. Then, in the time interval $1 \leq t \leq 51$, the beam is moving horizontally with $d_h = \sin(\frac{2\pi}{10}(t - 1))$. The simulation is performed with a time step size of $\Delta t = 0.1$. For the contact setting, the beam is chosen to be the master surface and the circle represents the slave surface. The wear coefficients for both sides are equal and defined to be $k_w^{(1)} = k_w^{(2)} = 7 \cdot 10^{-4}$ and the friction coefficient is $\mathfrak{f} = 0.1$. Spatial discretization is based on 3-node triangles with first-order Lagrange interpolation (tri3) and the simulation is performed using a plane-strain assumption. The resulting worn bodies as compared to their reference configurations are visualized in Figure 5.16. Here, both bodies significantly changed their material configuration due to material loss within the shape evolution steps. Nevertheless, not only element degeneration is prevented but also good mesh quality is guaranteed owing to the developed ALE-based shape evolution step. This is shown in Figure 5.17. Here, the mesh is plotted in the reference configuration and material configuration. For the analysis of the mesh quality, the aspect Frobenius norm

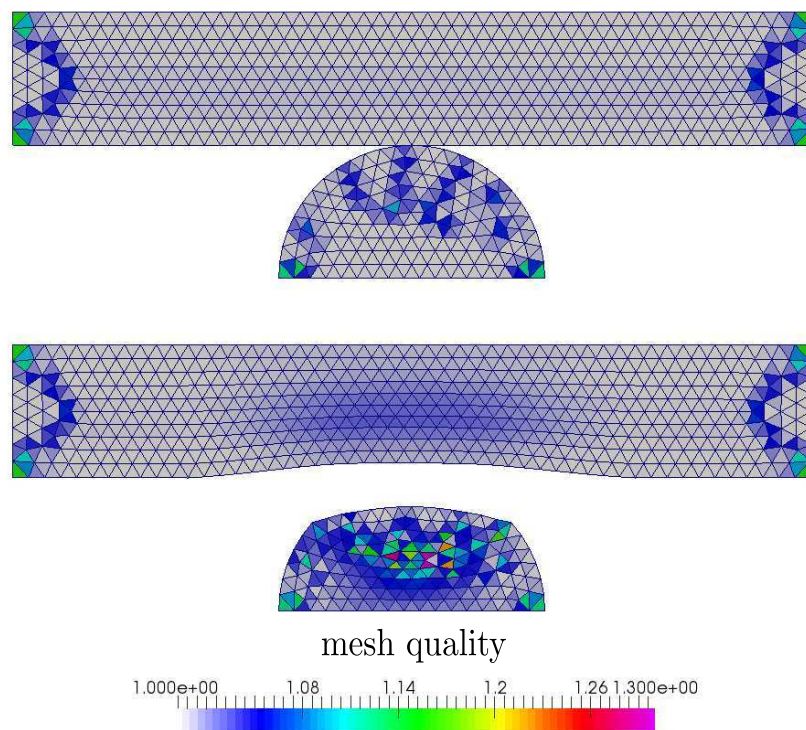


Figure 5.17: Mesh quality given in aspect Frobenius norm in reference configuration (top) and material configuration (bottom) at the end of the simulation, taken from Farah et al. [74].

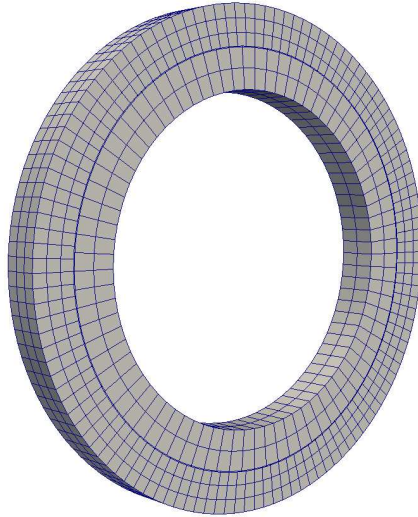


Figure 5.18: Problem setting and mesh for pseudo-3D cylinder press-fit example, taken from Farah et al. [74].

is employed, see Pébay and Baker [201]. This norm is defined as

$$q = \frac{l_0^2 + l_1^2 + l_2^2}{4A\sqrt{3}}, \quad (5.74)$$

where l_i are the edge lengths and A is the area of the triangle. The factor $\frac{1}{4\sqrt{3}}$ normalizes the term such that a unit equilateral triangle has a value of $q = 1$. The acceptable range of this norm is $1.0 \leq q \leq 1.3$. The shape evolution step with proper adaption of the bulk mesh results in a very good mesh quality measured in the aspect Frobenius norm. Even the three most critical elements in the bulk retain a mesh quality of approximately 1.29, which demonstrates the applicability of the shape evolution algorithm.

5.5.5.3. Comparison with fretting wear – 3D cylinder press-fit

The next example is a rotating cylinder press-fit, which only yields little material loss and is therefore ideally suited for comparisons with the internal state variable algorithm within the fretting wear algorithm from Section 5.4.2.1. This example is based on the assumption that no displacements in thickness direction will occur. The problem setting is shown in Figure 5.18. Here, two cylinders with the same thickness of $z = 1$ are given. The inner cylinder acts as slave body and is defined by its inner radius $r_i^1 = 4.022$ and its outer radius $r_o^1 = 5.022$. The outer cylinder acts as master body with radii $r_i^2 = 5.0$ and $r_o^2 = 6.0$. The resulting overlap at $t = 0$ causes an initially active state for the entire contact surface and an initial stress state. The employed material model for both bodies is the classical Neo-Hookean model from the last example with Young's modulus $E = 100.0$ and Poisson's ratio $\nu = 0.0$. The simulation is carried out in the time interval $0 \leq t \leq 5$ with 100 pseudo-time steps of size $\Delta t = 0.05$.

The outer cylinder's outer surface is completely supported during the simulation and the inner cylinder's inner surface is subjected to an angular acceleration of $\alpha = 0.2$ within $0 \leq t \leq 1$. The resulting angular velocity then remains constant for the rest of the simulation. Frictional effects at the contact interface are considered by Coulomb's law with a friction coefficient of $\mathfrak{f} = 0.1$. Spatial finite element discretization is done by 8-node hexahedral elements with an element size ratio of $\frac{2}{3}$ between slave and master body for thickness, radial and circumferential direction.

The results of the presented finite wear algorithm for purely slave-sided wear with a wear coefficient of $k_w^1 = 0.005$ are shown in Figure 5.19. Here, the normal contact tractions are represented by red arrows and mesh displacements are visualized by the solid coloring, each for steps 0, 33, 66 and 99. It can be clearly seen that the normal contact stresses decrease gradually because of a simultaneously increasing amount of wear, which leads to increasing mesh displacements. The results obtained with the finite wear algorithm for two-sided wear with wear coefficients of $k_w^1 = 0.0025$ and $k_w^2 = 0.0025$ are shown in Figure 5.20. Again, the simulation leads to the expected results of gradually decreasing normal contact stresses. Due to the two wear coefficients being identical, mesh-displacements are equally distributed for slave and master body and their magnitude is exactly half the magnitude that had been observed for the one-sided wear simulation. Now, the novel finite wear algorithm is compared to the internal state variable algorithm given in Section 5.4.2.1. The calculated wear depth is plotted for an exemplarily chosen node in Figure 5.28. For pure slave-sided wear, the newly developed finite wear algorithm nicely matches the internal state variable approach. This demonstrates that the presented finite wear algorithm is implicitly also capable to reproduce fretting wear effects. Again the two-sided wear case with $k_w^1 = k_w^2 = 0.0025$ leads to identical results for slave and master side. Moreover, as expected, adding slave and master wear depths yields exactly the same amount of wear as for the one-sided wear simulation with $k_w^1 = 0.005$. Finally, the normal contact stresses are visualized over time in Figure 5.28. The decrease of the normal stresses nicely matches for all simulations and corresponds to the calculated wear amount. The oscillations over time for all simulations result from the relatively coarse first-order finite element discretization. The interface stresses could be smoothed with higher-order elements as demonstrated in Farah et al. [73], where a very similar example has been investigated.

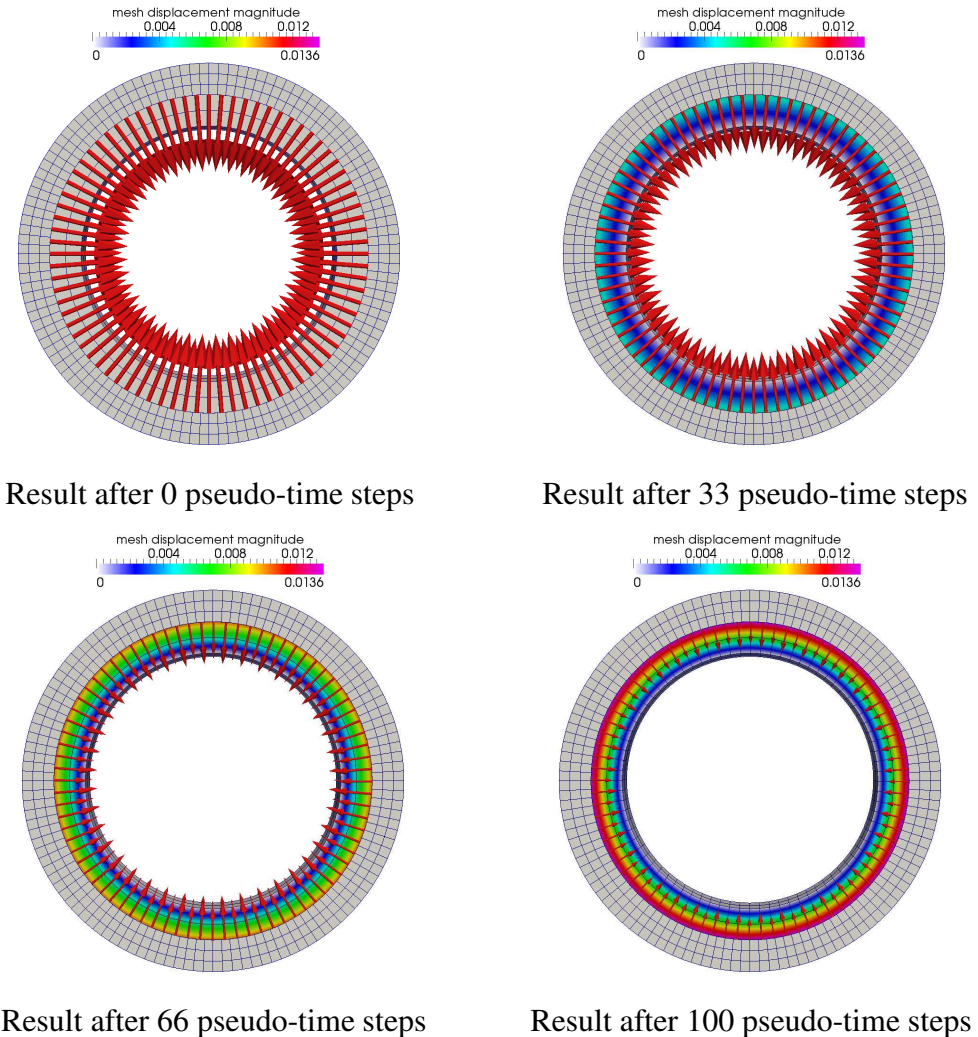


Figure 5.19: Visualized mesh displacements (color) and decreasing normal tractions (vectors) for press-fit example with slave-sided wear. Wear coefficient is chosen to 0.005, taken from Farah et al. [74].

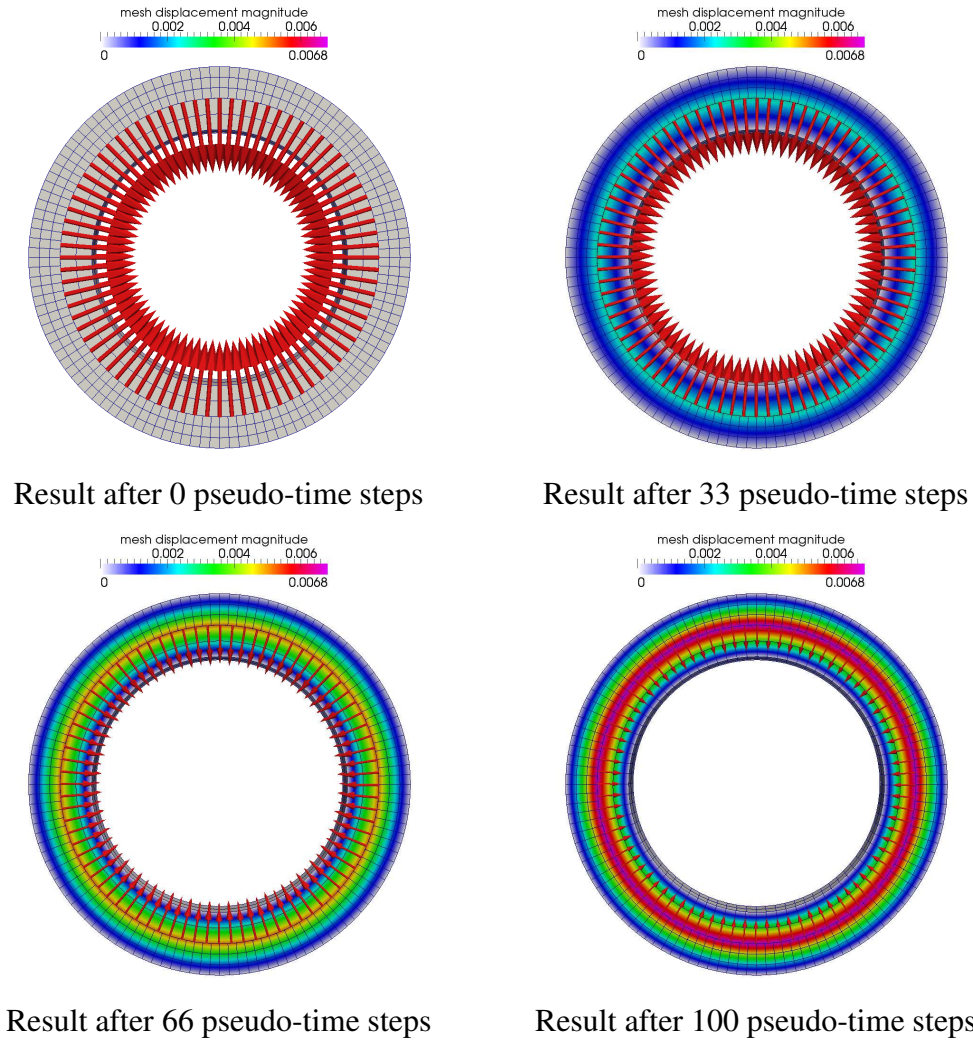


Figure 5.20: Visualized mesh displacements (color) and decreasing normal tractions (vectors) for press-fit example with two-sided wear. Wear coefficient for slave and master side is chosen to 0.0025, taken from Farah et al. [74].

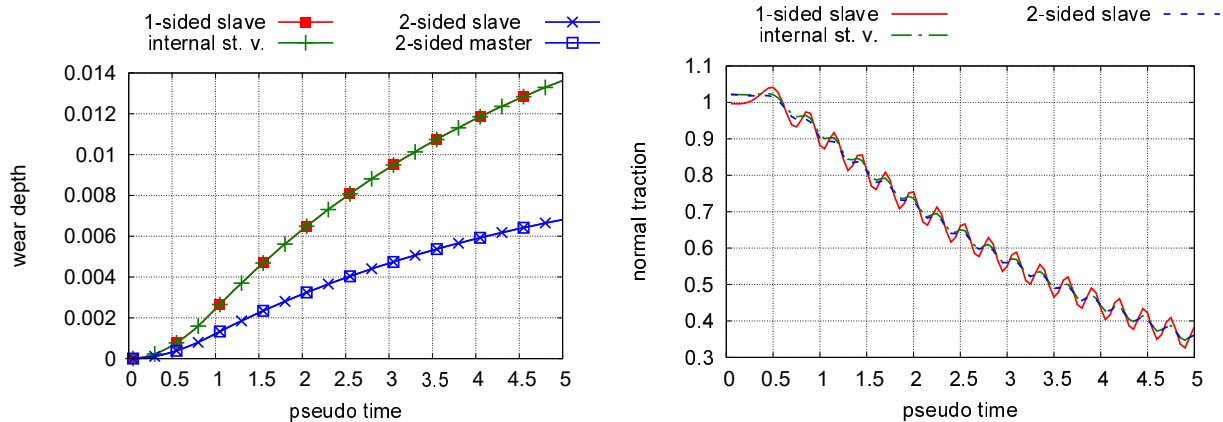


Figure 5.21: Resulting wear depth (left) and normal contact stress (right) for one-sided wear (red) and two-sided wear (blue) with the primary variable approach and the reference solution with internal state variable approach (green), taken from Farah et al. [74].

5.5.5.4. Finite deformation finite wear – oscillating cylinders

The last example is introduced to demonstrate the applicability of the presented algorithm to fully 3D settings in a finite wear and finite deformation regime. The example consists of two half-cylinders as shown in Figure 5.22. Both half-cylinders have identical dimensions and material parameters. Concretely, the length is given as $l = 5$ and the radius is set to $r_o = 2$. The cylinders are oriented in such a way that their main axes are forming the angle $\alpha = 60^\circ$. The employed material is the Neo-Hookean model with Young's modulus $E = 100$ and Poisson's ratio $\nu = 0.3$. The cylinders are equally discretized with first-order hexahedral elements as shown in Figure 5.22. To increase the accuracy of the contact simulation, fine outer mesh layers are tied to the bulk meshes with well-known mortar mesh tying algorithms. For a detailed description of mortar mesh tying algorithms the interested reader is referred to Puso and Laursen [218, 219]. The radius of the bulk mesh sections is chosen as $r_i = 1.8$. The simulation is carried out within 420 time steps with a time step size of $\Delta t = 0.1$. The movement of the cylinders is purely Dirichlet controlled. The lower body is fixed at its lower surface for the entire simulation. The upper body is subjected to a prescribed motion at its upper surface. Specifically, the upper half-cylinder is pressed into the lower half-cylinder within 10 time steps with a vertical displacement magnitude of $d_v = 0.8$. Thereafter, the vertical displacement is kept constant and the sliding process starts. The sliding motion is described by $d_h = \sin(\frac{2\pi}{10}(t - 1))$ for the time interval $1 < t \leq 41$. When the sliding is finished, the upper body is lifted to its initial location within the time interval $41 < t \leq 42$. The contact scenario is defined by the lower cylinder being the master body and the upper cylinder being the slave body, respectively. The friction coefficient is $\mathfrak{f} = 0.1$ and the wear coefficients are $k_w^1 = 2.1e - 3$ and $k_w^2 = 7e - 4$. The complementarity parameters are chosen as $c_n = 1$ and $c_t = 1000$ for the entire simulation. The resulting convergence behavior of the proposed implicit wear algorithm is exemplarily shown for one characteristic time step in Table 5.1. Here, it can be seen that 18 nonlinear solution steps

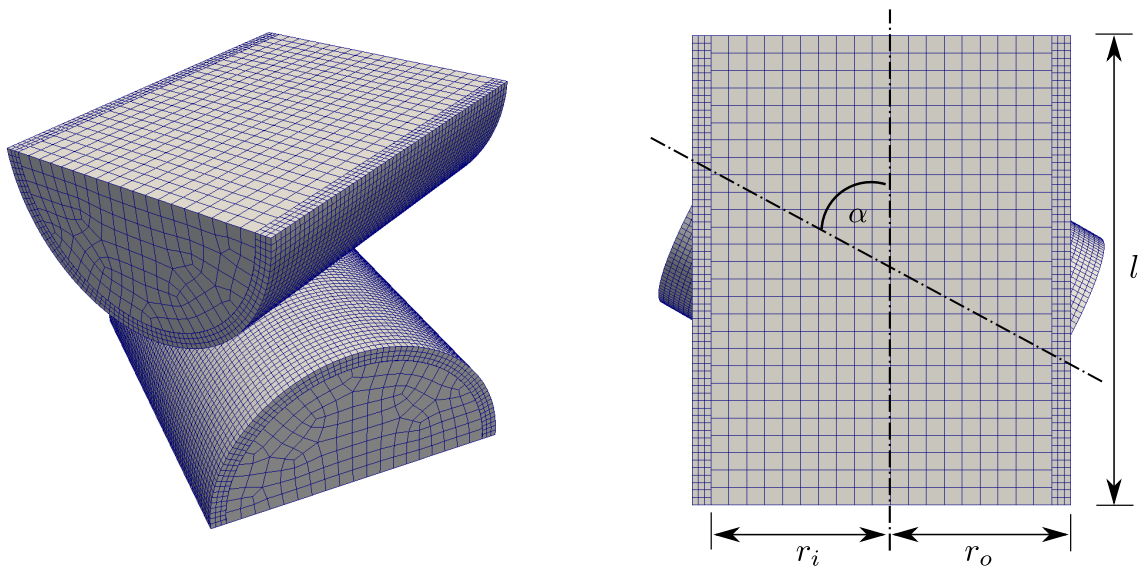


Figure 5.22: Problem setting and mesh for the cylinder wear test, taken from Farah et al. [74].

Table 5.1.: Convergence behavior in terms of the total residual norm for the proposed implicit wear algorithm for a characteristic time step.

step	Lagrangian step	shape evolution step
1	2.355e - 01 (*)	
2	1.408e - 01 (*)	
3	2.584e - 03 (*)	
4	3.549e - 04	
5	2.459e - 07	
6	3.526e - 09	
7	6.581e - 13	
8		9.154e - 03
9		2.086e - 06
10		1.527e - 11
11	1.218e - 03	
12	3.640e - 07	
13	8.886e - 12	
14		3.874e - 06
15		3.173e - 11
16	1.799e - 07	
17	2.146e - 12	
18		9.251e - 10

(*) = change in active and/or slip set

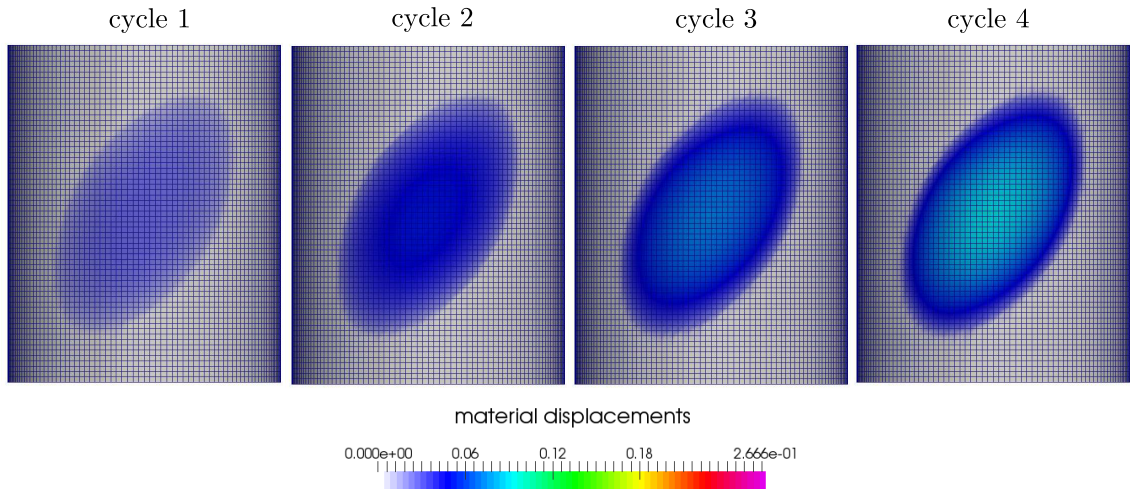


Figure 5.23: Material displacements at contact interface for master body with wear coefficient of $k_w^2 = 7e - 4$. The figure is based on Farah et al. [74].

in total have to be computed to meet a predefined convergence criterion of $1.0e - 9$ for the total residual norm of the Lagrangian step and for the total residual norm of the shape evolution step.

The resulting material displacements due to wear effects are shown for the master body in Figure 5.23 and for the slave body in Figure 5.24. Due to the wear coefficient ratio of $\frac{1}{3}$ between master surface and slave surface, the resulting ratio of material displacements at the interface, which corresponds to the wear depth, is $\frac{1}{3}$. The amount of material loss is visualized in the left part of Figure 5.25. There, the reference configuration is represented by the wire frame and the colored solid represents the material configuration. At the position where the largest wear depth occurs, three elements of the fine outer layer and more than one large bulk element are worn away. However, the shape evolution step still guarantees for a very good mesh quality in the material configuration, as can be seen in the right part of Figure 5.25. It is pointed out again that the material displacements correspond to the primary quantity of interest, i.e. the wear depth, at the contact interface. Inside the bulk of the domain, the material displacements have no physical interpretation, but are merely a consequence of the employed ALE algorithm to assure mesh quality. The mortar mesh tying interface does not affect the mesh shape evolution step and material displacements are consistently transferred through this interface. The corresponding normal contact stresses are visualized for the initial penetration state ($t=1$), the first ($t=11$), second ($t=21$), third ($t=31$) and fourth cycle ($t=41$) in Figure 5.26. It can be easily seen that the contact stresses drastically decrease due to the loss of material as expected.

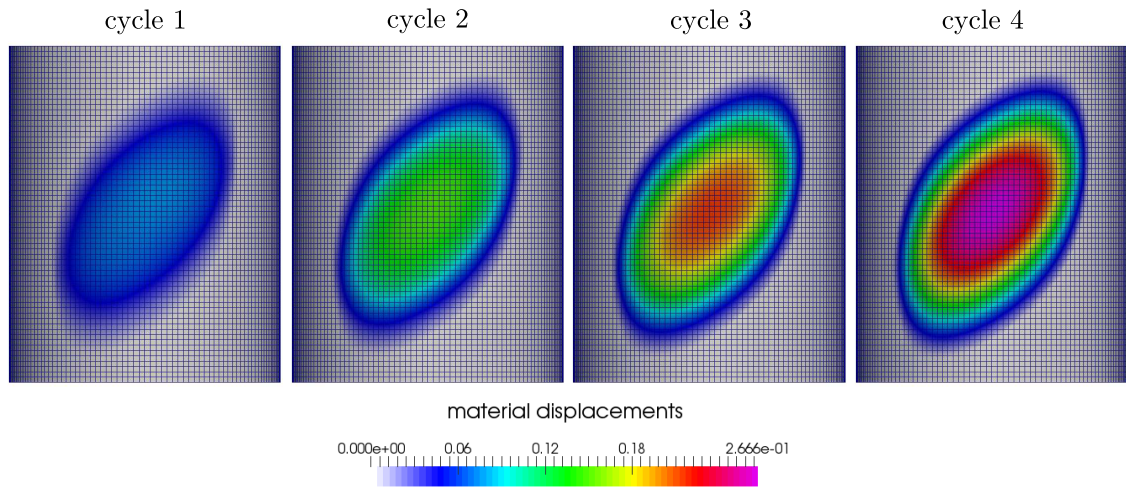


Figure 5.24: Material displacements at contact interface for slave body with wear coefficient of $k_w^1 = 2.1e - 3$. The figure is based on Farah et al. [74].

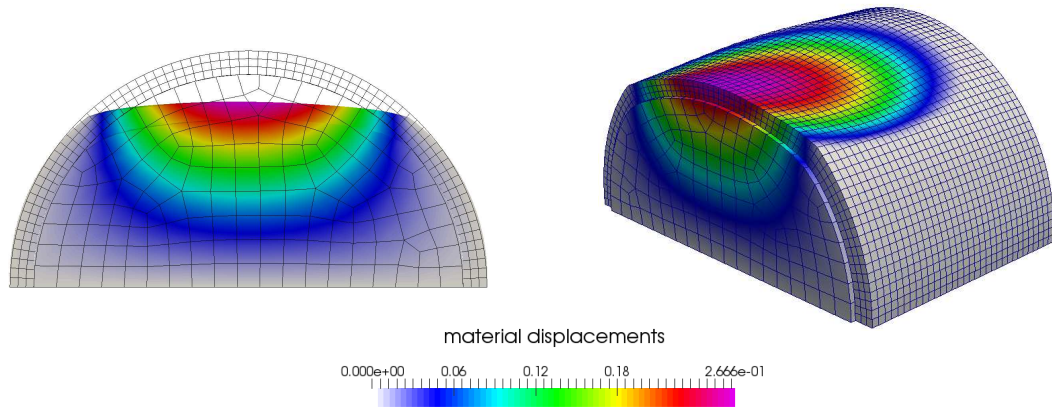


Figure 5.25: Material displacements for slave body: The wire frame on the left side represents the reference configuration and the solid represents the material configuration. On the right side, the pure material configuration with material displacements are shown. The figure is based on Farah et al. [74].

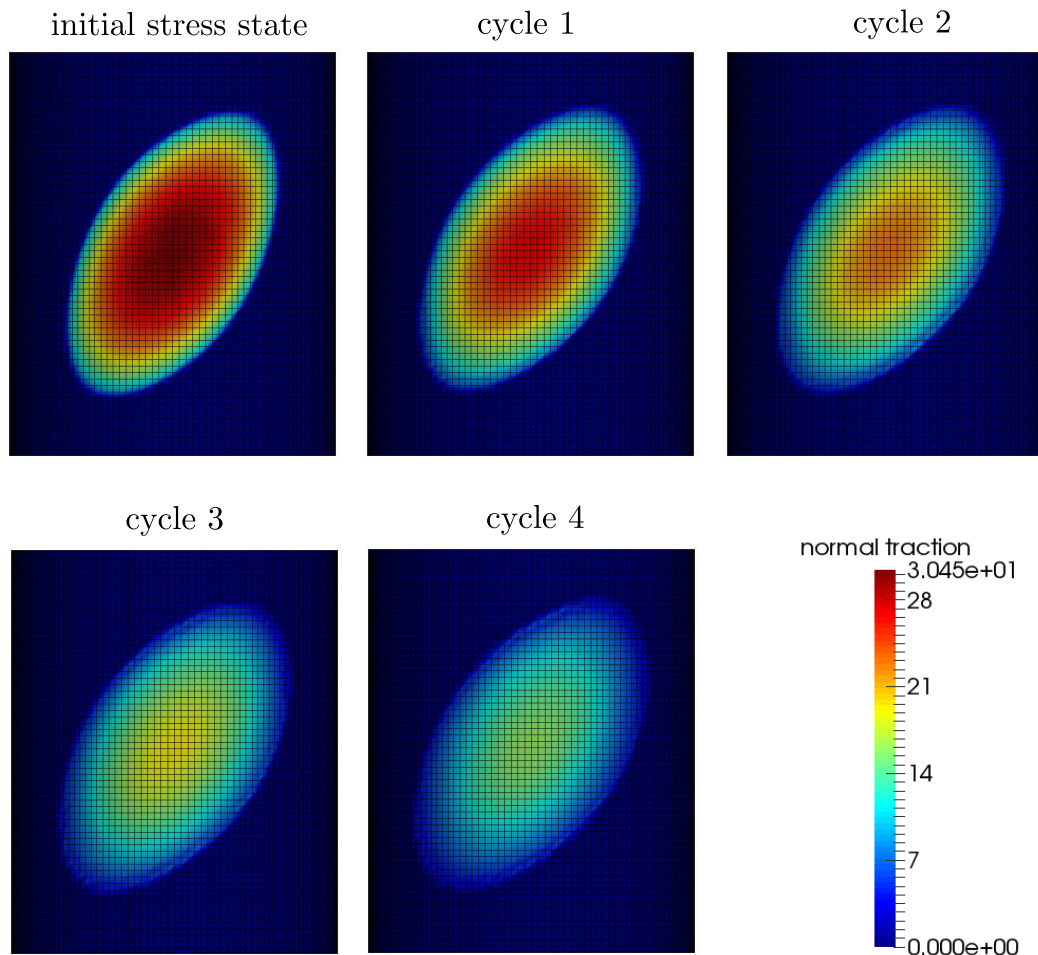


Figure 5.26: Normal contact stresses after 0, 1, 2, 3 and 4 wear cycles. The figure is based on Farah et al. [74].

5.6. Thermo-structure-contact-wear interaction with finite shape changes

Since wear phenomena are physically strongly connected to frictional dissipation, their interaction with thermal effects is very likely. This motivates the development of a thermo-structure-contact-wear interaction framework with finite shape changes.

The following investigations are based on the term paper Pröll [215], which has been supervised by the author. In order to derive an algorithm that is able to treat thermal wear effects, the standard frictional contact problem in Chapter 3 has to be extended towards thermo-mechanical interactions. Therefore, a general approach for thermo-structure interaction problems without contact was derived and described in great detail in Danowski [51] and Danowski et al. [52]. This approach has been extended towards contact interaction phenomena in Gitterle [87], Hüeber and Wohlmuth [116] and Seitz et al. [245]. Since the thermo-structure interaction framework including thermal contact effects is only employed in a black-box manner in the following, its governing equations are only briefly reviewed. In addition, the solution procedure is shortly sketched and two examples are presented at the end.

5.6.1. Problem setting

The temperature fields $\theta^{(1)}$ and $\theta^{(2)}$ for two bodies \mathcal{B}^1 and \mathcal{B}^2 are introduced. In order to derive a problem statement for the temperatures in the context of finite wear problems, thermal boundaries in material (worn) configuration are introduced:

$$\partial\Omega_m^{(i)} = \Gamma_{m,\theta}^{(i)} \cup \Gamma_{m,q}^{(i)} \cup \Gamma_{m,c}^{(i)}, \quad (5.75)$$

$$\Gamma_{m,\theta}^{(i)} \cap \Gamma_{m,q}^{(i)} = \Gamma_{m,\theta}^{(i)} \cap \Gamma_{m,c}^{(i)} = \Gamma_{m,q}^{(i)} \cap \Gamma_{m,c}^{(i)} = \emptyset, \quad (5.76)$$

where $\Gamma_{m,\theta}^{(i)}$ denotes the domain boundary with prescribed temperature and $\Gamma_{m,q}^{(i)}$ is the boundary with given heat fluxes. Again, their counterparts in spatial configuration are denoted with $\gamma_\theta^{(i)}$ and $\gamma_q^{(i)}$. Usually, thermo-mechanical problems are formulated with respect to a reference temperature θ_0 , where the bodies are stress free. Here, the reference temperature is also assumed to be equal to the material temperature in the material configuration. Therefore, no additional notation is introduced for the material temperature. Consequently, the relative temperature can be defined as

$$\Delta\theta^{(i)} = \theta^{(i)} - \theta_0. \quad (5.77)$$

The constitutive relations introduced in Section 2.1.2 are modified in order to describe thermo-elastic material behavior. Thus, the formulation for the Saint-Venant-Kirchhoff material model introduced in Danowski [51] is employed, which is defined by the strain energy function

$$\Psi_{TSVK} = \frac{\lambda(\theta)}{2}(\text{tr}\mathbf{E})^2 + \mu(\theta)\mathbf{E} : \mathbf{E} + m_0(\theta)\Delta\theta\text{tr}\mathbf{E} - \rho_0C_V\left(\theta \ln\frac{\theta}{\theta_0} - \Delta\theta\right). \quad (5.78)$$

Herein, the first two terms are equivalent to the classical Saint-Venant-Kirchhoff material model in (2.20) except for the dependency of the Lamé parameters on the temperature. The third term

represents the coupling between the thermal and structure field, where the stress-temperature modulus $m_0(\theta)$ is obtained by

$$m_0(\theta) = -(3\lambda(\theta) + 2\mu(\theta))\alpha_\theta. \quad (5.79)$$

The thermal expansion coefficient is denoted by α_θ . The last term in (5.78) is the thermal potential with the specific heat capacity C_V . This change in the definition of the strain energy function directly influences the balance of linear momentum. However, all remaining definitions for the boundary value problem remain unchanged and read

$$\operatorname{Div} \mathbf{P}_\phi^{(i)} + \hat{\mathbf{b}}_\phi^{(i)} = \mathbf{0} \quad \text{in } \Omega_m^{(i)} \times [0, T], \quad (5.80)$$

$$\mathbf{u}_\phi^{(i)} = \hat{\mathbf{u}}_\phi^{(i)} \quad \text{on } \Gamma_{m,u}^{(i)} \times [0, T], \quad (5.81)$$

$$\mathbf{P}_\phi^{(i)} \cdot \mathbf{N}_\phi^{(i)} = \hat{\mathbf{t}}_\phi^{(i)} \quad \text{on } \Gamma_{m,\sigma}^{(i)} \times [0, T]. \quad (5.82)$$

Additionally to the structural equations, the contact constraints for the structural part are still defined by the non-penetration conditions

$$g_n \geq 0, \quad p_n \leq 0, \quad p_n g_n = 0 \quad (5.83)$$

and the conditions for frictional sliding according to Coulomb's law

$$\Upsilon := \|\mathbf{t}_\tau\| - \mathfrak{F}|p_n| \leq 0, \quad \mathbf{v}_{\tau,\text{rel}} + \beta \mathbf{t}_\tau = \mathbf{0}, \quad \beta \geq 0, \quad \Upsilon \beta = 0. \quad (5.84)$$

Herein, it is assumed that the consideration of thermal effects directly influences the coefficient of friction, via

$$\mathfrak{F} = \mathfrak{F}_0 \frac{(\theta_c - \theta_d)^2}{(\theta_d - \theta_0)^2}. \quad (5.85)$$

This assumption is based on the explanations in Laursen [151]. In (5.85), the coefficient of friction at reference temperature is denoted with \mathfrak{F}_0 , the damage temperature is represented with θ_d and the temperature of the contact interface θ_c is defined to be the maximum temperature of the contact surfaces $\theta_c = \max(\theta^{(1)}, \theta^{(2)})$. Under consideration of this law, the coefficient of friction monotonically decreases from the initial friction coefficient \mathfrak{F}_0 to zero at the damage temperature θ_d .

Without any further details on the derivation, the problem formulation for the thermal field results from the first and second law of thermodynamics and reads

$$\rho_0^{(i)} C_V^{(i)} \dot{\theta}^{(i)} - \mathcal{H}^{(i)} + \operatorname{Div} \mathbf{Q}^{(i)} - \rho_0^{(i)} r^{(i)} = 0 \quad \text{in } \Omega_m^{(i)} \times [0, T], \quad (5.86)$$

$$\theta^{(i)} = \hat{\theta}^{(i)} \quad \text{on } \Gamma_{m,\theta}^{(i)} \times [0, T], \quad (5.87)$$

$$-\mathbf{Q}^{(i)} \cdot \mathbf{N}^{(i)} = \hat{q}_0^{(i)} \quad \text{on } \Gamma_{m,q}^{(i)} \times [0, T], \quad (5.88)$$

$$\theta^{(i)}(t = 0) = \theta_0^{(i)} \quad \text{in } \Omega_m^{(i)}. \quad (5.89)$$

Herein, \mathcal{H} describes heating due to the Joule effect and is given for the considered Saint-Venant-Kirchhoff material model:

$$\mathcal{H} = \theta m_0(\theta) \operatorname{tr} \dot{\mathbf{E}}. \quad (5.90)$$

Additionally, r is the source term energy density per unit mass and \mathbf{Q} denotes the heat flux in the material configuration, which is defined as

$$\mathbf{Q} = -Jk_\theta(\mathbf{F}^T \cdot \mathbf{F})^{-1}\text{Grad}\theta. \quad (5.91)$$

Here, J is the already introduced determinant of the deformation gradient, \mathbf{F} is the deformation gradient itself, $\text{Grad}\theta$ is the material gradient of the temperature and k_θ is the thermal conductivity. Furthermore, the prescribed boundary temperature is denoted with $\hat{\theta}$ and the prescribed heat flux reads \hat{q}_0 .

The thermal contact effects are defined by the heat fluxes of both bodies in inward normal direction of each considered body. Based on the local energy balance at the contact interface, the heat fluxes for the slave and master body read

$$q_c^{(1)} = \beta_c(\theta^{(1)} - \theta^{(2)}) - \delta_c(\mathbf{t}_\tau \cdot \mathbf{v}_{\tau,\text{rel}}), \quad (5.92)$$

$$q_c^{(2)} = -\beta_c(\theta^{(1)} - \theta^{(2)}) - (1 - \delta_c)(\mathbf{t}_\tau \cdot \mathbf{v}_{\tau,\text{rel}}). \quad (5.93)$$

Here, the first term of each definition is the heat flux due to the temperature difference and the second term is the generated heat due to dissipation effects. Thus, the second term of each equation is directly related to the dissipation rate density defined in (3.13). The parameters β_c and δ_c can be written as

$$\beta_c = \frac{\alpha_c^{(1)}\alpha_c^{(2)}}{\alpha_c^{(1)} + \alpha_c^{(2)}}, \quad \delta_c = \frac{\alpha_c^{(1)}}{\alpha_c^{(1)} + \alpha_c^{(2)}}, \quad (5.94)$$

where the heat transfer parameter $\alpha_c^{(i)}$ depends on the normal pressure, via

$$\alpha_c^{(i)} = \begin{cases} 0 & \text{for } p_n = 0 \\ \bar{\alpha}_c^{(i)}p_n & \text{for } p_n < 0 \end{cases}. \quad (5.95)$$

Despite the fact that the wear coefficient shows a dependence on temperatures as suggested in Molinari et al. [175] and Pearson et al. [200], a constant coefficient is assumed for the following investigations. However, the presented methods in this section are easily extendable to incorporate further dependencies on temperature and loading conditions.

Remark 5.6. *It is important to note that the additional mesh movement in the employed Arbitrary-Lagrangian-Eulerian approach leads to convective terms in the time derivatives of the temperatures. These convective effects are not implemented in the employed algorithm. However, since the loss of material due to wear is a very slow process and consequently the additional mesh motion is of small magnitude within one time step, the neglect of convective terms should be a valid assumption.*

5.6.2. Solution method

The consideration of wear effects and finite shape changes are again realized in a partitioned scheme as introduced in Section 5.5.2. Here, a Lagrangian step is performed followed by a shape evolution step. In contrast to Section 5.5.2, no wear effects are considered during the Lagrangian

step, which means that no modification of the gap function is performed. Thus, the Lagrangian step consists of a pure thermo-elastic problem which is solved in a fully monolithic manner. Herein, the structural field is considered as quasi-static problem and thus inertia effects are neglected. For the thermal field, dynamic effects are considered and time integration is done by the well-known One-Step- θ scheme. The contact interaction is discretized with the mortar method and the thermal heat fluxes are identified as additional Lagrange multipliers. However, further details on the spatial and temporal discretization of the coupled thermal-mechanical problem are beyond the scope of this thesis and the interested reader is referred to Danowski [51], Danowski et al. [52], Gitterle [87], Hüeber and Wohlmuth [116] and Seitz et al. [245] for detailed information on this topic. Therefore, the Lagrangian step can be considered in a black-box manner. After a completely converged Lagrangian step, the wear increment for the considered time step is post-processed according to Section 5.3.1 and afterwards utilized in the shape evolution step. The shape evolution procedure for the structural problem, i.e. for the material configuration, is identical to the explanations in Section 5.5.4. In addition, the temperatures have to be adapted according to the mesh movement. For this purpose, the discrete temperature $\theta_{j,h}^m$ at a considered relocated node j is consistently interpolated, via

$$\theta_{j,h}^m = \sum_{b=1}^{n_n} N_b(\tilde{\xi}_j) \theta_{b,h}, \quad (5.96)$$

where the parameter space coordinate $\tilde{\xi}_j$ of the updated node within the non-updated element is calculated as described in (5.72).

The complete algorithm for the thermo-structure-contact-wear interaction with finite shape changes follows to:

Algorithm 5.3. Explicit partitioned scheme

1. Solve the nonlinear thermo-mechanical contact problem including friction for fixed material displacements according to Seitz et al. [245] as Lagrangian step. Herein, no effects due to the actual wear increment are considered
2. Post-Process the wear increment for the completed Lagrangian step according to Section 5.3.1.
3. Solve the nonlinear shape evolution step as a pseudo-elasticity problem (ALE problem) for the calculated amount of wear. Then update the material and the spatial configuration as well as the temperatures with regard to the calculated wear by employing the advection map procedure.

5.6.3. Numerical examples

In the following, two numerical examples are investigated to verify the developed thermo-structure-contact-wear interaction algorithm and to demonstrate its applicability to finite deformations and finite shape changes.

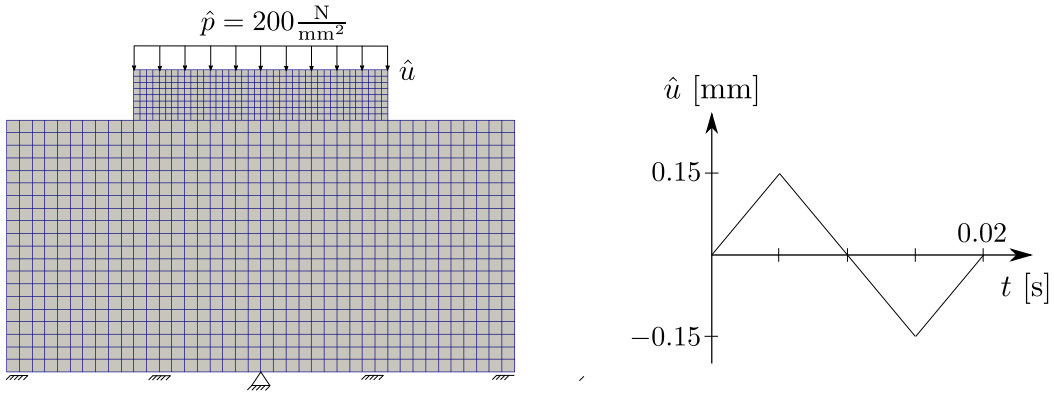


Figure 5.27: Geometry with finite element mesh and boundary conditions for the oscillating punch example. The right part visualizes the given displacements for one cycle.

5.6.3.1. Validation – oscillating punch

The first example is taken from Ireman et al. [125] and is employed to compare the accuracy of the developed thermo-structure-contact-wear interaction framework with already existing algorithms. The example consists of two thermo-elastic bodies, namely a punch and a foundation. The dimensions of the punch are $20\text{mm} \times 4\text{mm}$ and the dimensions of the foundation are $40\text{mm} \times 20\text{mm}$. In contrast to the original setting, a 3D simulation is performed. Thus, both bodies have a thickness of $d = 0.5\text{mm}$. The punch is loaded with a prescribed traction $\hat{p} = 200 \frac{\text{N}}{\text{mm}^2}$ in vertical direction, see Figure 5.27. Additionally, a horizontal oscillation \hat{u} is prescribed at the top of the punch, see again Figure 5.27. For the numerical tests, 100 cycles are carried out. The bottom of the foundation is completely supported in vertical direction and the midpoint is also fixed in horizontal direction. In order to achieve a problem setting, which corresponds to the plane strain assumption in Ireman et al. [125], symmetry conditions are enforced at the front and back of the bodies. The spatial discretization is visualized in 5.27 with one element layer in thickness direction. The finite element mesh employed in Ireman et al. [125] was initially matching at the contact interface and the mesh created in this thesis is non-matching in order to demonstrate the applicability of the mortar method to non-matching discretizations. The contact formulation is manipulated by an additional initial gap $g_i(x) = 0.0005x^2$, where x is the coordinate along the contact surface with its origin at the midpoint of the contact surface. This initial gap is included in the non-penetration constraints in the same way as the wear depth was included in (5.33). Consequently, the two bodies slightly overlap. The material properties are chosen corresponding to steel. Thus, Young's modulus is $E = 210000 \frac{\text{N}}{\text{mm}^2}$, Poisson's ratio is $\nu = 0.3$, the initial density is $\rho_0 = 7800 \frac{\text{kg}}{\text{m}^3}$, the thermal expansion coefficient is $\alpha_\theta = 12 \cdot 10^{-6} \frac{1}{\text{K}}$, the specific heat capacity is $C_V = 460 \frac{\text{J}}{\text{kg}\cdot\text{K}}$ and the thermal conduction is $k_\theta = 46 \frac{\text{W}}{\text{m}\cdot\text{K}}$. For the contact interaction, the friction coefficient is defined as $\mathfrak{F} = 0.3$ and no damage effects are assumed. Additionally, the thermal heat transfer parameters are assumed to be equal for the two bodies and set to $\bar{\alpha}_c^{(i)} = 10^{-3} \frac{\text{W}}{\text{N}\cdot\text{K}}$. Finally, the wear coefficient is defined as $k_w = 10^{-5} \frac{\text{mm}^2}{\text{N}}$. The time integration factor for the One-Step- θ scheme for thermal effects is chosen as $\theta_t = 0.5$ and the structural problem is considered to be quasi-static. Moreover, a time

5. Mortar Methods for Wear Modeling

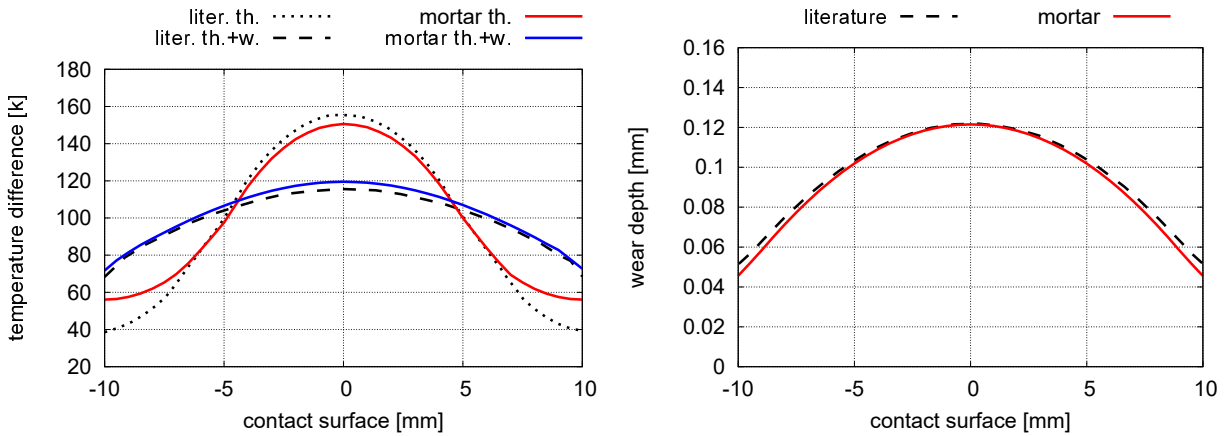


Figure 5.28: Results for oscillating punch compared to Ireman et al. [125] after 100 cycles: temperature difference with respect to reference temperature for simulations with wear effects and without wear effects (left) and wear depth when thermal effects are included (right).

step size of $\Delta t = 3.125 \cdot 10^{-4}$ s is chosen. The punch is defined to be the slave body and the foundation is the master body, respectively.

In order to judge the accuracy of the results, the basic differences in the employed finite element frameworks must be pointed out. The algorithm used in Ireman et al. [125] is based on the assumption of small displacements, small deviations from the reference temperature and a small wear depth. The contact discretization was realized in a node-to-node manner and thus the employed finite element mesh must initially match at the interface. Again, the algorithm developed in this thesis is created in order to be valid in a finite deformation and finite wear regime and the contact interaction is based on the mortar method. Consequently, it should also be able to perform in a small deformation regime with small expected wear depths.

The results compared to Ireman et al. [125] are visualized in the Figure 5.28. In the left part of this figure, the differences of the interface temperature compared to the reference temperature are plotted for simulations with included and excluded wear effects. When wear is not considered, the temperatures in the middle part of the contact interface match qualitatively well. At the outer parts of the contact zone relatively high discrepancies occur. This could originate from the additional initial gap $g_i(x)$ that becomes large at the outer parts of the contact zone. Therefore, the node-to-node contact assumption in Ireman et al. [125] is strongly violated for the outer contact regions and the solution quality drastically decreases. The presented mortar-based approach is constructed in order to deal with non-matching meshes and thus the solution quality is not drastically influenced by the mesh-to-mesh constellation. When wear is included, the overall temperature distribution of the contact interface matches very well with the result from literature. The additional loss of material, which reaches its peak at the center of the contact interface, balances the initial gap overlap and by an ongoing simulation the matching node assumption in Ireman et al. [125] becomes more and more valid. In the right part of Figure 5.28, the wear depth is plotted over the contact interface for included thermal effects. The maximum wear depth

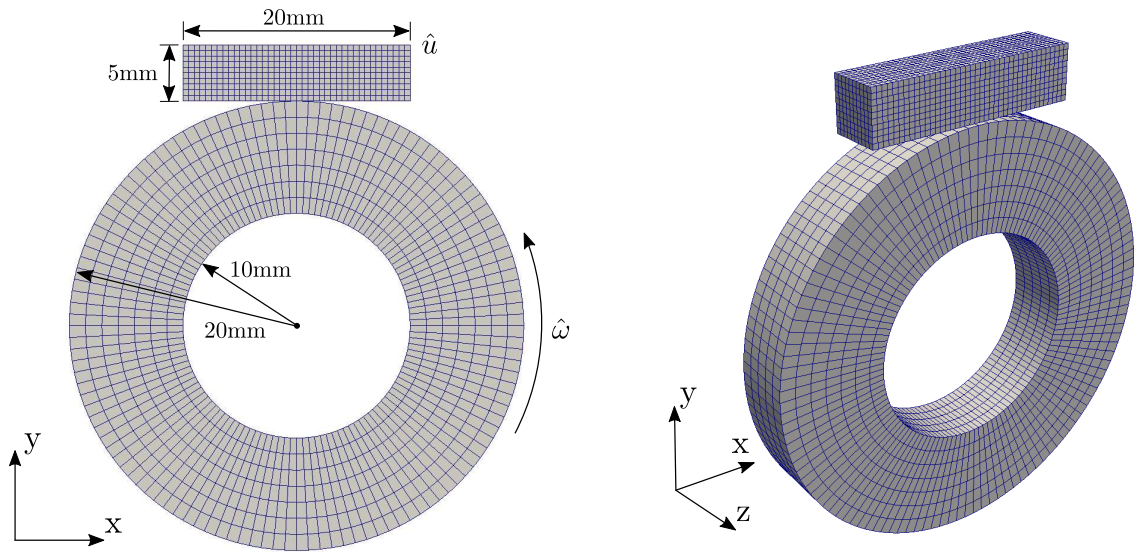


Figure 5.29: Geometry with finite element mesh and boundary conditions for block on rotating disc example.

at the center of the contact interface is excellently captured by the algorithm developed in this thesis. Also the wear depth distribution nicely matches the result from literature.

In summary, the presented algorithm yields excellent solutions and the results from Iremen et al. [125] can be reproduced.

5.6.3.2. Finite shape changes – block on rotating disc

The final wear example is introduced in order to demonstrate the applicability of the proposed thermo-structure-contact-wear interaction algorithm to finite deformations and finite shape changes. The example consists of a block which is pressed onto a rotating hollow cylinder. The geometry and the employed finite element mesh is shown in Figure 5.29. In addition to the information in 5.29, the thickness of the block is 5mm and the thickness of the disc is defined as 6mm. For both bodies, first-order hex8 elements are employed. The material properties for both bodies are chosen according to steel. Thus, the material parameters are equal to the previous example. The damage temperature for the friction coefficient is chosen as $\theta_d = 700\text{K}$ and the initial friction coefficient is $\mathfrak{f}_0 = 0.3$. The reference temperature is defined as $\theta_0 = 293\text{K}$. Again, the time integration factor for the One-Step- θ scheme for the thermal field is chosen to $\theta_t = 0.5$ and the structural problem is assumed to be quasi-static. The time step size is defined as $\Delta t = 0.01\text{s}$ and the overall simulation time is $T = 3.5\text{s}$. In the time interval $0\text{s} < t \leq 0.1\text{s}$, the block is completely fixed at its top surface and the hollow cylinders inner surface is subjected to an angular acceleration $\hat{\omega} = 4.0 \frac{\text{rad}}{\text{s}^2}$. Afterwards, in the time interval $0.1\text{s} < t \leq 3.5\text{s}$ the block is continuously pressed into the cylinder with a prescribed displacement amplitude of $\hat{u} = 1.75\text{mm}$ and the angular velocity of the cylinder is kept constant. The mortar contact is characterized by the block being the slave side and the cylinder is defined to act as master side, respectively. In addition, only the block is assumed to lose material due to wear.

The resulting temperatures are given in Figure 5.30. Here, the temperatures are shown for a

5. Mortar Methods for Wear Modeling

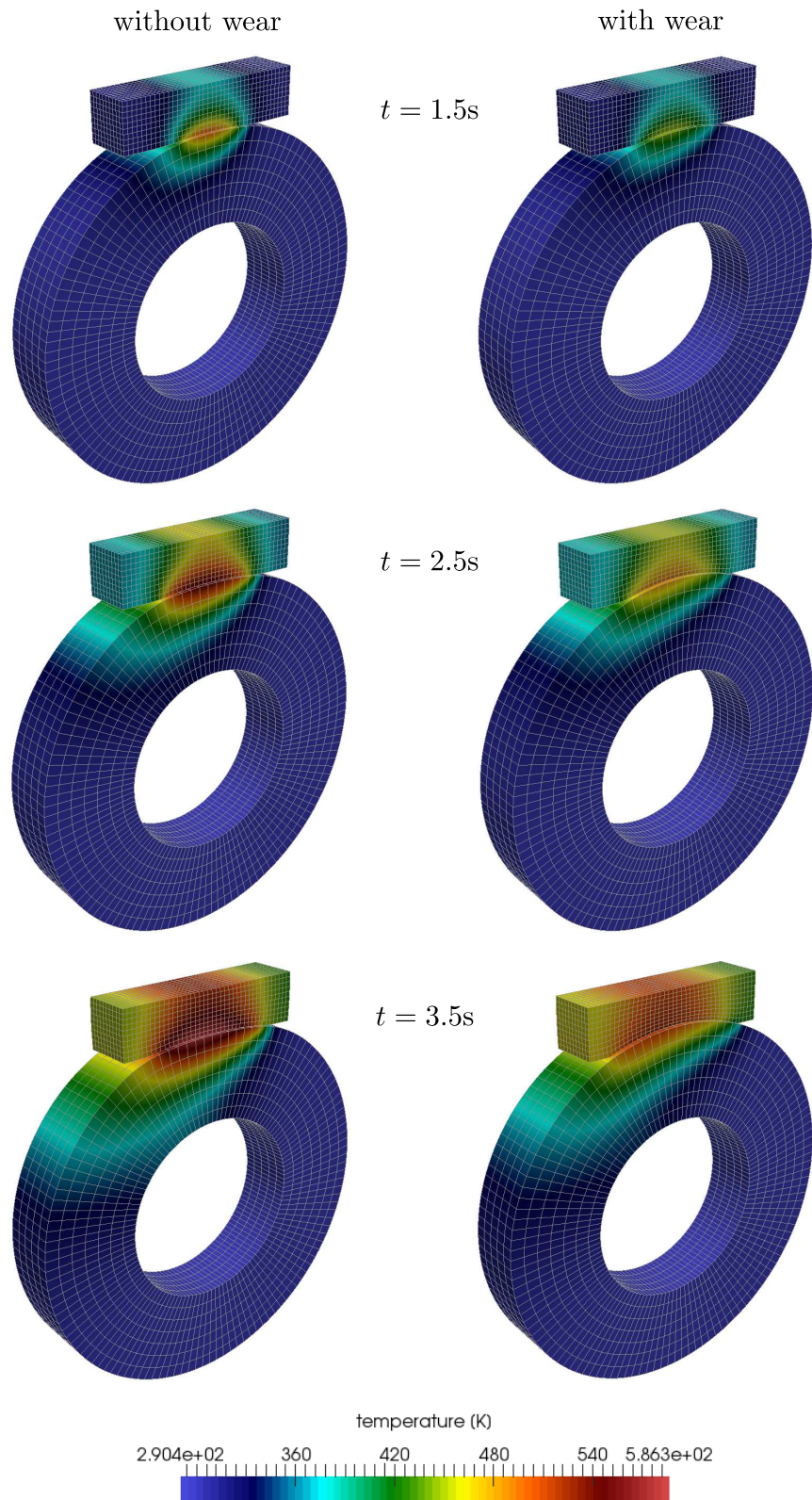


Figure 5.30: Temperature distribution for block on rotating disc example: results without wear (left) and when wear is included (right).

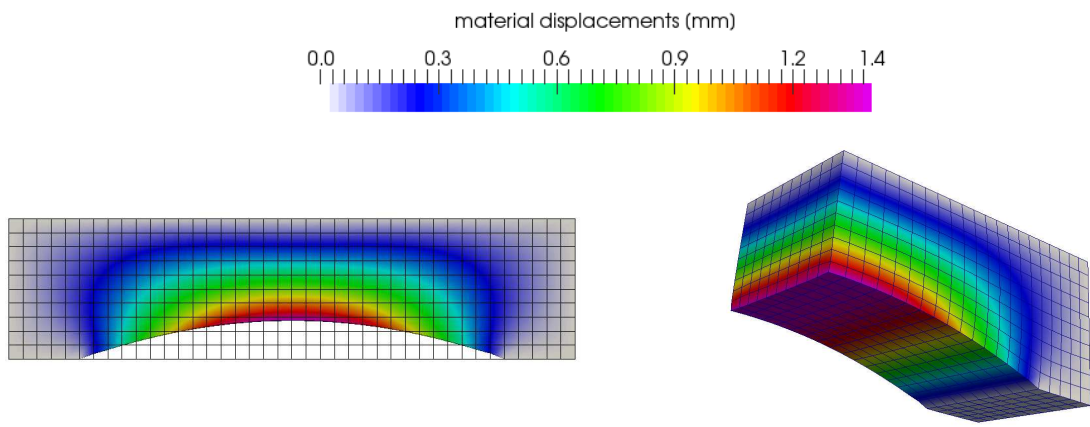


Figure 5.31: Material displacements for the block: The wire frame on the left-hand side represents the reference configuration and the solid represents the material configuration at the end of the simulation. On the right-hand side, the pure material configuration is shown with highlighting the material displacement contours.

simulation without any included wear phenomena and with considered wear effects. It can nicely be seen that the temperatures are much lower for the simulation with wear compared to the simulation with wear effects being ignored. This is due to the mass loss and corresponding finite shape change which naturally leads to decreased interface stresses compared to the simulation without wear. Of course, this effect results from the purely Dirichlet-controlled setting with prescribed displacements at the top of the block. In contrast, a setting with a force being applied at the top of the block would not lead to decreased contact traction to such an extent. However, this decrease in interface stresses causes a reduced dissipation at the contact interface and, according to (5.92) and (5.93), lower heat fluxes occur. During the entire simulation, no oscillations in the temperatures for the problem with wear being included are noticed. This shows that the developed explicit algorithm performs in a robust and stable manner for the chosen time step size.

Finally, the resulting shape change due to the material loss at the contact interface is shown in Figure 5.31. It can be seen that the material loss at the contact interface of the block corresponds to nearly three element layers. But again, the proposed algorithm, including the developed shape evolution procedure, guarantees for an excellent mesh quality despite the huge material loss.

6. Mortar Methods for Volume Coupled Problems

As already explained in this thesis, mortar methods were originally introduced in the context of Domain Decomposition (DD) applications and have usually been incorporated in a variational problem formulation. However, according to Dureisseix and Bavestrello [64], the mortar method can also be considered as an abstract transfer scheme that enforces conservation of nodal information in a weak sense. Thus, it perfectly suits the finite element idea and guarantees for high accuracy. While this approach yields excellent results, it is extremely costly when standard shape functions are employed. Up to now, no extension towards dual mortar methods in a complete 3D realm was ever made, which marks the first point of origin for this chapter. In addition, projection operators for nodal information transfer allow for multiphysics simulations on non-matching meshes, as firstly demonstrated for 2D problems in Dureisseix and Bavestrello [64] in the context of partitioned solution algorithms. However, this has never been extended towards 3D multiphysics problems within monolithic solution schemes and contact problems, which represent the further novel developments in this chapter.

This chapter focuses on details concerning the construction of a 3D projection operator based on dual mortar methods and its application to general multiphysics problems. Here, the presented information and methodologies are basically taken from the author's publication Farah et al. [70]. In addition, the multiphysics approach for non-matching meshes is extended towards contact interaction problems, where interface mortar operators and volume mortar operators are simultaneously employed within a single monolithic framework. Details on the extensions towards contact problems are basically taken from the Master's Thesis Jelich [128], which was supervised by the author.

The following chapter starts with a state-of-the-art overview of already existing approaches for nodal information transfer and their various applications. Then, the fundamentals on volume projection of nodal information are explained. Here, the mortar projection operator is derived in its general form and details on its numerical evaluation, dual shape functions for volume problems and conservation properties are provided. Afterwards, the performance of the projection operator is validated with two numerical examples. Then, the projection operator is employed on non-matching volume meshes in order to create a general methodology for multiphysics simulations. This approach is validated at several numerical simulations of coupled multiphysics problems. Finally, further applications of the projection operator are demonstrated.

6.1. Fundamental approaches and research objective

6.1.1. Fundamental approaches and applications

In the following, the fundamental approaches on nodal information transfer methods for volume coupled problems are reviewed. In addition, their strongly related counterparts in the field of computational contact mechanics are mentioned. Although contact mechanics and general interface mechanics are based on constraint enforcement techniques such as penalty regularization and Lagrange multiplier approaches, their type of constraint discretization is crucial for the performance of these methods. Therein, interface projection operators for nodal information transfer implicitly arise, which share a lot of conceptual similarities with abstract volume operators. Thus, the following explanations provide a state-of-the-art overview of general methodologies for nodal information transfer. Moreover, their various fields of application which are beyond the scope of computational contact mechanics are reviewed.

The easiest way of transferring nodal information is a *node-to-node* (NTN) approach, where each coupling pair consists of two nodes. It is also commonly known as *matching grid* discretization. Here, it is assumed that the nodes initially match and thus the coupling constraints or the information transfer can be enforced individually for each node pair. This approach was implicitly employed in many multiphysics problems, such as for poroelastic media simulations in Vuong et al. [278], thermo-structure interaction in Danowski et al. [52] and fluid-structure interaction problems with moving grid approach in Ramm and Wall [225] and Wall [280]. In the context of computational contact mechanics, such an approach has been employed in Francavilla and Zienkiewicz [84], Hughes et al. [120] and Ireman et al. [125]. In a regime of infinitesimal deformation this approach is valid since no significant relative movements between the domains are allowed. However, for classical structural applications in a finite deformation regime together with a pure Lagrangian description the NTN approach obviously fails. To overcome this problem, an Arbitrary-Lagrangian-Eulerian (ALE) approach was developed in Benson [24] and Haber [93], which split physical material point motion and mesh motion to enforce a matching grid setting at the contact interface. Such an approach was also applied for finite wear simulations in Chapter 5 and the interested reader is also referred to the explanations therein. However, this approach is still restricted to nearly equally discretized contact interfaces and thus it is not the approach of choice for contact simulations. For general domain decomposition applications with non-matching meshes the NTN approach is obviously not an adequate choice.

In order to treat the problem of non-matching discretizations that naturally restricts the NTN approach, a scheme based on coupling pairs consisting of a node and an element was developed, which is denoted as *node-to-segment* (NTS) scheme. A NTS scheme for nodal information transfer enforces the coupling point-wise (strong) at each node. It was employed for example in Bussetta et al. [35], Ortiz and Quigley [190], Ramm et al. [226] and Saksono and Perić [239]. The more general form of the NTS approach is denoted as *collocation scheme*, where the coupling pair consists of a general collocation point and an element. Then, the nodal information is interpolated at these collocation points and after the projection is completed, the nodal values from the target mesh can be recovered. In the literature on information transfer methods, these approaches are often termed collocation schemes although the information transfer is enforced at the nodes, see Dureisseix and Bavestrello [64]. Since this chapter focuses on information transfer schemes, the naming *collocation method* is maintained in the following of this thesis. In addi-

tion, it should be noted that among various other declarations, the NTS type of discretization is also usually called *element transfer method* in some publications, see for example Bussetta et al. [35]. In the context of computational contact mechanics, such node-wise enforcement is indeed commonly termed NTS discretization and has been proposed in Hallquist [97] and Hughes et al. [120]. It has successfully been extended to more general contact cases in Bathe and Chaudhary [14], Hallquist et al. [96], Papadopoulos and Taylor [195], Simo et al. [253] and Wriggers et al. [296].

Since the collocation approach enforces the nodal information transfer in a point-wise (strong) sense, it cannot guarantee for weak conservation properties and does not naturally fit in the finite element philosophy. To be consistent in a finite element sense, weak conservation methods have been developed, see for example Orlando and Perić [188] and Orlando [189]. These types of nodal information transfer schemes are denoted as *segment-to-segment* (STS) methods in the following. Due to their characteristic of weak information conservation, they naturally require for numerical integration procedures, which cause increased computational costs compared to the previously introduced methods. For computational contact methods, first investigations regarding the weak enforcement of contact constraints can be found in Papadopoulos and Taylor [195] and Simo et al. [253]. The *mortar method* can be identified as special type of STS methods. As already introduced in this thesis, it is based on a separation of a so-called slave (target) and master (source) mesh and the nodal information transfer is based on weak conservation assumptions over the slave side, see Bernardi et al. [25, 26]. The mortar method has been employed for the creation of general volume coupling operators in Dureisseix and Bavestrello [64] and Néron and Dureisseix [181]. Therein, the computation of the mortar operators is based on the construction of a so-called "super mesh", from which each element is included in only one element of the source and target mesh. This basically describes the integration cells/segments for the segment-based integration procedure from Section 3.4.2. This was also employed in Farrell and Maddison [76] and Farrell et al. [77] for the construction of projection operators, which are strongly related to mortar operators. Mortar methods for computational contact mechanics have been already introduced in Chapter 3 and the interested reader is referred to the explanations therein and the literature Gitterle [87], Gitterle et al. [88], Popp [210], Popp et al. [211, 212], Puso and Laursen [218] and Yang et al. [301]. For the sake of completeness, it should be noticed that operators for nodal information transfer based on weak conservation properties have also been developed based on finite volume (FV) schemes, see Alauzet and Mehrenberger [4] and Rashid [227].

Finally, besides the already mentioned field of computational contact mechanics, the various types of applications for nodal information transfer schemes are briefly given. One of the most obvious type of application is the remeshing operation, which might becomes necessary for structural mechanics where extremely large deformations occur. Remeshing procedures can be found in Bussetta et al. [35], Fernandes and Martins [78] and Perić et al. [203]. Other application types are global/local schemes in Gould and Hara [91], Mote [176] and Voleti et al. [276], the Arlequin method for structural problems in Dhia [58] and Dhia and Rateau [59], the Chimera scheme for fluid problems in Meakin [169], Renaud et al. [229], Steger and Benek [258] and Wall et al. [281] and geometrical multigrid methods in Adams [2] and Biotteau et al. [28]. Nodal information transfer schemes have also been applied for the simulation of volume coupled multiphysics problems on different meshes for the individual fields, see Dureisseix and Bavestrello [64] and Néron and Dureisseix [181]. Yet, in these publications only 2D multiphysics problems solved within a partitioned scheme are considered. However, it has been proven, that monolithic

solution schemes lead to superior robustness for coupled multiphysics problems, see for example Danowski et al. [52], Gee et al. [85] and Verdugo and Wall [275]. Hence, it seems promising to develop methodologies to allow for monolithic multiphysics solvers on non-matching meshes.

6.1.2. Specification of requirements

Based on the previous explanations on already existing coupling approaches, the most important requirements for the development of accurate and efficient mortar approaches for nodal information transfer and their application to multiphysics problems are listed in the following.

Computational efficiency due to dual shape functions Compared to collocation methods, mortar approaches require a much higher evaluation effort due to its characteristic weak enforcement of the information transfer and the consequently arising need for numerical integration. In addition, a standard mortar approach leads naturally to a fully coupled system for information transfer, meaning that one node of the target mesh is usually subjected to information of all nodes from the source mesh. In the algebraic form, this can be identified by a dense projection operator which inevitably causes high numerical effort for matrix-matrix and matrix-vector multiplications. Also the creation of the mortar projection operator itself is very costly since it requires the inversion of a non-diagonal, sparse matrix that is of global problem size. The use of dual shape functions based on biorthogonality conditions would significantly increase the computational efficiency of a mortar based projection operator, since they localize the coupling effect and lead to a NTS like, decoupled algebraic structure of the information transfer. Furthermore, the mentioned inversion of a global matrix becomes very efficient because it can be created in a way that it becomes of diagonal form. Up to now, the use of dual shape functions for coupling operators in a completely 3D setting for first- and second-order elements cannot be found in existing literature.

Application to general monolithic multiphysics problems In the existing literature, multiphysics problems are predominantly discretized in a NTN manner, meaning that nodes of the discretized single-fields match. In contrast, volume coupled multiphysics with different meshes for the involved physical fields are often highly desirable in terms of solution accuracy and computational costs. A first approach for multiphysics coupling on different meshes was outlined in Dureisseix and Bavestrello [64], but with restrictions to partitioned coupling schemes in a 2D setting. A comprehensive methodology for multiphysics simulations on non-matching and non-conforming meshes at the boundaries cannot be found in the existing literature so far.

Extension of the general coupling approach for monolithic multiphysics problems towards contact mechanics While the simulation of volume coupled problems on non-matching meshes is a rarely focused topic, the extension of such approaches towards contact mechanics problems, like thermo-structure-contact interaction, is a completely unanswered question. When considering a body with non-matching volume meshes in the most general case, usually its interface discretizations are also non-matching. Thus, a further coupling of the interface quantities, e.g. possibly employed Lagrange multipliers, is required in this case. Furthermore, the computational contact interaction with a second body in a finite deformation regime generally leads to non-matching interface meshes between these two bodies, see Chapter 3. Consequently, a very

complex interface and volume coupling scheme arises for such scenarios, which is presented throughout this thesis.

Extendable implementation regarding general volume coupled problems Despite the mentioned application to volume coupled multiphysics problems, the consideration of overlapping volumes with different meshes is also required for many other applications, such as remeshing schemes and so-called zooming procedures. The implementation of the presented algorithms can be realized in very general manner to allow for employing similarities for a bunch of numerical application such as a Hu-Washizu approach for first-order tetrahedral elements (cf. Lamichhane et al. [149]), a novel and computationally efficient algorithm for fluid-structure interaction problems and many more methods.

6.1.3. Proposal for a mortar approach for general volume coupled problems

The most important ingredients and new scientific contributions of the presented volume coupling approaches are given in the following:

- implementation of a mortar projection operator for nodal information transfer for 3D problems based on dual shape functions for first- and second-order elements, see also Farah et al. [70].
- application of the mortar based projection operator to various monolithic multiphysics problems, see also Farah et al. [70].
- extension of the coupling methodology for multiphysics problems on non-matching meshes towards computation contact mechanics.

Summing up, this chapter combines the gained knowledge of dual shape functions with volume coupled projection operators and provides a general and comprehensive methodology for volume coupled problems on different meshes.

6.2. Fundamentals on volume projection of nodal information

When dealing with incompatible meshes, the field s_1 defined on mesh Ω_1 is going to be transferred to mesh Ω_2 resulting in the field s_2 . The fields are represented by global vectors storing nodal values \mathbf{s}_i and finite element shape functions associated with the corresponding mesh \mathbf{N}_i for $i = 1, 2$. The total number of nodes for the meshes Ω_1 and Ω_2 is n_1 and n_2 , respectively. A connection between discrete nodal values on both meshes is given by

$$\mathbf{s}_2 = \mathbf{P}_{21} \mathbf{s}_1, \quad (6.1)$$

where \mathbf{P}_{21} is the projection operator to map from mesh Ω_1 to Ω_2 .

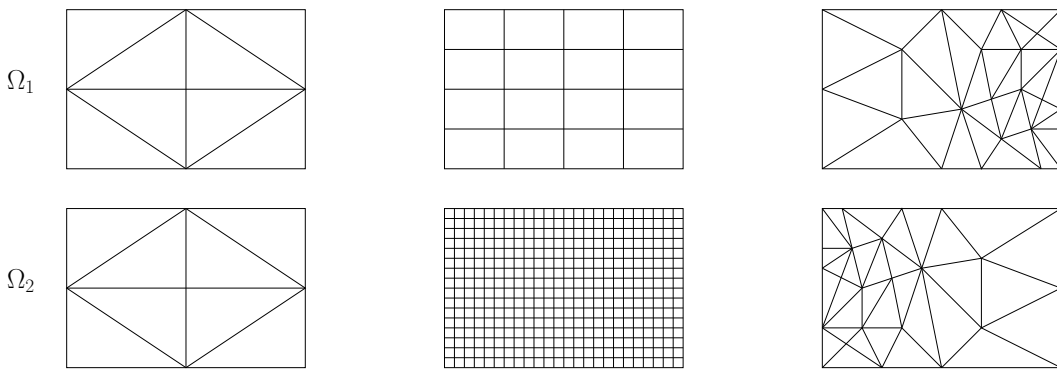


Figure 6.1: Representative mesh-to-mesh situations for nodal information transfer, adopted from [64]. From left to right: matching grids, nested meshes, dissimilar meshes. Figure taken from Farah et al. [70].

Throughout this thesis, various meshes will be compared in order to analyze the diverse demands on the information transfer methodology. For this purpose, a nomenclature for different mesh-to-mesh constellations is introduced and is shown in Figure 6.1. This classification is adopted from Dureisseix and Bavestrello [64] and was also employed in Farah et al. [70]. It consists of

- Matching grids: This case represents the most simple setting, where each node of the source mesh can be mapped onto a corresponding node of the target mesh.
- Nested meshes: Here, the finer mesh is able to exactly represent solutions based on the coarser mesh.
- General case of dissimilar meshes: This is the most difficult case with arbitrary dissimilar mesh sizes.

Within this thesis, two different approaches to define this projection operator are considered, namely the *collocation approach* and the *mortar approach*. Their basic work principle is demonstrated with a 1D example consisting of two first-order elements that are supposed to represent a Gaussian distribution, see Figure 6.2. In the left subfigure, the boundary between the elements is at $x = 0.0$, meaning that the middle node coincides with the location of the peak of the Gaussian distribution. The right subfigure represents a setting, where the middle node is located at $x = -3.0$, which corresponds to a value being nearly zero. It can be nicely seen that the collocation method fulfills information transfer point-wise at the nodes, whereas the mortar approach enforces the integral of the difference between the prescribed reference curve and the finite element approximation to be equal to zero, which fits very well to the philosophy of the finite element method. A detailed introduction of the two mentioned approaches to carry out the information transfer is given in the following subsections. Throughout this thesis, it is assumed without specifically addressing this topic that intersecting elements of the two meshes are found by an underlying search algorithm, see for example Massing et al. [162].

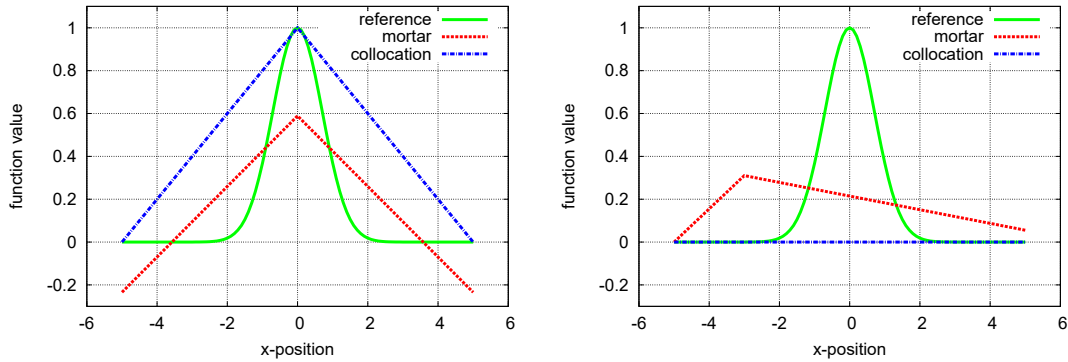


Figure 6.2: Two-element example of field transfer of a Gaussian distribution with the collocation approach and the mortar approach: placement of the middle node, i.e. element boundary at $x = 0.0$ (left) and at $x = -3.0$ (right). Figure taken from Farah et al. [70].

6.2.1. Derivation of the mortar method

The mortar method, originally developed in Bernardi et al. [25, 26] and Maday et al. [160], is based on the conservation of work between two different dual fields, i.e. the mortar method has a sound variational basis. In the context of computational contact mechanics, this is employed via the duality of the Lagrange multipliers and the displacement field, see Chapters 3 and 4. However, in the following, a more general approach is derived based on an abstract dual field d_2 , which is defined by its interpolation

$$d_2 = \Phi_2 \mathbf{d}_2. \quad (6.2)$$

It is employed for the transfer of the field s_1 defined on mesh Ω_1 onto mesh Ω_2 to get s_2 . The field d_2 is dual to the target field s_2 and the shape functions Φ_2 of the dual field d_2 are defined on nodes associated with mesh Ω_2 and can be chosen to be the same as for the field s_2 . However, dual shape functions which were already introduced in Section 3.4.1.2 will be extended towards 3D problems in Section 6.2.3 to increase numerical efficiency when used for the interpolation of d_2 . The energy pairing between field d_2 and s_2 reads

$$\langle d_2, s_2 \rangle_{\Omega_2} = \int_{\Omega_2} d_2 s_2 d\Omega_2 = \mathbf{d}_2^T \int_{\Omega_2} \Phi_2^T \mathbf{N}_2 d\Omega_2 \mathbf{s}_2 = \mathbf{d}_2^T \mathbf{D}_2 \mathbf{s}_2, \quad (6.3)$$

with the first mortar matrix \mathbf{D}_2 having characteristics of a mass matrix. Specifically, it is symmetric and positive definite and therefore invertible. Herein, the integral is defined over the target mesh Ω_2 . For the energy pairing of field s_1 , the same dual field as for s_2 is employed, which results in the expression

$$\langle d_2, s_1 \rangle_{\Omega_2} = \int_{\Omega_2} d_2 s_1 d\Omega_2 = \mathbf{d}_2^T \int_{\Omega_2} \Phi_2^T \mathbf{N}_1 d\Omega_2 \mathbf{s}_1 = \mathbf{d}_2^T \mathbf{M}_{21} \mathbf{s}_1. \quad (6.4)$$

The arising second mortar matrix \mathbf{M}_{21} is obtained by integrating a product of two shape functions defined on different meshes. Again, integration is performed over Ω_2 . By considering the

interface mortar matrices resulting from the contact formulation in (3.35) and (3.36), it becomes obvious that these matrices are strongly related to the mortar matrices for volume information transfer. Enforcing equality of the energy pairings yields

$$\mathbf{d}_2^T \mathbf{D}_2 \mathbf{s}_2 = \mathbf{d}_2^T \mathbf{M}_{21} \mathbf{s}_1, \quad (6.5)$$

which holds for any discrete dual field \mathbf{d}_2 . Thus, the mortar operator \mathbf{P}_{21}^m reads

$$\mathbf{s}_2 = \mathbf{D}_2^{-1} \mathbf{M}_{21} \mathbf{s}_1 = \mathbf{P}_{21}^m \mathbf{s}_1. \quad (6.6)$$

In addition, creation of the opposing projector \mathbf{P}_{12}^m can be realized by defining a dual field d_1 defined on nodes associated with Ω_1 and formulating the energy pairings over Ω_1 . The resulting projector \mathbf{P}_{12}^m is consequently defined as

$$\mathbf{s}_1 = \mathbf{D}_1^{-1} \mathbf{M}_{12} \mathbf{s}_2 = \mathbf{P}_{12}^m \mathbf{s}_2. \quad (6.7)$$

Evaluation of the arising mortar matrices causes the arguably quite high complexity of this approach. A detailed explanation on this topic is given in Section 6.2.4. For this purpose, the mortar matrices are reformulated as nodal blocks with problem specific dimensions. Concretely, the nodal blocks of the first mortar matrices \mathbf{D}_i for $i = 1, 2$ read

$$\mathbf{D}_1[a, b] = D_{1,ab} \mathbf{I}_{\text{ndof}} = \int_{\Omega_1} \Phi_{1,a} N_{1,b} \, d\Omega_1 \mathbf{I}_{\text{ndof}}, \quad a = 1, \dots, n_1, \quad b = 1, \dots, n_1, \quad (6.8)$$

$$\mathbf{D}_2[p, q] = D_{2,pq} \mathbf{I}_{\text{ndof}} = \int_{\Omega_2} \Phi_{2,p} N_{2,q} \, d\Omega_2 \mathbf{I}_{\text{ndof}}, \quad p = 1, \dots, n_2, \quad q = 1, \dots, n_2, \quad (6.9)$$

with the identity matrix \mathbf{I}_{ndof} defining the size of the nodal block based on the number of degrees of freedom per node. Correspondingly, the nodal blocks for the second mortar matrices \mathbf{M}_{ij} for $i, j = 1, 2$, $i \neq j$ are formulated as

$$\mathbf{M}_{12}[a, l] = M_{12,al} \mathbf{I}_{\text{ndof}} = \int_{\Omega_1} \Phi_{1,a} N_{2,l} \, d\Omega_1 \mathbf{I}_{\text{ndof}}, \quad a = 1, \dots, n_1, \quad l = 1, \dots, n_2, \quad (6.10)$$

$$\mathbf{M}_{21}[p, g] = M_{21,pg} \mathbf{I}_{\text{ndof}} = \int_{\Omega_2} \Phi_{2,p} N_{1,g} \, d\Omega_2 \mathbf{I}_{\text{ndof}}, \quad p = 1, \dots, n_2, \quad g = 1, \dots, n_1. \quad (6.11)$$

It has been shown in Dureisseix and Bavestrello [64] that the mortar projector satisfies the patch test and yields the same results as the collocation approach for nested meshes. Furthermore, the mortar operator reduces to the identity operator for matching meshes, which confirms the consistency of this method.

6.2.2. Degeneration to collocation method

The simplest possible projection operator can be created by a collocation approach, see Ortiz and Quigley [190] and Saksono and Perić [238]. Here, the interpolation of the field s_1 on mesh Ω_1 is employed to calculate the nodal values of the second mesh Ω_2 , i.e. to get s_2 . This is done in a point-wise (node-wise) sense which can be interpreted as mortar approach with shape functions of the dual field Φ becoming so-called Dirac impulses at the nodes. These Dirac functions are defined to be infinity at the corresponding nodes and zero at all other points. With these

Dirac functions, the integral (weak) conservation of the energy pairings reduces to a point-wise conservation. Therefore, the collocation approach is considered as degenerated mortar method. However, in practice, the physical position $\mathbf{X}_{2,k}$ of a node $n_{2,k}$ of mesh Ω_2 is going to be expressed in parameter space coordinates of a corresponding finite element $e_{1,m}$ of mesh Ω_1 as

$$\mathbf{X}_{2,k} - \sum_{i=1}^{n_{e_{1,m}}} N_{1,i}(\hat{\xi}) \mathbf{X}_{1,i} = \mathbf{0}. \quad (6.12)$$

Here, the sought-after parameter space position within element $e_{1,m}$ is $\hat{\xi}$ and n_{e_m} is the number of nodes attached to element $e_{1,m}$. The shape function $N_{1,i}$ is associated with the mesh Ω_1 and the index i corresponds to the local node numbering of element $e_{1,m}$. Solving this nodal parameter space projection can be achieved by employing a local Newton-Raphson scheme for each node of mesh Ω_2 . Due to the isoparametric concept underlying the finite element method, the obtained parameter space coordinate is used as interpolation of the field. The resulting projection operator reads

$$\mathbf{P}_{21}^c[j, l] = P_{21,jl}^c \mathbf{I}_{\text{ndof}} = N_{1,l}(\hat{\xi}_j) \mathbf{I}_{\text{ndof}}, \quad j = 1, \dots, n_2, \quad l = 1, \dots, n_1. \quad (6.13)$$

The size of the identity matrix $\mathbf{I}_{\text{ndof}} \in \mathbb{R}^{\text{ndof} \times \text{ndof}}$ is determined by the number of degrees of freedom ndof of each node. Construction of the opposing projection operator \mathbf{P}_{12}^c , which allows for information transfer from mesh Ω_2 to Ω_1 , is rather straightforward and basically requires the evaluation of the parameter space coordinates for nodes of mesh Ω_1 within element associated to mesh Ω_2 .

The computational costs for the collocation approach are quite low and mainly caused by having to solve a local Newton-Raphson scheme for the parameter space mapping. While appealingly simple, this method can still be termed as being consistent, since it is able to represent the identity operator for a matching grid case. Furthermore, this easy-to-implement approach satisfies the patch test Zienkiewicz and Taylor [306], because it allows for exact projection when the solution can be represented on both meshes, see Section 6.2.7.1.

6.2.3. Dual shape functions

For all considered coupled multiphysics problems which are going to be involved in the nodal information transfer within this thesis, the same solution space \mathcal{S} for the primary quantities of interest is employed. However, it is important to point out that there exist problems where this restriction is not valid due to stability reasons, like for example in fluid simulations. The solution space corresponds to an arbitrary continuous field s and reads

$$\mathcal{S} = \{s \in H^1(\Omega) \mid s(\mathbf{X}, t) = \hat{s}(\mathbf{X}, t) \text{ on } \partial\Omega_d\}. \quad (6.14)$$

Herein, $H^1(\Omega)$ denotes again the well-known Sobolev space of functions with square integrable values and first derivatives. Moreover, Ω is the continuous volume on which the problem is defined and $\partial\Omega_d$ is its Dirichlet boundary with prescribed values $\hat{s}(\mathbf{X}, t)$. For discretization in space into the considered non-matching meshes Ω_i for $i = 1, 2$, standard isoparametric, Langrangian finite elements are employed. This defines the usual finite dimensional subsets $\mathcal{S}_{i,h}$ for $i = 1, 2$, that are approximations of \mathcal{S} .

As it is aimed at solving monolithic systems of equations for coupled multiphysics problems, a globally assembled projection operator is required. At this point, it becomes obvious that inverting the first mortar matrices \mathbf{D}_i for $i = 1, 2$ in Equations (6.6) and (6.7) constitutes the major drawback of the standard mortar approach. For the mortar projection operators, any single nodal value on one mesh globally affects the entire other mesh and vice versa. However, there is a possibility to localize the influence domain (support) onto which a certain nodal value is mapped. Algebraically, this localized form is characterized by the mortar matrices \mathbf{D}_i for $i = 1, 2$ becoming diagonal. This can be achieved by employing the already introduced dual shape functions which are based on a biorthogonal relationship with the standard shape functions for the interpolation of the dual fields d_i for $i = 1, 2$, see Section 3.4.1.2. Within mortar methods for computational contact problems and wear modeling these dual shape functions have been successfully employed in Chapters 3, 4 and 5. However, in the following, these dual shape functions will be extended towards 3D problems.

6.2.3.1. Extension to 3D problems

For 4-node tetrahedral elements in 3D, dual shape functions have been used in Lamichhane [148], Lamichhane et al. [149] and Tkachuk and Bischoff [272]. However, up to the best knowledge of the author, dual shape functions for all other types of 3D Lagrangian finite elements have not yet been analyzed in recent publications. In order to be able to vary not only the mesh ratio, but also the element types and their polynomial order, dual shape functions for commonly used first- and second-order finite elements need to be considered in the following. The basic construction methodologies as described in Section 3.4.1.2 are still valid but will be shortly reviewed here. Thus, the biorthogonality condition for dual shape functions can be realized as linear combination of standard shape functions. Again, this can be written as multiplication of a vector containing standard shape functions within each element with an element coefficient matrix \mathbf{C}_e :

$$\Phi_j(\xi) = c_{jk} N_k(\xi), \quad \mathbf{C}_e = [c_{jk}] \in \mathbb{R}^{n_e \times n_e}. \quad (6.15)$$

The coefficient matrix itself reads

$$\mathbf{C}_e = \mathbf{D}_e \mathbf{M}_e^{-1}, \quad (6.16)$$

$$\mathbf{D}_e = [d_{jk}] \in \mathbb{R}^{n_e \times n_e}, \quad d_{jk} = \delta_{jk} \int_e N_k(\xi) J(\xi) de, \quad (6.17)$$

$$\mathbf{M}_e = [m_{jk}] \in \mathbb{R}^{n_e \times n_e}, \quad m_{jk} = \int_e N_j(\xi) N_k(\xi) J(\xi) de. \quad (6.18)$$

All these steps are based on the assumption that the number of nodes carrying discrete unknowns from the abstract dual fields d_i are equal to the nodes of the fields s_i , for $i = 1, 2$. The only difference compared to the construction rules for 2D elements is the integration of a volume element instead of a surface element. For the sake of clearness, the dual shape function of one node is shown for a regular hex8 element in Figure 6.3. Here, a dual shape function and a standard shape function are visualized for the red marked node at the bottom left with help of 4 characteristic slides (a-d) through the element. It can be nicely seen that the green shape function is of zero value at all nodes except its own (red) node, where a positive value occurs (not visualized in

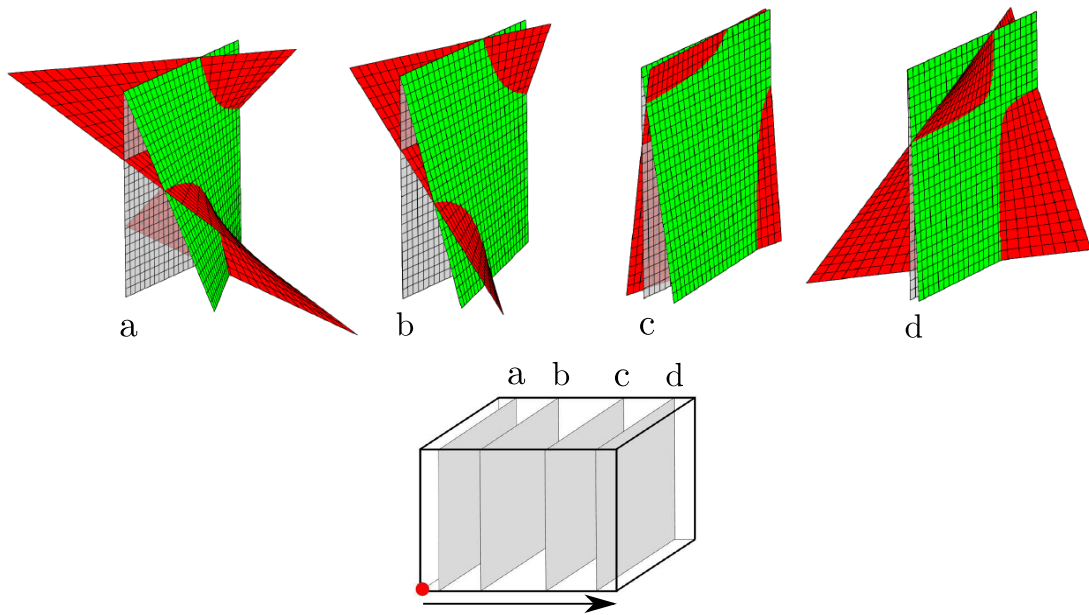


Figure 6.3: Standard (green) and dual (red) shape functions of the red node for an undistorted 4-node hexahedral element. Visualization is realized at 4 slices a-d.

Figure 6.3). When going from slide a to d, the value at the red node continuously decreases till it is zero. This corresponds to the general knowledge of standard shape functions. The dual shape function behaves completely different. It is discontinuous at the element boundaries and have higher values at the nodes. In addition, it changes the sign of its values, which is also well-known for 2D dual shape functions, see Popp et al. [213]. Special treatment of second-order shape functions in 3D is discussed in the following subsection.

6.2.3.2. Basis transformation for second-order elements

The creation of dual shape functions relies on the fact that the integrals of standard shape functions in (6.17) and (6.18) lead to non-zero values. Whereas this condition is readily fulfilled for first- and second-order elements for the integral in (6.18), non-zero values for the integral in (6.17) are only assured for first-order interpolation. This becomes obvious for a second-order, i.e. 10-node, tetrahedral element that is slightly distorted as shown in Figure 6.4. Here, the three edge nodes are relocated in such a way that the integral of the shape function associated with the top corner node vanishes. To overcome this problem, a simple basis transformation is employed for the standard shape functions as previously introduced for surface elements in the context of mortar contact algorithms, see Popp et al. [213]. The basic idea is to shift shape function values from edge to corner nodes to guarantee not only non-zero integral values in (6.17), but integral positivity. This is possible because the shape functions associated with the edge nodes are strictly positive for 10-node tetrahedral (tet10) elements. The modified shape functions due to the basis transformation are denoted with \tilde{N} . The corresponding dual shape functions are then built based

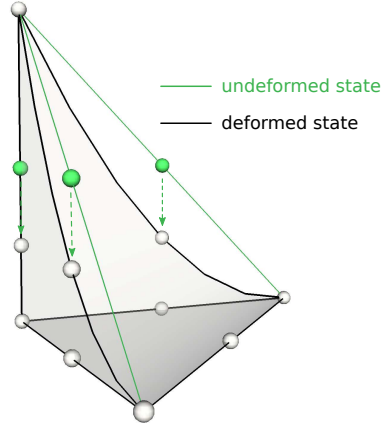


Figure 6.4: Critical scenario for a second-order (10-node) tetrahedral element: the undeformed domain represents the reference tetrahedron. In the deformed state, the marked edge nodes are moved downwards. The deformed state leads to a zero value for the standard shape function of the top node. Figure taken from Farah et al. [70].

on the transformed shape functions, viz.

$$\int_{e_i} \Phi_{i,j} \tilde{N}_{i,k} d\mathbf{e}_i = \delta_{jk} \int_{e_i} \tilde{N}_{i,k} d\mathbf{e}_i, \quad j, k = 1, \dots, n_{e_i}, \quad i = 1, 2. \quad (6.19)$$

There are a lot of possible basis transformations available, which can all sufficiently shift shape function values in a way that the integral positivity condition is fulfilled. In the following, one simple basis transformation is exemplarily shown for a tet10 element. This simple basis transformation will be employed for all numerical examples with second-order interpolation in this chapter. Based on a node numbering, where first all corner nodes are listed and afterwards all edge nodes, the basis transformation for a tet10 element reads

$$\begin{bmatrix} \tilde{N}^1 & \tilde{N}^2 & \tilde{N}^3 & \tilde{N}^4 & \tilde{N}^5 & \tilde{N}^6 & \tilde{N}^7 & \tilde{N}^8 & \tilde{N}^9 & \tilde{N}^{10} \end{bmatrix} = \underbrace{\begin{bmatrix} N^1 \\ N^2 \\ N^3 \\ N^4 \\ N^5 \\ N^6 \\ N^7 \\ N^8 \\ N^9 \\ N^{10} \end{bmatrix}^T \cdot \begin{bmatrix} 1 & 0 & 0 & 0 & 0 & 0 & 0 & 0 & 0 & 0 \\ 0 & 1 & 0 & 0 & 0 & 0 & 0 & 0 & 0 & 0 \\ 0 & 0 & 1 & 0 & 0 & 0 & 0 & 0 & 0 & 0 \\ 0 & 0 & 0 & 1 & 0 & 0 & 0 & 0 & 0 & 0 \\ \alpha_q & \alpha_q & 0 & 0 & 1 - 2\alpha_q & 0 & 0 & 0 & 0 & 0 \\ 0 & \alpha_q & \alpha_q & 0 & 0 & 1 - 2\alpha_q & 0 & 0 & 0 & 0 \\ \alpha_q & 0 & \alpha_q & 0 & 0 & 0 & 1 - 2\alpha_q & 0 & 0 & 0 \\ \alpha_q & 0 & 0 & \alpha_q & 0 & 0 & 0 & 1 - 2\alpha_q & 0 & 0 \\ 0 & \alpha_q & 0 & \alpha_q & 0 & 0 & 0 & 0 & 1 - 2\alpha_q & 0 \\ 0 & 0 & \alpha_q & \alpha_q & 0 & 0 & 0 & 0 & 0 & 1 - 2\alpha_q \end{bmatrix}}_{\mathbf{T}_e}. \quad (6.20)$$

This transformation matrix is symmetric, since it shifts edge node contributions equally to the adjacent corner nodes. Furthermore, partition of unity is assured, which simplifies the construction of the corresponding dual shape functions. The transformation parameter α_q has to be chosen large enough to guarantee integral positivity of the edge node shape functions, but is obviously limited by $\alpha_q < \frac{1}{2}$. Based on these considerations and the numerical experience, the transformation parameter is defined as $\alpha_q = \frac{1}{3}$. By modifying the standard shape functions, the interpolation of the continuous fields s_i for $i = 1, 2$ can be alternatively expressed with basis transformed nodal quantities

$$s_i = \mathbf{N}_i s_i = \tilde{\mathbf{N}}_i \tilde{s}_i. \quad (6.21)$$

A consistent node-wise assembly of the element transformation matrix \mathbf{T}_e in (6.20) yields the global transformation matrices \mathbf{T}_i for quantities on meshes Ω_i for $i = 1, 2$, viz.

$$\mathbf{s}_i = \mathbf{T}_i \tilde{\mathbf{s}}_i. \quad (6.22)$$

The global transformation matrices are sparse and have the same dimensions as the corresponding \mathbf{D} matrices. Applying the basis transformation for the duality pairing in (6.3) yields

$$\langle d_i, s_i \rangle_{\Omega_i} = \mathbf{d}_i^T \tilde{\mathbf{D}}_i \tilde{\mathbf{s}}_i = \mathbf{d}_i^T \tilde{\mathbf{D}}_i \mathbf{T}_i^{-1} \mathbf{s}_i. \quad (6.23)$$

Here, the mortar matrices $\tilde{\mathbf{D}}_i$ are square and diagonal due to the biorthogonality condition in (6.19) for the modified shape functions. Now, the final mortar projection operators for the non-modified quantities can be simply formulated by multiplying the transformation matrix and the basis-transformed projection operator:

$$\mathbf{s}_2 = \mathbf{T}_2 \tilde{\mathbf{D}}_2^{-1} \mathbf{M}_{21} \mathbf{s}_1 = \mathbf{T}_2 \tilde{\mathbf{P}}_{21}^m \mathbf{s}_1 = \mathbf{P}_{21}^m \mathbf{s}_1, \quad (6.24)$$

$$\mathbf{s}_1 = \mathbf{T}_1 \tilde{\mathbf{D}}_1^{-1} \mathbf{M}_{12} \mathbf{s}_2 = \mathbf{T}_1 \tilde{\mathbf{P}}_{12}^m \mathbf{s}_2 = \mathbf{P}_{12}^m \mathbf{s}_2. \quad (6.25)$$

With this modification at hand, the mortar approach for information transfer can be robustly employed for general second-order finite elements without loss of computational efficiency.

6.2.4. Integration schemes

No matter whether interface or volume coupled problems are considered, one of the major issues with regard to mortar methods is the design of adequate numerical integration schemes. Thus, strong similarities to the already introduced and developed integration schemes from Chapter 3 and Chapter 4 can be identified. The reason for the complex numerical integration is that the arising integrals contain a product of shape functions defined on different meshes, as can be seen in (6.4). The locally supported shape functions obviously have kinks at element nodes, edges and surfaces. Thus, non-matching meshes generally lead to a numerical integration over discontinuities. The way these discontinuities are treated crucially influences the efficiency and the accuracy of the integral evaluation. As already mentioned in the previous chapters, basically, two different types of integration procedures exist, which will be termed segment-based integration and element-based integration in the following. A detailed explanation of these integration schemes in the context of volume problems is given in the next subsections.

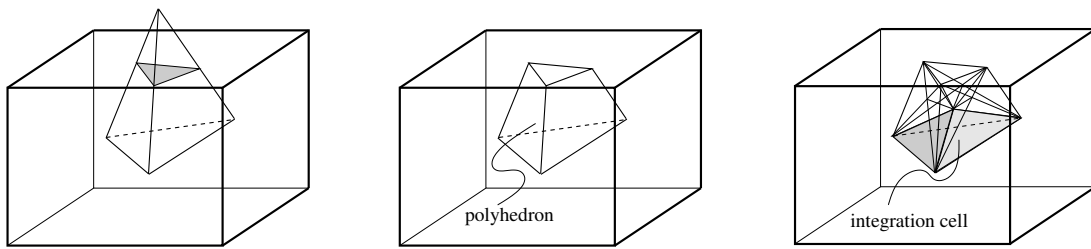


Figure 6.5: Main steps for 3D segment-based element coupling: initial state (left), polyhedron creation (middle) and tessellation (right). Figure taken from Farah et al. [70].

6.2.4.1. Segment-based integration

Having in mind the arising discontinuities within the integral in (6.4), the most intuitive way to perform numerical integration is to decompose the integration domain into parts containing only smooth shape function contributions from both meshes, see for example Dureisseix and Bavestrello [64], Popp et al. [211] and Puso and Laursen [218]. To maintain the introduced nomenclature for the evaluation processes of mortar terms from Section 4.8.6, this procedure will be called segment-based integration here. For 2D "volume" coupled problems, the segmentation procedure is identical to an integral evaluation of 3D interface coupled problems as introduced in Section 3.4.2. Therefore, the interested reader is referred to the mentioned section for a detailed algorithm of the 2D segment-based integration.

For the 3D case, the segmentation procedure becomes more intricate, but the underlying algorithmic concepts are nearly the same as for the 2D case. Instead of creating clip polygons, a polyhedron is created as overlapping volume of two elements. This polyhedron is then tessellated to create tetrahedra, see Figure 6.5. Afterwards, numerical integration is performed on these tetrahedral integration cells that contain only smooth contributions from both element shape functions. However, there are alternative, arguably more efficient approaches to integrate the polyhedron itself without further subdivision based on moment fitting algorithms or the direct divergence theorem, see Sudhakar and Wall [264] and Sudhakar et al. [265]. Yet, general integration procedures for arbitrary polyhedra are not the main topic of this thesis and therefore a 3D tessellation scheme is employed for segment-based integration here. For second-order elements, this segmentation procedure becomes even more intricate due to the possibly strongly curved element surfaces and edges. Usually, this problem is tackled by a subdivision of the second-order elements into first-order integration domains, i.e. the domain of a 27-node hexahedral is approximated by eight 8-node hexahedrals on which numerical integration is performed. However, a segment-based integration for second-order elements is not employed in the following. Thus, only first-order elements can be treated with segment-based integration scheme and consequently, second-order elements are exclusively evaluated with the element-based integration, which is specified in the following section.

6.2.4.2. Element-based integration

Beside the intuitive and most accurate segment-based integration, the element-based integration scheme can be predominantly found in the literature for mortar-based interface (i.e. surface)

coupling Fischer and Wriggers [80, 81] and was introduced for 3D problems in the context of information transfer due to remeshing procedures in Bussetta et al. [35]. It has been already introduced in Section 4.8.6 as efficient but less accurate alternative to the segment-based integration. This procedure is very attractive from an implementation point of view, because the high complexity and the excessive computational costs of a polygon clipping in 2D or polyhedron tessellation in 3D vanish in favor of an integration over entire element domains. Yet, this also means that the discontinuities arising at element nodes, edges and surfaces are quite simply ignored. The inevitably increased integration errors are tackled by an increased numbers of integration points per element domain. Consequently, this integration scheme strongly depends on the mesh size ratio and thus needs a certain experience of the user to guarantee sufficiently accurate results. However, as stated in Farah et al. [73], for moderate mesh size ratios and if only weak discontinuities arise within the considered domain, the element-based integration scheme is an attractive alternative to the segment-based integration. The general algorithm to construct the mortar operator \mathbf{P}_{21}^m can be directly adapted from Algorithm 4.5, which was introduced for mortar contact problems. However, the general methodology is the same. In contrast to the segment-based approach, the domain on which numerical integration of the opposing mortar operator \mathbf{P}_{12}^m is performed does not generally coincide with \mathbf{P}_{21}^m . Therefore, the creation of \mathbf{P}_{21}^m requires a suitable integration point definition for each element e_1 in Ω_1 in Step 1 of Algorithm 4.5.

Note, that the element-based integration procedure can easily be extended to second-order elements and requires no fundamental change in Algorithm 4.5 to do so. Therefore, it will be the algorithm of choice for 3D second-order elements in this thesis.

6.2.5. Boundary problems

Due to the geometrical approximation inherent to any discretization, incompatibilities on the geometry boundary $\partial\Omega$ could arise. Thus, for curved boundaries the discrete representations defined by the two volumes of the two involved meshes do not match anymore. This situation may become problematic in terms of accuracy for the collocation approach as well as for the mortar method, because nodes and integration points of one mesh are possibly located outside the respective other mesh. In the following, several enhanced strategies for evaluating projection operators in such cases, i.e. for elements and nodes attached to $\partial\Omega$ are introduced and discussed.

6.2.5.1. Collocation method for curved boundaries

When creating the collocation projector \mathbf{P}_{21}^c , some nodes of mesh Ω_2 might lie outside the mesh Ω_1 . Ignoring these critical nodes would lead to catastrophic results for the information transfer, because these critical nodes would not be able to obtain any information from mesh Ω_1 . A possibility to allow information transfer onto these nodes is to perform a geometrical mapping of the node position via a closest-point-projection (cf. Konyukhov and Schweizerhof [139]) onto the boundary of mesh Ω_1 , see Bussetta et al. [35]. The parameter space mapping in (6.12) is then performed with respect to the projected coordinates located on the boundary of mesh Ω_1 . However, this procedure requires implementation of a closest-point-projection in 3D, which must then be locally solved with an additional Newton-Raphson scheme.

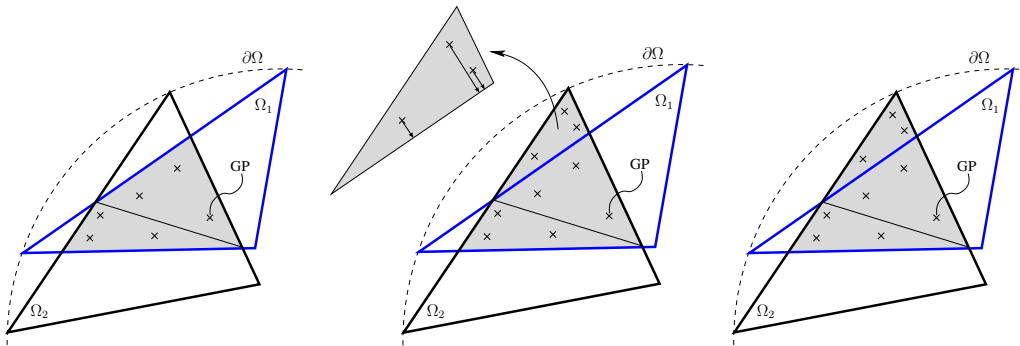


Figure 6.6: Three possible approaches to perform numerical integration of the entries of mortar projector \mathbf{P}_{21}^m at curved boundaries: integration over enclosed volume (left), element-wise integration over Ω_2 with closest-point-projection of integration points onto mesh Ω_1 (middle) and element-wise integration over Ω_2 with possible integration point evaluation outside mesh Ω_1 (right). Figure taken from Farah et al. [70].

In order to avoid this additional effort, a second possibility to evaluate the collocation method on curved boundaries is considered. Here, the closest element of mesh Ω_1 to a considered critical node is employed for the parameter space mapping in (6.12). The sought-after parameter space coordinate will then lie slightly outside the element parameter space boundaries. Nonetheless, this parameter space coordinate can be employed in (6.13) to calculate the projection operator. This can be interpreted as an artificial increase of nodal shape function support for boundary elements. In addition to being appealingly simple, it also does not require any additional geometrical projection of the nodes onto the boundary of mesh Ω_1 and the extent in shape function support for boundary elements is physically motivated, because in a continuous setting both meshes represent the same volume. Therefore, this approach is employed in the following.

6.2.5.2. Mortar method for curved boundaries

For the mortar approach, regardless of which integration procedure is chosen, there are three possible methods to treat such situations, see Figure 6.6. The first and most commonly used approach is to integrate over the enclosed volume, see left sketch in Figure 6.6 and the explanations in Dureisseix and Bavestrello [64]. However, with this approach, the elements attached to the boundaries are not completely integrated and the biorthogonality condition in (3.47) does no longer hold for this reduced integration domain. This problem also arises for mortar contact formulations in case of so-called dropping edge scenarios and could be handled by enforcing the biorthogonality condition for the reduced integration domain only, see Cichosz and Bischoff [45] and Popp et al. [214]. Yet, fulfilling the biorthogonality condition for reduced integration domains in 3D would become very intricate and thus two less complex approaches are introduced, see the middle and right sketches in Figure 6.6. Both approaches are based on an integration over the entire mesh Ω_2 for the projection operator \mathbf{P}_{21}^m or over the entire mesh Ω_1 for \mathbf{P}_{12}^m , respectively. Thus, an actual evaluation of integration points defined outside the other mesh is performed and no modifications concerning the biorthogonality condition have to be introduced.

The first approach for integration point evaluation (middle sketch) is based on a closest-point-projection of all integration points onto the boundary of the attached element. Here, no extension of shape functions support is required, but local Newton-Raphson schemes have to be performed for every integration point. Beside this additional effort for every integration point, an inconsistency in the integral evaluation is introduced here, because the physical integration point coordinates do not match anymore.

For the second approach (right sketch), shape functions of the nearest element to a considered integration point are evaluated at this point, which means that the support of the shape functions is slightly extended. However, the support of the shape functions is not extended when the considered element is employed as integration domain for the opposing projector. Thus, this approach introduces slight inconsistencies in the element evaluation. However, this approach makes lower demands on the computational complexity compared to the previous procedure and performs extremely well in the numerical examples, see Section 6.2.7.2. Therefore, it is exclusively used within this thesis.

6.2.6. Conservation properties of the projections

In the following, some fundamental conservation properties for the projection operators are analyzed. First, the standard patch test is reviewed. Second, weak conservation of nodal information during mesh transfer is investigated with respect to the employed integration domain.

6.2.6.1. Patch test

The scenario where a continuous field s can be exactly represented by the two considered meshes Ω_1 and Ω_2 is considered, i.e.

$$s = \mathbf{N}_1 \mathbf{s}_1 = \mathbf{N}_2 \mathbf{s}_2. \quad (6.26)$$

Then, the patch test is considered to be fulfilled if the projection operator introduces no errors, see Zienkiewicz and Taylor [306].

Since the collocation method is based on a node-wise information tracking as stated in (6.13), the patch test is automatically fulfilled when considering the assumed exact representation of field s by both meshes.

For the mortar method, this reads

$$\mathbf{P}_{21}^m \mathbf{s}_1 = \mathbf{D}_2^{-1} \mathbf{M}_{21} \mathbf{s}_1 = \mathbf{D}_2^{-1} \int_{\Omega_2} \boldsymbol{\Phi}_2^T \mathbf{N}_1 d\Omega_2 \mathbf{s}_1 = \mathbf{D}_2^{-1} \int_{\Omega_2} \boldsymbol{\Phi}_2^T \mathbf{N}_2 d\Omega_2 \mathbf{s}_2 = \mathbf{D}_2^{-1} \mathbf{D}_2 \mathbf{s}_2 = \mathbf{s}_2. \quad (6.27)$$

Thus, the mortar method also passes the patch test. Note, that this fact is completely independent from the chosen integration procedure, see Section 6.2.4.

6.2.6.2. Weak conservation of nodal information

Weak conservation of nodal information is fulfilled if the integral value of a continuous scalar field can be identically reproduced on the two considered meshes Ω_1 and Ω_2 , via

$$\int_{\Omega} s d\Omega = \int_{\Omega_1} \mathbf{N}_1 \mathbf{s}_1 d\Omega_1 = \int_{\Omega_2} \mathbf{N}_2 \mathbf{s}_2 d\Omega_2. \quad (6.28)$$

Following Equations (6.3) and (6.4), the mortar approach reads

$$\mathbf{d}_2^T \int_{\Omega_2} \Phi_2^T \mathbf{N}_2 d\Omega_2 \mathbf{s}_2 = \mathbf{d}_2^T \int_{\Omega_2} \Phi_2^T \mathbf{N}_1 d\Omega_2 \mathbf{s}_1. \quad (6.29)$$

This equation is valid for any discrete vector \mathbf{d}_2 . Therefore, the equation reduces to

$$\int_{\Omega_2} \Phi_2^T \mathbf{N}_2 d\Omega_2 \mathbf{s}_2 = \int_{\Omega_2} \Phi_2^T \mathbf{N}_1 d\Omega_2 \mathbf{s}_1. \quad (6.30)$$

The shape functions Φ_2 of the dual field d_2 fulfill the partition of unity requirement, which guarantees an unchanged integral value. Therefore, weak conservation of nodal information is automatically fulfilled in the mortar formulation for integration over the target mesh Ω_2 , i.e.

$$\int_{\Omega_2} \mathbf{N}_1 \mathbf{s}_1 d\Omega_2 = \int_{\Omega_2} \mathbf{N}_2 \mathbf{s}_2 d\Omega_2. \quad (6.31)$$

Note, however, that for curved boundaries and thus different volumes the weak integral conservation is not completely fulfilled for both domains in general, meaning that

$$\int_{\Omega_1} \mathbf{N}_1 \mathbf{s}_1 d\Omega_1 \neq \int_{\Omega_2} \mathbf{N}_2 \mathbf{s}_2 d\Omega_2. \quad (6.32)$$

The collocation method can be interpreted as a degeneration of the mortar method. Here, the shape functions of the dual field become Dirac functions $\Phi_2 = \delta_2$, being infinity at the corresponding nodes and zero at all other points, which leads to an integral value of 1. Therefore, the integral definition in (6.30) reduces to

$$\mathbf{I}_2 \mathbf{s}_2 = \tilde{\mathbf{N}}_{21} \mathbf{s}_1, \quad (6.33)$$

where \mathbf{I}_2 is the identity matrix and $\tilde{\mathbf{N}}_{21}$ is the collocation matrix. Since the Dirac functions do not fulfill the partition of unity requirement, weak conservation of nodal information is never guaranteed for the collocation approach.

6.2.7. Numerical examples

In the following, the conservation properties of the developed mortar projection operator based on dual shape functions and the collocation projection operator are tested with two examples. First, a classical structural patch test is employed in order to validate the abstract patch test requirement for projection operators as explained in Section 6.2.6.1. Second, the ability of weak conservation of nodal information is validated based on the investigations in Section 6.2.6.2. Therefore, thermal energy is mapped from a source onto a target mesh of a cylindrical body. Thus, also the boundary problems discussed in Section 6.2.5 are considered.

6.2.7.1. Consistency – Patch Test

As a first example, a purely structural patch test is considered. The idea of this first validation setup is to calculate a displacement solution on a first mesh, transfer the displacement field to

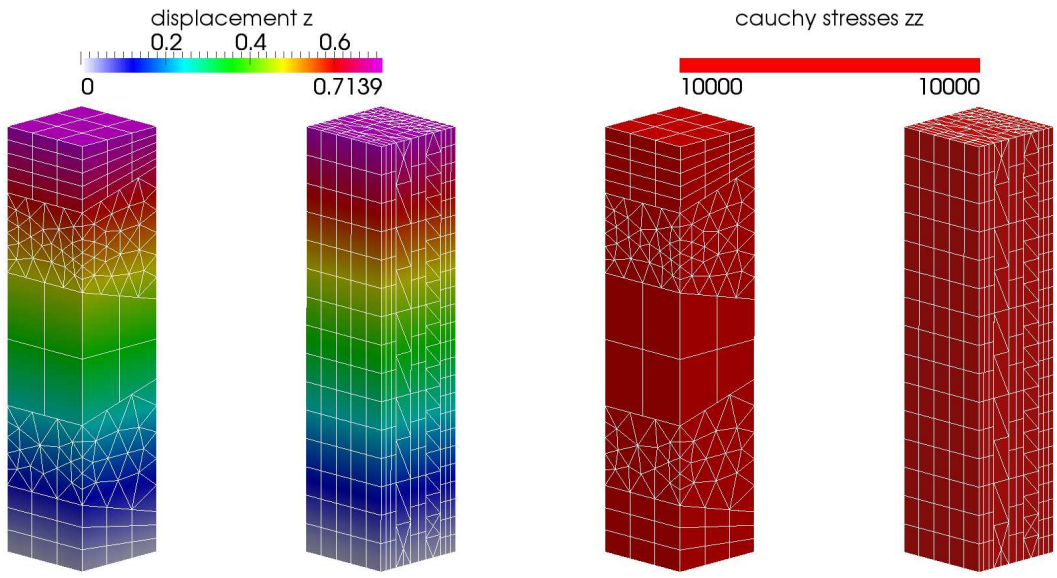


Figure 6.7: 3D structural patch test for combinations of 8-node hexahedral, 20-node hexahedral, 27-node hexahedral, 4-node tetrahedral and 10-node tetrahedral elements. Left subfigure: computed displacement solution on left mesh and projected displacement field on right mesh. Right subfigure: post-processed stress state for both meshes. Figure taken from Farah et al. [70].

a target mesh representing the same geometry and finally evaluate the resulting stress states on both meshes.

The geometrical setting is a cuboid of dimensions $4 \times 4 \times 16$ that is supported at its lower surface such that it is fixed in all directions. A constant pressure load of $p = 10,000$ is applied at the upper surface of the brick, thus leading to a uniaxially stretched deformation state. The material is modeled with a Saint-Venant-Kirchhoff law with Young's modulus $E = 210,000$ and Poisson's ratio $\nu = 0.0$. For both meshes, arbitrary combinations of first-order as well as second-order finite element patches are employed, namely 8-node hexahedral, 20-node hexahedral, 27-node hexahedral, 4-node tetrahedral and 10-node tetrahedral elements. The different patches are connected by mortar mesh tying interfaces. Thus it is related to the structural patch test in Section 4.9.1.1. The first mesh is horizontally divided by several mesh tying interfaces, and the second mesh is vertically divided. This rather academic setup is chosen as challenging as possible, i.e. requiring projections between all involved element types. The projectors for the volumetric mapping are created by the element-based integration scheme and the interface mortar mesh tying is evaluated by a segment-based integration scheme.

The resulting linear displacement field and the corresponding constant stress state on the first mesh are accurate up to machine precision. This is a characteristic feature of the interface mortar mesh tying method, see Puso [216] and the example in Section 4.9.1.1. The volumetric mapping of the displacement field onto the second mesh is done by employing the collocation and mortar projectors. Both projection methods are able to exactly transfer the displacement field, thus leading to the same constant stress state, see Figure 6.7. This result demonstrates that if a solution can be exactly represented on both meshes, the collocation approach as well as the mortar

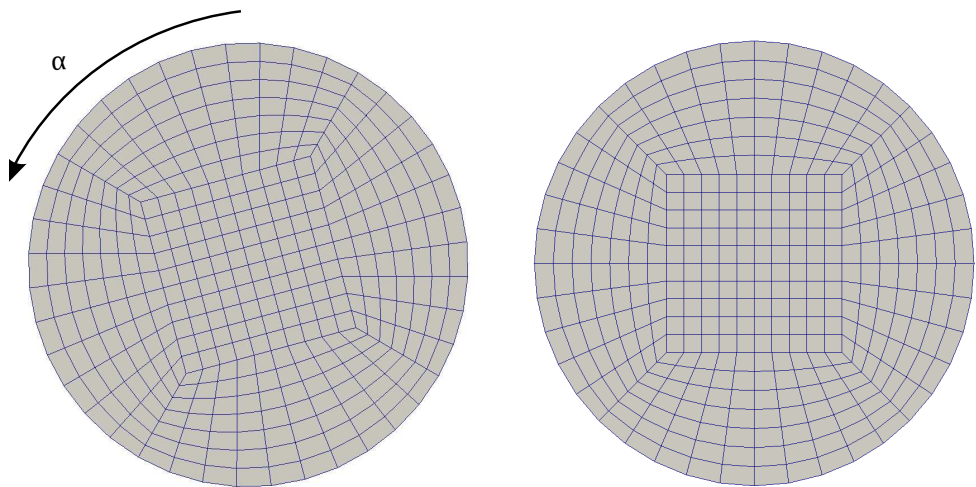


Figure 6.8: Employed fine meshes for the source mesh (left) and the target mesh (right) for a rotation angle of $\alpha = 30^\circ$. Figure taken from Farah et al. [70].

approach do not introduce errors due to the mapping. Thus, as stated in the previous sections, both methods successfully pass the patch test for volume coupling.

6.2.7.2. Weak conservation – Thermal energy

In the following example, conservation properties of the projection methods are discussed with the help of another pure mesh transfer problem. The quantity to map can be interpreted as temperature field and the conservation property tested will be the thermal energy

$$E_\theta = \int_{\Omega} C_V \theta d\Omega, \quad (6.34)$$

with a constant heat capacity C_V . The problem setting includes a cylindrical body, discretized with two different meshes, see Figure 6.8. On the source mesh, a given temperature field $\hat{\theta}(r) = 20 \cdot (1 - e^{0.1r^2})$, that depends on the radial coordinate r of the cylinder will be approximated. Note that the magnitude of $\hat{\theta}$ is deliberately chosen to have its highest value at the boundary of the cylinder in order to make the setup more challenging and to validate the boundary problems described in Section 6.2.5.2. The temperature field is projected onto the target mesh, where the thermal energy is re-evaluated. Thus, the error of the thermal energy on the target mesh with respect to the thermal energy on the source mesh is used as a measure for the global projection error. The target mesh is simply obtained by rotating the source mesh by an angle α around the cylinder axis. In Figure 6.9, the results of the mapping are depicted exemplarily for $\alpha = 15^\circ$. The collocation method was used for the evaluation of the projection operator. Another simulation with the mortar approach gives nearly indistinguishable results. The relative energy error over the rotation angle is depicted for first-order elements (8-node hexahedra) in Figure 6.10. Therein, the mortar and the collocation approach for a coarse mesh with 22 elements (left) and a finer mesh with 760 elements (right) are compared. In case of a zero rotation angle, both variants of course yield a perfect result, since the matching case is reproduced. Also, it becomes clear that the

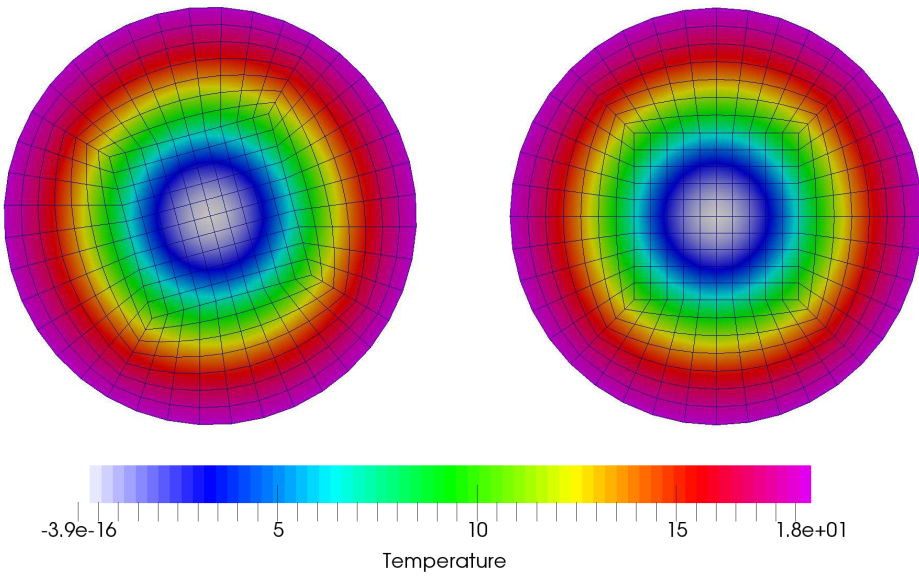


Figure 6.9: Temperature field on source mesh (left) and the target mesh (right) for a rotation angle of $\alpha = 15^\circ$. The collocation method was used for the evaluation of the projection operator. Another simulation with the mortar approach gives nearly indistinguishable results. Figure taken from Farah et al. [70].

coarser the mesh the higher the error, which is due to the non-matching boundary discretizations. Still, the obtained error is small in general. Comparing the two approaches, one can conclude that for all rotation angles other than zero, the mortar approach gives far better results than the collocation method. In addition, the accuracy of the mapping is investigated with a coarse mesh employing second-order elements (27-node hexahedra). As shown in Figure 6.11, the overall relative error of the thermal energy decreases even further as compared with first-order elements. However, the mortar method still yields far better results than the collocation approach.

Finally, the relative local errors of the thermal energy compared to the given temperature field are investigated. The results for the collocation method and the mortar method are shown in Figures 6.12 and 6.13, respectively. It can be seen that the collocation method yields an increased error on the target mesh. In contrast, the mortar method conserves the relative error and thus the discrete thermal energy. These results confirm the analysis of the global energy already presented in Figure 6.10 and demonstrate that the mortar projection operator performs excellently when weak conservation properties are required.

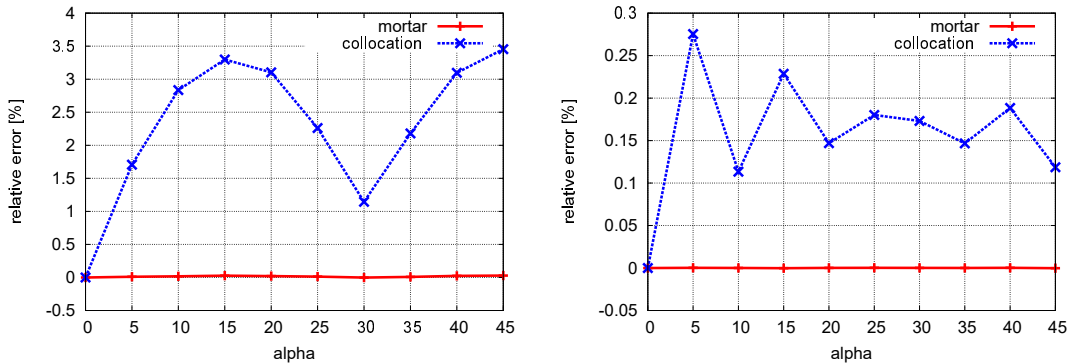


Figure 6.10: Relative error of the thermal energy compared to reference meshes with 8-node hexahedral elements. Results for coarse mesh (left) and finer mesh (right). Visualization for mortar and collocation approach. Figure taken from Farah et al. [70].

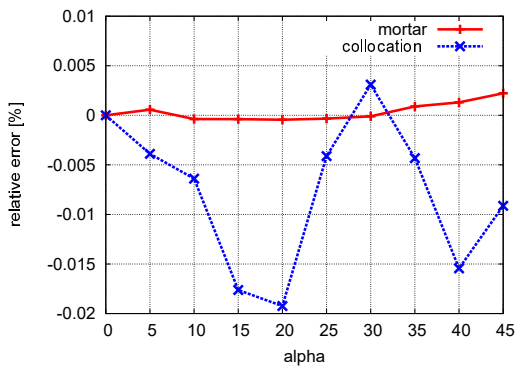


Figure 6.11: Relative error of the thermal energy compared to reference mesh with 27-node hexahedral elements. Results for mortar and collocation approach on a coarse mesh. Figure taken from Farah et al. [70].

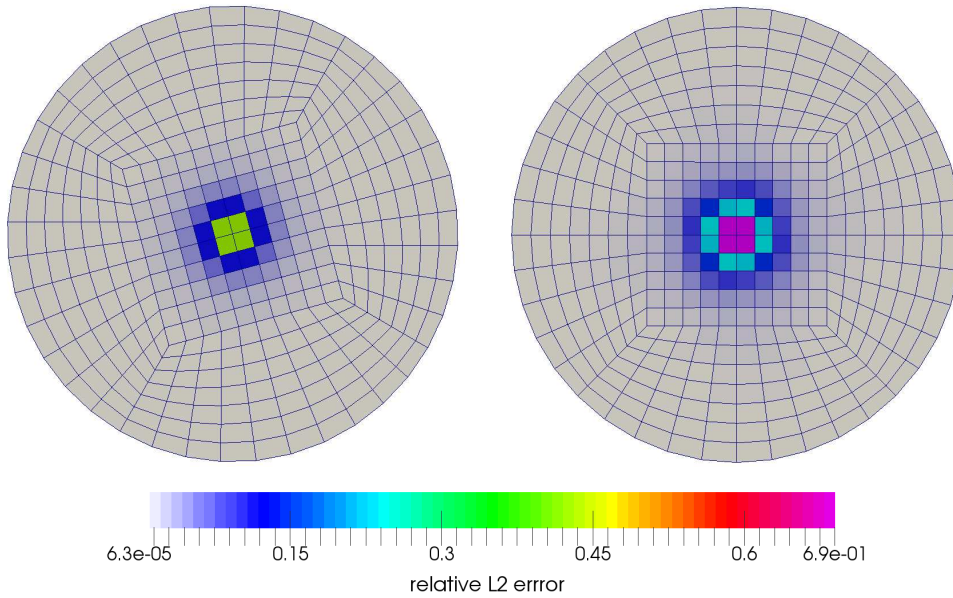


Figure 6.12: Relative L^2 -error of thermal energy compared to analytical solution evaluated on each element for collocation method. Source mesh on the left side, target mesh on the right side. Results are shown for $\alpha = 15^\circ$. Figure taken from Farah et al. [70].

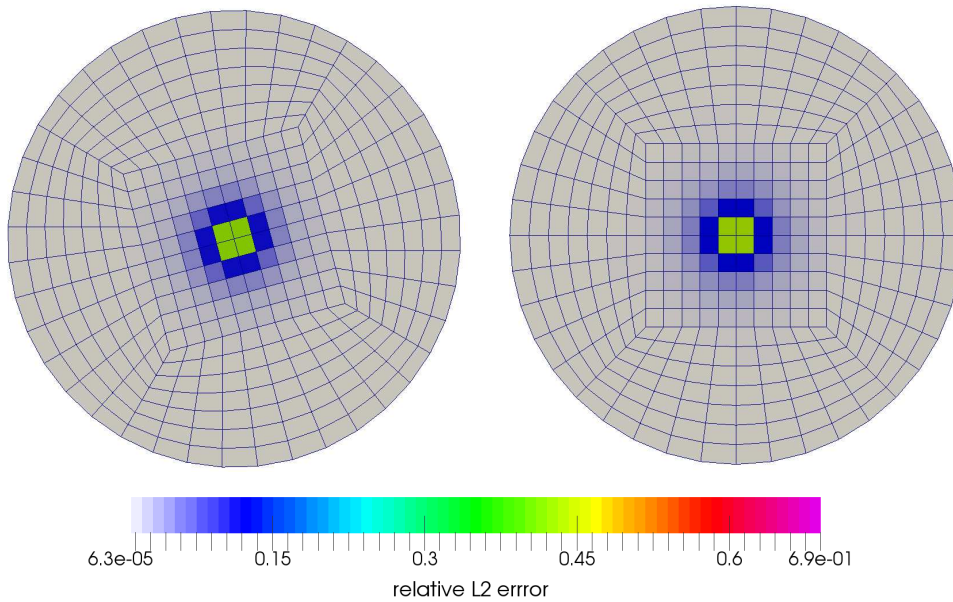


Figure 6.13: Relative L^2 -error of thermal energy compared to analytical solution evaluated on each element for mortar method. Source mesh on the left side, target mesh on the right side. Results are shown for $\alpha = 15^\circ$. Figure taken from Farah et al. [70].

6.3. Volumetric coupling approaches for multiphysics on non-matching meshes

Coupled multiphysics simulations are of high importance in various engineering and biomechanical applications, such as thermo-structure interaction Danowski et al. [52] and porous media mechanics Vuong et al. [278]. Possibly, the demands that each physical field makes on the finite element mesh completely differ from each other depending on the boundary conditions and the underlying partial differential equations. However, the quality of the finite element mesh and the employed shape functions strongly influence the accuracy and robustness of the solution. Therefore, the commonly used approach of matching-grid discretizations for volume coupled multiphysics represents a rather severe restriction, since the mesh size is determined by the field with the highest resolution requirements, thus possibly leading to unnecessary computational costs. This creates a high demand for solution algorithms that allow for different mesh resolutions for the considered sub-problems contained in a multiphysics problem. In the finite element context, this means that a method for transferring nodal values, i.e. motion variables such as displacements and load variables such as forces or stresses, between the discretizations needs to be applied.

In order to allow for such a flexibility in spatial discretization, the general methodology of coupling monolithic multiphysics on different meshes is introduced. Then, the proper enforcement of classical Dirichlet and Neumann boundary condition is for the different meshes is explained. Afterwards, the formulation is extended towards contact mechanics on different meshes and aspects of implementation are outlined. Finally, the formulation is validated with help of several numerical examples.

6.3.1. General methodology

For the sake of simplicity, only two physical fields are considered in the following. However, an extension to three or more fields is possible and rather straightforward. For the abstract spatially discretized problem setting, two discrete sets of primary unknowns \mathbf{p}_1 on Ω_1 and \mathbf{q}_2 on Ω_2 are considered, which represent the solutions of two governing partial differential equations α and β , both defined on the same continuous volume. The auxiliary counterparts of the primary unknowns are \mathbf{p}_2 on Ω_2 and \mathbf{q}_1 on Ω_1 , respectively. These quantities are not explicitly solved, but they are eliminated via the mesh transfer strategy. After spatial discretization, equation α is going to be solved on mesh Ω_1 and β on Ω_2 , respectively. Based on these partial differential equations, the discrete residuals

$$\mathbf{r}_1^\alpha(\mathbf{p}_1, \mathbf{q}_1) = \mathbf{0} \quad \text{and} \quad \mathbf{r}_2^\beta(\mathbf{p}_2, \mathbf{q}_2) = \mathbf{0} \quad (6.35)$$

are defined. The arising system of nonlinear discrete algebraic equations is going to be solved in a fully monolithic manner. As iterative nonlinear solution technique, a standard Newton-Raphson method is employed. This requires a linearization of the residuals with respect to the primary unknowns, which is obtained in complete analogy to Section 2.2.4 from a truncated Taylor series

expansion:

$$\text{Lin } \mathbf{r}_1^\alpha(\mathbf{p}_1^i, \mathbf{q}_1^i) = \mathbf{r}_1^\alpha(\mathbf{p}_1^i, \mathbf{q}_1^i) + \left. \frac{\partial \mathbf{r}_1^\alpha(\mathbf{p}_1, \mathbf{q}_1)}{\partial \mathbf{p}_1} \right|^i \Delta \mathbf{p}_1^{i+1} + \left. \frac{\partial \mathbf{r}_1^\alpha(\mathbf{p}_1, \mathbf{q}_1)}{\partial \mathbf{q}_1} \right|^i \Delta \mathbf{q}_1^{i+1} = \mathbf{0}, \quad (6.36)$$

$$\text{Lin } \mathbf{r}_2^\beta(\mathbf{p}_2^i, \mathbf{q}_2^i) = \mathbf{r}_2^\beta(\mathbf{p}_2^i, \mathbf{q}_2^i) + \left. \frac{\partial \mathbf{r}_2^\beta(\mathbf{p}_2, \mathbf{q}_2)}{\partial \mathbf{p}_2} \right|^i \Delta \mathbf{p}_2^{i+1} + \left. \frac{\partial \mathbf{r}_2^\beta(\mathbf{p}_2, \mathbf{q}_2)}{\partial \mathbf{q}_2} \right|^i \Delta \mathbf{q}_2^{i+1} = \mathbf{0}. \quad (6.37)$$

Here, the upper index i denotes the previously calculated Newton step and $i + 1$ the current one. In order to eliminate the auxiliary quantities $\Delta \mathbf{p}_2^{i+1}$ and $\Delta \mathbf{q}_1^{i+1}$ from the resulting system of equations, the nodal transfer operators

$$\Delta \mathbf{p}_2^{i+1} = \mathbf{P}_{21} \Delta \mathbf{p}_1^{i+1} \quad \text{and} \quad \Delta \mathbf{q}_1^{i+1} = \mathbf{P}_{12} \Delta \mathbf{q}_2^{i+1} \quad (6.38)$$

are employed. Both (6.36) and (6.37) have to be solved within each Newton step. At the end of each Newton step, the incremental solutions $\Delta \mathbf{p}_1^{i+1}$ and $\Delta \mathbf{q}_2^{i+1}$ are used to perform the updates

$$\mathbf{p}_1^{i+1} = \mathbf{p}_1^i + \Delta \mathbf{p}_1^{i+1}, \quad \mathbf{q}_2^{i+1} = \mathbf{q}_2^i + \Delta \mathbf{q}_2^{i+1}, \quad (6.39)$$

and the auxiliary quantities are recovered from the primary unknowns employing (6.38). Finally, the iteration counter is increased by one, i.e. $i \rightarrow i + 1$ and the procedure is repeated until a user-defined convergence criterion is met.

For the sake of clarity, the algebraic form of one Newton step $i + 1$ is given in the following. Based on the truncated Taylor series in (6.36) and (6.37), the following matrix blocks can be identified:

$$\mathbf{K}_{1,\mathbf{p}_1}^\alpha = \left. \frac{\partial \mathbf{r}_1^\alpha(\mathbf{p}_1, \mathbf{q}_1)}{\partial \mathbf{p}_1} \right|^i, \quad \mathbf{K}_{1,\mathbf{q}_1}^\alpha = \left. \frac{\partial \mathbf{r}_1^\alpha(\mathbf{p}_1, \mathbf{q}_1)}{\partial \mathbf{q}_1} \right|^i, \quad (6.40)$$

$$\mathbf{K}_{2,\mathbf{p}_2}^\beta = \left. \frac{\partial \mathbf{r}_2^\beta(\mathbf{p}_2, \mathbf{q}_2)}{\partial \mathbf{p}_2} \right|^i, \quad \mathbf{K}_{2,\mathbf{q}_2}^\beta = \left. \frac{\partial \mathbf{r}_2^\beta(\mathbf{p}_2, \mathbf{q}_2)}{\partial \mathbf{q}_2} \right|^i. \quad (6.41)$$

Here, the blocks in (6.40) are related to the partial differential equation α and the blocks in (6.41) are related to the partial differential equation β , respectively. Now, the global system of algebraic equations can be stated as

$$\begin{bmatrix} \mathbf{K}_{1,\mathbf{p}_1}^\alpha & \mathbf{K}_{1,\mathbf{q}_1}^\alpha & \mathbf{0} & \mathbf{0} \\ \mathbf{0} & \mathbf{0} & \mathbf{K}_{2,\mathbf{p}_2}^\beta & \mathbf{K}_{2,\mathbf{q}_2}^\beta \\ \mathbf{M}_{21} & \mathbf{0} & -\mathbf{D}_2 & \mathbf{0} \\ \mathbf{0} & -\mathbf{D}_1 & \mathbf{0} & \mathbf{M}_{12} \end{bmatrix}^i \begin{bmatrix} \Delta \mathbf{p}_1 \\ \Delta \mathbf{q}_1 \\ \Delta \mathbf{p}_2 \\ \Delta \mathbf{q}_2 \end{bmatrix}^{i+1} = - \begin{bmatrix} \mathbf{r}_1^\alpha \\ \mathbf{r}_2^\beta \\ \mathbf{0} \\ \mathbf{0} \end{bmatrix}^i, \quad (6.42)$$

with the set of discrete unknowns $(\Delta \mathbf{p}_1^{i+1}, \Delta \mathbf{q}_1^{i+1}, \Delta \mathbf{p}_2^{i+1}, \Delta \mathbf{q}_2^{i+1})$. The first two rows in the matrix in (6.42) represent the linearized and discretized partial differential equations. The last two rows in (6.42) represent the discrete nodal information transfers for the mortar projection approach. Reformulation of the nodal information transfer for the collocation approach could easily be realized, but is omitted here for the sake of brevity. Considering the last two rows naturally leads to the nodal transfer of the incremental solutions in (6.38). Thus, the auxiliary

unknowns $\Delta\mathbf{p}_2^{i+1}$ and $\Delta\mathbf{q}_1^{i+1}$ can be eliminated from the system of equations and the reduced system reads:

$$\begin{bmatrix} \mathbf{K}_{1,\mathbf{p}_1}^\alpha & \mathbf{K}_{1,\mathbf{q}_2}^\alpha \mathbf{P}_{12} \\ \mathbf{K}_{2,\mathbf{p}_2}^\beta \mathbf{P}_{21} & \mathbf{K}_{2,\mathbf{q}_2}^\beta \end{bmatrix}^i \begin{bmatrix} \Delta\mathbf{p}_1 \\ \Delta\mathbf{q}_2 \end{bmatrix}^{i+1} = - \begin{bmatrix} \mathbf{r}_1^\alpha \\ \mathbf{r}_2^\beta \end{bmatrix}^i. \quad (6.43)$$

Here, it can be seen, that applying the nodal information transfer to the solution increments is identical to multiplying the off-diagonal blocks of the resulting linear system of equations with the projection operators.

6.3.2. Boundary conditions

Enforcing boundary conditions for volume coupled problems can be intuitively realized by applying them onto the primary unknowns \mathbf{p}_1 on Ω_1 and \mathbf{q}_2 on Ω_2 . Under consideration of fundamental stability requirements for the projection operators in finite dimensional spaces, this choice is the easiest way to guarantee proper information transfer. This becomes obvious for the mortar operator \mathbf{P}_{21}^m , which originates from (6.6). Here, stability of the information transfer is ensured when the rows of the system

$$\begin{bmatrix} \mathbf{D}_2 & \mathbf{M}_{21} \end{bmatrix} \begin{bmatrix} \mathbf{s}_2 \\ \mathbf{s}_1 \end{bmatrix} = \mathbf{0} \quad (6.44)$$

are linearly independent, see Brezzi and Fortin [32]. This is guaranteed by employing the shape functions \mathbf{N}_2 and their dual counterpart Φ_2 as explained in Section 6.2.3. As discussed for interface mortar mesh tying methods in Puso and Laursen [217], applying Dirichlet boundary conditions on the target mesh leads to a column elimination in the \mathbf{D}_2 matrix in (6.44). Thus, linearly independent rows are not guaranteed anymore and the projection becomes unstable. Since the primary fields \mathbf{p}_1 on Ω_1 and \mathbf{q}_2 on Ω_2 represent the sets of unknowns that are going to be projected, Dirichlet boundary condition are only allowed to be defined on these fields, but not on the auxiliary field \mathbf{q}_1 on Ω_1 and \mathbf{p}_2 on Ω_2 .

In analogy to node-to-segment interface approaches in Hesch and Betsch [104] and Zavarise and De Lorenzis [303], the collocation methods can be interpreted as a degenerated mortar method that uses Dirac delta distributions for the interpolation of the dual quantities \mathbf{d}_i , for $i = 1, 2$. This leads to a degenerated formulation with \mathbf{D}_i for $i = 1, 2$ reducing to identity matrices \mathbf{I}_i and \mathbf{M}_{ij} for $i, j = 1, 2$ and $i \neq j$ reducing to collocation matrices $\tilde{\mathbf{N}}_{ij}$, see (6.13). The resulting system reads

$$\begin{bmatrix} \mathbf{I}_2 & \tilde{\mathbf{N}}_{21} \end{bmatrix} \begin{bmatrix} \mathbf{s}_2 \\ \mathbf{s}_1 \end{bmatrix} = \mathbf{0}. \quad (6.45)$$

This system of equations has the same stability requirements as the mortar system in (6.44). Thus, enforcing Dirichlet boundary conditions is again only allowed for the primary unknowns \mathbf{p}_1 on Ω_1 and \mathbf{q}_2 on Ω_2 .

Neumann boundary conditions are in general not problematic, but for the sake of consistency it is recommended to enforce them on the same mesh as the Dirichlet boundary conditions.

6.3.3. Contact mechanics for multiphysics on non-matching meshes

The following considerations concerning computational contact mechanics for non-matching volume and interface meshes are based on the Master's Thesis Jelich [128], which was supervised by the author. Here, it is assumed that a solid phase is involved in the coupled multiphysics problem, which is the case for porous media simulations and thermo-structure interaction problems. The extension of the presented methodology for monolithic multiphysics strongly depends on the employed approach for contact constraint enforcement and the characteristics of the interface meshes. Using a penalty approach for contact constraint enforcement would avoid additional unknowns due to the contact phenomena and no fundamental change in the methodology explained in Section 6.3.1 has to be made. The special case of non-matching volume meshes but matching interface meshes represents also a strong simplification in the resulting systems. Thus, the most challenging cases of an employed Lagrange multiplier approach for constraint enforcement and non-conforming (and consequently non-matching) interface meshes are discussed in the following.

Starting point for deriving a consistent formulation for computational contact of multiphysics problems for non-matching volume and interface meshes is, again, the definition of discrete residuals of two involved partial differential equations

$$\mathbf{r}_1^\alpha(\mathbf{p}_1, \mathbf{q}_1) = \mathbf{0} \quad \text{and} \quad \mathbf{r}_2^\beta(\mathbf{p}_2, \mathbf{q}_2) = \mathbf{0}, \quad (6.46)$$

with identical nomenclature as given in Section 6.3.1. Additionally to the discrete unknowns \mathbf{p}_1 , \mathbf{q}_1 , \mathbf{p}_2 and \mathbf{q}_2 , two sets of primary unknowns λ_1 and Λ_1 and two sets of auxiliary unknowns λ_2 and Λ_2 are introduced. All these newly introduced unknowns are exclusively defined at the slave contact interfaces. Here, the quantities λ_i are considered as discrete Lagrange multiplier unknowns due to the well-known contact constraint enforcement for the involved solid. For details on constraint enforcement for computational contact mechanics the interested reader is referred to Chapter 3 and Chapter 4. The interface unknowns Λ_i are problem specific interface quantities, which are required to define additional interface effects, such as the thermal heat flux as described in Hüeber and Wohlmuth [116]. With the new interface unknowns being introduced, the discrete residuals read:

$$\mathbf{r}_1^\alpha(\mathbf{p}_1, \mathbf{q}_1, \lambda_1, \Lambda_1) = \mathbf{0} \quad \text{and} \quad \mathbf{r}_2^\beta(\mathbf{p}_2, \mathbf{q}_2, \lambda_2, \Lambda_2) = \mathbf{0}. \quad (6.47)$$

Herein, the residuals for the interface equations are already included. Following the same procedure as for the general volume coupling methodology in Section 6.3.1, a Newton-Raphson scheme is applied as nonlinear solution technique. The required linearized residuals can be ob-

tained from a truncated Taylor series expansion, via

$$\begin{aligned} \text{Lin } \mathbf{r}_1^\alpha(\mathbf{p}_1^i, \mathbf{q}_1^i, \boldsymbol{\lambda}_1^i, \boldsymbol{\Lambda}_1^i) &= \mathbf{r}_1^\alpha(\mathbf{p}_1^i, \mathbf{q}_1^i, \boldsymbol{\lambda}_1^i, \boldsymbol{\Lambda}_1^i) \\ &\quad + \frac{\partial \mathbf{r}_1^\alpha(\mathbf{p}_1, \mathbf{q}_1, \boldsymbol{\lambda}_1, \boldsymbol{\Lambda}_1)}{\partial \mathbf{p}_1} \Big|_1^i \Delta \mathbf{p}_1^{i+1} + \frac{\partial \mathbf{r}_1^\alpha(\mathbf{p}_1, \mathbf{q}_1, \boldsymbol{\lambda}_1, \boldsymbol{\Lambda}_1)}{\partial \mathbf{q}_1} \Big|_1^i \Delta \mathbf{q}_1^{i+1} \\ &\quad + \frac{\partial \mathbf{r}_1^\alpha(\mathbf{p}_1, \mathbf{q}_1, \boldsymbol{\lambda}_1, \boldsymbol{\Lambda}_1)}{\partial \boldsymbol{\lambda}_1} \Big|_1^i \Delta \boldsymbol{\lambda}_1^{i+1} + \frac{\partial \mathbf{r}_1^\alpha(\mathbf{p}_1, \mathbf{q}_1, \boldsymbol{\lambda}_1, \boldsymbol{\Lambda}_1)}{\partial \boldsymbol{\Lambda}_1} \Big|_1^i \Delta \boldsymbol{\Lambda}_1^{i+1} = \mathbf{0}, \end{aligned} \quad (6.48)$$

$$\begin{aligned} \text{Lin } \mathbf{r}_2^\beta(\mathbf{p}_2^i, \mathbf{q}_2^i, \boldsymbol{\lambda}_2^i, \boldsymbol{\Lambda}_2^i) &= \mathbf{r}_2^\beta(\mathbf{p}_2^i, \mathbf{q}_2^i, \boldsymbol{\lambda}_2^i, \boldsymbol{\Lambda}_2^i) \\ &\quad + \frac{\partial \mathbf{r}_2^\beta(\mathbf{p}_2, \mathbf{q}_2, \boldsymbol{\lambda}_2, \boldsymbol{\Lambda}_2)}{\partial \mathbf{p}_2} \Big|_2^i \Delta \mathbf{p}_2^{i+1} + \frac{\partial \mathbf{r}_2^\beta(\mathbf{p}_2, \mathbf{q}_2, \boldsymbol{\lambda}_2, \boldsymbol{\Lambda}_2)}{\partial \mathbf{q}_2} \Big|_2^i \Delta \mathbf{q}_2^{i+1} \\ &\quad + \frac{\partial \mathbf{r}_2^\beta(\mathbf{p}_2, \mathbf{q}_2, \boldsymbol{\lambda}_2, \boldsymbol{\Lambda}_2)}{\partial \boldsymbol{\lambda}_2} \Big|_2^i \Delta \boldsymbol{\lambda}_2^{i+1} + \frac{\partial \mathbf{r}_2^\beta(\mathbf{p}_2, \mathbf{q}_2, \boldsymbol{\lambda}_2, \boldsymbol{\Lambda}_2)}{\partial \boldsymbol{\Lambda}_2} \Big|_2^i \Delta \boldsymbol{\Lambda}_2^{i+1} = \mathbf{0}. \end{aligned} \quad (6.49)$$

By employing the volume projection operators for nodal information transfer, the volume auxiliary quantities $\Delta \mathbf{p}_2^{i+1}$ and $\Delta \mathbf{q}_1^{i+1}$ can be eliminated from the resulting system of equations as described in (6.38). The auxiliary quantities defined at the contact interface are also eliminated, via

$$\Delta \boldsymbol{\lambda}_2^{i+1} = \bar{\mathbf{P}}_{21} \Delta \boldsymbol{\lambda}_1^{i+1} \quad \text{and} \quad \Delta \boldsymbol{\Lambda}_1^{i+1} = \bar{\mathbf{P}}_{12} \Delta \boldsymbol{\Lambda}_2^{i+1}, \quad (6.50)$$

with the interface projection operators $\bar{\mathbf{P}}_{21}$ and $\bar{\mathbf{P}}_{12}$. These operators are created in analogy to the volume operators, but are defined exclusively at the potential contact interface. Thus, they are strongly related to operators which are employed for classical mesh tying and domain decomposition applications, see (3.65). In this thesis, only mortar based interface operators are employed, but it is generally also possible to use collocation operators. When considering non-matching volume meshes but matching interface meshes, the interface projection operators become the identity matrix, which can be considered as special case and a huge simplification.

After a Newton iteration is completed, the auxiliary unknowns are recovered and the incremental solutions are employed to update all unknowns. Again, this is repeated until a user-defined convergence criterion is met. The final form of the algebraic system of equations is omitted here for the sake of brevity, but its creation is rather straightforward. The projection operators for the volume and interface information transfer are simply applied to the off-diagonal blocks. For details concerning the arising algebraic system of equations for thermo-structure interaction problems, the interested reader is referred to the Master's Thesis Jelich [128].

6.3.4. Numerical examples

In the following, the methodology for simulating non-matching multiphysics problems in a monolithic manner is validated with several examples. First, a thermo-structure interaction problem is considered and the accuracy of the mortar and collocation method is compared. Then, contact interaction phenomena in the context of thermo-structure interactions are investigated. Finally, a porous media problem is considered, which serves as example for comparing the two introduced integration techniques for the mortar based projection operator.

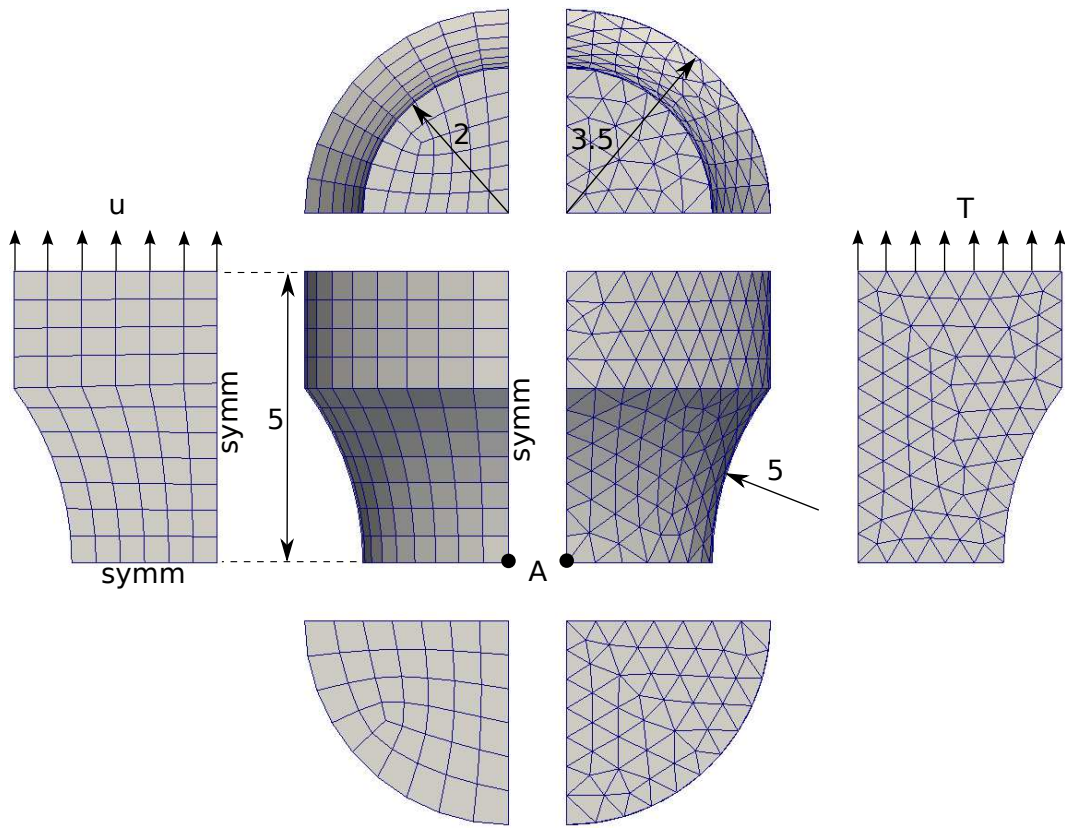


Figure 6.14: Problem setting for the thermo-structure interaction example. The left mesh represents the structural discretization and the right mesh represents the thermal counterpart. Figure is taken from Farah et al. [70].

6.3.4.1. Multiphysics problem – thermo-structure interaction

As first real volume coupled mutiphysics problem, thermo-structure interaction is employed for the following example. Therein, changes in temperature of a deformable solid induce thermal stresses, and, in return, strain rates can cause heating or cooling effects. The governing equations for the thermo-structure interaction problem can be found in Section 5.6, where they are employed for thermal wear coupling. Note, that now all thermal quantities are referred to the reference configuration and not to the material configuration anymore, since no mass loss due to wear is considered. For a more comprehensive overview and detailed derivations, the interested reader is referred to Danowski et al. [52].

In the following, spatial discretization of the structural linear momentum equation is realized on a different mesh than the temperature equation. The meshes and the problem setting in general are shown in Figure 6.14. The material parameters are Young's modulus $E = 2.1 \cdot 10^5$ and Poisson's ratio $\nu = 0.3$, resulting in the Lamé constants $\lambda = 121,153$ and $\mu = 80,769$. The reference density is $\rho_0 = 7.85 \cdot 10^{-6}$. The thermal parameters are chosen as $C_V = 700,637$, $k_\theta = 500$, $\theta_0 = 0$ and $\alpha_\theta = 7 \cdot 10^{-4}$. For the structural part, the displacements of the upper surface of the body are prescribed with a sinusoidal function in time, i.e. $u = 0.25 \sin(\pi t)$. Here, the time interval for the overall simulation is $t = [0, 10]$, which leads to five oscillation cycles. On

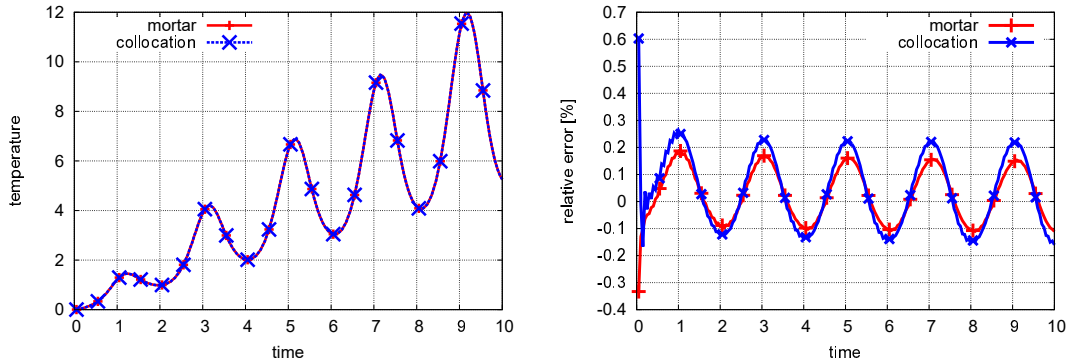


Figure 6.15: Left: total temperature evolution over time at a fixed point A for mortar and collocation approach. Right: Relative error with regard to matching grid solution for mortar and collocation approach. Figure is taken from Farah et al. [70].

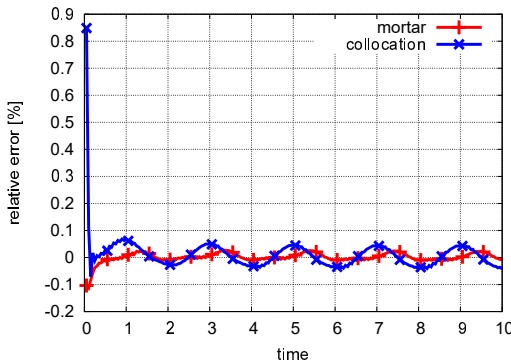


Figure 6.16: Relative error with regard to matching grid solution for mortar and collocation approach using second-order elements (20-node hexahedrals and 10-node tetrahedrals). Figure is based on Farah et al. [70].

the corresponding surface of the thermal mesh, a linearly increasing temperature of $\hat{\theta} = 0.8 t$ is prescribed. First-order hexahedral elements are employed for the structural mesh and first-order tetrahedrals are used for the thermal mesh. The volume mortar coupling is realized by a segment-based integration procedure. The resulting temperature over time at point A is shown in the left plot of Figure 6.15. Here, the mortar projection method leads to nearly the same results as the collocation approach. The right plot of Figure 6.15 visualizes the relative error with regard to the matching grid scenario calculated with a hexahedral mesh. Both methods yield errors that are negligible from an engineering point of view. Still, the mortar method yields better results than the collocation approach.

Furthermore, the same setting with second-order elements is analyzed, i.e. 20-node hexahedrals for the structural discretization and 10-node tetrahedrals for the thermal discretization are employed. In order to allow for a robust computation of dual shape functions for second-order elements, the shape function transformation from Section 6.2.3.2 is utilized. The absolute temperature distribution over time is virtually indistinguishable from the setting with first-order elements. The relative error with regard to the matching grid solution is given in Figure 6.16. Here,

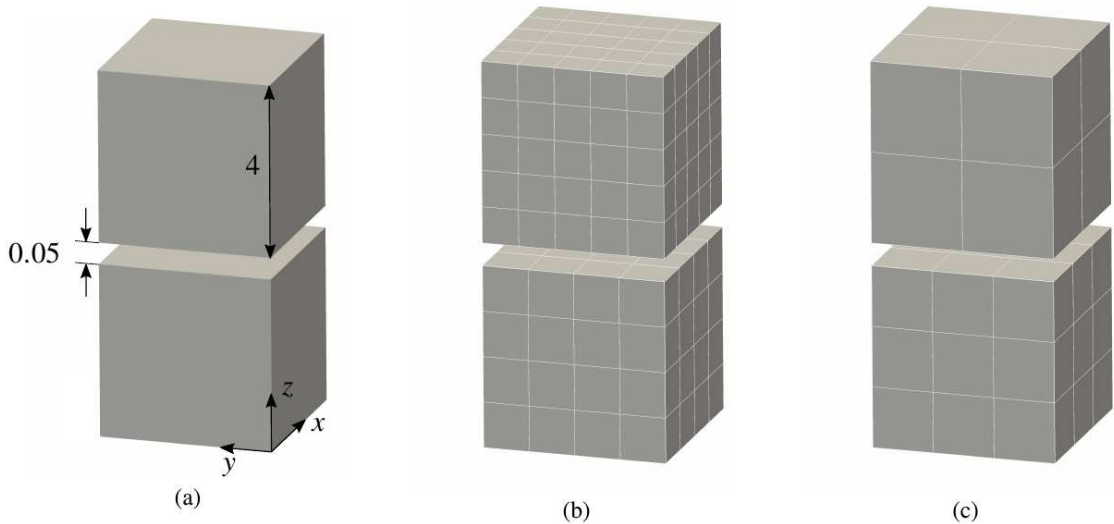


Figure 6.17: Heat conduction example: Problem setup with geometry information (a), finite element discretization for the structural field (b) and finite element discretization for the thermal field (c). The employed element type for both discretizations is 27-node second-order hexahedral element. Figure is taken from Jelich [128].

it can be seen that the relative errors of the collocation method and the mortar method are more than halved compared to the first-order elements. However, when compared with each other, the mortar method still yields slightly better results than the collocation method. Having in mind that the construction of the employed projection operators has to be performed only once at the beginning of a simulation and the computation time for this contributes only insignificantly to the overall simulation time, the use of mortar operators seems to be advantageous.

6.3.4.2. Contact mechanics on non-matching meshes – TSI

In the following two examples, the extension of the monolithic multiphysics framework on non-matching meshes towards contact mechanics is validated in the context of thermo-structure interaction problems. These examples are basically taken from the Master Thesis Jelich [128], which was supervised by the author. Details on the thermo-structure interaction problem including contact mechanics are already introduced in the context of wear phenomena in Section 5.6. Further information on mortar based thermo-structure-contact interaction frameworks can be found in Hüeber and Wohlmuth [116] and Seitz et al. [245].

6.3.4.2.1. Heat conduction The first example including contact effects is a classical heat conduction problem, which has already been investigated in the context of matching volume meshes in Gitterle [87]. Here, two identically shaped cubes with edge length of $l = 4$ are considered, see left part of Figure 6.17. The lower cube's bottom surface is subjected to a fixed temperature of $\hat{\theta}_1 = 100$ and at the upper cube's top surface a fixed temperature of $\hat{\theta}_2 = 0$ is prescribed. For the structural problem, the bottom surface of the lower cube is completely fixed

for the entire simulation and the upper cube's top surface is subjected to a total displacement in z direction of $w = -0.2$, which is enforced within 20 load steps. Both cubes are described by a Saint-Venant-Kirchhoff material model with Young's modulus $E = 400$, Poisson's ratio of $\nu = 0.0$, coefficient of thermal expansion of $\alpha_\theta = 0.0$ and a thermal conductivity of $k_\theta = 52$. Furthermore, the pressure dependent heat fluxes at the contact interface are defined via the interface parameters $\bar{\alpha}_c^{(1)} = \bar{\alpha}_c^{(2)} = 100$. For the contact scenario, the lower cube is defined to be the slave part and the upper block is the master part.

Two different spatial discretizations are employed for the thermal field and the structural field, see middle part and right part of Figure 6.17. This leads to non-matching volume and interface discretizations for the cubes themselves as well as for the contact interface. Consequently, the information transfer for the volumes and the interfaces becomes non-trivial since the projection operators differs from the identity operator. For the volume, interface and contact projections, mortar operators based on dual shape functions are employed and the resulting discrete problem is solved in a fully monolithic manner. The accuracy and consistency of these operators are validated by comparing the numerical solution with a 1D steady-state solution. As investigated in Oancea and Laursen [184] and Wriggers and Miehe [294], the temperature at the slave and master contact interfaces equals

$$\theta^{(1)} = \frac{\xi \cdot \hat{\theta}_1 + (1 + \xi) \cdot \hat{\theta}_2}{1 + 2\xi}, \quad \theta^{(2)} = \frac{\xi \cdot \hat{\theta}_2 + (1 + \xi) \cdot \hat{\theta}_1}{1 + 2\xi}, \quad \xi = \bar{\alpha}_c \frac{p_n}{2k_\theta}, \quad (6.51)$$

with p_n representing the normal contact pressure in the interface and the parameters $\bar{\alpha}_c$ and k_θ are assumed to be equal for both cubes. Here, it can be seen that the temperature distribution is directly influenced by the contact force and thus a strong thermo-mechanical coupling is present.

The resulting temperature distribution on both volume discretizations is visualized in Figure 6.18. At the beginning, the two cubes are separated and their temperature is constant and equal to the prescribed boundary temperatures. When the bodies are in contact, their temperature is not constant anymore, but is linearly distributed in z -direction with a jump at the contact interface. This jump in temperature decreases during the simulation since the contact pressure and the heat flux increase.

Finally, the temperature solution is given as function of the contact pressure and is compared with the analytical solution from (6.51). The result is visualized in Figure 6.19. It can be seen, that the numerical solutions for both contact sides match very well the analytical solution. This demonstrates the accuracy and consistency of the presented monolithic methodology for interface and volume coupled multiphysics problems.

6.3.4.2.2. Half torus The next example demonstrates the applicability of the proposed coupling methodology towards finite deformation contact interaction for thermo-structure problems. For this purpose, an elastic half hollow torus and a rigid plate are considered. Geometry information of both bodies can be taken from Figure 6.20. The half torus top surfaces are subjected to a prescribed motion, which firstly moves the torus in z -direction until the maximum $\hat{z} = -12$ is reached. Then, the z -displacement is kept constant and a movement along the y -axis is initiated with a maximum y -displacement of $\hat{y} = 10$. The overall simulation is performed within 50 time steps, where the first 26 steps are subjected to the z -movement and the remaining 24 steps are employed to enforce the y -movement. For the temperature field, zero fluxes are prescribed at the

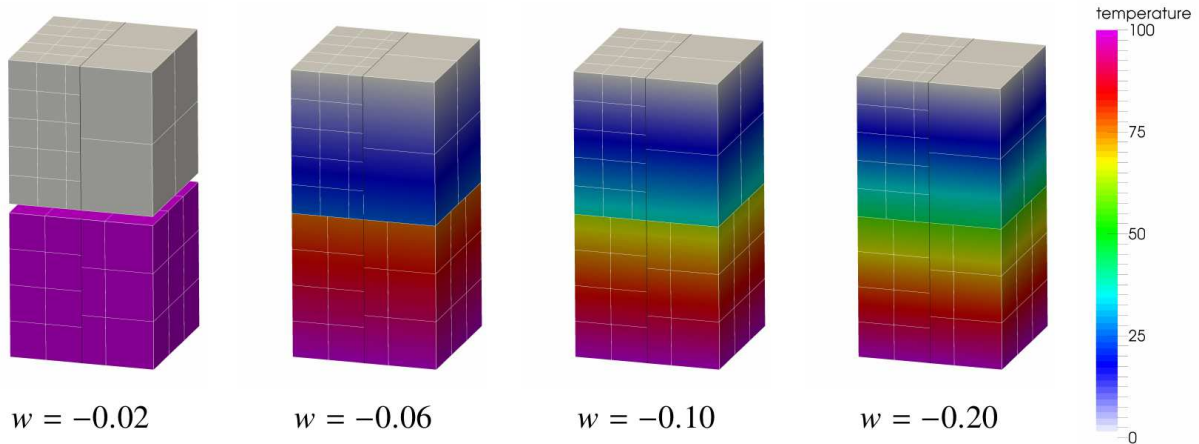


Figure 6.18: Heat conduction example: Temperature field visualized for four different time steps. Left parts of the cubes show the projected temperature on the structure field and the right parts are colored with the temperature on the thermal field. Figure is taken from Jelich [128].

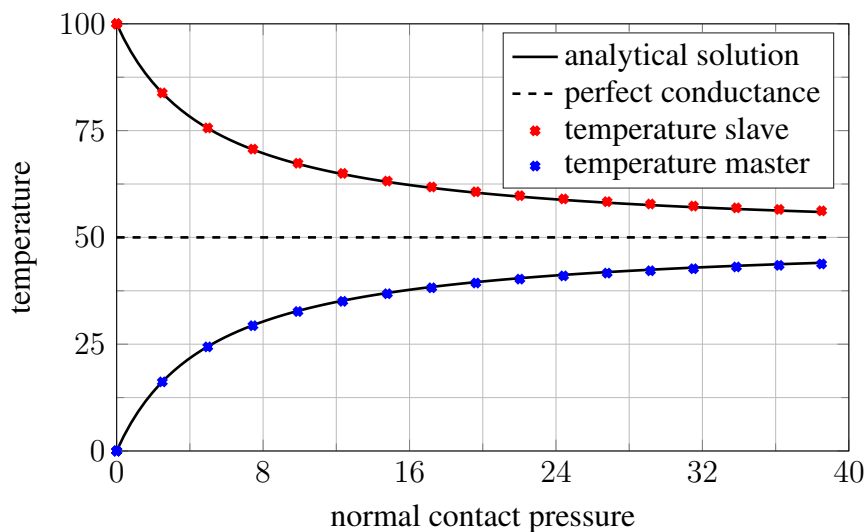


Figure 6.19: Analytical and numerical solution of the temperature at the slave and master contact interface as a function of the normal contact force. Figure is taken from Jelich [128].

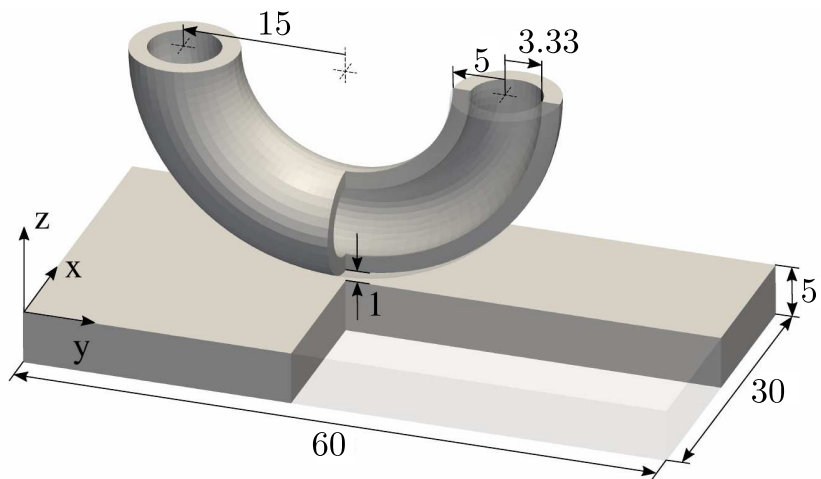


Figure 6.20: Half torus example: problem setup and geometry of the half torus and the plate.
Figure is based on Jelich [128].

two bodies. The material model for the two bodies is described by Young's modulus $E = 400$, Poisson's ratio $\nu = 0.0$, the coefficient of thermal expansion $\alpha_\theta = 1 \cdot 10^{-5}$, the thermal conductivity $k_\theta = 20$ and the heat capacity $C_V = 1$. The contact interaction is described with the torus being the slave body and the plate being the master body, respectively. The parameters for the contact heat fluxes are $\bar{\alpha}_c^{(1)} = 100$ and $\bar{\alpha}_c^{(2)} = 1$ and the coefficient of friction is $\mathfrak{f} = 0.1$.

The finite element discretization of the two bodies with different thermal and structural meshes and with a matching grid are visualized in Figure 6.21. Here, the matching grid discretization is denoted as Ω_{mg} , the structural mesh is named Ω_S and the thermal mesh reads Ω_T . For the non-matching case, the structural mesh is chosen in order to discretize the plate only with one element, since this is sufficient to represent the rigidness exactly. All other structure element are employed to resolve the torus relatively fine, because here finite deformations are expected. In contrast, the thermal mesh is defined in a way to resolve the plate with many elements, since here temperature gradients are expected. Please note, the approximately 7500 hex8 elements for the matching grid case should be considered as 7500 elements for the thermal field and additional 7500 elements for the structure field resulting in ca. 15000 elements for the overall simulation. When considering the non-matching case, an overall element number of ca. 7900 elements is employed.

The results for the simulation are exemplary shown for the time steps 26 and 50 in Figure 6.22. Here, the two figures on the left show the deformation of the torus with colored displacement magnitude on the structural mesh, whereas the right ones show the deformation with colored temperature distribution on the thermal mesh. It can be seen that the deformation is correctly mapped from the structural mesh onto the thermal mesh. In addition, the contact interaction works properly and thermal heating due to frictional sliding causes temperature gradients at the interface for both bodies. Here, it becomes obvious why the non-matching discretization approach for coupled multiphysics is advantageous for this example: the structural behavior of the rigid plate can be exactly captured by one finite element, but the heat flux due to frictional contact requires a fine thermal finite element resolution.

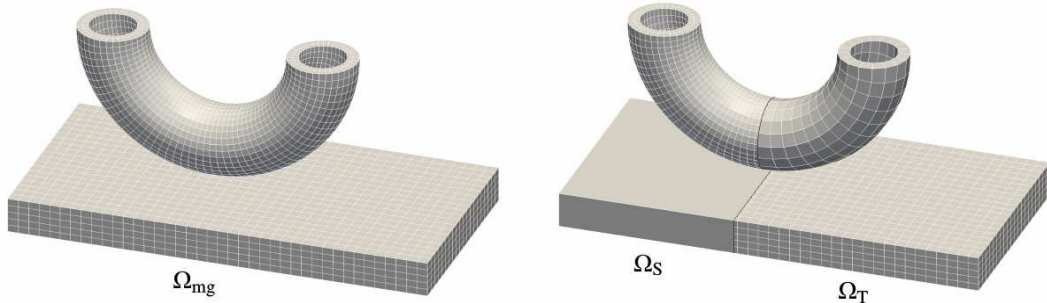


Figure 6.21: Half torus example: matching grid discretization with approximately 7500 hex8 elements (left) and non-matching discretization with structural mesh consisting of ca. 3500 hex8 elements and thermal mesh consisting of ca. 4400 hex8 elements (right). Figure is taken from Jelich [128].

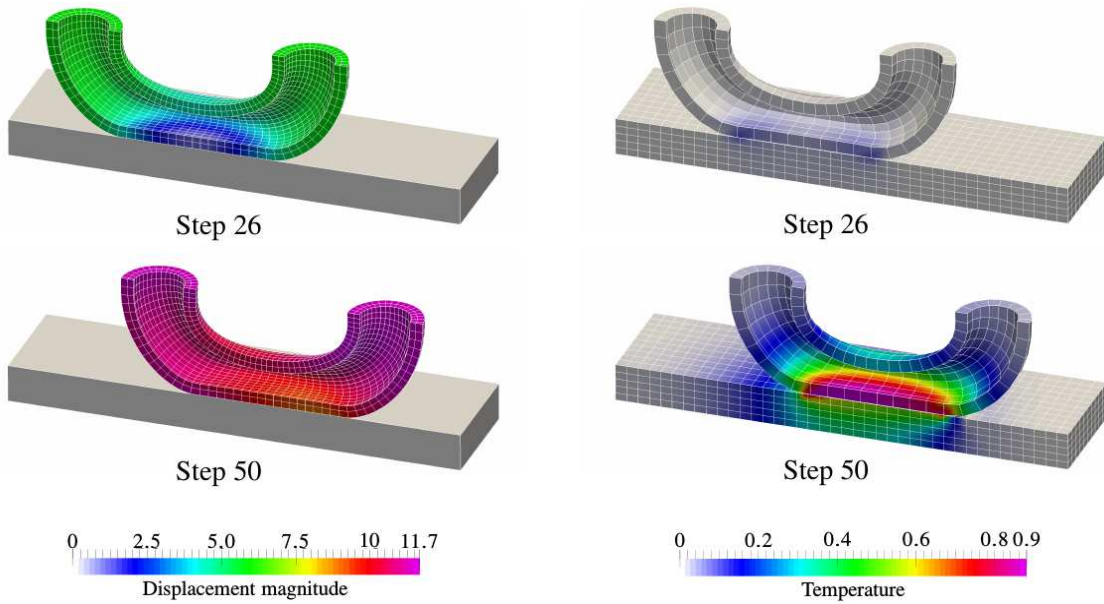


Figure 6.22: Half torus example: Numerical results for displacement magnitude and temperature at time steps 26 and 50. Figure is taken from Jelich [128].

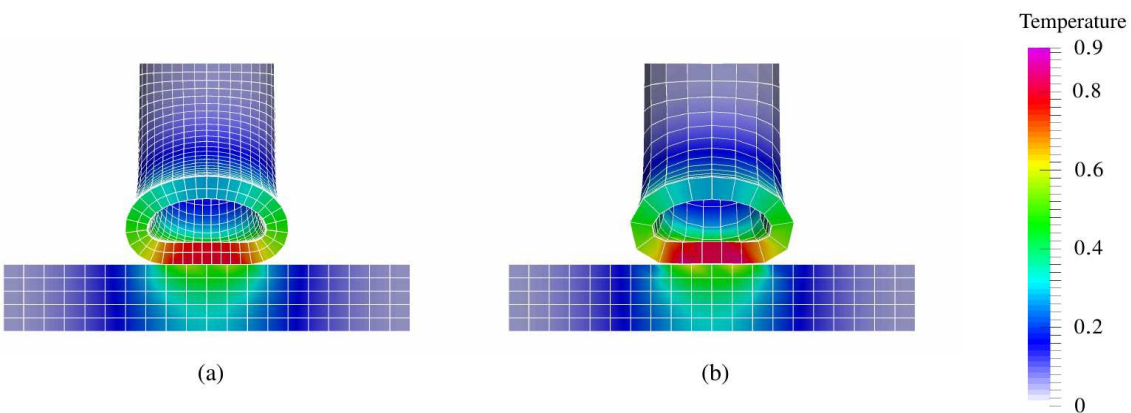


Figure 6.23: Half torus example: temperature distribution for torus and plate. matching grid solution (a) and non-matching grid solution for thermal discretization (b). Figure is taken from Jelich [128].

The deformation and the temperatures are compared with the matching grid solution in Figure 6.23. Here, both solutions are in good agreement.

6.3.4.3. Convergence analysis – porous media flow

This example is used to study convergence rates of the discretization error, similar to the investigations presented in Vuong et al. [279]. Therein, a mesh study was performed for matching discretizations. Investigations concerning non-matching meshes for this example have already been published in Vuong [277], but the following tests extend the example towards a comparison of the segment-based and element-based integration scheme, see 6.2.4.

The considered example represents a poroelasticity problem, which can be defined as a multiphysics system that consists of a structural phase being volumetrically coupled with a fluid phase. For a comprehensive introduction and the underlying theory, see Coussy [49]. The main characteristic quantity of a porous medium is its porosity $0 \leq \phi \leq 1$, which defines the volume ratio of the fluid phase with respect to the total volume, i.e. $\phi = 1$ in case of a pure fluid phase and $\phi = 0$ for a pure solid. In the following, quasi-static conditions and linear behavior of the porosity with respect to deformation and pore pressure are assumed. The problem is modeled in a 2D regime with different 'volume' meshes for discretizing the porosity and for discretizing fluid velocity and pressure, respectively. However, the problem itself is actually a 1D model, but the equations are solved on a 2D domain in order to be able to compare the presented approaches.

In order to analyze this porous media example, the most important equations describing the problem are given in the following and prescribed conditions are directly included. All quantities related to the involved fluid are denoted with the superscript $(\cdot)^F$ and all structural quantities are denoted with $(\cdot)^S$, respectively. The porous flow is determined by Darcy's law:

$$\frac{dp^F(x)}{dx} - \rho_0^F b(x) + \mu^F k^{-1} \phi v^F(x) = 0. \quad (6.52)$$

The pressure gradient $dp^F(x)/dx$ and the body forces $b(x)$ induce a flow velocity $v^F(x)$ which depends on the spatial coordinate x . Also, the fluid is assumed to have a constant density ρ_0^F and

dynamic viscosity μ^F . The spatial permeability $k(x)$ is calculated from the material permeability K_0 and the displacement field $d^S(x)$, via

$$k(x) = J(x)K_0 = \left(1 - \frac{d}{dx} d^S(x)\right)^{-1} K_0 , \quad (6.53)$$

with $J(x) = \left(1 - \frac{d}{dx} d(x)^S\right)^{-1}$ denoting the Jacobian determinant of the deformation. The continuity equation reads

$$\frac{d(\phi(x)v^F(x))}{dx} = 0. \quad (6.54)$$

The fluid pressure is related to the porosity by

$$p^F(x) = \kappa (\phi(x) - \phi_0 - (1 - \phi_0)(J(x) - 1)) , \quad (6.55)$$

with the initial porosity ϕ_0 and the bulk modulus κ . Inside the problem domain $\Omega = [-5, 5]$ the displacement $d^S(x)$ is prescribed as

$$d^S(x) = 0.5 \cdot \left(1 + \cos\left(\frac{\pi}{5}x\right)\right) . \quad (6.56)$$

Note, that even though the solid phase is fixed, the porosity is still allowed to vary due to pore pressure. On the entire domain the following body force is applied:

$$b(x) = 1 + 0.1\pi \sin(0.2\pi x) - 0.04\pi \cos\left(\frac{\pi}{5}x\right) + 0.01\pi^2 \cdot \frac{\cos(0.2\pi x)}{(1 + 0.1\pi \sin(0.2\pi x))^2} . \quad (6.57)$$

The chosen material parameters are the initial porosity $\phi_0 = 0.5$, the bulk modulus $\kappa = 1$, the dynamic viscosity of the fluid $\mu^F = 0.01$ and the material permeability $K_0 = 0.01$. All units are neglected in this example, since the parameters are chosen arbitrarily in order to obtain a simple analytical solution. Inserting the prescribed displacements (6.56), body forces (6.57) and the given material parameters into the strong form (6.52)-(6.55), it can be shown (cf. Vuong et al. [279]) that the analytical solutions for the porosity, the pressure and the fluid velocity are

$$\phi(x) = 0.5 - 0.2 \sin(0.2\pi x) , \quad (6.58)$$

$$p^F(x) = 0.5 - 0.2 \sin(0.2\pi x) - (2 + 0.2\pi \sin(0.2\pi x))^{-1} , \quad (6.59)$$

$$v^F(x) = (0.5 - 0.2 \sin(0.2\pi x))^{-1} . \quad (6.60)$$

Two meshes with a ratio of 1:1.5 between fine and coarse discretization are exemplary depicted in Figure 6.24. First-order elements are used for all primary fields. For the fluid a stabilized, mixed formulation is applied and the coupled system of equations is solved in a fully monolithic manner, see Vuong et al. [278] for more details. The displacement field is given on the same mesh as the porosity. First, the mortar integration is performed with the segment-based scheme. The convergence behavior of the fluid velocity is analyzed in the following. In the left part of Figure 6.25 the results are depicted for a fixed mesh ratio of 1:1.5 of the two meshes. A matching grid solution is used as reference (taken from Vuong et al. [279]) and the mortar approach (segment-based) is compared to the collocation method. If the fluid mesh is chosen to be the coarser mesh, both variants converge similarly to the matching grid case. However, when

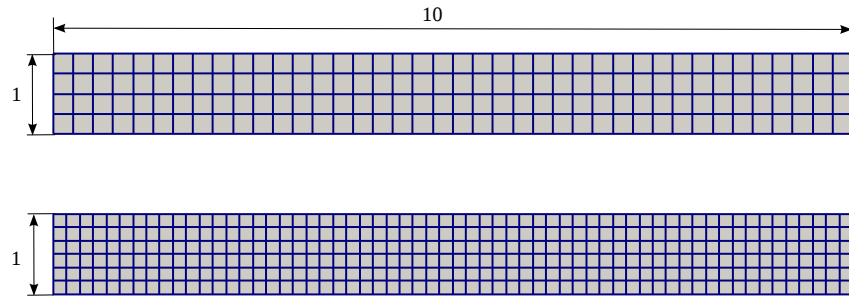


Figure 6.24: Problem setting for poroelasticity example. Two meshes with element size ratio of 1:1.5. Figure is taken from Farah et al. [70].

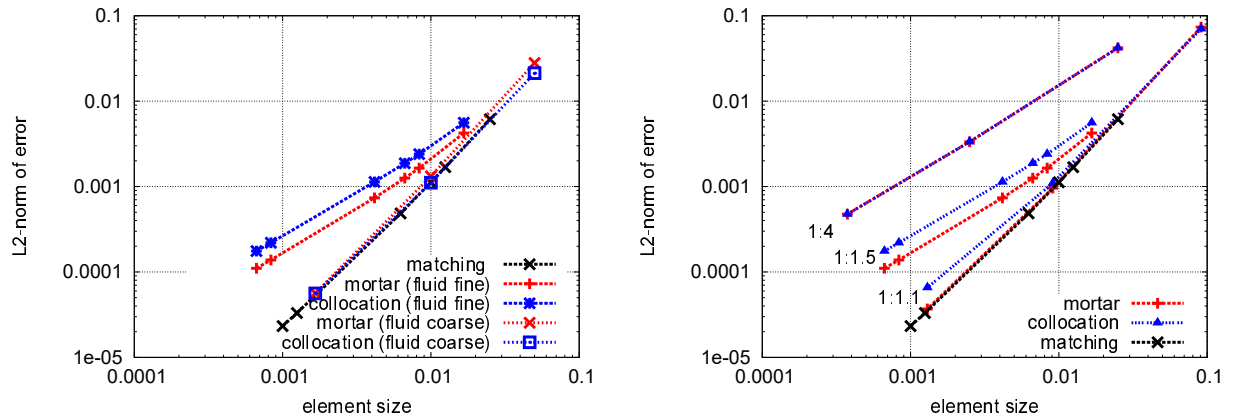


Figure 6.25: Convergence study. Error norm of the velocity plotted over the mesh size of the fluid field. Comparison of mortar and collocation method. Left subfigure: The mesh ratio is fixed to 1:1.5. Results for fluid field being discretized on the coarser and finer mesh, respectively. Right subfigure: Study for different mesh ratios. The fluid field is solved on a finer mesh than the porosity. Figure is taken from Farah et al. [70].

solving the porosity on the coarser mesh the convergence deteriorates for both variants. From this, one can conclude that the porosity solution strongly affects the quality of the velocity field. The porosity error on the coarser mesh seems to deteriorate the convergence of the fluid velocity. On the other hand, if the fluid mesh is coarser than the porosity mesh, the porosity solution is more accurate and does not affect the velocity convergence.

In the right part of Figure 6.25 the mesh ratio is varied, while the fluid field is solved on a finer mesh than the porosity. Again, both projection operator variants behave similarly, i.e. they approach the reference solution for mesh ratios close to 1. In general, the mortar approach shows smaller absolute error values than the collocation approach in this example. In the case of a mesh ratio of 1 : 4, both approaches lead to the same result. This is due to the fact that a nested mesh is obtained here. Thus, the projection matrices are the same and there is no difference between the two methods, see Section 6.2.1.

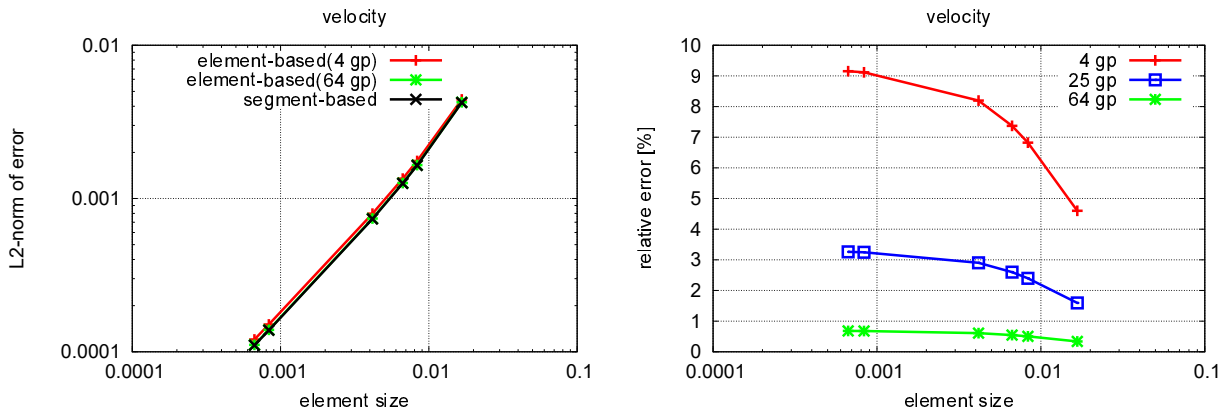


Figure 6.26: Comparison of segment-based integration and element-based integration. The mesh ratio is fixed at 1:1.5. Left subfigure: Error norm of the velocity plotted over the mesh size of the fluid field for segment-based integration and element-based integration. Right subfigure: Relative error norm of the velocity for element-based integration referred to segment-based integration. Figure is taken from Farah et al. [70].

In the following, the influence of the employed integration technique for the mortar projection operator on the convergence behavior of the solution is analyzed. In the left part of Figure 6.26 the absolute error norm of the velocity is shown for a fixed mesh ratio of 1:1.5 with a finer fluid mesh. For the element-based integration technique, 4 Gauss points and 64 Gauss points per element are used to compute the mortar projection operator. For the segment-based integration approach, 7 Gauss points per integration cell are employed. It can be seen that the convergence order is not significantly affected by the integration technique and the employed integration points. In the right part of Figure 6.26, the relative errors of the solutions computed with the element-based integration with 4, 25 and 64 Gauss points compared to the segment-based integration are visualized. The relative error directly decreases with an increased number of employed Gauss points. In case of coarse meshes, the integration errors are relatively small compared to the errors of the finite element approximation. By refining the mesh, the relative errors increase until they stagnate at a constant level, because the errors due to the numerical integration of the projection operator do not vanish by mesh refinement but become more and more dominant. These effects are in good agreement with investigations for mortar integration techniques for contact mechanics in Farah et al. [73] and in Appendix A.

Based on this result it could generally be summarized to prefer the element-based integration over the segment-based scheme, since the integration errors are acceptably small and the evaluation costs are drastically reduced.

6.4. Further applications

In addition to the use of volume projection operators for the monolithic simulation of coupled multiphysics problems on different meshes, a large variety of possible applications for such information transfer methods exists. This final section demonstrates the flexibility of the developed methods by means of two completely different applications. First, a novel grid motion approach for fluid-structure interaction problems is developed with advantageous characteristics in terms of computational robustness and efficiency. This approach has predominantly been implemented by the author and can be found in La Spina et al. [145]. Second, a linear tetrahedral element based on the so-called Hu-Washizu principle is implemented according to the investigations in Lamichhane et al. [149] and Shu [251]. As will be shown, such an approach shares numerical similarities with the presented mortar projection operators.

6.4.1. A novel grid motion approach for fluid-structure interaction

Fluid-structure interaction (FSI) is a classical problem in engineering science. Still, numerical simulations involving an incompressible fluid flow and an elastodynamic structure are very challenging. Such settings require special techniques to ensure robustness and stability of the chosen numerical method and the desired precision especially at the FSI interface. In general, one can distinguish between two approaches: *fixed grid* approaches use a stationary background mesh for the fluid problem. The structural problem is most often discretized independently and embedded into the fluid mesh. The geometrical position of the FSI interface and the corresponding coupling conditions can be tracked precisely, for instance using the XFEM method (cf. Gerstenberger and Wall [86]), or fulfilled in a smeared sense, as done in immersed methods, see Liu et al. [159] and Peskin [205]. In contrast, *moving grid* approaches resolve the FSI interface, see for example Ramm and Wall [225] and Wall [280]. Then, an additional strategy is needed in order to adapt the fluid mesh to the deformation of the structure and the interface. The most popular strategies are Arbitrary-Lagrangian-Eulerian formulations (ALE), where the fluid nodes are relocated without the necessity of costly remeshing and maintaining the original connectivity information. Such a moving grid approach is employed in the following and improved with a novel overlay grid approach. Therefore, discrete projection operators for nodal information transfer as introduced in this chapter are employed.

In the following, the problem statement for FSI is given in a very brief manner. Then, the novel grid motion approach is introduced and finally a benchmark example is analyzed.

6.4.1.1. Problem statement for fluid-Structure interaction

In this section the basic description of a FSI problem is briefly reviewed. As the already introduced ALE approach is employed, the FSI problem consists of three fields: two physical fields, i.e. structural and fluid field and, in order to account for deformation of the fluid mesh, a non-physical mesh field. In the following the governing equations for each field, as well as the coupling conditions between the fields and the partitioned solution algorithm are presented.

6.4.1.1.1. Fluid field An instationary, incompressible flow for a Newtonian fluid on a deformable fluid domain Ω^F is considered. Hence, the convective formulation of the ALE form of

the Navier-Stokes equations reads

$$\rho^F \frac{\partial \mathbf{v}^F}{\partial t} + \rho^F (\mathbf{c}^F \cdot \nabla) \mathbf{v}^F - 2\mu^F \nabla \cdot \boldsymbol{\varepsilon}(\mathbf{v}^F) + \nabla p^F = \rho^F \mathbf{b}^F, \quad (6.61)$$

$$\nabla \cdot \mathbf{v}^F = 0, \quad (6.62)$$

where the fluid velocity \mathbf{v}^F and the fluid pressure p^F are the unknown quantities. In the momentum equation (6.61), \mathbf{b}^F denotes a prescribed body force, $\boldsymbol{\varepsilon}(\mathbf{v}^F) = \frac{1}{2} (\nabla \mathbf{v}^F + (\nabla \mathbf{v}^F)^T)$ the strain rate tensor of the Newtonian fluid and μ^F its dynamic viscosity. The ALE convective velocity is denoted with $\mathbf{c}^F = \mathbf{v}^F - \mathbf{v}^G$, and can be interpreted as the relative velocity of the fluid with respect to the grid velocity \mathbf{v}^G . Equation (6.62) states the conservation of mass given that the fluid density ρ^F is constant. Suitable initial and boundary conditions need to be chosen in order to complete the problem formulation, but are skipped here for the sake of brevity. In this thesis, an implicit time integration method is utilized in combination with stabilized finite elements to discretize the fluid problem (6.61)-(6.62). Stabilization terms are applied to account for instabilities arising from equal-order discretization of fluid and pressure fields as well as for convection-dominated problems. For details on the finite element discretization of the fluid field and stabilization methods the interested reader is referred i.e. to Donéa and Huerta [63] and Hughes et al. [121].

6.4.1.1.2. Structure field The structure field is described by the balance of linear momentum for non-linear elastodynamics. It has already been introduced in Chapter 2 and is directly employed in the following without any change in the formulation. However, for the sake of readability and to achieve a clear distinction in the notation, all structure related quantities are denoted with the superscript $(\cdot)^S$ in the following.

6.4.1.1.3. Fluid Grid In order to allow finite deformations of the fluid domain, an ALE approach is applied for the fluid domain. Hence, the grid domain Ω^G is introduced which is equivalent to the fluid domain Ω^F in the continuous setting as well as in the spatially discretized setting. Here, the grid displacements \mathbf{u}^G define the grid motion. Generally, they are obtained by solving a type of equilibrium equation. However, the novel approach to calculate the grid displacements in an efficient and robust manner is explained in detail in Section 6.4.1.2.

6.4.1.1.4. FSI coupling conditions At the fluid-structure interface Γ_{FSI} , different kinematic and dynamic constraints have to be fulfilled. Equilibrium of forces requires the surface tractions \mathbf{t}_Γ^F and \mathbf{t}_Γ^S of fluid and structure to be equal, yielding

$$\mathbf{t}_\Gamma^S = -\mathbf{t}_\Gamma^F \quad \text{on } \Gamma_{FSI} \times (0, T). \quad (6.63)$$

In addition, the grid velocity \mathbf{v}_Γ^G has to match the fluid velocity \mathbf{v}_Γ^F at the interface:

$$\mathbf{v}_\Gamma^F = \mathbf{v}_\Gamma^G \quad \text{on } \Gamma_{FSI} \times (0, T). \quad (6.64)$$

Usually, both a mass flow across Γ_{FSI} and a relative tangential movement of fluid and structure at Γ_{FSI} are prohibited, i.e.

$$\frac{\partial \mathbf{u}_\Gamma^S}{\partial t} = \mathbf{v}_\Gamma^F \quad \text{on } \Gamma_{FSI} \times (0, T). \quad (6.65)$$

In combination with equation (6.64), this condition is equivalent to

$$\mathbf{u}_\Gamma^S = \mathbf{u}_\Gamma^G \quad \text{on} \quad \Gamma_{\text{FSI}} \times (0, T), \quad (6.66)$$

at least in the continuous setting. Hence, structural deformation and fluid movement (represented by the ALE-based fluid domain deformation \mathbf{u}_Γ^G) must match at Γ_{FSI} .

6.4.1.1.5. Global solution algorithm The balance of linear momentum of the structure field 6.4.1.1.2, the Navier-Stokes equations for the fluid field 6.4.1.1.1, the fluid grid motion 6.4.1.1.3 and the FSI coupling conditions 6.4.1.1.4 constitute a system of nonlinear algebraic equations which has to be solved within each time step, with the discretized displacements and velocities being denoted with \mathbf{d} and \mathbf{v} , respectively. For this purpose, a monolithic solver (cf. Mayr [165] and Mayr et al. [166]) or a partitioned solver (cf. Kütter and Wall [144]) can be employed. In this thesis, only a partitioned solution algorithm based on a Dirichlet-Neumann coupling scheme with Aitken relaxation (cf. Irons and Tuck [127]) is utilized. Here, the fluid field becomes the Dirichlet partition with prescribed interface velocities (6.65) and the structure field becomes the Neumann partition loaded with surface tractions (6.63). The solver coupling for each time step reads:

Algorithm 6.1. Dirichlet-Neumann scheme

1. Start with predicted structural interface displacements \mathbf{d}_Γ^S .
2. Solve fluid grid motion \mathbf{d}^G with interface displacements as Dirichlet condition (6.66).
3. Solve fluid field with interface velocities \mathbf{v}_Γ^F as Dirichlet condition (6.65).
4. Solve structure equations with fluid interface traction as Neumann condition (6.63).
5. Check for convergence: continue with next time step if algorithm is converged, otherwise return to step 2.

Here, the developed grid motion approach only affects solution step 2 and all other parts of the partitioned solution scheme remain unchanged. For a more detailed explanation on the partitioned solution scheme the interested reader is referred to Kütter and Wall [144].

6.4.1.2. Grid motion approach

By applying a dynamic mesh methodology the grid motion has to be iteratively calculated for each solving step to update the entire fluid mesh points. Under the assumption that the grids for the fluid field and the mesh motion are equivalent it is obvious that this procedure becomes very expensive for large scale applications. In addition, the demands, that the physical fluid field and the grid motion equations pose on the finite element mesh, completely differ from each other. The fluid field requires a very fine resolution at the FSI interface whereas the grid motion equations usually need a coarse resolution to prevent elements near the FSI interface from degeneration. These two aspects lead to the basic idea of the proposed grid moving strategy, that is to completely separate the fluid grid from the mesh on which the deformation is calculated. For this purpose, a new mesh is introduced, which is called overset grid Ω^O , which is employed

to calculate the grid displacements \mathbf{d}^O . The overlay grid is in general non-matching with the fluid grid and at the interface non-matching with the structure mesh. Therefore, step 2 of the solution algorithm 6.1 within one time step has to be modified as follows:

Algorithm 6.2. Grid motion approach

- 2.1 Project the structural interface displacements \mathbf{d}_Γ^S on the overlay grid.
- 2.2 Solve equilibrium equations on the overlay grid with projected interface displacements as Dirichlet condition to obtain overlay grid motion \mathbf{d}^O .
- 2.3 Project the overlay grid displacements onto the fluid grid to obtain $\tilde{\mathbf{d}}^G$. In general, these displacements do not fulfill the FSI conditions (6.66) and (6.65).
- 2.4 Perform a correction step to enforce equality of fluid grid displacements and structural displacements at the interface (6.66) as well as equality of structural velocities and fluid velocities (6.65). The final fluid grid displacements \mathbf{d}^G are obtained.

This procedure only affects the physically irrelevant mesh motion. The structural solver as well as the fluid solver are not influenced. Therefore, no change in physical results will arise as shown in Section 6.4.1.3. Note that step 2.2 of this strategy is conceptually equivalent to step 2 in the classic algorithm 6.1. However, here the solver costs are in general much less as the overlay grid can be chosen much coarser than the fluid mesh. The other steps 2.1, 2.3 and 2.4 are simple projection and correction steps in order to enforce consistency at the interface and do not involve inversion of a system of equations, i.e. are computationally cheap. Further details concerning these projections and the correction step are given in the following.

6.4.1.2.1. Projection of structure interface displacements The structural interface displacements \mathbf{d}_Γ^S have to be projected onto the interface part of the overlay grid to act as Dirichlet condition for the overlay grid

$$\mathbf{d}_\Gamma^O = \mathbf{P}_S \mathbf{d}_\Gamma^S \quad \text{on} \quad \Gamma_{FSI} \times (0, T). \quad (6.67)$$

Here, the projection operator for the structural displacements is denoted with \mathbf{P}_S . Since the overlay grid motion can be considered as an unphysical auxiliary deformation to reach a valid fluid grid motion, the projection operator of the strucral interface displacements does not have to fulfill any conservation properties. Therefore, it is recommended to employ the collocation approach to calculate the projection operator, see Section 6.2.2. With this projection the interface nodes of the overlay grid are strongly (point-wise) connected to the interpolation of the structural displacements at the interface. In other words, the interface nodes of the overlay grid are not allowed to change their position relatively to the structure node positions. Therefore, the evaluation of the projection operator has to be performed only once at the beginning of the simulation, which makes the computational costs negligible compared to the overall simulation time.

6.4.1.2.2. Equilibrium equation for grid motion The projected structural interface displacements act as Dirichlet boundary condition for the grid motion problem, i.e. \mathbf{d}_Γ^O is fixed.

Here, the overlay grid equilibrium is treated as a quasi-elastostatic pseudo-structure following Wall [280]. Hence, the mesh displacements \mathbf{d}^O are obtained by solving the equilibrium equation of motion as stated in Chapter 2 with the material parameters can be considered as pseudo material.

Remark 6.1. *Since the grid motion has no physical interpretation the grid equilibrium could be stated using other models, for example springs in Batina [15], torsion springs in Farhat et al. [75], geometrically nonlinear pseudo-structure equations and many more. The proposed grid motion algorithm is basically not affected by the choice of the equilibrium equation.*

6.4.1.2.3. Projection of overlay grid motion After the equilibrium equations are solved, the overlay grid displacements have to be projected onto the fluid grid. This is realized by a volume projection operator \mathbf{P}_G , via

$$\tilde{\mathbf{d}}^G = \mathbf{P}_G \mathbf{d}^O. \quad (6.68)$$

Again, the fluid grid motion has no physical interpretation and thus the projection operator \mathbf{P}_G does not have to fulfill any conservation properties. Therefore, the collocation approach is utilized again to construct a proper projection operator based on a strong (point-wise) coupling of fluid grid points with the interpolation of the overlay grid. For this volumetric projection, the point-wise coupling guarantees valid fluid grid elements because their node positions are directly associated with parameter space coordinates of overlay grid elements. Thus, if the (coarse) overlay grid is prevented from degeneration, then the (fine) fluid grid is also prevented from degeneration. This property causes the high robustness of the presented mesh motion algorithm.

6.4.1.2.4. Correction step at FSI interface It is obvious that the fluid grid deformation does not match the structural deformation at the interface since it is based on the coarse overlay grid solution. Therefore, a simple correction step has to be applied which guarantees the satisfaction of displacement and velocity equivalence in (6.65) and (6.66). Therefore, the fluid grid nodes at the interface are relocated in a way such that they exactly match the structure interface nodes:

$$\mathbf{d}_\Gamma^S - \tilde{\mathbf{d}}_\Gamma^G = \Delta\mathbf{d}_{\Gamma,c}^G \quad (6.69)$$

The resulting interface correction displacements are denoted with $\Delta\mathbf{d}_{\Gamma,c}^G$. After that, the fluid nodes which are near the interface are adapted properly. This is visualized in Figure 6.27. The adaption of the fluid grid near the interface is somehow arbitrary. It is suggested to spread the correction displacements with a linear distribution from the nearest interface node i to the considered volume node j , via

$$\Delta\mathbf{d}_{c,j}^G = \alpha_{FSI,ij} \Delta\mathbf{d}_{\Gamma,c,i}^G = \left(1 - \frac{l_{ij}}{L}\right) \Delta\mathbf{d}_{\Gamma,c,i}^G. \quad (6.70)$$

Here, l_{ij} is the distance between the interface node i and the volume node j in the reference configuration and L is the maximum distance from the FSI interface in which volume nodes are relocated in the reference configuration. By measuring the distances l and L in physical space, the choice of the maximum distance L depends on the fluid grid resolution and the expected range of interface correction displacements. However, by employing quadrilateral elements in

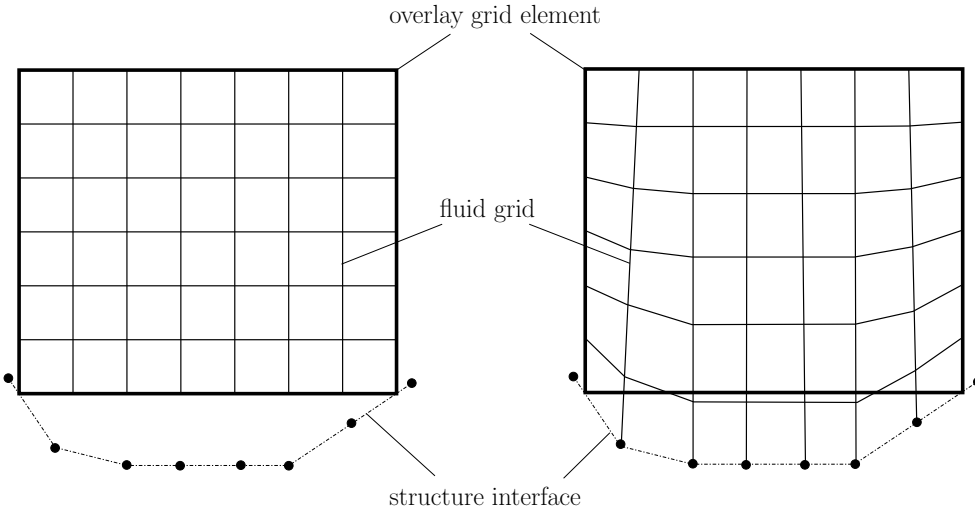


Figure 6.27: Correction step at FSI interface: before correction (left), after correction (right).
Figure is taken from La Spina et al. [145].

2D and hexahedral elements in 3D for the overlay grid, the distances can be measured in parameter space coordinates of the corresponding overlay grid element. Here, it is assumed that the correction of node positions is only performed for the fluid grid nodes located within an overlay grid element which is attached to the FSI interface. Consequently, the maximum relocation distance can be defined to $L = 2$, since the parameter space dimensions for quadrilaterals and hexahedral elements are defined to $[-1; 1]$ in each parameter space direction.

Regardless of whether the distances are measured in the physical space or in the parameter space it has to be performed only once at the beginning of the simulation. Thus, the scaling factor $\alpha_{\text{FSI},ij}$ is fixed for each node for the overall simulation and can be stored in a sparse correction matrix \mathbf{P}_c . All in all, the correction step reduces to a simple matrix vector product

$$\Delta \mathbf{d}_c^G = \mathbf{P}_c \Delta \mathbf{d}_{\Gamma,c}^G. \quad (6.71)$$

Finally, the fluid grid displacements read

$$\mathbf{d}^G = \tilde{\mathbf{d}}^G + \Delta \mathbf{d}_c^G. \quad (6.72)$$

Remark 6.2. *The grid motion algorithm presented in this thesis is also applicable for non-matching fluid and structure grids at the FSI interface, see for example Cebral and Lohner [39], Klöppel et al. [138] and Maman and Farhat [161]. The only algorithmic modification would be made in (6.69). Here, the fluid and structure nodes at the interface would not be forced to exactly match, but to be equal in a projected sense*

$$\mathbf{d}_\Gamma^S - \mathbf{P}_\Gamma \tilde{\mathbf{d}}_\Gamma^G = \Delta \mathbf{d}_{\Gamma,c}^G. \quad (6.73)$$

The interface coupling operator \mathbf{P}_Γ could be defined as mortar operator Klöppel et al. [138] to fulfill the FSI coupling in a weak sense. However, no further modification has to be done in the developed grid motion approach to allow for a non-conforming FSI interface.

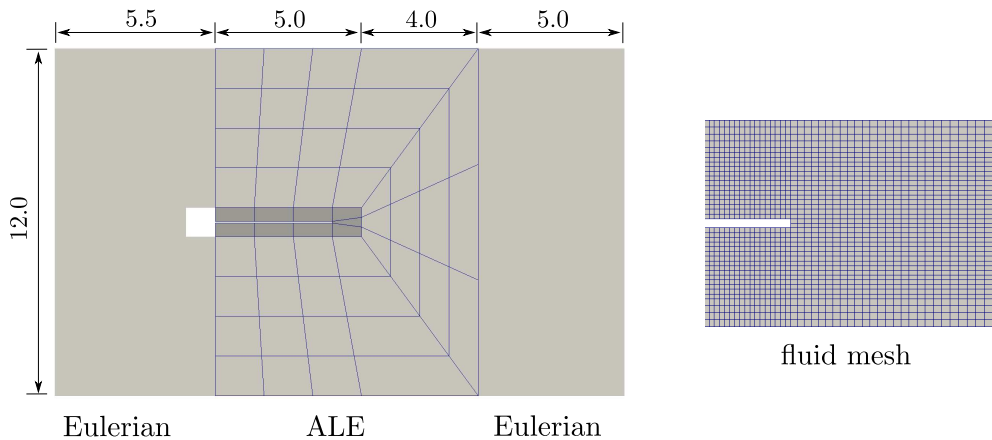


Figure 6.28: Problem setting for flow-induced vibration of a flexible structure. Figure is based on La Spina et al. [145].

6.4.1.3. Numerical example – flow induced vibration of a thin flexible structure

The validation example is the flow-induced vibration of a thin flexible structure originally presented in Ramm and Wall [225]. The same problem dimensions as introduced in Ramm and Wall [225] are used, see Figure 6.28. The solid consists of a rigid block of dimensions 1×1 and a thin flexible structure of dimensions 4×0.06 . The material model for the flexible structure is of Saint-Venant-Kirchhoff type with Poisson's ratio $\nu = 0.35$ and Young's modulus $E = 2.5 \times 10^6$. The structural density is set to $\rho_0^S = 0.1$.

For the fluid field, an inflow of $|\mathbf{v}^F| = 51.3$ is applied on the left side of the domain. The top and the bottom of the domain are defined as perfect slip boundaries. In addition, around the structure a no-slip condition is applied. The fluid viscosity is set to $\mu^F = 1.82 \times 10^{-4}$ and its density to $\rho^F = 1.18 \times 10^{-3}$. This leads to a Reynolds number of circa $Re = 333$. The fluid domain is split into 3 parts as shown in Figure 6.28: the left and the right part are not connected to the flexible structure and thus treated with a pure Eulerian formulation and the middle part is defined as Arbitrary-Lagrangian-Eulerian (ALE) domain. In Figure 6.28, the overlay grid for the ALE domain is visualized. The stiffness for elements in the dark grey region is 100 time higher than for the other elements of the overlay grid. Furthermore, the fluid mesh resolution is exemplarily shown at the tip of the flexible structure, see Figure 6.28. All in all, nearly 70.000 first-order fluid elements are employed for the simulation. The flexible structure is discretized with 60 second-order plane stress quadrilaterals (quad9). The overall simulation time is defined to $T = 10$ with a time step size of $\Delta t = 5 \times 10^{-3}$. By considering the mesh resolution it is obvious that the computational time for solving for the overlay grid displacements becomes negligible compared to the fluid evaluation.

The resulting tip displacements of the structure due to the flow vortices of the fluid are shown in Figure 6.29. Here, the mesh motion algorithm with overlay grid is employed to calculate the numerical solution. The resulting oscillation frequency as well as the amplitude nicely match the results proposed in Ramm and Wall [225]. Also a mesh refinement up to ca. 400.000 fluid elements has been performed by employing an equal overlay grid mesh as given in Figure 6.28. All simulations with overlay grid mesh finished the calculation and produced identical tip displace-

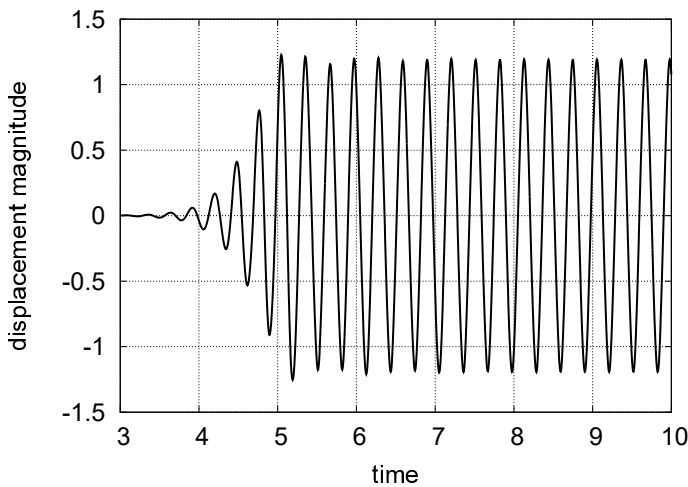


Figure 6.29: Structural tip displacement over time for mesh motion algorithm with overlay grid.
Figure is based on La Spina et al. [145].

ments as shown in Figure 6.29, which confirms the assumption that the overlay grid approach does not influence the physical solution. Thus, a completely independent meshing strategy for the overlay grid and the fluid grid can be employed. This marks a huge advantage compared to classical moving grid FSI approaches.

The overlay grid motion and the fluid pressure are exemplarily visualized for the largest structure tip displacement in Figure 6.30. The projected overlay grid deformation is visualized on the fluid grid in Figure 6.31. In the left part of Figure 6.31 the fluid grid displacements are shown in a grey shading to visualize the dependency on the overlay grid. It can be seen, that the fluid grid directly follows the overlay grid deformation. The deformed fluid grid elements are given in the right part of Figure 6.31. Here, even for strongly deformed fluid elements the mesh quality is still acceptable.

The problem has also been solved with a classical moving grid FSI approach without overlay grid in order to compare both algorithms. The results for the classical approach seem to be not as robust as for the overlay grid approach. Some runs with the classical approach failed due to degenerating elements in case of large mesh deformations. However, also some runs completed successfully with indistinguishable results compared to Figure 6.29. Nevertheless, even if it cannot be demonstrated that the robustness of the proposed overlay grid approach is in all cases better than the classical approach, it is at least at the same level. But, the computational costs are always lower since far less degrees of freedom have to be solved for the overlay grid. Maybe the most beneficial property of the proposed mesh motion algorithm with overlay grid is the flexibility in mesh creation. When a suitable and robust overlay grid is found, the fluid mesh can be gradually refined without loss of robustness. Thus, the developed approach allows for unproblematic mesh refinement studies and convergence analysis by keeping the costs for the mesh movement constantly at a low level.

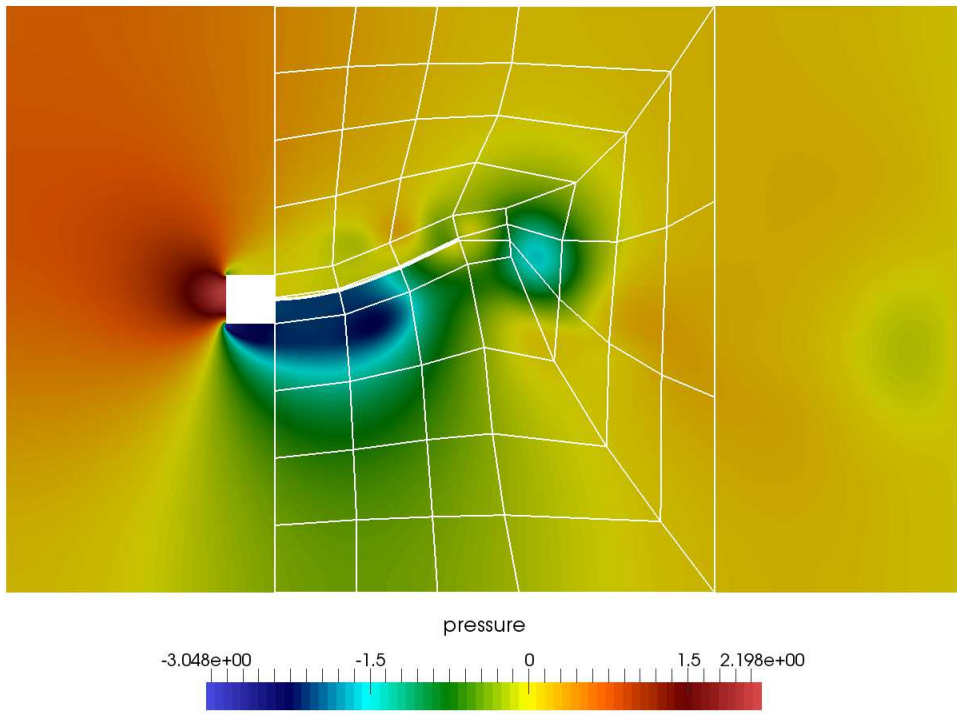


Figure 6.30: Overlay grid deformation and fluid pressure for largest structure tip deflection. Figure is based on La Spina et al. [145].

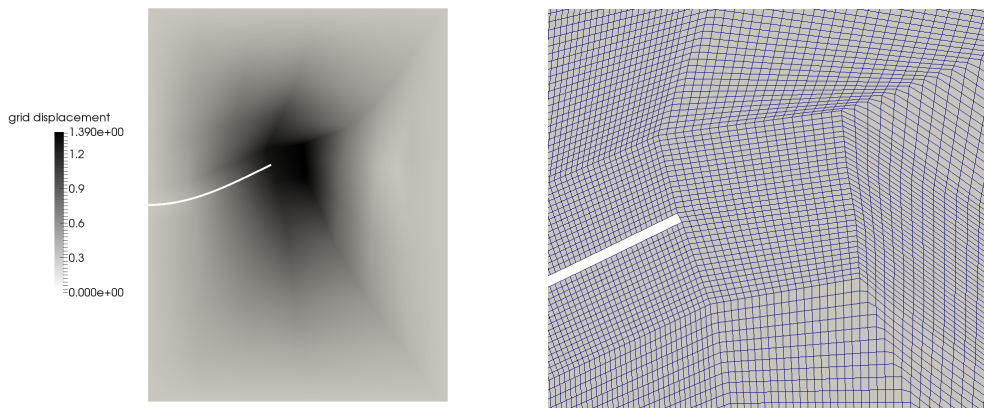


Figure 6.31: Projected overlay grid deformation state on fluid mesh for largest structure tip deflection. Figure is based on La Spina et al. [145].

6.4.2. Algorithmic flexibility – the Hu-Washizu principle

Finally it is demonstrated, that the developed mortar framework for volume couplings easily allows for extensions towards problems, which cannot be identified as classical volume couplings, but which share numerical similarities. As an example for the numerical flexibility of the proposed methods, the Hu-Washizu approach is employed based on the term paper Shu [251], which was supervised by the author. The Hu-Washizu approach according to Washizu [283] is a mixed three-field formulation for structural elasticity problems and was firstly introduced in de Veubeke [56]. It is usually employed to obtain locking-free methods near the incompressible regime in linear and nonlinear elasticity problems for quadrilateral and hexahedral finite elements, see for example Simo and Rifai [255] and Kasper and Taylor [133]. However, its application to tetrahedral elements is very challenging and thus, these elements usually perform very poor near the incompressible regime. Within the Hu-Washizu approach the discrete unknowns are displacements \mathbf{d} , stresses \mathbf{s} and strains \mathbf{e} and usually a saddle-point formulation arises. In Lamichhane et al. [149], this approach was utilized in order to construct locking free tetrahedral elements. Without pointing out the mathematical details of the method, the arising block system of equations is given as

$$\begin{bmatrix} \mathbf{K}_{uu} & \mathbf{K}_{ue} & \mathbf{K}_{us} \\ \mathbf{K}_{eu} & \mathbf{K}_{ee} & -\mathbf{D}^T \\ \mathbf{K}_{su} & -\mathbf{D} & \mathbf{0} \end{bmatrix}^i \begin{bmatrix} \Delta \mathbf{d} \\ \Delta \mathbf{e} \\ \Delta \mathbf{s} \end{bmatrix}^{i+1} = - \begin{bmatrix} \mathbf{r}_u \\ \mathbf{r}_e \\ \mathbf{r}_s \end{bmatrix}^i. \quad (6.74)$$

Here, dual shape functions were employed to form a biorthogonal system with respect to stresses and strains, which results in a diagonal matrix \mathbf{D} and thus allows for computationally efficient condensation procedures similar to the explanations in Chapter 3 and Chapter 4. The matrix \mathbf{D} is basically the same as for the construction of the mortar based projection operator in (6.8). Therefore, the final system of equations to be solved contains only displacement unknowns and the major number of unknowns, i.e. the stress and strain unknowns per node, vanish. For the sake of brevity, the condensed system is not given here but can be found in Shu [251]. This approach was successfully implemented in the employed in-house code BACI (cf. Wall et al. [282]) based on the developed volume coupling framework and numerical methods such as the evaluation of dual shape functions (see Section 6.2.3.1) were reused. Its performance compared to standard first-order tetrahedral elements is demonstrated with the benchmark example called Cooks membrane, also known as Cooks cantilever. This example is widely used in the literature to examine volumetric locking behavior of finite elements. It was firstly introduced in Cook [48] as 2D example and has been adapted to 3D settings by several authors, see for example Müller and Starke [180] and Nguyen-Thoi et al. [182]. It consists of a clamped cantilever with a Neumann load at the top of the body, which results in a bending dominated deformation state. Details on the commonly employed material parameters and loads can be found in the mentioned literature. The most important point is that a Poisson's ratio of $\nu = 0.4999$ is employed for the following comparison, which is very close to the incompressible limit of $\nu = 0.5$. The resulting stress state and the deformation are illustrated in Figure 6.32. The stress solution for standard first-order tetrahedral elements (tet4) shows strong and arbitrarily occurring oscillations, which demonstrate that this element type is absolutely not suited for such scenarios. In contrast, the tetrahedral element based on the Hu-Washizu approach (tet4-hw) performs very well and shows a reasonable stress state. Consequently, the standard tet4 element is stiffer than the tet4-hw ele-

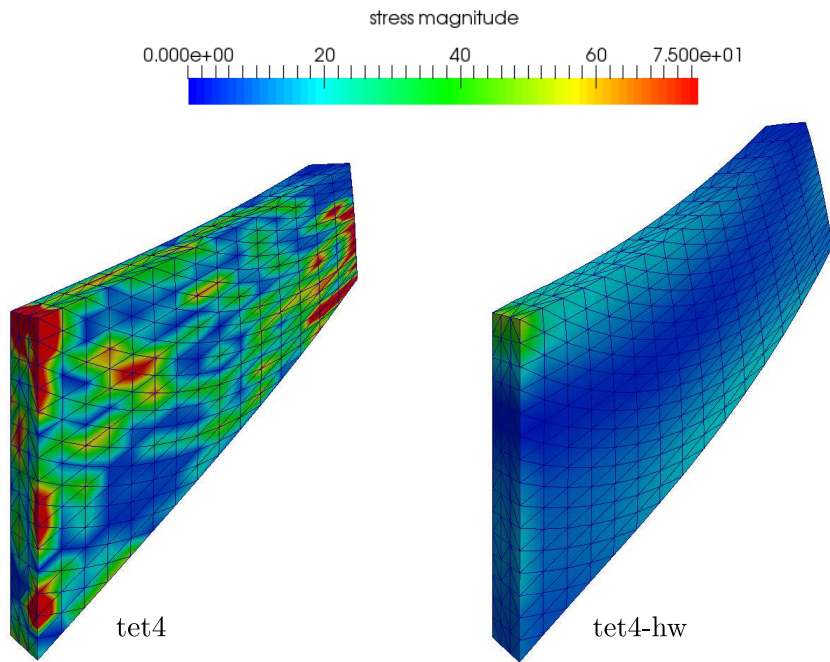


Figure 6.32: Cooks cantilever: Comparison of stress state and deformation for standard tet4 elements and tet4 Hu-Washizu elements (tet4-hw).

ment and leads to smaller deformations. Additionally to this comparison, also the convergence behavior and the performance compared with other element types have been investigated, but these details are beyond the scope of this thesis. All information and further investigations concerning the performance of this method can be found in Shu [251].

The realization of the Hu-Washizu approach for first-order tetrahedral elements demonstrates that the use of the implemented methods is not only restricted to classical volume coupling methods, but also allows for various related approaches.

7. Summary and Outlook

In this thesis, mortar finite element methods have been investigated in the context of three different fields:

- contact scenarios involving vertices, edges and surfaces, see Chapter 4,
- modeling of fretting wear and finite wear effects, see Chapter 5,
- general volume coupled problems, see Chapter 6.

On the basis of these topics, it has been demonstrated that basic methodologies from classical 2D mortar methods can be transferred towards problems of lower dimension (point and line contact), complex interface phenomena of equal dimension (wear modeling) and 3D problems (volume couplings). The following sections provide a detailed summary of achievements accomplished in the mentioned topics and give an outlook on possible future research.

7.1. Mortar methods for computational contact of vertices, edges and surfaces

In the first part, mortar methods have been investigated in the context of computational contact mechanics of vertices, edges and surfaces being simultaneously involved. These contact scenarios were rarely addressed in the existing literature on computational contact mechanics. The presented thesis contributes the first extensive scientific work on this topic in the context of mortar finite element methods. Thus, the main focus of this part of the thesis was a consistent extension of the frictional contact formulation for surface contact based on dual Lagrange multipliers towards scenarios of point, line and surface contact in a finite deformation regime.

Concerning this goal, three major contributions have been presented. Firstly, a variationally consistent problem formulation has been derived by the use of three different Lagrange multipliers, which define the point, line and surface contact, respectively. The point Lagrange multiplier has been defined on the boundary of all vertices, the line Lagrange multiplier has been defined on the boundary of all edges and the surface Lagrange multiplier has been used on all surfaces. Herewith, all contact scenarios except the contact of non-parallel edges are well defined. This special case has been treated with a penalty regularization in this thesis. Such a problem statement for combined complex contact scenarios has been stated in this thesis for the first time.

Secondly, a robust dual mortar approach for finite deformation line contact within implicit time integration schemes has been developed. While the naturally occurring contact of 1D boundaries for 2D problems has been well investigated by several authors, it was never developed for line contact of 3D bodies before this thesis. The employed dual Lagrange multipliers for line contact have the same beneficial properties as those for surface contact formulations

and those for classical domain decomposition (DD) applications. In addition, a novel numerical integration scheme has been developed in order to achieve highest possible accuracy and robustness of the line contact scenario. Mortar formulations of surface contact scenarios have already been developed and can be found in the vast amount of publications concerning this topic. Point contact resulting from interacting vertices was realized with a classical and well-known node-to-segment (NTS) approach since for the employed first-order Lagrangian discretizations a vertex is directly represented by a single node. Thus, robust spatial discretization and numerical integration of line contact was the missing piece for the all entity contact formulation and has been successfully developed and implemented in this thesis.

Thirdly, the point, line and surface contact formulations have been successfully combined to an all entity contact approach without requiring a heuristic transition parameter between the contact formulations. This has been achieved by a consistent modification of the Lagrange multiplier shape functions. While the modification of the shape functions was already developed for so-called crosspoints in mesh tying applications, it was used for contact interaction problems for the first time. The consistency of the proposed shape function modification has been demonstrated with several numerical examples. Furthermore, the shape function modification and the use of dual Lagrange multipliers for line and surface contact have been combined in a way, that still allows for very efficient solution procedures by the elimination of additional point, line and surface Lagrange multiplier unknowns. With this novel methodology, an undesirable increase in global system size is avoided.

All in all, it has been demonstrated that classic dual mortar approaches for surface-to-surface contact formulations, which are well-investigated in the existing literature, can be sufficiently extended towards complex scenarios of point, line and surface contact in a fully nonlinear realm. Although a substantial progress towards a general contact formulation with respect to the involved geometrical entities has been made, there is still room for improvements for mortar based contact formulations. Thus, in the following, an outlook concerning the all entity contact formulation as well as classical surface contact approaches is given.

The first obvious improvement of the presented all entity contact formulation is its extension towards second-order Lagrangian finite elements. This was already realized for surface contact in Popp [210] and Puso et al. [220], but it was not yet done for mortar line contact. When doing so, one important aspect is the adaption of the robust numerical integration scheme towards line contact of second-order elements. Following the idea of Puso et al. [220], a robust and accurate numerical integration could be achieved by subdividing the line and surface elements into first-order integration elements. This is visualized in Figure 7.1. Then, the proposed segment-based integration scheme could be applied for each pair of line and surface integration element. In addition, the choice of the Lagrange multiplier interpolation for line contact should be investigated when second-order elements are employed. In this context, it would be interesting whether first-order Lagrange multiplier shape functions are a suitable choice in combination with second-order displacement shape functions. Similar investigations for surface contact can be found in Popp et al. [213] and Puso et al. [220].

A more intricate point of improvement would be the avoidance of the developed penalty regularization for contact of non-parallel edges by the introduction of a Lagrange multiplier approach. Up to the best knowledge of the author, it would be very hard to do so from a mathematical point of view, since the problem would then tend to be over-constrained, which could be described as an interface/ contact locking phenomenon. In addition, the restriction that the lower dimensional

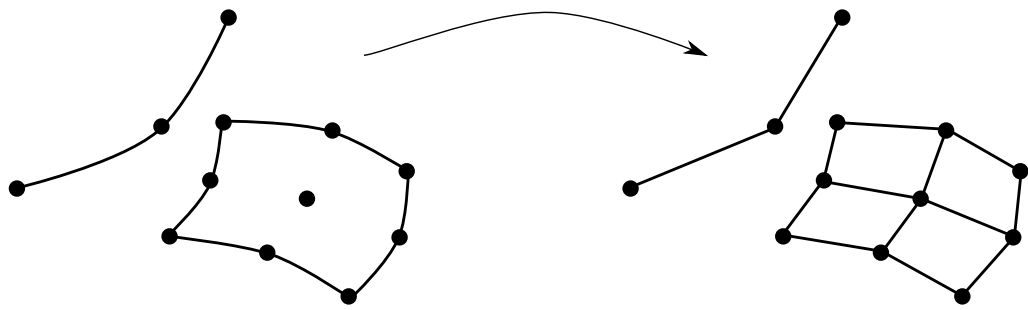


Figure 7.1: Suggested subdivision of a second-order line element and an exemplary second-order surface element (quad9) into integration elements for the segment-based integration scheme. Integration algorithm 4.3 can then be applied for each pair of line and surface integration elements.

entity is a priori defined as slave side could cause problems, as discussed in Section 4.8.5. As a basis for following investigations, two-pass algorithms seem promising to get rid of these problems, but usually they also suffer from interface locking, see Park et al. [196] and Taylor and Papadopoulos [266].

When setting special emphasis on accurate and robust contact interaction of non-smooth geometries, one should also think of smooth surface contact. Nowadays, a lot of publications focus on smooth mortar discretizations in the context of isogeometric analysis (IGA) and also approaches with dual Lagrange multipliers have been published very recently, see Brivadis et al. [33] and Seitz et al. [244]. Thus, it would be very interesting to combine the smooth and exact geometry representation of IGA with the developed all entity contact formulation. The shape function modification has already been discussed in the context of crosspoints in DD applications with IGA in Brivadis et al. [33], which makes it very promising that the all entity contact formulation is extendable to IGA.

7.2. Mortar methods for wear modeling

In the second part of this thesis, the complex interface and volume coupled phenomenon of wear has been investigated in the context of mortar surface contact. The main focus was set on the development of suitable numerical algorithms for the calculation of fretting wear effects and finite wear effects. Both types have never been investigated in the context of dual mortar contact methods for 3D bodies.

Thus, four major achievements regarding wear modeling have been presented. Firstly, two different spatial discretization approaches for the wear depth based on mortar methods have been investigated, namely the internal state variable approach and the primary variable approach. Each of these two approaches exhibits beneficial properties with regard to certain aspects, such as numerical efficiency and implementation effort. Both approaches were already available in the existing literature, but have never been implemented in combination with dual shape functions for contact of 3D bodies. This was firstly realized in this thesis. In addition, the application of these discretization approaches on fretting wear and finite wear simulations was outlined.

7. Summary and Outlook

Secondly, a numerical algorithm for simulating fretting wear has been developed based on earlier work in Gitterle [87], which was restricted to 2D problems. The developed algorithm manipulates the gap measure between the two involved bodies by the extent of the calculated wear depth. Such a procedure is well-established for modeling fretting wear problems. However, this thesis presented the first 3D implementation based on dual mortar methods including frictional effects.

Thirdly, a novel implicit finite wear algorithm has been developed without any restrictive simplifications or model assumptions like frictionless contact or steady-state motions. Herein, huge material loss and the accompanying shape change have been treated with an Arbitrary-Lagrangian-Eulerian (ALE) approach, which guarantees for highest element quality. Computational efficiency has been achieved by eliminating additional unknowns due to the Lagrange multiplier approach for constraint enforcement and wear unknowns with the help of dual shape functions.

Finally, the developed finite wear algorithm has been extended towards thermal effects. Material loss is explicitly calculated after a thermo-structure-contact interaction step is solved. This represents the first realization of a 3D thermo-structure-contact-wear interaction algorithm in a finite deformation regime.

Based on the wear algorithms presented in this thesis, further extensions towards complex volume and interface effects should be considered. In order to allow for numerical modeling of real world applications, it would be desirable to extend the finite wear algorithm towards plasticity effects, which usually require storage of plastic information at the discrete spatial integration points, see Seitz et al. [243]. Therefore, the proposed ALE approach has to be modified in order to allow for a consistent mapping of integration point quantities. Approaches for such mappings can be found in Bussetta et al. [35] and Ortiz and Quigley [190]. A first numerical model combining plastic effects and wear can be found in Doca [61].

In order to guarantee unconditional stability, the developed thermo-structure-contact-wear interaction algorithm should be improved to solve wear effects and shape change implicitly and fully coupled. In addition, dependencies of the temperatures on the wear coefficient could be developed. The created framework provides a suitable basis for this purpose. Also the contact interaction with debris represents an interesting aspect of future work. Here, one could think of manipulating the wear coefficient in order to take debris into account. Alternatively, debris could be resolved as particles within the contact zone, which would significantly increase the numerical complexity but likewise improve the modeling accuracy.

In addition, material loss at vertices and edges based on the previously developed all entity contact formulation is a very interesting and challenging aspect of future research. Here, a simple node relocation with an ALE approach is not desirable anymore since a worn vertex could instantly become a very small new surface bounded by newly created vertices as visualized in Figure 7.2 for 2D problems. Here, a finite element algorithm which captures the effect of the newly created surface is desirable.

Finally, extensions towards anisotropic effects are desirable, see Mróz and Stupkiewicz [179] and Zmitrowicz [307, 308]. In this context, a first numerical framework based on the boundary element method can be found in Rodríguez-Tembleque et al. [235]. Also the interaction of wear with other interface effects like adhesion in Sauer [241] and lubricated contact in Temizer and Stupkiewicz [269] and Yang and Laursen [300] could be an interesting field of future research.

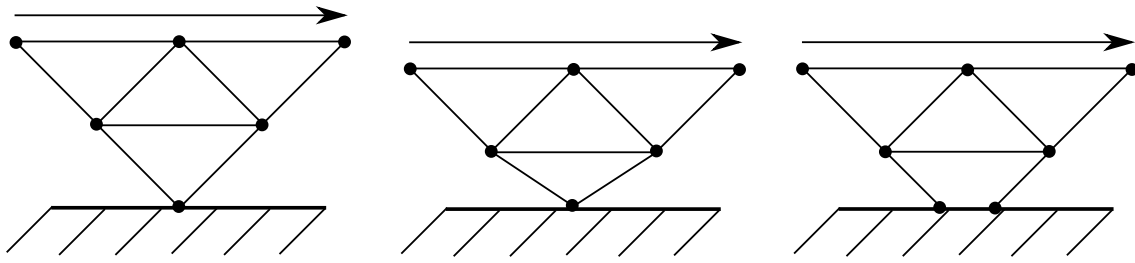


Figure 7.2: Wear at vertex: Contact without wear of a rigid foundation with a body discretized with four tri3 elements (left), node relocation due to wear with developed ALE algorithm (middle), desired and physically reasonable finite element approach for wear at sharp geometries (right).

7.3. Mortar methods for volume coupled problems

In the last part of this thesis, mortar methods have been investigated as basis for volume projections of nodal information. There, special focus was set on the use of dual mortar methods to reach an acceptable numerical effort to make these methods applicable to various fields of applications.

Therefore, three major contributions have been presented in this thesis. Firstly, a mortar based projection operator has been derived for general 3D problems. Its evaluation has been realized with two numerical integration schemes, namely the segment-based integration and the element-based integration, which are well-established in mortar formulations for interface problems. While the element-based integration technique was already employed in Bussetta et al. [35] for 3D problems, the most accurate segment-based integration has been employed in this thesis for the first time. Furthermore, dual shape functions for arbitrary first-order and second-order Lagrangian finite elements have been employed. For this purpose, the idea of a basis transformation from Popp et al. [213] has been extended towards 3D second-order elements to guarantee a robust evaluation of dual shape functions for arbitrary mesh distortions.

Secondly, a novel and general methodology for the monolithic solution process of volume coupled multiphysics on different meshes has been proposed in order to allow for the highest possible flexibility in terms of spatial discretization. Therein, also proper enforcement of boundary conditions and the potential contact interaction for volume coupled multiphysics have been investigated. To the author's best knowledge, the only publications addressing a similar topic are Dureisseix and Bavestrello [64] and Néron and Dureisseix [181], but these investigations are restricted to partitioned solution schemes in 2D without contact interactions.

Thirdly, the proposed dual mortar methods and numerical algorithms for volume coupled problems have been extended successfully to other volume problems. The result of these efforts is a novel grid motion approach for fluid-structure interaction problems with ALE formulation which is characterized by an increased computational efficiency. In addition, the flexible implementation of mortar tools also allows for the use in applications, which cannot be identified as mortar methods anymore, but share a lot of numerical similarities. This has been demonstrated by the implementation of the Hu-Washizu principle for nonlinear elasticity based on dual shape functions from Lamichhane et al. [149] to obtain computationally efficient and locking

free tetrahedral finite elements near the incompressible limit. Herewith, it has been shown that the developed tools and projection operators can be easily incorporated in various problem formulations to achieve increased robustness, solution accuracy and computational efficiency.

Future research can be split into improvements of the developed projection operators and methodologies and into possible applications of them. In order to increase the accuracy of the information transfer schemes, the boundary problems discussed in Section 6.2.5 should be investigated in more detail. The outlined possibility of performing numerical integration exclusively for the enclosed domain of both meshes seems reasonable, but would drastically increase computational complexity and cost. In addition, when applying these projection operators for the coupling of multiphysics problems, two projections from Ω_1 to Ω_2 and vice versa are required, see Section 6.3.1. In order to guarantee the highest possible consistency of the methods, the two projections should fulfill the following conditions for the initial setting of the meshes:

$$\mathbf{s}_1 = \mathbf{P}_{12} \mathbf{s}_2 , \quad \mathbf{s}_2 = \mathbf{P}_{21} \mathbf{s}_1 . \quad (7.1)$$

This can be equivalently expressed in terms of mesh position \mathbf{X}_i in the reference configuration instead of generic fields \mathbf{s}_i . The requirements in (7.1) are generally not achieved, since the boundary problems from Section 6.2.5 and the numerical integration schemes introduce errors. An analogy to this problem can be found in the context of classical mortar methods for DD applications, where the target mesh (slave side) is slightly modified in order to guarantee for balance of angular momentum, which is called mesh initialization, see Popp [210] and Puso [216]. Such a procedure is also applicable to the volume coupled problems, but with strongly increased complexity since projection operators themselves are dependent on the initial mesh positions and, compared to DD schemes, two conditions have to be fulfilled in (7.1).

The developed dual mortar projection operators and numerical methods allow for even more reasonable applications. A good example in this regard can be found in Hesch et al. [105], where it has been suggested to employ dual mortar methods for the projection between a fix grid fluid and an immersed structure for fluid-structure interaction problems. Up to now, only rather inefficient standard mortar methods are employed for this purpose and the use of the developed dual mortar projection operators seems very promising.

A. Comparison of Segment-Based and Element-Based Integration

While aspects for numerical efficiency of contact algorithms have been briefly discussed in Section 4.8.6, detailed information of the two introduced integration schemes have not been provided. Since these integration schemes represent the most time consuming algorithmic steps and, at the same time, the most critical steps regarding numerical accuracy for a contact evaluation, they should be carefully chosen. Thus, a fair comparison providing the most important aspects of these integration schemes is provided. The following comparison of segment-based integration (cf. Algorithm 3.1) and element-based integration (cf. Algorithm 4.5) is taken from the author's publication Farah et al. [73]. It is strongly referred to surface-to-surface contact scenarios, but the basic argumentation can directly be transferred to line contact scenarios introduced in Section 4.6. For volume coupled problems, both integration methods are briefly compared for a porous media example in Section 6.3.4.3.

A.1. Theoretical comparison

In this section, the segment-based integration and the element-based integration are compared with regards to their most important properties. Hence, the advantages and the drawbacks of each scheme are clearly demonstrated and discussed. Remember that all following statements refer to 3D surface-to-surface contact problems.

A.1.1. Choice of integration rule

The first issue to be highlighted is the choice of a suitable integration rule. In principle, there are two different approaches to perform a discrete numerical integration. First, the position and the weighting of each integration point could be calculated for each integration domain individually by using a moment-fitting related approach, which can be found in Mousavi and Sukumar [177], Mousavi et al. [178] and Xiao [297], or by employing methods based on the divergence theorem explained in Sommariva and Vianello [256, 257] and Sudhakar et al. [265]. The second possibility is to use simple predefined integration rules, for example Gauss-Legendre quadrature or Gauss-Lobatto quadrature. Due to the fact that using some algorithm for calculating the integration points for every integration domain individually requires a significantly higher implementational and computational effort than using predefined rules, only predefined quadrature rules are considered in the following.

For the segment-based integration scheme the domain resulting from the polygon clipping procedure in Algorithm 3.1 is in general an arbitrary convex polygon. Thus, adopting common

A. Comparison of Segment-Based and Element-Based Integration



Figure A.1: Triangulation methods: center-based triangulation (left), Delaunay triangulation (right). Figure is taken from Farah et al. [73].

quadrature rules first requires some preparation step, in which the polygon is divided into simply shaped domains. The preferred methods for that are triangulation approaches, especially the Delaunay triangulation in Lee and Schachter [156] or center-based triangulation (both shown in Figure A.1). As can be seen, using Delaunay triangulation creates the smallest possible number of triangular integration cells, i.e. $N - 2$ triangular cells for a convex polygon with N vertices. Here, it should be noted that the Delaunay triangulation is not a unique procedure. Therefore, small errors could occur if different-shaped integration cells are created within one time step. However, in all tested simulations no negative effect could be detected by employing the Delaunay triangulation. Therefore, it is the best triangulation approach for the segment-based integration scheme. However, it would also be possible to subdivide the polygon into quadrilateral and triangular integration cells by adopting the so-called ear-clipping algorithm in Meisters [172]. This was employed in Wilking and Bischoff [287] with positive effects on the efficiency of the mortar integration. However, this may lead to critical scenarios with strongly distorted quadrilaterals whose Jacobians become rational. Thus, they cannot be integrated with the desired accuracy by a polynomial based integration rule (e.g. any kind of Gauss quadrature). All in all, the preferred procedure is to subdivide the polygon into triangular cells having a constant Jacobian by Delaunay triangulation and to then employ standard Gauss-Legendre quadrature for these triangles. However, note that the highest polynomial degree that can be computed exactly by the integration rule should be chosen somewhat higher than the product of shape functions on slave and master side would indicate. This is due to the nonlinearity of the projections between auxiliary plane and actual contact surfaces. Based the experiences gained from the tested numerical examples, it is suggested to use 7 Gauss points per triangular integration cell, which are able to exactly calculate a polynomial degree of 5.

The choice of integration rule for the element-based integration method is simply based on the shape of the slave element, because the slave element parameter space equals the integration domain parameter space. However, for the element-based scheme the choice of the number of integration points is an extremely crucial issue. In many published articles, the authors aim at overcoming the negative influence due to the non-smoothness of the integrand with a very high number of integration points, see Fischer and Wriggers [80, 81]. To analyze the results of using polynomial based Gauss quadrature rules for integrands with weak discontinuities occurring within the contact boundary, a simple academic test case is provided, see Figure A.2. As can be seen, the set of functions $F_1(x)$ are piece-wise linear functions in $x \in [-1, 1]$ having a kink at k with $F_1(k) = 1$ and the boundary values $F_1(-1) = F_1(1) = 0$. Varying the kink position from -1 to 1 and performing the numerical integration with 2, 3, 4 and 5 Gauss-Legendre points gives the error plot also shown in Figure A.2. It is obvious that the maximum integration error indeed decreases with an increasing integration point number. Nevertheless, the integration error

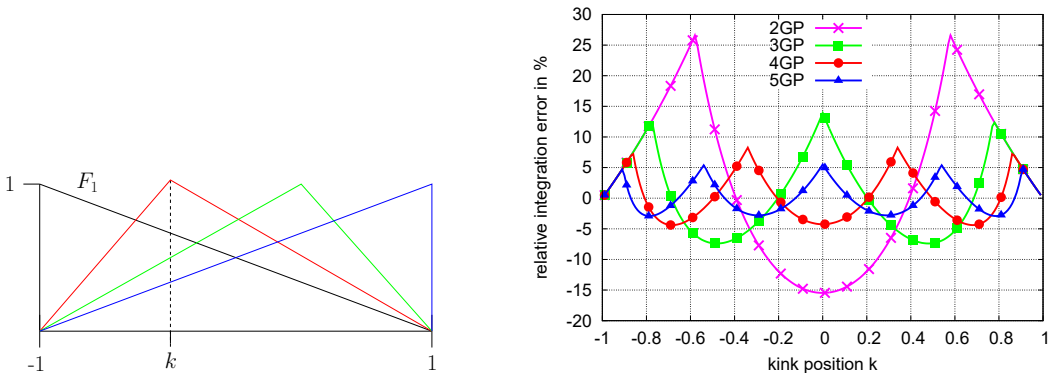


Figure A.2: Test case to analyze possible integration errors due to weak discontinuities. Figure is taken from Farah et al. [73].

strongly depends on the kink position. Therefore, using an increasing integration point number does not necessarily reduce the occurring error for any kink position. In other words, for certain kink positions Gauss rules with few integration points produce smaller errors than much higher Gauss point numbers. Having a closer look at the well-known Gauss point positions, one notices that the kink locations with the largest integration errors actually are the integration point positions. This interesting result can be also transferred to the 3D contact problems, i.e. 2D integration domains. In addition, when having a fine mesh for the master surface and a coarse mesh for the slave surface, the danger of kinks occurring in the integration domain of a slave element significantly increases. Thus, all in all, the element-based integration method is very sensitive to the employed integration point number and also to the mesh size ratio between slave and master surface. Therefore, defining a suitable integration point number is very problem-dependent and requires a certain amount of experience, which is a very crucial drawback compared to the segment-based method.

A.1.2. Geometry approximation and discrete projection

In this subsection all aspects concerning geometry approximation and the resulting impact on the discrete projections between slave and master surfaces are discussed. In a first step, any approximation of the interface geometry, which is involved in applying either of the two integration methods, will be reviewed and discussed in more detail. Then, the general problems of the discrete projection operations are considered and towards the end of this subsection the sensitivity of the two integration methods with regard to these projection problems is evaluated.

As described in Algorithm 3.1, a main step of performing the segment-based method is the construction of an auxiliary plane onto which the actual slave and master elements are projected to define the integration domain. In the general case of warped surface facets (e.g. quadrilaterals) this introduces a slight approximation of the actual slave surface. As a result of this approximation, all projections of slave nodes, master nodes and integration points are performed along the same auxiliary plane normal \mathbf{n}_0 .

Compared to the segment-based method, the element-based method does not require an auxiliary plane because there is no information from the master side which has to be processed on the

A. Comparison of Segment-Based and Element-Based Integration

slave side. Thus, the slave element parameter space becomes the integration domain parameter space right away and no geometric approximation is done. In addition, the discrete projections are computed along a continuous (and thus more consistent) normal field defined on the slave surface.

The projections from slave to master surface and vice versa are usually carried out by local Newton-Raphson iteration, which in general is very robust and guarantees local quadratic convergence. Nevertheless, there may be certain problems resulting in a divergent iterative solution process. The occurrence of such problems will be discussed in the following. In general, a Newton-Raphson scheme is given as

$$\mathbf{x}^{i+1} = \mathbf{x}^i - [\text{grad}(\mathbf{f}(\mathbf{x}^i))]^{-1} \mathbf{f}(\mathbf{x}^i), \quad (\text{A.1})$$

where $\mathbf{f}(\mathbf{x}^i)$ represents a real- and vector-valued function, \mathbf{x}^i is the vector-valued coordinate and the upper index i denotes the iteration number. The iteration outlined in (A.1) is repeated until the simple convergence criterion $\|\mathbf{f}(\mathbf{x}^{i+1})\| < \text{tol}$ is met. Considering the projection operation from a slave element to a master element, the vector-valued function \mathbf{f} , and thus the residual for the Newton-Raphson iteration, is given as

$$\mathbf{f}(\xi^{(2)}, \eta^{(2)}, \varpi) = \sum_j N_j(\xi^{(2)}, \eta^{(2)}) \mathbf{x}_j^{(2)} - \varpi \mathbf{n}_c - \mathbf{x}_{\text{int}}^{(1)} = \mathbf{0}, \quad (\text{A.2})$$

where N_j represents the shape function at each node of the master element, ϖ denotes the projection distance in direction of the employed normal vector \mathbf{n}_c and $\mathbf{x}_{\text{int}}^{(1)}$ is the location of the integration point onto the slave side in physical space. The unknowns are the coordinates $\xi^{(2)}, \eta^{(2)}$ of the projected point in the parameter space of the master element and the projection distance ϖ . These three quantities define the solution vector \mathbf{s} as

$$\mathbf{s} = \begin{bmatrix} \xi^{(2)} \\ \eta^{(2)} \\ \varpi \end{bmatrix}. \quad (\text{A.3})$$

A differentiation of \mathbf{f} with respect to the solution vector \mathbf{s} yields

$$\text{grad}(\mathbf{f}) = \left[\sum_j \frac{\partial N_j}{\partial \xi^{(2)}} \mathbf{x}_j^{(2)}, \quad \sum_j \frac{\partial N_j}{\partial \eta^{(2)}} \mathbf{x}_j^{(2)}, \quad -\mathbf{n}_c \right]. \quad (\text{A.4})$$

This matrix is also known as Jacobian of the projection. With these expressions at hand, possible problems that may occur due to degenerate cases of discrete projection are illustrated. As an example, a distorted but planar quadrilateral element to project on is given with its parameter space, see Figure A.3. The first critical projection can easily be identified around the singular point S , where no unique parameter space coordinates can be found. Evaluating $\text{grad}(\mathbf{f})$ at S yields a Jacobian with a zero-valued determinant. Thus, the Jacobian in (A.4) becomes singular and its inversion is impossible. The second critical case occurs when a point is projected into the inverted area I of the element parameter space, where the coordinate system is inverted with regard to the coordinate ξ . However, a projection is still possible in that case, Newton's method converges and mapping the projected point to spatial coordinates yields the correct result. Finally, the most critical case is considered, which is caused by a non-intersection of the projection normal \mathbf{n}_c with the generally warped element plane. Here, no solution can be found

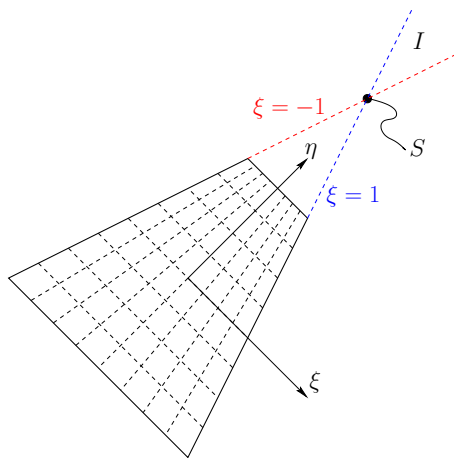


Figure A.3: Distorted, planar quadrilateral element to project on with the singular point S and the inverted space I . Figure is taken from Farah [72].

in (A.1) and therefore Newton's method does not converge. Such a projection arises when the element to project on is almost parallel to the projection normal or if it is warped.

In general, all the problems mentioned above could arise for both integration methods. Considering the segment-based integration scheme with its auxiliary plane approximation, only the projection of the integration points onto the slave and master surface is a nonlinear operation, and therefore possibly problematic. However, for the element-based integration method, problems occur much more frequently than for the segment-based integration. This is due to the fact that no geometric approximations (such as auxiliary planes) are introduced, and thus the actual surface normal is used as projection normal. However, this surface normal may change drastically in certain regions due to high curvatures of the contact surfaces and relatively coarse meshes. In contrast, the normal vector is assumed to be constant for each slave and master element pair in the segment-based approach.

In summary: If the local Newton-Raphson scheme diverges or yields an error, the projected point is either located on the singularity point, which is always outside a convex polygon, or the projection vector does not intersect the element plane. In both cases, the integration point is irrelevant for the integration and its contribution is set to zero. Therefore, despite the more frequent divergence of the local Newton-Raphson scheme for element-based integration, this situation can be dealt with relatively easily and discrete projection does not represent a critical drawback for this scheme.

A.1.3. Boundary problems

In the following subsection, possible problems at the boundary of the contact interface are discussed, which only arise for the element-based integration scheme.

There exist two characteristic problem settings associated with the boundary of the contact interface, see Figure A.4. Both problem settings share the fact that they introduce strong discontinuities (i.e. jumps) in the integrand of mortar matrix \mathbf{M} in addition to the usual weak discontinuities

A. Comparison of Segment-Based and Element-Based Integration

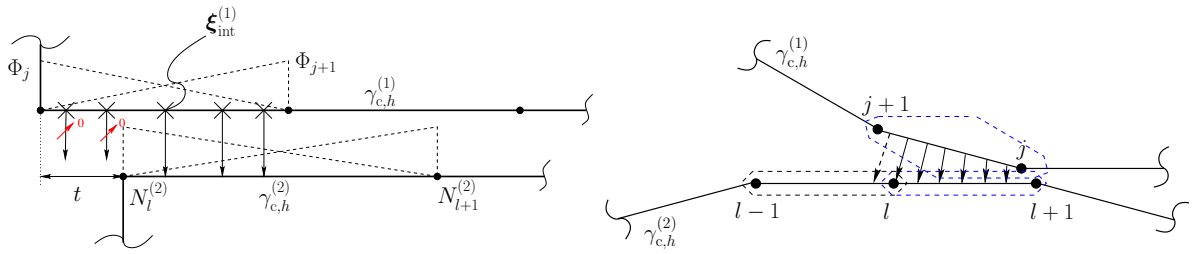


Figure A.4: Two characteristic problem settings of the element-based integration associated with the boundary of the contact interface. Dropping edge situation (left) and small contact search parameter (right). Figure is taken from Farah et al. [73].

(i.e. kinks). This significantly increases the requirements on the integration rule in terms of accuracy, and thus causes large integration errors in general.

The two characteristic problem settings shown in Figure A.4 are now analyzed in more detail. For the sake of simplicity, both scenarios are illustrated for 2D mortar contact, but all following considerations can be directly transferred to the 3D case. The first problematic setup is a dropping edge problem, see the left subfigure of Figure A.4. Here, parameter t defines the partition of the slave element which has a zero contribution to the integrand. At the position where the outermost master node l is projected onto the slave element, the integrand jumps from zero to a non-zero value. Thus, a strong discontinuity in the expression to be numerically integrated occurs. A possible remedy in order to avoid excessive integration errors for the element-based scheme will be proposed at the end of this subsection. Obviously, the segment-based approach does not encounter the described problem, since no contact segments are detected in the non-overlapping partition t .

Another contact scenario which produces a strong discontinuity is shown in the right subfigure of Figure A.4. The sketch illustrates two boundary meshes being located pretty near to each other and potentially coming into contact. The dashed lines represent the bounding boxes which are typically used for search algorithms. The specific search algorithms employed here are not presented in detail, but the reader is exemplarily referred to Yang and Laursen [299] instead. Only if the bounding boxes of a slave element and a corresponding master element overlap, then the numerical integration of the mortar matrices will be carried out for these elements. Thus the numerical integration will not be carried out for the master element containing the nodes $l-1$ and l . The projection of the integration points from slave element to the master is represented by arrows. Here, the red arrow represents a projection onto the master element that is not considered by the search algorithm. Due to this, the integration point associated with the red arrow has a zero contribution to the mortar integrals. This again leads to a strong discontinuity in the integrand. In contrast to the dropping edge situation, however, this problem can be avoided by an increased search radius. Thus, it does not pose a critical limitation to the accuracy of the element-based integration and will not be considered further.

Nevertheless, the dropping edge situation described above remains to be taken care of. Intuitively, eliminating the impact of strong discontinuities in an integral expression could be achieved by a significantly increased number of integration points. But as will be shown by the numerical results in Section A.2, this would require so many integration points that the element-

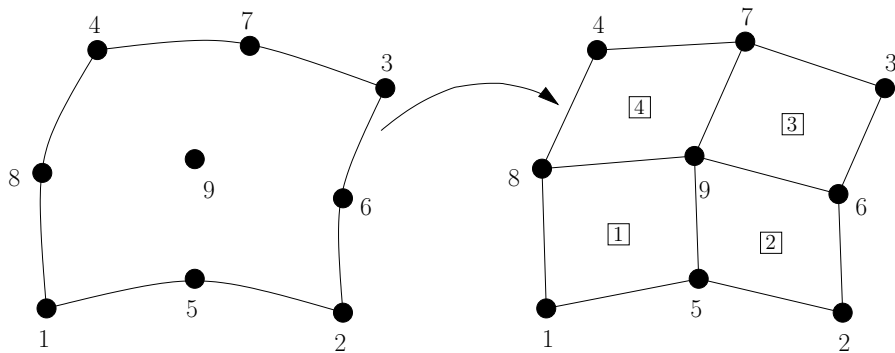


Figure A.5: Subdividing a second-order contact element for the segment-based integration scheme. Exemplarily, a 9-node quadrilateral element is split into four 4-node quadrilateral subelements, to which the segment-based algorithm 1 can then be applied nearly unchanged. Figure is taken from Popp [210].

based integration scheme becomes very inefficient. Thus, a different solution is needed. The developed approach to handle such boundary problems will be termed *boundary-segmentation* in the following. Herein, the segment-based integration scheme will be employed for problematic slave elements having strong discontinuities in the integrand and for non-critical slave elements within the contact zone the element-based integration is used. The critical slave elements will be identified by detecting integration points whose projection misses all of the master elements associated with this slave element. With this combination of segment-based and element-based integration, boundary problems can be avoided. Therefore, the preferred integration strategy consists of employing the element-based integration wherever possible and only if the problematic boundary scenarios occur, the integration algorithm will be changed to the segment-based scheme.

A.1.4. Second-order interpolation

The next aspect to be highlighted is mortar integration for higher-order finite element interpolation. Specifically, second-order Lagrangian elements are considered here. For the segment-based integration method, the authors in Puso et al. [220] have suggested a simple, but efficient modification as shown in Figure A.5. This approach can be interpreted as a direct extension to the segment-based integration scheme.

The modification generates linearly interpolated subelements and establishes geometric mappings from parent element space to subsegment space and vice versa. Thus, it is possible to evaluate higher-order shape function products in the integrand of the mortar matrices and the weighted gap without any algorithmic changes. This approach only affects the integration domain itself, which is less accurate in terms of geometry. Compared to the segment-based integration scheme, the element-based method requires no such modification step for second-order interpolation. Numerical integration is still simply carried out in the slave element parameter space without any geometric approximation. However, the impact of weak and strong discontinuities for quadratically interpolated elements is larger than for linearly interpolated elements.

A. Comparison of Segment-Based and Element-Based Integration

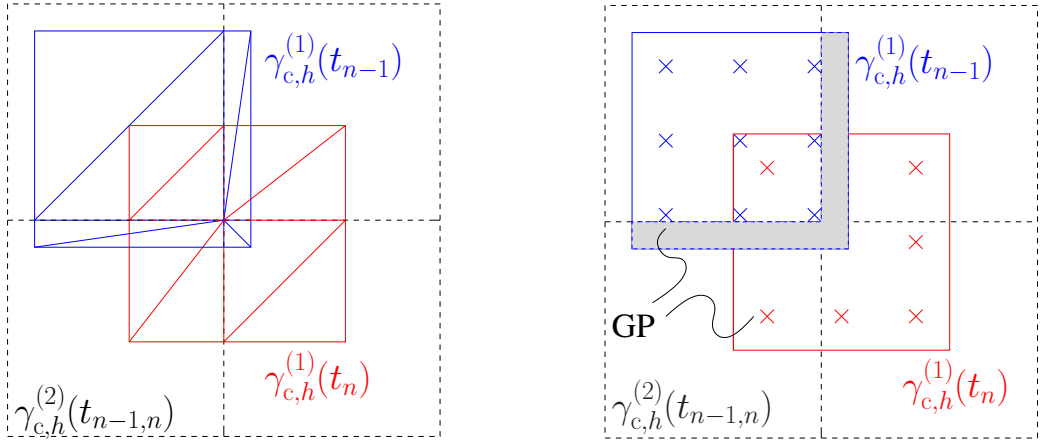


Figure A.6: Moving slave surface in time step t_{n-1} (blue) and t_n (red). With segment-based integration (left) and element-based integration (right). Figure is taken from Farah et al. [73].

Therefore, there exist greater demands on the employed integration formulas. Some examples concerning element-based integration with second-order elements are shown in Section A.2.

A.1.5. Frictional contact

As compared with frictionless mortar contact formulations, the frictional version requires not only the discrete weighted gap $\tilde{g}_{n,j}$ but also the discrete relative tangential velocity $(\tilde{\mathbf{v}}_{\tau,\text{rel}})_j$ of each slave node j as fundamental kinematic measure. As can be seen from (3.43), the definition of $(\tilde{\mathbf{v}}_{\tau,\text{rel}})_j$ contains time derivatives of the mortar matrices \mathbf{D} and \mathbf{M} . Introducing a local algorithmic time stepping procedure of backward Euler type at time t_n (see e.g. Gitterle et al. [88] and Yang et al. [301]) yields

$$\begin{aligned}\dot{\mathbf{D}}[j,k] &\approx \frac{\mathbf{D}[j,k](t_n) - \mathbf{D}[j,k](t_{n-1})}{\Delta t}, \\ \dot{\mathbf{M}}[j,l] &\approx \frac{\mathbf{M}[j,l](t_n) - \mathbf{M}[j,l](t_{n-1})}{\Delta t}.\end{aligned}\quad (\text{A.5})$$

Hence, the time derivatives in (3.43) are approximated by difference quotients of the mortar matrix entries evaluated at the current time step t_n and the last time step t_{n-1} . For the segment-based integration method these differences are in general not problematic because the mortar entries for both time steps are calculated with a high accuracy. In contrast, the element-based integration scheme is in general not able to compute the mortar integrals with a comparable accuracy (unless an excessive number of integration points is used). Thus, at both time steps there occur errors in the mortar expressions which could accumulate. Beside this effect, some entries in the mortar matrices might not even be detected by the element-based integration method. To illustrate this effect, both mortar integration schemes are shown at different time steps, see Figure A.6. Here, the black dashed lines represent four master elements not changing their position during the considered time interval. Additionally, the slave element is defined by blue lines for time step t_{n-1}

and by red lines for time step t_n . For standard Gauss rules, the integration points are located within the element and not on the element edges. Therefore, there exist element regions where the element-based integration is not able to detect contributions from master elements, see the gray colored area in Figure A.6. The resulting loss of accuracy for frictionless contact is not severe, because the evaluated terms within the element dominate the mortar matrices. In contrast, for frictional contact the non-detected contributions lead to a significantly increased relative error for the relative tangential velocity $(\tilde{\mathbf{v}}_{\tau,\text{rel}})_j$, which directly affects the decision, whether a node is in stick or slip state.

All in all, for frictional mortar contact the element-based integration is more sensitive than for the frictionless mortar contact. The segment-based integration is the best available integration scheme for this problems with regard to accuracy and ensures the highest possible robustness for a frictional mortar contact algorithm.

A.1.6. Conservation of linear and angular momentum

Finally, the ability to conserve linear and angular momentum is analyzed and compared for the two integration methods. All investigations are done in the semi-discrete setting, i.e. after spatial discretization but before time discretization, see also Section 4.8.3. First, as elaborated e.g. in Puso and Laursen [218] the requirement for linear momentum conservation can be expressed as

$$\mathbf{f}^{(1)} - \mathbf{f}^{(2)} = \sum_{j=1}^{m^{(1)}} \left(\sum_{k=1}^{n^{(1)}} \mathbf{D}[j, k] \boldsymbol{\lambda}_j - \sum_{l=1}^{n^{(2)}} \mathbf{M}[j, l] \boldsymbol{\lambda}_j \right) = \mathbf{0}, \quad (\text{A.6})$$

which can be simplified to

$$\sum_{k=1}^{n^{(1)}} \mathbf{D}[j, k] - \sum_{l=1}^{n^{(2)}} \mathbf{M}[j, l] = \mathbf{0} \quad \forall j = 1, \dots, m^{(1)}. \quad (\text{A.7})$$

Several authors, see e.g. Puso and Laursen [218], have shown, that this requirement is exactly satisfied for the segment-based integration when integrating both mortar matrices \mathbf{D} and \mathbf{M} with the same integration procedure. If the mortar integrals were evaluated independently of each other, conservation of linear momentum would not be guaranteed in general. Using the element-based integration scheme inevitably generates additional integration errors for the mortar matrix \mathbf{M} and the weighted gap \tilde{g}_j . However, these errors interestingly cancel out when evaluating the sum expressions in (A.7) due to the partition of unity property of the master side shape functions:

$$\sum_{k=1}^{n^{(1)}} \left(\int N_k \Phi_j \, dA \right) - \sum_{l=1}^{n^{(2)}} \left(\int N_l \Phi_j \, dA \right) = \int \Phi_j \, dA - \int \Phi_j \, dA = 0. \quad (\text{A.8})$$

Therefore, the element-based integration method also conserves linear momentum exactly. The influence of the generated integration errors could therefore be interpreted as a changed arrangement of the master side forces to the associated nodes. However, summing them up yields the same total force acting on slave and master side.

Enforcing an exact conservation of angular momentum is rather challenging in the context of mortar methods for unilateral contact. The basic requirement for conservation of angular momentum is given as

$$\mathbf{0} = \mathbf{m}^{(1)} - \mathbf{m}^{(2)} = \sum_{j=1}^{m^{(1)}} \left[\sum_{k=1}^{n^{(1)}} \mathbf{x}_k^{(1)} \times (\mathbf{D}[j, k] \boldsymbol{\lambda}_j) - \sum_{l=1}^{n^{(2)}} \mathbf{x}_l^{(2)} \times (\mathbf{M}[j, l] \boldsymbol{\lambda}_j) \right]. \quad (\text{A.9})$$

This condition is fulfilled when either the jump vector \mathbf{g}_j becomes zero for each active slave node j , i.e.

$$\mathbf{g}_j = \sum_{k=1}^{n^{(1)}} \mathbf{D}[j, k] \mathbf{x}_k^{(1)} - \sum_{l=1}^{n^{(2)}} \mathbf{M}[j, l] \mathbf{x}_l^{(2)} = \mathbf{0}, \quad (\text{A.10})$$

or alternatively when the discrete nodal Lagrange multiplier vector $\boldsymbol{\lambda}_j$ and \mathbf{g}_j are always collinear. As investigated in Yang and Laursen [299], both conditions will usually be slightly violated for the segment-based integration. Employing the element-based integration method one can obviously not expect any improvement with regard to angular momentum conservation, but rather a deterioration. However, as the examples in Section A.2 illustrate, almost identical results can be obtained for both integration methods concerning the conservation of angular momentum.

A.2. Numerical examples

In this section the theoretically discussed properties of the segment-based and element-based integration schemes are verified on the basis of four numerical examples. The first example is a classical contact patch test which is conducted to assess the accuracy of both integration methods and the effect of the newly proposed boundary-segmentation procedure. The second example analyzes the effect of numerical integration on the convergence properties for both first-order and second-order finite element interpolations. Thirdly, a two tori impact example is considered to evaluate the integration methods with regard to efficiency and conservation laws. Finally, an ironing example illustrates the applicability of both integration methods to frictional contact problems.

A.2.1. Consistency – patch test

The first example is supposed to demonstrate the accuracy of the introduced integration schemes and their influence on the consistency of the mortar method. The problem setting consists a lower block and a smaller upper block being in contact. This is basically the same example as introduced in Section 4.9.1.2 in the context of a combined contact algorithm for vertices, edges and surfaces being in contact.

The lower block is supported at the bottom surface and the upper block's top surface as well as the free part of the top surface of the lower block are loaded with a constant pressure $p = -0.5$ in vertical direction. Both blocks are defined with equal material parameters based on a neo-Hookean material model with Young's modulus $E = 100$ and Poisson's ratio $\nu = 0.0$. The discretization consists of linearly interpolated hexahedral elements. In the following, both

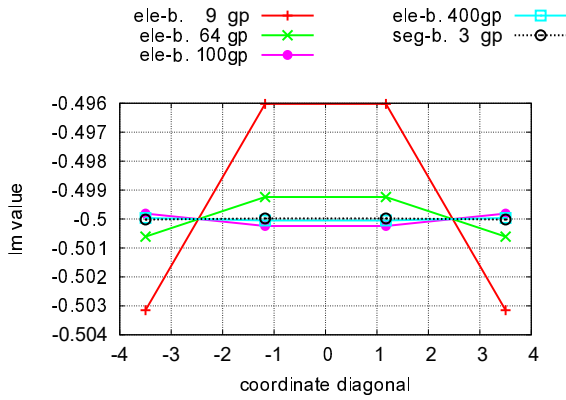


Figure A.7: Computed Lagrange multiplier values at the contact interface along a diagonal axis for overlapping master elements with element-based integration and segment-based integration. Figure is taken from Farah et al. [73].

possibilities of choosing slave and master surface are tested and compared. Independent from this choice, the mortar method should be able to exactly transmit constant contact pressure across the interface, which characterizes the physically correct solution.

The first simulations are carried out with a mortar setting where the lower surface of the upper block is the slave surface and the upper surface of the lower block is the master surface. Thus, all slave elements are covered with master elements causing only weak discontinuities in the integrand of the second mortar matrix and the weighted gap. The resulting Lagrange multiplier (i.e. contact pressure) values are exemplarily plotted along a diagonal line of the mortar surface, see Figure A.7. Here, the results are given for the segment-based integration method employing 3 Gauss points per triangular integration cell and for the element-based integration scheme employing 9, 64, 100 and 400 Gauss points per slave element. The analytical solution is represented by a constant contact pressure of -0.5 . The segment-based method passes this patch test. However, the element-based integration method fails the patch test and yields slight deviations of the discrete Lagrange multiplier values. However, even if only 9 Gauss points are employed, the errors introduced by the element-based integration scheme are very small as compared with typical engineering accuracies.

Now, the slave and master sides are switched, which results in an overlapping slave side. This yields not only weak discontinuities for the integration of slave elements located within the contact zone, but also strong discontinuities in the integrands of overlapping slave elements. Again, the computed Lagrange multiplier values are plotted along a diagonal line of the mortar interface for both segment-based and element-based integration methods, see Figure A.8. It can be seen that the Lagrange multiplier values are again exactly reproduced (to machine precision) for the segment-based integration scheme. The element-based integration method, however, yields unacceptably large errors for all investigated numbers of integration points, even for 400 Gauss points per slave element. The reason for this failure are the strong discontinuities (jumps) which occur in the mortar integrands for this setup. In addition, the results demonstrate how difficult it may be to predict the number of required Gauss points. Employing 64 Gauss points per slave element creates larger errors than 9 Gauss points in this case due the fact that to some points of

A. Comparison of Segment-Based and Element-Based Integration

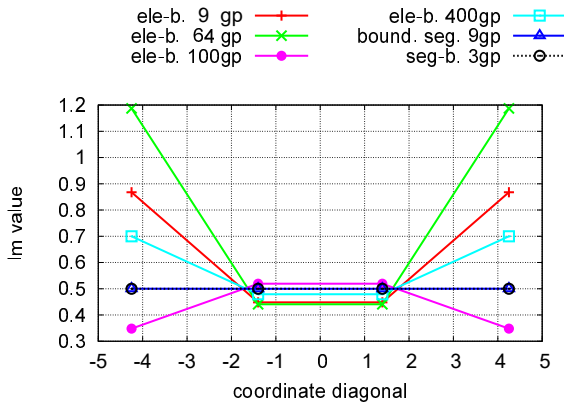


Figure A.8: Computed Lagrange multiplier values at the contact interface along a diagonal axis for overlapping slave elements with element-based integration, segment-based integration and boundary segmentation. Figure is taken from Farah et al. [73].

the 64-point rule are located very close to the occurring strong discontinuities. As discussed in Figure A.2 for the 2D case this proximity leads to a significant increase of the overall error level. To handle this problem, the proposed boundary-segmentation is tested, which employs element-based integration for slave elements located fully within the contact interface and segment-based integration scheme for overlapping elements at the boundary of the contact interface. The resulting Lagrange multipliers are much better approximated than for the element-based integration method, which demonstrates why boundary-segmentation is a natural choice in order to prevent excessive integration errors. However, the boundary-segmentation does obviously not reach an accuracy to machine precision, but the error levels are comparable to those of element-based integration for fully projecting slave elements, cf. Figure A.7.

A.2.2. Accuracy – bending beam

This numerical example is considered to investigate the convergence order of the discretization error measured in the energy norm. The problem setting is a classical domain decomposition setup with non-matching meshes, see Figure A.9. All problem data has been re-used from earlier investigations in Popp et al. [213] to which it is referred for further details. The example is based on a small deformation assumption and a linear-elastic material behavior. Therefore, an analytical solution of this problem is well-known from Gross et al. [92] and is going to be used as reference result. The small deformation assumption results in a linearized strain tensor $\epsilon = \frac{1}{2}(\nabla \otimes \mathbf{u} + (\nabla \otimes \mathbf{u})^T)$. In addition, the linear-elastic material behavior is based on Hookes law $\sigma = \mathbf{C} : \epsilon$, where \mathbf{C} represents the fourth-order constitutive tensor with the components

$$C_{ijkl} = \frac{E\nu}{(1+\nu)(1-2\nu)}(\delta_{ij}\delta_{kl}) + \frac{E}{2(1+\nu)}(\delta_{ik}\delta_{jl} + \delta_{il}\delta_{jk}). \quad (\text{A.11})$$

Within Equation (A.11), Young's modulus is represented by E and ν denotes Poisson's ratio. In the following, the material parameter are given as $E = 1000$ and $\nu = 0.3$. The considered bending structure is a cuboid with dimensions $l_x \times l_y \times l_z$ supported such that all rigid body

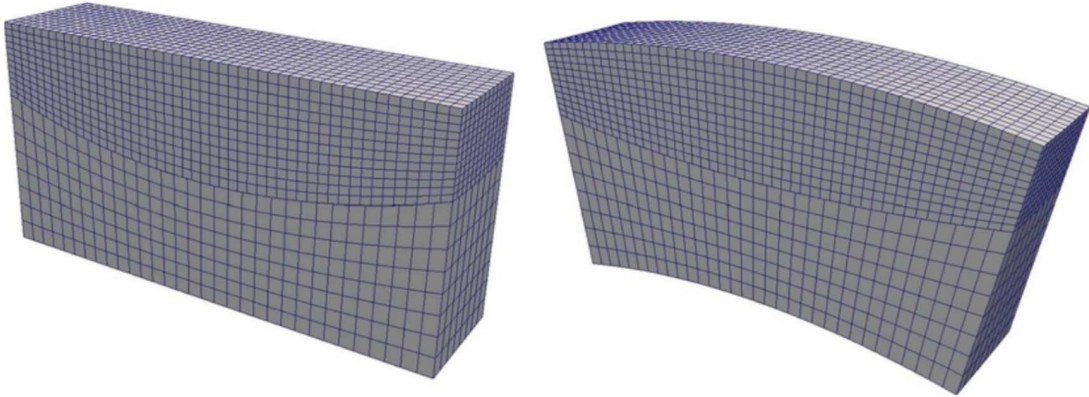


Figure A.9: Example with bending structure in initial configuration (left) and deformed configuration (right). Figure is taken from Farah et al. [73].

modes are removed, in detail with

$$u_x(0, 0, 0) = u_y(0, 0, 0) = u_z(0, 0, 0) = u_x(0, \frac{l_y}{2}, 0) = u_z(0, \frac{l_y}{2}, 0) = u_z(\frac{l_x}{2}, 0, 0) \equiv 0. \quad (\text{A.12})$$

The load case is defined as pure bending around the z -axis with the applied distributed loads $f_x = \pm 2p\frac{y}{l_y}$ at $x = \pm \frac{l_x}{2}$. Here, the load parameter is defined as $p = 100$. The analytical solution of this problem is well known Timoshenko and Goodier [271] and given as

$$u_x = \frac{2p}{El_y}xy, \quad u_y = \frac{p}{El_y}(-x^2 - \nu y^2 + \nu z^2), \quad u_z = -\frac{2p\nu}{El_y}yz. \quad (\text{A.13})$$

The simulations are performed for a geometrical setting of $l_x = 4$, $l_y = 2$ and $l_z = 1$. The following investigations heavily build upon the discretization error $\mathbf{u} - \mathbf{u}_h$ measured in the energy norm, which is defined as

$$\|\mathbf{u} - \mathbf{u}_h\|_{\text{energy}} = \sqrt{\int_{\Omega} (\boldsymbol{\epsilon} - \boldsymbol{\epsilon}_h) : \mathbf{C} : (\boldsymbol{\epsilon} - \boldsymbol{\epsilon}_h) d\Omega}, \quad (\text{A.14})$$

with the linearized strain tensor $\boldsymbol{\epsilon}$ and the linear-elastic constitutive tensor \mathbf{C} . The mortar interface is defined having a curved shape, with the ratio of the characteristic element sizes between the discretization of slave and master surface being fixed at $\frac{h^{(1)}}{h^{(2)}} = \frac{2}{3}$. Both sub-domains are discretized with hexahedral Lagrangian finite elements of polynomial degree $p = 1$ or $p = 2$, i.e. typical first- and second-order elements. This yields an expected convergence order of $\mathcal{O}(h^p)$. The interpolation of the Lagrange multipliers is done by dual shape functions of the same order as the displacement interpolation, see Popp et al. [213] for further details.

To numerically analyze convergence rates of the discretization error, the characteristic mesh size h is uniformly refined and the results are illustrated in Figure A.10. The expected convergence order of $\mathcal{O}(h^p)$ is perfectly represented by the segment-based integration schemes for both linearly and quadratically interpolated elements, as shown by the black dashed lines. For linear elements, element-based integration gives nearly the same errors as the segment-based

A. Comparison of Segment-Based and Element-Based Integration

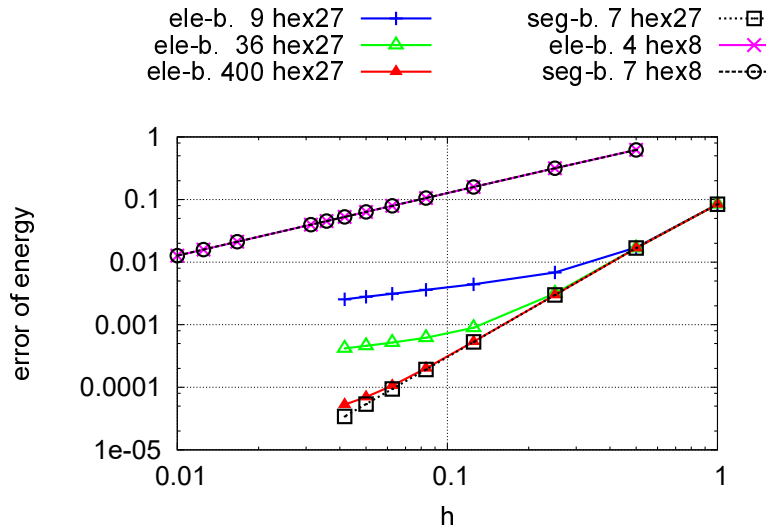


Figure A.10: Convergence of error in the energy norm with uniform mesh refinement for hexahedral meshes employing hex8 and hex27 elements with element-based and segment-based integration. Plot is taken from Farah et al. [73].

method. However, for quadratic elements, the element-based scheme fails to deliver an optimal convergence behavior for all employed numbers of Gauss points. The mesh size, below which the element-based method significantly differs from the segment-based solution depends on the number of used Gauss points. Employing more and more integration points reduces the undesirable effect of sub-optimal convergence rates, and the results slowly approach those of the segment-based version. It is very likely that this behavior would also occur for linearly interpolated elements, however only for very small characteristic element sizes, which arguably are irrelevant from a purely practical engineering point of view.

A.2.3. Efficiency – two tori impact

The impact of two tori, firstly introduced in the context of contact search algorithms in Yang and Laursen [299], is considered to compare the two integration methods concerning computational efficiency and conservation of linear and angular momentum in a large scale example. The problem setting taken up here is described in Popp et al. [214] and slightly differs from the original example. The thin-walled tori have the same size with a minor radius of 24, a major radius of 76 and a wall thickness of 4.5. The tori distance is 140 in the horizontal direction and 140 in the vertical direction. In addition, one torus is rotated by 45 degrees around the vertical axis. The contact interaction is described by an initial velocity $\hat{v} = [30.0 \ 23.0 \ 0.0]^T$ of the unrotated torus. The employed material is a neo-Hookean model with $E = 5500$, $\nu = 0.3$ and a density of $\rho_0 = 0.1$ for both bodies. The discretization is equal for both tori and results in a total number of 23.340 linearly interpolated hexahedral elements. For time integration, a generalized- α scheme is employed as introduced in Section 2.2.3 and 3.5.1. The calculation of contact interaction is based on 200 time steps, and the numerical solution is performed in parallel on 16 cores. Some characteristic stages of deformation during the impact process are shown in Figure A.11.

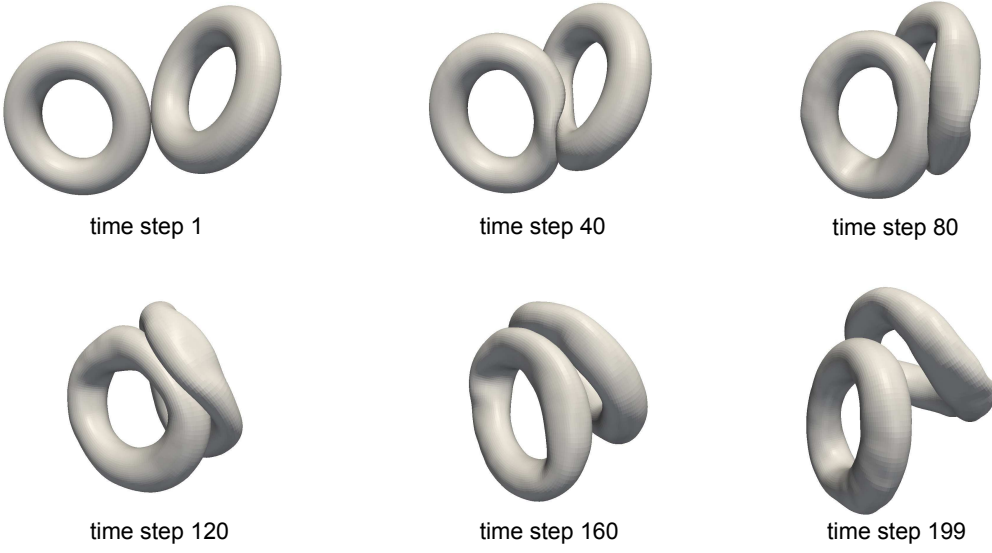


Figure A.11: Deformation of the two tori during frictionless impact. The time steps 1, 40, 80, 120, 160 and 199 are visualized. Figure is taken from Farah et al. [73].

First, the efficiency of the introduced integration methods is investigated. For this purpose, the average time required for integration for one Newton step within each time step are plotted in the left subfigure of Figure A.12. In addition, the accuracy of the integration schemes is validated by the right subfigure of Figure A.12, which visualizes the deviations of the relative L^2 -norm of the displacements with respect to a reference solution based on segment-based integration with 12 Gauss points per integration cell. Using 37 or 64 Gauss points per integration cell does not significantly change the displacement norm compared to 12 Gauss points. The relative error of the L^2 -norm, is given as

$$\epsilon_{\text{displ}} = \frac{\|\mathbf{d}_{\text{seg}12}\| - \|\mathbf{d}_n\|}{\|\mathbf{d}_{\text{seg}12}\|}, \quad (\text{A.15})$$

where \mathbf{d}_n represents the current numerical solution and $\mathbf{d}_{\text{seg}12}$ the reference solution. For this example, the segment-based integration is tested with 3 and 7 Gauss points per integration cell, and the element-based integration method employs 4 to 64 Gauss points per slave element. For the segment-based integration, 3 Gauss points per integration cell is the smallest sensible number of integration points. Thus, it can be seen that compared to the segment-based integration, the element-based integration method has the ability to significantly reduce the number of integration points. In addition, it is obvious that the required integration time scales linearly with the employed number of integration points, which is why all curves in A.12 have a similar shape. The characteristic shape of the curves depends strongly on the active set. Thus, ups and downs of the curves occur due to time steps with a correspondingly high or low number of nodes being in contact. From time step 190 onwards, the curves are zero-valued due to the fact that the two tori are not in contact any more. Interestingly, the L^2 -displacement errors are only small and decrease further with more and more integration points. Even 4 Gauss points per element are sufficient for

A. Comparison of Segment-Based and Element-Based Integration

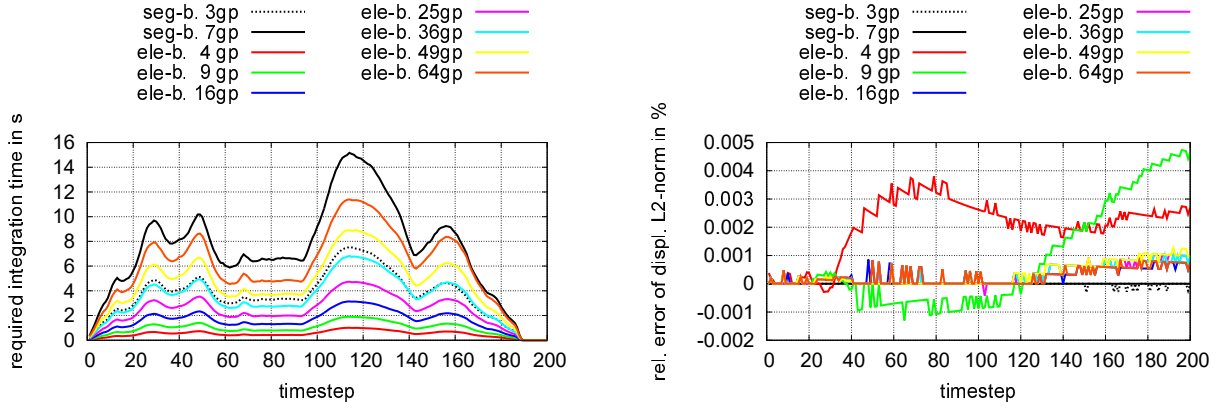


Figure A.12: Results for the frictionless tori impact with element-based and segment-based integration: averaged required integration time per Newton step (left) and relative error of computed displacement field (right). Plots are taken from Farah et al. [73].

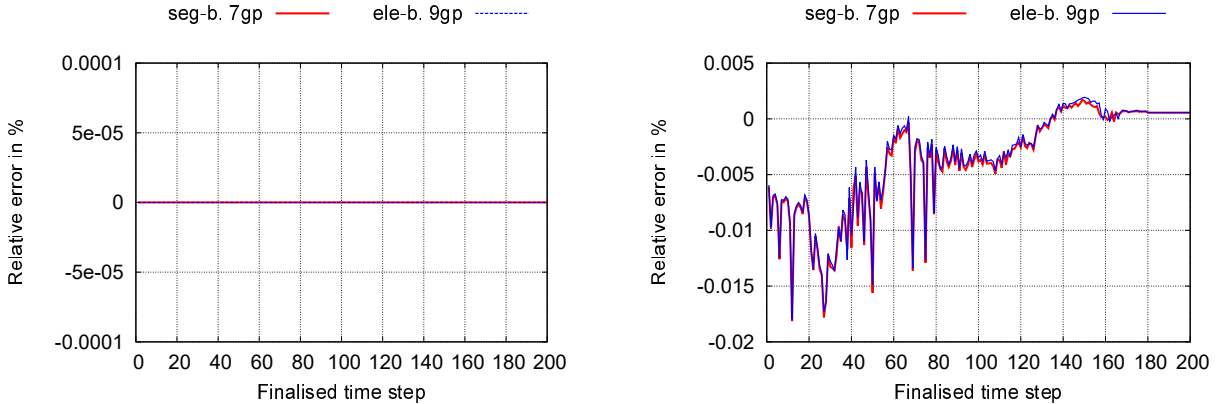


Figure A.13: Investigation concerning the conservation laws for the large scale two tori impact with element-based and segment-based integration. Plot of linear momentum (left) and Plot of angular momentum (right). Plots are taken from Farah et al. [73].

the L^2 -displacement error being negligible. However, with 4 Gauss points per element, only 7% of integration time of the segment-based integration employing 7 integration points per integration cell are required. All in all, it becomes obvious that the element-based integration scheme allows for dramatic reductions of the computational costs for practical applications, while still maintaining a sufficient level of accuracy.

The next aspect to be investigated is the conservation of linear and angular momentum. As described theoretically in Section A.1.6, the conservation of linear momentum is guaranteed for both integration methods, but the conservation of angular momentum may be slightly violated. Figure A.13 illustrates the numerical results with regard to conservation properties. The left subfigure confirms the exact fulfillment of linear momentum, whereas the right subfigure shows the relative error of the angular momentum. Again, element-based integration produces equally accurate results as segment-based integration. The element-based scheme with 9 Gauss points

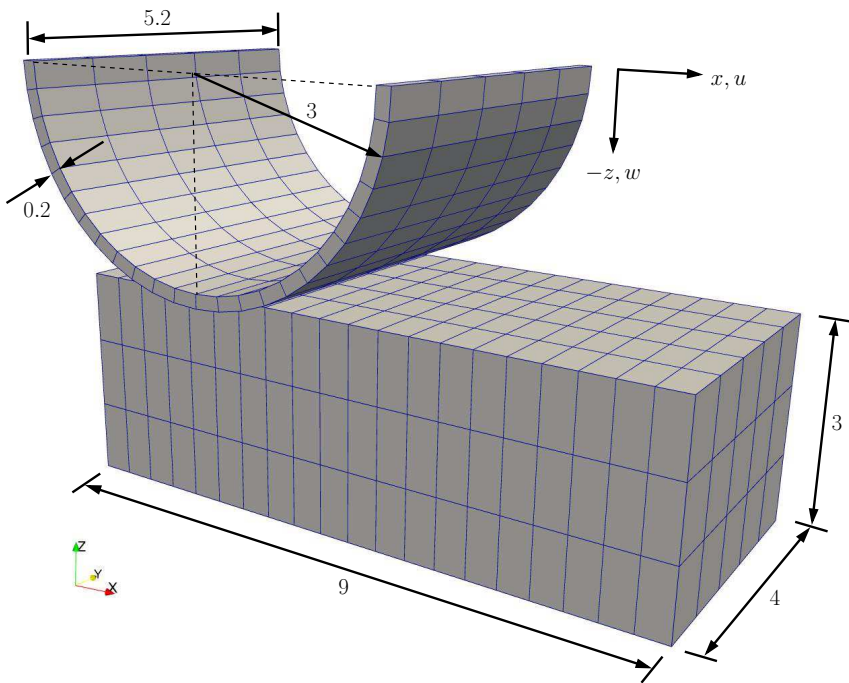


Figure A.14: Setup of the frictional ironing problem. Figure is taken from Gitterle [87].

per slave element exhibits the same error level as the segment-based integration scheme. Other Gauss rules for the element-based integration have also been tested and gave equal results with regard to conservation properties.

A.2.4. Frictional sliding – ironing

The last example is a frictional extension to the ironing problem investigated in Popp et al. [212]. The geometric setup is shown in Figure A.14. The upper body is a hollow half cylinder with a neo-Hookean material model with Young's modulus $E = 1000$ and Poisson's ratio $\nu = 0.3$. The other body is a block being fixed at the lower surface and has the material parameter $E = 1$ and $\nu = 0.3$. Frictional contact is modeled by Coulomb's law with the friction coefficient $\tilde{\gamma} = 0.2$. At the beginning of the simulation, the cylinder is pressed into the block by a prescribed vertical displacement of $w = 1.4$ within 20 steps. After this intrusion, the vertical displacement is held constant and the cylinder slides along the block with a prescribed displacement $u = 4.0$ within 130 additional steps. The problem is discretized with 8-node hexahedral elements as shown in Figure A.14. The top surface of the block is chosen as slave side and the bottom surface of the cylinder as master side, thus yielding only weak but no strong discontinuities in the mortar integrands. Typical stages of deformation during contact and associated patterns of tangential forces due to friction can be seen in Figure A.15.

To validate the accuracy of the element-based integration, the segment-based integration scheme is considered as reference solution. Despite the fact that the segment-based integration produces only marginal integration errors, some non-physical effects (e.g. slightly oscillating tractions) occur during the simulation. This could be avoided by well-known surface smoothing proce-

A. Comparison of Segment-Based and Element-Based Integration

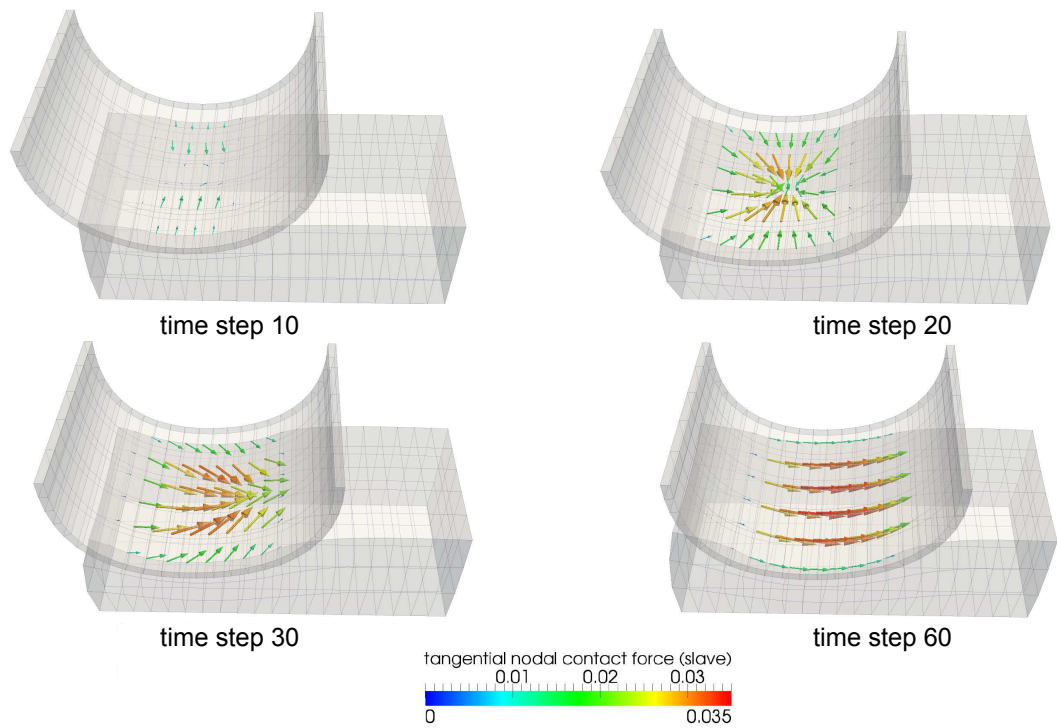


Figure A.15: Deformation and tangential nodal slave forces for the frictional ironing problem.
Figure is taken from Farah et al. [73].

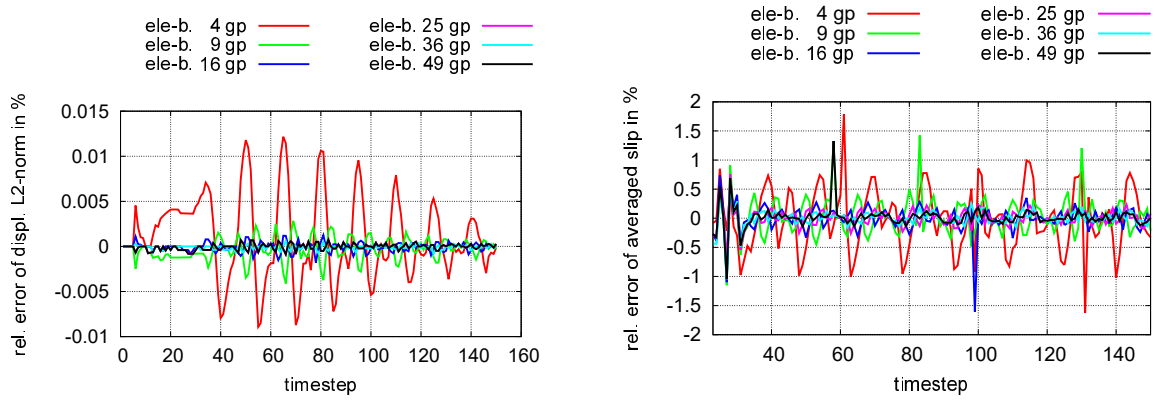


Figure A.16: Relative errors of the element-based integration for the L^2 -norm of the displacements and for the averaged incremental slip. Plots are taken from Farah et al. [73].

dures, see e.g. Tur et al. [274]. However, for an increasing number of integration points, the element-based solutions should still converge to the segment-based result. This is validated in Figure A.16. The first quantity to be analyzed is the relative error of the displacement field measured in the L^2 -norm compared to the segment-based reference solution, see the left subfigure in Figure A.16. During the first part of the simulation, the cylinder is pressed into the foundation and starts to slide. After roughly 30 steps all slave nodes are in the slip phase and no sticking effects occur anymore. From step 30 until the end of the calculation, the relative displacement errors of the element-based integration schemes slightly oscillate around the zero-reference. The error magnitude decreases for an increasing number of integration points. The damping effect of the oscillation during the simulation is due to the prescribed movement of the cylinder. Thus, the Dirichlet boundary condition dominates the displacement field for progressing time steps. The peaks of the displacement error are due to the master element edges sliding over parallel slave element edges. For 25 and more Gauss points, this effect vanishes due to the integration points being located near enough to the element edges.

The second investigation is concerning the slip increment, which represents the most crucial quantity for frictional mortar contact. Here, the slip increment of all slip nodes is summed up and divided by the number of slip nodes, thus yielding an averaged slip increment. This quantity is plotted over step index in the right subfigure of Figure A.16. Again, the relative error in the slip increment decreases with an increasing numbers of Gauss points, but in contrast to the L^2 -displacement error its magnitude is now considerable.

All in all, with an adequate number of integration points, the calculation of frictional mortar contact problems with the element-based integration scheme is possible, but the error in the slip increment could cause problems with respect to the rather sensitive search for the current stick and slip regions.

A.3. Concluding remarks

The two most commonly employed integration methods for mortar contact problems, segment-based and element-based integration, have been compared with each other and their respective

A. Comparison of Segment-Based and Element-Based Integration

advantages and drawbacks have been highlighted for classical surface contact scenarios. Furthermore, a so-called boundary-segmentation method has been proposed as an ideal compromise for an efficient and accurate integration scheme, because it combines the advantages of both schemes without taking over their deficiencies.

Several numerical examples have demonstrated acceptable results for both integration schemes but with a significantly reduced computation time for the element-based integration. For quadratic interpolation as well as for frictional problems with very sensitive stick/slip transitions, the quality of the solution is much better for the segment-based integration, which could not be reached by the element-based integration, even for very high numbers of integration points. Therefore, it is suggested to employ the segment-based integration as an accurate basis for further mortar-specific method development and the boundary-segmentation scheme together with a thorough error estimation of all relevant quantities (e.g. displacements, stick/slip behavior) for large-scale applications with first-order elements.

B. Details on Consistent Linearization for Line Contact

As the proposed mortar methods for contact of vertices, edges and surfaces in Chapter 4 and the mortar based computation of wear in Chapter 5 aim to be valid in the regime of finite deformations and to be solved in a fully implicit manner, they require consistent directional derivatives of all arising terms. However, the linearizations for wear modeling are strongly based on the investigations that have been made in Popp [210] for mortar surface contact formulations. Therefore, the directional derivatives of these terms can be evaluated in a straightforward manner and are omitted here. In addition, linearization of vertex contact is identical to well-investigated NTS formulations and thus also skipped. For contact of non-parallel edges, the only intricate to linearize quantity is the parameter space coordinate $\hat{\xi}_x^{(i)}$ corresponding to the contact point in (4.49). However, it can be calculated analogously to all other projections by linearizing a local Newton-Raphson scheme at its solution point. Related operations are outlined for the line contact in Section B.4.2 and a detailed explanation for non-parallel edge contact is not given here. Thus, this chapter focuses on the linearization details for the mortar line contact evaluation from Chapter 4. A detailed overview for consistent directional derivatives for a 2D mortar contact approach with penalty regularization can be found in Yang et al. [301], whereas linearizations for surface-to-surface mortar contact in 3D are outlined in great detail in Popp [210] and Popp et al. [212]. Again, details for the surface-to-surface contact part and the point contact part of the developed algorithm are not given in the following and the interested reader is referred to the mentioned literature for more information.

For all following details on consistent linearization, the directional derivative of an arbitrary quantity with respect to the discrete displacements \mathbf{d} is abbreviated with

$$\Delta(\cdot) = \frac{\partial(\cdot)}{\partial \mathbf{d}} \Delta \mathbf{d} . \quad (\text{B.1})$$

This notation has been employed in Popp [210] and allows for very compact writing of complex linearizations.

The general evaluation process for the mortar based line contact algorithm was outlined in Section 4.6. Here, a segment-based integration procedure was employed in order to evaluate the discrete integrals with the highest achievable accuracy. Thus, numerical integration is performed separately for each integration segment to integrate only smooth contributions from slave and master side. The following subsections provide the most important directional derivatives necessary for the linearization of this segment-based integration procedure.

B.1. General linearizations

Starting point for the following explanations is the consideration of the individual contribution of one mortar integration segment to the mortar matrices and the weighted gap:

$$D_{\text{t},jk} = \sum_{g=1}^{n_{\text{int}}} w_{\text{int},g} \Theta_j(\boldsymbol{\xi}^{(1)}(\tilde{\boldsymbol{\eta}}_g)) N_k^{(1)}(\boldsymbol{\xi}^{(1)}(\tilde{\boldsymbol{\eta}}_g)) J_{\text{seg}}, \quad (\text{B.2})$$

$$M_{\text{t},jl} = \sum_{g=1}^{n_{\text{int}}} w_{\text{int},g} \Theta_j(\boldsymbol{\xi}^{(1)}(\tilde{\boldsymbol{\eta}}_g)) N_l^{(2)}(\boldsymbol{\xi}^{(2)}(\tilde{\boldsymbol{\eta}}_g)) J_{\text{seg}}, \quad (\text{B.3})$$

$$\tilde{\mathbf{g}}_{\text{t},j} = \sum_{g=1}^{n_{\text{int}}} w_{\text{int},g} \Theta_j(\boldsymbol{\xi}^{(1)}(\tilde{\boldsymbol{\eta}}_g)) g_{\text{n},h}(\boldsymbol{\xi}^{(1)}(\tilde{\boldsymbol{\eta}}_g), \boldsymbol{\xi}^{(2)}(\tilde{\boldsymbol{\eta}}_g)) J_{\text{seg}}. \quad (\text{B.4})$$

Here, the contributions to the submatrices \mathbf{D}_{t} and $\mathbf{D}_{\text{t}*}$ are condensed to the general contribution $D_{\text{t},jk}$. The integration point weight is denoted with $w_{\text{int},g}$, the Jacobian of the integration segment reads J_{seg} and the number of integration points per integration segment is given as n_{int} . In all numerical examples, a standard Gauss quadrature rule with 5 integration points is employed. The positions of these integration points on the considered integration segment are denoted with $\tilde{\boldsymbol{\eta}}_g$. The linearization of the weighted relative tangential velocity is not considered in the following, since it basically consists of contributions from the mortar matrices, see (4.71).

The linearization of the \mathbf{D}_{t} matrix contribution with respect to the discrete nodal displacements reads:

$$\begin{aligned} \Delta D_{\text{t},jk} &= \sum_{g=1}^{n_{\text{int}}} w_{\text{int},g} \Delta \Theta_j(\boldsymbol{\xi}^{(1)}(\tilde{\boldsymbol{\eta}}_g)) N_k^{(1)}(\boldsymbol{\xi}^{(1)}(\tilde{\boldsymbol{\eta}}_g)) J_{\text{seg}} \\ &\quad + \sum_{g=1}^{n_{\text{int}}} w_{\text{int},g} \Theta_j(\boldsymbol{\xi}^{(1)}(\tilde{\boldsymbol{\eta}}_g)) \Delta N_k^{(1)}(\boldsymbol{\xi}^{(1)}(\tilde{\boldsymbol{\eta}}_g)) J_{\text{seg}} \\ &\quad + \sum_{g=1}^{n_{\text{int}}} w_{\text{int},g} \Theta_j(\boldsymbol{\xi}^{(1)}(\tilde{\boldsymbol{\eta}}_g)) N_k^{(1)}(\boldsymbol{\xi}^{(1)}(\tilde{\boldsymbol{\eta}}_g)) \Delta J_{\text{seg}}. \end{aligned} \quad (\text{B.5})$$

In addition, the linearization of the \mathbf{M}_{t} matrix contribution is given as:

$$\begin{aligned} \Delta M_{\text{t},jl} &= \sum_{g=1}^{n_{\text{int}}} w_{\text{int},g} \Delta \Theta_j(\boldsymbol{\xi}^{(1)}(\tilde{\boldsymbol{\eta}}_g)) N_l^{(2)}(\boldsymbol{\xi}^{(2)}(\tilde{\boldsymbol{\eta}}_g)) J_{\text{seg}} \\ &\quad + \sum_{g=1}^{n_{\text{int}}} w_{\text{int},g} \Theta_j(\boldsymbol{\xi}^{(1)}(\tilde{\boldsymbol{\eta}}_g)) \Delta N_l^{(2)}(\boldsymbol{\xi}^{(2)}(\tilde{\boldsymbol{\eta}}_g)) J_{\text{seg}} \\ &\quad + \sum_{g=1}^{n_{\text{int}}} w_{\text{int},g} \Theta_j(\boldsymbol{\xi}^{(1)}(\tilde{\boldsymbol{\eta}}_g)) N_l^{(2)}(\boldsymbol{\xi}^{(2)}(\tilde{\boldsymbol{\eta}}_g)) \Delta J_{\text{seg}}. \end{aligned} \quad (\text{B.6})$$

Finally, the linearization of the weighted nodal gap reads:

$$\begin{aligned}\Delta \tilde{g}_{\text{seg}} &= \sum_{g=1}^{n_{\text{int}}} w_{\text{int},g} \Delta \Theta_j(\boldsymbol{\xi}^{(1)}(\tilde{\eta}_g)) g_{\text{n},h}(\boldsymbol{\xi}^{(1)}(\tilde{\eta}_g), \boldsymbol{\xi}^{(2)}(\tilde{\eta}_g)) J_{\text{seg}} \\ &\quad + \sum_{g=1}^{n_{\text{int}}} w_{\text{int},g} \Theta_j(\boldsymbol{\xi}^{(1)}(\tilde{\eta}_g)) \Delta g_{\text{n},h}(\boldsymbol{\xi}^{(1)}(\tilde{\eta}_g), \boldsymbol{\xi}^{(2)}(\tilde{\eta}_g)) J_{\text{seg}} \\ &\quad + \sum_{g=1}^{n_{\text{int}}} w_{\text{int},g} \Theta_j(\boldsymbol{\xi}^{(1)}(\tilde{\eta}_g)) g_{\text{n},h}(\boldsymbol{\xi}^{(1)}(\tilde{\eta}_g), \boldsymbol{\xi}^{(2)}(\tilde{\eta}_g)) \Delta J_{\text{seg}}.\end{aligned}\quad (\text{B.7})$$

The linearization of the standard displacement shape functions reads

$$\Delta N_l^{(i)}(\boldsymbol{\xi}^{(i)}(\tilde{\eta}_g)) = N_{l,\boldsymbol{\xi}}^{(i)}(\boldsymbol{\xi}^{(i)}(\tilde{\eta}_g)) \Delta \boldsymbol{\xi}^{(i)}(\tilde{\eta}_g). \quad (\text{B.8})$$

with $N_{l,\boldsymbol{\xi}}^{(i)}$ being the derivative of the shape function with respect to the parameter space coordinate $\boldsymbol{\xi}$. In general, the linearization of dual shape functions reads

$$\Delta \Theta_j(\boldsymbol{\xi}^{(1)}(\tilde{\eta}_g)) = \Theta_{j,\boldsymbol{\xi}}(\boldsymbol{\xi}^{(1)}(\tilde{\eta}_g)) \Delta \boldsymbol{\xi}^{(1)}(\tilde{\eta}_g) + \Theta_{j,\mathbf{d}} \Delta \mathbf{d}. \quad (\text{B.9})$$

It can be seen, that the dual shape functions are generally deformation dependent since they are constructed in the spatial configuration, see Section 3.4.1.2. However, since only first-order elements are considered for the line contact, a line element is defined as a linear 1D element with 2 nodes that leads to a constant element Jacobian determinant. Thus, the directional derivative of the dual shape functions with respect to discrete displacements vanishes, i.e. $\Theta_{j,\mathbf{d}} = 0$. For details on linearization procedures for dual shape functions the interested reader is referred to Popp [210]. Evaluation of the linearizations in (B.5),(B.6) and (B.7) requires knowledge of the following elementary directional derivatives:

- the integration segment Jacobian determinant J_{seg}
- the integration segment vertices $\mathbf{x}_{j,\text{seg}}$
- the integration segment Gauss points $\boldsymbol{\xi}^{(1,2)}(\tilde{\eta}_g)$
- the normal and tangential vectors from the nodes and the auxiliary plane
- the discretized version of the gap function $g_{\text{n},h}$

All these linearizations are provided in the following subsections. Therein, it is implicitly assumed that the line element is a first-order 2-node element which results from a bulk discretization of tet4 and hex8 elements.

B.2. Linearization of integration segment Jacobian determinant

The Jacobian determinant of an integration cell reads

$$J_{\text{seg}} = \frac{1}{2} \|\mathbf{x}_{2,\text{seg}} - \mathbf{x}_{1,\text{seg}}\|. \quad (\text{B.10})$$

with the integration segment vertices $\mathbf{x}_{1,\text{seg}}$ and $\mathbf{x}_{2,\text{seg}}$. Its linearization is given as

$$\Delta J_{\text{seg}} = \frac{(\mathbf{x}_{2,\text{seg}} - \mathbf{x}_{1,\text{seg}})^T}{2 \|\mathbf{x}_{2,\text{seg}} - \mathbf{x}_{1,\text{seg}}\|} \cdot (\Delta \mathbf{x}_{2,\text{seg}} - \Delta \mathbf{x}_{1,\text{seg}}). \quad (\text{B.11})$$

Herein, the linearization of the integration segment vertices is employed, which is explained in the following subsection.

B.3. Linearization of integration segment vertices

The computation of the integration segment vertices and their directional derivative depends on the line clipping situation. The integration segment vertices can be classified as projected slave node, projected master node or as intersection of projected slave and master element edges. This is very similar to the computation of cell vertices for the evaluation of mortar surface contact, see Popp [210]. When the integration point is based on a projected slave or master node, its computation reads:

$$\mathbf{x}_{j,\text{seg}} = \mathbf{x}^{(i)} - \left[\left(\mathbf{x}^{(i)} - \mathbf{x}_0^{(1)} \right)^T \cdot \tilde{\mathbf{n}}_0^{(1)} \right] \tilde{\mathbf{n}}_0^{(1)}. \quad (\text{B.12})$$

This is a simple projection along the auxiliary plane normal $\tilde{\mathbf{n}}_0^{(1)}$ onto the auxiliary plane. Herein, $\mathbf{x}_0^{(1)}$ denotes the midpoint of the slave line element. The linearization of this type integration segment vertices reads

$$\begin{aligned} \Delta \mathbf{x}_{j,\text{seg}} &= \Delta \mathbf{x}^{(i)} - \left[\left(\Delta \mathbf{x}^{(i)} - \Delta \mathbf{x}_0^{(1)} \right)^T \cdot \tilde{\mathbf{n}}_0^{(1)} + \left(\mathbf{x}^{(i)} - \mathbf{x}_0^{(1)} \right)^T \cdot \Delta \tilde{\mathbf{n}}_0^{(1)} \right] \tilde{\mathbf{n}}_0^{(1)} \\ &\quad - \left[\left(\mathbf{x}^{(i)} - \mathbf{x}_0^{(1)} \right)^T \cdot \tilde{\mathbf{n}}_0^{(1)} \right] \Delta \tilde{\mathbf{n}}_0^{(1)}. \end{aligned} \quad (\text{B.13})$$

This expression contains the linearization of the auxiliary plane normal (see Section B.4) and of the midpoint of the slave line element, which is defined as

$$\Delta \mathbf{x}_0^{(1)} = \Delta \left(\frac{1}{2} \mathbf{x}_k^{(1)} + \frac{1}{2} \mathbf{x}_{k+1}^{(1)} \right) = \frac{1}{2} \Delta \mathbf{x}_k^{(1)} + \frac{1}{2} \Delta \mathbf{x}_{k+1}^{(1)}. \quad (\text{B.14})$$

When the integration segment vertex results from an intersection of projected slave and master nodes, the construction rule reads

$$\mathbf{x}_{j,\text{seg}} = \frac{(\tilde{\mathbf{x}}_s^{(1)} - \tilde{\mathbf{x}}_s^{(2)}) \times (\tilde{\mathbf{x}}_e^{(2)} - \tilde{\mathbf{x}}_s^{(2)}) \cdot \tilde{\mathbf{n}}_0^{(1)}}{(\tilde{\mathbf{x}}_e^{(1)} - \tilde{\mathbf{x}}_s^{(1)}) \times (\tilde{\mathbf{x}}_e^{(2)} - \tilde{\mathbf{x}}_s^{(2)}) \cdot \tilde{\mathbf{n}}_0^{(1)}} \left(\tilde{\mathbf{x}}_e^{(1)} - \tilde{\mathbf{x}}_s^{(1)} \right). \quad (\text{B.15})$$

The points with the lower index $(\cdot)_s$ define starting points of the projected element edges and the points with lower index $(\cdot)_e$ represent end points of the projected element edges. Their linearizations are identical to (B.13) since they result from slave and master node projections onto the auxiliary plane. The linearization of (B.15) is not given here but can be computed in a straightforward manner.

B.4. Linearization of normal and tangent vectors

B.4.1. Auxiliary plane normal:

The auxiliary plane normal for the evaluation of the line contact results from a projection of the averaged edge normal $\mathbf{n}_0^{(1)}$ into the normal plane of the edge element:

$$\tilde{\mathbf{n}}_0^{(1)} = \left(\mathbf{I}_3 - \boldsymbol{\tau}_0^{(1)} \otimes \boldsymbol{\tau}_0^{(1)} \right) \mathbf{n}_0^{(1)}. \quad (\text{B.16})$$

The consistent linearization of this term reads:

$$\Delta\tilde{\mathbf{n}}_0^{(1)} = -\left(\Delta\boldsymbol{\tau}_0^{(1)} \otimes \boldsymbol{\tau}_0^{(1)} + \boldsymbol{\tau}_0^{(1)} \otimes \Delta\boldsymbol{\tau}_0^{(1)} \right) \mathbf{n}_0^{(1)} + \left(\mathbf{I}_3 - \boldsymbol{\tau}_0^{(1)} \otimes \boldsymbol{\tau}_0^{(1)} \right) \Delta\mathbf{n}_0^{(1)}. \quad (\text{B.17})$$

Herein, the tangent of the line element $\boldsymbol{\tau}_0^{(1)}$ does not need to be normalized in order to define the normal plane. Thus, it can easily be calculated for a 2 node line element as difference of the line elements nodes:

$$\Delta\boldsymbol{\tau}_0^{(1)} = \Delta\left(\mathbf{x}_{k+1}^{(1)} - \mathbf{x}_k^{(1)}\right) = \Delta\mathbf{x}_{k+1}^{(1)} - \Delta\mathbf{x}_k^{(1)}. \quad (\text{B.18})$$

Here, it does not matter in which direction the tangent vector points. The calculation of the averaged edge normal $\mathbf{n}_0^{(1)}$ is defined as average of the node normals:

$$\Delta\mathbf{n}_0^{(1)} = \Delta\left(\frac{1}{2}\mathbf{n}_k^{(1)} + \frac{1}{2}\mathbf{n}_{k+1}^{(1)}\right) = \frac{1}{2}\Delta\mathbf{n}_k^{(1)} + \frac{1}{2}\Delta\mathbf{n}_{k+1}^{(1)}. \quad (\text{B.19})$$

The factor $\frac{1}{2}$ directly results from evaluating the displacement shape functions of the line element nodes at the midpoint of the edge. In (B.19), the linearization of the node normals $\Delta\mathbf{n}_l^{(1)}$ is required.

B.4.2. Nodal normal for node-to-surface CPP:

The nodal normals can possibly be defined by several closest-point-projections (cf. Section 4.4), which are analyzed in the following. First, a CPP with respect to a surface is considered. According to (4.42), the slave nodal normal vector is defined as negative master side normal vector resulting from a CPP:

$$\begin{aligned} \Delta\mathbf{n}_k^{(1)} &= -\Delta\mathbf{n}^{(2)}(\hat{\boldsymbol{\xi}}^{(2)}) = -\Delta\left(\sum_{l=1}^{n^{(2)}} N_l^{(2)}(\hat{\boldsymbol{\xi}}^{(2)})\mathbf{n}_l^{(2)}\right) \\ &= -\sum_{l=1}^{n^{(2)}} \left(N_{l,\xi}^{(2)}(\hat{\boldsymbol{\xi}}^{(2)})\Delta\hat{\boldsymbol{\xi}}^{(2)}\mathbf{n}_l^{(2)} - N_l^{(2)}(\hat{\boldsymbol{\xi}}^{(2)})\Delta\mathbf{n}_l^{(2)} \right). \end{aligned} \quad (\text{B.20})$$

Herein, the master side normal is expressed as nodal normal field and $\hat{\boldsymbol{\xi}}^{(2)}$ is the parameter space coordinate of the master side which corresponds the closest master point to the considered slave

node. The required linearization of the master side parameter space coordinate results from the expression of the CPP procedure:

$$\varpi \sum_{l=1}^{n^{(2)}} N_l^{(2)}(\hat{\xi}^{(2)}) \mathbf{n}_l^{(2)} + \sum_{l=1}^{n^{(2)}} N_l^{(2)}(\hat{\xi}^{(2)}) \mathbf{x}_l^{(2)} - \mathbf{x}_k^{(1)} = \mathbf{0}. \quad (\text{B.21})$$

It is solved with a local Newton-Raphson scheme and consistent linearization of the solution yields

$$\begin{bmatrix} \Delta\hat{\xi}^{(2)} \\ \Delta\varpi \end{bmatrix} = \mathbf{L}_{\text{cpp}}^{-1} \cdot \left[-\varpi \sum_{l=1}^{n^{(2)}} N_l^{(2)}(\hat{\xi}^{(2)}) \Delta\mathbf{n}_l^{(2)}(\hat{\xi}^{(2)}) - \sum_{l=1}^{n^{(2)}} N_l^{(2)}(\hat{\xi}^{(2)}) \Delta\mathbf{x}_l^{(2)} + \Delta\mathbf{x}_k^{(1)} \right], \quad (\text{B.22})$$

with $\mathbf{L}_{\text{cpp}} \in \mathbb{R}^{3 \times 3}$ being defined as

$$\mathbf{L}_{\text{cpp}} = \left[\begin{array}{c|c} \varpi \sum_{l=1}^{n^{(2)}} N_{l,\xi}^{(2)}(\hat{\xi}^{(2)}) \mathbf{n}_l^{(2)}(\hat{\xi}^{(2)}) + \sum_{l=1}^{n^{(2)}} N_{l,\xi}^{(2)}(\hat{\xi}^{(2)}) \mathbf{x}_l^{(2)} & \sum_{l=1}^{n^{(2)}} N_l^{(2)}(\hat{\xi}^{(2)}) \mathbf{n}_l^{(2)}(\hat{\xi}^{(2)}) \end{array} \right]. \quad (\text{B.23})$$

The only unknown linearization herein is the directional derivative of the master side nodal normals $\Delta\mathbf{n}_l^{(2)}$, which can be derived in complete analogy to the explanations for the slave side normal field in Popp [210]:

$$\Delta\mathbf{n}_l^{(2)} = \Delta \left(\frac{\hat{\mathbf{n}}_l^{(2)}}{\|\hat{\mathbf{n}}_l^{(2)}\|} \right) = \frac{\Delta\hat{\mathbf{n}}_l^{(2)}}{\|\hat{\mathbf{n}}_l^{(2)}\|} - \frac{(\hat{\mathbf{n}}_l^{(2),T} \Delta\hat{\mathbf{n}}_l^{(2)}) \hat{\mathbf{n}}_l^{(2)}}{\|\hat{\mathbf{n}}_l^{(2)}\|^3}, \quad (\text{B.24})$$

where $\hat{\mathbf{n}}_l^{(2)}$ denotes the non-normalized nodal normal vector. As stated in Section 4.4.1, the master side nodal normal vector $\hat{\mathbf{n}}_l^{(2)}$ results from averaging the element normal vectors at node l . Thus, the linearization reads

$$\Delta\hat{\mathbf{n}}_l^{(2)} = \Delta \left(\sum_{i=1}^{n_{\text{adj}}} \frac{\mathbf{n}_{l,ei}^{(2)}}{\|\mathbf{n}_{l,ei}^{(2)}\|} \right) = \sum_{i=1}^{n_{\text{adj}}} \left(\frac{\Delta\mathbf{n}_{l,ei}^{(2)}}{\|\mathbf{n}_{l,ei}^{(2)}\|} - \frac{(\mathbf{n}_{l,ei}^{(2),T} \Delta\mathbf{n}_{l,ei}^{(2)}) \mathbf{n}_{l,ei}^{(2)}}{\|\mathbf{n}_{l,ei}^{(2)}\|^3} \right). \quad (\text{B.25})$$

The linearization of the element normal vectors can be computed as

$$\begin{aligned} \Delta\mathbf{n}_{l,ei}^{(2)} &= \Delta(\mathbf{x}(\xi_l)_\xi \times \mathbf{x}(\xi_l)_\eta) = \left(\sum_{k=1}^{n_{ei}} N_{k,\xi}(\xi_l) \Delta\mathbf{x}_k \right) \times \left(\sum_{k=1}^{n_{ei}} N_{k,\eta}(\xi_l) \mathbf{x}_k \right) \\ &\quad + \left(\sum_{k=1}^{n_{ei}} N_{k,\xi}(\xi_l) \mathbf{x}_k \right) \times \left(\sum_{k=1}^{n_{ei}} N_{k,\eta}(\xi_l) \Delta\mathbf{x}_k \right), \end{aligned} \quad (\text{B.26})$$

with the number n_{ei} of all nodes associated to the considered adjacent element ei . In addition, the parameter space coordinate ξ_l corresponds to the position of master node l .

B.4.3. Nodal normal for node-to-line CPP:

If the slave side nodal normal is calculated with a node-to-line closest-point-projection, it is written as normalized difference of the slave node and the closest master point (cf. Section 4.4.2):

$$\mathbf{n}_j = \frac{\mathbf{x}_j^{(1)} - \sum_{l=1}^{n^{(2)}} N_l^{(2)}(\hat{\xi}^{(2)}) \mathbf{x}_l^{(2)}}{\|\mathbf{x}_j^{(1)} - \sum_{l=1}^{n^{(1)}} N_l^{(2)}(\hat{\xi}^{(2)}) \mathbf{x}_l^{(2)}\|}. \quad (\text{B.27})$$

The Linearization of this normalized vector can be done in analogy to (B.24). Then, the only intricate term is the linearization of the parameter space coordinate $\Delta\hat{\xi}^{(2)}$ of the closest master point on the considered line element. It reads

$$\begin{aligned}\Delta\hat{\xi}^{(2)} = & -L^{-1} \left(\Delta\boldsymbol{\tau}^{(2)}(\hat{\xi}^{(2)}) \left[\mathbf{x}_j^{(1)} - \sum_{l=1}^{n^{(2)}} N_l^{(2)}(\hat{\xi}^{(2)}) \mathbf{x}_l^{(2)} \right] \right. \\ & \left. + \boldsymbol{\tau}^{(2)}(\hat{\xi}^{(2)}) \left[\Delta\mathbf{x}_j^{(1)} - \sum_{l=1}^{n^{(2)}} N_l^{(2)}(\hat{\xi}^{(2)}) \Delta\mathbf{x}_l^{(2)} \right] \right) \end{aligned}\quad (\text{B.28})$$

with L being defined as

$$L = \boldsymbol{\tau}_{,\xi}^{(2)}(\hat{\xi}^{(2)}) \left[\mathbf{x}_j^{(1)} - \sum_{l=1}^{n^{(2)}} N_l^{(2)}(\hat{\xi}^{(2)}) \mathbf{x}_l^{(2)} \right] - \boldsymbol{\tau}^{(2)}(\hat{\xi}^{(2)}) \sum_{l=1}^{n^{(2)}} N_{l,\xi}^{(2)}(\hat{\xi}^{(2)}) \mathbf{x}_l^{(2)}. \quad (\text{B.29})$$

Herein, the tangent is defined as tangent field with averaged nodal tangents similar to the nodal normal field. Details for its linearization are omitted here.

The linearization of a nodal normal resulting from a node-to-node CPP is not given here since it can be computed in a straightforward manner.

B.5. Linearization of integration points

The slave and master side integration points result from a projection from the integration segment onto the slave and master element. The projection reads

$$\sum_{k=1}^{n^{(i)}} N_k^{(i)}(\boldsymbol{\xi}^{(i)}(\tilde{\boldsymbol{\eta}}_g)) \mathbf{x}_k^{(i)} - \varpi \tilde{\mathbf{n}}_0 - \mathbf{x}_g = \mathbf{0}. \quad (\text{B.30})$$

Again, this is a nonlinear equation which is solved with a Newton-Raphson scheme to obtain the sought after parameter space coordinates $\boldsymbol{\xi}^{(i)}(\tilde{\boldsymbol{\eta}}_g)$ and the distance ϖ . The linearization is defined similar to the investigations in Popp et al. [211] and Yang et al. [301] and reads

$$\begin{bmatrix} \Delta\hat{\boldsymbol{\xi}}^{(2)} \\ \Delta\varpi \end{bmatrix} = \mathbf{L}_{\text{gp}}^{-1} \cdot \left[\varpi \Delta\tilde{\mathbf{n}}_0 - \sum_{k=1}^{n^{(i)}} N_k^{(i)}(\boldsymbol{\xi}^{(i)}(\tilde{\boldsymbol{\eta}}_g)) \Delta\mathbf{x}_k^{(i)} + \Delta\mathbf{x}_g \right], \quad (\text{B.31})$$

with the matrix $\mathbf{L}_{\text{gp}} \in \mathbb{R}^{3 \times 3}$ being defined as

$$\mathbf{L}_{\text{gp}} = \left[\sum_{k=1}^{n^{(i)}} N_{k,\xi}^{(i)}(\boldsymbol{\xi}^{(i)}(\tilde{\boldsymbol{\eta}}_g)) \mathbf{x}_k^{(i)} \quad | \quad -\tilde{\mathbf{n}}_0 \right]. \quad (\text{B.32})$$

Note, the parameter space $\boldsymbol{\xi}^{(i)}$ of the target element is assumed to consist of two components, which corresponds to a 2D surface element. When projecting an integration point onto a line element, it would be sufficient to search for a scalar valued parameter space coordinate. However, writing it in vector formulation is still correct, since a line element parameter space can also be expressed as boundary of the attached surface element parameter space.

B.6. Linearization of gap function

The linearization of the discrete gap function at each Gauss point reads

$$\begin{aligned}\Delta g_{n,h} &= \Delta \left[-\mathbf{n}_g \cdot \left(\mathbf{x}_g^{(1)} - \hat{\mathbf{x}}_g^{(2)} \right) \right] \\ &= \Delta \left[- \left(\sum_{k=1}^{n^{(1)}} N_k^{(1)}(\boldsymbol{\xi}^{(1)}(\tilde{\boldsymbol{\eta}}_g)) \mathbf{n}_k \right) \cdot \left(\sum_{k=1}^{n^{(2)}} N_k^{(1)}(\boldsymbol{\xi}^{(1)}(\tilde{\boldsymbol{\eta}}_g)) \mathbf{x}_k^{(1)} - \sum_{l=1}^{n^{(2)}} N_l^{(2)}(\boldsymbol{\xi}^{(2)}(\tilde{\boldsymbol{\eta}}_g)) \hat{\mathbf{x}}_l^{(2)} \right) \right].\end{aligned}\quad (\text{B.33})$$

In detail, this formulation can be expressed as

$$\begin{aligned}\Delta g_{n,h} &= - \left(\mathbf{x}_g^{(1)} - \hat{\mathbf{x}}_g^{(2)} \right) \cdot \left(\sum_{k=1}^{n^{(1)}} \left(N_{k,\xi}^{(1)}(\boldsymbol{\xi}^{(1)}(\tilde{\boldsymbol{\eta}}_g)) \Delta \boldsymbol{\xi}^{(1)} \mathbf{n}_k + N_k^{(1)}(\boldsymbol{\xi}^{(1)}(\tilde{\boldsymbol{\eta}}_g)) \Delta \mathbf{n}_k \right) \right. \\ &\quad \left. - \mathbf{n}_g \left(\sum_{k=1}^{n^{(1)}} \left(N_{k,\xi}^{(1)}(\boldsymbol{\xi}^{(1)}(\tilde{\boldsymbol{\eta}}_g)) \Delta \boldsymbol{\xi}^{(1)} \mathbf{x}_k^{(1)} + N_k^{(1)}(\boldsymbol{\xi}^{(1)}(\tilde{\boldsymbol{\eta}}_g)) \Delta \mathbf{x}_k^{(1)} \right) \right) \right. \\ &\quad \left. + \mathbf{n}_g \left(\sum_{l=1}^{n^{(2)}} \left(N_{l,\xi}^{(2)}(\boldsymbol{\xi}^{(2)}(\tilde{\boldsymbol{\eta}}_g)) \Delta \boldsymbol{\xi}^{(2)} \hat{\mathbf{x}}_l^{(2)} + N_l^{(2)}(\boldsymbol{\xi}^{(2)}(\tilde{\boldsymbol{\eta}}_g)) \Delta \hat{\mathbf{x}}_l^{(2)} \right) \right) \right).\end{aligned}\quad (\text{B.34})$$

Herein, the global Gauss point coordinates $\mathbf{x}_g^{(i)}$ are defined via the parameter space coordinate of the corresponding element. The Gauss point normal \mathbf{n}_g results from shape function interpolation at the corresponding finite element parameter space coordinate.

Bibliography

- [1] Y. Achdou, G. Abdoulaev, J.-C. Hontand, Y. A. Kuznetsov, O. Pironneau, and C. Prud'homme, Nonmatching grids for fluids, *Contemporary Mathematics* **218**, 3–22, 1998.
- [2] M. F. Adams, Parallel multigrid solvers for 3D unstructured finite element problems in large deformation elasticity and plasticity, *International Journal for Numerical Methods in Engineering* **48**, 1241–1262, 2000.
- [3] P. Alart and A. Curnier, A mixed formulation for frictional contact problems prone to Newton like solution methods, *Computer Methods in Applied Mechanics and Engineering* **92**, 353–375, 1991.
- [4] F. Alauzet and M. Mehrenberger, P1-conservative solution interpolation on unstructured triangular meshes, *International Journal for Numerical Methods in Engineering* **84**, 1552–1588, 2010.
- [5] D. Aldham, J. Warburton, and R. Pendlebury, The unlubricated fretting wear of mild steel in air, *Wear* **106**, 177–201, 1985.
- [6] T. Arbogast, G. Pencheva, M. F. Wheeler, and I. Yotov, A multiscale mortar mixed finite element method, *Multiscale Modeling & Simulation* **6**, 319–346, 2007.
- [7] J. F. Archard, Contact and Rubbing of Flat Surfaces, *Journal of Applied Physics* **24**, 981–988, 1953.
- [8] I. Argatov, Asymptotic modeling of reciprocating sliding wear with application to local interwire contact, *Wear* **271**, 1147–1155, 2011.
- [9] I. Argatov and W. Tato, Asymptotic modeling of reciprocating sliding wear—comparison with finite-element simulations, *European Journal of Mechanics-A/Solids* **34**, 1–11, 2012.
- [10] F. Armero and E. Love, An Arbitrary Lagrangian-Eulerian finite element method for finite strain plasticity, *International Journal for Numerical Methods in Engineering* **57**, 471–508, 2003.
- [11] H. Bao and Z. Zhao, An alternative scheme for the corner–corner contact in the two-dimensional discontinuous deformation analysis, *Advances in Engineering Software* **41**, 206–212, 2010.
- [12] H. Bao and Z. Zhao, The vertex-to-vertex contact analysis in the two-dimensional discontinuous deformation analysis, *Advances in Engineering Software* **45**, 1–10, 2012.

- [13] K.-J. Bathe, *Finite element procedures*, Prentice Hall, Englewood Cliffs, 1996.
- [14] K.-J. Bathe and A. Chaudhary, A solution method for planar and axisymmetric contact problems, *International Journal for Numerical Methods in Engineering* **21**, 65–88, 1985.
- [15] J. T. Batina, Unsteady euler algorithm with unstructured dynamic mesh for complex-aircraft aerodynamic analysis, *AIAA journal* **29**, 327–333, 1991.
- [16] T. Belytschko, W. K. Liu, and B. Moran, *Nonlinear finite elements for continua and structures*, Wiley, 2000.
- [17] T. Belytschko, W. Daniel, and G. Ventura, A monolithic smoothing-gap algorithm for contact-impact based on the signed distance function, *International Journal for numerical methods in engineering* **55**, 101–125, 2002.
- [18] F. Ben Belgacem, The mortar finite element method with Lagrange multipliers, *Numerische Mathematik* **84**, 173–197, 1999.
- [19] F. Ben Belgacem, The mixed mortar finite element method for the incompressible Stokes problem: Convergence analysis, *SIAM Journal on Numerical Analysis* **37**, 1085–1100, 2000.
- [20] F. Ben Belgacem, P. Hild, and P. Laborde, The mortar finite element method for contact problems, *Mathematical and Computer Modelling* **28**, 263–271, 1998.
- [21] F. Ben Belgacem, L. K. Chilton, and P. Seshaiyer, The hp-mortar finite-element method for the mixed elasticity and stokes problems, *Computers & Mathematics with Applications* **46**, 35–55, 2003.
- [22] O. Ben-David and J. Fineberg, Static friction coefficient is not a material constant, *Physical review letters* **106**, 254301, 2011.
- [23] H. Ben Dhia and M. Torkhani, Modeling and computation of fretting wear of structures under sharp contact, *International Journal for Numerical Methods in Engineering* **85**, 61–83, 2011.
- [24] D. J. Benson, An efficient, accurate, simple ALE method for nonlinear finite element programs, *Computer methods in applied mechanics and engineering* **72**, 305–350, 1989.
- [25] C. Bernardi, Y. Maday, and A. Patera, Domain decomposition by the mortar element method, In H. Kaper, M. Garbey, and G. Pieper (eds.), *Asymptotic and Numerical Methods for Partial Differential Equations with Critical Parameters*, Volume 384 of *NATO ASI Series*, pages 269–286, Springer Netherlands, 1993.
- [26] C. Bernardi, Y. Maday, and A. T. Patera, A new nonconforming approach to domain decomposition: the mortar element method, In H. Brezis and J. Lions (eds.), *Nonlinear partial differential equations and their applications*, pages 13–51, Pitman/Wiley: London/New York, 1994.

- [27] D. P. Bertsekas, *Constrained optimization and Lagrange multiplier methods*, Academic press, London, 1982.
- [28] E. Biotteau, A. Gravouil, A. A. Lubrecht, and A. Combescure, Multigrid solver with automatic mesh refinement for transient elastoplastic dynamic problems, *International Journal for Numerical Methods in Engineering* **84**, 947–971, 2010.
- [29] H. Blum, H. Frohne, J. Frohne, and A. Rademacher, Semi-smooth Newton methods for mixed FEM discretizations of higher-order frictional, elasto-plastic two-body contact problems, *Computer Methods in Applied Mechanics and Engineering* **309**, 131–151, 2016.
- [30] E. G. Boman, Ü. V. Çatalyürek, C. Chevalier, and K. D. Devine, The Zoltan and Isorropia parallel toolkits for combinatorial scientific computing: Partitioning, ordering and coloring, *Scientific Programming* **20**, 129–150, 2012.
- [31] J. Bonet and R. D. Wood, *Nonlinear continuum mechanics for finite element analysis*, Cambridge university press, 1997.
- [32] F. Brezzi and M. Fortin, *Mixed and hybrid finite element methods*, Springer-Verlag, New York, 1991.
- [33] E. Brivadis, A. Buffa, B. Wohlmuth, and L. Wunderlich, Isogeometric mortar methods, *Computer Methods in Applied Mechanics and Engineering* **284**, 292–319, 2015.
- [34] S. Brunßen, F. Schmid, M. Schäfer, and B. Wohlmuth, A fast and robust iterative solver for nonlinear contact problems using a primal-dual active set strategy and algebraic multigrid, *International Journal for Numerical Methods in Engineering* **69**, 524–543, 2007.
- [35] P. Bussetta, R. Boman, and J.-P. Ponthot, Efficient 3D data transfer operators based on numerical integration, *International Journal for Numerical Methods in Engineering* **102**, 892–929, 2015.
- [36] F. J. Cavalieri and A. Cardona, Three-dimensional numerical solution for wear prediction using a mortar contact algorithm, *International Journal for Numerical Methods in Engineering* **96**, 467–486, 2013.
- [37] F. J. Cavalieri, F. Zenklusen, and A. Cardona, Determination of wear in internal combustion engine valves using the finite element method and experimental tests, *Mechanism and Machine Theory* **104**, 81–99, 2016.
- [38] F. Cavalieri and A. Cardona, An augmented Lagrangian technique combined with a mortar algorithm for modelling mechanical contact problems, *International Journal for Numerical Methods in Engineering* **93**, 420–442, 2013.
- [39] J. R. Cebral and R. Lohner, Conservative load projection and tracking for fluid-structure problems, *AIAA journal* **35**, 687–692, 1997.

Bibliography

- [40] V. Chawla and T. A. Laursen, Energy consistent algorithms for frictional contact problems, *International Journal for Numerical Methods in Engineering* **42**, 799–827, 1998.
- [41] F. Chouly and P. Hild, A Nitsche-based method for unilateral contact problems: numerical analysis, *SIAM Journal on Numerical Analysis* **51**, 1295–1307, 2013.
- [42] P. W. Christensen, A. Klarbring, J. S. Pang, and N. Strömberg, Formulation and comparison of algorithms for frictional contact problems, *International Journal for Numerical Methods in Engineering* **42**, 145–173, 1998.
- [43] J. Chung and G. M. Hulbert, A time integration algorithm for structural dynamics with improved numerical dissipation: The generalized- α method, *Journal of Applied Mechanics* **60**, 371–375, 1993.
- [44] M. Ciavarella, D. Hills, and G. Monno, The influence of rounded edges on indentation by a flat punch, *Proceedings of the Institution of Mechanical Engineers, Part C: Journal of Mechanical Engineering Science* **212**, 319–327, 1998.
- [45] T. Cichosz and M. Bischoff, Consistent treatment of boundaries with mortar contact formulations using dual Lagrange multipliers, *Computer Methods in Applied Mechanics and Engineering* **200**, 1317–1332, 2011.
- [46] F. Cirak and M. West, Decomposition contact response (DCR) for explicit finite element dynamics, *International Journal for Numerical Methods in Engineering* **64**, 1078–1110, 2005.
- [47] M. Comninou, Stress singularity at a sharp edge in contact problems with friction, *Zeitschrift für angewandte Mathematik und Physik ZAMP* **27**, 493–499, 1976.
- [48] R. D. Cook, Improved two-dimensional finite element, *Journal of the Structural Division* **100**, 1974.
- [49] O. Coussy, *Poromechanics*, John Wiley and Sons, West Sussex, 2004.
- [50] P. A. Cundall, A computer model for simulating progressive large scale movements in blocky rock systems, In *Proc. Symp. Rock Fracture (ISRM)*, Nancy, Volume 1, pages 1–8, 1971.
- [51] C. Danowski, *Computational Modelling of Thermo-Structure Interaction with Application to Rocket Nozzles*, PhD thesis, Technical University of Munich, 2014.
- [52] C. Danowski, V. Gravemeier, L. Yoshihara, and W. A. Wall, A monolithic computational approach to thermo-structure interaction, *International Journal for Numerical Methods in Engineering* **95**, 1053–1078, 2013.
- [53] L. De Lorenzis, I. Temizer, P. Wriggers, and G. Zavarise, A large deformation frictional contact formulation using NURBS-based isogeometric analysis, *International Journal for Numerical Methods in Engineering* **87**, 1278–1300, 2011.

- [54] C. A. de Saracibar and M. Chiumenti, On the numerical modeling of frictional wear phenomena, *Computer methods in applied mechanics and engineering* **177**, 401–426, 1999.
- [55] E. A. de Souza Neto, D. Perić, M. Dutko, and D. R. J. Owen, Design of simple low order finite elements for large strain analysis of nearly incompressible solids, *International Journal of Solids and Structures* **33**, 3277 – 3296, 1996.
- [56] B. F. de Veubeke, *Diffusion des inconnues hyperstatiques dans les voitures à longerons couplés*, Hayez, Bruxelles, 1951.
- [57] K. Devine, E. Boman, R. Heaphy, B. Hendrickson, and C. Vaughan, Zoltan data management service for parallel dynamic applications, *Computing in Science & Engineering* **4**, 90–97, 2002.
- [58] H. B. Dhia, Problèmes mécaniques multi-échelles: la méthode Arlequin, *Comptes Rendus de l'Académie des Sciences—Series {IIB}—Mechanics-Physics-Astronomy* **326**, 899–904, 1998.
- [59] H. B. Dhia and G. Rateau, The Arlequin method as a flexible engineering design tool, *International Journal for Numerical Methods in Engineering* **62**, 1442–1462, 2005.
- [60] T. Dickopf and R. Krause, Efficient simulation of multi-body contact problems on complex geometries: A flexible decomposition approach using constrained minimization, *International Journal for Numerical Methods in Engineering* **77**, 1834–1862, 2009.
- [61] T. Doca, *Energy wear methods for dual-mortar contact analysis of frictional problems at finite inelastic strains*, PhD thesis, University of Porto, 2014.
- [62] C. Dohrmann, S. Key, and M. Heinstein, Methods for connecting dissimilar three-dimensional finite element meshes, *International Journal for Numerical Methods in Engineering* **47**, 1057–1080, 2000.
- [63] J. Donéa and A. Huerta, *Finite element methods for flow problems*, Wiley, Chichester, 2003.
- [64] D. Dureisseix and H. Bavestrello, Information transfer between incompatible finite element meshes: Application to coupled thermo-viscoelasticity, *Computer Methods in Applied Mechanics and Engineering* **195**, 6523–6541, 2006.
- [65] A. Ehrl, A. Popp, V. Gravemeier, and W. A. Wall, A dual mortar approach for mesh tying within a variational multiscale method for incompressible flow, *International Journal for Numerical Methods in Fluids* **76**, 1–27, 2014.
- [66] N. El-Abbasi and K.-J. Bathe, Stability and patch test performance of contact discretizations and a new solution algorithm, *Computers & Structures* **79**, 1473–1486, 2001.
- [67] T. Erhart, W. A. Wall, and E. Ramm, Robust adaptive remeshing strategy for large deformation, transient impact simulations, *International Journal for Numerical Methods in Engineering* **65**, 2139–2166, 2006.

- [68] R. Fang, P. Farah, W. Wall, and A. Popp, A mortar-based, monolithic interface coupling scheme for finite-element simulations of lithium-ion cells, *in preparation*, 2017.
- [69] P. Farah, M. Gitterle, W. Wall, and A. Popp, Computational wear and contact modeling for fretting analysis with isogeometric dual mortar methods, *Key Engineering Materials* **681**, 1–18, 2016.
- [70] P. Farah, A.-T. Vuong, W. Wall, and A. Popp, Volumetric coupling approaches for multi-physics simulations on non-matching meshes, *International Journal for Numerical Methods in Engineering* **108**, 1550–1576, 2016.
- [71] P. Farah, W. Wall, and A. Popp, A mortar finite element approach for point, line and surface contact, *in preparation*, 2017.
- [72] P. Farah. Accurate and efficient numerical integration schemes for 2D/3D mortar contact simulations. Master's thesis, Technical University of Munich, 2012.
- [73] P. Farah, A. Popp, and W. A. Wall, Segment-based vs. element-based integration for mortar methods in computational contact mechanics, *Computational Mechanics* **55**, 209–228, 2015.
- [74] P. Farah, W. A. Wall, and A. Popp, An implicit finite wear contact formulation based on dual mortar methods, *International Journal for Numerical Methods in Engineering*, 2016.
- [75] C. Farhat, C. Degand, B. Koobus, and M. Lesoinne, Torsional springs for two-dimensional dynamic unstructured fluid meshes, *Computer Methods in Applied Mechanics and Engineering* **163**, 231 – 245, 1998.
- [76] P. Farrell and J. Maddison, Conservative interpolation between volume meshes by local galerkin projection, *Computer Methods in Applied Mechanics and Engineering* **200**, 89–100, 2011.
- [77] P. Farrell, M. Piggott, C. Pain, G. Gorman, and C. Wilson, Conservative interpolation between unstructured meshes via supermesh construction, *Computer Methods in Applied Mechanics and Engineering* **198**, 2632–2642, 2009.
- [78] J. Fernandes and P. Martins, All-hexahedral remeshing for the finite element analysis of metal forming processes, *Finite Elements in Analysis and Design* **43**, 666–679, 2007.
- [79] R. C. Fetecau, J. E. Marsden, M. Ortiz, and M. West, Nonsmooth lagrangian mechanics and variational collision integrators, *SIAM Journal on Applied Dynamical Systems* **2**, 381–416, 2003.
- [80] K. A. Fischer and P. Wriggers, Frictionless 2D contact formulations for finite deformations based on the mortar method, *Computational Mechanics* **36**, 226–244, 2005.
- [81] K. A. Fischer and P. Wriggers, Mortar based frictional contact formulation for higher order interpolations using the moving friction cone, *Computer Methods in Applied Mechanics and Engineering* **195**, 5020–5036, 2006.

- [82] B. Flemisch and B. I. Wohlmuth, Stable Lagrange multipliers for quadrilateral meshes of curved interfaces in 3D, *Computer Methods in Applied Mechanics and Engineering* **196**, 1589–1602, 2007.
- [83] B. Flemisch, M. Puso, and B. Wohlmuth, A new dual mortar method for curved interfaces: 2D elasticity, *International journal for numerical methods in engineering* **63**, 813–832, 2005.
- [84] A. Francavilla and O. C. Zienkiewicz, A note on numerical computation of elastic contact problems, *International Journal for Numerical Methods in Engineering* **9**, 913–924, 1975.
- [85] M. W. Gee, U. Küttler, and W. A. Wall, Truly monolithic algebraic multigrid for fluid–structure interaction, *International Journal for Numerical Methods in Engineering* **85**, 987–1016, 2011.
- [86] A. Gerstenberger and W. A. Wall, An extended finite element method/Lagrange multiplier based approach for fluid–structure interaction, *Computer Methods in Applied Mechanics and Engineering* **197**, 1699–1714, 2008.
- [87] M. Gitterle, *A dual mortar formulation for finite deformation frictional contact problems including wear and thermal coupling*, PhD thesis, Technical University of Munich, 2012.
- [88] M. Gitterle, A. Popp, M. W. Gee, and W. A. Wall, Finite deformation frictional mortar contact using a semi-smooth Newton method with consistent linearization, *International Journal for Numerical Methods in Engineering* **84**, 543–571, 2010.
- [89] M. Godet, The third-body approach: a mechanical view of wear, *Wear* **100**, 437–452, 1984.
- [90] O. Gonzalez, Exact energy and momentum conserving algorithms for general models in nonlinear elasticity, *Computer Methods in Applied Mechanics and Engineering* **190**, 1763–1783, 2000.
- [91] P. L. Gould and T. Hara, Recent advances in local–global FE analysis of shells of revolution, *Thin-walled structures* **40**, 641–649, 2002.
- [92] D. Gross, W. Hauger, J. Schröder, W. A. Wall, and J. Bonet, *Engineering Mechanics 2*, Springer Verlag Berlin Heidelberg, 2011.
- [93] R. B. Haber, A mixed Eulerian-Lagrangian displacement model for large-deformation analysis in solid mechanics, *Computer Methods in Applied Mechanics and Engineering* **43**, 277–292, 1984.
- [94] G. Haikal, *A stabilized finite element formulation of non-smooth contact*, PhD thesis, University of Illinois at Urbana-Champaign, 2009.
- [95] G. Haikal and K. Hjelmstad, A finite element formulation of non-smooth contact based on oriented volumes for quadrilateral and hexahedral elements, *Computer Methods in Applied Mechanics and Engineering* **196**, 4690–4711, 2007.

- [96] J. O. Hallquist, G. L. Goudreau, and D. J. Benson, Sliding interfaces with contact-impact in large-scale Lagrangian computations, *Computer Methods in Applied Mechanics and Engineering* **51**, 107–137, 1985.
- [97] J. Hallquist, NIKE2D: An implicit, finite-deformation, finite-element code for analyzing the static and dynamic response of two-dimensional solids, Technical report, California Univ., Livermore (USA). Lawrence Livermore Lab., 1979.
- [98] S. Hartmann, S. Brunssen, E. Ramm, and B. Wohlmuth, Unilateral non-linear dynamic contact of thin-walled structures using a primal-dual active set strategy, *International journal for numerical methods in engineering* **70**, 883–912, 2007.
- [99] S. Hartmann, J. Oliver, R. Weyler, J. Cante, and J. Hernández, A contact domain method for large deformation frictional contact problems. Part 2: Numerical aspects, *Computer Methods in Applied Mechanics and Engineering* **198**, 2607–2631, 2009.
- [100] S. Hartmann, R. Weyler, J. Oliver, J. Cante, and J. Hernández, A 3D frictionless contact domain method for large deformation problems, *Computer Modeling in Engineering and Sciences (CMES)* **55**, 211, 2010.
- [101] V. Hegadekatte, N. Huber, and O. Kraft, Finite element based simulation of dry sliding wear, *Modelling and Simulation in Materials Science and Engineering* **13**, 57, 2004.
- [102] M. A. Heroux, R. A. Bartlett, V. E. Howle, R. J. Hoekstra, J. J. Hu, T. G. Kolda, R. B. Lehoucq, K. R. Long, R. P. Pawlowski, E. T. Phipps, et al., An overview of the Trilinos project, *ACM Transactions on Mathematical Software (TOMS)* **31**, 397–423, 2005.
- [103] C. Hesch and P. Betsch, Transient three-dimensional domain decomposition problems: Frame-indifferent mortar constraints and conserving integration, *International Journal for Numerical Methods in Engineering* **82**, 329–358, 2010.
- [104] C. Hesch and P. Betsch, Transient 3D contact problems–NTS method: mixed methods and conserving integration, *Computational Mechanics* **48**, 437–449, 2011.
- [105] C. Hesch, A. Gil, A. A. Carreño, J. Bonet, and P. Betsch, A mortar approach for Fluid–Structure interaction problems: Immersed strategies for deformable and rigid bodies, *Computer Methods in Applied Mechanics and Engineering* **278**, 853–882, 2014.
- [106] C. Hesch and P. Betsch, A mortar method for energy-momentum conserving schemes in frictionless dynamic contact problems, *International Journal for Numerical Methods in Engineering* **77**, 1468–1500, 2009.
- [107] P. Hild, Numerical implementation of two nonconforming finite element methods for unilateral contact, *Computer Methods in Applied Mechanics and Engineering* **184**, 99–123, 2000.
- [108] D. A. Hills, Mechanics of fretting fatigue, *Wear* **175**, 107–113, 1994.

- [109] M. Hintermüller, K. Ito, and K. Kunisch, The Primal-Dual Active Set Strategy as a Semi-smooth Newton Method, *SIAM Journal on Optimization* **13**, 865–888, 2002.
- [110] T. Ho and M. Peterson, Wear formulation for aircraft brake material sliding against steel, *Wear* **43**, 199–210, 1977.
- [111] R. Hojjati Talemi, *Numerical modelling techniques for fretting fatigue crack initiation and propagation*, PhD thesis, Ghent University, 2014.
- [112] R. Holm, *Electric contacts*, Springer, Berlin, 1967.
- [113] G. A. Holzapfel, Nonlinear solid mechanics: a continuum approach for engineering science, *Meccanica* **37**, 489–490, 2002.
- [114] S. Hüeber, *Discretization techniques and efficient algorithms for contact problems*, PhD thesis, Universität Stuttgart, 2008.
- [115] S. Hüeber and B. I. Wohlmuth, A primal-dual active set strategy for non-linear multibody contact problems, *Computer Methods in Applied Mechanics and Engineering* **194**, 3147–3166, 2005.
- [116] S. Hüeber and B. I. Wohlmuth, Thermo-mechanical contact problems on non-matching meshes, *Computer Methods in Applied Mechanics and Engineering* **198**, 1338–1350, 2009.
- [117] S. Hüeber, G. Stadler, and B. I. Wohlmuth, A Primal-Dual Active Set Algorithm for Three-Dimensional Contact Problems with Coulomb Friction, *SIAM Journal on Scientific Computing* **30**, 572–596, 2008.
- [118] A. Huerta and F. Casadei, New ALE applications in non-linear fast-transient solid dynamics, *Engineering Computations* **11**, 317–345, 1994.
- [119] J. F. Hughes, A. Van Dam, J. D. Foley, and S. K. Feiner, *Computer graphics: principles and practice*, Pearson Education, New Jersey, 2014.
- [120] T. J. R. Hughes, R. L. Taylor, J. L. Sackman, A. Curnier, and W. Kanoknukulchai, A finite element method for a class of contact-impact problems, *Computer Methods in Applied Mechanics and Engineering* **8**, 249–276, 1976.
- [121] T. J. R. Hughes, G. Scovazzi, and L. P. Franca, Multiscale and stabilized methods, In E. Stein, R. de Borst, and T. J. R. Hughes (eds.), *Encyclopedia of Computational Mechanics*, pages 5–59, John Wiley & Sons, Chichester, 2004.
- [122] T. J. Hughes, J. A. Cottrell, and Y. Bazilevs, Isogeometric analysis: CAD, finite elements, NURBS, exact geometry and mesh refinement, *Computer methods in applied mechanics and engineering* **194**, 4135–4195, 2005.
- [123] T. J. Hughes, A. Reali, and G. Sangalli, Efficient quadrature for NURBS-based isogeometric analysis, *Computer methods in applied mechanics and engineering* **199**, 301–313, 2010.

Bibliography

- [124] P. Hurricks, The mechanism of fretting - a review, *Wear* **15**, 389–409, 1970.
- [125] P. Iremán, A. Klarbring, and N. Strömberg, Finite element algorithms for thermoelastic wear problems, *European Journal of Mechanics-A/Solids* **21**, 423–440, 2002.
- [126] B. M. Irons, Numerical integration applied to finite element methods, In *Proceedings Conference on the Use of Digital Computers in Structural Engineering*, University of Newcastle, 1966.
- [127] B. M. Irons and R. C. Tuck, A version of the Aitken accelerator for computer iteration, *International Journal for Numerical Methods in Engineering* **1**, 275–277, 1969.
- [128] C. Jelich. Thermo-Mechanical Mortar Contact Formulation for Non-Matching Volume and Interface Meshes. Master's thesis, Technical University of Munich, 2016.
- [129] Q. Jiang and M. Yeung, A model of point-to-face contact for three-dimensional discontinuous deformation analysis, *Rock Mechanics and Rock Engineering* **37**, 95–116, 2004.
- [130] K. L. Johnson, *Contact mechanics*, Cambridge University Press, Cambridge, 1985.
- [131] F. Jourdan and A. Samida, An implicit numerical method for wear modeling applied to a hip joint prosthesis problem, *Computer Methods in Applied Mechanics and Engineering* **198**, 2209–2217, 2009.
- [132] C. Kane, E. A. Repetto, M. Ortiz, and J. E. Marsden, Finite element analysis of nonsmooth contact, *Computer Methods in Applied Mechanics and Engineering* **180**, 1–26, 1999.
- [133] E. P. Kasper and R. L. Taylor, A mixed-enhanced strain method: Part II: Geometrically nonlinear problems, *Computers & Structures* **75**, 251–260, 2000.
- [134] N. Kikuchi and J. T. Oden, *Contact problems in elasticity: A study of variational inequalities and finite element methods*, SIAM, Philadelphia, 1988.
- [135] J.-Y. Kim and S.-K. Youn, Isogeometric contact analysis using mortar method, *International Journal for Numerical Methods in Engineering* **89**, 1559–1581, 2012.
- [136] M.-Y. Kim, E.-J. Park, S. G. Thomas, and M. F. Wheeler, A multiscale mortar mixed finite element method for slightly compressible flows in porous media, *Journal of the Korean Mathematical Society* **44**, 1103–1119, 2007.
- [137] T. W. Kim, S. M. Moon, and Y. J. Cho, Prediction of fretting wear using boundary element method, *Tribology International* **44**, 1571–1576, 2011.
- [138] T. Klöppel, A. Popp, U. Küttler, and W. A. Wall, Fluid-structure interaction for non-conforming interfaces based on a dual mortar formulation, *Computer Methods in Applied Mechanics and Engineering* **200**, 3111–3126, 2011.
- [139] A. Konyukhov and K. Schweizerhof, On the solvability of closest point projection procedures in contact analysis: Analysis and solution strategy for surfaces of arbitrary geometry, *Computer Methods in Applied Mechanics and Engineering* **197**, 3045–3056, 2008.

- [140] R. Krause and B. Wohlmuth, Nonconforming domain decomposition techniques for linear elasticity, *East West Journal of Numerical Mathematics* **8**, 177–206, 2000.
- [141] R. Krause, A nonsmooth multiscale method for solving frictional two-body contact problems in 2D and 3D with multigrid efficiency, *SIAM Journal on Scientific Computing* **31**, 1399–1423, 2009.
- [142] D. Kuhl and M. A. Crisfield, Energy-conserving and decaying algorithms in non-linear structural dynamics, *International Journal for Numerical Methods in Engineering* **45**, 569–599, 1999.
- [143] D. Kuhl and E. Ramm, Generalized energy–momentum method for non-linear adaptive shell dynamics, *Computer Methods in Applied Mechanics and Engineering* **178**, 343–366, 1999.
- [144] U. Küttler and W. A. Wall, Fixed-point fluid–structure interaction solvers with dynamic relaxation, *Computational Mechanics* **43**, 61–72, 2008.
- [145] A. La Spina, M. Kronbichler, A.-T. Vuong, P. Farah, and W. Wall, A robust, efficient and easy to implement moving grid approach to fluid-structure interaction based on a volumetric coupling scheme, *in preparation*, 2018.
- [146] B. P. Lamichhane and B. I. Wohlmuth, Biorthogonal bases with local support and approximation properties, *Mathematics of Computation* **76**, 233–249, 2007.
- [147] B. P. Lamichhane, R. P. Stevenson, and B. I. Wohlmuth, Higher order mortar finite element methods in 3D with dual Lagrange multiplier bases, *Numerische Mathematik* **102**, 93–121, 2005.
- [148] B. P. Lamichhane, A mixed finite element method for non-linear and nearly incompressible elasticity based on biorthogonal systems, *International journal for numerical methods in engineering* **79**, 870–886, 2009.
- [149] B. P. Lamichhane, A. McBride, and B. Reddy, A finite element method for a three-field formulation of linear elasticity based on biorthogonal systems, *Computer Methods in Applied Mechanics and Engineering* **258**, 109–117, 2013.
- [150] J. Lancaster, The formation of surface films at the transition between mild and severe metallic wear, In *Proceedings of the Royal Society of London A: Mathematical, Physical and Engineering Sciences*, Volume 273, pages 466–483. The Royal Society, 1963.
- [151] T. A. Laursen, *Computational contact and impact mechanics*, Springer-Verlag Berlin Heidelberg, 2002.
- [152] T. A. Laursen and V. Chawla, Design of energy conserving algorithms for frictionless dynamic contact problems, *International Journal for Numerical Methods in Engineering* **40**, 863–886, 1997.

Bibliography

- [153] T. A. Laursen and G. R. Love, Improved implicit integrators for transient impact problems—geometric admissibility within the conserving framework, *International Journal for Numerical Methods in Engineering* **53**, 245–274, 2002.
- [154] T. A. Laursen and J. C. Simo, A continuum-based finite element formulation for the implicit solution of multibody, large deformation-frictional contact problems, *International Journal for Numerical Methods in Engineering* **36**, 3451–3485, 1993.
- [155] C. Y. Lee, L. S. Tian, J. W. Bae, and Y. S. Chai, Application of influence function method on the fretting wear of tube-to-plate contact, *Tribology International* **42**, 951–957, 2009.
- [156] D. T. Lee and B. J. Schachter, Two algorithms for constructing a Delaunay triangulation, *International Journal of Computer Information Science* **9**, 219–242, 1980.
- [157] J. Lengiewicz and S. Stupkiewicz, Continuum framework for finite element modelling of finite wear, *Computer Methods in Applied Mechanics and Engineering* **205 - 208**, 178 – 188, 2012.
- [158] J. Lengiewicz and S. Stupkiewicz, Efficient model of evolution of wear in quasi-steady-state sliding contacts, *Wear* **303**, 611–621, 2013.
- [159] W. K. Liu, S. Tang, et al., Mathematical foundations of the immersed finite element method, *Computational Mechanics* **39**, 211–222, 2007.
- [160] Y. Maday, C. Mavriplis, and A. Patera, Nonconforming mortar element methods: Application to spectral discretizations, *Domain Decomposition Methods*, 392–418, 1989.
- [161] N. Maman and C. Farhat, Matching fluid and structure meshes for aeroelastic computations: a parallel approach, *Computers & Structures* **54**, 779–785, 1995.
- [162] A. Massing, M. Larson, and A. Logg, Efficient implementation of finite element methods on nonmatching and overlapping meshes in three dimensions, *SIAM Journal on Scientific Computing* **35**, C23–C47, 2013.
- [163] M. Matzen and M. Bischoff, A weighted point-based formulation for isogeometric contact, *Computer Methods in Applied Mechanics and Engineering* **308**, 73–95, 2016.
- [164] M. Matzen, T. Cichosz, and M. Bischoff, A point to segment contact formulation for isogeometric, NURBS based finite elements, *Computer Methods in Applied Mechanics and Engineering* **255**, 27–39, 2013.
- [165] M. Mayr, *A Monolithic Solver for Fluid-Structure Interaction with Adaptive Time Stepping and a Hybrid Preconditioner*, PhD thesis, Technical University of Munich, 2016.
- [166] M. Mayr, T. Klöppel, W. A. Wall, and M. W. Gee, A temporal consistent monolithic approach to fluid-structure interaction enabling single field predictors, *SIAM Journal on Scientific Computing* **37**, B30–B59, 2015.
- [167] I. McColl, J. Ding, and S. Leen, Finite element simulation and experimental validation of fretting wear, *Wear* **256**, 1114–1127, 2004.

-
- [168] T. W. McDevitt and T. A. Laursen, A mortar-finite element formulation for frictional contact problems, *International Journal for Numerical Methods in Engineering* **48**, 1525–1547, 2000.
 - [169] R. L. Meakin, Adaptive spatial partitioning and refinement for overset structured grids, *Computer Methods in Applied Mechanics and Engineering* **189**, 1077–1117, 2000.
 - [170] C. Meier, *Geometrically exact finite element formulations for slender beams and their contact interaction*, PhD thesis, Technical University of Munich, 2016.
 - [171] C. Meier, A. Popp, and W. A. Wall, A finite element approach for the line-to-line contact interaction of thin beams with arbitrary orientation, *Computer Methods in Applied Mechanics and Engineering* **308**, 377 – 413, 2016.
 - [172] G. H. Meisters, Polygons have ears, *The American Mathematical Monthly* **82**, 648–651, 1975.
 - [173] H. C. Meng and K. C. Ludema, Wear models and predictive equations: their form and content, *Wear* **181–183, Part 2**, 443 – 457, 1995.
 - [174] R. Mlika, Y. Renard, and F. Chouly, An unbiased nitsche's formulation of large deformation frictional contact and self-contact, 2017.
 - [175] J. F. Molinari, M. Ortiz, R. Radovitzky, and E. A. Repetto, Finite element modeling of dry sliding wear in metals, *Engineering Computations* **18**, 592–610, 2001.
 - [176] C. Mote, Global-local finite element, *International Journal for Numerical Methods in Engineering* **3**, 565–574, 1971.
 - [177] S. E. Mousavi and N. Sukumar, Numerical integration of polynomials and discontinuous functions on irregular convex polygons and polyhedrons, *Computational Mechanics* **47**, 535–554, 2011.
 - [178] S. E. Mousavi, H. Xiao, and N. Sukumar, Generalized Gaussian quadrature rules on arbitrary polygons, *International Journal for Numerical Methods in Engineering* **82**, 99–113, 2010.
 - [179] Z. Mróz and S. Stupkiewicz, An anisotropic friction and wear model, *International Journal of Solids and Structures* **31**, 1113–1131, 1994.
 - [180] B. Müller and G. Starke, Stress-Based Finite Element Methods in Linear and Nonlinear Solid Mechanics, In *Advanced Finite Element Technologies*, pages 69–104, Springer, 2016.
 - [181] D. Néron and D. Dureisseix, A computational strategy for thermo-poroelastic structures with a time–space interface coupling, *International Journal for Numerical Methods in Engineering* **75**, 1053–1084, 2008.

Bibliography

- [182] T. Nguyen-Thoi, G. Liu, H. Vu-Do, and H. Nguyen-Xuan, A face-based smoothed finite element method (FS-FEM) for visco-elastoplastic analyses of 3D solids using tetrahedral mesh, *Computer Methods in Applied Mechanics and Engineering* **198**, 3479–3498, 2009.
- [183] J. Nitsche, Über ein Variationsprinzip zur Lösung von Dirichlet-Problemen bei Verwendung von Teilräumen, die keinen Randbedingungen unterworfen sind, In *Abhandlungen aus dem mathematischen Seminar der Universität Hamburg*, Volume 36, pages 9–15. Springer, 1971.
- [184] V. Oancea and T. Laursen, A finite element formulation of thermomechanical rate-dependent frictional sliding, *International Journal for Numerical Methods in Engineering* **40**, 4275–4311, 1997.
- [185] R. W. Ogden, *Non-linear elastic deformations*, Courier Corporation, North Chelmsford, 1997.
- [186] J. Oliver, S. Hartmann, J. Cante, R. Weyler, and J. Hernández, A contact domain method for large deformation frictional contact problems. Part 1: theoretical basis, *Computer Methods in Applied Mechanics and Engineering* **198**, 2591–2606, 2009.
- [187] M. Öqvist, Numerical simulations of mild wear using updated geometry with different step size approaches, *Wear* **249**, 6–11, 2001.
- [188] A. Orlando and D. Perić, Analysis of transfer procedures in elastoplasticity based on the error in the constitutive equations: Theory and numerical illustration, *International Journal for Numerical Methods in Engineering* **60**, 1595–1631, 2004.
- [189] A. Orlando, *Analysis of adaptive finite element solutions in elastoplasticity with reference to transfer operation techniques*, PhD thesis, University of Wales Swansea, 2003.
- [190] M. Ortiz and J. J. Quigley, Adaptive mesh refinement in strain localization problems, *Computer Methods in Applied Mechanics and Engineering* **90**, 781–804, 1991.
- [191] I. Páczelt and Z. Mróz, On optimal contact shapes generated by wear, *International Journal for Numerical Methods in Engineering* **63**, 1250–1287, 2005.
- [192] I. Páczelt and Z. Mróz, Optimal shapes of contact interfaces due to sliding wear in the steady relative motion, *International journal of solids and structures* **44**, 895–925, 2007.
- [193] I. Páczelt, S. Kucharski, and Z. Mróz, The experimental and numerical analysis of quasi-steady wear processes for a sliding spherical indenter, *Wear* **274**, 127–148, 2012.
- [194] A. Pandolfi, C. Kane, J. E. Marsden, and M. Ortiz, Time-discretized variational formulation of non-smooth frictional contact, *International Journal for Numerical Methods in Engineering* **53**, 1801–1829, 2002.
- [195] P. Papadopoulos and R. L. Taylor, A mixed formulation for the finite element solution of contact problems, *Computer Methods in Applied Mechanics and Engineering* **94**, 373–389, 1992.

- [196] K. Park, C. Felippa, and G. Rebel, A simple algorithm for localized construction of non-matching structural interfaces, *International Journal for Numerical Methods in Engineering* **53**, 2117–2142, 2002.
- [197] C. Paulin, S. Fouvry, and C. Meunier, Finite element modelling of fretting wear surface evolution: application to a Ti–6Al–4V contact, *Wear* **264**, 26–36, 2008.
- [198] D. Pavelescu and M. Musat, Some relations for determining the wear of composite brake materials, *Wear* **27**, 91–97, 1974.
- [199] S. Pearson and P. Shipway, Is the wear coefficient dependent upon slip amplitude in fretting? Vingsbo and Söderberg revisited, *Wear* **330**, 93–102, 2015.
- [200] S. Pearson, P. Shipway, J. Abere, and R. Hewitt, The effect of temperature on wear and friction of a high strength steel in fretting, *Wear* **303**, 622–631, 2013.
- [201] P. P. Pébay and T. J. Baker, Analysis of Triangle Quality Measures, *Mathematics of Computation* **72**, 1817–1839, 2003.
- [202] D. Perić, C. Hochard, M. Dutko, and D. Owen, Transfer operators for evolving meshes in small strain elasto-plasticity, *Computer Methods in Applied Mechanics and Engineering* **137**, 331 – 344, 1996.
- [203] D. Perić, M. Vaz Jr., and D. Owen, On adaptive strategies for large deformations of elasto-plastic solids at finite strains: computational issues and industrial applications, *Computer Methods in Applied Mechanics and Engineering* **176**, 279–312, 1999.
- [204] B. N. Persson, O. Albohr, F. Mancosu, V. Peveri, V. Samoilov, and I. M. Sivebæk, On the nature of the static friction, kinetic friction and creep, *Wear* **254**, 835–851, 2003.
- [205] C. S. Peskin, The immersed boundary method, *Acta numerica* **11**, 479–517, 2002.
- [206] L. Piegl and W. Tiller, *The nurbs book*, Springer-Verlag Berlin Heidelberg, Heidelberg, 1997.
- [207] G. Pietrzak and A. Curnier, Large deformation frictional contact mechanics: continuum formulation and augmented lagrangian treatment, *Computer Methods in Applied Mechanics and Engineering* **177**, 351–381, 1999.
- [208] P. Podra and S. Andersson, Simulating sliding wear with finite element method, *Tribology International* **32**, 71–81, 1999.
- [209] V. Popov, *Contact Mechanics and Friction*, Springer-Verlag Berlin, 2010.
- [210] A. Popp, *Mortar methods for computational contact mechanics and general interface problems*, PhD thesis, Technical University of Munich, 2012.
- [211] A. Popp, M. W. Gee, and W. A. Wall, A finite deformation mortar contact formulation using a primal-dual active set strategy, *International Journal for Numerical Methods in Engineering* **79**, 1354–1391, 2009.

Bibliography

- [212] A. Popp, M. Gitterle, M. W. Gee, and W. A. Wall, A dual mortar approach for 3D finite deformation contact with consistent linearization, *International Journal for Numerical Methods in Engineering* **83**, 1428–1465, 2010.
- [213] A. Popp, B. I. Wohlmuth, M. W. Gee, and W. A. Wall, Dual quadratic mortar finite element methods for 3D finite deformation contact, *SIAM Journal on Scientific Computing* **34**, B421–B446, 2012.
- [214] A. Popp, A. Seitz, M. W. Gee, and W. A. Wall, Improved robustness and consistency of 3D contact algorithms based on a dual mortar approach, *Computer Methods in Applied Mechanics and Engineering* **264**, 67–80, 2013.
- [215] S. Pröll, *Thermo-Structure-Wear Interaction for Finite Deformation Contact Mechanics*, Term thesis, Technical University of Munich, 2016.
- [216] M. A. Puso, A 3D mortar method for solid mechanics, *International Journal for Numerical Methods in Engineering* **59**, 315–336, 2004.
- [217] M. A. Puso and T. A. Laursen, Mesh tying on curved interfaces in 3D, *Engineering Computations* **20**, 305–319, 2003.
- [218] M. A. Puso and T. A. Laursen, A mortar segment-to-segment contact method for large deformation solid mechanics, *Computer Methods in Applied Mechanics and Engineering* **193**, 601–629, 2004.
- [219] M. A. Puso and T. A. Laursen, A mortar segment-to-segment frictional contact method for large deformations, *Computer Methods in Applied Mechanics and Engineering* **193**, 4891–4913, 2004.
- [220] M. A. Puso, T. A. Laursen, and J. Solberg, A segment-to-segment mortar contact method for quadratic elements and large deformations, *Computer Methods in Applied Mechanics and Engineering* **197**, 555–566, 2008.
- [221] L. Qi and J. Sun, A nonsmooth version of Newton's method, *Mathematical programming* **58**, 353–367, 1993.
- [222] A. Quarteroni, R. Sacco, and F. Saleri, *Numerical mathematics*, Volume 37, Springer Science & Business Media, New York, 2010.
- [223] E. Rabinowicz, *Friction and wear of materials*, Wiley, New York, 1995.
- [224] A. Ramalho and J. Miranda, The relationship between wear and dissipated energy in sliding systems, *Wear* **260**, 361 – 367, 2006.
- [225] E. Ramm and W. A. Wall, Fluid-structure interaction based upon a stabilized (ALE) finite element method, In *4th World Congress on Computational Mechanics: New Trends and Applications, CIMNE, Barcelona*, pages 1–20, 1998.

- [226] E. Ramm, E. Rank, R. Rannacher, K. Schweizerhof, E. Stein, W. Wendland, G. Wittum, P. Wriggers, and W. Wunderlich, *Error-controlled adaptive finite elements in solid mechanics*, John Wiley & Sons, Chichester, 2003.
- [227] M. M. Rashid, Material state remapping in computational solid mechanics, *International Journal for Numerical Methods in Engineering* **55**, 431–450, 2002.
- [228] J. N. Reddy, *An introduction to nonlinear finite element analysis*, Oxford University Press, 2004.
- [229] T. Renaud, M. Costes, and S. Péron, Computation of GOAHEAD configuration with Chimera assembly, *Aerospace Science and Technology* **19**, 50–57, 2012.
- [230] S. Rhee, Wear equation for polymers sliding against metal surfaces, *Wear* **16**, 431–445, 1970.
- [231] S. Rhee, Wear mechanisms for asbestos-reinforced automotive friction materials, *Wear* **29**, 391–393, 1974.
- [232] A. Rodríguez-Ferran, A. Pérez-Foguet, and A. Huerta, Arbitrary Lagrangian–Eulerian (ALE) formulation for hyperelastoplasticity, *International Journal for Numerical Methods in Engineering* **53**, 1831–1851, 2002.
- [233] L. Rodríguez-Tembleque, R. Abascal, and M. Aliabadi, A boundary element formulation for wear modeling on 3D contact and rolling-contact problems, *International Journal of Solids and Structures* **47**, 2600–2612, 2010.
- [234] L. Rodríguez-Tembleque, R. Abascal, and M. Aliabadi, A boundary elements formulation for 3D fretting-wear problems, *Engineering Analysis with Boundary Elements* **35**, 935–943, 2011.
- [235] L. Rodríguez-Tembleque, R. Abascal, and M. H. Aliabadi, Anisotropic wear framework for 3D contact and rolling problems, *Computer Methods in Applied Mechanics and Engineering* **241**, 1–19, 2012.
- [236] D. F. Rogers, *An introduction to NURBS: with historical perspective*, Academic Press, San Diego, 2001.
- [237] Y. Saad, *Iterative methods for sparse linear systems*, SIAM, Philadelphia, 2003.
- [238] P. H. Saksono and D. Perić, On finite element modelling of surface tension: Variational formulation and applications–Part II: Dynamic problems, *Computational Mechanics* **38**, 251–263, 2006.
- [239] P. Saksono and D. Perić, On finite element modelling of surface tension Variational formulation and applications–Part I: Quasistatic problems, *Computational Mechanics* **38**, 265–281, 2006.

Bibliography

- [240] L. Salles, L. Blanc, F. Thouverez, and A. M. Gouskov, Dynamic analysis of fretting-wear in friction contact interfaces, *International Journal of Solids and Structures* **48**, 1513–1524, 2011.
- [241] R. A. Sauer, Enriched contact finite elements for stable peeling computations, *International Journal for Numerical Methods in Engineering* **87**, 593–616, 2011.
- [242] L. R. Scott and S. Zhang, Finite element interpolation of nonsmooth functions satisfying boundary conditions, *Mathematics of Computation* **54**, 483–492, 1990.
- [243] A. Seitz, A. Popp, and W. A. Wall, A semi-smooth newton method for orthotropic plasticity and frictional contact at finite strains, *Computer Methods in Applied Mechanics and Engineering* **285**, 228–254, 2015.
- [244] A. Seitz, P. Farah, J. Kremheller, B. I. Wohlmuth, W. A. Wall, and A. Popp, Isogeometric dual mortar methods for computational contact mechanics, *Computer Methods in Applied Mechanics and Engineering* **301**, 259–280, 2016.
- [245] A. Seitz, W. A. Wall, and A. Popp, A computational approach for thermo-elasto-plastic frictional contact based on a monolithic formulation employing non-smooth nonlinear complementarity functions, *submitted*, 2017.
- [246] I. Serre, M. Bonnet, and R.-M. Pradeilles-Duval, Modelling an abrasive wear experiment by the boundary element method, *Comptes Rendus de l'Académie des Sciences-Series IIB-Mechanics* **329**, 803–808, 2001.
- [247] P. Seshaiyer and M. Suri, hp submeshing via non-conforming finite element methods, *Computer Methods in Applied Mechanics and Engineering* **189**, 1011–1030, 2000.
- [248] G. K. Sfantis and M. H. Aliabadi, A boundary element formulation for three-dimensional sliding wear simulation, *Wear* **262**, 672 – 683, 2007.
- [249] G. Sfantis and M. Aliabadi, Wear simulation using an incremental sliding boundary element method, *Wear* **260**, 1119–1128, 2006.
- [250] G.-H. Shi, Discontinuous deformation analysis: a new numerical model for the statics and dynamics of deformable block structures, *Engineering computations* **9**, 157–168, 1992.
- [251] A. Shu, *The Hu-Washizu approach for nonlinear finite elements based on dual trial functions for nearly incompressible elements*, Term thesis, Technical University of Munich, 2017.
- [252] J. C. Simo and N. Tarnow, The discrete energy-momentum method. Conserving algorithms for nonlinear elastodynamics, *Zeitschrift für Angewandte Mathematik und Physik (ZAMP)* **43**, 757–792, 1992.
- [253] J. C. Simo, P. Wriggers, and R. L. Taylor, A perturbed Lagrangian formulation for the finite element solution of contact problems, *Computer Methods in Applied Mechanics and Engineering* **50**, 163–180, 1985.

- [254] J. C. Simo and T. J. Hughes, *Computational inelasticity*, Volume 7, Springer Science & Business Media, New York, 2006.
- [255] J. C. Simo and M. Rifai, A class of mixed assumed strain methods and the method of incompatible modes, *International journal for numerical methods in engineering* **29**, 1595–1638, 1990.
- [256] A. Sommariva and M. Vianello, Product Gauss cubature over polygons based on Green's integration formula, *BIT Numerical Mathematics* **47**, 441–453, 2007.
- [257] A. Sommariva and M. Vianello, Gauss-Green cubature and moment computation over arbitrary geometries, *Journal of Computational and Applied Mathematics* **231**, 886–896, 2009.
- [258] J. L. Steger and J. A. Benek, On the use of composite grid schemes in computational aerodynamics, *Computer Methods in Applied Mechanics and Engineering* **64**, 301–320, 1987.
- [259] D. E. Stewart, Rigid-body dynamics with friction and impact, *SIAM review* **42**, 3–39, 2000.
- [260] N. Strömberg, An augmented Lagrangian method for fretting problems, *European Journal of Mechanics – A/Solids* **16**, 573–593, 1996.
- [261] N. Strömberg, L. Johansson, and A. Klarbring, Derivation and analysis of a generalized standard model for contact, friction and wear, *International Journal of Solids and Structures* **33**, 1817–1836, 1996.
- [262] N. Strömberg, A method for structural dynamic contact problems with friction and wear, *International journal for numerical methods in engineering* **58**, 2371–2385, 2003.
- [263] S. Stupkiewicz, An ALE formulation for implicit time integration of quasi-steady-state wear problems, *Computer Methods in Applied Mechanics and Engineering* **260**, 130 – 142, 2013.
- [264] Y. Sudhakar and W. A. Wall, Quadrature schemes for arbitrary convex/concave volumes and integration of weak form in enriched partition of unity methods, *Computer Methods in Applied Mechanics and Engineering* **258**, 39–54, 2013.
- [265] Y. Sudhakar, J. M. de Almeida, and W. A. Wall, An accurate, robust, and easy-to-implement method for integration over arbitrary polyhedra: Application to embedded interface methods, *Journal of Computational Physics* **273**, 393–415, 2014.
- [266] R. L. Taylor and P. Papadopoulos, On a patch test for contact problems in two dimensions, In P. Wriggers and W. Wagner (eds.), *Computational Methods in Nonlinear Mechanics*, Springer-Verlag Berlin Heidelberg, 1991.
- [267] R. L. Taylor, J. C. Simo, O. C. Zienkiewicz, and A. C. H. Chan, The patch test: A condition for assessing FEM convergence, *International Journal for Numerical Methods in Engineering* **22**, 39–62, 1986.

Bibliography

- [268] I. Temizer, A mixed formulation of mortar-based contact with friction, *Computer Methods in Applied Mechanics and Engineering* **255**, 183–195, 2013.
- [269] I. Temizer and S. Stupkiewicz, Formulation of the reynolds equation on a time-dependent lubrication surface, In *Proc. R. Soc. A*, Volume 472, page 20160032. The Royal Society, 2016.
- [270] I. Temizer, P. Wriggers, and T. J. R. Hughes, Three-dimensional mortar-based frictional contact treatment in isogeometric analysis with NURBS, *Computer Methods in Applied Mechanics and Engineering* **209–212**, 115–128, 2012.
- [271] S. P. Timoshenko and J. N. Goodier, *Theory of elasticity*, McGraw-Hill, New York, 1970.
- [272] A. Tkachuk and M. Bischoff, Direct and sparse construction of consistent inverse mass matrices: general variational formulation and application to selective mass scaling, *International Journal for Numerical Methods in Engineering* **101**, 435–469, 2015.
- [273] M. Tur, F. J. Fuenmayor, and P. Wriggers, A mortar-based frictional contact formulation for large deformations using Lagrange multipliers, *Computer Methods in Applied Mechanics and Engineering* **198**, 2860–2873, 2009.
- [274] M. Tur, E. Giner, F. J. Fuenmayor, and P. Wriggers, 2D contact smooth formulation based on the mortar method, *Computer Methods in Applied Mechanics and Engineering* **247–248**, 1–14, 2012.
- [275] F. Verdugo and W. A. Wall, Unified framework for the efficient solution of n-field coupled problems with monolithic schemes, *submitted to Computer Methods in Applied Mechanics and Engineering*, 2015.
- [276] S. Voleti, N. Chandra, and J. Miller, Global-local analysis of large-scale composite structures using finite element methods, *Computers & Structures* **58**, 453–464, 1996.
- [277] A.-T. Vuong, *A Computational Approach to Coupled Poroelastic Media Problems*, PhD thesis, Technical University of Munich, 2016.
- [278] A.-T. Vuong, L. Yoshihara, and W. A. Wall, A general approach for modeling interacting flow through porous media under finite deformations, *Computer Methods in Applied Mechanics and Engineering* **283**, 1240–1259, 2015.
- [279] A.-T. Vuong, C. Ager, and W. Wall, Two finite element approaches for Darcy and Darcy–Brinkman flow through deformable porous media—Mixed method vs. NURBS based (isogeometric) continuity, *Computer Methods in Applied Mechanics and Engineering* **305**, 634–657, 2016.
- [280] W. A. Wall, *Fluid-Struktur-Interaktion mit stabilisierten Finiten Elementen*, PhD thesis, Universität Stuttgart, 1999.
- [281] W. A. Wall, P. Gamnitzer, and A. Gerstenberger, Fluid–structure interaction approaches on fixed grids based on two different domain decomposition ideas, *International Journal of Computational Fluid Dynamics* **22**, 411–427, 2008.

- [282] W. A. Wall et al., *BACI: A multiphysics simulation environment*, Technical report, Technical University of Munich, 2017.
- [283] K. Washizu, *Variational methods in elasticity and plasticity*, Pergamon press, New York, 1975.
- [284] R. B. Waterhouse, Fretting fatigue, *International materials reviews* **37**, 77–98, 1992.
- [285] R. Weyler, J. Oliver, T. Sain, and J. Cante, On the contact domain method: A comparison of penalty and lagrange multiplier implementations, *Computer methods in applied mechanics and engineering* **205**, 68–82, 2012.
- [286] T. Wiesner, *Flexible Aggregation-based Algebraic Multigrid Methods for Contact and Flow Problems*, PhD thesis, Technical University of Munich, 2015.
- [287] C. Wilking and M. Bischoff, Alternative integration algorithms for three-dimensional mortar contact, *Computational Mechanics*, 1–16, 2016.
- [288] B. I. Wohlmuth, A mortar finite element method using dual spaces for the Lagrange multiplier, *SIAM Journal on Numerical Analysis* **38**, 989–1012, 2000.
- [289] B. I. Wohlmuth, *Discretization methods and iterative solvers based on domain decomposition*, Springer-Verlag Berlin Heidelberg, 2001.
- [290] B. I. Wohlmuth, Variationally consistent discretization schemes and numerical algorithms for contact problems, *Acta Numerica* **20**, 569–734, 2011.
- [291] B. I. Wohlmuth, A. Popp, M. W. Gee, and W. A. Wall, An abstract framework for a priori estimates for contact problems in 3D with quadratic finite elements, *Computational Mechanics* **49**, 735–747, 2012.
- [292] B. I. Wohlmuth and R. H. Krause, Monotone multigrid methods on nonmatching grids for nonlinear multibody contact problems, *SIAM journal on scientific computing* **25**, 324–347, 2003.
- [293] P. Wriggers, *Computational contact mechanics*, Springer-Verlag Berlin Heidelberg, 2006.
- [294] P. Wriggers and C. Miehe, Contact constraints within coupled thermomechanical analysis - a finite element model, *Computer Methods in Applied Mechanics and Engineering* **113**, 301–319, 1994.
- [295] P. Wriggers and G. Zavarise, A formulation for frictionless contact problems using a weak form introduced by Nitsche, *Computational Mechanics* **41**, 407–420, 2008.
- [296] P. Wriggers, T. V. Van, and E. Stein, Finite element formulation of large deformation impact-contact problems with friction, *Computers & Structures* **37**, 319–331, 1990.
- [297] Z. Xiao, H. Gimbutas, A numerical algorithm for the construction of efficient quadratures in two and higher dimensions, *Computers & Mathematics with Applications* **59**, 663–676, 2010.

Bibliography

- [298] B. Yang and T. A. Laursen, A large deformation mortar formulation of self contact with finite sliding, *Computer Methods in Applied Mechanics and Engineering* **197**, 756–772, 2008.
- [299] B. Yang and T. A. Laursen, A contact searching algorithm including bounding volume trees applied to finite sliding mortar formulations, *Computational Mechanics* **41**, 189–205, 2008.
- [300] B. Yang and T. A. Laursen, A mortar-finite element approach to lubricated contact problems, *Computer Methods in Applied Mechanics and Engineering* **198**, 3656–3669, 2009.
- [301] B. Yang, T. A. Laursen, and X. Meng, Two dimensional mortar contact methods for large deformation frictional sliding, *International Journal for Numerical Methods in Engineering* **62**, 1183–1225, 2005.
- [302] M. Yeung, Q. Jiang, and N. Sun, A model of edge-to-edge contact for three-dimensional discontinuous deformation analysis, *Computers and Geotechnics* **34**, 175–186, 2007.
- [303] G. Zavarise and L. De Lorenzis, A modified node-to-segment algorithm passing the contact patch test, *International Journal for Numerical Methods in Engineering* **79**, 379–416, 2009.
- [304] G. Zavarise and P. Wriggers, A segment-to-segment contact strategy, *Mathematical and Computer Modelling* **28**, 497–515, 1998.
- [305] O. C. Zienkiewicz and R. L. Taylor, *The finite element method for solid and structural mechanics*, Elsevier Butterworth-Heinemann, Oxford, 2005.
- [306] O. Zienkiewicz and R. L. Taylor, The finite element patch test revisited a computer test for convergence, validation and error estimates, *Computer methods in applied mechanics and engineering* **149**, 223–254, 1997.
- [307] A. Zmitrowicz, Constitutive equations for anisotropic wear, *International journal of engineering science* **31**, 509–528, 1993.
- [308] A. Zmitrowicz, Wear patterns and laws of wear—a review, *Journal of theoretical and applied mechanics* **44**, 219–253, 2006.

Verzeichnis der betreuten Studienarbeiten

Im Rahmen dieser Dissertation entstanden am Lehrstuhl für Numerische Mechanik (LNM) in den Jahren von 2013 bis 2017 unter wesentlicher wissenschaftlicher, fachlicher und inhaltlicher Anleitung des Autors die im Folgenden aufgeführten studentischen Arbeiten. Der Autor dankt allen Sudierenden für Ihr Engagement bei der Unterstützung dieser wissenschaftlichen Arbeit.

Studierende(r)	Studienarbeit
Christopher Müller	<i>Cubic Hermite surface smoothing for 2D mortar contact</i> , Semesterarbeit, 2013
Johannes Kremheller	<i>Isogeometric mortar contact formulations in 2D</i> , Bachelorarbeit, 2014, eingeflossen in Abschnitt 5.4.3.3
Josef Winter	<i>Closest point projection for 2D mortar contact formulations</i> , Bachelorarbeit, 2014
Jasper Rieser	<i>Contact surface smoothing with additional interface discretizations</i> , Semesterarbeit, 2015
Lukas Scheucher	<i>Coupling methods for an overlapping domain decomposition using lagrange multipliers</i> , Bachelorarbeit, 2015
Boris Link	<i>Monolithic interface coupling for electrochemistry problems based on mortar approaches</i> , Bachelorarbeit, 2015
Raphael Gebhart	<i>Mixed finite element approach based on dual shape functions for nearly incompressible elasticity</i> , Bachelorarbeit, 2015
Christopher Jelich	<i>Thermo-mechanical mortar contact formulation for non-matching volume and interface meshes</i> , Masterarbeit, 2016, eingeflossen in Abschnitt 6.3.3 und 6.3.4.2
Theo Gilch	<i>A frame indifferent penalty approach for frictional mortar contact</i> , Semesterarbeit, 2016
Johannes Herb	<i>Construction of locally linear dual shape functions for mortar contact with second order interpolation</i> , Semesterarbeit, 2016
Sebastian Pröll	<i>Thermo-structure-contact-wear interaction with finite shape changes</i> , Semesterarbeit, 2016, eingeflossen in Abschnitt 5.6
Anton Shu	<i>The Hu-Washizu approach for nonlinear finite elements based on dual shape functions for nearly incompressible elasticity</i> , Semesterarbeit, 2016, eingeflossen in Abschnitt 6.4.2